MECHANISTIC INVESTIGATION OF CATALYTIC CHLORITE DECOMPOSITION BY CHLORITE DISMUTASE

A Dissertation
Submitted to the Graduate Faculty
of the
North Dakota State University
of Agriculture and Applied Science

By

Zachary Geeraerts

In Partial Fulfillment of the Requirements
for the Degree of
DOCTOR OF PHILOSOPHY

Major Program:
Chemistry

December 2020

Fargo, North Dakota

North Dakota State University
Graduate School

Title

MECHANISTIC INVESTIGATION OF CATALYTIC CHLORITE DECOMPOSITION BY CHLORITE DISMUTASE

By

Zachary Geeraerts

The Supervisory Committee certifies that this ***disquisition*** complies with North Dakota State University's regulations and meets the accepted standards for the degree of

DOCTOR OF PHILOSOPHY

SUPERVISORY COMMITTEE:

Kenton Rodgers
Chair

John Hershberger

Christopher Colbert

Birgit Pruess

Approved:

01/05/2021
Date

Gregory Cook
Department Chair

ABSTRACT

Water purification processes often involve chlorine-based disinfectants which consequently leads to formation of chloro oxyanions (ClO_x^-), potent water-soluble oxidizing agents. These chlorine species are kinetically stable in water which allows them to persist and buildup to hazardous concentrations. Chlorite (ClO_2^-), a common contaminant in water purification processes, has been labeled as a top ten major water contaminant by the United States Environmental Protection Agency. Therefore, there is pressing interest in developing methods for removal of ClO_x^- species from water. Chlorite dismutases are heme *b* dependent enzymes that catalyze the unimolecular decomposition of ClO_2^- into chloride (Cl^-) and molecular oxygen (O_2) with remarkable efficiency. Catalytic O−O bond formation is a rare process in Nature as the only other well characterized example occurs in photosystems II. Clds are great candidates for bioremediation purposes and an excellent model for investigating catalytic O−O bond formation as the catalyzed reaction is not hindered by the need to pump protons.

The goal of this work is to gain mechanistic insight into catalytic ClO_2^- decomposition by Cld and to investigate the structural features that tune the reaction pathway for productive O_2 evolution. Cld from *Klebsiella pneumoniae* and *Dechloromonas aromatica* are the representatives used in this work. Since heme is the cofactor in these enzymes, a variety of spectroscopic tools have been utilized to probe the electrostatic landscape of the active site. Vibrational (resonance Raman and infrared), optical absorbance, and electron paramagnetic resonance spectroscopies were used to characterize the heme environment. Various ligand complexes were prepared to probe non-reactionary states of the enzymes while reactionary states were directly observed through use of stopped-flow spectrophotometry and freeze-quenched

methods. Site directed mutagenesis studies of key amino acids were performed in combination with the above techniques to elucidate how changes in the electronics of the heme pocket alter catalytic activity. These studies have allowed for development of a proposed mechanism that describes the sequential steps and identification of the reactive intermediates leading to catalytic O_2 production that accounts for the pH dependency of the reaction that was previously not understood.

ACKNOWLEDGMENTS

I would like to thank both Dr. Kenton R. Rodgers and Dr. Gudrun S. Lukat-Rodgers for being amazing mentors during my time at NDSU. They provided me the opportunity to work in their laboratory since I was a wee undergraduate and welcomed me as a graduate student soon after. Their expertise, knowledge, and guidance have molded me into the scientist that I am today. I hold them in high regard, and I am eternally grateful for the time they have invested in me. They have made an everlasting impact on my life that I will indefinitely cherish.

I would also like to thank the Rodgers group, both past and present. My undergraduate experience in the Rodgers lab coincided with Kyle Conner, a fellow undergraduate and friend, who also successfully pursued a doctoral degree in chemistry. I had the opportunity to meet and spend a great deal of time with Seth Adrian and Sabine Volla, both of which helped me in my early years as a graduate student. During the later years of my graduate career, I had the chance to develop a life-long relationship with Olivia R. Stiller, who has been one of my greatest supporters as I proceeded to finish my degree. Her continued encouragement has been a motivating force for me and will be wholly reciprocated as our time together evolves.

Many thanks are also owed to my committee of Dr. Christopher Colbert, Dr. John Hershberger, and Dr. Birgit Pruess for committing their time and providing me with insight over the course of my graduate career. Numerous staff and faculty members in the Department of Chemistry and Biochemistry are also owed thanks for their assistance in teaching, communication, and organization throughout my time at NDSU. The facilities provided here aided my scientific growth and merited experiences that I otherwise may never have had. Funding of my dissertation project through NIH grants and the ND EPSCoR fellowship were also appreciated.

Last, but never least, I must thank my family for supporting me throughout my endeavors. My father nurtured my curiosity in science and medicine from a young age which inevitably propelled my immersion into studying the chemistry of life processes. My mother has been my greatest advocate during my adventure of post-secondary education and has instilled in me the confidence to pursue my interests. I have learned a lot from my siblings, whether intentional or not, that has shaped me into the person I am now.

TABLE OF CONTENTS

LIST OF TABLES

LIST OF FIGURES

LIST OF SCHEMES

LIST OF ABBREVIATIONS

Da.....*Dechloromonas aromatica*

Kp.....*Klebsiella pneumoniae*

Cld.....Chlorite Dismutase

ClO_2^-.....Chlorite

BrO_2^-.....Bromite

rR.....Resonance Raman

EPR.....Electron Paramagnetic Resonance

UV/Vis.....Ultraviolet/Visible Absorbance Spectroscopy

IR.....Infrared Spectroscopy

HS.....High Spin

LS.....Low Spin

5c.....Five coordinate

6c.....Six coordinate

LMCT.....Ligand to Metal Charge Transfer

WT.....Wild type

LIST OF APPENDIX TABLES

LIST OF APPENDIX FIGURES

1. INTRODUCTION TO CHLORITE DISMUTASES

1.1. Overview

1.1.1. General description of Clds.

Chlorite dismutases (Cld) are heme *b* dependent enzymes that occur in Gram-negative bacteria and catalyze the rapid decomposition of chlorite (ClO_2^-) to chloride (Cl^-) and molecular oxygen (O_2). This reaction is novel in Nature, as the only other well characterized example for catalytic O–O bond formation occurs at the tetramanganese center in photosystems II (PSII). Chlorite dismutase is a misnomer as the catalyzed reaction does not involve disproportionation where two ClO_2^- ions undergo reduction and oxidation. Rather, it is a unimolecular decomposition reaction in which both O atoms and the Cl atom in the products come from a single ClO_2^- ion. Phylogenetic analysis of homologous sequences to Clds shows there are three distinct clades (Figure 1.1): two functional Cld clades and one ChdC clade. Clade 1 Clds are found primarily in (per)chlorate reducing bacteria (PCRB) where Cld catalyzes the terminal step of the perchlorate reduction pathway (Scheme 1.1).

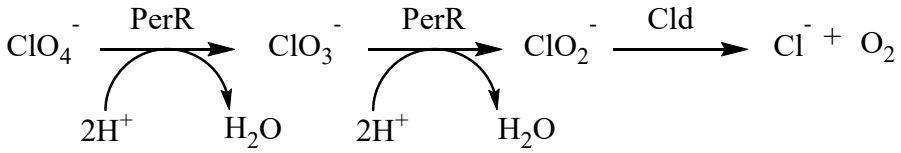

Scheme 1.1. Perchlorate respiration pathway.

The first two steps are catalyzed by perchlorate reductase (PerR) and involve the reduction of perchlorate (ClO_4^-) to chlorate (ClO_3^-) which is subsequently reduced to ClO_2^-.[1] The final step involves the catalytic decomposition of ClO_2^- by Cld generating O_2 and Cl^-. All clade 1 Clds are in the periplasmic space and the first characterized Clds were isolated from the periplasm of *Azospira oryzae* and *Ideonella dechlorotans*.[2] Subsequently, potential homologous

gene sequences have been identified in bacterial genomes and cloned into commercially available bacterial expression vectors for transformation, heterologous expression and purification from *Escherichia coli* cells.[3] Clade 2 Clds are found in bacteria that do not contain genes encoding for PerR and are hypothesized to be in the cytoplasm due to lack of a signal peptide.[4] These Clds do not have a well characterized *in vivo* function; however, the gene that encodes for them is located on plasmid DNA as opposed to genomic DNA like clade 1 Clds. Thus, bacteria that have clade 2 Clds likely inherited them through horizontal gene transfer. In the case of *Klebsiella pneumoniae*, a human pathogen, the gene that encodes for Cld is located on a plasmid that also contains an ampicillin resistance gene.[5] Therefore, there may be an attributable *in vivo* function related to virulence or resistance to host defense. If future work reveals such a function, the Cld and/or any pathway that regulates it when identified could be a potential drug target. The third clade contains Cld-like proteins formerly known as HemQ, which were recently renamed as coproheme decarboxylase (ChdC). These enzymes, while homologous to the functional Cld clades, do not catalyze the decomposition of ClO_2^-. Instead, they catalyze the terminal step in the coproporphyrin dependent pathway of heme *b* biosynthesis in Gram-positive bacteria.[6] These enzymes are outside the scope of this study.

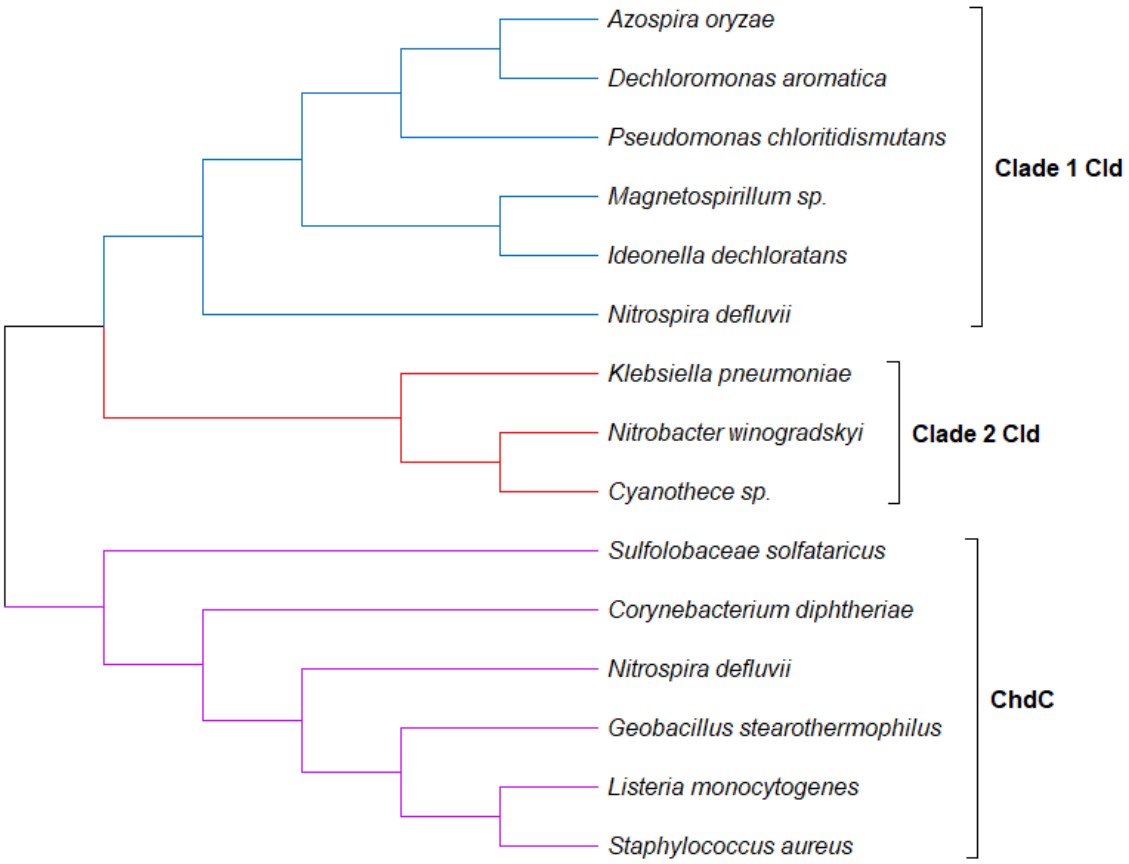

Figure 1.1. Phylogenetic tree based on the primary protein sequences of isolated Cld and ChdC (Cld-like) proteins. Tree was generated using MEGA-X software[7] using parameters outlined in Chapter 2.[8] Protein sequences were obtained from UniProt: E2DI02 (*Ao*Cld), Q47CX0| (*Da*Cld), B1AAM3 (*Pc*Cld), Q9F437, (*Id*Cld), A0A0M3KL46 (*Ma*Cld), B3U4H7 (*Nd*Cld), Q3SPU6 (*Nw*Cld), A0A1K0ELF2 (*Kp*Cld), B8HNS6 (*C*Cld), Q6NGV6 (*Cd*ChdC), Q8Y5F1 (*Lm*ChdC), D8PHP0 (*Nd*ChdC), Q97WP2 (*Ss*ChdC), A6QEP0 (*Sa*ChdC), and A0A0K2H9D8 (*Gs*ChdC).

1.1.2. Significance of studying Clds.

The oxyanions ClO_4^-, ClO_3^-, ClO_2^-, and ClO^- are major water contaminants that are kinetically stable with respect to water oxidation. Their high solubility in water allows for their accumulation to potentially hazardous concentrations, causing oxidative stress in some organisms. Chlorine dioxide ($\bullet ClO_2$), which disproportionates to ClO_2^- and ClO_3^-, especially under alkaline conditions (Figure 1.2), is a common disinfectant in water treatment.[9-10] The disproportionation of $\bullet ClO_2$ is catalyzed by trace transition metal ions such as Fe(II) and Cu(II). Some organic compounds can also reduce $\bullet ClO_2$ to ClO_2^- and Cl^-.[11] The photo reactivity of $\bullet ClO_2$ in sunlight leads to the formation of ClO_3^-, ClO_2^-, and Cl^-.[12-13] NaOCl or $Ca(OCl)_2$, which dissolve in water to yield aqueous OCl^-, are commonly used in pools as disinfectants. The hypochlorite anioni is unstable with respect to disproportination,[14] the products of which include ClO_2^-, ClO_3^-, and ultimately ClO_4^-.[15] The ubiquitous contamination of water by chloro oxyanions has led the United States Environmental Protection Agency to rate ClO_2^- specifically as a top ten water contaminant and has a maximum contaminant level of 1.0 mg / L.[16] Both ClO_3^- and ClO_2^- cause hemolytic anemia and liver damage[11] while ClO_3^- and ClO_4^- impact hormone regulation of the thyroid.[17-18] Several methods are used to remove ClO_2^- from water which include activated charcoal, sulfur reducing agents, ferrous iron, and anion exchange.[9] However, there is no low-cost method available to remove ClO_3^- ions in drinking water which typically originates from aged ClO^- solutions where ClO_2^- is briefly formed during the decomposition process.[9] Consequently, there is interest in developing bioremediation methods to strategically remove ClO_3^- from water. Currently, Clds are the only enzymes known to catalytically decompose ClO_2^- into Cl^- and O_2. As ClO_2^- is typically a precursor to ClO_3^-, Clds are a strong candidate for prevention of ClO_3^- buildup in drinking water. These enzymes do not

require channeling of protons nor do they require a reducing agent making them ideal candidates for bioremediation.

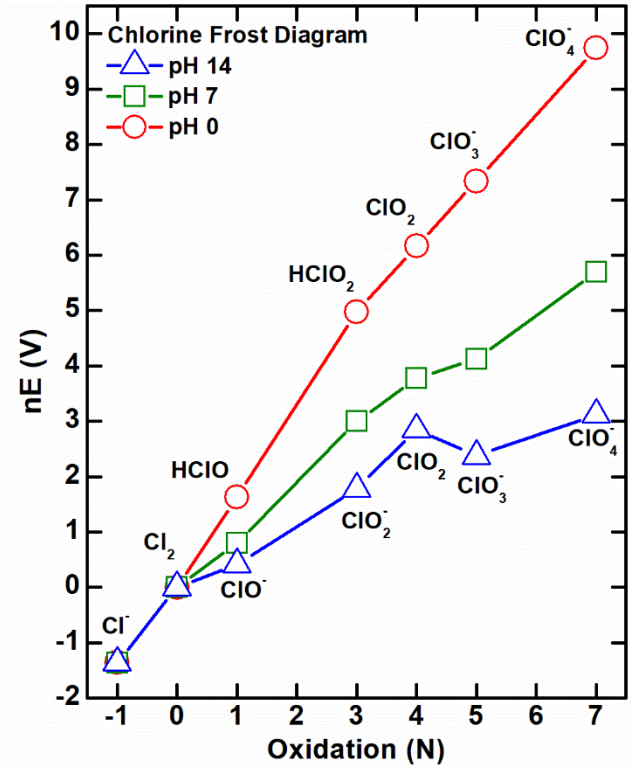

Figure 1.2. Frost diagram of chlorine in its various oxidation states at pH 0, 7, and 14. Species that lay above two other species at the same pH are thermodynamically driven to disproportionate (i.e. ClO_2). Species that lay below two other species at the same pH are formed by comproportionation of the oxidation states above and below them (e.g. ClO_3^-). Reduction potentials used to generate this plot were obtained from literature.[19]

1.2. Summary of Previous Work

1.2.1. Structure of Clds.

Clds of different clades vary by sequence length and consequently molecular weight. Clade 1 Clds are longer than clade 2 Clds which is highlighted by their differing molecular weights.[20] On average, clade 2 Clds are 21.0 kDa per monomer while clade 1 Clds are 30.5 kDa per monomer based on Clds isolated to date. This difference in molecular weight manifests itself in two ways. All isolated clade 1 Clds, except for Cld from *Magnetospirillum sp.* (*Ma*Cld), have a secretion signal peptide sequence on the N-terminus.[4] This signal peptide directs Cld to the periplasmic space where PerR is also found in PCRBs.[1, 21-22] However, since not all clade 1 Clds are found in PCRBs, it remains uncertain what purpose Cld serves in the periplasmic space for those other micro-organisms. All clade 1 Clds have a N-terminal domain that does not bind heme but contains the contacts that facilitates their quaternary structure. Since all clade 2 Clds do not contain this N-terminus domain, they are often referred to as "truncated" Clds. Nonetheless, both clade 1 and clade 2 Clds have highly homologous C-terminal heme -binding domains.[23]

Clade 1 and clade 2 Clds have both alpha helical (α) and beta-strand (β) secondary structures and belong to the $\alpha+\beta$ class since their beta-strands are all antiparallel.[24] The N-terminal and C-terminal domains are best described as ferredoxin-like folds ($\beta\alpha\beta\beta\alpha\beta$) in clade 1 Clds.[25-28] Contrastingly, the N-terminal fold in clade 2 Clds consists of a strict $\beta\beta\beta\beta$-β configuration. However, their C-terminal heme binding domain is structurally similar to clade 1 and is also described as a ferredoxin-like fold (Figure 1.3A).[4, 8, 29] Not only is the C-terminal domain highly homologous between clade 1 and clade 2 Clds, the orientation of the heme cofactor in the catalytic active site is nearly identical.

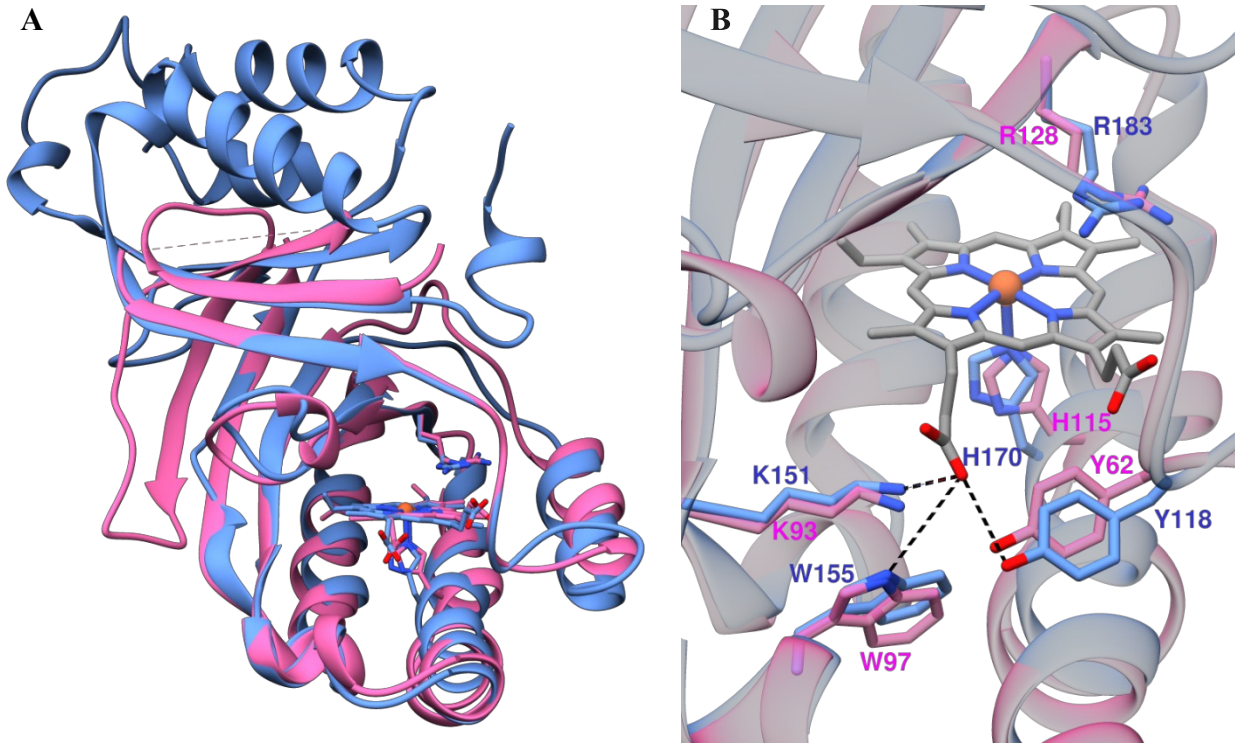

Figure 1.3. Clade 1 and clade 2 Clds have high structural homology. A) Monomeric structure overlay (RMSD = 0.965 Å) between *Da*Cld (PDB 3q08 - blue) and CCld (PDB 5mau - pink) via the MatchMaker tool in UCSF Chimera software.[30] B) Heme active site overlay between *Da*Cld (blue) and *Kp*Cld homology model (pink). The *Kp*Cld homology model was generated from CCld (PDB 5mau) using SWISS-MODEL.[31] The heme *b* displayed originates from the *Da*Cld crystal structure with select invariant residues displayed for both clade representatives.

The C-terminal domain contains numerous homologous and invariant residues between both clades (Figure 1.4). Residues with the highest similarity are located around the bound heme (Figure 1.3B). Both clades coordinate the heme iron through an invariant histidine residue on the proximal side. The distal side (uncoordinated) contains four invariant residues that cage the heme iron: leucine, phenylalanine, serine, and arginine. The importance of the distal arginine to catalytic ClO_2^- decomposition will be discussed in Section 1.2.2. Several residues within the heme periphery are conserved as well, specifically a lysine, tryptophan, and tyrosine which are within hydrogen bonding distance (< 3 Å) of propionate 6. The relevance of these residues during enzymatic turnover will be discussed in Chapter 6.

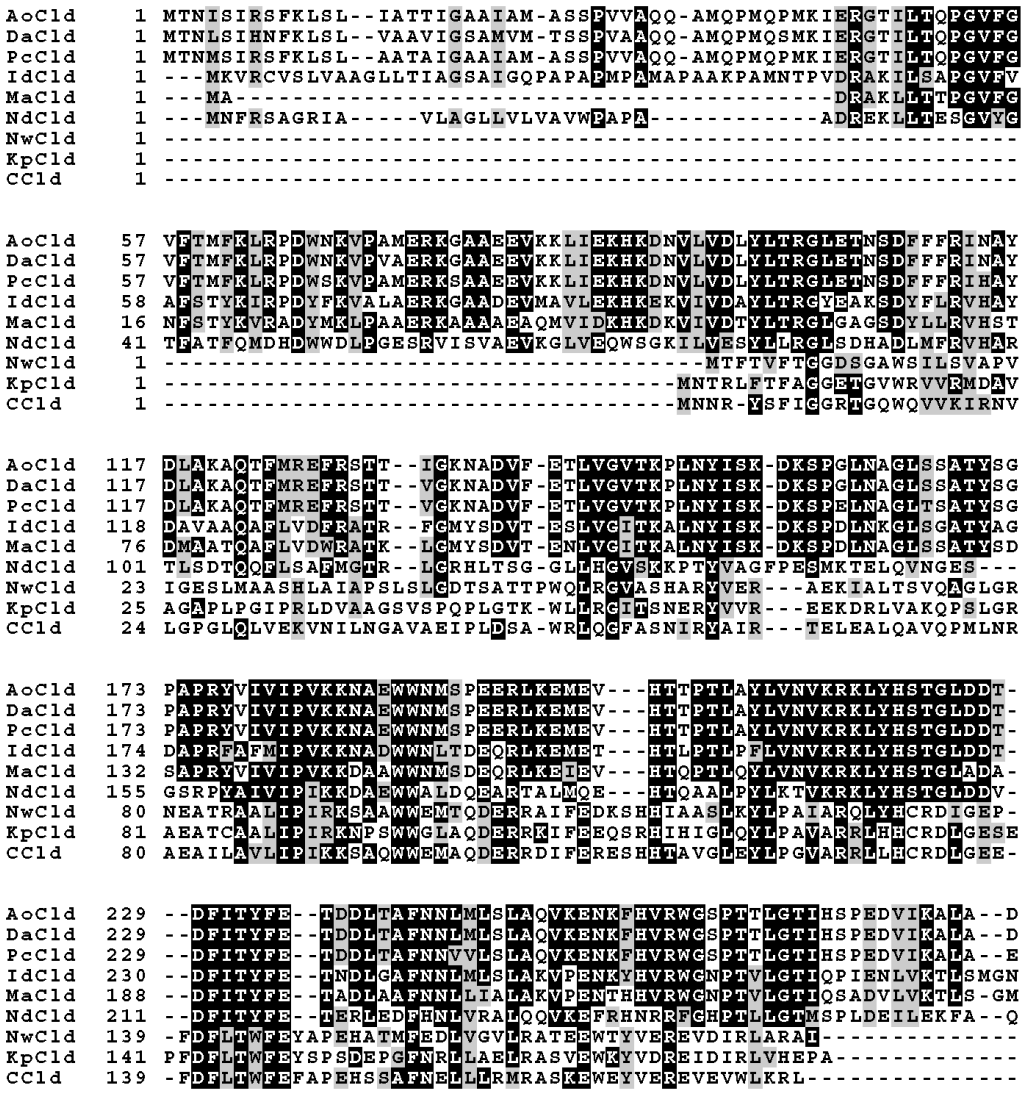

Figure 1.4. Multiple protein sequence alignment of all characterized Clds using the Constraint-based Multiple Alignment Tool (COBALT).[32] Totally conserved residues are highlighted in black while similar residues are highlighted in gray. The alignment image was generated by BoxShade version 3.21. Protein sequences were obtained from UniProt: E2DI02 (*Ao*Cld), Q47CX0| (*Da*Cld), B1AAM3 (*Pc*Cld), Q9F437, (*Id*Cld), A0A0M3KL46 (*Ma*Cld), B3U4H7 (*Nd*Cld), Q3SPU6 (*Nw*Cld), A0A1K0ELF2 (*Kp*Cld) and B8HNS6 (*C*Cld).

Table 1.1 summarizes the structural properties of all currently characterized Clds. Clade 1 Clds form a higher order homopentameric oligomer. Several techniques were used to determine the oligomeric state for *Ao*Cld which resulted in either a homotetramer or homohexamer. It was concluded that the enzyme adopted a homopentameric state in solution when accounting for its hydrodynamic radius in the gel filtration determination which was consistent with the mass spectrometry determination.[25] Contrastingly, all clade 2 Clds characterized so far form homodimeric oligomers.[23] This striking difference in oligomeric state is manifested by the N-terminal domain which has several inter subunit contacts in clade 1 Clds. Interestingly, X-ray crystallography showed a calcium cation (Ca^{2+}) can serve as an inter subunit contact in *Da*Cld. However, it is likely that the presence of Ca^{2+} is due to the crystallization conditions and may not be physiologically relevant.[26] Contacts from the N-terminal domain do not exist in clade 2 Clds due to their truncated N-terminus. The isoelectric points (pI), the pH in which the protein is charge neutral, are also distinctly different between clades. Clade 1 enzymes, with the exception of *Nd*Cld, all have alkaline pIs ranging from 8.7 to 9.1. These high values are attributed to their numerous surface lysine residues, whose side chain pK_a is ~10.6.[33]

Table 1.1. Protein properties of characterized Clds.

Enzyme	MW (kDa)[a]	pI[b]	Oligomer	Method	PDBID	Ref
			Clade 1			
*Ao*Cld	28.2 (31.6)	9.1	Tetramer	Analytical Gel Filtration		21, 25
			Pentamer	Electrospray Ionization Mass Spectrometry		25
			Hexamer	X-ray Crystallography	2vxh	25
*Id*Cld	27.7 (31.4)	9.0	Tetramer	Analytical Gel Filtration		22
*Da*Cld	28.1 (31.6)	9.1	Tetramer	Analytical Gel Filtration		34
			Pentamer	X-ray Crystallography	3q08, 3q09	26
*Pc*Cld	28.2 (31.6)	8.7	Tetramer	Analytical Gel Filtration		35
*Nd*Cld	27.1 (29.8)	6.7	Pentamer	Analytical Gel Filtration		27
			Pentamer	X-ray Crystallography	3nn1, 3nn2, 3nn3, 3nn4, 4m05, 4m06, 4m07, 4m08	27, 36
*Ma*Cld	26.7	9.1	Pentamer	Analytical Gel Filtration		28
			Pentamer	X-ray Crystallography	5a12, 5a13	28, 37
			Clade 2			
*Nw*Cld	20.4	5.9	Dimer	Analytical Gel Filtration		29
			Dimer	X-ray Crystallography	3qpi	29
*Kp*Cld	21.3	8.3	Dimer	Analytical Gel Filtration		38
CCld	21.2	6.5	Dimer	Analytical Gel Filtration		4
			Dimer	X-ray Crystallography	5mau, 5nku, 5nkv, 5k8z, 5k90, 5k91	39

[a]Molecular weights determined by primary sequences obtained from UniProt. Molecular weights in parentheses include a signal peptide sequence, as predicted by SignalP5[40], for the respective clade 1 proteins.
[b]The isoelectric points (pI) were estimated based on the primary sequences without the predicted signal peptide sequence via Serial Cloner version 2.6.

1.2.2. Cld chlorite decomposition kinetics.

All reported Cld catalytic activities have been determined from the rates of O_2 product formation. These rates are monitored either polarographically, by tracking cathode current in a Clark cell during electrochemical reduction of O_2 to H_2O,[41] or by measuring luminescence

quenching rate of an excited state luminophore by O_2.[42] Both methods require a calibration curve to correlate cell current or luminescence quenching rate with known solution concentrations of O_2. This is typically done by altering the partial pressure of O_2 above an aqueous solution and using barometric pressure and Henry's Law to quantify the concentration of dissolved O_2.[43] The latter method has a faster response time (< 1 second) than the former, which varies by the thickness of the gas-permeable membrane used to separate the Pt cathode of the Clark cell from the bulk solution. Additionally, O_2 is consumed via the polarographic method but not in the luminescence quenching method. Detection of O_2 is the preferred method for two reasons. First, solubility of O_2 in aqueous media is 1.1×10^{-3} M at $P(O_2)$ = 1 atm and 25 °C.[43] While this puts an upper limit on detection of dissolved O_2 production, it also precludes detection via optical absorbance spectroscopy due to the generation of bubbles that scatter light which artificially increases measured absorbance. Second, the maximal extinction coefficient for the substrate, ClO_2^-, is 155 M^{-1} cm^{-1} at 260 nm.[44] Coupled with the O_2 production constraint, a maximum signal change of 0.171 will only be observed assuming 1:1 stoichiometry. This does not allow for a sufficiently wide range of ClO_2^- concentrations necessary for proper kinetic analysis.

All Clds characterized to date have their ClO_2^- decomposing activity modeled by Michaelis-Menten kinetics.[45] The respective parameters are summarized in Table 1.2. Both Cld clades have acidic pH optimums ranging between 5.0 and 6.5. High resolution pH activity profiles (ΔpH = 0.5) for *Da*Cld, *Kp*Cld, and *Ma*Cld revealed a pK_a at 6.6[17], 7.0[18], and 6.7[28], respectively. Histidine is the only amino acid with a pK_a within range (6.0) of the kinetic pK_as. The only histidine residue within proximity to the catalytic center is coordinated to the heme *b* iron. However, site directed mutagenesis studies revealed that upon mutating the distal arginine residue to a glutamine residue, ClO_2^- decomposition activity decreases and is no longer

dependent on pH.[46] Therefore, the pH dependence of O_2-evolving activity was initially attributed to the distal arginine side chain. Considering the high pK_a of the guanidinium group (13.8)[47], it was suggested that the pH dependency in activity was due to the distal arginine residue occupying two conformers: an open, less active form and a closed, more active form. This was supported by resonance Raman (rR) spectra of the Cld carbonyl complexes previously published.[46] Wild-type *Da*Cld had two unique sets of ν(C-O) and ν(Fe-CO) vibrations which were assigned based on isotope labeling with ^{13}CO. Both ν(C-O) and ν(Fe-CO) frequencies are known to be sensitive to hydrogen-bonding. An increase in hydrogen-bonding leads to a lower ν(C-O) frequency and a higher ν(Fe-CO) frequency because of its influence on the distribution of valence electrons in the FeCO π-backbonding molecular orbital (MO). Therefore, it was concluded that the higher ν(C-O) / lower ν(Fe-CO) frequency set corresponded to the open conformer while the lower ν(C-O) / higher ν(Fe-CO) frequency set corresponded to the closed conformer. Considering the various R183 mutant carbonyl complexes and their respective positions on the π-backbonding correlation line, it was hypothesized that positive charge in the pocket was more important than hydrogen-bonding alone for catalytic ClO_2^- decomposing activity.[46]

Table 1.2. Michaelis-Menten kinetic parameters for characterized Clds.

Enzyme	pH optimum	Temp optimum (°C)	k_{cat} (s^{-1})	K_M (M)	k_{cat} / K_M ($M^{-1}s^{-1}$)	Ref
			Clade 1			
*Ao*Cld	6.0	30	1.2×10^{3}	1.7×10^{-4}	6.9×10^{6}	[21]
*Id*Cld	7.0*	25[a]	1.8×10^{3}	2.6×10^{-4}	6.9×10^{6}	[22]
*Da*Cld	5.2	4[a]	2.0×10^{3}	6.2×10^{-4}	3.2×10^{7}	[48]
*Pc*Cld	6.0	25	2.3×10^{2}	8.0×10^{-5}	2.7×10^{6}	[35]
*Nd*Cld	6.0	25	3.5×10^{1}	5.8×10^{-5}	6.0×10^{5}	[27]
*Ma*Cld	6.5	5	1.6×10^{3}	5.9×10^{-4}	2.7×10^{6}	[28]
			Clade 2			
*Nw*Cld	5.5	20	1.9×10^{2}	9.0×10^{-5}	2.1×10^{6}	[29]
*Kp*Cld	5.0	20[a]	1.9×10^{2}	7.6×10^{-5}	2.5×10^{6}	[8]
CCld	5.0	30	1.1×10^{2}	1.6×10^{-4}	7.1×10^{6}	[4]

[a]The optimum pH and/or temperature was not reported. All kinetic parameters correspond with the tabulated pH and temperature.

1.2.3. Heme properties of Clds.

All Clds characterized to date have high spin (HS) resting states and have variable coordination numbers (5-coordinate or 6-coordinate) in their resting state at low pH (Table 1.3). These spin states and coordination numbers are inferred from their respective optical absorbance spectra and directly determined by either resonance Raman or electron paramagnetic resonance spectroscopies. Under alkaline conditions, all Clds coordinate a hydroxide (OH^-) which has been shown to be stabilized by the totally conserved cationic distal arginine residue in *Da*Cld.[46] The coordinated OH^- yields a spin-state equilibrium between 6-coordinate high spin (6cHS) and 6-coordinate low spin (6cLS) states. The reported pK_as for OH^- coordination range between 8.1 and 8.7. Clade 2 Clds fall on the lower end while clade 1 Clds span the full range. X-ray crystal structures of *Nw*Cld and CCld demonstrate that water can occupy the pocket and coordinate to the heme iron. This is consistent with a small amount of 6cHS heme observed for *Kp*Cld at low pH, which increases proportionally with Cl^- concentration.[38] No water has been observed in the

distal heme pocket of X-ray crystal structures for any clade 1 Cld except in that of *Nd*Cld (1.9 Å resolution, PDBID 3NN1 and 3NN2). The lower pK_a for OH^- of clade 2 Clds is hypothesized to correlate with their more solvent exposed distal heme pocket. Numerous anionic ligands such as fluoride form stable complexes in Clds unlike other heme proteins that lack a positive charge in the distal pocket. This has allowed for extensive probing of the heme active site by reporter ligands whose vibrational frequencies are impacted by both nonbonding (i.e. H-bonding) and bonding (*trans* effect) interactions.[38]

The oxidation state of the heme iron for resting Clds is Fe(III), commonly known as the ferric state. One electron reduction of the heme iron to Fe(II), or the ferrous state, has been characterized as well to gain insight into their redox properties. Similar to the ferric state, all ferrous Clds are 5cHS. However, unlike ferric Clds, the ferrous forms do not undergo a change in their coordination number or spin state as a function of pH. The Fe(III) | Fe(II) redox couple of Clds vary between clades. Clade 2 Clds generally have lower reduction potentials than clade 1 by approximately 100 mV and become more negative as pH increases as shown by CCld.[39] As far as it is reasonable to compare, trends in the Fe(III) | Fe(II) redox couple can be used to rationalize the thermodynamic accessibility of the proposed intermediate (see Section 1.2.4.) Compound I (Cpd I), an Fe(IV)=O (ferryl) π−cation radical, from Fe(III). A comparison was made between *Da*Cld and Horseradish peroxidase (HRP), whose Cpd I | Fe(III) and Fe(III) | Fe(II) redox potentials have been measured,[49] supporting that the ClO_2^- | HOCl redox couple at pH 7.0 is sufficient to oxidize *Da*Cld to Cpd I. By extension, all clade 2 enzymes with their lower Fe(III) | F(II) reduction potentials are predicted to have a larger thermodynamic driving force to form Cpd I upon reaction with ClO_2^-. Proximal iron−histidine bond strengths can be inferred from the ν(Fe^{2+}−His) vibrational frequencies based on Badger's Rule since the

ν(Fe^{3+}−His) vibrations are not readily detectable in the rR spectrum.[50] In general, higher frequency vibrations correlate with shorter bond distances and, therefore, higher bond strengths. Based on the ν(Fe^{2+}−His) frequencies reported for Clds, clade 2 enzymes have a stronger iron−histidine bond than clade 1 enzymes. Consequently, ligands trans to the iron−histidine bond, such as a ferryl, are likely to become weaker with increasing iron−histidine bond strength.[51] Since the Cpd I | Fe(III) redox couple involves change of coordination of an oxygen atom, it is reasonable to expect that the corresponding Fe^{IV}=O bond of the ferryl group will be weaker for clade 2 enzymes than for clade 1. How these effects translate to catalytic ClO_2^- decomposition activity will be discussed in Chapter 6.

Table 1.3. Heme properties of characterized Clds.

Enzyme	Ferric Resting CN / SS	pK_a (OH^-)	Fe^{3+} | Fe^{2+} (mV vs. SHE)	ν(Fe^{2+}−His) (cm^{-1})	Ref
			Clade 1		
*Ao*Cld	5cHS	8.2	−23	n.r.	[52]
*Id*Cld	5cHS	8.5	−21	n.r.	[22]
*Da*Cld	5cHS	8.7	−23	224 / 226[a]	[46, 48]
*Pc*Cld	5cHS	n.r.	n.r.	n.r.	[35]
*Nd*Cld	5c/6cHS	n.r.	−113	n.r.	[53]
MaCld	5cHS	n.r.	n.r.	n.r.	[28]
			Clade 2		
*Nw*Cld	6cHS	n.r.	−119	n.r.	[53]
*Kp*Cld	5c/6cHS	8.3	n.r.	229[b]	[8]
CCld	5c/6cHS	8.1	−82 / −126 / −173[d]	231[c]	[4, 39]

n.r. = not reported.
[a]Frequencies reported at pH 6.0 and 8.0, respectively.
[b]Frequency reported at pH 7.
[c]Frequency reported at pH 5.8.
[d]Reduction potentials reported at pH 5.0, 7.0, and 10, respectively.

1.2.4. Proposed mechanism for catalytic chlorite decomposition by Clds.

Scheme 1.2 shows the proposed mechanistic pathways for catalytic ClO_2^- generation by Cld. Three primary mechanisms have been proposed: one based on homolytic O−Cl bond cleavage, another on heterolytic cleavage, and a concerted isomerization reaction. All pathways share an initial step, formation of the O-coordinated chlorito complex of the hemin cofactor (enzyme substrate complex). This complex has never been directly observed. However, the geometry of the chlorite complex is hypothesized to be similar to the nitrito complex observed in the X-ray crystal structure for *Da*Cld−ONO^-.[26] The three mechanisms diverge at the O−Cl bond cleavage step. The heterolytic pathway involves two electron oxidation of hemin to Compound I (Cpd I), a Fe(IV)=O π−cation radical porphyrinate, and a two electron reduction of ClO_2^- to OCl^- upon cleaving of a O−Cl bond. In contrast, the homolytic pathway involves one electron oxidation of hemin to Compound II (Cpd II), a Fe(IV)=O porphyrinate, and a one electron reduction of ClO_2^- to OCl• upon cleavage of an O−Cl bond. Cpd I has been directly observed for *Da*Cld when reacted with peracetic acid (PAA), a two-electron oxidant, which readily converts to Cpd II at acidic pH. In the reaction with PAA under alkaline conditions, Cpd II is the first intermediate observed. This work has revealed that whenever Cpd II is observed, a protein-based radical is also detected.[54] Although these data support the accessibility of the heterolytic bond cleavage pathway and establish a correlation between the accumulation of its two-electron intermediate, Cpd I and O_2-evolving activity, they rule out neither a homolytic bond cleavage pathway nor a concerted pathway. Both pathways involve recombination of their respective geminate pairs to form the hypothetical hemin−peroxyhypochlorite complex. This step involves nucleophilic attack by the oxygen atom of the OCl fragment to the ferryl oxygen, reducing the ferryl to Fe(III) upon formation of the putative peroxo ($Fe^{III}O$−OCl) bond. The newly formed

complex spontaneously decomposes by reduction of the Cl atom to Cl^- and oxidation of the peroxide to O_2 regenerating the uncoordinated Fe(III) catalyst. The third pathway invokes concerted isomerization from the chlorite complex to the peroxyhypochlorite complex, bypassing the need to distinguish between homolytic or heterolytic bond cleavage pathways. However, like the chlorite complex, the peroxyhypochlorite complex has never been observed. Therefore, although the above described sequence accounts for electrons transferred and for bonds made and broken, precisely how the decomposition occurs once the geminate pair recombines remains unclear. The unimolecular nature of this reaction was deduced from the poor peroxidase activity exhibited by *Da*Cld due to its inability to oxidize organic substrates when ClO_2^- was used as the oxidant.[55] Furthermore, reactions involving H_2O_2 and *Da*Cld do not yield Cpd I, likely due to the lack of a histidine or other basic side chain in the distal pocket, which acts as the catalytic base in heme peroxidases.[54] The source of O_2 was determined to be directly from ClO_2^- and not from H_2O based on ^{18}O isotope studies.[35, 55] This thesis aims to determine which mechanistic pathway yields O_2 through the catalytic decomposition of ClO_2^- by Cld. Structural differences and similarities from each clade that impacts O_2 evolving activity are also investigated through *Da*Cld and *Kp*Cld, representatives of their respective clade.

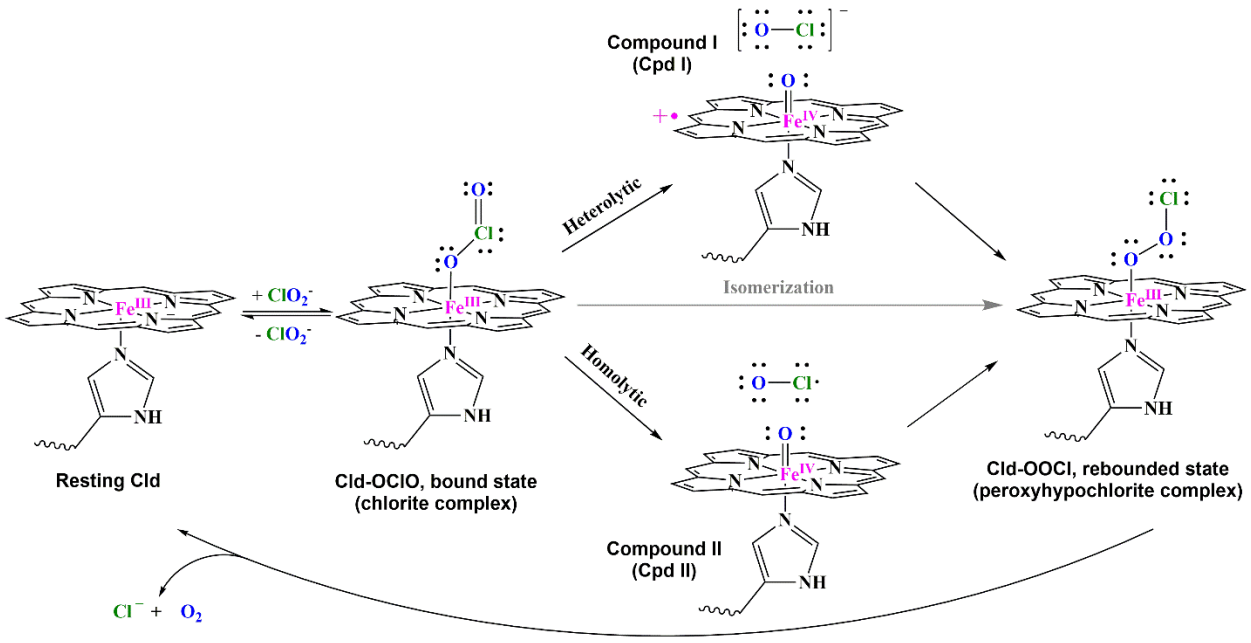

Scheme 1.2. Proposed mechanistic pathways for catalytic ClO_2^- decomposition into O_2 and Cl^-.

1.3. Physical Methods

1.3.1. Light-matter interactions.

When a photon collides with a molecule, there are several interactions that can occur, two of which are absorption and scattering. Absorption occurs when the incident photon energy is in resonance with the energy difference between stationary states of a molecule. The energy absorbed by the molecule leads to an electronic and/or vibrational transition. In both cases, the intensity of the transition is proportional to the molecular transition dipole moment. These transitions lead to an observable (stationary) state that gradually decays to its ground state through other processes. One process is non-radiative relaxation wherein energy is dispersed thermally via interaction with other molecules. Another process is radiative relaxation where a photon is emitted from the excited molecule, typically with lower energy than the incident photon.[56]

Elastic scattering occurs when the electric field of the incident photon induces polarization of electron density in a molecule which forces the electrons to oscillate at the same

frequency as the incident photon. Energy is subsequently radiated in all directions from the oscillating dipole known as scattering. Most scattered photons are scattered elastically, which means the scattered photon has the same energy as the incident photon, a process known as Rayleigh scattering. A much smaller fraction of scattered photons are scattered inelastically, which means the energy of the scattered photon is not equal to that of the incident photon. This process is known as Raman scattering, which reradiates photons whose energies differ from the incident energy by one rotational, vibrational, or rovibrational quantum. In this work, vibrational Raman scattering has been used extensively to probe structural properties of heme species under equilibrium and non-equilibrium conditions. The latter are typically reaction intermediates that are examined in real time or in reaction mixtures that have been quenched by rapid freezing. Hereinafter, the term Raman scattering will refer to vibrational Raman scattering.[57]

When the scattered photon is in lower energy than the incident photon, a quantum of energy has been transferred to a molecule that is typically in its ground vibrational state, which is described as a Stokes shift. Inversely, when the scattered photon is higher in energy than the incident photon, energy has been transferred from a vibrationally excited molecule to the scattered photon, which is described as an anti-Stokes shift. In both cases, molecular vibrational transitions occur in concert with these transfers of energy quanta, and the intensity of the Raman scattered light scales with the polarizability of the molecule and the frequency of the incident photons. However, the relative intensities between Stokes shift and anti-Stokes shift transitions is dependent on the Boltzmann distribution of the ground and first vibrational excited states. Scattering is not a dominant process of photon-molecular interactions as Rayleigh scattering occurs for approximately one out of a thousand photons and Raman scattering only occurs for one in a million.[57] Therefore, a very intense light source is required to observe Raman scattering.

Light Amplification by Stimulated Emission of Radiation (LASER) is commonly used for Raman experiments as its photon coherence produces very high electric field amplitudes, even for modest powers, and the emitted light is highly polarized. Since the polarization properties of Raman scattered photons carry with them structural information about the scattering molecule, the typically highly polarized and coherent light emission (same phase and frequency) from LASERs is useful for probing vibrational and, therefore, molecular symmetry.[58]

A molecule has symmetry if it can be reoriented to generate an indistinguishable orientation. This is accomplished by use of symmetry operations which are unique permutations of atoms in a molecule. Each symmetry operation has a corresponding symmetry element which can be an axis, plane, line, or point, about which the symmetry operation occurs and which contains the center point of the molecule.[59] Depending on its symmetry, a molecule's structure is characterized by a group of such point-based symmetry operations. Point groups form the symmetry basis for the structurally based interpretation of molecular spectra. Molecules are categorized in point groups by an algorithm that systematically eliminates possible combinations of symmetry operations. The number of vibrational modes that a molecule has is expressed by $3N-6$ (or $3N-5$ for linear molecules) where N equals the number of atoms. Molecular symmetry dictates which vibrational modes are Raman active and which modes are observable by Infrared (IR) absorbance spectroscopy.[60]

Infrared absorbance spectroscopy follows the absorption selection rules that dictate whether vibrationally excited states are accessible via absorption of IR photons. Intensities are proportional to the change induced in a molecule's dipole moment by vibrational motion along a normal vibrational mode. Infrared and Raman spectroscopies are often said to be complementary because of their different selection rules. They can give rise to common and/or unique

vibrational transitions or frequencies, depending on the molecular symmetry and whether its group of symmetry elements includes a center of inversion. If the molecule has an inversion center, then the rule of mutual exclusivity applies, and unique vibrational transitions only appear in either the IR or Raman spectrum.[60]

The symmetry of a vibrational mode can be inferred by Raman spectroscopy. When a plane-polarized light source is used, the orientation of the plane of polarization for the Raman scattered light with respect to the exciting polarization depends on the symmetry of the corresponding vibrational mode. Consequently, some photons are scattered perpendicular to the excitation polarization while others are scattered parallel to it. The parallel and perpendicular intensities can be determined by recording spectra with a polarization filter in the collection telescope oriented in parallel and perpendicular orientations, respectively. The ratio of the integrated peak intensities from the parallel and perpendicular spectra is known as the depolarization ratio (Equation 1.1).

$$\rho = \frac{I_{\perp}}{I_{\parallel}} \qquad \text{(Eq. 1.1)}$$

Totally symmetric vibrations have a depolarization ratio less than 0.75. These bands are also referred to as polarized bands. Non-totally symmetry vibrations have a depolarization ratio equal to 0.75 which are also referred to as depolarized bands.[58, 60] These spectroscopic techniques can be readily applied to porphyrins such as heme *b*, the cofactor in Cld.

1.3.2. Resonance Raman and optical absorbance spectra of porphyrins.

All porphyrins have the basic tetrapyrrole core structure shown in Figure 1.5. They are conjugated tetrapyrrole macrocycles that follow Huckle's rule of aromaticity: cyclic, planar, conjugated, and have 4n+2 π electrons. Porphyrins have 22, π electrons where n = 5, represented by the 11 double bonds. Porphyrins are characterized by π→π* transitions in the visible and near

UV regions of the spectrum because of their extensive π conjugation. A typical absorption spectrum of a metalloporphyrin includes three bands: the Q_{00} and Q_{01} bands, and the Soret or B band.[61-62] These bands correspond to π→π* electronic transitions and were described by Gouterman in his Four-Orbital Model (Scheme 1.3).[63] The frontier molecular orbitals for a metallated porphyrin include the two highest occupied molecular orbitals (HOMOs), designated as a_{1u} and a_{2u}, in accord with their symmetries, and the doubly degenerate lowest unoccupied molecular orbitals (LUMOs) designated as e_g. Four possible excited state electronic configurations are accessible for these four frontier MOs. Configurations having half-filled a_{1u} and a_{2u} MOs have E_u symmetry. Because these nearly-degenerate states have the same symmetry, their configurations interact. Configuration interaction generates two new excited states, one at the difference between the energies of the E_u states and one at their sum. The B- or Soret band corresponds to the higher-energy, fully allowed $S_0 \rightarrow S_2$ transition, which occurs at wavelengths in the near UV with $\varepsilon > 10^5$ M^{-1} cm^{-1}. The Q_{00} band corresponds to the lowest-energy, partially allowed π→π* transition and occurs in the visible region with $\varepsilon \sim 10^4$ M^{-1} cm^{-1}. The remaining Q_{01} band is a vibrational side band to the Q_{00} electronic transition. It falls between the B- and Q_{00} bands and has approximately 10% of the B-band molar absorptivity. Since metalloporphryins have four-fold symmetry, the *x*- and *y*-polarized π→π* transitions have the same energy (i.e. $B_x = B_y$ and $Q_x = Q_y$). However, since protonated free-base porphyrins have reduced symmetry, D_{2h} (two-fold symmetry). Consequently, four Q-bands are observed in the visible spectrum (Q_{x00}, Q_{y00}, Q_{x01}, and Q_{y01}). Hypothetically, B_x and B_y occur at different energies but are usually not sufficiently resolved to be observed in a room temperature optical absorption spectrum.[62-63] Depending on the axial ligand(s), a ligand to metal charge transfer (LMCT) may be observed in the visible spectra of metalloporphyrins.

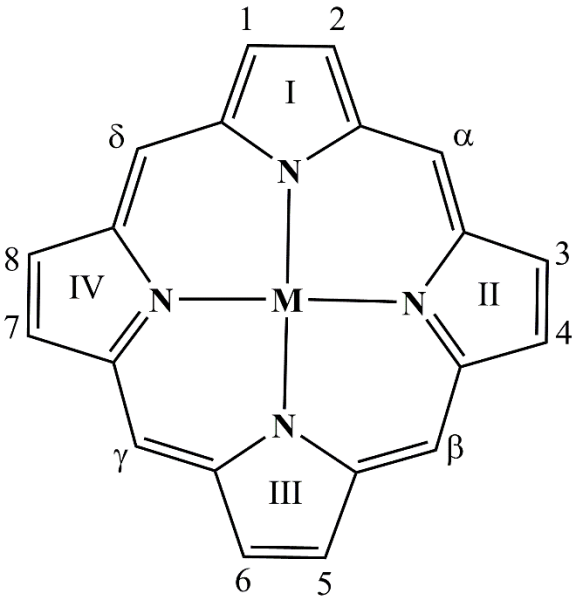

Figure 1.5. Labeled structure of a D_{4h} metallated porphyrin. Heme *b* has vinyl groups at positions 2 and 4, methyl groups at positions 1, 3, 5, and 8, and propionate groups at positions 6 and 7.

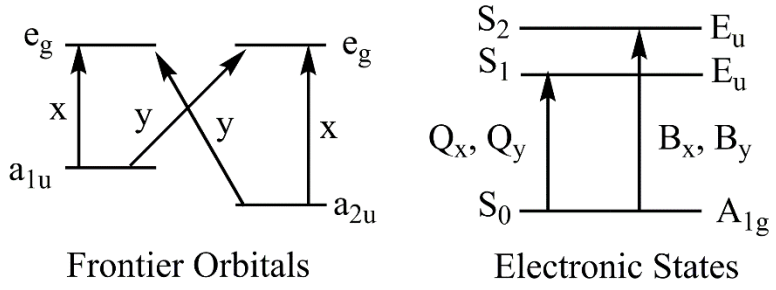

Scheme 1.3. Representation of the Gouterman Four Orbital Model. Symmetry elements are indicated for each orbital and electronic state. Relative energies of the states and orbitals are not to scale.

Oxidation state, spin state, and coordination number of the metal all have varying impacts on the porphyrin optical absorption spectrum. Substituents along the porphyrin ring also alter its electronic structure consequently affecting its absorption spectrum. Nonetheless, optical absorbance spectra are not particularly sensitive to changes in the porphyrin environment due to non-bonding interactions. Vibrational spectroscopy is a more sensitive tool for probing these interactions and are information rich. However, for proteins having thousands of atoms, small

changes in overall structure can be difficult to detect due to the enormous number of vibrational modes, even though such small changes can be deterministic for reaction mechanism. Furthermore, IR spectroscopy is not practical in aqueous solutions since water has a large absorption cross section effectively occluding the majority of the useful IR spectrum. Resonance Raman (rR) spectroscopy is often used to counter these problems for proteins that contain a chromophore like a porphyrin. Raman scattering is greatly enhanced by selecting the excitation wavelength within an electronic absorbance band. Vibrational modes that undergo a change in their force constant in an excited state have dramatically increased polarizability. Consequently, Raman scattering intensities by vibrational modes whose distortions mimic the excited state geometry show resonance enhancement.[58] Soret or B-band excitation is commonly used for metalloporphyrins and greatly enhances Raman scattering by totally symmetric vibrational modes. The enhancement is so large for porphyrins that none of the myriad amino acid vibrations are typically observed, and useful spectra can be recorded from only micromolar metalloporphyrin concentrations . Much work has been done to characterize and assign rR bands to their metalloporphyrin vibrational modes. A complete normal mode analysis was done for nickel(II) porphine, nickel(II) tetraphenylporphyrin, and nickel(II) octaethylporphyrin.[64-66] Similar normal mode analyses were performed on heme in proteins such as cytochrome *c*[67] and metmyoglobin[68]. These studies have identified core-size marker bands that are useful diagnostic tools for determining metal oxidation state, spin state, and coordination number in metalloporphyrins. The core-size, which is the distance between *trans* nitrogen atoms from the pyrrole groups, is responsive to metal ion radius and consequently impacts the porphyrin skeletal bond strengths. This influence depends not only on the metal ion radius, but whether it lies in the porphyrin plane or is displaced from it along the 4-fold symmetry axis. Higher oxidation state

metals have smaller core sizes which correspond to greater skeletal bond strengths and, consequently, their relatively high vibrational frequencies. Spin state, which is related to the electronic configuration of molecular orbitals with *d*-character, also impacts the core size. Metal ions in high-spin configurations can have *d*-based MOs of antibonding character occupied. These metal ions have larger radii than their low-spin counterparts and their metalloporphyrins have larger porphyrin core sizes than their low-spin cousins. Low spin configurations consist of mostly spin paired electrons that populate lower energy *d*-based MOs of bonding or nonbonding $M-N_{pyrrole}$ character, favoring smaller porphyrin core-sizes. Coordination number also impacts porphyrin skeletal bond strengths by positioning the metal ion in or out of the plane. The metal ions in five-coordinate complexes are typically out of the porphyrin plane, thereby allowing the porphyrin skeletal bonds to relax, especially for high spin complexes. Six coordinate metal ions typically lie in the porphyrin plane and force the its skeletal bonds to elongate. The general trend of increasing frequencies for porphyrin skeletal vibrations occurs as follows in heme *b*: Fe(II) 5cHS < Fe(III) 6cHS < Fe(III) 5cHS < Fe(III) 5c/6c LS < Fe(IV) 5c/6cLS.[58]

1.3.3. EPR spectroscopy of metalloporphyrins and protein radicals.

Electron paramagnetic resonance (EPR) or electron spin resonance (ESR) spectroscopy is a magnetic technique where microwave radiation at a specific frequency is absorbed by a molecule that contains an unpaired electron(s). This phenomenon is akin to nuclear magnetic resonance (NMR) spectroscopy where a molecule absorbs radio-frequency radiation when placed in an applied magnetic field. In NMR, the applied magnetic field removes the degeneracy between nuclear spin states which arises from the alignment of nuclear magnetic moments relative to the applied field. In EPR, the applied magnetic field removes the degeneracy between unpaired electron spin states as their magnetic moments align with the applied field. Removal of

degenerate nuclear states and unpaired electron spin states when within an applied magnetic field is known as the Zeeman effect. The resonance frequency (ΔE) for an EPR transition is expressed in Equation 1.2 where *g* = the proportionality factor akin to the chemical shift in NMR, β = Bohr magneton, and H = applied external field.[69]

$$\Delta E = g\beta H \qquad \text{(Eq. 1.2)}$$

Since the absorption spectrum of an EPR transition is orientationally broadened in a sample with randomly oriented molecules, it is typically reported as the first derivative of the absorption spectrum. This allows for clear resolution of the g_{xx}, g_{yy}, and g_{zz} signal components. For a free electron, one that is not tied to a molecule or atom, the *g*-factor = 2.0023. However, much like NMR, the effective applied external field deviates from a free electron due to the electronic structure of the molecule in which the unpaired electron(s) resides. The change in resonance frequency from that of a free electron is typically reported as a change in the *g*-factor which encompasses the gyromagnetic ratio of the electron. A primary component in this deviation stems from spin-orbit coupling which occurs between the spin angular momentum of the unpaired electron and the orbital angular momentum for the molecular orbital in which it resides. Therefore, the symmetry of an orbital alters the effective magnetic field felt by an unpaired electron causing a dependency of the observed g-factor on the molecule's orientation with respect to the applied field. This is known as *g*-anisotropy and is useful in identifying what orbital the unpaired electron resides. Hyperfine coupling can occur which stems from the interaction between the magnetic field of a nucleus and that of the unpaired electron. Depending on the distance and spin of the nucleus, the principle resonance frequency splits according to 2nI+1 where n = the number of nuclei and I = the respective nuclear spin. Hyperfine coupling is useful for identifying which atom(s) an unpaired electron may reside on or near in a molecule.[70]

Metalloporphyrins commonly contain unpaired electrons depending on their oxidation and spin state which merits them to be investigated by EPR. Systems with multiple unpaired electrons, such as HS ferric hemin (S = 5/2), have broadened EPR lines due to spin-spin interactions which sharply decreases their relaxation time. Linewidth in an EPR spectrum is inversely proportional to T_{2e} (spin-spin relaxation time), thus spin systems that relax quickly are significantly broader. Consequently, most heme EPR spectra are recorded at very low temperatures (4–10 K). HS ferric hemin complexes generally have high *g*-factors with respect to a free electron (5–7) while LS ferric hemin complexes (S= ½) have only slightly higher *g*-factors (2–3).[70] This contrasts with unpaired electrons localized on organic molecules whose *g*-factors are very close to 2. A common set of organic radicals observed in proteins include tyrosyl and tryptophanyl radicals, where the unpaired electron is delocalized throughout the respective side chain π system. These radicals have smaller *g*-anisotropy with respect to metal-based radicals, have slower relaxation times allowing them to be observed at higher temperatures (> 77 K), and exhibit hyperfine coupling, a significant fraction of which arises from the two β methylene hydrogens.[71] Due to the stark differences in their molecular environments, the spectral signatures between a protein based radical and a metal based radical are readily distinguishable. Numerous heme proteins show evidence of tyrosyl and tryptophanyl after formation of their high valent iron states by various oxidants.[72] Cld-like proteins also form a tyrosyl radical to catalyze their respective reactions.[73] Therefore, it is possible that a protein based radical is involved in catalytic decomposition of ClO_2^- by Clds. The combination of hyperfine coupling constants and the respective anisotropic *g*-values will allow for assignment of any protein radicals formed during catalysis as either a tyrosyl or tryptophanyl radical.

1.4. References

1. Bender, K. S.; O'Connor, S. M.; Chakraborty, R.; Coates, J. D.; Achenbach, L. A., Sequencing and transcriptional analysis of the chlorite dismutase gene of Dechloromonas agitata and its use as a metabolic probe. *Appl Environ Microbiol* 2002, *68* (10), 4820-6.
2. Clark, I. C.; Melnyk, R. A.; Engelbrektson, A.; Coates, J. D., Structure and Evolution of Chlorate Reduction Composite Transposons. *mBio* 2013, *4* (4), e00379-13.
3. Danielsson Thorell, H.; Beyer, N. H.; Heegaard, N. H. H.; Öhman, M.; Nilsson, T., Comparison of native and recombinant chlorite dismutase from Ideonella dechloratans. *European Journal of Biochemistry* 2004, *271* (17), 3539-3546.
4. Schaffner, I.; Hofbauer, S.; Krutzler, M.; Pirker, K. F.; Bellei, M.; Stadlmayr, G.; Mlynek, G.; Djinovic-Carugo, K.; Battistuzzi, G.; Furtmüller, P. G.; Daims, H.; Obinger, C., Dimeric chlorite dismutase from the nitrogen-fixing cyanobacterium Cyanothece sp. PCC7425. *Molecular microbiology* 2015, *96* (5), 1053-68.
5. Liu, P.; Li, P.; Jiang, X.; Bi, D.; Xie, Y.; Tai, C.; Deng, Z.; Rajakumar, K.; Ou, H.-Y., Complete Genome Sequence of Klebsiella pneumoniae subsp. pneumoniae HS11286, a Multidrug-Resistant Strain Isolated from Human Sputum. *Journal of Bacteriology* 2012, *194* (7), 1841.
6. Dailey, H. A.; Dailey, T. A.; Gerdes, S.; Jahn, D.; Jahn, M.; Brian, M. R.; Warren, M. J., Prokaryotic Heme Biosynthesis: Multiple Pathways to a Common Essential Product. *Microbiology and Molecular Biology Reviews* 2017, *81* (1), e00048-16.
7. Kumar, S.; Stecher, G.; Li, M.; Knyaz, C.; Tamura, K., MEGA X: Molecular Evolutionary Genetics Analysis across Computing Platforms. *Mol Biol Evol* 2018, *35* (6), 1547-1549.
8. Celis, A. I.; Geeraerts, Z.; Ngmenterebo, D.; Machovina, M. M.; Kurker, R. C.; Rajakumar, K.; Ivancich, A.; Rodgers, K. R.; Lukat-Rodgers, G. S.; DuBois, J. L., A Dimeric Chlorite Dismutase Exhibits O2-Generating Activity and Acts as a Chlorite Antioxidant in Klebsiella pneumoniae MGH 78578. *Biochemistry* 2015, *54* (2), 434-446.
9. M. Asami, R. J. B., J. Cotruvo, A. Eckhardt, J.K. Fawell, M. Giddings, A. Hirose, P. Marsden, Y. Matsui, M.E. Meek, E. Ohanian, C.N. Ong, S. Ramasamy, S. Snyder, Chlorine Dioxide, Chlorite and Chlorate in Drinking-water. *World Health Organization Guidelines for Drinking-water Quality* 2016.
10. Odeh, I. N.; Francisco, J. S.; Margerum, D. W., New Pathways for Chlorine Dioxide Decomposition in Basic Solution. *Inorganic Chemistry* 2002, *41* (24), 6500-6506.
11. Gan, W.; Ge, Y.; Zhong, Y.; Yang, X., The reactions of chlorine dioxide with inorganic and organic compounds in water treatment: kinetics and mechanisms. *Environmental Science: Water Research & Technology* 2020, *6* (9), 2287-2312.
12. Cosson, H.; Ernst, W. R., Photodecomposition of Chlorine Dioxide and Sodium Chlorite in Aqueous Solution by Irradiation with Ultraviolet Light. *Industrial & Engineering Chemistry Research* 1994, *33* (6), 1468-1475.
13. Lee, Y.-j.; Kim, H.-t.; Lee, U.-g., Formation of chlorite and chlorate from chlorine dioxide with Han river water. *Korean Journal of Chemical Engineering* 2004, *21* (3), 647-653.
14. Adam, L. C.; Fabian, I.; Suzuki, K.; Gordon, G., Hypochlorous acid decomposition in the pH 5-8 region. *Inorganic Chemistry* 1992, *31* (17), 3534-3541.

15. Stanford, B. D.; Pisarenko, A. N.; Snyder, S. A.; Gordon, G., Perchlorate, bromate, and chlorate in hypochlorite solutions: Guidelines for utilities. *Journal AWWA* 2011, *103* (6), 71-83.
16. Perchlorate Environmental Contamination: Toxicological Review and Risk Characterization. *United States Environmental Protection Agency* 2002.
17. J. Cotruvo, J. J. K. F., M. Giddings, P. Jackson, Y. Magara, E. Ohanian,, Chlorite and Chlorate in Drinking-water. *World Health Organization Guidelines for Drinking-water Quality* 2005.
18. Leung, A. M.; Pearce, E. N.; Braverman, L. E., Perchlorate, iodine and the thyroid. *Best Practice & Research Clinical Endocrinology & Metabolism* 2010, *24* (1), 133-141.
19. Bard, A.; Parsons, R.; Jordan, J., Standard potentials in aqueous solution. Marcel Dekker, New York. 1985, -.
20. Goblirsch, B.; Kurker, R. C.; Streit, B. R.; Wilmot, C. M.; DuBois, J. L., Chlorite dismutases, DyPs, and EfeB: 3 microbial heme enzyme families comprise the CDE structural superfamily. *J Mol Biol* 2011, *408* (3), 379-98.
21. van Ginkel, C. G.; Rikken, G. B.; Kroon, A. G.; Kengen, S. W., Purification and characterization of chlorite dismutase: a novel oxygen-generating enzyme. *Arch Microbiol* 1996, *166* (5), 321-6.
22. Stenklo, K.; Thorell, H. D.; Bergius, H.; Aasa, R.; Nilsson, T., Chlorite dismutase from Ideonella dechloratans. *J Biol Inorg Chem* 2001, *6* (5-6), 601-7.
23. Celis, A. I.; DuBois, J. L., Substrate, product, and cofactor: The extraordinarily flexible relationship between the CDE superfamily and heme. 2015, (1096-0384 (Electronic)).
24. Hofbauer, S.; Pfanzagl, V.; Michlits, H.; Schmidt, D.; Obinger, C.; Furtmüller, P. G., Understanding molecular enzymology of porphyrin-binding α + β barrel proteins - One fold, multiple functions. *Biochimica et Biophysica Acta (BBA) - Proteins and Proteomics* 2021, *1869* (1), 140536.
25. de Geus, D. C.; Thomassen, E. A.; Hagedoorn, P. L.; Pannu, N. S.; van Duijn, E.; Abrahams, J. P., Crystal structure of chlorite dismutase, a detoxifying enzyme producing molecular oxygen. *J Mol Biol* 2009, *387* (1), 192-206.
26. Goblirsch, B. R.; Streit, B. R.; Dubois, J. L.; Wilmot, C. M., Structural features promoting dioxygen production by Dechloromonas aromatica chlorite dismutase. *J Biol Inorg Chem* 2010, *15* (6), 879-88.
27. Kostan, J.; Sjoblom, B.; Maixner, F.; Mlynek, G.; Furtmuller, P. G.; Obinger, C.; Wagner, M.; Daims, H.; Djinovic-Carugo, K., Structural and functional characterisation of the chlorite dismutase from the nitrite-oxidizing bacterium "Candidatus Nitrospira defluvii": identification of a catalytically important amino acid residue. *J Struct Biol* 2010, *172* (3), 331-42.
28. Freire, D. M.; Rivas, M. G.; Dias, A. M.; Lopes, A. T.; Costa, C.; Santos-Silva, T.; Van Doorslaer, S.; González, P. J., The homopentameric chlorite dismutase from Magnetospirillum sp. *Journal of inorganic biochemistry* 2015, *151*, 1-9.
29. Mlynek, G.; Sjoblom, B.; Kostan, J.; Fureder, S.; Maixner, F.; Gysel, K.; Furtmuller, P. G.; Obinger, C.; Wagner, M.; Daims, H.; Djinovic-Carugo, K., Unexpected diversity of chlorite dismutases: a catalytically efficient dimeric enzyme from Nitrobacter winogradskyi. *J Bacteriol* 2011, *193* (10), 2408-17.

30. Meng, E. C.; Pettersen, E. F.; Couch, G. S.; Huang, C. C.; Ferrin, T. E., Tools for integrated sequence-structure analysis with UCSF Chimera. *BMC Bioinformatics* 2006, *7* (1), 339.
31. Waterhouse, A.; Bertoni, M.; Bienert, S.; Studer, G.; Tauriello, G.; Gumienny, R.; Heer, F. T.; de Beer, T. A P.; Rempfer, C.; Bordoli, L.; Lepore, R.; Schwede, T., SWISS-MODEL: homology modelling of protein structures and complexes. *Nucleic Acids Research* 2018, *46* (W1), W296-W303.
32. Papadopoulos, J. S.; Agarwala, R., COBALT: constraint-based alignment tool for multiple protein sequences. *Bioinformatics (Oxford, England)* 2007, *23* (9), 1073-9.
33. Pahari, S.; Sun, L.; Alexov, E., PKAD: a database of experimentally measured pKa values of ionizable groups in proteins. *Database* 2019, *2019*.
34. Streit, B. R.; DuBois, J. L., Chemical and steady-state kinetic analyses of a heterologously expressed heme dependent chlorite dismutase. *Biochemistry* 2008, *47* (19), 5271-80.
35. Mehboob, F.; Wolterink, A. F.; Vermeulen, A. J.; Jiang, B.; Hagedoorn, P. L.; Stams, A. J.; Kengen, S. W., Purification and characterization of a chlorite dismutase from Pseudomonas chloritidismutans. *FEMS Microbiol Lett* 2009, *293* (1), 115-21.
36. Hofbauer, S.; Gysel, K.; Bellei, M.; Hagmuller, A.; Schaffner, I.; Mlynek, G.; Kostan, J.; Pirker, K. F.; Daims, H.; Furtmuller, P. G.; Battistuzzi, G.; Djinovic-Carugo, K.; Obinger, C., Manipulating conserved heme cavity residues of chlorite dismutase: effect on structure, redox chemistry, and reactivity. *Biochemistry* 2014, *53* (1), 77-89.
37. De Schutter, A.; Correia, H. D.; Freire, D. M.; Rivas, M. G.; Rizzi, A.; Santos-Silva, T.; González, P. J.; Van Doorslaer, S., Ligand Binding to Chlorite Dismutase from Magnetospirillum sp. *The Journal of Physical Chemistry B* 2015, *119* (43), 13859-13869.
38. Geeraerts, Z.; Rodgers, K. R.; DuBois, J. L.; Lukat-Rodgers, G. S., Active Sites of O2-Evolving Chlorite Dismutases Probed by Halides and Hydroxides and New Iron–Ligand Vibrational Correlations. *Biochemistry* 2017, *56* (34), 4509-4524.
39. Schaffner, I.; Mlynek, G.; Flego, N.; Pühringer, D.; Libiseller-Egger, J.; Coates, L.; Hofbauer, S.; Bellei, M.; Furtmüller, P. G.; Battistuzzi, G.; Smulevich, G.; Djinović-Carugo, K.; Obinger, C., Molecular Mechanism of Enzymatic Chlorite Detoxification: Insights from Structural and Kinetic Studies. *ACS Catalysis* 2017, *7* (11), 7962-7976.
40. Almagro Armenteros, J. J.; Tsirigos, K. D.; Sønderby, C. K.; Petersen, T. N.; Winther, O.; Brunak, S.; von Heijne, G.; Nielsen, H., SignalP 5.0 improves signal peptide predictions using deep neural networks. *Nature Biotechnology* 2019, *37* (4), 420-423.
41. Pouvreau, L. A. M.; Strampraad, M. J. F.; Berloo, S. V.; Kattenberg, J. H.; de Vries, S., Chapter Six - NO, N2O, and O2 Reaction Kinetics: Scope and Limitations of the Clark Electrode. In *Methods in Enzymology*, Poole, R. K., Ed. Academic Press: 2008; Vol. 436, pp 97-112.
42. Di Russo, N. V.; Bruner, S. D.; Roitberg, A. E., Applicability of fluorescence-based sensors to the determination of kinetic parameters for O2 in oxygenases. *Analytical Biochemistry* 2015, *475*, 53-55.
43. Sander, R., Compilation of Henry's law constants (version 4.0) for water as solvent. *Atmos. Chem. Phys.* 2015, *15* (8), 4399-4981.
44. Philippi, M.; dos Santos, H. S.; Martins, A. O.; Azevedo, C. M. N.; Pires, M., Alternative spectrophotometric method for standardization of chlorite aqueous solutions. *Analytica Chimica Acta* 2007, *585* (2), 361-365.

45. Michaelis, L.; Menten, M. L.; Johnson, K. A.; Goody, R. S., The original Michaelis constant: translation of the 1913 Michaelis-Menten paper. *Biochemistry* 2011, *50* (39), 8264-8269.
46. Blanc, B.; Mayfield, J. A.; McDonald, C. A.; Lukat-Rodgers, G. S.; Rodgers, K. R.; DuBois, J. L., Understanding how the distal environment directs reactivity in chlorite dismutase: spectroscopy and reactivity of Arg183 mutants. *Biochemistry* 2012, *51* (9), 1895-910.
47. Fitch, C. A.; Platzer, G.; Okon, M.; Garcia-Moreno E, B.; McIntosh, L. P., Arginine: Its pKa value revisited. *Protein Science* 2015, *24* (5), 752-761.
48. Streit, B. R.; Blanc, B.; Lukat-Rodgers, G. S.; Rodgers, K. R.; DuBois, J. L., How active-site protonation state influences the reactivity and ligation of the heme in chlorite dismutase. *J Am Chem Soc* 2010, *132* (16), 5711-24.
49. Hayashi Y Fau - Yamazaki, I.; Yamazaki, I., The oxidation-reduction potentials of compound I/compound II and compound II/ferric couples of horseradish peroxidases A2 and C. 1970, (0021-9258 (Print)).
50. Green, M. T., Application of Badger's Rule to Heme and Non-Heme Iron−Oxygen Bonds: An Examination of Ferryl Protonation States. *Journal of the American Chemical Society* 2006, *128* (6), 1902-1906.
51. Oertling, W. A.; Kean, R. T.; Wever, R.; Babcock, G. T., Factors affecting the iron-oxygen vibrations of ferrous oxy and ferryl oxo heme proteins and model compounds. *Inorganic Chemistry* 1990, *29* (14), 2633-2645.
52. Hagedoorn, P. L.; De Geus, D. C.; Hagen, W. R., Spectroscopic characterization and ligand-binding properties of chlorite dismutase from the chlorate respiring bacterial strain GR-1. *Eur J Biochem* 2002, *269* (19), 4905-11.
53. Hofbauer, S.; Bellei, M.; Sundermann, A.; Pirker, K. F.; Hagmuller, A.; Mlynek, G.; Kostan, J.; Daims, H.; Furtmuller, P. G.; Djinovic-Carugo, K.; Oostenbrink, C.; Battistuzzi, G.; Obinger, C., Redox thermodynamics of high-spin and low-spin forms of chlorite dismutases with diverse subunit and oligomeric structures. *Biochemistry* 2012, *51* (47), 9501-12.
54. Mayfield, J. A.; Blanc, B.; Rodgers, K. R.; Lukat-Rodgers, G. S.; DuBois, J. L., Peroxidase-type reactions suggest a heterolytic/nucleophilic O-O joining mechanism in the heme-dependent chlorite dismutase. *Biochemistry* 2013, *52* (40), 6982-94.
55. Lee, A. Q.; Streit, B. R.; Zdilla, M. J.; Abu-Omar, M. M.; DuBois, J. L., Mechanism of and exquisite selectivity for O-O bond formation by the heme-dependent chlorite dismutase. *Proc Natl Acad Sci U S A* 2008, *105* (41), 15654-9.
56. Drago, R. S., Chapter 5. Electronic Absorption Spectroscopy. In *Physical Methods for Chemists Second Edition*, Saunders College Publishing: 1992; pp 109 - 148.
57. Drago, R. S., Chapter 6. Vibration and Rotation Spectroscopy: Infrared, Raman, and Microwave. In *Physical Methods for Chemists Second Edition*, Saunders College Publishing: 1992; pp 149 - 210.
58. Thomas G. Spiro, R. S. C., Chapter 2. Resonance Raman Spectroscopy. In *Physical Methods in Bioinorganic Chemistry: Spectroscopy and Magnetism*, Lawrence Que, J., Ed. University Science Books: 2010; pp 59 - 120.
59. Carter, R. L., Chapter 1. Fundamental Concepts. In *Molecular Symmetry and Group Theory*, John Wiley & Sons, Inc.: 1998; pp 1 - 39.

60. Carter, R. L., Chapter 6. Vibrational Spectroscopy. In *Molecular Symmetry and Group Theory*, John Wiley & Sons, Inc.: 1998; pp 164 - 200.
61. McMillin, D. R., Chapter 1. Electronic Absorption Spectroscopy. In *Physical Methods in Bioinorganic Chemistry: Spectroscopy and Magnetism*, Lawrence Que, J., Ed. University Science Books: 2010; pp 1 - 58.
62. Gouterman, M., Spectra of porphyrins. *Journal of Molecular Spectroscopy* 1961, *6*, 138-163.
63. Gouterman, M.; Wagnière, G. H.; Snyder, L. C., Spectra of porphyrins: Part II. Four orbital model. *Journal of Molecular Spectroscopy* 1963, *11* (1), 108-127.
64. Li, X. Y.; Czernuszewicz, R. S.; Kincaid, J. R.; Su, Y. O.; Spiro, T. G., Consistent porphyrin force field. 1. Normal-mode analysis for nickel porphine and nickel tetraphenylporphine from resonance Raman and infrared spectra and isotope shifts. *The Journal of Physical Chemistry* 1990, *94* (1), 31-47.
65. Li, X. Y.; Czernuszewicz, R. S.; Kincaid, J. R.; Stein, P.; Spiro, T. G., Consistent porphyrin force field. 2. Nickel octaethylporphyrin skeletal and substituent mode assignments from nitrogen-15, meso-d4, and methylene-d16 Raman and infrared isotope shifts. *The Journal of Physical Chemistry* 1990, *94* (1), 47-61.
66. Li, X. Y.; Czernuszewicz, R. S.; Kincaid, J. R.; Spiro, T. G., Consistent porphyrin force field. 3. Out-of-plane modes in the resonance Raman spectra of planar and ruffled nickel octaethylporphyrin. *Journal of the American Chemical Society* 1989, *111* (18), 7012-7023.
67. Hu, S.; Morris, I. K.; Singh, J. P.; Smith, K. M.; Spiro, T. G., Complete assignment of cytochrome c resonance Raman spectra via enzymic reconstitution with isotopically labeled hemes. *Journal of the American Chemical Society* 1993, *115* (26), 12446-12458.
68. Hu, S.; Smith, K. M.; Spiro, T. G., Assignment of Protoheme Resonance Raman Spectrum by Heme Labeling in Myoglobin. *Journal of the American Chemical Society* 1996, *118* (50), 12638-12646.
69. Drago, R. S., Chapter 9. Electron Paramagnetic Resonance Spectroscopy. In *Physical Methods for Chemists Second Edition*, Saunders College Publishing: 1992; pp 360 - 408.
70. Palmer, G., Chapter 3. Electron Paramagnetic Resonance of Metalloproteins. In *Physical Methods in Bioinorganic Chemistry: Spectroscopy and Magnetism*, Lawrence Que, J., Ed. University Science Books: 2010; pp 121 - 186.
71. Un, S., The g-values and hyperfine coupling of amino acid radicals in proteins: comparison of experimental measurements with ab initio calculations. *Magnetic Resonance in Chemistry* 2005, *43* (S1), S229-S236.
72. Østdal, H.; Andersen, H. J.; Davies, M. J., Formation of Long-Lived Radicals on Proteins by Radical Transfer from Heme Enzymes—A Common Process? *Archives of Biochemistry and Biophysics* 1999, *362* (1), 105-112.
73. Streit, B. R.; Celis, A. I.; Moraski, G. C.; Shisler, K. A.; Shepard, E. M.; Rodgers, K. R.; Lukat-Rodgers, G. S.; DuBois, J. L., Decarboxylation involving a ferryl, propionate, and a tyrosyl group in a radical relay yields heme b. *Journal of Biological Chemistry* 2018, *293* (11), 3989-3999.

2. A DIMERIC CHLORITE DISMUTASE EXHIBITS O_2-GENERATING ACTIVITY AND ACTS AS A CHLORITE ANTIOXIDANT IN KLEBSIELLA PNEUMONIAE MGH 78578[1]

2.1. Abstract

Chlorite dismutases (Clds) convert chlorite to O_2 and Cl^-, stabilizing heme in the presence of strong oxidants and forming the O−O bond with high efficiency. The Cld from the pathogen *Klebsiella pneumoniae* (*Kp*Cld) represents a clade of Clds which share most of their active site structure with efficient O_2-producing Clds, even though they have a truncated monomeric structure, exist as a dimer rather than a pentamer, and come from Gram-negative bacteria without a known need to degrade ClO_2^-. We hypothesized that *Kp*Cld, like others in its clade, should be able to make O_2 and may serve an in vivo antioxidant function. Here, it is demonstrated that it degrades ClO_2^- with limited turnovers relative to the pentameric Clds, due in part to loss of HOCl from the active site and destruction of the heme. The observation of HOCl, the expected leaving group accompanying oxygen-atom transfer to the ferric heme, is consistent with the more open, solvent-exposed heme environment predicted by spectroscopic measurements and inferred from the crystal structures of related proteins. *Kp*Cld is more susceptible to oxidative degradation under turnover conditions than the well-characterized Clds associated with perchlorate respiration. However, wild type *K. pneumoniae* has a significant growth advantage in the presence of chlorate relative to a Δ*cld* knock out strain, specifically

[1]The material in this chapter is from a collaborative manuscript published in the journal Biochemistry (https://doi.org/10.1021/bi501184c) co-authored by Arianna I. Celis, Zachary Geeraerts, David Ngmenterebo, Melodie M. Machovina, Richard C. Kurker, Kumar Rajakumar, Anabella Ivancich, Kenton R. Rodgers, Gudrun S. Lukat-Rodgers, and Jennifer L. DuBois. Zachary Geeraerts had primary responsibility in isolating, characterizing by resonance Raman and UV/Visible absorbance spectroscopies, and measuring the pH dependent oxygen evolution activity of *Kp*Cld. He also had responsibility interpreting data he collected and writing sections associated with his work.

under nitrate-respiring conditions. This suggests that a physiological function of *Kp*Cld may be detoxification of endogenously produced ClO_2^-.

2.2. Introduction

O_2-bond forming processes are rare in biology. At present, two examples are well-described. First, the water-splitting reaction catalyzed by photosystem II (PSII) drives the photosynthetic fixation of CO_2 into carbohydrates.[1] Second, a much more unusual reaction found in perchlorate (ClO_4^-)-respiring bacteria is used to detoxify chlorite (ClO_2^-), the end product of the perchlorate respiratory pathway. ClO_2^- is rapidly converted to O_2 and Cl^- via an enzyme known as chlorite dismutase (Cld).[2] In sharp contrast with the complexity of PSII,[1] Clds are soluble enzymes catalyzing an O−O bond-forming reaction with heme *b* as the sole cofactor.

Clds from perchlorate-respiring bacteria catalyze this reaction with great efficiency. The Cld from *Dechloromonas aromatica* (*Da*Cld), which we have characterized extensively and use here as an example of a highly-adapted respiratory Cld, turns over >20,000 eq of chlorite per heme at rates nearing the diffusion limit before it is irreversibly inactivated.[3-7] The proposed mechanisms for O_2 formation (Scheme 2.1) involves initial transfer of an oxygen atom from ClO_2^- to the ferric heme through a fleeting enzyme substrate (i.e. chlorite bound) complex to make a Fe^{IV}=O Porphyrin (Por) π-cation radical (Compound I). The resulting hypochlorite (OCl^-) leaving group is stabilized in its nucleophilic, anionic state by a positively charged arginine residue in a sterically confined pocket above the heme plane.[8-11] The "trapped" hypochlorite is then poised for nucleophilic attack on the electron-deficient ferryl oxygen atom to generate a putative ferric peroxyhypochlorite ($OOCl^-$), likely a transition state, that decomposes to yield Cl^- and O_2.

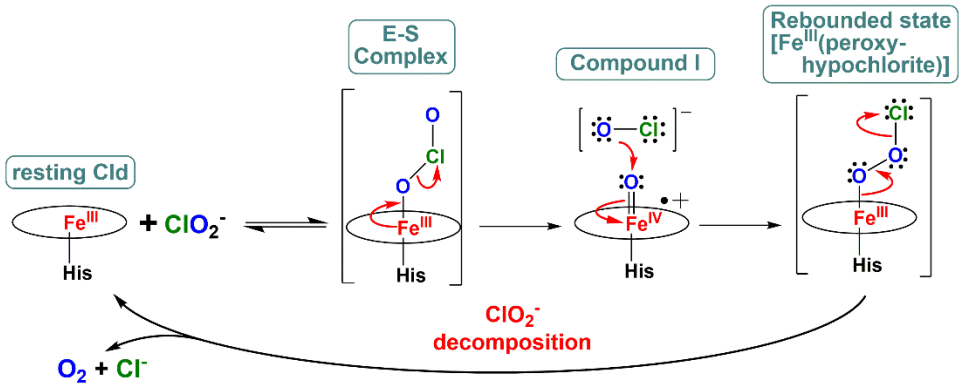

Scheme 2.1. Proposed catalytic mechanisms of chlorite decomposition by Cld.

The requirement for the Cld-catalyzed reaction by perchlorate-respiring bacteria is absolute; without it, ClO_2^- rapidly accumulates to toxic levels.[2] However, Clds are found in almost all bacterial phyla and in many archaea, the overwhelming majority of which are not involved in ClO_4^- respiration.[12] These Clds subdivide according to sequence into groups that may be functionally distinct from their respiration-associated counterparts and from each other (Figure 2.1), in spite of their close sequence similarity.[13] Investigation of the Cld from *Staphylococcus aureus*, a Gram-positive bacterium, provided a striking example. In its heme-bound form, it is completely inactive in the conversion of ClO_2^- to Cl^- and O_2.[14] Genetic and biochemical evidence instead suggests that the protein is essential for a terminal step in heme biosynthesis,[14-15] a biological function that appears to be common to the Clds from Gram-positive bacteria and potentially other species.[13, 15]

The Cld from *Klebsiella pneumoniae* strain MGH 78578 (*Kp*Cld) represents another clade that may have yet a third biochemical function. These enzymes are found in non-perchlorate-respiring bacteria from Gram-negative phyla (Figure 2.1).[12-13] As a consequence, they are not expected to be involved in either ClO_4^- respiration or heme biosynthesis. Unlike the respiration-associated Clds, they are homodimers rather than homopentamers, leading to a very different monomer-monomer interface and resulting structural context for their bound hemes

(Figure 2.2A-C). Locally, however, they possess very similar active site residues and share structural attributes essential for efficient ClO_2^- / O_2 conversion. In particular, they share the functionally important distal arginine above the ferric heme's open coordination position (Figure 2.2D).[8, 11] Consistent with chemical expectation, O_2 production has been demonstrated for at least one protein from this subgroup, the Cld from *Nitrobacter winogradskyi* (*Nw*Cld; structure shown in Figure 2.2A & D) [11] however, the dimeric enzymes have presumably not had the selection pressure to evolve to the same level of efficiency as respiratory Clds.

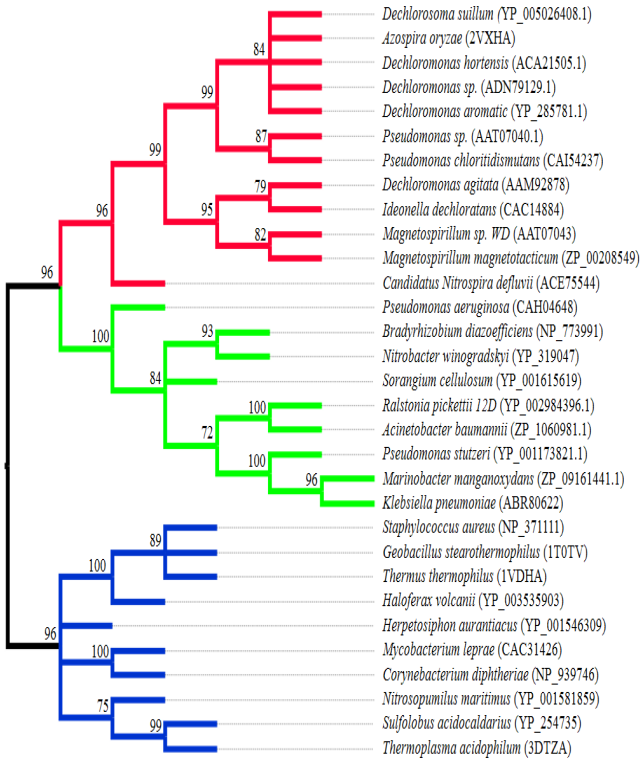

Figure 2.1. Phylogenetic tree illustrating the major subdivisions of the Cld protein family discussed in the text. The respiratory Clds, coming mostly from Proteobacteria with some exceptions due to lateral gene transfer, form the first group (red). A second group of dimeric Clds (green), including *Kp*Cld, come from non-perchlorate respiring species but retain active site features critical for ClO_2^- conversion to O_2. A third broad group of Clds (blue) catalyze a terminal step in heme biosynthesis in Gram-positive bacteria and potentially some Archaea. These have consequently been renamed HemQs.[11] Sequence accession numbers are given in parentheses, with PDB codes used to indicate where structures are available. The phylogenetic tree was generated using MEGA6.[16] The bootstrap consensus tree inferred from 1000 replicates is taken to represent the evolutionary history of the taxa analyzed. Branches corresponding to partitions reproduced in less than 70% bootstrap replicates are collapsed. Initial tree(s) for the heuristic search were obtained by applying the Neighbor-Joining method to a matrix of pairwise distances estimated using a JTT model. A discrete Gamma distribution was used to model evolutionary rate differences among sites (5 categories (+G, parameter = 2.4895)). 5% alignment gaps, missing data, and ambiguous bases were allowed at any position. The resulting tree is consistent with those previously reported by others.[7, 13, 17]

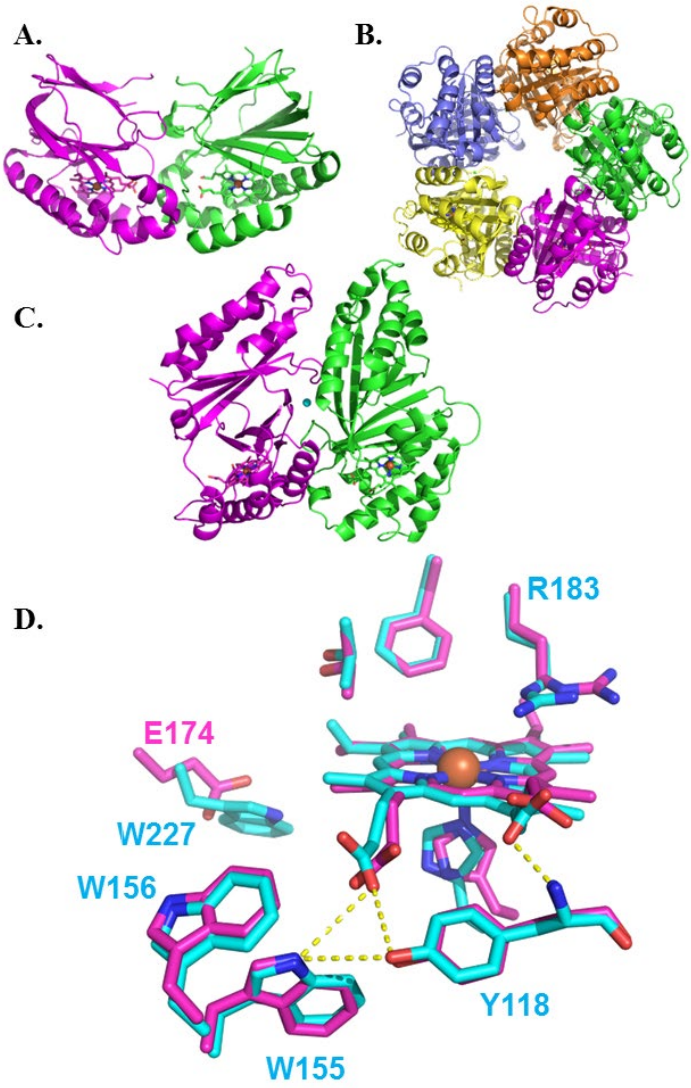

Figure 2.2. Clds from perchlorate-respiring and non-respiring Proteobacteria. A) *Kp*Cld, like the *Nw*Cld structure shown (3QPI),[7] has a truncated monomer relative to the respiratory Clds. Both form functional homodimers. Protein monomers are rendered as cartoons in different colors. Hemes are rendered as sticks. B) The respiration-associated *Da*Cld (PBD ID 3Q08) forms a functional homopentamer, shown looking down the C_5 axis.[4] C) A monomer-monomer interface from the structure in (B) suggests differences in heme accessibility in the pentameric and dimeric Clds. D) Active site environments for *Da*Cld (carbon cyan) and the *Nw*Cld (carbon magenta) are superimposed with several conserved residues around the heme labeled (*Da*Cld numbering). The two active sites are highly similar; two notable exceptions are the orientation of the distal Arg side chain and the identity of the residue at the position of W227, which is a conserved glutamate in *Nw*Cld and other dimeric Clds.

Why bacteria like *K. pneumoniae* MGH 78578, a respiratory pathogen, possess a potential means for ClO_2^- detoxification is not clear. *K. pneumoniae* and other non-perchlorate

respiring species generally do not encode perchlorate or chlorate reductase enzymes.[15] Yet, pathogenic strains of clinically pervasive[18] species including *K. pneumoniae, Acinetobacter baumanii,* and *Pseudomonas aeruginosa* all possess genes from this *cld* subtype, often on plasmids or as part of pathogenicity islands. These genes appear unlikely to guard against environmental chlorite, due to its chemical instability and the inability of negatively charged ClO_2^- to passively enter cells.[19] However, an indirect antioxidant function against ClO_3^- or ClO_4^- is possible, if these can enter the cell and be reduced by endogenous enzymes. To test this hypothesis, and to better understand the influence of the unusual monomer and oligomerization states on an otherwise similar heme environment, *Kp*Cld was characterized in parallel with the Δ*cld* strain of *K. pneumoniae* MGH 78578. The results presented here report on both the biological function of this group of Clds as well as the biochemical properties that make them unique.

2.3. Experimental Methods

2.3.1. Chemicals.

Chemicals were purchased from Alfa Aesar, Sigma-Aldrich or VWR. Sodium chlorite, 2,2'-azino-bis(3-ethylbenzothiazoline-6-sulfonic acid) diammonium salt (ABTS), guaiacol and 2-chloro-5,5-dimethyl-1,3-cyclohexanedione (MCD) stock solutions were made fresh daily in buffers prepared from distilled/deionized water and their concentrations determined spectrophotometrically: ε_{262} = 160 $M^{-1}cm^{-1}$ ($NaClO_2$), ε_{415} = 3.6×10^4 $M^{-1}cm^{-1}$ (ABTS) and ε_{290} = 20,100 $M^{-1}cm^{-1}$ (MCD).[20] Iodometric titration was routinely used to quantify working solutions of sodium chlorite or hypochlorite (diluted from a 10−14% w/w stock), as well as unreacted ClO_2^- remaining at the end of experiments.[21] Each substrate was dissolved directly in

the specified aqueous buffers with the exception of guaiacol, for which a 0.9 M stock was prepared in DMSO. Stocks of hemin were prepared in DMSO.

2.3.2. Generation of Δ*cld* strain.

Mutagenesis of *K. pneumoniae* MGH 78578 was carried out as described previously.[22] Briefly, a derivative of pKOBEG coding for apramycin resistance, pKOBEGApra, was used to facilitate lambda Red based replacement of *cld* with a 1652 bp FRT site-flanked hygromycin resistance cassette (FRT-*hph*-FRT) amplified from pJTAG-hyg (Deenathayalaguptha and Rajakumar, unpublished data) using primers GmF and GmR.[23] Targeting flanking sequences TS1 (572 bp) and TS2 (527 bp) were amplified using primer pairs P1/P2 and P3/P4. TS1, TS2 and FRT-*hph*-FRT were joined by splicing overlap extension-PCR (SOE-PCR) to produce a 2702 bp amplicon (Figure A1). Arabinose-induced electrocompetent *K. pneumoniae* MGH 78578/pKOBEGApra maintained at 30°C was electroporated with 100 ng of the SOE-PCR product and transformants recovered on LB + 200 μg/ml hygromycin agar at 37 °C after overnight culture. Several hygromycin resistant colonies were examined and the Δ*cld* mutant was validated by PCR analysis (Figure A1). Bacteria and plasmids used for *cld* mutagenesis are listed in Table A1.

2.3.3. Phenotypic characterization of Δ*cld* strain.

Frozen (−80°C) glycerol stocks of wild type (WT) and *Δcld* strains of *K. pneumoniae* were revived by streaking on Luria broth (LB)-agar or LB-agar + hygromycin B (75 mg/mL) plates respectively. Hygromycin B was used in all growth experiments to maintain the mutant free of contamination. Single colonies were inoculated into 5 mL of LB or LB + hygromycin B and grown to an $OD_{600} = 0.4$. Cells were harvested in microcentrifuge tubes and washed three times with M9 media (0.2% (v/v) glycerol, 58 mM K_2HPO_4, 22 mM Na_2HPO_4, 85 mM NaCl,

18.7 mM NH_4Cl) supplemented with the following trace elements in 134 μM EDTA: 6.15 μM ZnO, 570 nM $CuCl_2•2H_2O$, 340 nM $CoNO_3•6H_2O$, and 1.6 μM H_3BO_3. Cells were resuspended to a final optical density at 600 nm [OD_{600}] = 0.4 and used as a uniform inoculate (1:100) for all experiments.

For determination of minimal inhibitory concentrations of ClO_X^- (X = 2−4), cells were inoculated into 10 mL of anaerobic/N_2-purged media in sealed glass crimp-topped bottles containing increasing concentrations of $NaClO_2$, $NaClO_3$ or $KClO_4$ (0.5−200 mM) and 50 mM KNO_3. The sealed bottles were placed in a 37°C incubator with gentle shaking. The minimal inhibitory concentration (MIC) was defined as the lowest concentration of a reagent that would inhibit the visible growth of *K. pneumoniae* after 24 h of incubation.[24] No-nitrate controls were carried out in tandem under aerobic conditions. Finally, for generation of growth curves, cells were inoculated into aerobic media and their growth monitored via periodic measurement of their OD_{600} over time.

2.3.4. Growth, purification, and characterization of wild type (WT) and mutant *Kp*Cld.

DNA containing the full-length coding region of chlorite dismutase from *Klebsiella pneumoniae* MGH 78578 (accession no. CP000650.1) was PCR-amplified with the primers KpCldFor (5'- CGC CATATG AAT ACA CGA TTA TTT ACG TTC GCT GG -3') and KpCldRev (5'- TTT GGATCC CTA GGC CGG CTC ATG CA -3') from a *K. pneumoniae* genomic DNA template (added cut sites for NdeI and BamHI at the 5' and 3' ends underlined, respectively). The product was subsequently cloned into the pET-15b (Merck/Novagen) expression vector for production of protein with an N-terminal His-tag. The Y62F and W97F mutants of *Kp*Cld and the Y118F mutant of *Da*Cld were generated from the WT via PCR-based

single codon substitution using a QuikChange kit. The W227F, W155F, and W156F mutants of *Da*Cld were generated in a similar manner and available from prior work.[25]

All *Kp*Clds were expressed in *Escherichia coli* Tuner (DE3) cells (Merck/Novagen) grown in Terrific Broth (TB) plus ampicillin (100 μg/mL). Expression cultures were grown at 37°C in a shaker incubator (250 rpm) to mid-logarithmic phase (OD_{600} = 0.5). 1 mM isopropyl-β-D-thiogalactopyranoside (IPTG) and 50 mg/L delta-aminolevulinic acid were added to induce heme protein expression and the temperature lowered to 20°C. After 16 h, cell pellets were collected by centrifugation and stored at −80°C. Cells were thawed/resuspended (20 mM phosphate buffer, 500 mM NaCl, and 20 mM imidazole, 1 mM phenylmethylsulfonylfluoride, pH=7.4) and lysed by pulsed sonication on ice (7 min). The lysates were clarified by centrifugation and supernatants loaded onto a 20-mL HisTrap column. The protein was eluted using a 20−500 mM linear gradient of imidazole in the resuspension buffer. Eluted proteins were screened by SDS-PAGE and pure fractions buffer-exchanged into 0.1 M phosphate buffer (0.1 M, pH 6.8) using Amicon centrifugal concentrators (10,000 MWCO). Pure protein was concentrated to 10 mg/mL (20% glycerol), frozen in liquid N_2, and stored at −80°C. All *Kp*Cld concentrations are given as heme-bound monomer, where [heme] and [protein] were determined by the pyridine hemochromagen[26] and Bradford assays, respectively.

2.3.5. Measurement of initial rates of chlorite-decomposing activity in the steady state.

A commercial luminescence-based probe was used to measure O_2 evolution by *Kp*Cld during chlorite decomposition under steady state conditions. Samples were 12 nM WT*Kp*Cld and 0.05−2 mM chlorite in the following buffer solutions: 50 mM phosphate-citrate (pH < 6), 100 mM phosphate (pH 6−8), or 100 mM glycine (pH >8). The probe was equilibrated in the

buffered chlorite solution for 5–10 minutes prior to initiation of the reaction by introduction of enzyme. Kinetic traces were recorded at 1 s intervals for 3–10 minutes.

2.3.6. Monitoring heme chromophore loss due to $NaClO_2$ or NaOCl.

10 μM samples (200 μL) of heme-containing *Kp*Cld were titrated in quartz cuvettes with a concentrated ClO_2^- or $HOCl/OCl^-$ stock (600 mM) added in 1 μL increments (all solutions in 0.1 M citrate-phosphate buffer, pH 6.6). Samples were allowed to come to equilibrium following each addition and absorbances were corrected for dilution.

Chromophore loss was also monitored over time following the addition of varying amounts of NaOCl as a function of pH. Reactions were carried out in 0.1 M citrate-phosphate at pH values spanning 6−8. 10 μM samples (200 μL) of heme-containing *Kp*Cld in quartz cuvettes were manually mixed with NaOCl stock, yielding final [NaOCl] of 0−1 mM (0−2000 eq). Spectra were measured every 6 s after mixing. The absorbance at the Soret band maximum (409 nm) was plotted versus time and fitted to a single exponential equation in order to obtain a first order rate constant (k_{obs}). Values of k_{obs} measured at a given pH were plotted versus [NaOCl] to obtain second order rate constants (k = slope).

2.3.7. Measurement of residual activities and turnover numbers.

The potency of ClO_2^- as a suicide substrate was assessed by the method of Silverman.[27] Briefly: 5 μM samples of *Kp*Cld were incubated for 1 h at room temperature with increasing equivalents of chlorite up to 3×10^4, with or without 0.5 mM of added guaiacol, MCD, or ABTS (0.1 M citrate-phosphate buffer, pH 6.6). Reactions were dialyzed against chlorite-free buffer for two one-hour cycles to remove any unreacted substrate. Remaining *Kp*Cld reactivity was measured using a Clark oxygen electrode by adding 5 μL of each dialysate to 1.5 mL of 2 mM ClO_2^- and measuring the initial rate of O_2 production. Rates were measured three times,

corrected for dilution, and averaged. Residual activity was computed by referencing the activity remaining after incubation in a given ClO_2^- concentration to the activity of the zero-chlorite control. The turnover number, defined as the total number of molecules of ClO_2^- catalyzed per *Kp*Cld heme before the catalyst is irreversibly inactivated, was obtained by extrapolating a plot of residual activity versus [ClO_2^-] / [*Kp*Cld] to the x-intercept.

2.3.8. Vibrational characterization of *Kp*Cld.

Resonance Raman (rR) spectra were obtained with 413.1-nm or 441.6-nm excitation from a Kr^+ and HeCd lasers, respectively. The laser beam was focused to a line at the sample using a cylindrical lens. Scattered light was collected in the 135° backscattering geometry using a f/1 lens to collect and collimate the light. Rayleigh scattered light was attenuated with a holographic notch filter and the remaining light passed through a polarization scrambler. Collection was f-matched to a single f/4.7 0.67-m Czerny-Turner spectrograph fitted with a 120×140 mm 1200 groove/mm holographic grating and operated with a 10 μm (0.74 cm^{-1}) slit. The spectrograph was fitted with a LN_2-cooled CCD detector having a 26.8 mm (1340 pixel) × 8.0 mm (400 pixel) image area. The spectrometer was calibrated against Raman frequencies of toluene, dimethylformamide, acetone, and methylene bromide. Spectra were recorded at ambient temperature from samples in spinning 5 mm NMR tubes. UV-visible absorbance spectra were recorded from the rR samples before and after spectral acquisition to assess whether sample integrity had been compromised by exposure to the laser beam. Laser power at ferric and ferrous samples ranged from 5 to 10 mW; no spectral artifacts due to photoinduced chemistry were observed with these irradiation powers. Ferric *Kp*Cld samples for the rR pH dependence study were prepared in the following 100 mM buffers: potassium phosphate pH 5.7−7.5, Tris/HCl pH 8.6−9.7, and borate buffer pH 10.1.

2.3.9. Electron paramagnetic resonance (EPR) spectroscopy.

The 9-GHz EPR spectra were recorded on a Bruker EleXsys E500 spectrometer equipped with a standard Bruker ER 4102 X-band resonator and a liquid helium cryostat (Oxford Instruments, ESR 900). The spectra for WT *Kp*Cld at pH 6.0 were recorded at 4 K, 1 mW microwave power, 4 G modulation amplitude, 100 kHz modulation frequency. The spectra at pH 8.0 were recorded at 12 K, 10 G modulation amplitude, 0.5 mW microwave power, 100 kHz modulation frequency. Spectra for the mutant *Kp*Clds were recorded at 4 K, 1 mW microwave power, 4 G modulation amplitude, 100 kHz modulation frequency. In order to avoid significant changes of pH upon freezing, Tris-maleate buffer, which covers the range $5.2 < pH < 8.6$ with minor changes (0.1 pH unit) upon freezing, was used. No effect on the ferric EPR signal was observed for the Tris-maleate buffer as compared to phosphate buffer. Typically, EPR samples of ferric *Kp*Cld and *Da*Cld (in 0.1 mM Tris-maleate at pH 6.0 or 8.0, and at 0.6 mM enzyme concentration) were measured in 4-mm quartz tubes. The buffer exchange in the pH range 5.0−8.0, done with Centricon microconcentrators (Amicon), could be reversibly obtained without enzyme precipitation, degradation or iron release as judged by the UV/visible absorbance and EPR spectra recorded after each buffer exchange. Freezing and thawing cycles at high enzyme concentrations used for the EPR characterization did not induce any enzyme precipitation or detectable changes in the heme environment.

2.4. Results

2.4.1. The heme environment in *Kp*Cld as probed by UV/vis and rR spectroscopy.

*Kp*Cld has a reversible pH-dependent transition in UV/visible spectrophotometric titrations. Experiments in which the enzyme was titrated with base (Figure 2.3A) and acid (data not shown) yielded the same pK_a. Fits of UV/vis data at 390 nm (Figure 2.3A, inset), 413 nm,

and 574 nm (not shown) indicated a pK_a of 8.3, the same as that reported for the *Azospira oryzae* Cld[28] and slightly lower than that for Clds from *Ideonella dechloratans* (8.5)[29] and *D. aromatica* (8.7).[5] Heme proteins with neutral proximal histidine ligands have lower pK_as (heme oxygenases-1 and -2 [7.6, 8.5]; *Sm*FixL [9.6]; HmuO [9.0] than those with a proximal histidinate (peroxidases [pK_as 11−12]).[30-32] Consistent with a pK_a in this range, the Fe(II)−His vibrational frequency measured by rR for *Kp*Cld suggests a charge-neutral proximal histidine (Figure A2; discussed further below).

At pH 6.0, ferric *Kp*Cld's exhibits a Soret band maximum at 405 nm, a broad α/β band envelope at 505 nm with a small shoulder at 540 nm, and a charge transfer (CT) band at 645 nm (Figure 2.3A). This spectrum is similar to that reported for the related dimeric *Nw*Cld (405, 506, 543, 640 nm) and the pentameric Cld from Candidatus *Nitrospira defluvii* at pH 7.0,[10-11] but different from Clds from *D. aromatica* (393, 506, 648 nm, pH 7.0), *Azospira oryzae* (392-394 nm), and *Ideonella dechloratans* (392, 509, 648 nm, pH 7).[5, 9, 29] The latter three proteins, which come from ClO_4^- respirers, share similar five coordinate, high spin (5cHS) heme sites, pentameric oligomerization states, and hydrophobic, solvent-enclosed heme environments, to which their blue-shifted Soret bands have been attributed. In contrast, the visible spectrum of acidic *Kp*Cld corresponds to a mixture of coordination states; this is confirmed by its rR spectra.

The rR spectra (Figure 2.3B) of ferric *Kp*Cld in mildly acidic solution have a broad HS ν_3 envelope spanning 1482−1490 cm^{-1}, consistent with a mixture of six coordinate high spin (6cHS) and 5cHS heme. The temperature dependence of the HS ν_3 envelope supports the presence of 5c and 6c HS hemes. Upon lowering the temperature of ferric *Kp*Cld from 19 °C at pH 6.0, the 6cHS intensity of the ν_3 envelope at 1484 cm^{-1} increases at the expense of the 5cHS component at 1491 cm^{-1}. At temperatures below −14 °C, the envelope narrows to a single band

centered at 1484 cm^{-1}, indicating complete conversion of the HS heme to a 6c complex that is likely an aqua complex, whose formation is exothermic. The acid-base behavior of this complex supports this assignment. These data indicate that a considerable fraction of the resting HS enzyme is coordinatively saturated at near-physiological temperatures. In contrast, the acidic form of *Da*Cld contains only 5cHS heme.[5]

Another small ν_3 band occurs at 1505 cm^{-1} at 19 °C and pH near 6 (Figure 2.3B). This band increases in intensity in concert with a new 6cHS band at 1478 cm^{-1} as the pH is raised. Bands in the 1505 cm^{-1} frequency range can be consistent with 6cLS species or 5cQS (5c quantum-mechanical spin admixture of S=3/2 and S=5/2 ferric heme). The appearance of UV/visible bands near 572 nm (typical for 6cLS species) and 646 nm (CT) at pH 7.0 argue for assignment of the ν_3 band to a 6cLS species. At pH 10, ferric *Kp*Cld has a Soret maximum at 413 nm, α/β bands at 572 and 540 nm, and small absorbance bands near 490 and 603 nm. The 572 and 540 nm bands are consistent with a 6cLS complex, while the bands at 490 and 603 nm are suggestive of a 6cHS species (Figure 2.3A). These features are very similar to those reported for alkaline ferric *Da*Cld.[5] The mixture of spin states suggested by the UV-visible spectrum is confirmed by the appearance of two ν_3 bands at 1478 and 1505 cm^{-1} in the rR spectrum of alkaline *Kp*Cld. Growth of these bands is accompanied by the appearance of a shoulder at 1640 cm^{-1}, attributable to ν_{10} for 6cLS heme, and a 2 cm^{-1} upshift in the frequency of ν_4 (not shown), both indicating growth in the population of 6cLS heme. The formation of heme hydroxides is often characterized by parallel growth in intensity of bands arising from 6cHS and 6cLS hemes, which indicate its presence as a thermal spin state equilibrium. Similar mixtures attributed to such equilibria have been reported for a number of heme proteins, including the alkaline forms of *Da*Cld, myoglobin, hemoglobin, *Mycobacterium tuberculosis* HbN, and *Sm*FixL.[5, 33-36]

To determine whether the sixth ligand in *Kp*Cld is hydroxide at pH 9.8, the ν_{Fe-OH} modes were identified by isotopic substitution (Figure 2.3C). Bands at 509 and 442 cm^{-1} were assigned to the Fe−OH stretching modes for the LS and HS heme hydroxides, respectively. The LS ν_{Fe-OH} band shifts to 494 cm^{-1} in D_2O and to 488 cm^{-1} in $H_2{}^{18}O$. In the case of the HS heme, no deuterium shift is detected. In $^{18}OH_2$, the $\nu_{Fe-{}^{18}OH}$ band shifts by 22 cm^{-1} to 420 cm^{-1}. Thus, the pK_a of 8.3 corresponds to the formation of the *Kp*Cld−OH complex. Consistent with our previous report for *Da*Cld−OH,[5] the ν_{Fe-OH} bands of both HS and LS *Kp*Cld−OH fall at the low end of Fe−OH stretching frequency range for heme hydroxides.

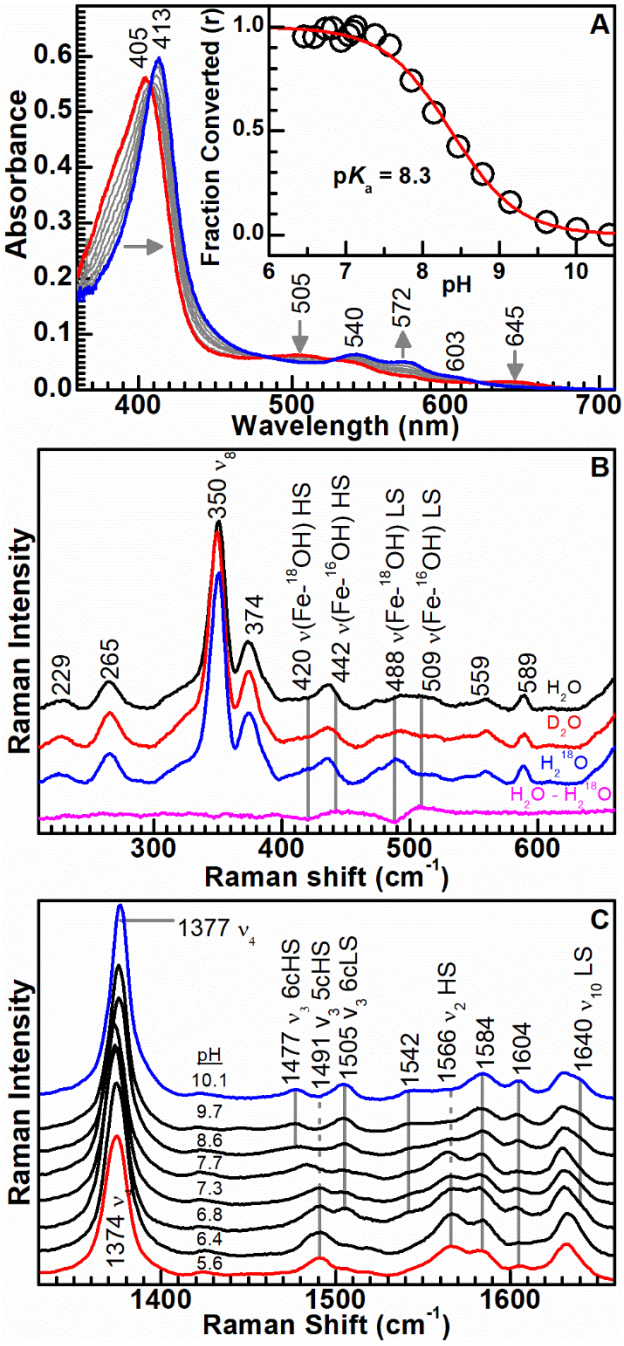

Figure 2.3. The pH-dependent behavior of *Kp*Cld indicates a water-accessible heme. A) UV-visible pH titration of *Kp*Cld. Spectra shown between pH 6.4 and 10.4. Arrows indicate the direction of the absorbance change with pH. Inset: Fraction converted at 390 nm as a function of pH; least squares fit to the data (•) a pK_a of 8.3. B) Speciation of ferric *Kp*Cld as observed in rR pH titration. Resonance Raman spectra were obtained with 413.1 nm excitation at the indicated pHs. C) Soret-excited rR spectra of the oxygen Isotopologues of alkaline *Kp*Cld (50 mM Ches, pH 9.8). The top three spectra were measured in the indicated solvent under identical acquisition times. The bottom trace is the difference spectrum generated by a 1:1 digital subtraction (H_2O – $H_2{}^{18}O$).

Finally, the UV/visible spectrum of ferrous *Kp*Cld (pH 7.0) generated by reduction of the ferric protein with a 12-fold redox excess of sodium dithionite exhibited a Soret band maximum at 433 nm, typical of 5cHS ferrous heme, and α/β bands at 586 and 555 nm, respectively (Figure A2). The 413.1-nm excited Fe(II) *Kp*Cld spectrum at pH 7.0 has ν_4 at 1356 cm^{-1}, typical of ferrous heme, and ν_3 at 1472 cm^{-1}, typical of 5cHS ferrous heme. The 441.6-nm excited Fe(II) *Kp*Cld spectrum revealed a Fe−His stretching band at 229 cm^{-1}, 7 cm^{-1} higher than that observed for *Da*Cld (222 cm^{-1} at pH 6.8),[5] consistent with the Fe−His bond being slightly stronger in *Kp*Cld assuming similar normal mode compositions in the two enzymes.

2.4.2. Structural features of the *Kp*Cld heme environment, including second-sphere interactions as revealed by 9-GHz EPR spectroscopy.

EPR spectroscopy is a sensitive probe of the extended hydrogen bonding network of heme active sites, including structural water molecules as well as second-sphere (and beyond) amino acid residues.[37-38] In the absence of a crystal structure for *Kp*Cld and in order to expand the structural view of the heme site provided by rR, the ferric EPR spectra of wild-type *Kp*Cld and key variants in its heme extended environment were examined as a function of pH. These were compared to their *Da*Cld counterparts, for which the WT crystal structure has been solved.[8]

Figure 2.4 shows the 9-GHz EPR spectra of wild-type *Kp*Cld recorded at cryogenic temperatures (4 K and 12 K). The ferric EPR spectrum of *Kp*Cld remained invariant in the pH range 5.5 to 7.9 (top, black trace) but showed a dramatic change at pH 8.0 (top, gray trace). At pH 6.0 (Figure 2.4, top, black trace) the EPR spectrum of *Kp*Cld showed an axial signal, with observed g_{eff} values of $g_{\perp} = 5.92$ and $g_{\parallel} = 1.99$, consistent with a ferric high-spin species. At pH 8.0 (Figure 2.4, top, gray trace), the *Kp*Cld EPR spectrum showed a distinct LS ferric species, with effective g-values of $g_{Cx} = 2.54$, $g_{Cy} = 2.19$, and $g_{Cz} = 1.87$. The almost complete conversion

of the ferric EPR signal from high-spin to low-spin at pH 8.0, observed in frozen solutions, differs from the more gradual effect observed in the rR experiments in solution (Figure 2.3B), and most possibly reflects the preferential configurations of the heme environment locked in the frozen samples. The ferric LS EPR spectrum overall is consistent with a nitrogenous amino-acid side chain not directly coordinated to the heme iron, in the vicinity of the Fe−OH bond revealed by the rR characterization described in the previous section. The relatively lower contribution of another LS signal with a large g_{max} of 3.10 (the other two components being very weak and too broad to be detected) consistent, in this case, with a nitrogenous ligand on the heme distal side,[8] was also observed. The identity of this ligand is not known. It is possible that, even after thorough dialysis, some imidazole used in the purification of the protein remained in the active site. Alternatively, repositioning of the distal arginine, with a deprotonated guanidinium group replacing water molecules close to the iron (for example, in the structural water molecules shown in the *Nw*Cld structure, Figure 2.2), could be envisioned if considering the crystal structures of the *N. defluvii* Cld with thiocyanate bound in the sixth coordination position of the heme.[10]

The EPR spectra of *Da*Cld differed substantially from *Kp*Cld's. Specifically, the spectrum at pH 6.0 showed the contribution of two ferric HS EPR signals (Figure 2.4, labelled with subscripts A and B), with effective *g*-values of (g_{Ax} = 6.67, g_{Ay} = 5.20, g_{Az} = 1.96) and (g_{Bx} = 6.25, g_{By} = 5.24, g_{Bz} = 1.99). Two distinct LS ferric species (Figure 2.4, subscripts C and D), with effective *g*-values of (g_{Cx} = 2.56, $g_{Cy} \approx$ 2.18, g_{Cz} = 1.87) and (g_{Dx} = 2.64, $g_{By} \approx$ 2.18, g_{Bz} = 1.82), were consistently observed at pH 8.0. These observations of two HS and two LS EPR signals are consistent with our earlier reports that closed (more active) and open (less active) *Da*Cld conformers are present between pH 5.6 and 9.1.[39]

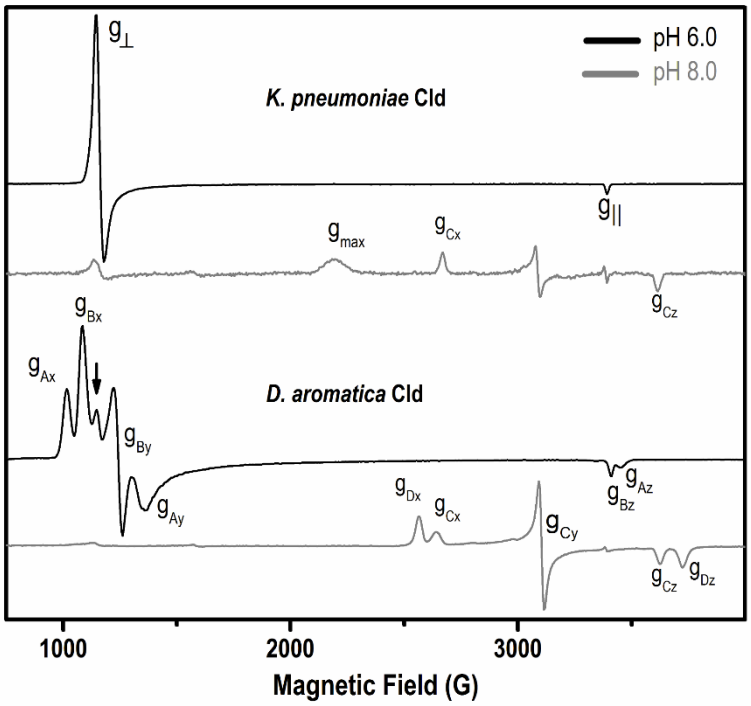

Figure 2.4. The 9-GHz EPR spectra of ferric Clds from *K. pneumonia* (top) and *D. aromatica* (bottom) as a function of pH. A spin-switch from high-spin ferric (black trace) to the low-spin ferric (gray trace) is observed at pH ≥ 8.0. The conversion of the high-spin ferric signal was estimated at 95% in *Da*Cld and 85% in *Kp*Cld. Experimental conditions: the spectra at pH 6.0 were recorded at 4 K, 1 mW microwave power, 4 G modulation amplitude, 100 kHz modulation frequency. The spectra at pH 8.0 were recorded at 12 K, 10 G modulation amplitude, 0.5 mW microwave power, 100 kHz modulation frequency.

To better understand the lack of pH-induced changes in the HS EPR spectra as well as the difference in ferric heme signals of the various Clds, structurally conservative mutations at highly conserved W and Y residues within hydrogen bonding distance to the heme propionates were constructed. Specifically, the crystal structures of the *Da* and *Nw* Clds show that a highly conserved tyrosine (numbered Y118 and Y61, respectively) appears to make hydrogen bonding contacts to both heme propionates via their phenol oxygen atoms and their amide nitrogens (Figure 2.2). The indole N atom of a conserved tryptophan (W155, *Da*Cld or W96, *Kp*Cld) lies within hydrogen bonding distance of one heme propionate. A second strictly conserved Trp (W156, *Da*Cld or W97, *Kp*Cld) is sterically close to the same propionate, but oriented such that

the indole nitrogen cannot form a hydrogen bond to it. Accordingly, we anticipated that substitutions of these conserved residues could considerably affect the orientation of the propionate(s) and/or heme planarity, resulting in measurable changes in the ferric EPR spectra.

Figure 2.5 shows dramatic changes observed in the ferric EPR spectra of *Kp*Cld and *Da*Cld upon mutation of these active site residues. The axial HS EPR signal of WT *Kp*Cld (Figure 2.5, top, dotted black trace) fully converted to a rhombically-distorted spectrum in the Y62F mutant (Figure 2.5, top, magenta trace), with the contribution of two species [effective *g*-values of (6.46, 5.39, 1.98) and (6.57, 5.54,1.99)]. The W97F mutation in *Kp*Cld induced a partial conversion of the wild-type axial signal to one of the rhombically-distorted HS forms of the Y62F variant, with effective *g*-values of (6.57,5.54, 1.99), plus a contribution of the 6cLS form with a large gmax of 3.10 (Figure 2.5, top, purple trace). The same LS large-gmax form was observed in WT *Kp*Cld, but only at basic pH (Figure 2.4, top, gray trace). In the Y118F mutant of *Da*Cld, positionally equivalent to Y62F in *Kp*Cld, the EPR component with the largest rhombic distortion disappears (Figure 2.5, bottom, magenta trace). The ferric EPR spectrum of the *Da*Cld(Y118F) variant then becomes very similar to the previously reported rhombic EPR spectra of the Clds from *A. oryzae and I. dechloratans*,[9, 29] and also similar to that of *Kp*Cld(Y62F). Accordingly, these results show that breaking the hydrogen bonds to the propionates allows more flexibility of the heme.

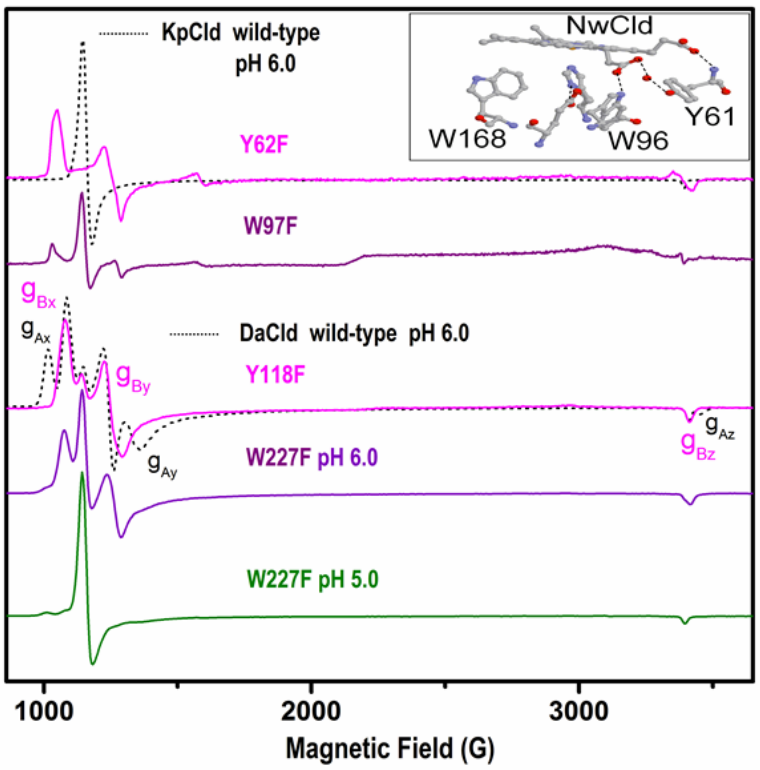

Figure 2.5. The 9-GHz EPR spectra of selected mutation on the heme environment of *Kp*Cld (top) and *Da*Cld (bottom) at pH 6.0. Both spectra of the wild-type Clds (black dotted traces) are shown for comparison. Figure 2.2D shows the crystallographic structure of the extended heme environment of *Nw*Cld (pdb accession code 3QPI), in which the amino acid residues (Trp96 and Tyr61) at equivalent positions to those mutated in *Kp*Cld (Y62F and W97F) are shown. The other Trp mutated in *Da*Cld (Trp227) is not conserved in *Nw*Cld. Experimental conditions: spectra were recorded at 4 K, 1 mW microwave power, 4 G modulation amplitude, 100 kHz modulation frequency.

To explore these differences further, we investigated the *Da*Cld W227F mutant. This residue is conserved among the Clds from known perchlorate respirers but not in the dimeric Clds (Figures 2.1 and 2.2) and could represent a key differentiation between the two groups. Trp227 is not connected to the heme by hydrogen bonds yet is sterically close to those other residues having hydrogen bonding interactions to the heme. Interestingly, two significant changes were observed in the ferric EPR spectrum of W227F *Da*Cld relative to WT: the disappearance of the component with the largest rhombic distortion, as in *Da*Cld Y118F, plus an increase in the axial EPR signal (Figure 2.5, bottom, violet trace). Moreover, the ratio of the

axial and rhombically distorted signals of the W227F *Da*Cld EPR spectrum became pH-dependent, as in the case of *Burkholderia pseudomallei* KatG,[40] fully converting to the axial signal at pH 5.0 (Figure 2.5, bottom, green trace). Hence, the resulting EPR spectrum for *Da*Cld W227F at pH 5.0 is the same as that of the wild-type *Kp*Cld (Figure 2.5, top, dotted black trace). Notably, the mutant protein could be isolated in a stably heme-bound state at low pH if concentrated and frozen immediately following purification (see Experimental Methods).[25] These results reinforce the idea that second sphere coordination influences the electronic structure of the heme iron. They also suggest that the conserved residue W227 is indeed important for distinguishing the heme environments of *Da*Cld and *Kp*Cld even though it is not directly connected to the heme via hydrogen bonding.

2.4.3. *Kp*Cld exhibits chlorite decomposing activity.

*Kp*Cld is a competent catalyst of chlorite decomposition; values of k_{cat} and k_{cat}/K_M maximize near pH 5.0, at $(1.9\pm0.2)\times10^3$ s^{-1} and $(2.5\pm 0.4)\times10^6$ $M^{-1}s^{-1}$, respectively (20 °C) (Figure A3). These values are approximately 10-fold lower than the corresponding parameters for *Da*Cld measured at its pH 5.2 optimum (4 °C): $k_{cat} = (2.0 \pm0.6)\times10^4$ s^{-1} and $k_{cat}/K_M = (3.2\pm0.4)\times10^7$ M^{-1} s^{-1}.[5] A pH optimum between pH 5−6 was recently measured for the k_{cat} for the *N. defluvii* Cld.[10, 41]

Steady state pH-rate profiles for *Kp*Cld (Figure A3) and *Da*Cld[5] are broadly similar, with each protein possessing a more active acidic form and less active alkaline form. Turning points in the plots of log k_{cat} versus pH were fit at pH 6.5 and 8.7 (*Da*Cld).[5] A transition from a highly active low pH form to a less active alkaline form is apparent near pH 7 for *Kp*Cld. Turning points in log-log plots of kinetic constants are associated with pK_as. Though not explicitly assigned here for *Kp*Cld, the lower pH turning point in *Da*Cld was previously assigned to the

distal arginine, first modeled as an explicit deprotonation and later associated with movement of the distal pocket Arg between less reactive "out" (alkaline) and more reactive "in" (acidic) conformations (Figure 2.2). The latter model is supported by both spectroscopic evidence and reactivity data with H_2O_2.[5-6, 39]

2.4.4. Chlorite acts as a potent suicide substrate.

Titration of *Kp*Cld with chlorite (Figure 2.6A) demonstrated near-complete elimination of the heme Soret band following exposure to roughly $(6.0\pm0.3)\times10^3$ equivalents of the oxidant. This value is intermediate between *Da*Cld's (2.0×10^4) and *Sa*Cld's (≤5).[5, 14] To relate heme destruction quantitatively with loss of catalytic activity, *Kp*Cld's turnover number was measured (Figure 2.6B). A line fit to a plot of residual activity versus chlorite eq intercepts the x-axis at 5.3×10^3. The same data could also be fit to an exponential decay curve, consistent with some protection of the enzyme from degradation by the accumulation of high product concentrations.[42] The exponential curve predicts heme degradation after exposure to even fewer equivalents of chlorite; that is, the number of equivalents extrapolated from where the initial, linear phase intercepts the x-axis. The number extrapolated from a straight line fit to all of the data is therefore likely an upper limit for turnovers.

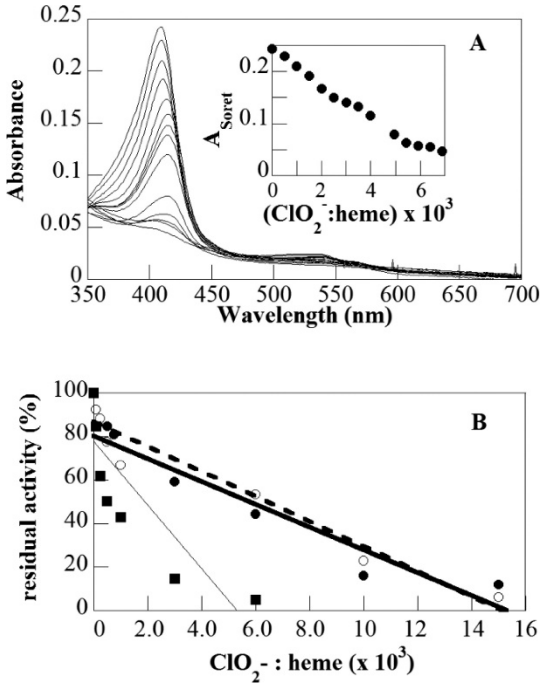

Figure 2.6. Chlorite acts as a suicide substrate and is rescued by H-atom donors and chlorination substrates. A) ClO_2^- was added in 300 eq increments and the heme chromophore observed to diminish to baseline after roughly 6×10^3 eq. Inset: the Soret band absorbance plotted versus added chlorite eq. B) Residual enzymatic activity following incubation with increasing eq of chlorite. Linear extrapolation to the x-axis yields the turnover number: no additives, (5.3×10^3, dark squares), with added ABTS (dark circles, solid line, 1.5×10^4), and with added MCD (open circles, dashed line, 1.5×10^4).

The measured turnover number is similar to but slightly less than the number of equivalents required to completely eliminate the Soret band (Figure 2.6A, inset), suggesting that loss of activity is correlated with destruction of the heme and also some degree of protein damage. Consistent with these results, a detailed study of chlorite-mediated damage to the pentameric Cld from *N. defluvii* showed that chlorite effected damage in a number of ways, including oxidation of methionine residues, chlorination of aromatic side chains, and heme lysis.[43]

2.4.5. H-atom donors and chlorination traps increase *Kp*Cld's turnover number.

The turnover number was remeasured in the presence of excess guaiacol and ABTS, which can act as sacrificial hydrogen-atom donors toward highly reactive oxidants. These could

include ferryl heme species, (H)OCl produced as intermediates in the O_2 generating reaction, or chlorine dioxide (ClO_2) from the one-electron oxidation of chlorite by a ferryl heme. In the presence of guaiacol, the turnover number for *Da*Cld increased by approximately ten-fold.[3] Here, in guaiacol or ABTS, the turnover number increased more modestly, to 1.5×10^4 (~2-fold larger). The same trend was observed in the presence of MCD, a trap used to detect chlorinating agents (HOCl, $\bullet ClO_2$, or OCl^-) in enzymatic reactions.[44-45] These results indicated that a species capable of reacting with guaiacol, ABTS, and MCD was responsible for chlorite-mediated inactivation of *Kp*Cld.

2.4.6. (H)OCl is produced by *Kp*Cld during steady state turnover with chlorite.

In order to directly detect the species generated during turnover, the reaction between ClO_2^- (3 mM) and *Kp*Cld (0.1 μM) was monitored via UV/vis under steady state conditions. Unreacted ClO_2^- was quantified by iodometric titration. ClO_2^- decomposition was incomplete: 36%±5% of the initially present chlorite had degraded by the end of the experiment, indicating $(6.7\pm0.3)\times10^3$ turnovers per heme; representative results are shown and turnover numbers are an average of three experiments (Figure 2.7A). Decomposition of ClO_2^- moreover occurred with no observable accumulation of ClO_2 (ε_{262} = 160 $M^{-1}cm^{-1}$). When 50 μM MCD was added to the same reaction, conversion of the MCD to DCD was readily detectable via the loss of the MCD chromophore (Figure 2.7B). The reaction with ClO_2^- also proceeded much closer to completion: 73%±5% consumed, or $(1.4\pm 0.1)\times10^4$ turnovers per heme.

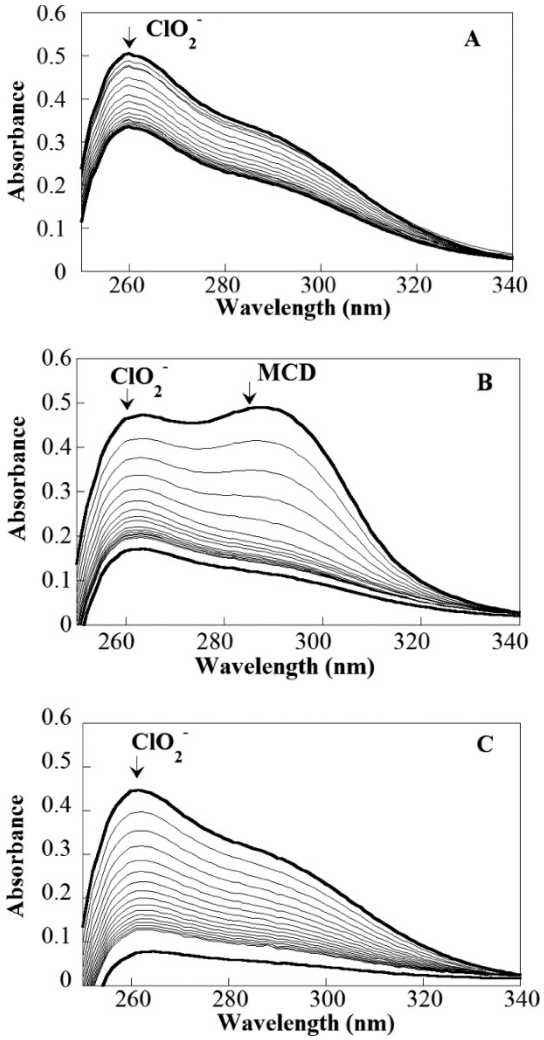

Figure 2.7. Chlorite decomposition is enhanced by the presence of (H)OCl trapping agents. A) An inhibitory concentration of ClO_2^- (3 mM) was added to a catalytic amount (0.1 μM) of *Kp*Cld (0.1 M citrate-phosphate, pH 6.6). Spectra were measured every 30 s (gray lines) until the reaction went to completion (black lines: t = 0 and 30 min). 36% of the initially present ClO_2^- decomposed without the appearance of ClO_2. B) In the presence of 50 μM MCD and the same amount of ClO_2^-, the turnover number more than doubles. MCD's chromophore disappears, consistent with conversion to the chlorinated product DCD. C) Colorless DMSO, used as a HOCl-specific trap, enhances ClO_2^- turnover to a similar extent.

To distinguish definitively between HOCl or ClO_2 as the MCD-reactive species, dimethylsulfoxide (DMSO) was assayed for its ability to enhance turnover. DMSO has previously been used as a highly selective trapping agent for HOCl in aqueous mixtures of ClO_2/ClO_2^-.[46] Neutral HOCl is the reactive species ($HOCl \rightleftharpoons OCl^- + H^+$, $pK_a = 7.5$), serving as an electrophilic oxidant via transfer of OH^+ to a nucleophilic acceptor substrate (here, the lone

pair of electrons on the sulfoxide).[46] When the *Kp*Cld/ClO_2^- reaction shown in Figure 2.7A was monitored in the presence of 50 μM DMSO (Figure 2.7C), the reaction proceeded rapidly and nearly to completion (86±7%; (1.6± 0.2×10^4 turnovers per heme). This strongly suggested that HOCl and not •ClO_2 is released from *Kp*Cld during turnover with ClO_2^-. The results in Figure 2.6A-B are moreover consistent with the measured turnover number for chlorite and expected increases in turnover afforded by MCD (Figure 2.6), and they support the conclusion that MCD's protective function is due to its reaction with HOCl.

2.4.7. Hypochlorous acid avidly degrades *Kp*Cld's heme.

To quantify the influence of chlorite-derived HOCl on heme degradation, the effect of exogenously added NaOCl on the heme spectrum was measured titrimetrically at pH 6.6, where it is expected to equilibrate rapidly to form HOCl. The spectrum diminished to baseline following addition of (800±20) eq of NaOCl (Figure A5), versus (6.0±0.3)×10^3 eq of ClO_2^- (Figure 2.3A). If HOCl alone were responsible for catalytic inactivation, this would suggest that approximately 1 in 8 turnovers would lead to HOCl rather than O_2 during catalysis of ClO_2^-. This number is likely an upper estimate, since the Fe(IV)=O Por▪+ generated concomitantly with OCl^- (Scheme 2.1) would also likely lead to protein damage in the absence of a reductant.

The measurements examining heme and catalytic stability above (Figures 2.6 and 2.7) were carried out at a single pH (6.6). However, both the enzyme and the HOCl suicide reactant are known to undergo pH-dependent transitions. Second order rate constants for the heme/NaOCl reaction (k) were therefore measured 1.5 pH units below and 0.5 above the HOCl/OCl^- pK_a of 7.5 in order to assess which is the more likely reactive form. Heme decomposition was an order of magnitude faster in the presence of HOCl (pH 6, k = 0.13 $M^{-1}s^{-1}$) rather than OCl^- (pH 8, k = 0.010 $M^{-1}s^{-1}$) (Figure A6). However, the spin state of the heme also

clearly undergoes changes from HS to LS within this pH range (Figures 2.3 and 2.4). Changes in the heme electronic state could therefore also contribute to these differences in reaction rate.

2.4.8. Measurement of MICs.

K. pneumoniae exhibits substantial ClO_4^- and ClO_3^- tolerance under aerobic conditions, withstanding concentrations ≥100 mM without significant growth defects. It is much more strongly affected by ClO_2^-. No growth was observed even at 20 mM $NaClO_2$, the lowest concentration tested. The mechanism of toxicity of ClO_2^- administered in the extracellular environment of bacteria has not been described. Lipid epoxidation, protein unfolding, and amino acid side chain modifications have all been observed in the presence of (H)OCl, and could occur in the presence of ClO_2^-.[47] However, the $ClO_2^-/HClO_2$ pK_a (1.8) is significantly lower than for $OCl^-/HOCl$.[48-49] Hence, chlorite and not chlorous acid is expected to predominate under biological conditions, where its negative charge should bar its passive entry into cells. Consistent with an expected extracytoplasmic mechanism of toxicity, ClO_2^- is equally toxic to cells possessing *Kp*Cld in the cytoplasm and those in which it is absent.

We hypothesized that ClO_3^- could be more toxic to *K. pneumoniae* that is actively reducing NO_3^- as a respiratory substrate. Consistent with that hypothesis, WT *K. pneumoniae* appears to become sensitized specifically to ClO_3^- (not ClO_4^- or ClO_2^-) under nitrate-respiring conditions (anaerobic, 50 mM KNO_3) exhibiting an MIC near 70 mM (Table 2.1). This shifts to 60 mM for the Δ*cld* mutant. These results suggest that *K. pneumoniae* metabolizes ClO_3^- under these conditions, and that *Kp*Cld affords some protection against ClO_2^- produced endogenously from ClO_3^-. By contrast, ClO_4^- has no effect (up to 80 mM) on either the WT or Δ*cld* mutant strains of *K. pneumoniae*, under either aerobic or nitrate-respiring conditions. These results collectively suggest that ClO_4^- is not incorporated and/or metabolized by *K. pneumoniae*.

Table 2.1. Determination of ClO_3^- MICs for WT and Δ*cld K. pneumoniae* MGH under aerobic and nitrate-respiring conditions. All cultures were grown in the presence of 50 mM added KNO_3. Legend: (++) robust growth; (+) minor growth; (–) no observable growth.

	WT		Δ*cld*	
$[ClO_3^-]$ (mM)	Aerobic	Anaerobic	Aerobic	Anaerobic
30	++	++	++	++
40	++	++	++	+
50	++	++	++	+
60	++	+	++	−
70	++	+	++	−
80	++	−	++	−
100	++	−	++	−

2.5. Discussion

Chlorite dismutases are a family of heme-binding proteins catalyzing steps in biological processes as divergent as perchlorate respiration and heme biosynthesis. Genetic and biological evidence has pointed toward a third, functionally distinct subgroup of the Cld family (Figure 2.2), members of which are found in diverse Gram-negative bacteria including many obligate pathogens.[11, 50] These bacteria are not known to respire (per)chlorate, nor do they lack any of the canonical genes required for making heme.[51] Their Cld proteins nonetheless share an almost identical active site with the respiration-associated Clds, though the overall monomer structure and oligomerization state differ. The biological role and distinct molecular features of this subgroup have been examined here, through biochemical investigation of *Kp*Cld and phenotypic characterization of the corresponding gene knock-out in a pathogenic strain of *Klebsiella pneumoniae* (MGH 78578).

The Δ*cld* strain of *K. pneumoniae* had neither a growth defect nor any obvious sign of impaired heme metabolism. This contrasts sharply with the Δ*cld* strain of *Staphylococcus aureus*, a slow-growing small colony variant with global deficiencies in its cellular heme

levels.[14] We therefore investigated the hypothesis that the *cld* acts as an antioxidant toward chlorite or a related chlorine oxoanion. It was discovered that WT *K. pneumoniae* gains a noticeable growth advantage over its Δ*cld* counterpart in the presence of ClO_3^-. This advantage is observed specifically under anaerobic, nitrate-respiring conditions (Table 2.1), even though *K. pneumoniae* does not have a dissimilatory reductase for either ClO_4^- or ClO_3^-, nor have these anions been shown to support anaerobic growth. It has been suggested that ClO_3^- might be taken up and metabolized by widespread bacterial nitrate-associated pathways.[52-53] Catalytic reduction of ClO_3^- could be catalyzed by nitrate reductases due to the favorable reduction potential and kinetic lability of ClO_3^- relative to ClO_4^-; indeed, some nitrate reductases have been shown to accept ClO_3^- as a substrate *in vitro*.[54-55] The product ClO_2^-, trapped inside the cell due to its charge, would be expected to quickly reach toxic levels if not enzymatically removed.[2] Hence, the Cld acts as an antioxidant against the ClO_2^- generated endogenously from ClO_3^-.

Such an antioxidant function, even in the absence of ClO_4^- or ClO_3^- respiration, is consistent with both the catalytic properties of *Kp*Cld and the potent toxicity of ClO_2^-. Like superoxide dismutase or catalase, antioxidant enzymes against reduced oxygen species, *Kp*Cld is relatively fast (k_{cat} = [1.9 ±0.2]×10^3 s^{-1}, k_{cat}/K_M = [2.5± 0.4]×10^6 $M^{-1}s^{-1}$, 25 °C, pH 5). This suggests that it may effectively out-compete reactions between ClO_2^- and reactive intra- or extracellular components. Potential targets of ClO_2^- mediated damage are not as well characterized as those of HOCl.[47] However, ClO_2^- is known to act as an oxygen-atom donor toward heme Fe(III) and reactive double bonds, as well as a source of highly-reactive •ClO_2 and HOCl[43-44, 56] These properties support its industrial use as a microbicide and bleach.[57]

*Kp*Cld's reactivity toward ClO_2^-, while rapid, is limited by the instability of the heme cofactor in the presence of its strongly oxidizing substrate. The heme spectrum and catalytic

activity are completely eliminated by exposure to roughly 6,000 eq of ClO_2^- (Figure 2.6). The turnover number is enhanced by the inclusion of sacrifical reductants or chlorination traps in the reaction mixture, including DMSO: a reagent which combines rapidly and specifically with HOCl.[46] This strongly suggests that OCl^-, generated along with Fe^{IV}=O $Por^{\bullet+}$ from the heterolytic cleavage of the O–ClO^- bond (Scheme 2.1), is partially responsible for loss of the heme and its associated catalytic activity. This is consistent with recently reported results for a respiratory-type Cld from *N. defluvii* (discussed further below).[43]

The results also indirectly support the mechanism for O_2 generation proposed in Scheme 2.1, wherein the OCl^- leaving group recombines with the Fe(IV)=O $Por^{\bullet+}$ to produce O_2 and Cl^-. Kinetic sluggishness in the recombination would create the opportunity for release of OCl^-. Thus, the role of the arginine likely involves both steering the OCl^- leaving group and maintaining it in its more nucleophilic, anionic form, thereby mechanistically favoring the O–O bond forming reaction, as illustrated in Scheme 2.1. Evidence in support of this model is found in the sensitivity of Clds lacking the distal Arg to oxidative conditions. For example, the Cld from *S. aureus*, which contains a glutamine at the homologous position, undergoes complete beaching of the heme following exposure to only 5 equivalences of ClO_2^-.[14] By the same token, substitution of the arginine in the *N. defluvii* Cld with a neutral residue strongly sensitizes its heme toward oxidant-mediated degradation.[43]

Yet, while HOCl is readily observed during chlorite turnover with *Kp*Cld, no MCD-trappable HOCl was detectable for *Da*Cld under conditions similar to those used here (Figure A7).[3] *Da*Cld is at the same time significantly less prone to catalytic inactivation (20,000 turnovers versus 6,000) and (H)OCl loss (Figure 2.6).[3-4] Hence, in spite of their shared O_2-evolving activity and conserved active site residues, including the distal Arg, the heme

environment in dimeric *Kp*Cld and its pentameric *Da*Cld counterpart must be in some ways distinct.

The best insight into the nature of these distinctions comes from spectroscopic analysis of *Da*Cld and *Kp*Cld, which provides a nuanced view of the heme environment. First, it is clear from both EPR and rR that *Kp*Cld and *Da*Cld are different. The occurrence of a single axial ferric high-spin signal in the EPR spectrum of *Kp*Cld at pH < 8.0 strongly contrasts with *Da*Cld, which exhibits two rhombically distorted ferric EPR signals. In fact, among the few Clds for which the ferric EPR spectra have been reported so far, only *Nw*Cld shows the same axial signal as *Kp*Cld.[40] While the rR spectra of *Da*Cld and *Kp*Cld at pH 6 indicate high spin heme, the enzymes differ in coordination state with *Da*Cld being 5c and *Kp*Cld having a significant population of 6c heme. Second, both EPR and rR spectra are consistent with water as the sixth ligand in *Kp*Cld at neutral pH. Increased access of water to the active site pocket in *Kp*Cld relative to *Da*Cld is suggested by the crystal structures of these two enzymes (Figure 2.8).

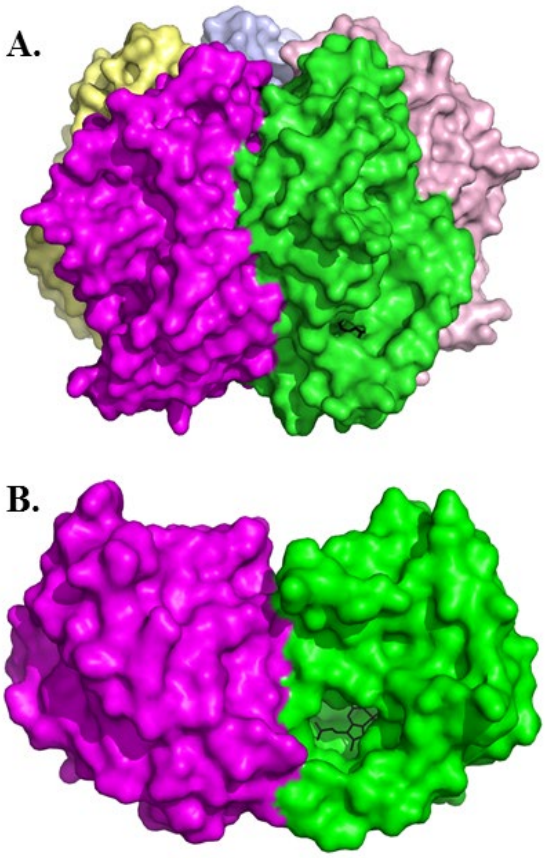

Figure 2.8. Surface rendering of *Nw*Cld and *Da*Cld in their expected native oligomerization states, showing differences in the entryway leading to the heme. A) *Da*Cld pentamer (3Q08). B) *Nw*Cld dimer (3QPI). The monomers are rendered in different colors and the hemes in the green monomers shown in black sticks. The tunnel leading from the surface to the heme is more open in *Nw*Cld than in *Da*Cld. Figures generated by PyMol (www.pymol.com).

Functionally, a more open catalytic pocket could explain the postulated lower fidelity in the recombination of Fe(IV)=O $Por^{\bullet+}$ with OCl^-, leading to a lower turnover number and higher frequency of HOCl escape in *Kp*Cld (Figure 2.8). The Cld from *N. defluvii* shares spectral features with *Kp*Cld that are consistent with a more solvated distal pocket.[11] It likewise produces readily trappable HOCl during turnover with ClO_2^-,[43] and the EPR spectrum of its bound heme becomes undetectable after exposure to roughly 3,000 eq of ClO_2^-. Third, EPR characterization of mutants positioned within hydrogen-bonding distance of the heme propionates (Y118F in *Da*Cld, Y62F in *Kp*Cld), or within the second coordination sphere of the heme (W227 and W156

in *Da*Cld, W96 in *Kp*Cld) clearly indicates that both direct and indirect interactions influence the electronic structure of the heme. The fact that some of these (W227) are conserved only in the respiratory Clds suggests that they could contribute to the unique functional characteristics of those enzymes. Finally, the absence of second-sphere nitrogenous ligands that could explain the spin-switch observed in frozen solution at pH 8 (85% conversion of high-spin to low spin of the ferric EPR signal, see Figure 2.4) strongly argues for a repositioning of the guanidinium group of the distal side Arg in concert with formation of the Cld−OH complex and/or changes in hydrogen bonding interactions to the heme propionates. Effects of these kinds were reported for cytochrome *c* peroxidase, in relation to the formation of the ferryl-oxo intermediate.[58]

The relatively less robust heme in *Kp*Cld and potentially other proteins in this clade is consistent with a biological role in providing intermittent protection against environmental ClO_3^-. The same may perhaps be true of the *N. defluvii* Cld which, though pentameric in structure like *Da*Cld and the other respiratory Clds (Figure 2.1, red), is extraordinary for being found within a species that is both non-perchlorate or -chlorate respiring and phylogenetically distinct from any known respirers.[12] The gene's presence in this organism appears to be the result of lateral transfer; hence, like *Kp*Cld, it may provide protection against environmental chlorate that is metabolized via nitrate-reducing pathways.

Of course, a chlorate-directed antioxidant role for *Kp*Cld and related enzymes (Figure 2.1, green) depends on the availability of ClO_3^- in the natural environment. ClO_4^- is used as an oxidant and propellant for rockets and fireworks, while chlorate is a common constituent of herbicides.[59] Because of their pervasive industrial use and the lack of a known geochemical mechanism for their formation, perchlorate and chlorate have long been thought to be largely unnatural in origin. However, the discovery of widespread perchlorate in pristine ground waters,

ice cores, and undisturbed deserts prompted deeper investigation into its natural sources.[60-62] Potentially ancient atmospheric mechanisms for the generation of both ClO_4^- and ClO_3^- are now favored on Earth and on Mars, where abundant ClO_4^- has been discovered.[63-68] Hence, Clds of the *Kp*Cld subtype may presently play an unaccounted-for role in Earth's chlorine cycle, and could have done so for some time. It is likewise possible that they could serve a similar role against other halogen oxide species (e.g., iodate) that are especially abundant in non-terrestrial environments such as the open ocean.[16, 69-70]

2.6. Associated Content

Additional data referred to in the text are in Appendix A: Figures A1 to A7 and Tables A1 to A2.

2.7. Funding Sources

Support is gratefully acknowledged from the National Institutes of Health grants R01GM090260 (to J.D.), GM094039 (to G. L.-R.), AI072719 (to K. R. R) and from the French CNRS (UMR 8221) and CEA-Saclay (to A.I.).

2.8. Acknowledgments

Dr. Thomas Chen is thanked for the generation of the *Kp*Cld Y62F and W97F mutants, as well as preliminary work related to but eventually not published as part of this manuscript. Dr. Béatrice Blanc is thanked for generating the *Da*Cld W227F, W155F, and W156F mutants used in this work. Garrett Moraski is thanked for helpful discussions.

2.9. References

1. Tagore, R.; Crabtree, R. H.; Brudvig, G. W., Oxygen evolution catalysis by a dimanganese complex and its relation to photosynthetic water oxidation. *Inorg. Chem.* 2008, *47*, 1815.
2. Coates, J. D.; Achenbach, L. A., Microbial perchlorate reduction: Rocket-fuelled metabolism. *Nat. Rev. Microbiol.* 2004, *2*, 569.

3. Streit, B. R.; DuBois, J. L., Chemical and steady state kinetic analyses of a heterologously expressed heme dependent chlorite dismutase. *Biochemistry* 2008, *47*, 5271.
4. Lee, A. Q.; Streit, B. R.; Zdilla, M. J.; Abu-Omar, M. M.; DuBois, J. L., Mechanism of and exquisite selectivity for O-O bond formation by the heme-dependent chlorite dismutase. *Proc. Natl. Acad. Sci. U.S.A.* 2008, *105*, 15654.
5. Streit, B. R.; Blanc, B.; Lukat-Rodgers, G. S.; Rodgers, K. R.; DuBois, J. L., How active-site protonation state influences the reactivity and ligation of the heme in chlorite dismutase. *J. Am. Chem. Soc.* 2010, *132*, 5711.
6. Mayfield, J. A.; Blanc, B.; Rodgers, K. R.; Lukat-Rodgers, G. S.; DuBois, J. L., Peroxidase-type reactions suggest a heterolytic/nucleophilic O-O joining mechanism in the heme-dependent chlorite dismutase. *Biochemistry* 2013, *52*, 6982.
7. DuBois, J. L.; Kroneck, P. M. H.; Sosa-Torres, M. E.; Sigel, A.; Sigel, H.; Sigel, R. K. O., *The Metal-Driven Biogeochemistry of Gaseous Compounds in the Environment*. 2014.
8. Goblirsch, B. R.; Streit, B. R.; DuBois, J. L.; Wilmot, C. M., Structural features promoting dioxygen production by Dechloromonas aromatica chlorite dismutase. *JBIC, J. Biol. Inorg. Chem.* 2010, *15*, 879.
9. de Geus, D. C.; Thomassen, E. A. J.; Hagedoorn, P. L.; Pannu, N. S.; van Duijn, E.; Abrahams, J. P., Crystal structure of chlorite dismutase, a detoxifying enzyme producing molecular oxygen. *J. Mol. Biol.* 2009, *387*, 192.
10. Kostan, J.; Sjoeblom, B.; Maixner, F.; Mlynek, G.; Furtmueller, P. G.; Obinger, C.; Wagner, M.; Daims, H.; Djinovic-Carugo, K., Structural and functional characterisation of the chlorite dismutase from the nitrite-oxidizing bacterium "Candidatus Nitrospira defluvii": Identification of a catalytically important amino acid residue. *J. Struct. Biol.* 2010, *172*, 331.
11. Mlynek, G.; Sjoeblom, B.; Kostan, J.; Fuereder, S.; Maixner, F.; Gysel, K.; Furtmueller, P. G.; Obinger, C.; Wagner, M.; Daims, H.; Djinovic-Carugo, K., Unexpected diversity of chlorite dismutases: A catalytically efficient dimeric enzyme from Nitrobacter winogradsky. *J. Bacteriol.* 2011, *193*, 2408.
12. Maixner, F.; Wagner, M.; Luecker, S.; Pelletier, E.; Schmitz-Esser, S.; Hace, K.; Spieck, E.; Konrat, R.; Le Paslier, D.; Daims, H., Environmental genomics reveals a functional chlorite dismutase in the nitrite-oxidizing bacterium 'Candidatus Nitrospira defluvii'. *Environ. Microbiol.* 2008, *10*, 3043.
13. Goblirsch, B.; Kurker, R. C.; Streit, B. R.; Wilmot, C. M.; DuBois, J. L., Chlorite dismutases, DyPs, and EfeB: 3 Microbial heme enzyme families comprise the CDE structural superfamily. *J. Mol. Biol.* 2011, *408*, 379.
14. Mayfield, J. A.; Hammer, N. D.; Kurker, R. C.; Chen, T. K.; Ojha, S.; Skaar, E. P.; DuBois, J. L., The chlorite dismutase (HemQ) from Staphylococcus aureus has a redox-sensitive heme and is associated with the small colony variant phenotype. *J. Biol. Chem.* 2013, *288*, 23488.
15. Dailey, T. A.; Boynton, T. O.; Albetel, A. N.; Gerdes, S.; Johnson, M. K.; Dailey, H. A., Discovery and characterization of HemQ an essential heme biosynthetic component. *J. Biol. Chem.* 2010, *285*, 25978.
16. Tamura, K.; Stecher, G.; Peterson, D.; Filipski, A.; Kumar, S., MEGA6: Molecular Evolutionary Genetics Analysis version 6.0. *Mol. Biol. Evol.* 2013, *30*, 2725.

17. Melnyk, R. A.; Engelbrektson, A.; Clark, I. C.; Carlson, H. K.; Byrne-Bailey, K.; Coates, J. D., Identification of a perchlorate reduction genomic island with novel regulatory and metabolic genes. *Appl. Environ. Microbiol.* 2011, *77*, 7401.
18. Wisplinghoff, H.; Bischoff, T.; Tallent, S. M.; Seifert, H.; Wenzel, R. P.; Edmond, M. B., Nosocomial bloodstream infections in US hospitals: Analysis of 24,179 cases from a prospective nationwide surveillance study. *Clin. Infect. Dis.* 2004, *39*, 309.
19. Fabian, I.; Gordon, G., Complex-formation reactions of the chlorite ion. *Inorg. Chem.* 1991, *30*, 3785.
20. Manoj, K. M.; Hager, L. P., A colorimetric method for detection and quantification of chlorinating activity of hemeperoxidases. *Anal. Biochem.* 2006, *348*, 84.
21. Jeffery, G. H.; Bassett, J.; Mendham, J.; Denney, R. C., *Vogel's Textbook of Quantitative Chemical Analysis*. 1989; Vol. 5.
22. Zhang, Y.; Jiang, X.; Wang, Y.; Li, G.; Tian, Y.; Liu, H.; Ai, F.; Ma, Y.; Wang, B.; Ruan, F.; Rajakumar, K., Contribution of β-lactamases and porin proteins OmpK35 and OmpK36 to carbapenem resistance in clinical isolates of KPC-2-producing Klebsiella pneumoniae. *Antimicrob. Agents Chemother.* 2014, *58*, 1214.
23. Chaveroche, M.; Ghigo, J.; d'Enfert, C., A rapid method for efficient gene replacement in the filamentous fungus Aspergillus nidulans. *Nucleic Acids Res.* 2000, *28*, e97.
24. Andrews, J., Determination of minimum inhibitory concentrations. *J. Antimicrob. Chemother.* 2001, *48*, 5.
25. Blanc, B.; Rodgers, K. R.; Lukat-Rodgers, G. S.; DuBois, J. L., Understanding the roles of strictly conserved tryptophan residues in O2 producing chlorite dismutases. *Dalton Trans.* 2013, *42*, 3156.
26. Berry, E. A.; Trumpower, B. L., Simultaneous determination of hemes a, b, and c from pyridine hemocrome spectra. *Anal. Biochem.* 1987, *161*, 1.
27. Silverman, R. B., Mechanism based enzyme inactivators. *Methods Enzymol.* 1995, *249*, 240.
28. Hagedoorn, P. L.; de Geus, D. C.; Hagen, W. R., Spectroscopic characterization and ligand-binding properties of chlorite dismutase from the chlorate respiring bacterial strain GR-1. *Eur. J. Biochem.* 2002, *269*, 4905.
29. Stenklo, K.; Thorell, H. D.; Bergius, H.; Aasa, R.; Nilsson, T., Chlorite dismutase from Ideonella dechloratans. *JBIC, J. Biol. Inorg. Chem.* 2001, *6*, 601.
30. Bellelli, A.; Antonini, G.; Brunori, M.; Springer, B. A.; Sligar, S. G., Transient spectroscopy of the reaction of cyanide with ferrous myoglobin: Effect of distal side residues. *J. Biol. Chem.* 1990, *265*, 18898.
31. Chu, G. C.; Tomita, T.; Sonnichsen, F. D.; Yoshida, T.; Ikeda-Saito, M., The heme complex of HmuO, a bacterial heme degradation enzyme from Corynebacterium diphtheriae: Structure of the catalytic site. *J. Biol. Chem.* 1999, *274*, 24490.
32. Smulevich, G.; Neri, F.; Marzocchi, M.; Welinder, K., Versatility of heme coordination demonstrated in a fungal peroxidase. Absorption and resonance Raman studies of Coprinus cinereus peroxidase and the Asp245 → Asn mutant at various pH values. *Biochemistry* 1996, *35*, 10576.
33. Asher, S. A.; Schuster, T. M., Resonance Raman examination of axial ligand bonding and spin-state equilibria in metmyoglobin hydroxide and other heme derivatives. *Biochemistry* 1979, *18*, 5377.

34. Feis, A.; Marzocchi, M. P.; Paoli, M.; Smulevich, G., Spin state and axial ligand bonding in the hydroxide complexes of metmyoglobin, methemoglobin, and horseradish-peroxidase at room and low-temperatures. *Biochemistry* 1994, *33*, 4577.
35. Yeh, S. R.; Couture, M.; Ouellet, Y.; Guertin, M.; Rousseau, D. L., A cooperative oxygen finding hemoglobin from Mycobacterium tuberculosis: Stabilization of heme ligands by a distal tyrosine residue. *J. Biol. Chem.* 2000, *275*, 1679.
36. Lukat-Rodgers, G. S.; Rodgers, K. R., Spin-state equilibria and axial ligand bonding in FixL hydroxide: A resonance Raman study. *JBIC, J. Biol. Inorg. Chem.* 1998, *3*, 274.
37. Colin, J.; Wiseman, B.; Switala, J.; Loewen, P.; Ivancich, A., Distinct role of specific tryptophans in facilitating electron transfer or as [Fe(IV)═O Trp•] intermediates in the peroxidase reaction of Bulkholderia pseudomallei catalase-peroxidase: A multifrequency EPR spectroscopy investigation. *J. Am. Chem. Soc.* 2009, *131*, 8557.
38. Deemagarn, T.; Wiseman, B.; Carpena, X.; Ivancich, A.; Fita, I.; Loewen, P., Two alternative substrate paths for compound I formation and reduction in catalase-peroxidase KatG from Burkholderia pseudomallei. *Proteins: Struct., Funct., Bioinf.* 2007, *66*, 219.
39. Blanc, B.; Mayfield, J. A.; McDonald, C. A.; Lukat-Rodgers, G. S.; Rodgers, K. R.; DuBois, J. L., Understanding how the distal environment directs reactivity in chlorite dismutase: Spectroscopy and reactivity of Arg183 mutants. *Biochemistry* 2012, *51*, 1895.
40. Singh, R.; Switala, J.; Loewen, P. C.; Ivancich, A., Two [Fe(IV)═O Trp*] intermediates in M. tuberculosis catalase-peroxidase discriminated by multifrequency (9–285 GHz) EPR spectroscopy: Reactivity toward isoniazid. *J. Am. Chem. Soc.* 2007, *129*, 15954.
41. Hofbauer, S.; Bellei, M.; Sundermann, A.; Pirker, K.; Hagmuller, A.; Mlynek, G.; Kostan, J.; Daims, H.; Furtmuller, P.; Djinovic-Carugo, K.; Oostenbrink, C.; Battistuzzi, G.; Obinger, C., Redox thermodynamics of high-spin and low-spin forms of chlorite dismutases with diverse subunit and oligomeric structures. *Biochemistry* 2012, *51*, 9501.
42. Silverman, R. B., *Mechanism-Based Enzyme Inactivation: Chemistry and Enzymology*. 1988; Vol. I.
43. Hofbauer, S.; Gruber, C.; Pirker, K.; Sundermann, A.; Schaffner, I.; Jakopitsch, C.; Oostenbrink, C.; Furtmuller, P.; Obinger, C., Transiently produced hypochlorite is responsible for the irreversible inhibition of chlorite dismutase. *Biochemistry* 2014, *53*, 3145.
44. Jakopitsch, C.; Pirker, K.; Flemmig, J.; Hofbauer, S.; Schlorke, D.; Furtmuller, P.; Arnhold, J.; Obinger, C., Mechanism of reaction of chlorite with mammalian heme peroxidases. *J. Inorg. Biochem.* 2014, *135*, 10.
45. Shahangian, S.; Hager, L. P., The reaction of chloroperoxidase with chlorite and chlorine dioxide. *J. Biol. Chem.* 1981, *256*, 6034.
46. Lehtimaa, T.; Kuitunen, S.; Tarvo, V.; Vuorinen, T., Kinetics of aldehyde oxidation by chlorous acid. *Ind. Eng. Chem. Res.* 2010, *49*, 2688.
47. Winter, J.; Ilbert, M.; Graf, P. C. F.; Oezcelik, D.; Jakob, U., Bleach activates a redox-regulated chaperone by oxidative protein unfolding. *Cell* 2008, *135*, 691.
48. Shriver, D.; Atkins, P., *Inorganic Chemistry*. 2009; p 830.
49. Panek, H.; O'Brian, M. R., A whole genome view of prokaryotic haem biosynthesis. *Microbiology (Reading, U.K.)* 2002, *148*, 2273.
50. Clark, I. C.; Melnyk, R. A.; Engelbrektson, A.; Coates, J. D., Structure and evolution of chlorate reduction composite transposons. *MBio* 2013, *4*, e00379-13.

51. Parsonage, D.; Ferguson, S., Reassessment of pathways of electron flow to nitrate reductase that are coupled to energy-conservation in Paracoccus denitrificans. *FEBS Lett.* 1983, *153*, 108.
52. Stewart, V., Nitrate respiration in relation to facultative metabolism in enterobacteria. *Microbiol. Rev.* 1988, *52*, 190.
53. Yoshimatsu, K.; Sakurai, T.; Fujiwara, T., Purification and characterization of dissimilatory nitrate reductase from a denitrifying halophilic archaeon, Haloarcula marismortui. *FEBS Lett.* 2000, *470*, 216.
54. Afshar, S.; Johnson, E.; de Vries, S.; Schroder, I., Properties of a thermostable nitrate reductase from the hyperthermophilic archaeon Pyrobaculum aerophilum. *J. Bacteriol.* 2001, *183*, 5491.
55. Jakopitsch, C.; Spalteholz, H.; Fürtmuller, P. G.; Arnhold, J.; Obinger, C., Mechanism of reaction of horseradish peroxidase with chlorite and chlorine dioxide. *J. Inorg. Biochem.* 2008, *102*, 293.
56. Richardson, S. D., Disinfection by-products and other emerging contaminants in drinking water. *Trends Anal. Chem.* 2003, *22*, 666.
57. Bonagura, C. A.; Bhaskar, B.; Shimizu, H.; Li, H. Y.; Sundaramoorthy, M.; McRee, D. E.; Goodin, D. B.; Poulos, T. L., High-resolution crystal structures and spectroscopy of native and compound I cytochrome c peroxidase. *Biochemistry* 2003, *42*, 5600.
58. Urbansky, E. T., Perchlorate chemistry: Implications for analysis and remediation. *Biorem. J.* 1998, *2*, 81.
59. Rao, B.; Anderson, T.; Orris, G.; Rainwater, K.; Rajagopalan, S.; Sandvig, R.; Scanlon, B.; Stonestrom, D.; Walvoord, M.; Jackson, W., Widespread natural perchlorate in unsaturated zones of the southwest United States. *Environ. Sci. Technol.* 2007, *41*, 4522.
60. Scanlon, B. R.; Reedy, R. C.; Jackson, W. A.; Rao, B., Mobilization of naturally occurring perchlorate related to land-use change in the southern high plains, Texas. *Environ. Sci. Technol.* 2008, *42*, 8648.
61. Furdui, V. I.; Tomassini, F., Trends and sources of perchlorate in arctic snow. *Environ. Sci. Technol.* 2010, *44*, 588.
62. Rao, B. A.; Wake, C. P.; Anderson, T.; Jackson, W. A., Perchlorate depositional history as recorded in North American ice cores from the Eclipse Icefield, Canada, and the Upper Fremont Glacier, USA. *Water, Air, Soil Pollut.* 2012, *223*, 181.
63. Rao, B.; Mohan, S.; Neuber, A.; Jackson, W. A., Production of perchlorate by laboratory simulated lightning process. *Water, Air, Soil Pollut.* 2012, *223*, 275.
64. Catling, D.; Claire, M.; Zahnle, K.; Quinn, R.; Clark, B.; Hecht, M.; Kounaves, S., Atmospheric origins of perchlorate on Mars and in the Atacama. *J. Geophys. Res.: Planets* 2010, *115*, E00E11.
65. Kounaves, S.; Carrier, B.; O'Neil, G.; Stroble, S.; Claire, M., Evidence of martian perchlorate, chlorate, and nitrate in Mars meteorite EETA79001: Implications for oxidants and organics. *Icarus* 2014, *229*, 206.
66. Hecht, M. H.; Kounaves, S. P.; Quinn, R. C.; West, S. J.; Young, S. M. M.; Ming, D. W.; Catling, D. C.; Clark, B. C.; Boynton, W. V.; Hoffman, J.; DeFlores, L. P.; Gospodinova, K.; Kapit, J.; Smith, P. H., Detection of perchlorate and the soluble chemistry of Martian soil at the Phoenix Lander site. *Science* 2009, *325*, 64.
67. Balaji Rao, B. R.; Hatzinger, P. B.; Bohlke, J. K.; Sturchio, N. C.; Andraski, B. J.; Eckardt, F. D.; Jackson, W. A., Natural chlorate in the environment: Application of a new

IC-ESI/MS/MS method with a Cl18O3-internal standard. *Environ. Sci. Technol.* 2010, *44*, 8429.
68. Lu, Z.; Jenkyns, H.; Rickaby, R., Iodine to calcium ratios in marine carbonate as a paleo-redox proxy during oceanic anoxic events. *Geology* 2010, *38*, 1107.
69. Xu, S.; Xie, Z.; Li, B.; Liu, W.; Sun, L.; Kang, H.; Yang, H.; Zhang, P., Iodine speciation in marine aerosols along a 15000-km round-trip cruise path from Shanghai, China, to the Arctic Ocean. *Environ. Chem.* 2010, *7*, 406.
70. Le, S. Q.; Dang, C. C.; Gascuel, O., Modeling protein evolution with several amino acid replacement matrices depending on site rates. *Mol. Biol. Evol.* 2012, *29*, 2921.

3. ACTIVE SITES OF O_2-EVOLVING CHLORITE DISMUTASES PROBED BY HALIDES, HYDROXIDES AND NEW IRON-LIGAND VIBRATIONAL CORRELATIONS[2]

3.1. Abstract

O_2-evolving chlorite dismutases (Clds) fall into two clades, which efficiently convert ClO_2^- to O_2 and Cl^-. The Cld from *Dechloromonas aromatica* (*Da*Cld) represents the chlorite-decomposing homopentameric enzymes found in perchlorate and chlorate respiring bacteria. The Cld from the Gram-negative, human pathogen *Klebsiella pneumoniae* (*Kp*Cld) is representative of the second clade, comprising homodimeric enzymes having truncated N-termini. Here steric and nonbonding properties of the *Da*Cld and *Kp*Cld active sites have been probed via kinetic, thermodynamic and spectroscopic behaviors of their fluorides, chlorides and hydroxides. Cooperative Cl^- binding to *Kp*Cld drives formation of a hexacoordinate, high-spin aqua heme, whereas *Da*Cld remains pentacoordinate and high-spin under analogous conditions. Fluoride coordinates to the heme iron in *Kp*Cld and *Da*Cld, exhibiting $\nu(Fe^{III}–F)$ bands at 385 and 390 cm^{-1}, respectively. Correlation of these frequencies with their CT1 energies reveals strong H-bond-donation to the F^- ligand, indicating that atoms directly coordinated to heme iron are accessible by distal H-bond donation. New vibrational frequency correlations between either $\nu(Fe^{III}–F)$ or $\nu(Fe^{III}–OH)$ and $\nu(Fe^{II}–His)$ of Clds and other heme proteins are reported. These correlations orthogonalize proximal and distal effects on the bonding between iron and

[2]The material in this chapter is from a manuscript published in the journal Biochemistry (https://doi.org/10.1021/acs.biochem.7b00572) co-authored by Zachary Geeraerts, Kenton R. Rodgers, Jennifer L. DuBois, and Gudrun S. Lukat-Rodgers. Zachary Geeraerts had primary responsibility in isolating, characterizing complexes by resonance Raman and UV/Visible absorbance spectroscopies, determining oligomeric states, and measuring specific activity for oxygen evolution in the presence of various ligands of *Kp*Cld and *Da*Cld. His responsibilities also include data analysis, interpretation, figure-making, and writing each section with guidance from the corresponding authors.

exogenous π-donor ligands. The axial Fe−X vibrations and the relationships between them illuminate both similarities and differences in the H-bonding and electrostatic properties of the distal and proximal heme environments in pentameric and dimeric Clds. Moreover, they provide general insight into the structural basis of reactivity toward substrates in heme-dependent enzymes and their mechanistic intermediates, especially those containing the ferryl moiety.

3.2. Introduction

The formation of an O–O bond is achieved in a unique manner by chlorite dismutases (Clds) that rapidly and efficiently catalyze the decomposition of a single chlorite ion (ClO_2^-) to O_2 and Cl^-.[1-2] Clds are soluble enzymes containing heme *b*, the sole cofactor required for catalyzing its O–O bond-forming reaction. The simplicity of this system derives from its intramolecular redox nature, which does not require coupling to a proton pump. This is in sharp contrast to the complexity of O_2 production, in the water-splitting reaction catalyzed by the tetramanganese center in the oxygen-evolving complex of photosystem II (PSII), a key step in the pathway for photosynthetic fixation of CO_2 into carbohydrates.[3]

Clds have been identified in almost all bacterial phyla and in many archaea. However, the vast majority of them occur in organisms that do not utilize perchlorate as a respiratory oxidant.[4-5] Three major subdivisions of the Cld protein family have been identified in phylogentic studies.[6-10] Two of the clades, referred to as functional Clds, catalyze the decomposition of ClO_2^- and differ in subunit size and oligomeric state. The first of these consists predominantly of the respiratory Clds that are pentameric and found mainly in proteobacteria. The second clade is populated by Clds from non-perchlorate-respiring species; their subunit size is significantly smaller than that of the respiratory Clds due to a truncated N-terminus. The third Cld clade contains Cld-like proteins,[11] which catalyze the oxidative decarboxylation of coproheme in the

terminal step of heme *b* biosynthesis in Gram-positive bacteria and, potentially, in some Archaea.[12-16] The encoding gene for these coproheme decarboxylases is *hemQ*.[12]

In perchlorate-respiring bacteria, the ClO_2^- decomposing reaction constitutes the terminal step in perchlorate (ClO_4^-) or chlorate (ClO_3^-) respiration; Cld catalyzes the reaction to efficiently detoxify the ClO_2^- produced by catalytic ClO_3^- reduction.[17] The Cld from *Dechloromonas aromatica* (*Da*Cld), a representative of Clds from (per)chlorate-respiring bacteria, turns over >20,000 equivalents of ClO_2^- per heme, with catalytic efficiency nearing the diffusion limit, before it is irreversibly inactivated (k_{cat}/K_M = (3.2± 0.4)×10^7 $M^{-1}s^{-1}$ at pH 5.2, 4 °C).[18] The proposed mechanism for O_2 formation involves initial transfer of an oxygen atom from ClO_2^- to the ferric heme in a two- or one-electron oxidation to yield, either a Fe^{IV}=O porphyrin π-cation radical (Compound I),[19] or a Fe^{IV}=O heme (Compound II), respectively.[20-21] It and the resulting OCl fragment, either hypochlorite (OCl^-) or chlorine monoxide (OCl•), are maintained as a geminate pair in the distal pocket, which comprises a positively charged Arg residue and a number of hydrophobic residues.[6, 22-24] The sequestered OCl fragment is thought to be poised for nucleophilic attack on the electron-deficient ferryl oxygen atom to generate a putative ferric peroxyhypochlorite ($OOCl^-$) intermediate that decomposes to yield Cl^-, O_2 and the resting enzyme.

Although members of the second clade are efficient catalysts for ClO_2^- decomposition (k_{cat}/K_M.= 10^6 $M^{-1}s^{-1}$, pH 5.0−6.0, 20−30 °C),[6, 10-11] their function is not definitively understood. For the Cld from *Klebsiella pneumoniae* strain MGH 78578 (*Kp*Cld), a Gram-negative, non-perchlorate-respiring bacterium, studies of a Δ*cld* knockout strain suggest that it may function in the detoxification of chlorite produced endogenously by nitrate reductases, from ClO_4^- or ClO_3^-.[10] *Kp*Cld and perhaps Clds from other non-perchlorate-respiring species may therefore be

part of a system that protects against the effects of environmental ClO_4^- or ClO_3^-, each of which has minute but ubiquitous natural sources.[1, 25-26]

The heme environments of the two ClO_2^--decomposing Cld clades consist of similar active site residues, including a highly conserved proximal histidine, through which the heme cofactor is bound to the enzyme,[22-23] and a conserved distal arginine (Figure 3.1).[24, 27-28] Spectroscopic data and crystal structures reveal that the distal arginine has two main conformations: one in which its guanidinium group points toward the heme and one where the side chain is directed toward the main access channel into the heme pocket.[6, 22, 24, 29] Substantial loss of ClO_2^- degrading activity upon mutation of the distal Arg indicates that it is catalytically important but not essential for activity.[24, 27-28] One role of the distal Arg is confining ClO^- generated during ClO_2^- decomposition in the heme pocket.[30] In the case of *Da*Cld, ClO^- is not detected during catalytic turnover (although it may contribute to inactivation of the enzyme oxidative destruction of the heme).[18, 31] In contrast, ClO^- escape from the active sites of *Kp*Cld and the Cld from *Candidatus Nitrospira defluvii* (*Nd*Cld), a pentameric Cld, has been detected as HOCl.[10, 30] This HOCl is responsible for the limited turnover observed for *Kp*Cld (6700 ± 300 turnovers/heme) relative to *Da*Cld.[10] This suggests that although the general heme site characteristics of Clds are similar, there are subtle variations in their active site structures and/or dynamics that modulate accessibility of the active site to bulk solvent.

In addition to varying turnover numbers, physical differences have been reported between the active sites of *Kp*Cld and *Da*Cld. Notably, Trp227 of *Da*Cld, located on the periphery of the heme (Figure 3.1A), is highly conserved among known (per)chlorate respirers but replaced by a Glu in dimeric Clds (Figure 3.1B).[5] Also, both the rR core size marker frequencies and rhombicity differences in the HS EPR spectra indicate differing ligation states in the resting,

ferric *Da*Cld and *Kp*Cld.[10] Since the distal heme environment is a major determinant of heme enzyme activity, numerous spectroscopic methods using physiological and nonphysiological heme ligands have been developed to probe the distal landscape of the heme pocket. Here we examine ferric Cld complexes with chloride, fluoride, and hydroxide to probe the heme environments of various Clds with the goal of identifying structural elements that differentially modulate the ClO_2^--degrading activities of the two functional clades. New vibrational frequency correlations between either $\nu(Fe^{III}–F)$ or $\nu(Fe^{III}–OH)$ and $\nu(Fe^{II}–His)$ for the *trans* (proximal) His of ferric Clds and other heme proteins are reported. These correlations orthogonalize the effects of proximal and distal heme environments on the bonding between iron and exogenous π-donor ligands. The Fe-axial ligand vibrations and the relationships between them illuminate both similarities and differences in the H-bonding and electrostatic properties of the distal and proximal heme environments in pentameric and dimeric Clds.

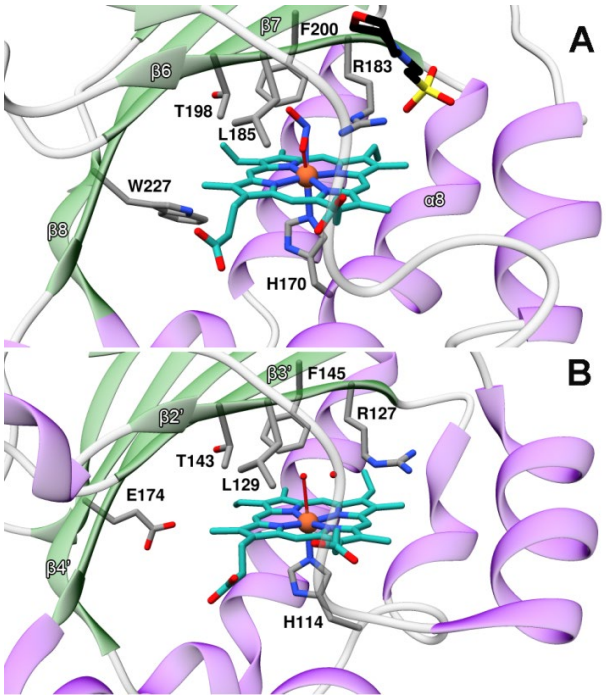

Figure 3.1. Active site structures of pentameric and dimeric. Active site environments for A) the respiration-associated, pentameric *Da*Cld (PBD ID 3Q08)[22] as a nitrite complex and B) the dimeric *Nw*Cld (3QPI) as an aqua complex,[6] which like *Kp*Cld is from proteobacteria that do not respire perchlorate, are shown. Heme carbons are cyan, protein side chain carbons are gray; nitrogen and oxygen atoms are blue and red, respectively. The distal face contains conserved threonine, phenylalanine, leucine, and arginine which form a cage around the sixth coordination site of the heme. Differences between the two active sites are the orientation of the distal Arg side chain and the identity of the residue at the position of W227, which is a conserved glutamate in *Nw*Cld and other dimeric Clds. In the *Da*Cld structure (A), a MES buffer molecule (shown in black, yellow and red) is H-bonded to Arg183. Secondary structure elements are labeled according to the ferredoxin fold using the labeling schemes consistent with those used for *Ao*Cld[23] in A and *Nd*Cld[24] in (B). All of the structures are displayed using UCSF Chimera.[32]

3.3. Experimental Methods

3.3.1. Growth, purification, and characterization of *Da* and *Kp*Cld enzymes.

DNA containing the full-length coding region of chlorite dismutase from *Klebsiella pneumoniae* MGH 78578 (accession no. CP000650.1) was PCR-amplified and cloned into the pET-15b (Merck/Novagen) expression vector for production of protein with a N-terminal His-tag as previously described.[10] The resulting vector was mutated to replace the thrombin protease site (CTG GTG CCG CGC GGC AGC) with a TEV protease site (GAA AAC CTG TAT TTT CAG

GGC) for removal of the 6-His tag post purification. A Q5 Site-Directed Mutagenesis Kit was used with primers TEV_F (5'-t ttt cag ggc CAT ATG AAT ACA CGA TTA TTT ACG TTC G-3') and TEV_R (5'-ta cag gtt ttc GCC GCT GCT GTG ATG ATG-3'). Mutated plasmid was transformed in Tuner DE3 *E. coli* cells and *Kp*Cld was expressed, isolated, and purified as previously described.[10] The N-terminal His-tag of *Kp*Cld was removed by incubation with TEV(S219V) at 1 mol TEV per 10 mol Cld in 50 mM sodium phosphate pH 8.0, 2 mM DTT, and 0.5 mM EDTA overnight at 4 °C.[33] The proteolysis mixture was passed over a 5-mL HisTrap column equilibrated in 20 mM imidazole, 100 mM NaPhos pH 7.4. A linear gradient (20–500 mM imidazole) was used to separate cleaved *Kp*Cld from tagged *Kp*Cld during elution. Imidazole was removed with a PD-10 desalting column and exchanged into 100 mM sodium phosphate pH 6.8. Purity and cleavage were verified by SDS-PAGE.

Plasmids for the over-expression of WT *Da*Cld, *Da*Cld(R183Q), and *Da*Cld(W227F) were available from previous work.[27, 31, 34] These *Da*Clds were expressed, isolated, and purified using published protocols.[18] All Cld concentrations are given as heme-bound monomer, where [Cld] was determined using reported extinction coefficients. The activity with ClO_2^- was routinely monitored to confirm the competency of each enzyme preparation.[10, 18] Molecular weights for both ferric *Da*Cld and *Kp*Cld were determined by gel filtration on a 26×1200 mm S-200 Sephacryl HR column in 0.1 M sodium phosphate pH 6.8 at 0.7 mL / min. The gel filtration column was calibrated with horse heart cytochrome *c* (12.4 kDa), bovine erythrocyte carbonic anhydrase (29 kDa), bovine serum albumin (66 kDa), yeast alcohol dehydrogenase (150 kDa), sweet potato β-amylase (200 kDa), and blue dextran (2,000 kDa). Chromatograms were recorded for each marker and Cld by tracking absorbance at 280 nm or 254 nm. After each chromatographic run, UV/vis absorbance spectra were recorded for relevant fractions

corresponding to eluted markers/proteins. *Kp*Cld gel filtration was also performed in the presence of 10 mM imidazole and 200 mM sodium chloride on separate chromatographic runs.

3.3.2. Quantification of halide binding to Clds by UV/visible spectrophotometric titrations.

Titrations of Clds with F^- (pH 5.8, 100 mM phosphate), Cl^- (pH 6.2, 100 mM phosphate) and Br^- (pH 6.0, 100 mM phosphate) ligands (as aqueous NaX solutions) were carried out using 6–8 μM enzyme and [NaX] ranging from 10 μM to 0.5 M; ligand solutions were added to 800 μL enzyme samples in aliquots ranging from 1 to 5 μL. UV/visible absorbance (UV/vis) spectra were acquired after each addition until the samples reached equilibrium. The titration was considered complete when no spectral changes were observed upon addition of a 5 μL aliquot of concentrated ligand stock. Individual spectra were corrected for sample dilution; these corrected spectra were used to generate difference spectra for obtaining ΔA values. The fraction of enzyme with the ligand bound (r) was represented by $\Delta A/\Delta A_\infty$ where $\Delta A = A_i - A_x$, $\Delta A_\infty = A_i - A_f$; A_i is the initial absorbance, A_x is the absorbance at a given ligand concentration, and A_f is the final absorbance (*i.e.* at saturating ligand concentrations). Plots of r versus free ligand concentration ($[X^-]_F$) were constructed for absorbance data at the wavelength of maximal absorption change and fit by nonlinear regression to equation 3.1 for a single binding site and to equation 3.2 to consider cooperative ligand binding:

$$r = \frac{[X^-]_F}{(K_D + [X^-]_F)} \qquad \text{(Eq 3.1)}$$

$$r = \frac{[X^-]_F^n}{(K_D + [X^-]_F^n)} \qquad \text{(Eq 3.2)}$$

In the experiments described here, $[X^-]_T$ was always >> [heme–X], such that $[X^-]_T \approx [X^-]_F$.

3.3.3. Chlorite-decomposing activity in the presence of coordinating and non-coordinating anions.

Initial rates of chlorite-decomposing activity by *Kp*Cld were determined by monitoring O_2 evolution with a commercial luminescence-based probe with varying substrate (ClO_2^-) concentrations and NaCl as a potential inhibitor with concentrations fixed at 1, 5, 10, 100, or 200 mM. These measurements were carried out under pseudo-first order conditions with 2.0×10^{-8} M enzyme and [ClO_2^-] concentrations ranging from 0.1 mM to 2.0 mM in 100 mM sodium phosphate, pH 6.0. Concentrations of freshly prepared stock $NaClO_2$ solutions were determined via iodometric titration or spectrophotometrically by measuring absorbance at 260 nm using ε_{260} = 155 $M^{-1}cm^{-1}$.[35] *Kp*Cld samples were equilibrated with Cl^- prior to the assay. Reactions were initiated by introducing the enzyme solution with a 10 μL syringe, and kinetic runs, done in quadruplicate, were carried out by recording probe luminescence at 0.1 s intervals for 60 s. Analogous initial rate measurements were performed with *Kp*Cld in 100 mM $NaClO_4$, 50 mM NaF (*Kp*Cld−F), and 50 μM KCN (*Kp*Cld−CN).

3.3.4. Vibrational characterization of Cld halide and hydroxide complexes.

Resonance Raman (rR) scattering was excited with either 406.7-nm or 413.1-nm emission from a Kr^+ laser, or 441.6-nm emission from a HeCd laser. The laser beam was focused to a line at the sample using a cylindrical lens. Scattered light was collected in the 135° backscattering geometry using a f/1 lens to collect and collimate the light. Rayleigh scattered light was attenuated with a holographic notch filter and the remaining light passed through a polarization scrambler. Collection was f-matched to a single f/4.7 0.67-m Czerny-Turner spectrograph fitted with a 120×140 mm 1200 groove/mm holographic grating and operated with a 10 μm (0.74 cm^{-1}) slit. The spectrograph was fitted with a LN_2-cooled CCD detector having a

26.8 mm (1340 pixel) × 8.0 mm (400 pixel) image area. The spectrometer was calibrated against Raman frequencies of toluene, dimethylformamide, acetone, and methylene bromide. Spectra were recorded at ambient temperature from samples in spinning, 5-mm NMR tubes. Laser power at samples ranged from 5 to 10 mW; no spectral artifacts due to photoinduced chemistry were observed with these irradiation powers. UV/visible spectra were recorded from the rR samples before and after spectral acquisition to assess whether sample integrity had been compromised by exposure to the laser beam.

Both WT Clds were examined in the presence of varying chloride ion concentrations in potassium phosphate buffer at pH 5.7 or 6.0 which are below the kinetic pK_a of *Da*Cld, and pH 7.5, which is above the kinetic pK_a of *Da*Cld and below the pK_as for heme−OH formation in both *Da*Cld and *Kp*Cld. Resonance Raman spectra of WT Clds in the presence of 100 mM sodium sulfate and sodium perchlorate were acquired as control experiments. Ferric *Kp*Cld−F, *Da*Cld−F, *Da*Cld(W227F) −F samples for rR spectroscopy were prepared in 100 mM potassium phosphate buffer at pH 5.8.

3.4. Results

3.4.1. Chloride binding to *Kp*Cld facilitates formation of a heme-aqua complex.

The sensitivity of the *Kp*Cld active site to its Cl^- product has been examined by UV/vis and rR spectroscopic methods. Figure 3.2A shows the spectral changes in the UV/vis absorbance spectrum of ferric *Kp*Cld at pH 6.2 in response to increasing [Cl^-]. In the absence of Cl^-, ferric *Kp*Cld exhibits a B band maximum at 403 nm with an intense shoulder at ~380 nm, Q bands at 504 and 540 nm, and a charge transfer (CT1) band at 645 nm. Upon addition of Cl^-, the B-band shifts to the red and sharpens while its high-energy shoulder disappears. The CT1 band shifts from 645 to 638 nm. However, the positions of the Q bands are not measurably altered. These

spectral characteristics are similar to those observed for aqua complexes of metMb and metHb (*c.f.* Sperm Whale aquametMb pH 6.0, 409.5, 505, and 635 nm; Horse aquametMb pH 6.4, 408, 502, and 630 nm; aquametHb pH 6.4, 405, 500, and 631 nm) or the 6cHS *Coprinus cinereus* peroxidase-benzohydroxamic acid complex (CIP-BHA 407, 503, 638 nm).[36-38] Since the changes observed in the UV/vis spectra of the Cl^- titration are consistent with formation of an aqua-heme complex, it suggests that the Cl^- may bind in or near the heme pocket so as to favor water binding to the heme in resting *Kp*Cld.

Isosbestic points observed in the *Kp*Cld spectra upon titration with Cl^- (348, 402 and 432 nm) suggest an equilibrium between two heme species (Figure 3.2A). However, consistent with the sigmoidal shape of the titration curve (inset, Figure 3.2A), attempts to fit it to a single binding site model (dashed red line) did not converge. The data were well modeled by the Hill function with $n = 2.3 \pm 0.1$, suggestive of positive cooperativity in the binding of Cl^- to the enzyme; the same fit yields a composite K_D for the cooperative binding of Cl^- to *Kp*Cld of $(1.4\pm0.3)\times10^{-3}$ M (solid blue line, Figure 3.2A inset). The isosbestic points reflect conversion of the five-coordinate high spin (5cHS) ferric heme in the resting enzyme to a six-coordinate high spin (6cHS) aqua complex with the relative amounts of 5cHS and 6cHS heme being influenced by Cl^- binding.

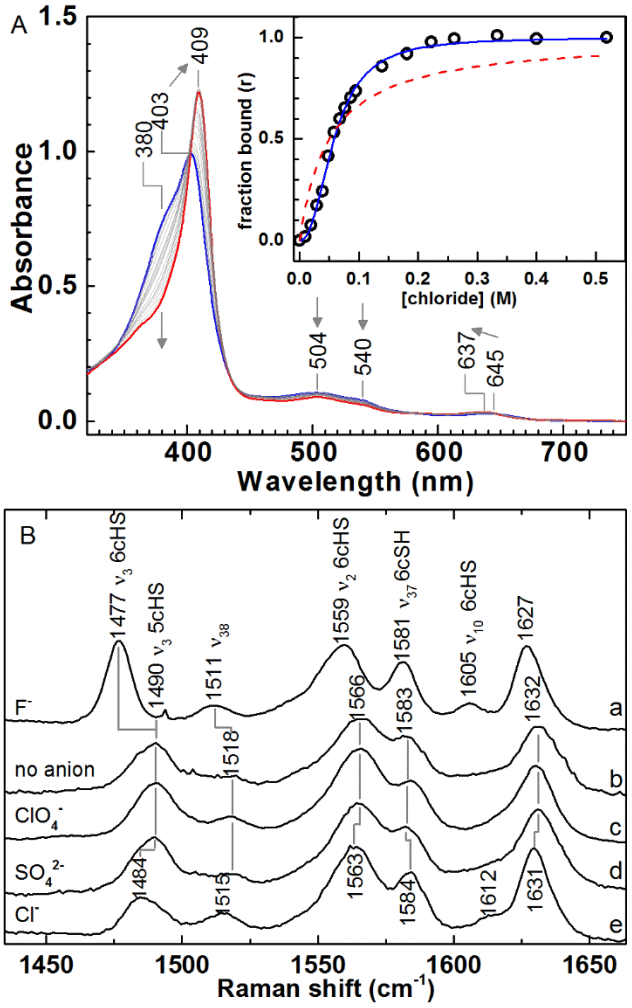

Figure 3.2. In the presence of chloride ion, ferric *Kp*Cld exhibits a 6cHS species. A) The spectrophotometric titration of *Kp*Cld in 100 mM sodium phosphate pH 6.2 is shown with the initial spectrum (0 mM Cl^-) in blue and the final spectrum (500 mM Cl^-) in red. Spectra corresponding to intermediate concentrations of chloride are grey. Aliquots of a stock chloride solution prepared in the same buffer were added to the enzyme to increase the chloride ion concentration in 0.010-0.025 M steps. Equilibrium was reached prior to each sequential addition. Arrows indicate the direction of change in the spectra as the chloride concentration increases. Inset: The fraction of *Kp*Cld with chloride bound ($r = (A_{Cl} - A_{initial})/(A_{final} - A_{initial})$) calculated using the absorbance data at 412 nm, the wavelength of greatest change in the titration, is plotted as a function of chloride concentration. The dashed line shows the fit obtained using a single chloride binding model (Eq. 3.1); the solid line is the fit to the Hill equation (Eq 3.2) where the Hill coefficient measured is 2.3 $\pm$ 0.1. B) Resonance Raman spectra of *Kp*Cld in 100 mM sodium phosphate buffer pH 6 were obtained with 413.1 nm excitation in the presence of the following anions: a) 500 mM sodium fluoride, b) no additional anion (buffer only), c) 100 mM sodium perchlorate, d) 100 mM sodium sulfate, and e) 100 mM sodium chloride. Enzyme concentration is 25 µM. The spectrum of *Kp*Cld−F is shown for comparison purposes; the complex is 6cHS.

To address the possibility that this behavior is a general ionic strength effect rather than being specific to Cl^-, UV/vis and rR spectra of ferric *Kp*Cld with NaCl, KCl, KBr, $NaClO_4$, or Na_2SO_4 were recorded. UV/vis spectra obtained for *Kp*Cld in 100 mM $NaClO_4$ or Na_2SO_4 have features comparable to ferric *Kp*Cld (Figure B1). The UV/vis spectral signature of *Kp*Cld in the presence of Cl^- was insensitive to whether the counter ion was Na^+ or K^+. Spectrophotometric titration of resting *Kp*Cld with Br^- yielded spectral changes similar to those observed upon titration with Cl^-; albeit for a single binding site and with K_D=(1.22±0.03)×10^{-2} M, approximately ten-fold greater than that for Cl^- (Figure B2). The radii of the anions used to probe this effect increase in the order Cl^- (180 pm) < Br^- (198 pm) < SO_4^{2-} (242 pm) ≈ ClO_4^- (241 pm).[39] Thus, the conversion of the active-site heme state to 6cHS under the influence of anions depends upon their ionic radii with the upper limit being ~200. pm. An upper limit on the size of the anions that induce hexacoordination is consistent with steric constraints on access to the sites whose interactions with the anions drives the change in heme coordination number. This ionic radius effect raises the question of whether the smaller anions bind inside or outside the heme pocket. This question is discussed below following presentation of the rR results.

Under acidic conditions, the Soret-excited rR spectrum of heme in ferric *Kp*Cld exhibited a broad ν_3 band, a coordination and spin-state state marker centered at 1490 cm^{-1}. This feature is consistent with the presence of an equilibrium mixture of 5cHS and 6cHS water-bound heme states.[10] The presence of Cl^- favors the 6cHS heme, as judged by a shift in ν_3 to 1484 cm^{-1} and the growth of the 1515 cm^{-1} band corresponding to the in-plane ν_{38} mode for 6cHS hemes (Figure 3.2B). Neither ClO_4^- nor SO_4^{2-} exert this effect on the coordination number. The aforementioned frequencies are comparable to those reported for other aqua heme complexes,

such as aqua metMb at pH 6.4 (ν_3, 1482; ν_{38}, 1512 cm^{-1}).[40] For comparison purposes, *Kp*Cld−F with its ν_3 at 1477 cm^{-1} and ν_{38} at 1511 cm^{-1} is an example of a 6cHS complex of *Kp*Cld.

No ν(Fe−Cl) band is observed in the low frequency spectrum of *Kp*Cld in the presence of 100 mM Cl^-. The apparent lack of a LMCT band in the visible region of [Fe(por)Cl] absorbance spectra[41] precludes identification of a ν(Fe−Cl) band via selective excitation of Raman scattering by that mode (*c.f.* ν(Fe−F)). Thus, the question of whether Cl^- coordinates to the heme iron must be addressed by other means. A prominent band appears at 325 cm^{-1} in the Soret-excited rR spectrum and the feature around 344 cm^{-1} broadens in the presence of saturating [Cl^-], suggesting at least two bands within that envelope (Figure B3). This broad peak likely includes the ν_8 band at 347 cm^{-1} and a band near 338 cm^{-1}. These new features are very similar to those observed in the spectrum of *Kp*Cld−F for which bands at 323 and 338 cm^{-1} have been tentatively assigned to γ_{16} and γ_6, respectively, based on analogy to Mb. These are out-of-plane B_{2u} and A_{2u} modes, respectively, that correspond to pyrrole tilting.[42] Their frequencies are consistent with the presence of Cl^- favoring a 6cHS heme complex.

Interestingly, the 6cHS *Kp*Cld species in the presence of Cl^- exhibits rR features of acidic ferric *Kp*Cld at low temperature in the absence of Cl^-. At −29 °C the rR spectrum of *Kp*Cld at pH 6.0 exhibits ν_3, ν_2, ν_{10}, and ν_{37} bands at 1483, 1565, 1612, 1584 cm^{-1},[10] respectively, consistent with a 6cHS aqua complex.[42] Additionally, the shoulder at 323 cm^{-1} becomes well defined, as it does in the presence of Cl^-.[10] These data, together with those presented above, suggest that Cl^- does not bind to the heme iron but that it interacts with the enzyme to alter the active site conformation in such a way that it favors the 6cHS aqua heme complex.

3.4.2. *Da*Cld heme coordination number is insensitive to chloride.

Spectrophotometric titration of *Da*Cld with Cl^- revealed only subtle spectral changes within the Cl^- concentration range of 0−400 mM. Changes in the ferric *Da*Cld UV/vis spectrum (392 nm B-band, 509 and 540 nm Q bands, and 645 nm CT) upon titration with Cl^- at pH 6.0 were limited to a shift of the B-band to 395 nm with a 2.5% change in B-band extinction but constant band width; the Q- and CT bands were unchanged (Figure B4). Consistent with lack of a significant effect of Cl^- on the *Da*Cld UV/vis spectrum, no changes were detected in the *Da*Cld rR spectrum with Cl^-concentrations below 100 mM. Difference spectra generated by subtracting the ferric *Da*Cld spectrum from those recorded at high [Cl^-] revealed features consistent with the generation of some 6cHS heme (ν_3, 1483 cm^{-1}; ν_{38}, 1515 cm^{-1}; ν_{10}, 1618 cm^{-1} Figure 3.3A). These 6cHS features are quite small *i.e.* ν_3 for the 5cHS enzyme remains the dominant feature between 1480 and 1510 cm^{-1}. This is in contrast to *Kp*Cld, whose heme is completely converted to a 6cHS complex at much lower [Cl^-] with its spectral features being invariant between 100 and 500 mM NaCl (Figures 3.2A and 3.3B).

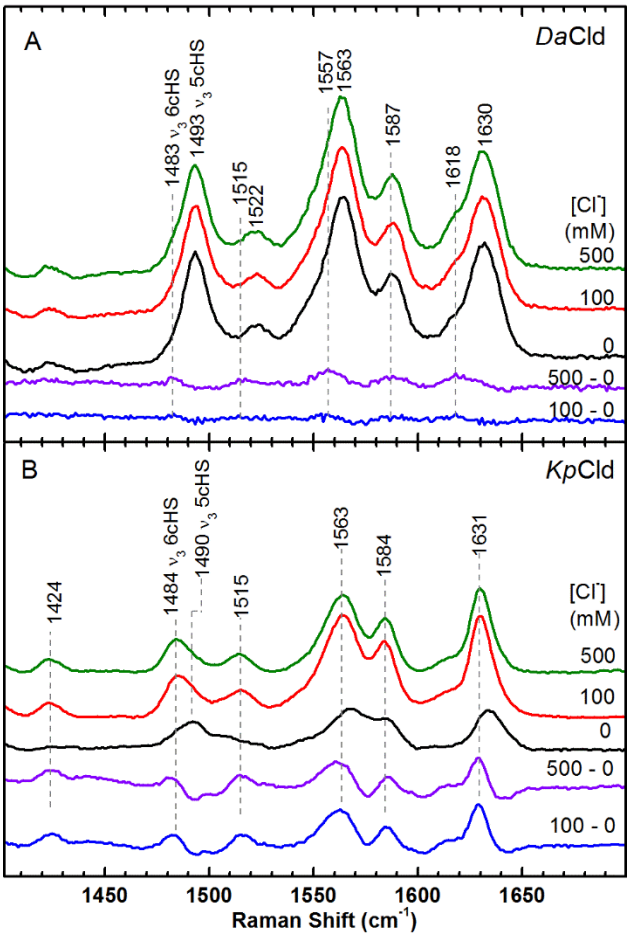

Figure 3.3. Titration of pentameric and dimeric Clds with chloride. A) rR spectra of *Da*Cld with varying [Cl^-]: 0 mM Cl^-, black; 100 mM Cl^-, red; 500 mM Cl^-, green; difference spectrum generated by subtracting the 0 mM Cl^-/*Da*Cld spectrum from the 500 mM Cl^-/*Da*Cld spectrum, purple; difference spectrum generated by subtracting the 0 mM Cl^-/*Da*Cld spectrum from the 100 mM Cl^-/*Da*Cld spectrum, blue. *Da*Cld concentration was 25 µM in sodium phosphate buffer pH 6.0. B) rR spectra of *Kp*Cld with varying [Cl^-]. Spectra as described in (A) *Kp*Cld concentration was 40 µM in sodium phosphate buffer pH 6.0. Comparison of (A) and (B) shows that *Da*Cld is predominantly a 5cHS species even at 500 mM Cl^- while *Kp*Cld is completely converted to a 6cHS species at 100 mM Cl^-.

The rR spectrum of *Da*Cld(R183Q) reveals the same insensitivity of its coordination number to Cl^- as WT *Da*Cld (data not shown). However, the heme in ferric *Da*Cld(R183Q) is a mixture of 5cHS and 6cHS heme,[27] analogous to the Cl^--free ferric *Kp*Cld. In the two former cases, the aqua complex is thermodynamically favored over the 5cHS complex that dominates the speciation of WT *Da*Cld at pH 6.0.[29] Thus, replacement of the cationic Arg side chain by the

shorter, neutral side chain of Gln appears to allow coordination of water in the acidic form of *Da*Cld(R183Q). Given that the binding of other anionic ligands is less favorable without the native distal Arg, it seems unlikely that its replacement with Gln would facilitate Cl^- binding to the heme. Yet the rR spectra clearly report the formation of a hexacoordinate heme. Another possibility is that Cl^- forms an ion pair with the distal guanidinium group, thereby neutralizing the distal charge (vis-à-vis *Da*Cld(R183Q)) and allowing water to occupy the open heme coordination site. If this were the case, two influences to the alkaline form of WT *Kp*Cld would be anticipated. First, neutralization of the positive charge would be expected to drive the pK_a to higher values. The pK_a was, in fact, shown by spectrophotometric titration to increase to 9.0. However, this is likely a general anion effect, as it is observed for Cl^-, ClO_4^- and SO_4^{2-} (data not shown). Second, because the low ν(Fe−OH) frequencies in the Clds are attributable to the non-bonded interaction between the OH^- ligand and the distal Arg, neutralization of the distal positive charge would very likely shift ν(Fe−OH) to higher frequency. The Soret-excited rR spectra of WT *Kp*Cld in the presence and absence of Cl^- are indistinguishable at pH 10.5 (data not shown). As the evidence at hand supports neither the binding of Cl^- to the heme nor its presence in the heme pocket and, given the consistency of UV/vis and rR spectral signatures with *Kp*Cld−OH_2 in the presence of Cl^-, the possibilities for its binding outside the heme pocket were examined.

Given the difference in sensitivity of the heme spectroscopic signatures of *Kp*Cld and *Da*Cld to the presence of Cl^-, the oligomeric state of *Kp*Cld in the absence and presence of Cl^- was evaluated to determine whether conformational changes induced by Cl^- influence subunit interactions. *Kp*Cld eluted from the S-200 size exclusion column as a single band with an elution volume of 330 mL under both sets of conditions (Figure B5). The theoretical mass of dimeric

*Kp*Cld is 42.6 kDa and, like the short Clds from *Nitrobacter winogradskyi* (*Nw*Cld)[6] and *Cyanothece* sp. PCC7425 (CCld)[11], the data in Figure B5 are consistent with *Kp*Cld being a dimer in solution, whether Cl^- is present, or not. Therefore, the conformational and coordination changes that occur in the heme pocket when Cl^- is present do not affect the oligomeric state of the enzyme.

3.4.3. *Kp*Cld chlorite decomposition activity is not inhibited by water coordination to its resting high spin heme.

The effect of Cl^- on the ClO_2^- decomposition reaction was assessed by measuring the rate of O_2 evolution as a function of $[Cl^-]$. Plots of initial rate versus $[ClO_2^-]$ at $[Cl^-]$ ranging from 0 to 200 mM were constructed and fit to the Michaelis-Menten function to determine k_{cat} and K_M (Table B1). As their values at various $[Cl^-]$ were all within statistical uncertainty of one another, only the data set at 200 mM $[Cl^-]$ is shown in Figure B6. Values of 2,910±70 s^{-1} and (3.8±0.2)×10^{-4} M for k_{cat} and K_M, respectively, in the presence of saturating Cl^- were both quite close to the k_{cat} and K_M of ferric *Kp*Cld in the absence of chloride (2,600±100 s^{-1} and [3.0±0.4]×10^{-4} M). The effect of Cl^- on the ClO_2^- decomposing activity of *Kp*Cld, as revealed here by activity assays, indicates comparable enzyme efficiency in the presence and absence of Cl^-; k_{cat}/K_M values under both conditions are within the statistical uncertainties of the determination (Table B1). If Cl^- facilitates formation of a 6cHS *Kp*Cld−OH_2 complex, the coordination of water does not inhibit the enzyme measurably. Thus, replacement of the water ligand by an incoming substrate ion is not the rate limiting step in the decomposition reaction.

In the *Kp*Cld−F case, both k_{cat} and K_M are also on the same order of magnitude as those of the halide-free, resting enzyme, although k_{cat}/K_M decreased by a factor of 2 relative to halide-free enzyme, suggesting a small decrease in enzyme efficiency (Table B1). As in the case with

coordinated water, coordinated F^- is not a significant inhibitor of chlorite decomposition, even under conditions where the 6cHS species account for >99.9 % of the heme at equilibrium.

3.4.4. Probing the Cld distal pocket with ferric heme−F complexes.

Fluoride complexes of heme proteins are sensitive probes of distal H-bond donation to atoms directly bonded with the heme iron atom. A strong linear correlation is observed between the Fe−F stretching (ν(Fe−F)) frequency and the CT1 transition energy. The position of a heme-fluoride complex on this correlation line has been shown to be a general spectroscopic indicator of the extent of H-bond donation from its distal pocket. Strong H-bond donation, such as that in peroxidases (distal His and Arg) or the bacterial truncated hemoglobin from *Thermobifida fusca* (*Tf*-trHb) (distal Trp and Tyr), is revealed by a low ν(Fe−F) frequency and a red-shifted CT1 band. Weaker H-bonding environments found in Mb or dehaloperoxidase (DHP) exhibit higher ν(Fe−F) frequencies.[43-44] The only possible endogenous distal H-bond donor in the Cld pocket is the conserved Arg side chain. Here, *Da*Cld and *Kp*Cld fluoride complexes are used to evaluate whether their distal Arg is indeed capable of providing H-bond stabilization to a ligand atom bonded directly to the heme iron atom.

EPR data suggest that Trp227, which is conserved among pentameric Clds from known perchlorate respirers but not in dimeric Clds,[5-6, 10] plays an important role in differentiating the heme environments of *Kp*Cld and *Da*Cld. *Kp*Cld has Glu in the position analogous to Trp227 of *Da*Cld. Under acidic conditions, constraints on the heme of *Da*Cld(W227F) are relaxed such that its rhombicity is lost and it presents an axial EPR signal, analogous to that of *Kp*Cld.[10] Since mutation at this peripheral position of the heme does not abolish F^- binding to *Da*Cld(W227F) ($K_D = 3.8\times10^{-3}$ M),[34] *Da*Cld(W227F)−F was characterized and compared to WT *Da*Cld−F and

*Kp*Cld−F to determine how the distal pocket interactions in *Da*Cld(W227F) compare to those in the WT Clds.

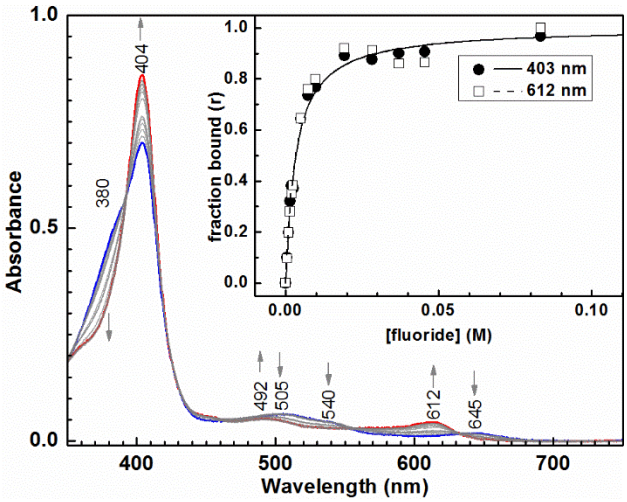

Figure 3.4. Fluoride complex characterized by spectrophotometric titration of *Kp*Cld with fluoride ion. The spectrophotometric titration of *Kp*Cld in 100 mM sodium phosphate pH 5.8 is shown with the initial spectrum (0 mM F^-) in blue and the final spectrum (83 mM F^-) in red. Spectra corresponding to intermediate concentrations of fluoride are grey. Aliquots of a stock sodium fluoride solution prepared in the same buffer were added to the enzyme in 0.5-10.0 mM steps. Equilibrium was reached prior to each sequential addition. Arrows indicate the direction of change in the spectra as the fluoride concentration increases. Inset: The fraction of *Kp*Cld with fluoride bound ($r = (A_F - A_{initial})/(A_{final} - A_{initial})$) calculated using the absorbance data at 403 nm and 612 nm, the wavelengths of greatest change in the titration, are plotted as a function of free fluoride concentration. The solid line (403 nm) and dashed line (612 nm) are fits obtained using a single fluoride binding model (Eqn 1) which both generate a $K_D = 3.3 \pm 0.2$ mM.

Titration of *Kp*Cld with F^- revealed its K_D to be $(3.3\pm0.2)\times10^{-3}$ M (Figure 3.4). The UV/vis spectrum of the *Kp*Cld−F complex at pH 5.8 exhibits a B band at 403 nm and a weak Q band at 491 nm. The CT1 [$a_{2u}(\pi)\rightarrow e_g(d_\pi)$] and CT2 [$a'_{2u}(\pi)\rightarrow a_{1g}(d_{z2})$] bands observed at 16,347 cm^{-1} (611.7 nm) and 22,150 cm^{-1} (451.5 nm), respectively, (Figure 3.5 Inset) are assigned based on comparison to spectra of typical 6cHS complexes.[43] The high frequency rR spectrum shows ν_4 at 1369 cm^{-1} and ν_3 at 1477 cm^{-1}, consistent with a 6cHS F^- complex (Figure 3.2B). Although the K_D for WT *Da*Cld with F^- is 1.5×10^{-2} M, about 5-fold greater than that for *Kp*Cld, the UV-visible (Figures 3.5B and 5C Insets) and rR (Figure B7) spectra for WT *Da*Cld−F and

*Da*Cld(W227F)−F have characteristics similar to those described for *Kp*Cld−F. Comparison of low frequency, Soret-excited rR spectra of ferric Cld−F complexes facilitated assignment of the ν(Fe−F) frequencies (Figure 3.5). The Fe−F stretching mode is observed in the spectra of the Cld−F complexes but is absent in the corresponding ligand-free ferric enzymes. Assignment of the ν(Fe−F) bands at 385, 390, and 393 cm^{-1} for *Kp*Cld−F, *Da*Cld−F, and *Da*Cld(W227F)−F, respectively, was facilitated by Raman excitation within both the Soret and CT2 transitions using 406.7- and 441.6-nm light, respectively. Resonance enhancement of scattering by the *z*-polarized ν(Fe−F) modes of heme fluorides has been reported with excitation at the frequency of the *x,y*–polarized CT1 transition, where scattering by ν(Fe−F) gains resonance enhancement in hemes exhibiting equilibrium out-of-plane distortion.[45] More recently, scattering by the ν(Fe−F) modes has been achieved via excitation within the *z*-polarized CT2 transition, whose energy lies between the B and Q_{01} transitions (Figure 3.5, insets).[43] There are a couple advantages to this approach. First, even though the molar absorbtivities of the CT2 and CT1 bands are similar, scattering efficiency in the blue region of the spectrum is substantially higher than in the red. Second, since the hemes in proteins and enzymes are typically distorted from planarity, it is usually possible to mark the appearance of any candidate ν(Fe−F) bands in rR spectra excited within the in-plane Soret transition by comparison with the spectrum in the absence of F^-. As ν(Fe−F) modes have been shown to be isolated (i.e. they behave as diatomic oscillators[45]), the compositions of the other normal heme modes are sufficiently unperturbed by F^- binding that they are easily correlated between the spectra recorded in the absence and presence of F^-. Finally, by moving the exciting wavelength away from the B band and toward or within the *z*-polarized CT2 absorbance band, the *z*-polarized ν(Fe−F) band gains resonance enhancement while the relative intensities of the in-plane polarized heme bands are diminished. This behavior

facilitates assignment of the ν(Fe−F) band and is easily seen by comparing the three rR spectra in each panel of Figure 3.5 The only complication of this approach is that precise determination of the ν(Fe−F) frequency requires fitting of the overlapping ν(Fe−F) and heme bands. However, the clear correlation of heme bands between the spectra (Figure 3.5) defines the number of bands to use in the fit. So, as long as different initial frequencies converge to the same best fit frequencies for a given spectrum, the possibility of errors due to degenerate solutions is easily minimized or eliminated. With attention paid to these nuances, the widespread availability of fitting routines makes this determination of ν(Fe−F) frequencies reliable and straight-forward.

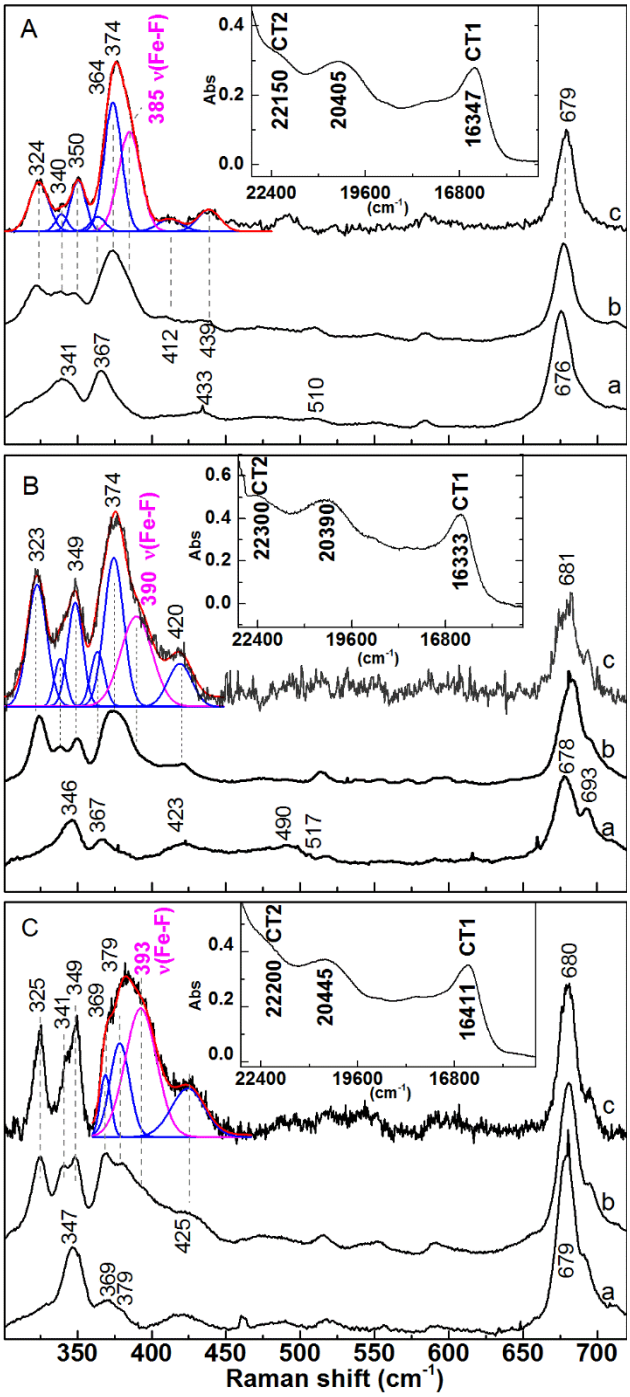

Figure 3.5. Fluoride complexes of Clds compared to ferric Clds: A) WT *Kp*Cld, B) WT *Da*Cld, and C) *Da*Cld(W227F). Each panel contains Soret-excited rR spectra of a) ferric Cld and b) Cld−F at pH 5.8 with 406.7 excitation and c) Cld−F with 441.6 nm (22,645 cm^{-1}) excitation for identification of the Fe(III)−F stretch. The data are shown in black while the components of the fit spectrum and the composite fit spectrum are shown in blue and red, respectively and the band assigned to the Fe−F stretch is shown in magenta. Insets: UV-vis spectrum of Cld−F at pH 5.8.

Variability along the positive correlation between the ν(Fe−F) frequency and the CT1 energy reflects the H-bond donor ability of the distal environment, as revealed by the plot shown in Figure 3.6. Points with low ν(Fe−F) frequency and CT1 energy are consistent with strong distal H-bond donation to the coordinated F^- ligand, like those known for *Tf*Hb and horseradish peroxidase C (HRPC).[43, 46] Weaker distal H-bond donation is manifested in increased ν(Fe−F) and CT1 energies. The position of WT *Da*Cld−F and *Kp*Cld−F on the correlation plot is consistent with strong H-bond donations from the distal cavity to the coordinated F^-. By analogy to HRPC−F where its distal Arg38 and water have been reported to form a H-bond network to F^-,[43] the *Da*Cld−F and *Kp*Cld−F data suggest that the distal Arg, with the possible participation of a water molecule, is responsible for H-bond donation to the coordinated F^- ligand. *Da*Cld−F complexes at pH 5.8 and 7.9 fall at a similar location on the correlation line, consistent with comparable H-bonding interactions over this pH range. This insensitivity of the ν(Fe−F) frequency to pH on either side of the kinetic pK_a of 6.5 is in strong agreement with the earlier conclusion that Arg183 is not deprotonated above the pK_a.[27] Fluoride anion has been shown to displace hydroxide in *Da*Cld even at pHs greater than 9.0. It was speculated that this is attributable to direct interaction with a well-positioned H-bond-donating distal Arg183.[29]

For *Da*Cld(W227F)−F, its ν(Fe−F)/CT1 energy correlation, *i.e.* its position on the correlation plot (Figure 3.6), reveals that distal H-bond donation to the coordinated F^- ligand in *Da*Cld(W227F) is weaker than in both *Da*Cld and *Kp*Cld. Despite the lack of direct H-bonding between Trp227 and the heme (Figure 3.1A), the distinct positions of WT *Da*Cld and *Da*Cld(W227F) on the ν(Fe−F)/CT1 correlation plot suggest that Trp227 plays a remote role in maintaining the electrostatic and H-bonding environment of the distal heme pocket, where the substrate, ClO_2^-, binds.

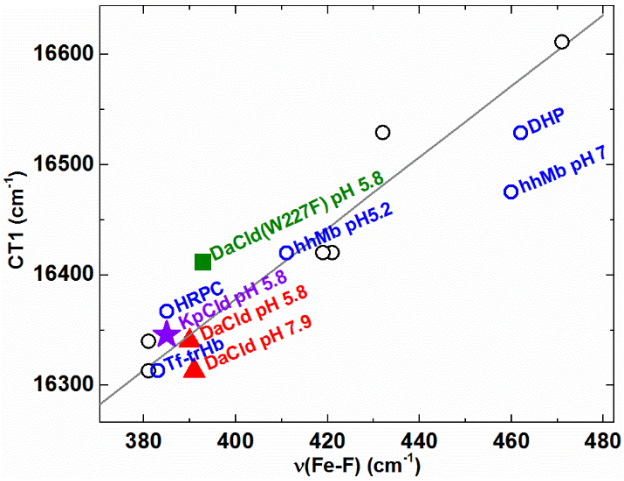

Figure 3.6. Correlation plot showing the relationship between the ν(Fe−F) frequency and the CT1 energy. *Da*Cld−F, red triangles; *Da*Cld(W227F)−F, green square; *Kp*Cld−F, purple star; data points for other heme proteins (hhMb, horse heart myoglobin; HRPC, horseradish peroxidase isozyme C; DHP, dehaloperoxidase; *Tf*-trHb, truncated hemoglobin from *Thermobifida fusca*), blue circles ;a series of *Tf*-trHb mutants, black squares.[44]

3.4.5. Distal ν(Fe^{III}–F) and proximal ν(Fe^{II}–His) frequencies are inversely correlated for Clds and other heme proteins.

The scatter of points about the positive correlation line discussed above (Figure 3.6) is greater than the uncertainty with which the frequencies can be experimentally determined. This suggests that ν(Fe^{III}–F) frequency is likely influenced by factors other than simply the CT1 energy. One clear candidate is the nature of bonding between the heme iron atom and its proximal His ligand as a reporter of the proximal H-bonding environment. Given that ν(Fe^{III}–F) modes in heme fluorides behave essentially as diatomic oscillators, [45] a simple way to assess whether proximal (i.e. *trans*) Fe^{III}–His bonding affects systematic influence on distal Fe^{III}–F bond strength is to plot ν(Fe^{III}–F) frequencies versus ν(Fe^{III}–His) frequencies for a series of hemeprotein fluorides. However, ν(Fe^{III}–His) frequencies for HS hemins are not generally available. Hence, as is typically done, their ν(Fe^{II}–His) counterparts were used here as proxies for distal environmental effects on the Fe^{III}–His bond in hemin fluorides. The validity of this proxy finds support in EXAFS data on resting HRP-C and metMb, which, in accord with their

respective 5cHS ν(Fe^{II}–His) frequencies of 244[47] and 220 cm^{-1},[48] provide proximal Fe^{III}–His bond lengths of 1.92 Å and 2.09 Å.[49] Thus, the ν(Fe^{II}–His) frequencies for 5cHS ferrous heme proteins were used as reporters of proximal H-bond accepting factors known to be deterministic for σ-donor strength of the proximal His ligand.[50] The question is whether *trans*-Fe^{III}–F bonding, as reported by ν(Fe^{III}–F) frequencies in the corresponding ferric hemin fluorides is responsive to environmental modulations of proximal Fe–His bonding.[50] Plots of ν(Fe^{III}–F) frequency versus ν(Fe^{II}–His) frequency for the Clds studied here, along with a variety of other heme proteins for which literature data are available, (Figure 3.7A and Table B2) reveal linear and negative correlations between them. These correlations constitute experimental evidence for the effects predicted previously by DFT calculations[51] and provide more detailed insight into the roles of both distal and proximal heme environments on Fe^{III}–F bonding. Although all the heme proteins on this plot have proximal His ligands, the protein environments that dictate their nonbonded interactions with the distal and proximal axial heme ligands vary considerably.

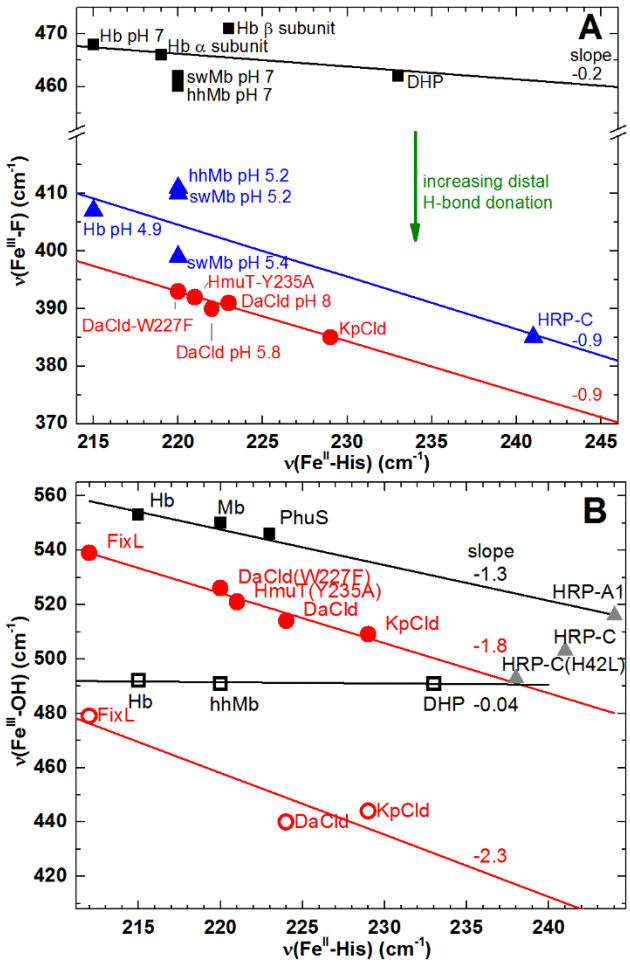

Figure 3.7. Correlation plots illustrating the inverse correlation between ν(Fe^{III}–X) and ν(Fe^{II}–His). A) X = F^-. Heme proteins with Arg in their distal pocket, red circles; other heme proteins with no H-bonding to bound F^-, black squares; other heme proteins with H-bonding to bound F^-, blue triangles.[43, 48, 52-55] B) X = OH^- Low spin heme hydroxide complexes: heme proteins with Arg in their distal pocket, red circles;[10, 29, 56] heme proteins with distal His, black squares.[47, 57-62] HRP proteins with His and/or Arg available as H-bond donator in the pocket are shown as gray triangles. The HRP−C(H42L) variant contains only a distal Arg. High spin heme hydroxides: same as low-spin hydroxides with open symbols.[10, 29, 48, 54, 57, 59-60, 63]

3.4.5.1. Distal environments.

The Clds and a variant of the bacterial hemin trafficking protein HmuT have single distal Arg residues.[52] Myoglobin (Mb), Hb and dehaloperoxidase (DHP)[64] have single distal His residues while the distal pocket of HRP contains a single His *and* a single Arg.[65] The ν(Fe^{III}–F) frequencies of metHb and metMb fluorides are sensitive to pH, which has been reported to result from protonation of the distal His under acidic conditions with consequent donation of a H-bond

to the bound F^- ligand.[53] On the correlation plot in Figure 3.7A, the increased H-bond donation from the distal, cationic imidazolium moiety places the acidic metMb and metHb fluorides well below their neutral counterparts. The vertical dispersion of these complexes along the $\nu(Fe^{III}–F)$ axis is attributable to the range in distal charge and number of hydrogen bond donors for a set of heme pockets having the same proximal environment. Thus, for a given proximal environment, $\nu(Fe^{III}–F)$ frequencies reveal differences in the protonation states and charges of their distal H-bond donors. Inspection of the entire graph reveals three correlation lines whose heights on the $\nu(Fe^{III}–F)$ axis reflect a range of H-bond donor environments. Each line comprises proteins having the same amino acid-based distal H-bond donor, with the highest line corresponding to neutral His, and those for $HisH^+$ and Arg being negatively displaced by offsets that reflect increasing H-bond donation. According to this analysis, the distal Arg of the Clds constitutes a stronger H-bond donor environment than either the neutral or protonated distal His in the globins, likely due to its ability to donate two hydrogen bonds to the coordinate F^-. In general, for a given proximal environment, $\nu(Fe^{III}–F)$ frequencies appear to reveal differences in the number of distal hydrogen bonds donated to the coordinated F^- ligand. The heights of these new correlation lines on the $\nu(Fe^{III}–F)$ axis in Figure 3.7A are related to positions of the corresponding proteins along the $\nu(Fe^{III}–F)$/CT1 correlation line in Figure 3.6.

3.4.5.2. Proximal environments.

In addition to the distal H-bonding effects on $\nu(Fe^{III}–F)$ described above, the plots in Figure 3.7A reveal an inverse correlation between $\nu(Fe^{III}–F)$ and $\nu(Fe^{II}–His)$ frequencies for a given number of distal hydrogen bonds to F^-. Insofar as it is reasonable to relate the trend in $\nu(Fe^{II}–His)$ frequency to a trend in $Fe^{III}–His$ bond strength, the inverse correlation lines revealed in Figure 3.7A can be classified as a *trans* effect. The *trans* effect of the proximal ligand on the

Fe^{III}–F bond strength is reported by the negative slopes of the individual correlation lines. This behavior is consistent with a *trans* effect that weakens the ν(Fe^{III}–F) force constant as that for ν(Fe^{II}–His) increases. For the Clds reported here, the largest *trans* effect is observed for *Kp*Cld; so even though *Da* and *Kp*Clds have the same distal amino acid-based H-bond donors, the Fe–F bond strength in *Kp*Cld–F is less than in *Da*Cld–F.

Interestingly, ferric heme proteins such as Mb and Hb at pH 7 and DHP, which exhibit only weak or no distal H-bond donation to a coordinated F^- ligand, fall on a nearly horizontal correlation line (slope = −0.2±0.3). Among the possible explanations for this behavior is that distal H-bond donation somehow activates the *trans* effect (*i.e*. there is no clear *trans* effect on ν(Fe^{III}–F) in the absence of at least a single distal H-bond donor). Although such a H-bond switch is difficult to rationalize, it is reasonable to consider the possibility of one or more effects on ν(Fe^{III}–F) whose trends offset that of the *trans* ligand. A considerable database of proximal ν(Fe^{II}–His) frequencies for 5cHS ferrous hemes is consistent with high ν(Fe^{II}–His) frequencies being correlated with the presence of an anionic H-bond acceptor in the proximal heme pocket. Proteins having anionic carboxylate acceptors from Asp or Glu generally exhibit the highest ν(Fe^{II}–His) frequencies, which is attributed to the imidazolate character of the proximal His, whose σ donor strength is greater than neutral imidazole.[66-67] The accumulation of negative charge on the axial F^- ligand, which might otherwise result from its competition with the proximal imidazole for the d_{z^2} orbital, is moderated by increased π donation from p_π orbitals of F^- to the iron d_π orbitals. In other words, there is synergy between axial valence electron delocalization through the σ and π pathways that minimizes the separation of charge with increased anionic character of the proximal ligand. This self-balancing of the σ and π contributions to Fe–F bond strength renders it relatively insensitive to the trend in σ *trans* effect

of the proximal His ligand. This behavior accounts for the very small negative slope of the correlation line representing heme pockets providing little or no H-bond donation (top line in Figure 3.7A).

By contrast, in heme pockets that provide strong H-bond donation to the coordinated F^- ligand, the Fe−F π electron density is polarized toward the F atom, thereby diminishing the π character of the Fe−F bond. Accordingly, distal H-bond donation diminishes the ability of the system to compensate, through increased Fe−F π bonding, for *trans*-induced diminution of Fe−F σ bonding. This H-bond induced decoupling of σ and π donation by the F^- ligand is manifested in a steeper negative slope of the *trans*–effect correlation lines for heme proteins having distal imidazolium and guanidinium H-bond donors. Interestingly, the slopes of those lines are the same within experimental uncertainty (−0.91±0.05 and −0.90±0.07, respectively). The common slope of the imidazolium and guanidinium lines is consistent with the *trans* effect on Fe−F σ bonding being independent of or insensitive to the distal effect on its π bonding. Dispersion of proteins having a given number of distal H-bonds along the $\nu(Fe^{III}–F)$ axis is attributable to variation in the strength of the Fe−F σ bond as the proximal ligand takes on more or less imidazolate character. These plots orthogonalize proximal and distal contributions to the exogenous $Fe^{III}–X$ bond strength, as revealed by trends in the $\nu(Fe^{III}–F)$ frequencies. Thus, the plots in Figure 3.7A provide direct insight into the heme pocket properties of the resting *ferric* states of the proteins. In the case of the Clds, these are the properties that govern their interactions with the anionic substrate, ClO_2^-.

The additive proximal and distal effects revealed in Figure 3.7A synergistically weaken the $Fe^{III}–X$ bonds in 6cHS π-donor complexes of the Clds investigated here. Both F^- and water form such 6cHS complexes with resting *Kp*Cld. The kinetic barrier to dissociation of these

ligands is expected to be low with high dissociation rates, as has been reported for HRP (k_{off} = 4.2×10^2 s^{-1}).[68] Based on this reasoning, the labialization of these ligands is expected to render them poor competitive inhibitors of Cld activity. Indeed, the K_I for inhibition by F^- and H_2O is too large to measure (Figure B6).

3.4.6. Distal ν(Fe^{III}−OH) and proximal ν(Fe^{II}−His) frequencies are inversely correlated for Clds and other heme proteins.

Like the fluorides of *Da*Cld and *Kp*Cld, their hydroxides are also enzymatically active.[10, 29] Also like the fluorides, the stabilities of their hydroxides are highly dependent on the distal Arg. *Da*Cld variants R183Q and R183A do not bind OH^- under conditions where the WT enzyme is completely converted to the heme hydroxide.[27] To test our understanding of the proximal and distal effects described above and its general applicability to π donor ligand complexes of heme proteins, ν(Fe^{III}−OH) frequencies were plotted versus ν(Fe^{II}−His) frequencies for the Clds studied here, along with a variety of other heme proteins for which literature data are available (Figure 3.7B and Table B2). The hydroxide complexes of numerous heme proteins, including the Clds, exist as equilibrium mixtures of 6cLS and 6cHS forms. Under conditions where heme hydroxides form, distal His residues are expected to have neutral imidazole side chains whereas Arg maintains its positively charged guanidinium side chain throughout the pH range over which the protein fold is stable. As illustrated in Figure 3.7B, the 6cHS hydroxide complexes exhibit trends similar to the 6cHS fluoride complexes in Figure 3.7A. Specifically, the points fall on two correlation lines. One comprises proteins whose distal pockets contain a neutral His and, like its F^- counterpart, is nearly horizontal. The other contains proteins whose distal pockets donate H-bonds from Arg and has a negative slope. As in the case of the heme fluorides, the vertical offset of the individual lines report the dependence of the

Fe−OH bond strength, as reported by the ν(Fe^{III}−OH) frequency, on the number of amino acid-based distal hydrogen bonds to the coordinated OH^-. The slope of the correlation lines (−0.04±0.04 for HS OH^- with neutral distal His and −2.3±0.9 for HS OH^- with Arg) can be explained in the same terms as heme fluorides. The slope of the ν(Fe^{III}−OH)/ν(Fe^{II}−His) Arg line in Figure 3.7B is steeper than the corresponding F^- line in Figure 3.7A, ostensibly because OH^- is a weaker π donor ligand than F^-, making its susceptibility to Fe−OH bond weakening by the *trans* effect greater than that in the heme fluorides. Note that there is no line for distal imidazolium because the pK_a of imidazolium lies far below that for heme hydroxide formation.

The ν(Fe^{III}−OH) frequencies of LS heme hydroxides are also sensitive to both proximal and distal environments. The top of Figure 3.7B shows that, like the HS heme hydroxides and fluorides, the LS hydroxides for which frequencies are available, from this study and literature sources (Table B2), fall on two ν(Fe^{III}−OH)/ν(Fe^{II}−His) correlation lines. Their positions along the ν(Fe^{III}−OH) axis distinguish between distal pockets comprising neutral His (higher line) and Arg (lower line) as single and double H-bond donors, respectively. In contrast to the HS cases, both lines correlating the ν(Fe^{III}−OH) and ν(Fe^{II}−His) frequencies have similar negative slopes (slopes of the correlation lines are −1.3±0.5 and −1.8±0.2, respectively, Figure 3.7B). Thus, the *trans* effect on the Fe−OH σ bonding is the dominant factor in modulating the overall Fe−OH bond strength, as reported by the ν(Fe^{III}−OH) frequency, even for proteins in which the distal H-bond donor is a charge-neutral His. The most likely reason for this is that, even though hydroxide is a weak π donor ligand, the filled d_π orbitals preclude significant π bonding in the LS hydroxides.

3.5. Discussion

The O_2-evolving Clds constitute an unusual example of rapid and efficient catalytic O−O bond-formation. Vibrational signatures of halide and hydroxide complexes with the resting ferric enzyme are sensitive probes of the heme environment. They have been used here to compare and contrast the anion complexes of *Kp*Cld and *Da*Cld, having low and high turnover numbers, respectively, in order to gain insight into the structural properties crucial to high-fidelity O_2 generation.

3.5.1. Differential sensitivity of Cld active sites to the presence of halides reveals distinctions between the nonbonding interactions that shape their heme pockets.

The binding of Br^- and the cooperative binding of Cl^- to *Kp*Cld drives formation of a 6cHS heme complex. There are two ways this could occur: coordination of the halides to the heme iron or binding to one or more non-heme sites, inducing a conformational change that favors coordination of a water molecule. There are a few examples of Cl^- coordination to the iron center in heme-dependent enzymes. As bacterial dye-decolorizing peroxidases (DyPs) belong to the CDE (Clds, DyPs, EfeB) superfamily, the most relevant examples are several distal pocket DypB variants in which Cl^- coordinates to their heme iron.[69] However, a ν(Fe−Cl) band is not observed in the low frequency spectrum of *Kp*Cld at [Cl^-] where the formation of 6cHS heme is known, by spectrophotometric titration and the high-frequency rR spectrum, to be complete. In contrast, there are examples in which Cl^- binds to heme enzymes at sites removed from the iron. For example the distal heme pockets of lactoperoxidase and myeloperoxidase contain Cl^- binding sites that accommodate the halide without its direct coordination to the iron.[70-71] The spectral similarities among the 6cHS *Kp*Cld complex at saturating [Cl^-] with other heme aqua complexes in globins and peroxidases is consistent with Cl^- binding at a site removed

from the heme iron and inducing a conformational change that facilitates water binding at the heme. The crystal structure of *Nw*Cld (Figure 3.1B), a dimeric enzyme like *Kp*Cld, shows a water molecule coordinated to the heme iron. Several steps of the published isolation procedure expose *Nw*Cld to [NaCl] ≥ 150 mM.[6] Thus, if sensitivity to Cl^- binding is a general characteristic of dimeric Clds, a 6cHS aqua complex of *Nw*Cld would be anticipated in the presence of high [Cl^-]. Furthermore, solutions of *Nw*Cld isolated in the absence of Cl^- are hypothesized to contain at least some 5cHS heme.

Although Cl^- and Br^- drive a change in the coordination number of the HS iron from 5c to 6c in *Kp*Cld, its ClO_2^- decomposition activity remains essentially unchanged (Table B1). So Cl^- formed during the ClO_2^- decomposition reaction is not an inhibitor of *Kp*Cld. For the pentameric *Da*Cld and the Cld from *Magnetospirillum sp*. (*Ma*Cld), Cl^- has been shown to be a weak mixed hyperbolic inhibitor: K_I =225 mM and K'_I = 95.6 mM for *Da*Cld[18] and K_I = 460 mM and K'_I = 480 mM for the *Ma*Cld.[72] These K_I values are approximately two orders of magnitude larger than the composite K_D of 1.44 mM for cooperative Cl^- binding to *Kp*Cld. This is consistent with the observation that the *Da*Cld heme remains 5cHS at Cl^- concentrations that drive *Kp*Cld to be 6c (Figure 3.3). Thus, *Da*Cld is more resistant to chloride-induced conformational changes than *Kp*Cld. A possible explanation for this is revealed by comparing the crystal structures of pentameric and dimeric Clds, as shown in Figure 3.8 In the *Da*Cld structure, the heme pocket is formed by hydrophobic interactions between residues on the alpha helix (α9) and the beta sheets (β5, β8, and β9), shaping the heme pocket: L205/L233, F208/I145, M212/I147, M212/W227 (Figure 3.8A). These hydrophobic residues are not strongly driven to interact with ions like Cl^-. Additionally, access to these residues is blocked because they are located near the subunit interface in the pentamers. In dimeric *Nw*Cld, the heme pocket is shaped

by ionic interactions between residues on the alpha helix (α5') and on the beta sheets (β4' and β1'): E156/R178, R163/D176, R163/E174, and W168/E174 (Figure B8). Similar pairwise ionic interactions are also observed in the homology structure for *Kp*Cld: E155/R181, R166/D179, R166/E177, and W171/E177. An additional interacting pair of residues (N159/R181) along this face of the heme pocket is noted in the *Kp*Cld homology structure (Figure 3.8B). Any of these ionic interactions could be disrupted or perturbed by the incursion of Cl^-. The cooperative nature of Cl^- binding (n = 2.3 per heme) suggests that its energetically coupled participation in more than one of these ionic interactions results in conformational changes that, as discussed above, drive formation of a heme−OH_2 complex in *Kp*Cld.

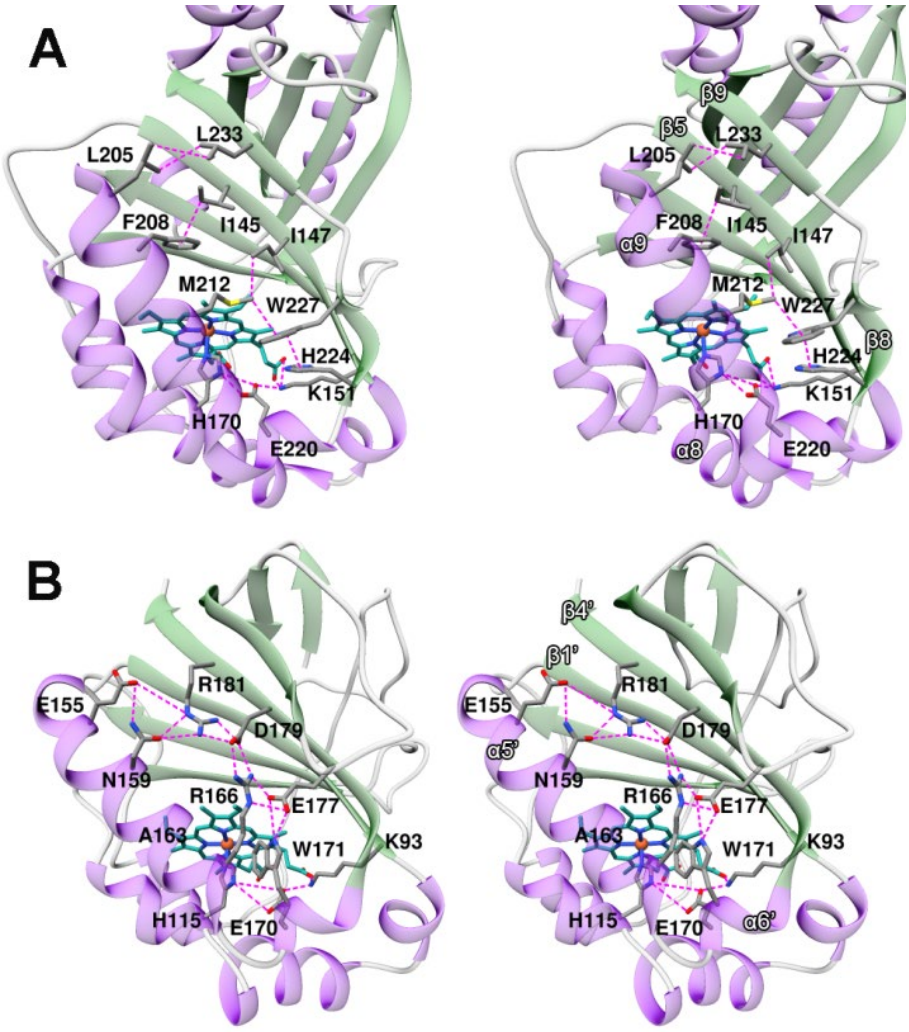

Figure 3.8. Secondary structure of pentameric and dimeric Clds shaping the heme pocket. A) Cross-eyed stereo view of the crystal structure of *Da*Cld (3Q08)[22] depicting residues with nonbonding interactions (2.9 – 4.2 Å) between α9 and β5, β8, & β9 as indicated by dashed magenta lines; these define a side of the heme pocket. These residues are hydrophobic suggesting their interactions are a mixture between London dispersion forces and the hydrophobic effect. This hydrophobic region is located at one intersubunit interface within the pentameric structure and is therefore not solvent exposed. B) Cross-eyed stereo view of the Swiss Model homology model of *Kp*Cld (generated using *Nw*Cld (3QPI))[6] as a template) depicting residues with nonbonding interactions (2.5–4.6 Å) between α5' & α6' and β4' as indicated by dashed magenta lines. Nitrogen and oxygen atoms of the amino acid side chains and heme are shown in blue and red, respectively. The carbons of the heme are shown in cyan and the iron is orange. The heme cofactor is an overlay from *Nw*Cld onto the *Kp*Cld homology model. These residues are similar to *Nw*Cld and are hydrophilic suggesting their interactions are primarily ionic in nature. This region is not located at an intersubunit interface. Secondary structure elements are labeled according to the ferredoxin fold using the labeling schemes consistent with those used for *Ao*Cld[23] in (A) and *Nd*Cld[24] in (B). All of the structures are displayed using UCSF Chimera.[32]

Crystal structures of pentameric *Da*Cld and *Ma*Cld indicate that the conserved Trp227, one of the residues lining the heme pocket, is within 4.3 to 5.0 Å of a heme vinyl group.[22, 73] Thus, although Trp227 is not directly H-bonded to the heme, the participation of its indole side chain in hydrophobic stacking interactions with Met212 and His224 contributes to stabilization of tertiary structure involving α9, β8 and β9, which shape the back of the *Da*Cld heme pocket. Subtle disruption of that triad is achieved by mutation of Trp227 to Phe, likely due to the difference in the extents of their π systems. Based on the position of *Da*Cld(W227F) on the $\nu(Fe^{III}–F)$/CT1 correlation plot (Figure 3.6), one might conclude that this peripheral perturbation manifests as weakened distal H-bond donation. However, Figure 3.7 reveals that this disruption in peripheral hydrophobic interactions actually diminishes the *trans* effect on both $\nu(Fe^{III}–F)$ and $\nu(Fe^{III}–OH)$. Interestingly, in dimeric Clds the residue at this position is Glu (E177 in *Kp*Cld; E174 in *Nw*Cld). This natural substitution contributes to stabilization of the heme pocket in *Kp*Cld by ionic interactions. The positions of *Da* and *Kp*Cld on the $\nu(Fe^{III}–F)$/CT1 correlation plot (Figure 3.6), suggest that the ionic interactions between Arg166, Glu177, and Trp171 in *Kp*Cld are effective in maintaining a distal heme environment similar to that shaped by the corresponding hydrophobic interactions in *Da*Cld. In this case, the fact that, both enzymes fall on the same $\nu(Fe^{III}–F)/\nu(Fe^{II}–His)$ and $\nu(Fe^{III}–OH)/\nu(Fe^{II}–His)$ lines in Figure 3.7 also supports similarity in their distal H-bonding environments, albeit under the influence of different *trans* environments.

All reported clade 1 Clds contain a signal peptide which designates them to the periplasm. The lack of a signal peptide in clade 2 suggests that these enzymes are localized to the cytoplasm.[11] Thus, different subcellular localizations of Clds from clades 1 and 2 exposes them to different Cl^- concentrations. A $[Cl^-]$ gradient is maintained such that cytoplasmic $[Cl^-]$ at 10

to 100 mM is less than in the extracellular fluid. Since the outer membrane of Gram-negative bacteria contains porins, which allow for passive diffusion of small anions, such as Cl^-, the periplasm has a similar Cl^- concentration as the extracellular fluid.[74] Therefore, clade 1 Clds are likely exposed to higher [Cl^-] than their counterparts in clade 2. The distinct sensitivities of *Da* and *Kp*Clds to [Cl^-] reflect the different subcellular Cl^- concentrations. Measurable loss of chlorite-decomposing activity in the presence of Cl^- is observed for *Da*Cld, at concentrations up to 200 mM.[18] Despite the measurable activity loss, heme spectroscopic features reveal that the cofactor speciation in *Da*Cld is not significantly altered in the presence of excess Cl^-. This is in stark contrast to *Kp*Cld which exhibits no measurable activity loss when exposed to Cl^-. Interestingly, however, the affinity of its heme for water as a sixth ligand is increased in the presence of Cl^-. Therefore, the physiologically relevant form of the heme in resting *Kp*Cld may be 6cHS, as opposed to the 5cHS heme in resting *Da*Cld.[29] Thus, distribution of the heme between 5c and 6c states in *Kp*Cld is likely to be strongly dependent on the cytosolic Cl^- concentration over the physiological range of 10 to 100 mM.[75]

3.5.2. Strong H-bond donation to the coordinating atom of exogenous heme ligands is characteristic of Clds.

The affinity of pentameric Clds for F^- (K_D: *Da*Cld, 15 mM;[29] *Nd*Cld, 5.9 mM[76]) is comparable to that determined here for dimeric Clds (K_D: *Kp*Cld, 3.3 mM). That *Da*Cld distal pocket mutants R183Q, R183K, and R183A and analogous *Nd*Cld distal pocket variants do not bind F^- points to an important role of the distal Arg in stabilizing heme-anion complexes in Clds.[27, 76] The similar positions of *Kp*Cld and *Da*Cld on the plot in Figure 3.6, which shows the correlation of ν(Fe−F) frequency with CT1 energy, suggests similarity among their distal H-bond donation to the coordinated F^- ligands. The more detailed view provided by the correlations in

Figure 3.7 reveal that *Da* and *Kp* Clds fall on the same low $\nu(Fe^{III}–X)/\nu(Fe^{II}–His)$ correlation lines, where X is either $F^–$ or $OH^–$, consistent with the distal Arg residue in each enzyme providing two H-bonds to the bound $X^–$ ligand. Therefore, the two H-bond donating distal environments in these enzymes are expected to contribute similarly to the stabilities of exogenous anion complexes, including putative ferryl intermediates. The Clds examined here all fall on correlation lines that reveal inverse relationships between $Fe^{III}–F^–$ and $Fe^{III}–His$ bond strengths. Analogous trends are seen for HS and LS heme hydroxides. A similar inverse correlation between $\nu(Fe^{IV}=O)$ and $\nu(Fe^{II}–His)$ has been reported for Mb and a number of peroxidases.[50] These four inverse correlations illustrate the importance of variability in the *trans* effect on the exogenous Fe−X bond strength for a given number of H-bonds donated by the distal pocket. Interestingly, that variability, as reported by the slopes of the correlation lines, is similar for the aforementioned $\nu(Fe^{IV}=O)/\nu(Fe^{II}–His)$ correlation[50] and the LS $\nu(Fe^{III}–OH)/\nu(Fe^{II}–His)$ correlation reported here. The *Kp*Cld complexes, being lower (more to the right) on their correlation lines (Figure 3.7), reveal a greater *trans*-effect of their proximal His on their Fe−X bonds than *Da*Cld. However, neither experiences a *trans* effect as large as the $Fe^{III}–OH$ bond in peroxidases, as illustrated by their position well to the right of the Clds. Indeed, Clds are poor peroxidases[19] because, in addition to lacking a distal catalytic base, they lack sufficient "push" because their proximal His residues are weaker σ donors than the imidazolates of the peroxidases (Figure 3.7). Moreover, the polarizing cationic side chain of the distal Arg in Clds is sufficiently close to the heme that it donates two H-bonds to the coordinating atom in $Fe–X^–$ complexes. This arrangement is unlikely to be optimal for polarizing the peroxo bond toward the heterolytic O−O bond cleavage characteristic of peroxidases. By contrast, strong polarization of the O−Cl bond in the Cld−$OClO^–$ complex is likely less critical to heterolytic bond cleavage, as that bond

is already slightly polar. Rather, the distal Arg in the Clds appears to facilitate formation of the enzyme substrate complex and maintaining the Fe^{IV}=O/OCl geminate pair after the putative O−Cl bond scission.

3.5.3. ν(Fe^{III}−X)/ν(Fe^{II}−His) correlations are general reporters of ferric heme pocket properties.

Given that two of the distal H-bond donors considered in Figure 3.7A are cationic, the importance of charge in displacement along the ν(Fe^{III}–F) axis must be considered. To test the general applicability of the ν(Fe^{III}–F)/ν(Fe^{II}–His) correlation plots, a set of *Tf* trHb−F^- variants representing a range of charge-neutral distal H-bonding environments were placed on the plot. The active site of *Tf* trHb contains distal Trp and Tyr residues known to stabilize complexes of exogenous ligands with a second Tyr providing indirect H-bonding to the heme ligand via a bridging water molecule.[44, 46, 77] Figure B9 shows that the vertical distribution of the ν(Fe^{III}–F) frequencies for these proteins on the correlation plot is consistent with the number of H-bonds predicted by molecular dynamics simulations to be donated to the coordinated F^- ligand. While charge appears to have some systematic effect on vertical displacement along the ν(Fe^{III}–F) axis, ν(Fe^{III}–F) frequencies cluster in ranges corresponding to the number of H-bonds donated to the F^- ligand.

Support for the HS OH^- line with two H-bonds come from the *Mt* trHbN and *Mt* trHbO proteins that have been reported to undergo a conformational change upon spin state change. The LS OH^- complexes of these proteins exhibit little to no H-bonding to OH^- in their distal pocket, and they are positioned near the LS OH^- weak H-bonding line. The conformational change accompanying a spin state change to HS results in their OH^-complexes falling on or close to the HS OH^- two-H-bond line. The H-bond donors are for trHbN and trHbO are Tyr/Gln and

Tyr/Trp, respectively.[78] This indicates that the trends illustrated in the correlation plot are general in nature and not just applicable to distal pocket H-bond donation from amino acid side chains containing nitrogen (His, Arg, Trp versus Tyr).[78]

An enzyme's position on these correlation plots yields insight into the extent to which it weakens π bonding between Fe and the π-donor ligands, F^- and OH^-, through distal H-bond donation and σ bonding via the *trans* effect (*vide supra*). As such, it may provide insight into why and whether π-donor ligands, such as F^- and OH^-, and OH_2 are poor competitive inhibitors of enzymes whose substrate binding site is an axial coordination site on the heme iron center. Specifically, such ligands that accept multiple distal H-bonds and lie to the high-frequency end of the $\nu(Fe^{II}–His)$ axis are likely to exhibit low barriers to Fe−L bond dissociation, a necessary prelude to formation of the enzyme-substrate complex. Worthy of note is that *Kp*Cld−F and *Kp*Cld−OH lie to the right of their *Da*Cld analogues on the respective correlation lines. On that basis, it is hypothesized that *Kp*Cld will be inhibited to a lesser extent by F^-, OH^-, and OH_2 than is *Da*Cld.

3.5.3.1. Intersecting or overlapping correlation lines.

Heme hydroxides of the trHbs are similarly dispersed along the $\nu(Fe^{III}–OH)$ frequency axis in accord with the number of H-bonds to the O atom of coordinated OH^-. As seen in Figure B10, the HS and LS *Tf* and *Mycobacterium tuberculosis* (*Mt*) trHbs fall remarkably close to the HS and LS correlation lines established in Figure 3.7B. Interestingly, the LS *Tf* trHb hydroxides that are predicted by MD simulations to have three distal hydrogen bonds[46, 79] lie, as these new correlations would predict, lower on the $\nu(Fe^{III}–OH)$ axis than those having two hydrogen bonds. Noteworthy is that these LS heme hydroxides fall near the line for HS hydroxides having only weak or no H-bond donors. Hence, even though the position of a heme protein hydroxide on this

correlation plot can appear to indicate a particular spin state and number of H-bonds for a given $\nu(Fe^{II}–His)$ frequency, the $\nu(Fe^{III}–OH)$ frequency alone may not be sufficient to assign these two parameters because, as seen in Figure B10, correlation lines can intersect due to offsetting effects of spin state and number of H-bonds. Therefore, using these correlations to assign number of H-bonds and properties of the proximal ligand may require assignment of the spin state by an independent means at the same temperature, such as high frequency rR, NMR or EPR spectroscopy.

3.5.3.2. Clarification of ambiguous assignments.

This approach has the potential to clarify assignments that may be ambiguous on the basis of $\nu(Fe^{III}–OH)$ frequency alone. For example, for HRP enzymes whose distal pockets comprise both Arg and His, the positions of HRP-A1 and HRP-C[61] on the $(Fe^{III}–OH)/\nu(Fe^{II}–His)$ plot suggest that these two amino acids contribute differently to distal H-bonding in these isozymes. The HRP-C variant HRP-C (H42L), which has no distal His, leaves only the distal Arg to stabilize anion coordination by H-bond donation. Although the core-size marker region of the rR spectrum indicates an equilibrium mixture of HS and LS heme hydroxides, only a single $\nu(Fe–OH)$ band is detected in the low-frequency rR spectrum. This single $\nu(Fe^{III}–OH)$ band was assigned to the HS hydroxide based on $\nu(Fe^{III}–OH)$ frequency similarity with Hb.[80] The $\nu(Fe^{III}–OH)$ and $\nu(Fe^{II}–His)$ frequencies for HRP-C (H42L) place it close to the intersection of the LS correlation line comprising Clds that also have only a distal Arg and the correlation line for HS hydroxides with little to no H-bond donation from the distal pocket. This raises the question of whether this is a LS heme hydroxide under the influence of a distal Arg, or a HS hydroxide in which the mutation preludes H-bond donation by the distal Arg. Since the distal Arg in peroxidases is important to the H-bond network in the distal cavity, essential for

stabilizing peroxidase anion complexes, and stabilizes the enzymes at alkaline pH,[81] distal Arg interaction with hydroxide in HRP-C (H42L) is reasonable. If the Arg were a H-bond donator to the HS HRP-C (H42L)−OH, the correlation line for HS hydroxide heme in strongly H-bond donating environments predicts that its ν(Fe^{III}−OH) would be lower than those observed for HS *Da*- and *Kp*Cld−OHs; this was not observed. In light of the (Fe^{III}−OH)/ν(Fe^{II}−His) correlation plot, the possibility of the ν(Fe^{III}−OH) band arises from a LS hydroxide with significant H-bond donation from the distal Arg cannot be eliminated and its assignment to the HS heme hydroxide should be considered tentative.

3.5.3.3. Sensitivity of the ν(Fe^{III}−X) frequencies to proximal and distal effects.

Table B2 shows the relationship between the ν(Fe^{III}−F) and ν(Fe^{III}−OH) frequencies and the respective bond lengths, calculated in accord with Badger's Rule.[82-83] The estimated equilibrium bond lengths (r_e(Fe−X)) within a set of heme fluorides or hydroxides on the same correlation line fall within a range of only ~3% and ~5% of the average values, respectively. Thus, these ν(Fe^{III}−X) frequency trends reflect changes in heme environment that elicit changes in r_e(Fe−X) that are on the cusp of being too small to be reliably reported by other structural methods. Insofar as catalysis in heme-dependent oxidoreductases is linked to the facility with which bonds between the heme iron and exogenous ligands are made and broken, understanding the structural basis of Fe−X bond strength sensitivity to differences between or changes in heme environments is a necessary prelude to understanding the structural basis of mechanism. The relationships described herein constitute an exquisitely sensitive reporter of such mechanistically relevant structural changes.

3.6. Conclusions

Examination of halide and hydroxide complexes of Clds highlights both similarities and differences between dimeric *Kp* and pentameric *Da*Cld active sites. Strong H-bond donation occurs from the distal Arg residue to the atom directly bonded to the heme iron in Clds from clades 1 and 2. This is apparent from their similar positions on the plot showing the direct correlation between the $\nu(Fe^{III}–F)$ and CT1 frequencies.

Inverse correlations, reported here for the first time, between $\nu(Fe^{III}–X)$, where $X = F^-$ or OH^-, and $\nu(Fe^{II}–His)$ provide a more detailed account of the proximal and distal environments and their effects on the Fe−X bond strength. The positions of *Da*Cld−X and *Kp*Cld−X on those lines clearly shows that the effects of their distal environments on Fe−X bonding are strikingly similar. Where the two enzymes differ is in their proximal environments, which impose *trans* effects of different magnitudes on the Fe–X bond. These inverse correlations hold for other His-ligated heme proteins that donate different numbers of distal H-bonds of various strengths to the bound X^- ligand. They reveal that the H-bond donating character in the distal pocket increases in the order: neutral His < protonated His < Arg. Thus, these correlations reveal additive effects of distal H-bond donation and *trans* (i.e. proximal) ligand influence on the Fe–X bond strength, as reported by $\nu(Fe^{III}–X)$ frequencies for π-donor ligands. As such, these two effects can combine to labialize ligands, such as F^-, OH^-, and OH_2 toward ligand exchange with heme-binding substrates like ClO_2^- in the case of Clds. Consequently, these ligands do not strongly inhibit *Kp*Cld activity.

The proximal ligands in the Clds, Mb and most heme-dependent peroxidases are the imidazole side chains of His residues and proximal $\nu(Fe^{II}–His)$ frequencies are governed by the same environmental factors. Thus, it is reasonable to hypothesize that the *trans* effect on distal

Fe−OH and Fe=O bond strengths would be similar. This hypothesis is supported by similarity between the slopes of the $\nu(Fe^{III}–OH)/\nu(Fe^{II}–His)$ and $\nu(Fe^{IV}=O)/\nu(Fe^{II}–His)$ frequency correlations (−1.8±0.2 and −1.2±0.5, respectively), which characterize the *trans* effect. Using the inverse correlation between the $\nu(Fe^{III}–OH)$ and $\nu(Fe^{II}–His)$ frequencies as a gauge for the *trans* effects on $\nu(Fe^{IV}=O)$ frequencies for *Kp* and *Da*Clds, they are predicted to fall between those for Mb and HPRC.[50] This suggests that the $Fe^{IV}=O$ bond strength required for ClO_2^- decomposing activity is lower than that in heme peroxidases, consistent with a lowered barrier for $Fe^{IV}=O$ bond scission in an oxo-atom transfer step with the putative OCl fragment. This may lend kinetic facility to the penultimate O−O bond forming step of ClO_2^- decomposition hypothesized to yield an $Fe^{III}–OOCl$ intermediate.[31]

*Kp*Cld binds Cl^- cooperatively (n = 2.3±0.1), likely at or near salt bridges remote from the heme and deterministic for heme pocket conformation. Although binding of anionic π-donor ligands is not specific to Cl^-, only Cl^- was observed to bind cooperatively. Because cooperativity places the steepest region of the Cl^- binding curve for *Kp*Cld in the physiological [Cl^-] range (Figure 3.2A) of the cytosol, the heme coordination number is a steep function of that Cl^- concentration. While cooperative binding of Cl^- is expected to affect the coordination state of cytosolic, dimeric Clds, the coordination state of periplasmic, pentameric Clds remains insensitive to Cl^-. This is consistent with a role for Cl^- in modulating ligand/substrate access to the *Kp*Cld heme pocket in this pathogenic organism.[10]

3.7. Associated Content

Additional data referred to in the text are located in Appendix B: Figures B1 to B10 and Tables B1 to B2.

3.8. Funding Sources

Support is gratefully acknowledged from the National Institutes of Health Grants GM114787 (to G. S. L.-R.) and GM090260 (to J. L. D.).

3.9. Acknowledgments

The authors wish to thank Garrett Moraski for his helpful suggestions during the preparation of this manuscript.

3.10. References

1. DuBois, J. L.; Ojha, S., Production of dioxygen in the dark: dismutases of oxyanions. *Met Ions Life Sci* 2015, *15*, 45-87.
2. Schaffner, I.; Hofbauer, S.; Krutzler, M.; Pirker, K. F.; Furtmueller, P. G.; Obinger, C., Mechanism of chlorite degradation to chloride and dioxygen by the enzyme chlorite dismutase. *Arch. Biochem. Biophys.* 2015, *574*, 18-26.
3. Tagore, R.; Crabtree, R. H.; Brudvig, G. W., Oxygen Evolution Catalysis by a Dimanganese Complex and Its Relation to Photosynthetic Water Oxidation. *Inorg. Chem.* 2008, *47* (6), 1815-1823.
4. Maixner, F.; Wagner, M.; Lueker, S.; Pelletier, E.; Schmitz-Esser, S.; Hace, K.; Spieck, E.; Konrat, R.; Le Paslier, D.; Daims, H., Environmental genomics reveals a functional chlorite dismutase in the nitrite-oxidizing bacterium '*Candidatus Nitrospira defluvii*'. *Environ.Microbiol.* 2008, *10* (11), 3043-3056.
5. Goblirsch, B.; Kurker, R. C.; Streit, B. R.; Wilmot, C. M.; DuBois, J. L., Chlorite dismutases, DyPs, and EfeB: 3 microbial heme enzyme families comprise the CDE structural superfamily. *J. Mol. Biol.* 2011, *408*, 379.
6. Mlynek, G.; Sjoeblom, B.; Kostan, J.; Fuereder, S.; Maixner, F.; Gysel, K.; Furtmueller, P. G.; Obinger, C.; Wagner, M.; Daims, H.; Djinovic-Carugo, K., Unexpected diversity of chlorite dismutases: a catalytically efficient dimeric enzyme from *Nitrobacter winogradskyi*. *J. Bact.* 2011, *193*, 2408-2417.
7. Melnyk, R. A.; Engelbrektson, A.; Clark, I. C.; Carlson, H. K.; Byrne-Bailey, K.; Coates, J. D., Identification of a perchlorate reduction genomic island with novel regulatory and metabolic genes. *Appl. Environ. Microbiol.* 2011, *77*, 7401-7404.
8. Clark, I. C.; Melnyk, R. A.; Engelbrektson, A.; Coates, J. D., Structure and evolution of chlorate reduction composite transposons. *mBio* 2013, *4*, e00379, 12 pp.
9. Hofbauer, S.; Schaffner, I.; Furtmueller, P. G.; Obinger, C., Chlorite dismutases - a heme enzyme family for use in bioremediation and generation of molecular oxygen. *Biotechnol. J.* 2014, *9*, 461.
10. Celis, A. I.; Geeraerts, Z.; Ngmenterebo, D.; Machovina, M. M.; Kurker, R. C.; Rajakumar, K.; Ivancich, A.; Rodgers, K. R.; Lukat-Rodgers, G. S.; DuBois, J. L., A Dimeric Chlorite Dismutase Exhibits O2-Generating Activity and Acts as a Chlorite Antioxidant in *Klebsiella pneumoniae* MGH 78578. *Biochemistry* 2015, *54*, 434-446.

11. Schaffner, I.; Hofbauer, S.; Krutzler, M.; Pirker, K. F.; Bellei, M.; Stadlmayr, G.; Mlynek, G.; Djinovic-Carugo, K.; Battistuzzi, G.; Furtmueller, P. G.; Daims, H.; Obinger, C., Dimeric chlorite dismutase from the nitrogen-fixing cyanobacterium Cyanothece sp. PCC7425. *Mol. Microbiol.* 2015, *96*, 1053-1068.
12. Dailey, H. A.; Gerdes, S.; Dailey, T. A.; Burch, J. S.; Phillips, J. D., Noncanonical coproporphyrin-dependent bacterial heme biosynthesis pathway that does not use protoporphyrin. *Proc. Natl. Acad. Sci. U. S. A.* 2015, *112*, 2210-2215.
13. Dailey, H. A.; Gerdes, S., HemQ: An iron-coproporphyrin oxidative decarboxylase for protoheme synthesis in Firmicutes and Actinobacteria. *Arch. Biochem. Biophys.* 2015, *574*, 27-35.
14. Dailey, T. A.; Boynton, T. O.; Albetel, A.-N.; Gerdes, S.; Johnson, M. K.; Dailey, H. A., Discovery and Characterization of HemQ: an essential heme biosynthetic pathway component. *J. Biol. Chem.* 2010, *285*, 25978-25986.
15. Celis, A. I.; Streit, B. R.; Moraski, G. C.; Kant, R.; Lash, T. D.; Lukat-Rodgers, G. S.; Rodgers, K. R.; DuBois, J. L., Unusual Peroxide-Dependent, Heme-Transforming Reaction Catalyzed by HemQ. *Biochemistry* 2015, *54*, 4022-4032.
16. Lobo, S. A. L.; Scott, A.; Videira, M. A. M.; Winpenny, D.; Gardner, M.; Palmer, M. J.; Schroeder, S.; Lawrence, A. D.; Parkinson, T.; Warren, M. J.; Saraiva, L. M., Staphylococcus aureus haem biosynthesis: characterisation of the enzymes involved in final steps of the pathway. *Mol. Microbiol.* 2015, *97*, 472-487.
17. Coates, J. D.; Achenbach, L. A., Microbial perchlorate reduction: rocket-fueled metabolism. *Nat.Rev.Microbiol.* 2004, *2* (7), 569-580.
18. Streit, B. R.; DuBois, J. L., Chemical and Steady-State Kinetic Analyses of a Heterologously Expressed Heme Dependent Chlorite Dismutase. *Biochemistry* 2008, *47* (19), 5271-5280.
19. Mayfield, J. A.; Blanc, B.; Rodgers, K. R.; Lukat-Rodgers, G. S.; DuBois, J. L., Peroxidase-Type Reactions Suggest a Heterolytic/Nucleophilic O–O Joining Mechanism in the Heme-Dependent Chlorite Dismutase. *Biochemistry* 2013, *52* (40), 6982-6994.
20. Sun, S.; Li, Z.-S.; Chen, S.-L., A dominant homolytic O-Cl bond cleavage with low-spin triplet-state Fe(IV)=O formed is revealed in the mechanism of heme-dependent chlorite dismutase. *Dalton Trans.* 2014, *43* (Copyright (C) 2015 American Chemical Society (ACS). All Rights Reserved.), 973-981.
21. Su, J.-X.; Chen, H.-L., Significant electron transfer in heme catalysis: The case of chlorite dismutase. *J. Catal.* 2017, *348*, 40-46.
22. Goblirsch, B. R.; Streit, B. R.; DuBois, J. L.; Wilmot, C. M., Structural features promoting dioxygen production by Dechloromonas aromatica chlorite dismutase. *J.Biol.Inorg.Chem.* 2010, *15* (6), 879-888.
23. de Geus, D. C.; Thomassen, E. A. J.; Hagedoorn, P. L.; Pannu, N. S.; van Duijn, E.; Abrahams, J. P., Crystal Structure of Chlorite Dismutase, a Detoxifying Enzyme Producing Molecular Oxygen. *J. Mol. Biol.* 2009, *387* (1), 192-206.
24. Kostan, J.; Sjoeblom, B.; Maixner, F.; Mlynek, G.; Furtmueller, P. G.; Obinger, C.; Wagner, M.; Daims, H.; Djinovic-Carugo, K., Structural and functional characterisation of the chlorite dismutase from the nitrite-oxidizing bacterium "Candidatus Nitrospira defluvii": Identification of a catalytically important amino acid residue. *J.Struct.Biol.* 2010, *172* (3), 331-342.

25. Catling, D. C.; Claire, M. W.; Zahnle, K. J.; Quinn, R. C.; Clark, B. C.; Hecht, M. H.; Kounaves, S. Atmospheric origins of perchlorate on Mars and in the Atacama *J. Geophys. Res., [Planets]* [Online], 2010, p. E00E11/1-E00E11/15. http://onlinelibrary.wiley.com/store/10.1029/2009JE003425/asset/jgre2709.pdf?v=1&t=ihsbp3ol&s=9fa6fd93eee324c7fdcfb1972eab931312dd2dd1.
26. Rao, B.; Hatzinger, P. B.; Bohlke, J. K.; Sturchio, N. C.; Andraski, B. J.; Eckardt, F. D.; Jackson, W. A., Natural Chlorate in the Environment: Application of a New IC-ESI/MS/MS Method with a Cl18O3- Internal Standard. *Environ. Sci. Technol.* 2010, *44*, 8429-8434.
27. Blanc, B.; Mayfield, J. A.; McDonald, C. A.; Lukat-Rodgers, G. S.; Rodgers, K. R.; DuBois, J. L., Understanding How the Distal Environment Directs Reactivity in Chlorite Dismutase: Spectroscopy and Reactivity of Arg183 Mutants. *Biochemistry* 2012, *51*, 1895-1910.
28. Hofbauer, S.; Gysel, K.; Bellei, M.; Hagmueller, A.; Schaffner, I.; Mlynek, G.; Kostan, J.; Pirker, K. F.; Daims, H.; Furtmueller, P. G.; Battistuzzi, G.; Djinovic-Carugo, K.; Obinger, C., Manipulating conserved heme cavity residues of chlorite dismutase: Effect on structure, redox chemistry, and reactivity. *Biochemistry* 2014, *53*, 77-89.
29. Streit, B. R.; Blanc, B.; Lukat-Rodgers, G. S.; Rodgers, K. R.; DuBois, J. L., How Active-Site Protonation State Influences the Reactivity and Ligation of the Heme in Chlorite Dismutase. *J. Am. Chem. Soc.* 2010, *132*, 5711-5724.
30. Hofbauer, S.; Gruber, C.; Pirker, K. F.; Suendermann, A.; Schaffner, I.; Jakopitsch, C.; Oostenbrink, C.; Furtmueller, P. G.; Obinger, C., Transiently produced hypochlorite is responsible for the irreversible inhibition of chlorite dismutase. *Biochemistry* 2014, *53*, 3145-3157.
31. Lee, A. Q.; Streit, B. R.; Zdilla, M. J.; bu-Omar, M. M.; DuBois, J. L., Mechanism of and exquisite selectivity for O-O bond formation by the heme-dependent chlorite dismutase. *Proc. Natl. Acad. Sci. U. S. A.* 2008, *105* (41), 15654-15659.
32. Pettersen, E. F.; Goddard, T. D.; Huang, C. C.; Couch, G. S.; Greenblatt, D. M.; Meng, E. C.; Ferrin, T. E., UCSF Chimera—A visualization system for exploratory research and analysis. *J. Comput. Chem.* 2004, *25* (13), 1605-1612.
33. Tropea, J. E. C., Scott; Waugh, David S., Expression and purification of soluble His_6-tagged TEV protease. In *Methods in Molecular Biology: High Throughput Protein Expression and Purification*, Doyle, S. A., Ed. Humana Press: Totowa, NJ, 2009; Vol. 498, pp 297-306.
34. Blanc, B.; Rodgers, K. R.; Lukat-Rodgers, G. S.; DuBois, J. L., Understanding the roles of strictly conserved tryptophan residues in O2 producing chlorite dismutases. *Dalton Trans.* 2013, *42*, 3156-3169.
35. Philippi, M.; dos Santos, H. S.; Martins, A. O.; Azevedo, C. M.; Pires, M., Alternative spectrophotometric method for standardization of chlorite aqueous solutions. *Anal Chim Acta* 2007, *585* (2), 361-5.
36. Antonini, E.; Brunori, M., *Frontier in Biology; Hemoglobin and Myoglobin in Their Reactions with Ligands* North-Holland Publishing Co.: Amsterdam, 1971.
37. Indiani, C.; Feis, A.; Howes, B. D.; Marzocchi, M. P.; Smulevich, G., Benzohydroxamic Acid-Peroxidase Complexes: Spectroscopic Characterization of a Novel Heme Spin Species. *J. Am. Chem. Soc.* 2000, *122* (30), 7368-7376.

38. Indiani, C.; Santoni, E.; Becucci, M.; Boffi, A.; Fukuyama, K.; Smulevich, G., New Insight into the Peroxidase-Hydroxamic Acid Interaction Revealed by the Combination of Spectroscopic and Crystallographic Studies. *Biochemistry* 2003, *42* (47), 14066-14074.
39. Marcus, Y., Ionic radii in aqueous solutions. *Chem, Rev.* 1988, *88* (8), 1475-1498.
40. Rwere, F.; Mak, P. J.; Kincaid, J. R., Resonance Raman determination of vinyl group disposition in different derivatives of native myoglobin and its heme-disoriented form. *J. Raman Spectrosc.* 2014, *45* (1), 97-104.
41. Paulat, F.; Praneeth, V. K. K.; Naether, C.; Lehnert, N., Quantum Chemistry-Based Analysis of the Vibrational Spectra of Five-Coordinate Metalloporphyrins [M(TPP)Cl]. *Inorg. Chem.* 2006, *45*, 2835-2856.
42. Hu, S.; Smith, K. M.; Spiro, T. G., Assignment of protoheme resonance Raman spectrum by heme labeling in myoglobin. *J. Am. Chem. Soc.* 1996, *118* (50), 12638-12646.
43. Droghetti, E.; Nicoletti, F. P.; Bonamore, A.; Sciamanna, N.; Boffi, A.; Feis, A.; Smulevich, G., The optical spectra of fluoride complexes can effectively probe H-bonding interactions in the distal cavity of heme proteins. *J. Inorg. Biochem.* 2011, *105*, 1338-1343.
44. Nicoletti, F. P.; Droghetti, E.; Boechi, L.; Bonamore, A.; Sciamanna, N.; Estrin, D. A.; Feis, A.; Boffi, A.; Smulevich, G., Fluoride as a Probe for H-Bonding Interactions in the Active Site of Heme Proteins: The Case of Thermobifida fusca Hemoglobin. *J. Am. Chem. Soc.* 2011, *133*, 20970-20980.
45. Asher, S. A.; Schuster, T. M., Differences in iron-fluoride bonding between the isolated subunits of human methemoglobin fluoride and sperm whale metmyoglobin fluoride as measured by resonance Raman spectroscopy. *Biochemistry* 1981, *20* (7), 1866-1873.
46. Droghetti, E.; Nicoletti, F. P.; Bonamore, A.; Boechi, L.; Arroyo, M. P.; Estrin, D. A.; Boffi, A.; Smulevich, G.; Feis, A., Heme pocket structural properties of a bacterial truncated hemoglobin from Thermobifida fusca. *Biochemistry* 2010, *49*, 10394-10402.
47. Teraoka, J.; Kitagawa, T., Structural implication of the heme-linked ionization of horseradish peroxidase probed by the iron-histidine stretching Raman line. *J. Biol. Chem.* 1981, *256* (8), 3969-3977.
48. Kitagawa, T.; Nagai, K.; Tsubaki, M., Assignment of the iron-nitrogen (His F8) stretching band in the resonance Raman spectra of deoxymyoglobin. *FEBS Letters* 1979, *104* (2), 376-378.
49. Chance, M.; Powers, L.; Kumar, C.; Chance, B., X-ray absorption studies of myoglobin peroxide reveal functional differences between globins and heme enzymes. *Biochemistry* 1986, *25* (Copyright (C) 2017 American Chemical Society (ACS). All Rights Reserved.), 1259-65.
50. Oertling, W. A.; Kean, R. T.; Wever, R.; Babcock, G. T., Factors affecting the iron-oxygen vibrations of ferrous oxy and ferryl oxo heme proteins and model compounds. *Inorg. Chem.* 1990, *29* (Copyright (C) 2012 American Chemical Society (ACS). All Rights Reserved.), 2633-45.
51. Zhao, J.; Moretto, J.; Le, P.; Franzen, S., Measurement of Internal Substrate Binding in Dehaloperoxidase–Hemoglobin by Competition with the Heme–Fluoride Binding Equilibrium. *J. Phys. Chem. B* 2015, *119* (7), 2827-2838.
52. Draganova, E. B.; Akbas, N.; Adrian, S. A.; Lukat-Rodgers, G. S.; Collins, D. P.; Dawson, J. H.; Allen, C. E.; Schmitt, M. P.; Rodgers, K. R.; Dixon, D. W., Heme

Binding by Corynebacterium diphtheriae HmuT: Function and Heme Environment. *Biochemistry* 2015, *54*, 6598-6609.
53. Asher, S. A.; Adams, M. L.; Schuster, T. M., Resonance Raman and absorption spectroscopic detection of distal histidine-fluoride interactions in human methemoglobin fluoride and sperm whale metmyoglobin fluoride: measurements of distal histidine ionization constants. *Biochemistry* 1981, *20* (12), 3339-3346.
54. Asher, S. A.; Schuster, T. M., Resonance Raman examination of axial ligand bonding and spin-state equilibriums in metmyoglobin hydroxide and other heme derivatives. *Biochemistry* 1979, *18* (24), 5377-5387.
55. Jeyarajah, S.; Kincaid, J. R., Resonance Raman studies of hemoglobins reconstituted with mesoheme. Unperturbed iron-histidine stretching frequencies in a functionally altered hemoglobin. *Biochemistry* 1990, *29* (Copyright (C) 2017 American Chemical Society (ACS). All Rights Reserved.), 5087-94.
56. Lukat-Rodgers, G. S.; Rexine, J. L.; Rodgers, K. R., Heme Speciation in Alkaline Ferric FixL and Possible Tyrosine Involvement in the Signal Transduction Pathway for Regulation of Nitrogen Fixation. *Biochemistry* 1998, *37*, 13543-13552.
57. Feis, A.; Marzocchi, M. P.; Paoli, M.; Smulevich, G., Spin State and Axial Ligand Bonding in the Hydroxide Complexes of Metmyoglobin, Methemoglobin, and Horseradish Peroxidase at Room and Low Temperatures. *Biochemistry* 1994, *33* (15), 4577-4583.
58. Lansky, I. B.; Lukat-Rodgers, G. S.; Block, D.; Rodgers, K. R.; Ratliff, M.; Wilks, A., The Cytoplasmic Heme-binding Protein (PhuS) from the Heme Uptake System of Pseudomonas aeruginosa Is an Intracellular Heme-trafficking Protein to the δ-Regioselective Heme Oxygenase. *J. Biol. Chem.* 2006, *281*, 13652-13662.
59. Belyea, J.; Belyea, C. M.; Lappi, S.; Franzen, S., Resonance Raman Study of Ferric Heme Adducts of Dehaloperoxidase from Amphitrite ornata. *Biochemistry* 2006, *45* (48), 14275-14284.
60. Franzen, S.; Roach, M. P.; Chen, Y.-P.; Dyer, R. B.; Woodruff, W. H.; Dawson, J. H., The Unusual Reactivities of *Amphitrite ornata* Dehaloperoxidase and *Notomatus lobatus* Chloroperoxidase Do Not Arise from a Histidine Imidazolate Proximal Heme Iron Ligand. *J. Am. Chem. Soc.* 1998, *120*, 4658-4661.
61. Sitter, A. J.; Shifflett, J. R.; Terner, J., Resonance Raman spectroscopic evidence for heme iron-hydroxide ligation in peroxidase alkaline forms. *J Biol Chem* 1988, *263* (Copyright (C) 2012 U.S. National Library of Medicine.), 13032-8.
62. Smulevich, G.; Feis, A.; Focardi, C.; Tams, J.; Welinder, K. G., Resonance Raman Study of the Active Site of Coprinus cinereus Peroxidase. *Biochemistry* 1994, *33* (51), 15425-15432.
63. Lukat-Rodgers, G. S.; Rodgers, K. R., Spin-state equilibria and axial ligand bonding in FixL hydroxide: a resonance Raman study. *J. Biol. Inorg. Chem.* 1998, *3* (Copyright (C) 2012 American Chemical Society (ACS). All Rights Reserved.), 274-281.
64. McCombs, N. L.; D'Antonio, J.; Barrios, D. A.; Carey, L. M.; Ghiladi, R. A., Nonmicrobial Nitrophenol Degradation via Peroxygenase Activity of Dehaloperoxidase-Hemoglobin from Amphitrite ornata. *Biochemistry* 2016, *55* (17), 2465-2478.
65. Smulevich, G.; Feis, A.; Howes, B. D., Fifteen years of Raman spectroscopy of engineered heme containing peroxidases: What have we learned? *Accounts of Chemical Research* 2005, *38* (5), 433-440.

66. Teraoka, J.; Job, D.; Morita, Y.; Kitagawa, T., Resonance Raman study of plant tissue peroxidases. Common characteristics in iron coordination environments. *Biochim. Biophys. Acta, Protein Struct. Mol. Enzymol.* 1983, *747* (Copyright (C) 2017 American Chemical Society (ACS). All Rights Reserved.), 10-15.
67. Desbois, A.; Mazza, G.; Stetzkowski, F.; Lutz, M., Resonance Raman spectroscopy of protoheme-protein interactions in oxygen-carrying hemoproteins and in peroxidases. *Biochim. Biophys. Acta, Protein Struct. Mol. Enzymol.* 1984, *785* (Copyright (C) 2017 American Chemical Society (ACS). All Rights Reserved.), 161-76.
68. Ellis, W. D.; Dunford, H. B., The kinetics of cyanide and fluoride binding by ferric horseradish peroxidase. *Biochemistry* 1968, *7* (6), 2054-2062.
69. Singh, R.; Grigg, J. C.; Armstrong, Z.; Murphy, M. E. P.; Eltis, L. D., Distal Heme Pocket Residues of B-type Dye-decolorizing Peroxidase: Arginine but not Aspartate is Essential for Peroxidase Activity. *J. Biol. Chem.* 2012, *287*, 10623-10630.
70. Singh, A. K.; Pandey, N.; Sinha, M.; Kaur, P.; Sharma, S.; Singh, T. P., Structural evidence for the order of preference of inorganic substrates in mammalian heme peroxidases: crystal structure of the complex of lactoperoxidase with four inorganic substrates, SCN^-, I^-, Br^- and Cl^-. *Int. J. Biochem. Mol. Biol.* 2011, *2*, 328-339.
71. Fiedler, T. J.; Davey, C. A.; Fenna, R. E., X-ray crystal structure and characterization of halide-binding sites of human myeloperoxidase at 1.8 Å resolution. *J. Biol. Chem.* 2000, *275* (Copyright (C) 2017 American Chemical Society (ACS). All Rights Reserved.), 11964-11971.
72. Freire, D. M.; Rivas, M. G.; Dias, A. M.; Lopes, A. T.; Costa, C.; Santos-Silva, T.; Van Doorslaer, S.; Gonzalez, P. J., The homopentameric chlorite dismutase from *Magnetospirillum sp*. *J. Inorg. Biochem.* 2015, *151*, 1-9.
73. De Schutter, A.; Correia, H. D.; Freire, D. M.; Rivas, M. G.; Rizzi, A.; Santos-Silva, T.; Gonzalez, P. J.; Van Doorslaer, S., Ligand binding to chlorite dismutase from *Magnetospirillum sp*. *J. Phys. Chem. B* 2015, *119*, 13859-13869.
74. Benz, R.; Schmid, A.; Hancock, R. E., Ion selectivity of gram-negative bacterial porins. *J. Bact.* 1985, *162* (2), 722-727.
75. Schultz, S. G.; Wilson, N. L.; Epstein, W., Cation Transport in Escherichia coli II. Intracellular chloride concentration. *J. Gen. Physiol.* 1962, *46* (1), 159-166.
76. Hofbauer, S.; Howes, B. D.; Flego, N.; Pirker, K. F.; Schaffner, I.; Mlynek, G.; Djinovic-Carugo, K.; Furtmueller, P. G.; Smulevich, G.; Obinger, C., From chlorite dismutase towards HemQ-the role of the proximal H-bonding network in haeme binding. *Biosci. Rep.* 2016, *36*, e00312.
77. Nicoletti, F. P.; Droghetti, E.; Howes, B. D.; Bustamante, J. P.; Bonamore, A.; Sciamanna, N.; Estrin, D. A.; Feis, A.; Boffi, A.; Smulevich, G., H-bonding networks of the distal residues and water molecules in the active site of Thermobifida fusca hemoglobin. *Biochim. Biophys. Acta, Proteins Proteomics* 2013, *1834* (Copyright (C) 2014 American Chemical Society (ACS). All Rights Reserved.), 1901-1909.
78. Egawa, T.; Yeh, S.-R., Structural and functional properties of hemoglobins from unicellular organisms as revealed by resonance Raman spectroscopy. *J. Inorg. Biochem.* 2005, *99* (Copyright (C) 2017 American Chemical Society (ACS). All Rights Reserved.), 72-96.
79. Nicoletti, F. P.; Bustamante, J. P.; Droghetti, E.; Howes, B. D.; Fittipaldi, M.; Bonamore, A.; Baiocco, P.; Feis, A.; Boffi, A.; Estrin, D. A.; Smulevich, G., Interplay of the H-Bond

Donor-Acceptor Role of the Distal Residues in Hydroxyl Ligand Stabilization of Thermobifida fusca Truncated Hemoglobin. *Biochemistry* 2014, *53* (Copyright (C) 2017 American Chemical Society (ACS). All Rights Reserved.), 8021-8030.
80. Howes, B. D.; Rodriguez-Lopez, J. N.; Smith, A. T.; Smulevich, G., Mutation of Distal Residues of Horseradish Peroxidase: Influence on Substrate Binding and Cavity Properties. *Biochemistry* 1997, *36* (6), 1532-1543.
81. Neri, F.; Indiani, C.; Welinder, K. G.; Smulevich, G., Mutation of the distal arginine in Coprinus cinereus peroxidase. Structural implications. *Eur. J. Biochem.* 1998, *251* (3), 830-838.
82. Badger, R. M., The Relation Between the Internuclear Distances and Force Constants of Molecules and Its Application to Polyatomic Molecules. *J. Chem. Phys.* 1935, *3* (11), 710-714.
83. Badger, R. M., A Relation Between Internuclear Distances and Bond Force Constants. *J. Chem. Phys.* 1934, *2* (3), 128-131.

4. DISTINGUISHING ACTIVE SITE CHARACTERISTICS OF CHLORITE DISMUTASES WITH THEIR CYANIDE COMPLEXES[3]

4.1. Abstract

O_2-evolving chlorite dismutases (Clds) efficiently convert chlorite (ClO_2^-) to O_2 and Cl^-. *Dechloromonas aromatica* Cld (*Da*Cld) is a highly active chlorite-decomposing homopentameric enzyme, typical of Clds found in perchlorate and chlorate respiring bacteria. The Gram-negative, human pathogen *Klebsiella pneumoniae* contains a homodimeric Cld (*Kp*Cld) that also decomposes ClO_2^-, albeit with a 10-fold lower activity and a lower turnover number compared to *Da*Cld. The interactions between the distal pocket and heme ligand of the *Da*Cld and *Kp*Cld active sites have been probed via kinetic, thermodynamic and spectroscopic behaviors of their cyanide complexes for insight into active site characteristics that are deterministic for chlorite decomposition. At 4.7×10^{-9} M, the K_D for *Kp*Cld−CN^- is two orders of magnitude smaller than that of *Da*Cld−CN^- and indicates an affinity for CN^- that is greater than that of most heme proteins. The difference in CN^- affinity between *Kp* and *Da*Clds is predominantly due to differences in k_{off}. The kinetics of cyanide binding to *Da*Cld, *Da*Cld(R183Q) and *Kp*Cld between pH 4 and 8.5 corroborate the importance of distal Arg183 and a pK_a ~ 7 in stabilizing complexes of anionic ligands, including substrate. The Fe−C stretching and FeCN bending modes of *Da*Cld−CN^- ($\nu_{Fe\text{-}C}$, 441 cm^{-1}; δ_{FeCN}, 396 cm^{-1}) and *Kp*Cld−CN^- ($\nu_{Fe\text{-}C}$, 441 cm^{-1}; δ_{FeCN}, 356 cm^{-1}) reveal differences in their FeCN angle, which suggest different distal pocket interactions with their bound cyanide. Conformational differences

[3]The material in this chapter is from a collaborative manuscript published in the journal Biochemistry (https://doi.org/10.1021/acs.biochem.7b01278) co-authored by Zachary Geeraerts, Arianna I. Celis, Jeffery A. Mayfield, Megan Lorenz, Kenton R. Rodgers, Jennifer L. DuBois, and Gudrun S. Lukat-Rodgers. Zachary Geeraerts had primary responsibility in isolating, characterizing cyano complexes by resonance Raman and UV/visible absorbance spectroscopies, and measuring specific activity for oxygen evolution of *Kp*Cld and *Da*Cld. His responsibilities also included data analysis, interpretation, generating figures, and writing of sections related to the aforementioned data.

in their catalytic sites are also reported by the single ferrous *Kp*Cld carbonyl complex, which is in contrast to the two conformers observed for *Da*Cld−CO.

4.2. Introduction

O_2-evolving chlorite dismutases (Clds) catalyze the rapid decomposition of a single chlorite ion (ClO_2^-) to O_2 and Cl^- with heme *b* as the sole cofactor required for this unique O–O bond-forming reaction.[1-2] Unlike the water-oxidation reaction catalyzed by the tetramanganese center in the oxygen-evolving complex of photosystem II,[3] Cld catalyzes the reaction without being coupled to generation of a proton gradient. Instead, the Cld-catalyzed reaction serves to detoxify chlorite generated from respiratory reduction of perchlorate or chlorate.[4]

The Cld protein family consists of three major clades identified in phylogentic studies.[5-9] Although members of two of these clades differ in subunit size and oligomeric state, they are referred to as functional Clds because they catalyze the decomposition of ClO_2^-. The first clade consists predominantly of the respiratory pentameric Clds found mainly in Proteobacteria.[10] Dimeric Clds from non-perchlorate-respiring species constitute the second clade; their subunit size is significantly smaller than that of the respiratory Clds due to a truncated N-terminus.[9, 11] The third Cld clade contains coproheme decarboxylases.[12] While these enzymes share structural similarities with the first two clades, they catalyze a completely different reaction, the oxidative decarboxylation of coproheme as the terminal step of heme biosynthesis in Gram-positive bacteria.[12-16]

In perchlorate-respiring bacteria like *Dechloromonas aromatica*, Cld's function is the efficient detoxification of the ClO_2^- produced by metabolic reduction of ClO_4^-.[4] *Dechloromonas aromatica* Cld (*Da*Cld) is capable of turning over >20,000 equivalents of ClO_2^- per heme prior to irreversible inactivation ($k_{cat}/K_M = (3.2\pm0.4)\times10^7\ M^{-1}s^{-1}$ at pH 5.2, 4 °C).[17] Although members

of the second clade are efficient catalysts for ClO_2^- decomposition ($k_{cat}/K_M = 10^6\ M^{-1}{\cdot}s^{-1}$, pH 5.0−6.0, 20−30 °C)[5, 9, 11], their *in-vivo* function is not clear. Growth studies of a Δ*cld* knockout strain of *Klebsiella pneumoniae* strain MGH 78578, a Gram-negative, non-perchlorate-respiring bacterium, suggest that its Cld (*Kp*Cld) may have a role in detoxification of ClO_2^- produced endogenously by nitrate reductases, acting upon ClO_4^- or ClO_3^-.[9] It has been hypothesized that a general function of Clds from non-perchlorate-respiring species may be protection against the effects of environmental ClO_4^- or ClO_3^-.[1, 18-19]

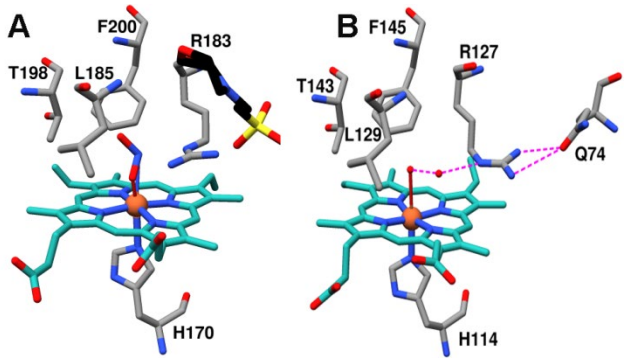

Figure 4.1. Active site structures of a pentameric and a dimeric Cld. Heme environments for A) the ferric nitrite complex of the respiration-associated, pentameric *Da*Cld (PBD ID 3Q08)[20] and B) ferric aqua complex of *Nw*Cld (3QPI),[5] which like *Kp*Cld is a dimeric enzyme, are shown. Heme carbons are cyan, protein carbons are gray; nitrogen and oxygen atoms are blue and red, respectively. The distal face contains conserved threonine, phenylalanine, leucine, and arginine which form a cage around the sixth coordination site of the heme. The two distal pockets differ in the orientation of the distal Arg side chain. In the *Da*Cld structure (A), a MES buffer molecule (shown in black, yellow and red) is H-bonded to Arg183. A Gln, the H-bond partner to the distal Arg in *Nw*Cld (B), stabilizes the Arg in its open conformation. The structures are displayed using UCSF Chimera.[21]

The heme active sites of representatives of the two ClO_2^--decomposing Cld clades are shown in Figure 4.1. In both representative enzymes the heme is bound to the protein through a highly conserved proximal histidine,[20, 22] and the distal pocket contains a conserved arginine .[23-25] The distal arginine side chain position is flexible resulting in the accessibility of two conformations: one in which its guanidinium group is oriented toward the heme and one where the guanidinium group is directed toward the main access channel into the heme pocket.[5, 20, 23, 26]

The catalytic importance of the distal Arg is illustrated by substantial loss of chlorite degrading activity upon its mutation to Ala or Gln.[23-25] Recent evidence suggests that one role of the distal Arg is confining ClO^- generated during ClO_2^- decomposition to the heme pocket.[27] In *Da*Cld the Arg is quite effective in this role as ClO^- is not detected during catalytic turnover.[17, 28] When ClO^- escapes from the heme pocket, as observed for *Kp*Cld and the Cld from *Candidatus Nitrospira defluvii* (*Nd*Cld), a pentameric Cld, it is readily detected as HOCl.[9, 27] Enzyme degradation by HOCl limits *Kp*Cld to a significantly lower number of turnovers (6700 ± 300 equivalents ClO_2^- /heme) relative to *Da*Cld.[9] Thus, although the general heme site characteristics of Clds are similar, subtle variations in their active site structures and/or dynamics appear to modulate their ClO_2^--decomposing activity and turnover.

The resting axial ligation states of five-coordinate high spin (5cHS) and 5cHS/six-coordinate high spin (6cHS) heme in ferric *Da*Cld and *Kp*Cld, respectively, also point to differences in their active sites.[9] Ligand binding to heme proteins is sensitive to various factors such as the identity of the heme proximal ligand, amino acid composition of the distal pocket and the ability of distal residues to stabilize exogenous heme ligands with H-bonding, electrostatic, or steric interactions. Numerous spectroscopic methods using nonphysiological heme ligands have been developed to probe the distal landscape of the heme pocket to ascertain its influence on enzymatic activity. The reaction of cyanide with ferric heme proteins is widely used to probe their active site structure.[25, 29-35] Since it does not oxidize the heme iron center subsequent to coordination and its binding can readily be monitored spectrophotometrically to obtain k_{on}, k_{off} and equilibrium constants, cyanide can be used as an anionic reporter ligand. Additionally, subtle structural differences in heme−CN^- complexes due to different distal heme environments are discernible via rR spectroscopy.[36-43] Here we examine ferric Cld complexes with cyanide to

probe the distal environments of Clds from the two functional clades with the goal of identifying structural elements that differentially modulate their ClO_2^--degrading activities.

4.3. Experimental Methods

4.3.1. Growth, purification, and characterization of *Da* and *Kp*Cld enzymes.

DNA containing the full-length coding region of chlorite dismutase from *Klebsiella pneumoniae* MGH 78578 (accession no. CP000650.1) was PCR-amplified and cloned into the pET-15b (Merck/Novagen) expression vector for production of protein with a N-terminal His-tag as previously described.[9] The resulting vector was mutated to replace the thrombin protease site (CTG GTG CCG CGC GGC AGC) with a TEV protease site (GAA AAC CTG TAT TTT CAG GGC) for removal of the 6-His tag post purification. A Q5 Site-Directed Mutagenesis Kit was used with primers TEV_F (5'-T TTT CAG GGC CAT ATG AAT ACA CGA TTA TTT ACG TTC G-3') and TEV_R (5'-TA CAG GTT TTC GCC GCT GCT GTG ATG ATG-3'). Mutated plasmid was transformed in Tuner DE3 *E. coli* cells and *Kp*Cld was expressed, isolated, and purified as previously described.[9] The N-terminal His-tag of *Kp*Cld was removed by incubation with TEV(S219V) at 1 mol TEV per 10 mol Cld in 50 mM sodium phosphate pH 8.0, 2 mM DTT, and 0.5 mM EDTA overnight at 4 °C.[44] The proteolysis mixture was passed over a 5 mL HisTrap column equilibrated in 20 mM imidazole, 100 mM sodium phosphate pH 7.4. A linear gradient (20–500 mM imidazole) was used to separate cleaved *Kp*Cld from tagged *Kp*Cld during elution. Imidazole was removed with a PD-10 desalting column and exchanged into 100 mM sodium phosphate pH 6.8. Purity and cleavage were verified by SDS-PAGE.

Plasmids for the over-expression of WT *Da*Cld and *Da*Cld(R183Q) were available from previous work.[24, 28, 45] These *Da*Clds were expressed, isolated, and purified using published protocols.[17] All Cld concentrations are given as heme-bound monomer, where [Cld] was

determined using reported extinction coefficients. The activity with chlorite was routinely monitored to confirm the competency of each enzyme preparation.[9, 17] Initial rates of chlorite-decomposing activity by Clds were determined by monitoring O_2 evolution with a commercial luminescence-based probe under pseudo-first order conditions with 20 nM enzyme and [ClO_2^-] concentrations from 0.1–2.0 mM in 100 mM sodium phosphate pH 6.0 at 25 °C. Concentrations of freshly prepared stock chlorite solutions were determined via iodometric titration or spectrophotometrically by measuring its absorbance using $\varepsilon_{260} = 155\ M^{-1}cm^{-1}$.[46]

4.3.2. Equilibrium binding of cyanide to Cld.

Potassium cyanide (KCN) stock solutions were prepared anaerobically under nitrogen in 0.2 M potassium phosphate pH 5 – 8 and 0.2 M glycine pH > 8. Stock KCN concentrations were determined analytically via titration against a known silver nitrate ($AgNO_3$) solution in KOH with *p*-dimethylaminobenzylidene rhodanine as the indicator.[47-48] Titrations were done anaerobically to insure that the cyanide concentration did not change during the course of the experiment due to oxidation.[49]

For each spectrophotometric titration, a 4−8 μM Cld sample was prepared in a 1 mL volume of anaerobic buffer. Stock KCN solution was added in 1−2 μL aliquots. Spectra were repeatedly measured after each addition until the reaction mixtures had reached equilibrium. At the end of the titration, a cyanide stock of 10-fold higher concentration was added in 10 μL aliquots to ensure a clear endpoint had been reached. Difference spectra were generated from spectra which had been corrected for sample dilution. The wavelength of maximum absorbance change was used to construct a plot of ΔA versus $[L]_T$ (total concentration of added ligand) and for tight binding ligands such as cyanide, where the binding of ligand to the enzyme (E) affects

the overall concentration of ligand in solution, the data were fit to the quadratic form of the one-to-one titration equation:[34, 50]

$$\Delta A = \Delta A_{\infty}([E] + [L]_T + K_D - \{([E] + K_D + [L]_T)^2 - 4[E]\,[L]_T\}^{1/2})/(2[E]) \qquad \text{(Eq. 4.1)}$$

4.3.3. Transient kinetic reactions with KCN.

Rapid kinetic measurements were made using a Hi-Tech SF-61DX2 stopped-flow system. Spectra were measured from 320–700 nm with a diode array detector. Reactions were carried out under pseudo-first order conditions (≥ 10-fold ligand excess over heme) by rapidly mixing *Da*Cld, *Kp*Cld, or *Da*Cld(R183Q) (1−10 μM final concentrations) with varied final concentrations of potassium cyanide (10 μM−100 mM for WT and R183Q *Da*Cld and 5−200 μM for *Kp*Cld). Both the enzyme and ligand were diluted into the same buffer prior to binding experiments.

Observed rate constants (k_{obs}) were calculated by fitting ΔA time courses at either 420 nm (*Da*Cld), or 405 and 419 nm (*Kp*Cld) to the single-exponential function:

$$\Delta A_t = \Delta A_{tot} e^{-k_{obs} t} \qquad \text{(Eq. 4.2)}$$

Values for the second-order association rate constant (k_{on}) and the first-order dissociation constant (k_{off}) were determined from fitting plots of k_{obs} versus [KCN] to the following:

$$k_{obs} = k_{on}[KCN] + k_{off} \qquad \text{(Eq. 4.3)}$$

Dissociation constants for the *Da*Cld−CN^- complexes were determined from the ratio of rate constants:

$$K_D = \frac{k_{off}}{k_{on}} \qquad \text{(Eq. 4.4)}$$

In the case of *Kp*Cld, values for k_{off} extrapolated to negative values near the origin. In each case, k_{off} is on the order of 10% or less of the corresponding value for k_{on}. We interpret these results as indicative of a small k_{off} across the pH range. Since the uncertainties in the intercepts for

*Kp*Cld−CN^- are larger than the k_{off} itself, K_Ds were measured using spectrophotometric titrations and then used to calculate k_{off} using equation 4.

The rate constants k_{on} and k_{off} were measured in citrate-phosphate buffers as a function of pH from 4 to 8.5, as described above. The $\log_{10}$ values of these rate constants were computed and plotted versus pH. The data were then fit to either a one (Equation 4.5) or two (Equation 4.6) K_a model, depending on whether single or dual inflection points were observed in the data. These fits in turn yielded values for acid dissociation constants:

$$\log(k) = \log\left[\frac{c}{1+\frac{[H^+]}{K_a}}\right] \quad \text{(Eq. 4.5)}$$

$$\log(k) = \log\left[c \times \frac{1+\frac{[H^+]}{K_{a1}}}{1+\frac{[H^+]}{K_{a2}}}\right] \quad \text{(Eq. 4.6)}$$

All data were plotted using KaleidaGraph. Fits to equation 1 were made using the KinetAssyst software from Tgk Scientific. Fits to equations 2−5 were generated using the least squares fitting program in KaleidaGraph. All values for k_{obs} were based on measurements made in triplicate or more. The reported uncertainties are based on the standard deviations of *k*, which were determined from these multiple runs.

4.3.4. Vibrational characterization of Cld cyanide and CO complexes.

Resonance Raman (rR) spectra were recorded with 413.1-nm emission from a Kr^+ laser. Scattered light was collected in the 135° backscattering geometry using a f/1 lens to collect and collimate the light. Rayleigh scattered light was attenuated with a holographic notch filter and the remaining light passed through a polarization scrambler. Collection was f-matched to a single f/4.7 0.67-m Czerny-Turner spectrograph fitted with a 120×140 mm 1200 groove/mm holographic grating and operated with a 10 μm (0.74 cm^{-1}) slit. The spectrograph was fitted with a LN2-cooled CCD detector having a 26.8 mm (1340 pixel) × 8.0 mm (400 pixel) image area.

The spectrometer was calibrated against Raman frequencies of toluene, dimethylformamide, acetone, and methylene bromide. Spectra were recorded at ambient temperature from samples in spinning, 5-mm NMR tubes. Laser power at samples ranged from 2 mW for CO complexes to 5−12 mW for CN^- complexes; no spectral artifacts due to photoinduced chemistry were observed with these irradiation powers. UV-visible spectra were recorded from the rR samples before and after spectral acquisition, and they confirmed that sample integrity had not been compromised by exposure to the laser beam.

The vibrational parameters for Cld cyanide complexes were examined at pH 5.8, 6.8, 8.8, and 10.0 using ^{13}C and ^{15}N isotopologs of cyanoferric Clds (40 μM enzyme and 25-50 mM cyanide). Isotopically labeled potassium cyanides $K^{13}CN$ (99 atom % ^{13}C), $KC^{15}N$ (98 atom % ^{15}N) and $K^{13}C^{15}N$ (99 atom % ^{13}C; 98 atom % ^{15}N) were used. For the spectral range of 600−250 cm^{-1} no baseline corrections were applied. The original spectra were simulated using Origin® to calculate frequencies, intensities and widths of overlapping Gaussian bands. The number of bands and their widths were held constant whenever possible during peak fitting of the spectra for the four cyanide isotopolog complexes for a given Cld while the frequencies were allowed to vary. The simulated spectra were then subtracted from one another and the resulting simulated difference spectra were compared by superposition to the experimental difference spectra.

Enzyme samples in ^2H_2O were prepared from concentrated stock protein solutions. Samples were exchanged into 100 mM sodium phosphate buffer prepared in ^2H_2O (99.9% ^2H) at the desired pH by a 25-fold dilution with the buffer followed by concentration of the sample back to its original volume. This procedure was performed three times to obtain a final solution enrichment of 99 % ^2H_2O.

The Fe−C and C−O stretching frequencies were assigned for ferrous *Kp*Cld−CO using the ^{13}C isotopolog. Ferrous *Kp*Cld was generated anaerobically by reduction of ferric *Kp*Cld with an excess of buffered stock sodium dithionite solution. The corresponding CO complexes were prepared by flushing the ferrous proteins with natural abundance CO (^{12}CO) or ^{13}CO (99 atom % ^{13}C). Protein concentration was 40 μM *Kp*Cld.

4.4. Results

4.4.1. Comparison of kinetic parameters for ClO_2^- decomposition by Clds.

Activities have been reported for a number of Clds.[5, 9, 17, 23, 26, 51-53] Nevertheless, the kinetic parameters for the various Clds are difficult to compare because the pHs, buffers, ionic strengths, temperatures, and detection methods used in these assays differ among the literature reports. The *Da*Cld and *Kp*Cld used here were assayed near the peaks of their pH activity profiles and under identical solution conditions to support comparisons of their kinetic parameters (Table C1). These data show that the enzyme efficiencies differ only by a factor of about four (k_{cat}/K_M: *Da*Cld (4±1)×10^7 $M^{-1}s^{-1}$; *Kp*Cld (9±1)×10^6 $M^{-1}s^{-1}$), while their activities differ by an order of magnitude (k_{cat}: *Da*Cld (2.3±0.4)×10^4 s^{-1}; *Kp*Cld (2.6±0.1)×10^3 s^{-1}).

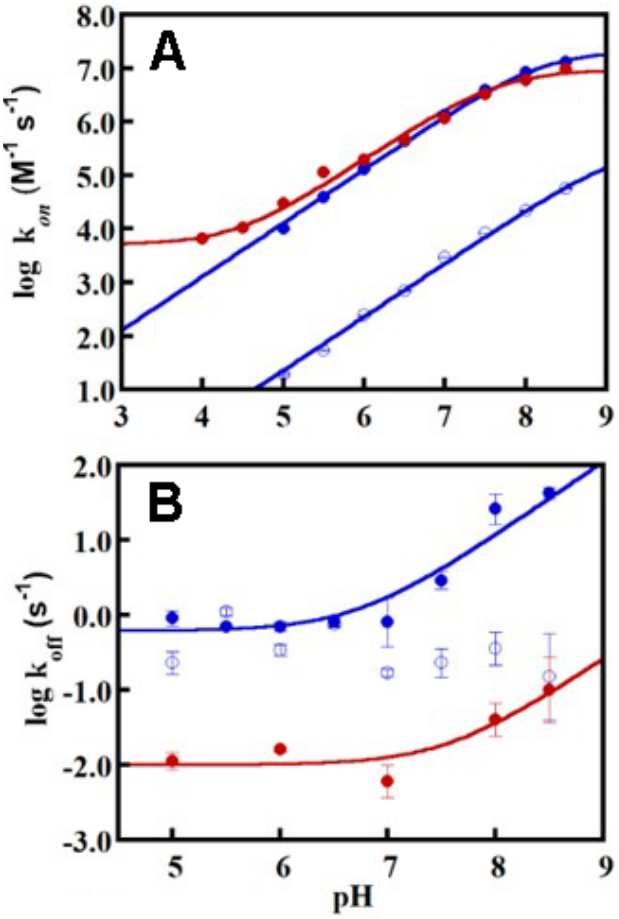

Figure 4.2. Kinetics of formation and dissociation for cyano-complex formation with ferric *Da*Cld (closed circles, blue), *Da*Cld(R183Q) (open circles, blue), and *Kp*Cld (closed circles, red). Values for (A) logk_{on} and (B) logk_{off} are plotted as a function of pH. Lines represent the fit of equations 5 and 6 to the data, as described in the text.

4.4.2. Low spin ferric Cld−CN as a probe of the catalytic site.

Conversion of high spin ferric *Da*- and *Kp*Clds to six-coordinate, low spin (6cLS) heme complexes upon cyanide binding is readily monitored by the changes in their UV-vis spectra, as shown in Figure C1. Their cyanide complexes exhibit UV-vis spectra (B band at 418-420 nm, Q bands at 540 and 565 nm)[24, 26] comparable to those reported for *Nd*Cld (420 nm, 540 nm)[25] and the dimeric Cld from *Cyanothece* sp. PCC7425 (CCld) (421 nm, 538 nm).[54] The UV-vis spectra of the three 6cLS Cld−CN complexes examined here do not change with pH.

4.4.2.1. Kinetics of cyanide association and dissociation as a function of pH.

Changes in absorbance at 419 nm upon binding of cyanide to the ferric form of all three proteins at each pH and [CN^-] examined were monophasic with time, yielding high quality fits to a single-term exponential decay function (Equation 4.1, Figure C2) having R^2 values ≥ 0.98. The resulting values for k_{obs} were plotted versus [KCN] and used to determine k_{on}, k_{off}, and K_D (Equations 3 and 4). Above pH 8.5, the binding events became too fast to track with rapid-mixing techniques, reflected by linear changes in absorbance over time. The k_{on}, k_{off}, and K_D values over the pH range of 4.0 to 8.5 are tabulated in Table C2.

Values of log k_{on} measured for CN^- and WT *Da*Cld, *Da*Cld(R183Q), and WT *Kp*Cld are plotted as a function of pH (Figure 4.2A). In every case, the log k_{on} increased roughly linearly with pH, having slopes ≈ 1, consistent with affinity for CN^- being modulated by a single deprotonation event. For *Da*Cld at the highest pH values, the data plateau, suggesting a nearby pK_a. Fitting the data to a single-pK_a model (Equation 4.5) yielded 8.1 ± 0.2, which is an approximation since values for k_{on} above pH 8.5 were too fast to be measured. The R183Q mutant showed a similar pH dependence for k_{on}, albeit with values ~500-fold smaller than their WT counterparts. Fitting the data to Equation 4.5 reflects both the expected linearity of the data and the slope ≈ 1; however, the pK_a was too high to be determined and is therefore designated as >8.5. Finally, the values and pH-dependent trends in log k_{on} for *Kp*Cld were similar to those of WT *Da*Cld. Given the inflection in its plot (Figure 4.2A), the data were fit to a two pK_a model (Equation 4.6) which yielded pK_a values of 7.7±0.1 and 4.4±0.2. The lower pK_a corresponds to irreversible protein denaturation, which makes it an apparent pK_a. A similar pH profile of k_{on} for CN^- binding to dimeric CCld has been recently reported.[54]

Values of log k_{off} for *Da*Cld, *Da*Cld(R183Q), and *Kp*Cld cyanide complexes are plotted as a function of pH in Figure 4.2B. The k_{off} for *Da*Cld is approximately four orders of magnitude smaller than its k_{on} at the lowest pH where rates were measured. The log k_{off} remains unchanged until ~ pH 6.5, whereupon it begins to rise with a slope near 1. Fitting the curve to Equation 4.5 yields pK_a = 6.7±0.3. By contrast, k_{off} for the R183Q variant appeared to be unaffected by pH, remaining small (<1 s^{-1}) at all pH values measured. Finally, the k_{off} values for *Kp*Cld are approximately two orders of magnitude smaller than those for *Da*Cld. As a function of pH, they exhibit the similar behavior as those for *Da*Cld, unchanging until ~ pH 7 followed by a linear rise; a fit of the log k_{off} versus pH to Equation 4.5 reveals a pK_a = 7.6 ± 0.2.

4.4.2.2. Comparison of cyanide affinities.

Under alkaline conditions (pH 8.5) *Da*Cld and *Da*Cld(R183Q) had similar binding affinities for cyanide ($K_D \approx 3\times10^{-6}$ M) while *Kp*Cld exhibited a much larger cyanide affinity ($K_D \approx 1\times10^{-8}$ M) (Table C2). This difference in cyanide affinity is clearly revealed by spectrophotometric titrations of *Kp*Cld and *Da*Cld with cyanide (Figure 4.3).

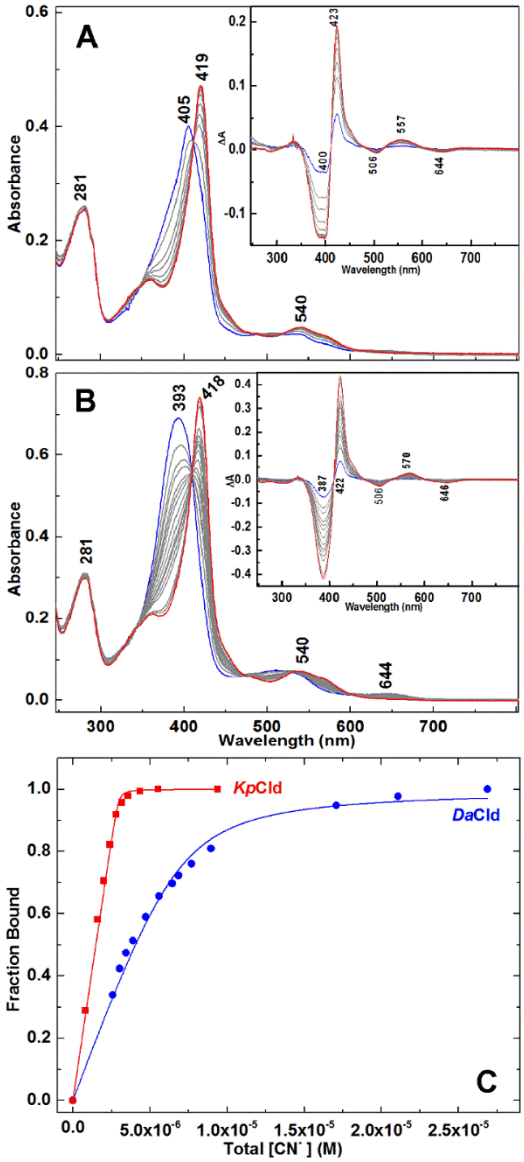

Figure 4.3. Spectrophotometric determination of K_D values for the reaction of Clds with cyanide. A) UV-visible spectra of 2.97 µM *Kp*Cld in 0.2 M potassium phosphate titrated with KCN at pH 7.0. Starting spectrum, blue; final spectrum, red; spectra at intermediate cyanide concentrations, gray. [CN^-] = 0, 1.59, 1.99, 2.39, 2.78, 3.17, 3.57, 4.35, 5.52, and 9.38 µM. Inset: ΔA spectra generated from spectra in A by subtraction of starting ferric *Kp*Cld spectrum from each spectrum for subsequent CN^- addition. B) Spectrophotometric titration of 6.8 µM *Da*Cld in 0.2 M potassium phosphate with KCN at pH 7.0. Color scheme is the same as in A. [CN^-] = 0, 0.86, 1.73, 2.59, 3.02, 3.45, 3.88, 4.73, 5.58, 6.43, 6.85, 7.69, 8.95, 17.1, 21.1, and 26.9 µM. Inset: ΔA spectra generated from spectra in B by subtraction of starting ferric *Da*Cld spectrum from each spectrum for subsequent CN^- addition. C) Plots of fraction of protein bound with cyanide versus total [KCN] (M); *Kp*Cld, red squares; *Da*Cld blue circles. Since cyanide binding to both enzymes is quite strong, the fraction bound ($\Delta A_{obs}/\Delta A_{max}$) is a quadratic function of the total [KCN]. Nonlinear least squares regression was used to fit ΔA_{422} vs [CN^-] to equation 1.

The difference in cyanide affinity is attributed to differences in the k_{off} values, as k_{on} for *Kp*Cld and *Da*Cld were essentially the same across the pH range examined. Trends in K_D with pH reflected the trends observed independently in k_{on} and k_{off}. Diminution followed by some degree of flattening in K_D values was observed for *Kp*Cld, *Da*Cld, and *Da*Cld(R183Q) dominated by the much larger magnitude linear increases in log k_{on}, relative to log k_{off}, over much of the measurable range of pH. The K_D data were not well modelled by either the single or double pK_a functions of Equations 4.2 and 4.3, respectively.

The spectrophotometrically determined K_D for *Da*Cld−CN^- of $(6.0\pm0.5)\times10^{-7}$ M at pH 7.0 (Figure 4.3) is in excellent agreement with K_D calculated from kinetic constants using Equation 4.4 (Table C2). The previously reported spectrophotometrically determined K_D for *Da*Cld(R183Q)−CN^- of 8.4×10^{-5} M[24] is close to the 6.0×10^{-5} M calculated here using kinetic constants (Table C2). Agreement between the kinetically and spectroscopically determined K_D values was taken as an indication that use of our spectrophotometrically determined K_D values for *Kp*Cld−CN^- to calculate k_{off} is reasonable.

4.4.2.3. Identification of the FeCN vibrational modes.

The low frequency range of the Soret-excited rR spectra of *Kp*Cld−CN^- and *Da*Cld−CN^- at pH 5.8 are shown in Figures 4.4A and 4.4C. The ferric Cld−CN^- complexes were generated with cyanide isotopologs $^{12}C^{14}N^-$, $^{13}C^{14}N^-$, $^{12}C^{15}N^-$ and $^{13}C^{15}N^-$ to identify bands arising from the modes involving distortions of the $Fe^{III}CN$ fragment. As these frequencies and isotope shift patterns are responsive to properties of the distal heme pocket, they constitute a probe of its structural properties. Since several strong heme deformation modes are observed in the 270-500 cm^{-1} region, the difference spectra shown in Figures 4B and 4D were generated by digital subtraction of various pairs of Cld−CN^- isotopolog spectra to facilitate identification of the

isotope-sensitive modes. Peak-fitting analyses of the experimental spectra identified the bands responsible for features in the difference spectra; multiple isotope-sensitive bands were observed and their Raman shifts are listed in Table C3. The frequencies indicated at the minima and maxima of the difference spectra (Figures 4.4B and 4.4D) differ from the actual Raman shifts obtained from the fits of the experimental data (Figures 4.4A and 4.4C) because the isotope shifts are less than the widths of the $^{13}CN^-$- and $C^{15}N^-$-sensitive bands. The FeCN angle in cyanide complexes of synthetic iron porphyrinates is typically near 180˚. Distortions that alter the Fe−C−N angle can be imposed by electronic and/or steric factors in the heme pocket of proteins, lending both stretching (ν_{Fe-C}) and bending (δ_{FeCN}) character to the $^{13}CN^-$ and $C^{15}N^-$-sensitive normal modes. The FeCN fragment exhibits a ν_{Fe-C} band that shifts monotonically to lower frequency with increasing total mass of the cyanide ligand and a δ_{FeCN} band whose frequency shifts in a "zigzag" pattern upon isotopic substitution of the carbon (in order: $^{12}C^{14}N^-$, $^{13}C^{14}N^-$, $^{12}C^{15}N^-$, $^{13}C^{15}N^-$, the frequency decreases, increases, and then decreases). In heme protein cyanide complexes where there are small equilibrium distortions, the nearly linear FeCN fragments exhibit a ν_{Fe-C} frequency that is greater than the δ_{FeCN} frequency (Table 4.1). For bent FeCN fragments (∠FeCN between ~160-130˚), the relative frequencies of ν_{Fe-C} and δ_{FeCN} are less clear, possibly because of the effect of lower force constants for the Fe−C stretching (f_{Fe-C}) and FeCN bending (f_{FeCN}) internal coordinates relative to those for a linear FeCN fragment (*vide infra*).[43]

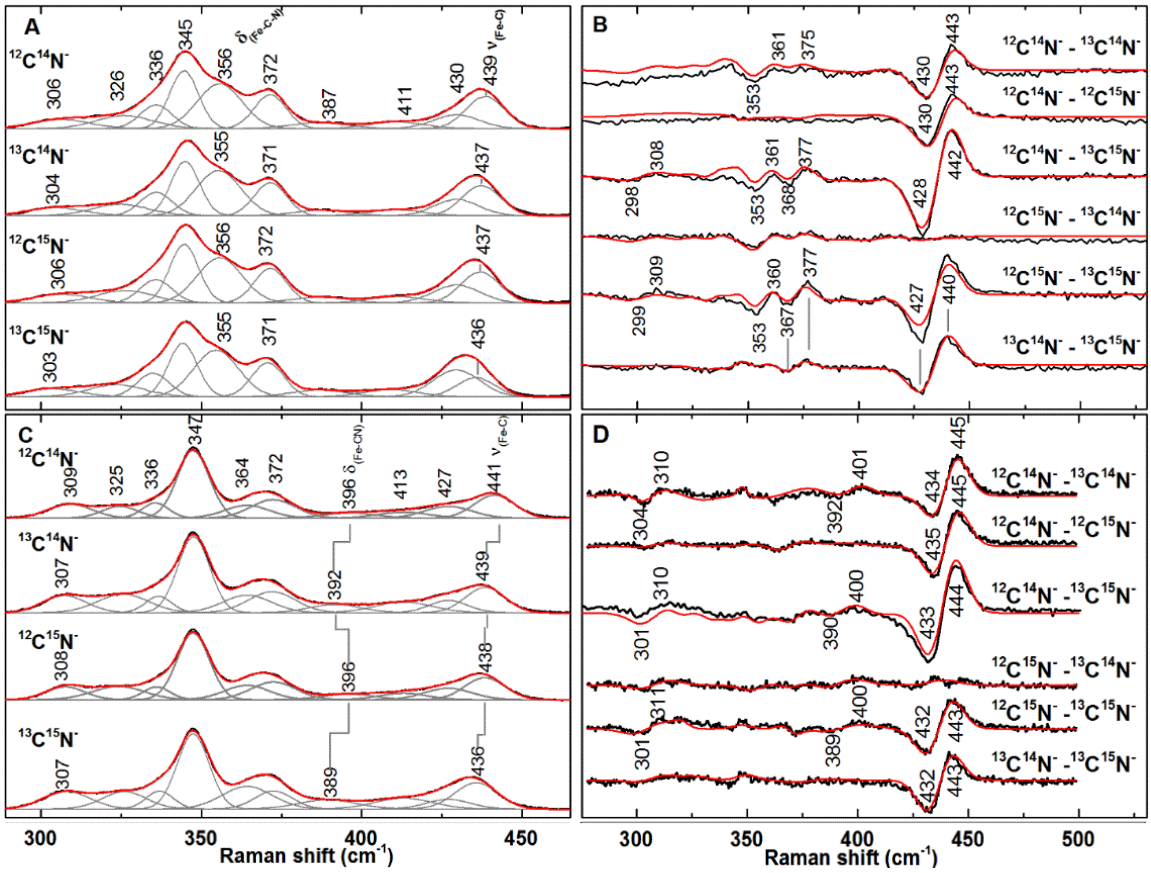

Figure 4.4. Fits of cyanoferric *Kp*Cld isotopologs at low pH. A) Low-frequency resonance Raman spectra of isotopically labeled cyanoferric *Kp*Cld pH 5.8. The cyanoferric *Kp*Cld complexes were 20 μM *Kp*Cld and 25 mM cyanide in 100 mM sodium phosphate buffer. *Kp*Cld−CN^- ν_{Fe-C} and δ_{FeCN} frequencies are consistent with a bent FeCN unit. B) Isotope difference spectra for *Kp*Cld−CN^-. Difference spectra generated by digital subtraction of the spectra shown in A. C) Low-frequency resonance Raman spectra of isotopically labeled cyanoferric *Da*Cld pH 5.8. The cyanoferric *Da*Cld complexes were 20 μM *Da*Cld and 25 mM cyanide in 100 mM sodium phosphate buffer. *Da*Cld−CN^- ν_{Fe-C} and δ_{FeCN} frequencies are consistent with a larger FeCN angle than that of *Kp*Cld−CN^-. D) Isotope difference spectra for *Da*Cld−CN^-. Difference spectra generated by digital subtraction of the spectra shown in C. E) Low-frequency resonance Raman spectra of isotopically labeled cyanoferric *Da*Cld(R183Q) pH 5.8. The cyanoferric *Da*Cld(R183Q) complexes were 25 μM *Da*Cld(R183Q) and 25 mM cyanide in 100 mM Tris/sulfate buffer. *Da*Cld(R183Q) −CN^- ν_{Fe-C} and δ_{FeCN} are consistent with a nearly linear FeCN unit. F) Isotope difference spectra for *Da*Cld(R183Q)−CN^-. Difference spectra generated by digital subtraction of the spectra shown in E. The excitation wavelength was 413.1 nm; laser power at the sample was 12 mW. Spectra were acquired at 20 °C. Original spectral data are shown in black, bands used to fit the spectra are grey, and the calculated spectra are shown in red. Difference spectra generated from subtraction of spectral data are shown in black; the fit difference spectra are shown in red. Fits for the difference spectra were obtained by generating fits for the experimental spectra and then subtracting those best-fit spectra.

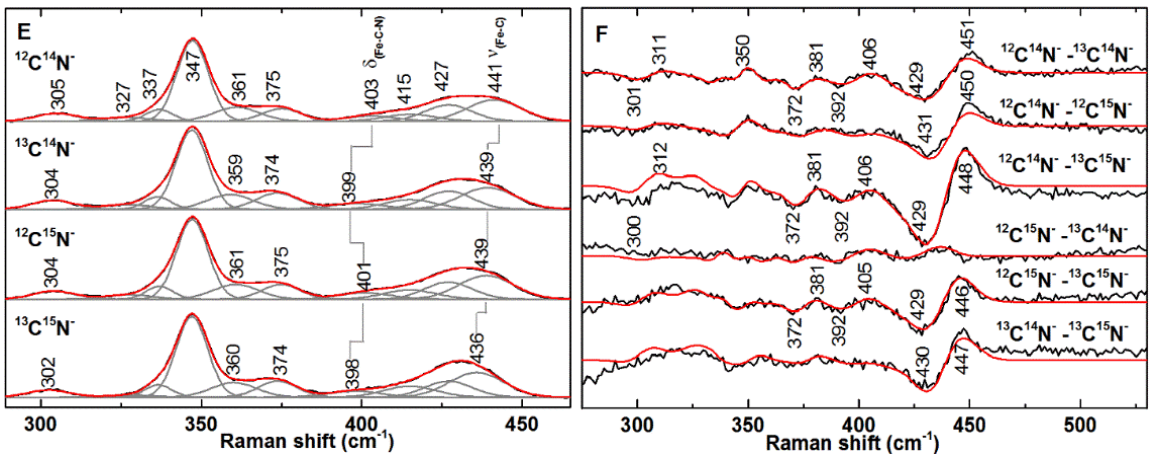

Figure 4.4. Fits for cyanoferric isotopologs at low pH (continued). A) Low-frequency resonance Raman spectra of isotopically labeled cyanoferric *Kp*Cld pH 5.8. The cyanoferric *Kp*Cld complexes were 20 μM *Kp*Cld and 25 mM cyanide in 100 mM sodium phosphate buffer. *Kp*Cld−CN^- ν_{Fe-C} and δ_{FeCN} frequencies are consistent with a bent FeCN unit. B) Isotope difference spectra for *Kp*Cld−CN^-. Difference spectra generated by digital subtraction of the spectra shown in A. C) Low-frequency resonance Raman spectra of isotopically labeled cyanoferric *Da*Cld pH 5.8. The cyanoferric *Da*Cld complexes were 20 μM *Da*Cld and 25 mM cyanide in 100 mM sodium phosphate buffer. *Da*Cld−CN^- ν_{Fe-C} and δ_{FeCN} frequencies are consistent with a larger FeCN angle than that of *Kp*Cld−CN^-. D) Isotope difference spectra for *Da*Cld−CN^-. Difference spectra generated by digital subtraction of the spectra shown in C. E) Low-frequency resonance Raman spectra of isotopically labeled cyanoferric *Da*Cld(R183Q) pH 5.8. The cyanoferric *Da*Cld(R183Q) complexes were 25 μM *Da*Cld(R183Q) and 25 mM cyanide in 100 mM Tris/sulfate buffer. *Da*Cld(R183Q) −CN^- ν_{Fe-C} and δ_{FeCN} are consistent with a nearly linear FeCN unit. F) Isotope difference spectra for *Da*Cld(R183Q)−CN^-. Difference spectra generated by digital subtraction of the spectra shown in E. The excitation wavelength was 413.1 nm; laser power at the sample was 12 mW. Spectra were acquired at 20 °C. Original spectral data are shown in black, bands used to fit the spectra are grey, and the calculated spectra are shown in red. Difference spectra generated from subtraction of spectral data are shown in black; the fit difference spectra are shown in red. Fits for the difference spectra were obtained by generating fits for the experimental spectra and then subtracting those best-fit spectra.

Table 4.1. Stretching (ν) and bending (δ) frequencies (cm^{-1}) for the FeCN fragment in the cyanide complex of various ferric heme proteins with proximal histidine ligation.

protein[a]	"nearly linear" FeCN			"bent" Fe−CN			Potential distal H-bond donors to CN^-	references
	ν_{Fe-C}	δ_{FeCN}	$\Delta(\nu - \delta)$	ν_{Fe-C}	δ_{FeCN}	$\Delta(\nu - \delta)$		
Chlorite dismutases								
*Kp*Cld pH 5.8				439	356	83	Arg/H_2O	This work
*Kp*Cld pH 8.0				440	359	81	Arg/H_2O	This work
*Da*Cld pH 5.8	441	396	45				Arg	This work
*Da*Cld pH 8.8	441	398	43				Arg	This work
*Da*Cld(R183Q)	441	403	38				Gln	This work
Nitrophorin								
Rhodnius prolixus NP 1	454	397	57	443[b]	357[c]	86	H_2O	[39]
Globins								
trHbC				440[d]	nd[e]	nd[e]	Gln/Tyr/Gln	[42]
trHbC E7Gln6Gly	452	nd[e]	nd[e]				Tyr/Gln	[42]
Tf-trHb				439	380	59	Trp/Tyr	[55]
Horse Mb pH 8.0	452	441	11				His	[41]
Human HbA, pH 8.0	452	434	18				His	[41]
Chironomus Hb	453	412	41				His	[56]
C. jejuni single domain Hb	440	403	37	353	417	-64	Gln/Tyr	[57]
Peroxidases								
HRP pH 11.6	444	405	35	355	420	−65	Arg	[38]
HRP pH 5.5	453	405	48	360	422	−62	His/Arg	[38, 58]
HPR(H42Q) pH 7.0	443	nd[e]	nd[e]				Gln/Arg	[59]
LPO, pH 7.0				360	453	−93	His/Arg	[60]
MPO				361	453	−92	His/Arg	[43]

[a]Hb, hemoglobin; Mb, myoglobin; *Tf* trHb, *Thermobifida fusca* truncated Hb II; trHbC, *Chlamydomonas eugametos* trHb-I; *Chironomus* Hb, *Chironomus thummi thummi* Hb; *C. jejuni* single domain Hb, *Campylobacter jejuni* single domain Hb; HRP, horseradish peroxidase; LPO, lactoperoxidase; MPO, myeloperoxidase.

[b]Normal mode calculations indicate that band has contributions from modes ν(Fe−CN), δ(FeCN), and ν(Fe−His).

[c]Normal mode calculations indicate that band has contributions from δ(FeCN), δ(His−Fe−C), and ν(Fe−His).

[d]Assignment made based on comparison to ν(Fe−CN) frequencies for Mb and Hb. Isotopic shifts from $^{12}C^{14}N^-$ to $^{13}C^{15}N^-$ were comparable to those observed for *Kp*Cld-CN^-.

[e]not determined

4.4.2.4. FeCN geometry and vibrational signatures.

The ν_{Fe-C} frequencies for *Kp*Cld−CN^- and *Da*Cld−CN^- at pH 5.8 are observed at 439 and 441 cm^{-1}, respectively. Both bands shift monotonically (Figures 4.4A and 4.4C) by 3 cm^{-1} (*Kp*Cld) and 5 cm^{-1} (*Da*Cld) between $^{12}C^{14}N^-$ and $^{13}C^{15}N^-$ complexes. These assignments are further supported by the difference spectra of Cld−CN^- isotopolog complexes which have differing total cyanide mass but carbon atoms of equal mass; in these difference spectra, the features arising from the stretching vibrations are predominant and, since the bending vibrations occur at the same frequencies, they are removed by the subtraction process. The difference spectra of [$^{12}C^{14}N^- - {}^{12}C^{15}N^-$] and [$^{13}C^{14}N^- - {}^{13}C^{15}N^-$] in Figure 4.4B and 4.4D exhibit a prominent feature corresponding to a single stretching mode in each Cld. The observed shifts are considerably smaller than the ~11 cm^{-1} calculated for a linear FeCN;[42] the myoglobin cyanide complexes, which have "nearly linear" FeCN geometries (πFeCN= 166˚ for sperm whale Mb−CN^-; pdb code: 1EBC),[61] exhibit isotope shifts of 8−10 cm^{-1}.[41] The smaller isotope sensitivity of *Kp*Cld−CN^- relative to *Da*Cld−CN^- and cyanometMb is consistent with delocalized modes, attributable to the FeCN triad of *Kp*Cld-CN having the greater deviation from linearity.

In *Kp*Cld−CN^- at pH 5.8, there are two possibilities for the δ_{FeCN} bending mode; bands at 356 and 372 cm^{-1} exhibit small, but clearly discernable, zigzag patterns in their cyanide isotopolog frequencies. The band at 356 cm^{-1} is tentatively assigned to the δ_{FeCN} mode because it is absent in the ferric *Kp*Cld spectrum whereas a 371 cm^{-1} band, assigned to a propionate bending mode, $\delta(C_\beta C_c C_d)$, is present (Figure C3). The zigzag pattern due to the isotope sensitivity of the 356-cm^{-1} band yields a difference feature with a maximum at 361 cm^{-1} and a minimum at 353 cm^{-1} in [$^{12}C^{14}N^- - {}^{13}C^{14}N^-$], [$^{12}C^{14}N^- - {}^{13}C^{15}N^-$], and [$^{12}C^{15}N^- - {}^{13}C^{15}N^-$]

difference spectra (Figure 4.4B). A similar difference feature for the 372-cm^{-1} band (max. at 377 cm^{-1}, min. at 368 cm^{-1}) is tentatively attributed to kinematic or vibrational coupling of a FeCN coordinate, involving displacement of the iron along a vector having a nonzero projection on the mean porphyrin plane, and in-plane porphyrin coordinates .[41] The 372 cm^{-1} difference feature is not observed in the *Da*Cld−CN^- spectra (Figure 4.4D), suggesting that the kinematic coupling is activated by a bent FeCN geometry in *Kp*Cld−CN^-. One additional isotope-sensitive band at 306 cm^{-1}, attributed to kinematic coupling of the FeCN and Fe−His distortions,[42] is observed for *Kp*Cld−CN^- at pH 5.8.

The δ_{FeCN} mode is assigned for *Da*Cld−CN^- pH 5.8 at 396 cm^{-1} based on its zigzag isotope shift pattern (Figure 4.4C). The difference feature due to this zigzag pattern has a maximum at 401 cm^{-1} and a minimum at ~390 cm^{-1} in the [$^{12}C^{14}N^- - {}^{13}C^{14}N^-$], [$^{12}C^{14}N^- - {}^{13}C^{15}N^-$], and [$^{12}C^{15}N^- - {}^{13}C^{15}N^-$] difference spectra (Figure 4.4D). One additional band at 309 cm^{-1} is isotope-sensitive with shifts of ~2 cm^{-1} to lower frequency upon substitution of natural abundance CN^- (hereinafter designated by $^{12}C^{14}N^-$) with $^{13}C^{15}N^-$. A similar isotope-sensitive mode has been reported for other ferric heme protein cyanides and, like the 306 cm^{-1} band in *Kp*Cld−CN^-, is attributed to vibrational coupling between the local Fe−His stretching coordinate and the FeCN distortion coordinates.[42-43]

Two major differences are observed when comparing vibrational data for cyanide complexes of *Da*Cld(R183Q), shown in Figure 4.4E and 4.4F, and WT *Da*Cld. First, although the ν_{Fe-C} frequency at 441 cm^{-1} for the mutant is the same as that of the WT, the line width of the band increases by a factor of approximately 1.5 (from 12 to 17 cm^{-1}); this is visualized by the greater difference between maxima/minima in the difference spectra; for example, in the [$^{12}C^{14}N^- - {}^{13}C^{15}N^-$] spectrum the maximum and minimum for WT appear at 444 and 433 cm^{-1}

while for the R183Q mutant they are observed at 448 and 429 cm^{-1}. This band width increase is consistent with greater conformational inhomogeneity in the distal pocket of the mutant. It suggests that the Arg side chain constrains the FeCN fragment to a narrower distribution of geometries (FeCN angles) than the amide side chain of Gln. Secondly, the δ_{FeCN} frequency (403 cm^{-1}) is 7 cm^{-1} higher than its WT counterpart. This is consistent with some contribution from a less strained FeCN unit. Several additional isotope sensitive bands are observed in the *Da*Cld(R183Q)−CN^- spectra. An isotope sensitive band at 305 cm^{-1} appears comparable to that observed in WT at 309 cm^{-1} due to coupling between the Fe−His stretching and FeCN distortions.[42-43] Isotope shifts of 1−2 cm^{-1} are observed for bands at 375 and 361 cm^{-1}; sensitivity of these modes is similar to that reported for cyanide complexes of Mb and Hb and are likely due to kinematic coupling of in-plane coordinates having Fe−$N_{pyrrole}$ stretching character with the Fe−CN stretching coordinate.[41] Although the shifts in these bands are small, the bands overlap with other bands, some of which are also isotope sensitive, and they appear in the difference spectra as features around 381 and 350 cm^{-1}.

4.4.2.5. FeCN geometry and Δ(ν – δ).

In contrast to bent FeCN of peroxidases, for which the δ_{FeCN} frequency is greater than the ν_{Fe-C} frequency, the *Kp*Cld−CN^- ν_{Fe-C} frequency is higher than its δ_{FeCN} frequency (Table 4.1). These cyanide-sensitive normal vibrational modes comprise displacements along both the ν_{Fe-C} and δ_{FeCN} coordinates, with their frequencies depending upon both the FeCN geometry and force constants of the Fe−C stretching (f_{Fe-C}) and FeCN bending (f_{FeCN}) internal coordinates. Each of these frequencies has a potential energy distribution that includes contributions from internal Fe−C stretching, FeCN bending and Fe-His_{prox} stretching coordinates. The relative contributions of displacements along these internal coordinates determine which of the normal modes

comprises more stretch than bend or more bend than stretch as illustrated in Figure C5.[43] As f_{Fe-C} increases, a point is reached where the Fe-His_{prox} stretching contribution changes dramatically and the relative frequencies of the predominantly stretching and bending normal modes reverse. The value of f_{Fe-C} at which this reversal occurs depends on the equilibrium FeCN angle; for angles of 170° and 155°, reversal occurs near f_{Fe-C} = 1.80 mdyn/Å and 1.45 mdyn/Å, respectively.[43] *Kp*Cld−CN^- has observed frequencies and isotopic sensitivities comparable to the nonlinear form of NP1−CN^-. In fitting the vibrational data of NP1−CN^-, a f_{Fe-C} of 1.55 mdyn/Å and an πFeCN of 155.0° reproduced the observed isotope shift pattern (Table C4).[39] Thus, the occurrence of the Fe−C stretch at a higher frequency than the FeCN bend in the spectra of *Kp*Cld−CN^- and NP1−CN^- (Table 4.1) indicates that f_{Fe-C} for these two cyanide complexes are greater than 1.45 mdyn/Å. By contrast, the bent cyanide complexes of other heme proteins (Table 4.1, Figure C5) exhibit lower values of f_{Fe-C} (< 1.45 mdyn/Å), thereby pushing their δ_{FeCN} modes to higher frequencies than their ν_{Fe-C} modes.[43]

The frequency separations between modes of predominantly ν_{Fe-C} and δ_{FeCN} character are 83, 45, and 38 cm^{-1} at pH 5.8 for *Kp*Cld−CN^-, *Da*Cld−CN^- and *Da*Cld(R183Q)−CN^-, respectively. Since the frequency difference between ν_{Fe-C} and δ_{FeCN} modes is larger for bent FeCN geometries (65−106 cm^{-1}) than for the "nearly linear" forms (11−58 cm^{-1}) of cyanoheme proteins,[37-39, 41] these frequency separations together with isotope sensitivities (*vide supra*) support a bent geometry for *Kp*Cld−CN^- (~155°). Nearly linear geometries, wherein ∠FeCN lies between ~166° and 176°, are observed for *Da*Cld−$CN^-$and *Da*Cld(R183Q)−CN^-. The smaller Δ(ν−δ) for *Da*Cld(R183Q)−CN^- is consistent with the largest ∠FeCN of the three cyanide complexes probably due to the distal Gln exerting less off-axis force on the coordinated CN^- than the native Arg side chain.

4.4.2.6. pH sensitivity of FeCN modes.

As the pH of *Kp*Cld−CN^- is increased from 5.8 to 8.0, the bands assigned to ν_{Fe-C} and δ_{FeCN} modes both sharpen with line widths decreasing by ~2 cm^{-1}, while their frequencies increase slightly from 439 cm^{-1} to 440 cm^{-1} and from 356 cm^{-1} to 359 cm^{-1}, respectively (Figures 4.4A, 4.4B, and C4). Isotope shifts of 1−3 cm^{-1} were observed upon substitution of $^{12}C^{14}N^-$ by $^{13}C^{15}N^-$. As already noted for the pH 5.8 case, these observed shifts are considerably smaller than the calculated 11 cm^{-1} for a linear FeCN.[42] Under alkaline conditions, the isotope-sensitive ν_{Fe-C} and δ_{FeCN} bands both exhibit a zigzag isotope shift pattern. Zigzag patterns for the band predominantly due to the stretch have on occasion been observed in proteins where the FeCN has a bent geometry and the ν_{Fe-C} and δ_{FeCN} internal coordinates both contribute to the isotope-sensitivity of the frequencies. Thus, the band assigned to the "stretching" mode has a significant contribution from the bending coordinate and vice versa.[36]

Comparison of the *Kp*Cld−CN^- spectra at pH 5.8 and 8.0 suggests that increasing pH causes subtle changes in the heme environment which alter the contributions of the stretching and bending coordinates to the isotope-sensitive bands. The frequency separation between the predominantly ν_{Fe-C} and δ_{FeCN}–dominated modes ($\nu-\delta$) for *Kp*Cld−CN^- at pH 8.0 remains large at 82 cm^{-1}. Large $\nu-\delta$, the small isotope shifts, and the zigzag shift pattern for the band at 440 cm^{-1} support the conclusion that the overall geometry of *Kp*Cld−CN^- remains bent over the pH range examined in this study.

The FeCN modes of *Da*Cld−CN^- also exhibit very small shifts with increasing pH. The ν_{Fe-C} frequency decreases from 442 to 441 cm^{-1} while that of δ_{FeCN} increases from 396 to 398 cm^{-1} going from pH 5.8 to 8.8 (Figures 4.4C and C6). Thus, no dramatic changes in FeCN geometry occur as the pH is raised. However, several low frequency porphyrin modes (309, 336,

and 347 cm^{-1}) exhibit band width increases of 2−4 cm^{-1} and 1−2 cm^{-1} shifts in frequency as the pH is increased. These changes are the source of the features observed in the [pH 8.8–5.6] rR difference spectra (Figure 4.5A). By analogy to previously assigned modes, these bands correspond to ν_{Fe-His}, γ_6, and ν_8.[42, 62] In contrast, neither the FeCN nor the out of plane porphyrin modes of *Da*Cld(R183Q)−CN^- are altered by increases in pH, consistent with the lack of features in the *Da*Cld(R183Q)−CN^- [pH 8.0–5.6] difference spectrum (Figure 4.5B). Since these pH-dependent shifts for WT are not observed for *Da*Cld(R183Q)−CN^-, they may be correlated with the kinetically observed pK_a of 6.7 for *Da*Cld−CN^-.

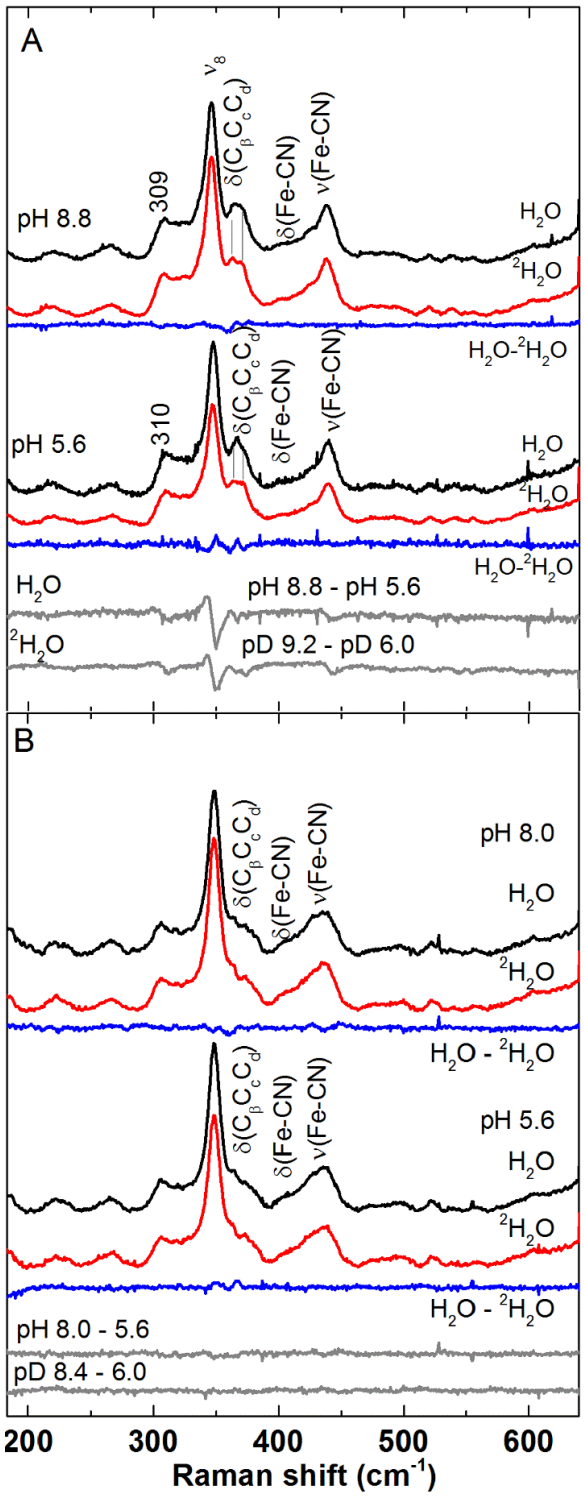

Figure 4.5. Low-frequency resonance Raman spectra of A) cyanoferric *Da*Cld and B) cyanoferric *Da*Cld(R183Q) as a function of pH and ^2H_2O. The parent spectra at pH 8.8, 8.0, and 5.6 in H_2O (black) and in ^2H_2O (red) were used to generate the [$H_2O - {}^2H_2O$] difference spectra (blue). Difference spectra highlighting changes that occur upon increased pH were obtained by subtraction of spectra of acidic enzymes from those under alkaline conditions (grey).

To probe for H-bonding interactions between bound cyanide and the distal pocket, rR spectra of the cyanide complexes of *Da*Cld at pH 5.6 and 8.8 and *Da*Cld(R183Q) at pH 5.6 and 8.0 were recorded in H_2O and in ^2H_2O (Figure 4.5). These [H_2O – ^2H_2O] difference spectra indicate that no significant perturbation occurs in the ν_{Fe-C} and δ_{FeCN} frequencies of either enzyme upon isotope substitution, regardless of pH. A similar lack of $H_2O/^2H_2O$ sensitivity is observed for *Kp*Cld−CN^- (data not shown). Although the lack of deuterium isotope shifts in ν_{Fe-C} and δ_{FeCN} frequencies does not eliminate the possibility of hydrogen bonding between the bound cyanide and residues in the distal pocket,[36, 42, 63] it is consistent with a bound cyanide that does not have strong hydrogen bonding along the Fe−C−N axis. This suggests that the distal Arg is not positioned for optimal hydrogen bonding to the cyanide nitrogen.

4.4.3. Low spin ferrous Cld−CO as a probe of the catalytic site.

The Soret-excited rR spectra of *Kp*Cld−CO (Figure 4.6) reveal three isotope-sensitive bands at 495, 588, and 1944 cm^{-1}. They are assigned to ν_{Fe-C}, δ_{FeCO}, and ν_{C-O} modes, respectively. These data report a single form of *Kp*Cld−CO; its position on the ν_{Fe-C}/ν_{C-O} correlation plot (Figure 4.6) is consistent with little or no non-bonded interaction between the distal Arg and the bound CO ligand. The CO complexes of WT *Da*Cld and *Da*Cld(R183Q) have open and closed conformers, likely corresponding to different orientations of the distal Arg side chain.[24] In contrast, *Kp*Cld−CO exhibits a single form, having a Raman fingerprint comparable to the open form of WT *Da*Cld−CO.

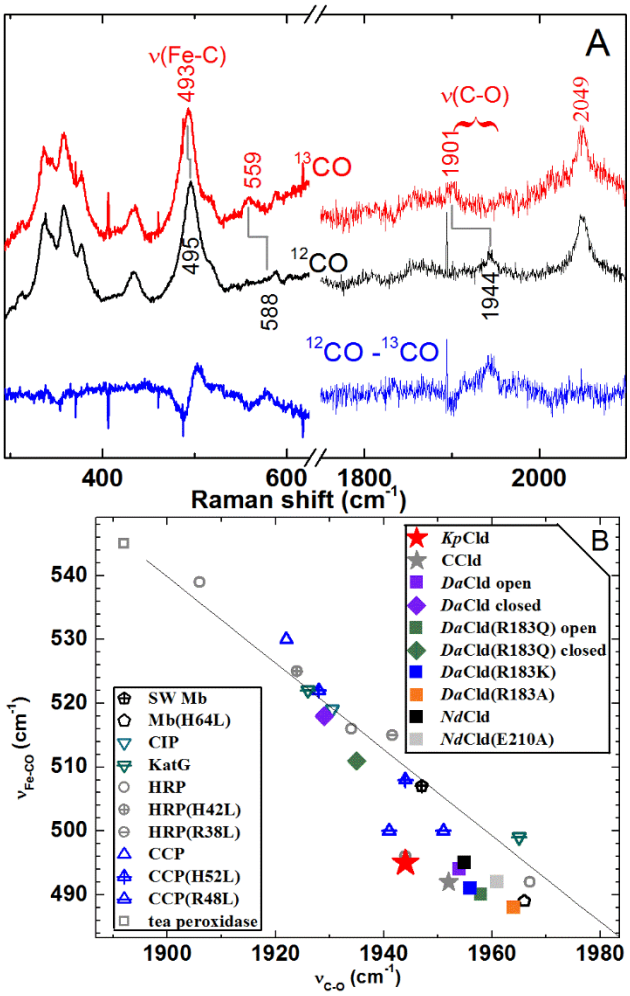

Figure 4.6. Resonance Raman characterization of ferrous CO complex of *Kp*Cld reports on its proximal ligands and distal environments. A) Soret-excited rR spectra of the isotopomers of CO complexes of KpCld−CO at pH 8.0. Spectra were acquired with 413.1 nm excitation and 2 mW power at the sample. ^{12}CO complex, black; ^{13}CO complex, red; difference spectra ^{12}CO–^{13}CO, blue. B) Backbonding correlation plot of ν_{Fe-C} versus ν_{C-O} for ferrous carbonyls of heme proteins shows the dependences of their positions on axial ligation and distal pocket properties. The black line correlates ν_{Fe-C} with ν_{C-O} for six-coordinate FeCO adducts in which the sixth ligand is histidine (neutral imidazole). Solid symbols represent Clds: dimeric Clds, stars; pentameric Clds, squares and diamonds. Data for *Da*Clds, *Nd*Clds and CCld are from references 24, 64 and 54, respectively. Raman shifts for other heme carbonyls are tabulated in Table C1 of reference 24 and their plot positions are shown as open symbols.

4.5. Discussion

The O_2-evolving Clds constitute an unusual example of rapid and efficient catalytic O−O bond-formation. Despite the similarities in protein folds and active sites in the catalytic domains of enzymes in both the homodimeric and homopentameric Cld clades, there is variability in their

catalytic activities, enzyme efficiencies, and turnover numbers. Cyanide complexes, which are sensitive probes of the heme environment, have been used here to evaluate the active sites of the *Kp*Cld dimer and *Da*Cld pentamer as a means of gaining insight into the structural and electronic features responsible for their high-fidelity O_2 generation.

4.5.1. Anion binding to Clds and catalytic efficiency.

Cyanide is known to be a strong, competitive inhibitor of *Kp*Cld[64] and *Azospira oryzae* strain GR-1 Cld.[51] This is not unexpected for the strong field CN^- ligand, which readily forms stable 6cLS complexes with the ferric Clds, thereby blocking access of the substrate to the exogenous (i.e. distal) ligand site of the catalytic hemin center. In the pH-dependent reactions between resting Clds and CN^-, the CN^- ligand can be considered in some ways a non-reactive surrogate for ClO_2^- ($pK_a = 1.96$; $HClO_2 \rightleftharpoons H^+ + ClO_2^-$). The pH-dependent behavior of the chlorite reaction with *Da*Cld was previously studied,[26] and interconversions associated with two pK_as were previously shown to modulate its activity and spectroscopic properties. The lowest pK_a of 6.5 involves the conformation reorganization of distal Arg183,[26] which is strictly conserved among all O_2-evolving Clds.[10, 23] Activity, spectroscopic, crystallographic, and molecular dynamics studies suggest that the Arg side chain can rotate from a catalytically optimal position in a closed conformer to a less active position in an open conformer.[20, 23, 26, 65] Conversion of the most active 5cHS heme to a 6cLS heme hydroxide occurs with a pK_a of 8.7.[26] The analogous pK_as for the distal heme pocket conformation and heme hydroxide formation in *Kp*Cld are 7.0 and 8.3.[9] Based on the pH profiles of their chlorite decomposing activities, these Clds are most active in their acidic form, which has been hypothesized to have a heme-substrate complex wherein the side chain of the conserved distal Arg points inward over the heme plane (closed conformation).

In contrast to the chlorite reaction, the second-order rate constant for CN^- binding, k_{on}, increased with pH for both *Kp*Cld and *Da*Cld, having values of 10^6 $M^{-1}s^{-1}$ near the estimated pK_as of 7.7 and ~8.1, respectively. These pK_a values are consistent with k_{on} being limited by the deprotonation of HCN to yield the anion (pK_a = 9.2, 25 °C), exchange of the heme OH^- ligand [9, 26] for CN^-, or both. The similarity in magnitudes of k_{on} and k_{cat}/K_M at their respective pH maxima, however, suggests that values of k_{on} near 10^6 $M^{-1}s^{-1}$ define the limiting rate for *Kp*Cld and *Da*Cld complexation with anions. Moreover, based on the similarity among values of k_{on} reported for CN^- binding to other Clds,[11, 23, 66, 54]rapid anion binding appears to be characteristic of Clds (Table 4.2).

Table 4.2. Kinetic and thermodynamic parameters for cyanide binding to selected heme proteins with varying distal pockets

Protein	conditions	k_{on} ($M^{-1}s^{-1}$)	k_{off} (s^{-1})	K_D (M)	reference
*Kp*Cld	20 °C, pH 7.0	$(1.15\pm0.01)\times10^{6}$	$(5.8\pm3.2)\times10^{-3}$[a]	$(4.7\pm2.8)\times10^{-9}$[b]	This work
*Da*Cld	20 °C, pH 7.0	$(1.30\pm0.02)\times10^{6}$	$(8\pm1)\times10^{-1}$	$(6.1\pm0.4)\times10^{-7}$[c]	This work
*C*Cld	25 °C, pH 7.0	1.6×10^{5}	1.4	8.6×10^{-6}	11
*Nw*Cld	25 °C, pH 7.0	1.0×10^{6}	2.4	2.4×10^{-6}	66
*Nd*Cld	25 °C, pH 7.0	2.57×10^{6}	9.3	3.6×10^{-6}	23
CcP	25 °C, pH 7.0	1.1×10^{5}	9.0×10^{-1}	8×10^{-6}	67
CcP(H52L)	25 °C, pH 7.0	7.0×10^{3}	1.5×10^{-1}	6.3×10^{-6}	34
HRP	25 °C, pH 7.05	9.8×10^{4}	2.8×10^{-1}	2.9×10^{-6}	35
Cj trHbP[d]	20 °C, pH 7.0	$\geq 2\times10^{4}$	$\geq 1\times10^{-4}$	5.8×10^{-9}	68-69
Mt trHbN[d]	20 °C, pH 7.0	3.80×10^{2}	6.8×10^{-4}	1.8×10^{-6}	68-69
Mt trHbO[d]	20 °C, pH 7.0	3.20×10^{2}	3.5×10^{-4}	1.1×10^{-6}	68-69
human Mb	20 °C, pH 7.0	2.30×10^{2}	3.8×10^{-4}	1.67×10^{-6}	70-71
SW Mb	20 °C, pH 7.0	3.20×10^{2}	4.0×10^{-4}	1.25×10^{-6}	70-71
human Mb(H64A)	20 °C, pH 7.0	1.1×10^{2}	4.6×10^{-4}	4.17×10^{-6}	71
human Mb(H64Q)	20 °C, pH 7.0	1.8×10^{2}	1.0×10^{-5}	5.6×10^{-8}	70-71
*Bj*FixLH[d]	25 °C, pH 7.0	1.8×10^{1}	1.2×10^{-4}	5.2×10^{-6}	72
*Sm*FixLH[d]	25 °C, pH 7.0	1.4×10^{1}	1.7×10^{-4}	1.04×10^{-5}	72
*Sm*FixLN[d]	22 °C, pH 7.0	3.2×10^{1}	14.7×10^{-4}	1.48×10^{-5}	49
MP-11	20 °C, pH 7.0	8.9×10^{3}	1.5×10^{-3}	1.7×10^{-7}	73
*Da*Cld(R183Q)	20 °C, pH 7.0	$(3.0\pm0.02)\times10^{3}$	$(1.7\pm0.2)\times10^{-1}$	$(6.0\pm0.6)\times10^{-5}$	This work
*Nd*Cld(R173Q)	25 °C, pH 7.0	2.3×10^{3}	5×10^{-1}	2.164×10^{-4}	25
*Nd*Cld(R173K)	25 °C, pH 7.0	1.62×10^{3}	3.0×10^{-1}	1.85×10^{-4}	23
*Nd*Cld(R173A)	25 °C, pH 7.0	3.43×10^{3}	5.01×10^{-1}	1.46×10^{-4}	23
*Nd*Cld(R173E)	25 °C, pH 7.0	7.3×10^{1}	3.0×10^{-1}	3.874×10^{-3}	25
CcP(H52Q)	25 °C, pH 6.0	8.4×10^{1}	4.9×10^{-2}	6.1×10^{-3}	33
Gd II Hb[+d]	20 °C, pH 7.0	4.91×10^{-1}	9.82×10^{-8}	2×10^{-7}	74
Gd III Hb[+d]	20 °C, pH 7.0	3.02×10^{-1}	2.9×10^{-6}	1×10^{-5}	75
Gd IV Hb[+d]	20 °C, pH 7.0	1.82	2.2×10^{-5}	1.2×10^{-5}	75

[a]Calculated from spectrophotometric K_D and kinetically determined k_{on}.
[b]Measured via spectrophotometric titration.
[c]Kinetic and spectrophotometric titration yield the same value for *Da*Cld K_D.
[d]*Cj*, *Campylobacter jejuni*;*Mt*, *Mycobacterium tuberculosis*; *Bj, Bradyrhizobium japonicum*; *Sm, Sinorhizobium meliloti*; *Gd*, *Glycera dibranchiate.*

In *Da*Cld(R183Q), where the side chain of the distal Gln bears no overall charge, k_{on} diminishes by 2 to 3 orders of magnitude (Table C2). Similar decreases in k_{on} relative to WT enzyme have been reported for R173Q, R173K, and R173A mutants (*Nd* distal Arg numbering) of *Nd*Cld (Table 4.2).[23, 25] Notably, k_{on} does not exhibit a pK_a near 6.5, attributed to the impact of the open/closed transition on k_{cat}/K_M, for either ferric WT *Da*Cld or its R183Q mutant.[26] This suggests that closing of the Arg "gate" is not important for forming the Fe−CN bond in the *Da* enzymes but for a subsequent step in the catalytic cycle. Comparison of k_{off} values at pH 7.0 for pentameric Cld−CN^-s and their distal Arg mutants (Table 4.2) reveals that these mutations have a ~10^2 fold smaller effect on k_{off} relative to their effect on k_{on}.

The pH dependence of k_{off}, in contrast, yields pK_as for *Da*Cld and *Kp*Cld, which are very close to those reported for these Clds and their chlorite decomposition reaction. Based on X-ray structures of pentameric Cld ligand complexes,[20, 22, 53] a closed conformation of the charged distal Arg appears to be readily accessible in *Da*Cld where its interaction with the bound CN^- imparts maximum stability and activity under acidic conditions. Above the pK_a k_{off} increases; the coordinated CN^- is more readily lost from *Da*Cld suggesting that an open orientation is more accessible as conditions become more alkaline. In contrast, X-ray structures for dimeric Clds, *Nw*Cld and CCld, show the distal Arg held in an open conformation by H-bonding to a Gln residue (Figure 4.1).[5, 54] In turn, the Arg is H-bonded to a water molecule that is within H-bonding distance of heme ligands such as hydroxide and fluoride.[54] Examination of a *Kp*Cld homology model reveals a similar Gln residue poised to facilitate a comparable open conformer. In such an open conformer of *Kp*Cld−CN, the Fe-C bond would be exposed to considerably less influence of Coulombic or steric interaction with Arg. The distancing of the Arg charge from the Fe-C bond stabilizes the bond against dissociation; this is supported by the two orders of

magnitude slower dissociation rate observed for *Kp*Cld relative to pentameric Clds. In addition stabilization of an open conformation via H-bonding between the distal Arg and a conserved Gln in dimeric Clds is an attractive explanation for the decreased activity and chlorite turnover number of *Kp*Cld relative to *Da*Cld which lacks a H-bond partner in the comparable position.

4.5.2. FeCN vibrational distortions as indicators of FeCN geometry and distal pocket landscape.

Open and closed conformers of the ferrous *Da*Cld−CO complex, forming with Arg183 in its open and closed configuration, respectively, have been observed.[24] Their positions on the π backbonding correlation plot are consistent with different distal H-bond donor strengths.[24, 26] It was anticipated, that in *Da*Cld−CN^-, the open conformer would lack H-bonding between Arg183 and CN^- while the closed conformer, with its inward-oriented guanidinium group, would interact more strongly with the coordinated CN^- through H-bond donation. However, only one *Da*Cld−CN^- conformer was observed. Since the polar non-bonding interactions between distal H-bond donors and the anionic CN^- ligand are expected to be stronger than their CO counterparts,[36, 38] one explanation for the single *Da*Cld−CN^- conformer is that the stronger non-bonding interaction coupled with the ionic interaction between the anionic ligand and the cationic Arg result in a closed conformation.

The ^2H_2O insensitivity of the FeCN modes of the nearly linear *Da*Cld−CN^- leaves the question of H-bonding in the distal pocket unresolved.[63, 76] Insensitivity of the ν_{Fe-C} frequencies to ^2H_2O suggests that either there is no hydrogen bond or the hydrogen bond is so weak as to be undetectable by a shift of the ν_{Fe-C} frequencies in ^2H_2O because its geometry is not optimal for polarizing electron density in the FeCN unit.[36, 42, 63]

The FeCN angle in heme protein cyanides is quite sensitive to distal steric interactions. In and out movement of the distal Arg in *Da*Cld would certainly alter steric interactions between CN^- and the distal heme pocket. Modulation of distal steric interactions with coordinated CN^- could be directly associated with dynamics of the distal Arg183 side chain or indirectly, through its influence on the side chain conformations of other distal residues, including Phe200, Thr198 and Leu185. In either case, the ∠FeCN could be influenced by the position of the distal Arg. As judged by its ν_{Fe-C} and δ_{FeCN} frequencies, the *Da*Cld−CN^- ∠FeCN is unaffected by pH; this also supports a single conformation for the cyanide complex. There is, however, a pH-dependent broadening of ν_{Fe-His} and ν_8 rR bands indicating some conformational inhomogeneity of the heme pocket. This decrease in homogeneity could correspond to the kinetic pK_a estimated from k_{off}. These data support the hypothesis that at low pH, where k_{off} for *Da*Cld−CN^- is small, the active site is in a closed conformation while at alkaline pH open Arg conformational states become more accessible, lowering the barrier to CN^- dissociation with a corresponding increase in k_{off} values. However, it is likely that, even in the absence of distal H-bond interactions, the closed conformation dominates the rR spectrum of the ferric cyanide complex due to the ionic interaction between the cationic Arg side chain and the negatively charged cyanide ligand. Such a salt bridge-type interaction is not available to *Da*Cld−CO with its neutral CO ligand, resulting in CO complexes mostly in the open Arg conformation.

Although the low pK_a governing the Arg183 gating of the active site in ferric WT *Da*Cld is not observed kinetically in the R183Q mutant, two forms of its heme carbonyl have been reported and interpreted as this mutant accessing two conformations analogous to those of the WT enzyme, one with the Gln183 side chain oriented towards the heme and a second in which it is oriented away.[24] Although WT *Da*Cld−CN^- and *Da*Cld(R183Q)−CN^- exhibited similar ν_{Fe-C}

frequencies, the broadened ν_{Fe-C} band of the R183Q mutant reveals a decrease in structural homogeneity of the FeCN unit analogous to that seen for alkaline WT enzyme (*vide infra*). The smaller $\Delta(\nu-\delta)$ for *Da*Cld(R183Q)−CN^- relative to WT enzyme indicates that its FeCN geometry is less constrained. This suggests that lack of charge in the R183Q distal pocket or the difference in Gln side chain size and/or its hydrogen bond donor strength result in a weaker distal interaction with the bound cyanide in the mutant than in WT. Conformational inhomogeneity and the less constrained FeCN unit of *Da*Cld(R183Q)−CN^- indicate that the open conformer is accessible. However, based on the lack of pH sensitivity of the k_{off} for *Da*Cld(R183Q)−CN^- and its similarity to the WT *Da*Cld−CN^- k_{off} under acidic conditions, it is likely that an active-site conformer of *Da*Cld(R183Q)−CN^- analogous to the WT closed conformer is also accessible. Taken together, these lines of evidence suggest why *Da*Cld(R183Q) retains a modicum of its chlorite-decomposing activity;[24] while its closed conformation is responsible for the mutant's residual activity, its diminished ability to bind and retain substrate in the open conformation significantly attenuates its activity.

In contrast to *Da*Cld and its R183Q mutant, a single conformer is observed for *Kp*Cld−CO; its position on the ν_{Fe-C}/ν_{C-O} correlation plot indicates that there is only weak interaction between heme−CO and distal pocket of *Kp*Cld (Figure 4.6). By analogy to its CO complex, *Kp*Cld−CN^- would be expected to exist as a single conformer with a minimal H bonding environment around the CN^-. The insensitivity of FeCN frequencies in *Kp*Cld−CN^- to ^2H_2O substitution could be consistent with this; however, only very small isotope shifts are anticipated for H bonding to the cyanide making it difficult to detect. One FeCN geometry with very subtle frequency differences on either side of the pK_a is observed for *Kp*Cld−CN^-, suggesting that, like *Da*Cld−CN^-, its distal Arg is in a single conformation. Interestingly,

*Nd*Cld−CO exhibits a single open conformation in which its distal Arg does not interact with the CO (Figure 4.6).[77] Molecular dynamics simulations for ferrous *Nd*Cld predict that its distal Arg is in the open position 62% of the time, while in ferric *Nd*Cld−CN^- the distal Arg is predominantly in the closed position (85% of the time). This suggests that, while the open conformation is observed for *Kp*Cld−CO, the form of *Kp*Cld−CN^- observed spectroscopically is mostly likely closed due to nonbonding interactions comparable to those described above for *Da*Cld.

4.5.2.1. Distal Arg versus Gln – effects of charge and steric bulk.

The small differences between the FeCN frequencies of the *Da*Cld and *Da*Cld(R183Q) cyanides suggest that the structural features influencing the force constants and reduced masses of these modes are similar in the WT and mutant enzymes. Increased breadth of the mutant ν_{Fe-C} band relative to that of WT (Figure 4.4) reflects greater structural flexibility (*i.e.* inhomogeneity) in the heme pocket structure. This points toward the Arg charge being important in controlling its side chain conformation.

Interestingly, several heme proteins having a distal Gln residue exhibit ν_{Fe-C} frequencies comparable to those of the three Cld−CN^- complexes reported here (Table 4.1). Increases in these ν_{Fe-C} frequencies have been attributed to removal of constraints on the FeCN unit based on "strapped" heme cyanide model complexes with $(CH_2)_n$ chains over the heme, where lengthening or eliminating the strap hindering the bound CN^- caused the ν_{Fe-C} to shift to higher frequencies (n=13 to 15, 445−447 cm^{-1}; no strap, 451 cm^{-1}).[78] A similar trend is observed in heme protein cyanide complexes. For example, the crystal structure of *Chlamydomonas* Hb−CN^- (pdb code:1DLY) revealed that its FeCN angle is 130° due to a H-bonding network involving a Tyr and two Gln in its distal pocket.[79] Disruption of this H-bonding network resulted in a less

hindered FeCN (*i.e.* more linear FeCN moiety), which was reported by the ν_{Fe-C} of *Chlamydomonas* Hb−CN^- shifting from 440 cm^{-1} to 454 cm^{-1} upon mutation of its distal Gln to Gly.[42] Replacing the distal His in HRP−CN^- with Gln elicits a downshift of its ν_{Fe-C} frequency from 453 to 443 cm^{-1}, consistent with steric reorganization of the distal heme pocket accompanying loss of the H-bond donation to the terminal N atom of the CN^- ligand.[59] A similar ν_{Fe-C} frequency (444 cm^{-1})[38] reported for HRP at pH 12.5 (*c.f.* pK_a of ~14 for ImH of aqueous histidine) is probably due to loss of the H bond to the CN^- ligand in addition to relaxing structural factors influencing the FeCN angle. Another possibility is that in the absence of H-bonding from the distal His, the distal Arg of HRP interacts with the coordinated CN^- in a manner comparable to the distal Gln in the examples described here. This idea is supported by the fact that the WT Cld−CN^- complexes with their distal Arg residues exhibit similar ν_{Fe-C} frequencies (439-441 cm^{-1}). Steric interactions dictated by Gln or Arg in these distal pockets appear to provide comparable nonbonding environments, which restrict the FeCN moiety, in their respective heme cyanides.

Relative insensitivities of ν_{Fe-C} frequencies in the Cld−CN^-s to Arg/Gln mutation and $H_2O/^2H_2O$ substitution suggest that neither the distal Arg nor distal Gln serve as significant H-bond donors to the terminal N atom of coordinated CN^-. Interestingly, the distal Arg does donate two hydrogen bonds to coordinated F^-.[64] Therefore, the apparent lack of hydrogen bonding with coordinated CN^- leads to the conclusion that heme pocket structure precludes it. In other words, the Cld heme pockets are organized to favor hydrogen bond donation to the coordinated atom of exogenous ligands.[64] This is the first experimental evidence that supports a structurally based explanation for the poor peroxidase activity[28] of the Clds. Specifically, their heme pocket structure disfavors peroxidase and catalase reactions by disfavoring the terminal hydrogen bond

necessary to polarize the peroxo bond, which is responsible, in part, for its heterolytic cleavage in the conversion of compound 0 to compound I in heme peroxidases.

While *Da*Clds and other heme proteins like peroxidases, Mb and Hb, have comparable affinities for cyanide ($K_D \sim 10^{-6}$ M), their k_{on} and k_{off}, values vary significantly (Table 4.2). The k_{on} values for cyanide binding to Clds are 1 to 2 orders of magnitude greater than those for cytochrome *c* peroxidase (CcP) and HRP, which have distal pockets containing His and Arg, and 4 orders of magnitude greater than Mb and Hb with a His in their distal pockets. The distal Arg in Cld is partially responsible for these greater k_{on} values, which drop from 10^6 to 10^3 $M^{-1}\cdot s^{-1}$ upon its replacement with Gln. The series of *Nd*Cld Arg mutants and *Da*Cld(R183Q) still have greater k_{on} values than Mb or Hb indicating that factors intrinsic to Clds other than their distal Arg, such as the hydrophobicity of the distal pocket, contribute to their low kinetic barriers to cyanide binding.

The significantly higher affinity of *Kp*Cld for CN^- relative to *Da*Cld, driven by the much smaller k_{off} value in the former, is surprising. An affinity for CN^- of similar magnitude has been reported for the truncated Hb from *Camplyobacter jejuni* (*Cj* trHbP). However, its distal heme pocket is quite different than that of *Kp*Cld. In *Cj* trHbP, a Tyr and a Trp (pdb code: 2IG3) provide direct H bonds to stabilize bound CN^-.[80] How the pocket characteristics that promote the high CN^- affinity of *Kp*Cld are relevant to its function is currently unclear.

4.5.2.2. Differing FeCN geometries in DaCld and KpCld.

The stretching and bending frequencies reported here for *Da*Cld and *Kp*Cld cyanides are compared to those of other cyanoferric heme proteins in Table 4.1. The frequencies for WT *Da*Cld and its R183Q mutant are similar to other nearly linear (166°−179°) cyanide complexes, especially those of HRP.[38, 43] While the ν_{Fe-C} and δ_{FeCN} frequencies of *Kp*Cld−CN^- are close to

those of bent NP1−CN^-, the Raman shift patterns of their $^{13}CN^-$ and $C^{15}N^-$ isotopologs reveal that their ν_{Fe-C} and δ_{FeCN} frequencies are reversed from those for bent peroxidase, catalase, and P450 cyanides. The bent FeCN geometry of the *Kp*Cld−CN^- indicates that there are interactions in the distal pocket that are strong enough to generate large off-axis distortions of the FeCN unit that are absent in *Da*Cld. The presence of one or two water molecules in the *Kp*Cld active site, as is the case in dimeric ferric *Nw*Cld and CCld and pentameric *Nd*Cld−CN^-,[5, 23, 54] could provide the steric interactions and possibly H bonds responsible for the off-axis distortions in *Kp*Cld−CN^- that contribute in slower k_{off} relative to *Da*Cld−CN^-. This is also consistent with the "nearly linear" *Da*Cld−CN^- having an active site that is less accessible to water than the *Kp*Cld heme pocket.[9, 26] Given that the chlorite decomposition activity of these enzymes differs by an order of magnitude and assuming that both enzymes react via similar intermediates, it appears that the factors responsible for the differences in FeCN geometry could play a significant role in their oxygen-evolving activity. The presence of water in the *Kp*Cld heme pocket would weaken the ion pair presumably formed between the distal Arg and ClO^-, possibly explaining the decrease in activity. This may also be the reason that *Kp*Cld leaks ClO^- more readily than *Da*Cld, resulting in oxidative damage to the enzyme, lowering its turnover number.

While crystal structures of various Cld-ligand complexes have been reported,[5, 20, 22-23, 53-54, 81] only one cyanide complex structure is available.[23] In the *Nd*Cld−CN^- crystal structure (3NN2), ∠FeCN ranges from 140.9 to 177.0˚ with an O atom of a glycerol molecule within H-bonding distance of the terminal cyanide nitrogen atom. The guanidinium group of the distal Arg is pointed away from the heme and lies beyond H-bonding distance from the cyanide ligand (Figure C7).[23] It is unclear how the glycerol in the heme pocket of the *Nd*Cld−CN^- structure influences the geometry of the FeCN unit or the orientation of the distal Arg. It does illustrate

that a wide range of ∠FeCN can be accommodated. Since there is no glycerol present in the experiments described here and a bent FeCN unit is also observed for *Kp*Cld−CN^-, it is possible that 1) its Arg is in a position analogous to the glycerol, pointed into the pocket toward the cyanide or 2) a water molecule can occupy the glycerol position and provide a bridge between the Arg and the cyanide.

4.6. Conclusions

*Kp*Cld has one of the highest affinities for CN^- reported for heme proteins. Its particularly small K_D of 4.7×10^{-9} M for CN^- dissociation is attributable to slow dissociation kinetics. While the rates of CN^- association with WT *Da*Cld and *Kp*Cld are similar to one another, their k_{on} values are at least an order of magnitude larger than those reported for peroxidases and four orders of magnitude greater than those of Mbs. The distal Arg is an important factor in the high CN^- association rates, of both Cld clades. Substitution of Arg with Gln reveals that the charge of the distal residue is important in controlling the homogeneity of the ligand-bound pentameric enzyme conformation and the pK_a of ~7 is important in stabilizing the CN^- complex. Differing FeCN geometries between *Da*Cld (nearly linear) and *Kp*Cld (bent) reveal that their distal pocket environments, and possibly those between the clades they represent, are distinct. Factors responsible for the bent FeCN geometry in *Kp*Cld, such as the possibility of water being positioned between the ligand and the distal Arg in the active site, could also affect the stability of the intermediates and/or transition states. Associated differences in kinetic barriers likely account for *Kp*Cld's 10-fold lower oxygen-evolving activity relative to *Da*Cld. That larger kinetic barrier is also likely the reason that escape of enzyme-inactivating HOCl from the catalytic heme pocket under turnover conditions competes with product

formation, thereby limiting the turnover number. Whether these distal pocket characteristics are conserved within the Cld clades remains to be determined.

4.7. Associated Content

Additional data referred to in the text are in Appendix C: Figures C1 to C7 and Tables C1 to C4.

4.8. Funding Sources

Support is gratefully acknowledged from the National Institutes of Health Grants GM114787 (to G. S. L.-R.) and GM090260 (to J. L. D.).

4.9. References

1. DuBois, J. L.; Ojha, S., Production of dioxygen in the dark: dismutases of oxyanions. *Met Ions Life Sci* 2015, *15*, 45-87.
2. Schaffner, I.; Hofbauer, S.; Krutzler, M.; Pirker, K. F.; Furtmueller, P. G.; Obinger, C., Mechanism of chlorite degradation to chloride and dioxygen by the enzyme chlorite dismutase. *Arch. Biochem. Biophys.* 2015, *574*, 18-26.
3. Tagore, R.; Crabtree, R. H.; Brudvig, G. W., Oxygen Evolution Catalysis by a Dimanganese Complex and Its Relation to Photosynthetic Water Oxidation. *Inorg. Chem.* 2008, *47* (6), 1815-1823.
4. Coates, J. D.; Achenbach, L. A., Microbial perchlorate reduction: rocket-fueled metabolism. *Nat.Rev.Microbiol.* 2004, *2* (7), 569-580.
5. Mlynek, G.; Sjoeblom, B.; Kostan, J.; Fuereder, S.; Maixner, F.; Gysel, K.; Furtmueller, P. G.; Obinger, C.; Wagner, M.; Daims, H.; Djinovic-Carugo, K., Unexpected diversity of chlorite dismutases: a catalytically efficient dimeric enzyme from *Nitrobacter winogradskyi*. *J. Bact.* 2011, *193*, 2408-2417.
6. Melnyk, R. A.; Engelbrektson, A.; Clark, I. C.; Carlson, H. K.; Byrne-Bailey, K.; Coates, J. D., Identification of a perchlorate reduction genomic island with novel regulatory and metabolic genes. *Appl. Environ. Microbiol.* 2011, *77*, 7401-7404.
7. Clark, I. C.; Melnyk, R. A.; Engelbrektson, A.; Coates, J. D., Structure and evolution of chlorate reduction composite transposons. *mBio* 2013, *4*, e00379, 12 pp.
8. Hofbauer, S.; Schaffner, I.; Furtmueller, P. G.; Obinger, C., Chlorite dismutases - a heme enzyme family for use in bioremediation and generation of molecular oxygen. *Biotechnol. J.* 2014, *9*, 461-473.
9. Celis, A. I.; Geeraerts, Z.; Ngmenterebo, D.; Machovina, M. M.; Kurker, R. C.; Rajakumar, K.; Ivancich, A.; Rodgers, K. R.; Lukat-Rodgers, G. S.; DuBois, J. L., A Dimeric Chlorite Dismutase Exhibits O2-Generating Activity and Acts as a Chlorite Antioxidant in *Klebsiella pneumoniae* MGH 78578. *Biochemistry* 2015, *54*, 434-446.

10. Goblirsch, B.; Kurker, R. C.; Streit, B. R.; Wilmot, C. M.; DuBois, J. L., Chlorite dismutases, DyPs, and EfeB: 3 microbial heme enzyme families comprise the CDE structural superfamily. *J. Mol. Biol.* 2011, *408* (3), 379-398.
11. Schaffner, I.; Hofbauer, S.; Krutzler, M.; Pirker, K. F.; Bellei, M.; Stadlmayr, G.; Mlynek, G.; Djinovic-Carugo, K.; Battistuzzi, G.; Furtmueller, P. G.; Daims, H.; Obinger, C., Dimeric chlorite dismutase from the nitrogen-fixing cyanobacterium Cyanothece sp. PCC7425. *Mol. Microbiol.* 2015, *96*, 1053-1068.
12. Dailey, T. A.; Boynton, T. O.; Albetel, A.-N.; Gerdes, S.; Johnson, M. K.; Dailey, H. A., Discovery and Characterization of HemQ: an essential heme biosynthetic pathway component. *J. Biol. Chem.* 2010, *285*, 25978-25986.
13. Dailey, H. A.; Gerdes, S.; Dailey, T. A.; Burch, J. S.; Phillips, J. D., Noncanonical coproporphyrin-dependent bacterial heme biosynthesis pathway that does not use protoporphyrin. *Proc. Natl. Acad. Sci. U. S. A.* 2015, *112*, 2210-2215.
14. Dailey, H. A.; Gerdes, S., HemQ: An iron-coproporphyrin oxidative decarboxylase for protoheme synthesis in Firmicutes and Actinobacteria. *Arch. Biochem. Biophys.* 2015, *574*, 27-35.
15. Celis, A. I.; Streit, B. R.; Moraski, G. C.; Kant, R.; Lash, T. D.; Lukat-Rodgers, G. S.; Rodgers, K. R.; DuBois, J. L., Unusual Peroxide-Dependent, Heme-Transforming Reaction Catalyzed by HemQ. *Biochemistry* 2015, *54*, 4022-4032.
16. Lobo, S. A. L.; Scott, A.; Videira, M. A. M.; Winpenny, D.; Gardner, M.; Palmer, M. J.; Schroeder, S.; Lawrence, A. D.; Parkinson, T.; Warren, M. J.; Saraiva, L. M., Staphylococcus aureus haem biosynthesis: characterisation of the enzymes involved in final steps of the pathway. *Mol. Microbiol.* 2015, *97*, 472-487.
17. Streit, B. R.; DuBois, J. L., Chemical and Steady-State Kinetic Analyses of a Heterologously Expressed Heme Dependent Chlorite Dismutase. *Biochemistry* 2008, *47* (19), 5271-5280.
18. Catling, D. C.; Claire, M. W.; Zahnle, K. J.; Quinn, R. C.; Clark, B. C.; Hecht, M. H.; Kounaves, S. Atmospheric origins of perchlorate on Mars and in the Atacama *J. Geophys. Res., [Planets]* [Online], 2010, p. E00E11/1-E00E11/15. http://onlinelibrary.wiley.com/store/10.1029/2009JE003425/asset/jgre2709.pdf?v=1&t=ihsbp3ol&s=9fa6fd93eee324c7fdcfb1972eab931312dd2dd1.
19. Rao, B.; Hatzinger, P. B.; Bohlke, J. K.; Sturchio, N. C.; Andraski, B. J.; Eckardt, F. D.; Jackson, W. A., Natural Chlorate in the Environment: Application of a New IC-ESI/MS/MS Method with a Cl18O3- Internal Standard. *Environ. Sci. Technol.* 2010, *44*, 8429-8434.
20. Goblirsch, B. R.; Streit, B. R.; DuBois, J. L.; Wilmot, C. M., Structural features promoting dioxygen production by Dechloromonas aromatica chlorite dismutase. *J.Biol.Inorg.Chem.* 2010, *15* (6), 879-888.
21. Pettersen, E. F.; Goddard, T. D.; Huang, C. C.; Couch, G. S.; Greenblatt, D. M.; Meng, E. C.; Ferrin, T. E., UCSF Chimera—A visualization system for exploratory research and analysis. *J. Comput. Chem.* 2004, *25* (13), 1605-1612.
22. de Geus, D. C.; Thomassen, E. A. J.; Hagedoorn, P. L.; Pannu, N. S.; van Duijn, E.; Abrahams, J. P., Crystal Structure of Chlorite Dismutase, a Detoxifying Enzyme Producing Molecular Oxygen. *J. Mol. Biol.* 2009, *387* (1), 192-206.
23. Kostan, J.; Sjoeblom, B.; Maixner, F.; Mlynek, G.; Furtmueller, P. G.; Obinger, C.; Wagner, M.; Daims, H.; Djinovic-Carugo, K., Structural and functional characterisation

of the chlorite dismutase from the nitrite-oxidizing bacterium "Candidatus Nitrospira defluvii": Identification of a catalytically important amino acid residue. *J.Struct.Biol.* 2010, *172* (3), 331-342.

24. Blanc, B.; Mayfield, J. A.; McDonald, C. A.; Lukat-Rodgers, G. S.; Rodgers, K. R.; DuBois, J. L., Understanding How the Distal Environment Directs Reactivity in Chlorite Dismutase: Spectroscopy and Reactivity of Arg183 Mutants. *Biochemistry* 2012, *51*, 1895-1910.
25. Hofbauer, S.; Gysel, K.; Bellei, M.; Hagmueller, A.; Schaffner, I.; Mlynek, G.; Kostan, J.; Pirker, K. F.; Daims, H.; Furtmueller, P. G.; Battistuzzi, G.; Djinovic-Carugo, K.; Obinger, C., Manipulating conserved heme cavity residues of chlorite dismutase: Effect on structure, redox chemistry, and reactivity. *Biochemistry* 2014, *53*, 77-89.
26. Streit, B. R.; Blanc, B.; Lukat-Rodgers, G. S.; Rodgers, K. R.; DuBois, J. L., How Active-Site Protonation State Influences the Reactivity and Ligation of the Heme in Chlorite Dismutase. *J. Am. Chem. Soc.* 2010, *132*, 5711-5724.
27. Hofbauer, S.; Gruber, C.; Pirker, K. F.; Suendermann, A.; Schaffner, I.; Jakopitsch, C.; Oostenbrink, C.; Furtmueller, P. G.; Obinger, C., Transiently produced hypochlorite is responsible for the irreversible inhibition of chlorite dismutase. *Biochemistry* 2014, *53*, 3145-3157.
28. Lee, A. Q.; Streit, B. R.; Zdilla, M. J.; bu-Omar, M. M.; DuBois, J. L., Mechanism of and exquisite selectivity for O-O bond formation by the heme-dependent chlorite dismutase. *Proc. Natl. Acad. Sci. U. S. A.* 2008, *105* (41), 15654-15659.
29. Graves, A. B.; Morse, R. P.; Chao, A.; Iniguez, A.; Goulding, C. W.; Liptak, M. D., Crystallographic and spectroscopic insights into heme degradation by Mycobacterium tuberculosis MhuD. *Inorg. Chem.* 2014, *53* (Copyright (C) 2014 American Chemical Society (ACS). All Rights Reserved.), 5931-5940.
30. Yoshida, T.; Tsuge, H.; Konno, H.; Hisabori, T.; Sugano, Y., The catalytic mechanism of dye-decolorizing peroxidase DyP may require the swinging movement of an aspartic acid residue. *FEBS J.* 2011, *278* (Copyright (C) 2013 American Chemical Society (ACS). All Rights Reserved.), 2387-2394.
31. Rwere, F.; Mak, P. J.; Kincaid, J. R., Resonance Raman Interrogation of the Consequences of Heme Rotational Disorder in Myoglobin and Its Ligated Derivatives. *Biochemistry* 2008, *47* (Copyright (C) 2011 American Chemical Society (ACS). All Rights Reserved.), 12869-12877.
32. La Mar, G. N.; Chen, Z.; Vyas, K.; McPherson, A. D., An Interpretive Basis of the Hyperfine Shifts in Cyanide-Inhibited Horseradish Peroxidase Based on the Magnetic Axes and Ligand Tilt. Influence of Substrate Binding and Extensions to Other Peroxidases. *J. Am. Chem. Soc.* 1995, *117*, 411-19.
33. Foshay, M. C.; Vitello, L. B.; Erman, J. E., Effect of alternative distal residues on the reactivity of cytochrome c peroxidase: Properties of CcP mutants H52D, H52E, H52N, and H52Q. *Biochim.Biophys.Acta, Proteins Proteomics* 2011, *1814* (5), 525-535.
34. Bidwai, A.; Witt, M.; Foshay, M.; Vitello, L. B.; Satterlee, J. D.; Erman, J. E., Cyanide Binding to Cytochrome c Peroxidase (H52L). *Biochemistry* 2003, *42*, 10764-10771.
35. Ellis, W. D.; Dunford, H. B., The kinetics of cyanide and fluoride binding by ferric horseradish peroxidase. *Biochemistry* 1968, *7* (6), 2054-2062.
36. Simianu, M. C.; Kincaid, J. R., Resonance Raman Spectroscopic Detection of Both Linear and Bent Fe-CN Fragments for the Cyanide Adducts of Cytochrome P-450

Camphor and Its Substrate-Bound Forms. Relevance to the "Charge Relay" Mechanism. *J. Am. Chem. Soc.* 1995, *117*, 4628-36.
37. Al-Mustafa, J.; Sykora, M.; Kincaid, J. R., Resonance Raman investigation of cyanide ligated beef liver and *Aspergillus niger* catalases. *J. Biol. Chem.* 1995, *270* (18), 10449-10460.
38. Al-Mustafa, J.; Kincaid, J. R., Resonance Raman Study of Cyanide-Ligated Horseradish Peroxidase.Detection of Two Binding Geometries and Direct Evidence for the "Push-Pull" Effect. *Biochemistry* 1994, *33*, 2191-7.
39. Maes, E. M.; Walker, F. A.; Montfort, W. R.; Czernuszewicz, R. S., Resonance Raman Spectroscopic Study of Nitrophorin 1, a Nitric Oxide-Binding Heme Protein from Rhodnius prolixus, and Its Nitrosyl and Cyano Adducts. *J. Am. Chem. Soc.* 2001, *123*, 11664-11672.
40. Boffi, A.; Chiancone, E.; Takahashi, S.; Rousseau, D. L., Stereochemistry of the Fe(II)- and Fe(III)-cyanide complexes of the homodimeric Scapharca inaequivalvis hemoglobin. A resonance Raman and FTIR study. *Biochemistry* 1997, *36* (15), 4505-4509.
41. Hirota, S.; Ogura, T.; Shinzawa-Itoh, K.; Yoshikawa, S.; Kitagawa, T., Observation of Multiple CN-Isotope-Sensitive Raman Bands for CN Adducts of Hemoglobin, Myoglobin, and Cytochrome c Oxidase: Evidence for Vibrational Coupling between the Fe-C-N Bending and Porphyrin In-Plane Modes. *J. Phys. Chem.* 1996, *100* (37), 15274-15279.
42. Das, T. K.; Couture, M.; Guertin, M.; Rousseau, D. L., Distal Interactions in the Cyanide Complex of Ferric Chlamydomonas Hemoglobin. *J. Phys. Chem. B* 2000, *104*, 10750-10756.
43. Lopez-Garriga, J. J.; Oertling, W. A.; Kean, R. T.; Hoogland, H.; Wever, R.; Babcock, G. T., Metal-ligand vibrations of cyanoferric myeloperoxidase and cyanoferric horseradish peroxidase: evidence for a constrained heme pocket in myeloperoxidase. *Biochemistry* 1990, *29*, 9387-95.
44. Tropea, J. E. C., Scott; Waugh, David S., Expression and purification of soluble His_6-tagged TEV protease. In *Methods in Molecular Biology: High Throughput Protein Expression and Purification*, Doyle, S. A., Ed. Humana Press: Totowa, NJ, 2009; Vol. 498, pp 297-306.
45. Blanc, B.; Rodgers, K. R.; Lukat-Rodgers, G. S.; DuBois, J. L., Understanding the roles of strictly conserved tryptophan residues in O2 producing chlorite dismutases. *Dalton Trans.* 2013, *42*, 3156-3169.
46. Philippi, M.; dos Santos, H. S.; Martins, A. O.; Azevedo, C. M.; Pires, M., Alternative spectrophotometric method for standardization of chlorite aqueous solutions. *Anal Chim Acta* 2007, *585* (2), 361-5.
47. Ryan, J. A.; Culshaw, G. W., The use of p-dimethylaminobenzylidene rhodanine as an indicator for the volumetric determination of cyanides. *Analyst* 1944, *69* (825), 370-371.
48. Breuer, P. L.; Sutcliffe, C. A.; Meakin, R. L., Cyanide measurement by silver nitrate titration: Comparison of rhodanine and potentiometric end-points. *Hydrometallurgy* 2011, *106* (3), 135-140.
49. Rodgers, K. R.; Lukat-Rodgers, G. S.; Barron, J. A., Structural basis for ligand discrimination and response initiation in the heme-based oxygen sensor FixL. *Biochemistry* 1996, *35* (Copyright (C) 2012 American Chemical Society (ACS). All Rights Reserved.), 9539-9548.

50. Bidwai, A. K.; Ok, E. Y.; Erman, J. E., pH Dependence of Cyanide Binding to the Ferric Heme Domain of the Direct Oxygen Sensor from Escherichia coli and the Effect of Alkaline Denaturation. *Biochemistry* 2008, *47* (Copyright (C) 2017 American Chemical Society (ACS). All Rights Reserved.), 10458-10470.
51. Van Ginkel, C. G.; Rikken, G. B.; Kroon, A. G. M.; Kengen, S. W. M., Purification and characterization of chlorite dismutase. A novel oxygen-generating enzyme. *Arch. Microbiol.* 1996, *166* (5), 321-326.
52. Stenklo, K.; Danielsson Thorell, H.; Bergius, H.; Aasa, R.; Nilsson, T., Chlorite dismutase from Ideonella dechloratans. *JBIC Journal of Biological Inorganic Chemistry* 2001, *6* (5), 601-607.
53. Freire, D. M.; Rivas, M. G.; Dias, A. M.; Lopes, A. T.; Costa, C.; Santos-Silva, T.; Van Doorslaer, S.; Gonzalez, P. J., The homopentameric chlorite dismutase from *Magnetospirillum sp*. *J. Inorg. Biochem.* 2015, *151*, 1-9.
54. Schaffner, I.; Mlynek, G.; Flego, N.; Puehringer, D.; Libiseller-Egger, J.; Coates, L.; Hofbauer, S.; Bellei, M.; Furtmueller, P. G.; Battistuzzi, G.; Smulevich, G.; Djinovic-Carugo, K.; Obinger, C., Molecular Mechanism of Enzymatic Chlorite Detoxification: Insights from Structural and Kinetic Studies. *ACS Catal.* 2017, *7*, 7962-7976.
55. Nicoletti, F. P.; Droghetti, E.; Howes, B. D.; Bustamante, J. P.; Bonamore, A.; Sciamanna, N.; Estrin, D. A.; Feis, A.; Boffi, A.; Smulevich, G., H-bonding networks of the distal residues and water molecules in the active site of Thermobifida fusca hemoglobin. *Biochim. Biophys. Acta, Proteins Proteomics* 2013, *1834* (Copyright (C) 2014 American Chemical Society (ACS). All Rights Reserved.), 1901-1909.
56. Yu, N. T.; Benko, B.; Kerr, E. A.; Gersonde, K., Iron-carbon bond lengths in carbonmonoxy and cyanomet complexes of the monomeric hemoglobin III from Chironomus thummi thummi: a critical comparison between resonance Raman and x-ray diffraction studies. *Proc Natl Acad Sci U S A* 1984, *81* (Copyright (C) 2017 U.S. National Library of Medicine.), 5106-10.
57. Lu, C.; Mukai, M.; Lin, Y.; Wu, G.; Poole, R. K.; Yeh, S.-R., Structural and Functional Properties of a Single Domain Hemoglobin from the Food-borne Pathogen Campylobactor jejuni. *J. Biol. Chem.* 2007, *282* (Copyright (C) 2017 American Chemical Society (ACS). All Rights Reserved.), 25917-25928.
58. Al-Mustafa, J. I.; Alshbool, T., Fourier Transform Infrared Spectroscopic Investigation of the Binary and Ternary Cyanide Adducts of the Oxidized Horseradish Peroxidase: Identification of a Second Stretching Mode for the Carbon-Nitrogen Bond of the Bound Cyanide Ion. *Spectrosc. Lett.* 2014, *47*, 281-291.
59. Tanaka, M.; Ishimori, K.; Mukai, M.; Kitagawa, T.; Morishima, I., Catalytic activities and structural properties of horseradish peroxidase distal His42 -> Glu or Gln mutant. *Biochemistry* 1997, *36* (32), 9889-9898.
60. Hu, S.; Treat, R. W.; Kincaid, J. R., Distinct heme active-site structure in lactoperoxidase revealed by resonance Raman spectroscopy. *Biochemistry* 1993, *32*, 10125-30.
61. Bolognesi, M.; Rosano, C.; Losso, R.; Borassi, A.; Rizzi, M.; Wittenberg, J. B.; Boffi, A.; Ascenzi, P., Cyanide binding to Lucina pectinata hemoglobin I and to sperm whale myoglobin: an x-ray crystallographic study. *Biophys J* 1999, *77*, 1093-9.
62. Hu, S.; Smith, K. M.; Spiro, T. G., Assignment of protoheme resonance Raman spectrum by heme labeling in myoglobin. *J. Am. Chem. Soc.* 1996, *118* (50), 12638-12646.

63. Deng, T.-j.; Macdonald, I. D. G.; Simianu, M. C.; Sykora, M.; Kincaid, J. R.; Sligar, S. G., Hydrogen-Bonding Interactions in the Active Sites of Cytochrome P450cam and Its Site-Directed Mutants. *J. Am. Chem. Soc.* 2001, *123* (Copyright (C) 2011 American Chemical Society (ACS). All Rights Reserved.), 269-278.
64. Geeraerts, Z.; Rodgers, K. R.; DuBois, J.; Lukat-Rodgers, G. S., Active sites of O_2-evolving chlorite dismutases probed by halides, hydroxides and new iron-ligand vibrational correlations. *Biochemistry* 2017.
65. Suendermann, A.; Reif, M. M.; Hofbauer, S.; Obinger, C.; Oostenbrink, C., Investigation of Ion Binding in Chlorite Dismutases by Means of Molecular Dynamics Simulations. *Biochemistry* 2014, *53*, 4869-4879.
66. Hofbauer, S.; Bellei, M.; Suendermann, A.; Pirker, K. F.; Hagmueller, A.; Mlynek, G.; Kostan, J.; Daims, H.; Furtmueller, P. G.; Djinovic-Carugo, K.; Oostenbrink, C.; Battistuzzi, G.; Obinger, C., Redox Thermodynamics of High-Spin and Low-Spin Forms of Chlorite Dismutases with Diverse Subunit and Oligomeric Structures. *Biochemistry* 2012, *51*, 9501-9512.
67. Erman, J. E., Kinetic and equilibrium studies of cyanide binding by cytochrome c peroxidase. *Biochemistry* 1974, *13* (1), 39-44.
68. Milani, M.; Ouellet, Y.; Ouellet, H.; Guertin, M.; Boffi, A.; Antonini, G.; Bocedi, A.; Mattu, M.; Bolognesi, M.; Ascenzi, P., Cyanide Binding to Truncated Hemoglobins: A Crystallographic and Kinetic Study. *Biochemistry* 2004, *43* (18), 5213-5221.
69. Bolli, A.; Ciaccio, C.; Coletta, M.; Nardini, M.; Bolognesi, M.; Pesce, A.; Guertin, M.; Visca, P.; Ascenzi, P., Ferrous Campylobacter jejuni truncated hemoglobin P displays an extremely high reactivity for cyanide - a comparative study. *FEBS J.* 2008, *275* (Copyright (C) 2017 American Chemical Society (ACS). All Rights Reserved.), 633-645.
70. Brancaccio, A.; Cutruzzola, F.; Allocatelli, C. T.; Brunori, M.; Smerdon, S. J.; Wilkinson, A. J.; Dou, Y.; Keenan, D.; Ikeda-Saito, M.; Brantley, R. E. J.; Olson, J. S., Structural factors governing azide and cyanide binding to mammalian metmyoglobins. *J. Biol. Chem.* 1994, *269* (19), 13843-13853.
71. Dou, Y.; Olson, J. S.; Wilkinson, A. J.; Ikeda-Saito, M., Mechanism of Hydrogen Cyanide Binding to Myoglobin. *Biochemistry* 1996, *35* (22), 7107-7113.
72. Bidwai, A. K.; Ahrendt, A. J.; Sullivan, J. S.; Vitello, L. B.; Erman, J. E., pH dependence of cyanide and imidazole binding to the heme domains of Sinorhizobium meliloti and Bradyrhizobium japonicum FixL. *J. Inorg. Biochem.* 2015, *153* (Copyright (C) 2017 American Chemical Society (ACS). All Rights Reserved.), 88-102.
73. Ascenzi, P.; Sbardella, D.; Santucci, R.; Coletta, M., Cyanide binding to ferrous and ferric microperoxidase-11. *J. Biol. Inorg. Chem.* 2016, *21* (4), 511-522.
74. Mintorovitch, J.; Satterlee, J. D., Anomalously slow cyanide binding to Glycera dibranchiata monomer methemoglobin component II: implication for the equilibrium constant. *Biochemistry* 1988, *27* (21), 8045-8050.
75. Mintorovitch, J.; Van Pelt, D.; Satterlee, J. D., Kinetic study of the slow cyanide binding to Glycera dibranchiata monomer hemoglobin components III and IV. *Biochemistry* 1989, *28* (14), 6099-6104.
76. Unno, M.; Christian, J. F.; Olson, J. S.; Sage, J. T.; Champion, P. M., Evidence for Hydrogen Bonding Effects in the Iron Ligand Vibrations of Carbonmonoxy Myoglobin. *J. Am. Chem. Soc.* 1998, *120* (11), 2670-2671.

77. Hofbauer, S.; Howes, B. D.; Flego, N.; Pirker, K. F.; Schaffner, I.; Mlynek, G.; Djinovic-Carugo, K.; Furtmueller, P. G.; Smulevich, G.; Obinger, C., From chlorite dismutase towards HemQ-the role of the proximal H-bonding network in haeme binding. *Biosci. Rep.* 2016, *36*, e00312.
78. Tanaka, T.; Yu, N. T.; Chang, C. K., Resonance Raman studies of sterically hindered cyanomet \"strapped\" hemes. Effects of ligand distortion and base tension on iron-carbon bond. *Biophysical Journal* 1987, *52* (5), 801-805.
79. Egawa, T.; Yeh, S.-R., Structural and functional properties of hemoglobins from unicellular organisms as revealed by resonance Raman spectroscopy. *J. Inorg. Biochem.* 2005, *99* (Copyright (C) 2017 American Chemical Society (ACS). All Rights Reserved.), 72-96.
80. Nardini, M.; Pesce, A.; Labarre, M.; Richard, C.; Bolli, A.; Ascenzi, P.; Guertin, M.; Bolognesi, M., Structural Determinants in the Group III Truncated Hemoglobin from Campylobacter jejuni. *J. Biol. Chem.* 2006, *281* (Copyright (C) 2017 American Chemical Society (ACS). All Rights Reserved.), 37803-37812.
81. De Schutter, A.; Correia, H. D.; Freire, D. M.; Rivas, M. G.; Rizzi, A.; Santos-Silva, T.; Gonzalez, P. J.; Van Doorslaer, S., Ligand binding to chlorite dismutase from *Magnetospirillum sp*. *J. Phys. Chem. B* 2015, *119*, 13859-13869.

5. STRUCTURE AND REACTIVITY OF CHLORITE DISMUTASE NITROSYLS[4]

5.1. Abstract

Ferric nitrosyl ({FeNO}^{6}) and ferrous nitrosyl ({FeNO}^{7}) complexes of the chlorite dismutases (Cld) from *Klebsiella pneumoniae* and *Dechloromonas aromatica* have been characterized using UV-visible absorbance and Soret-excited resonance Raman spectroscopy. Both of these Clds form kinetically stable {FeNO}^{6} complexes and they occupy a unique region of ν(Fe−NO) / ν(N−O) correlation space for proximal histidine liganded heme proteins, characteristic of weak Fe−NO *and* N−O bonds. This location is attributed to admixed Fe^{III}–$NO^{\bullet}$ character of the {FeNO}^{6} ground state. Cld {FeNO}^{6} complexes undergo slow reductive nitrosylation to yield {FeNO}^{7} complexes. The affects of proximal and distal environment on reductive nitroylsation rates for these dimeric and pentameric Clds are reported. The ν(Fe−NO) and ν(N−O) frequencies for Cld {FeNO}^{7} complexes reveal both six-coordinate (6c) and five-coordinate (5c) nitrosyl hemes. These 6c and 5c forms are in a pH dependent equilibrium. The 6c and 5c {FeNO}^{7} Cld frequencies provided positions of both Clds on their respective ν(Fe−NO) vs ν(N−O) correlation lines. The 6c {FeNO}^{7} complexes fall below (along the ν(Fe−NO) axis) the correlation line that reports hydrogen-bond donation to N_{NO}, which is consistent with a relatively weak Fe−NO bond. Kinetic and spectroscopic evidence is consistent with the 5c {FeNO}^{7} Clds having NO coordinated on the proximal side of the heme, analogous to 5c {FeNO}^{7} hemes in proteins known to have NO sensing functions.

[4] The material in this chapter is from a manuscript published in the Journal of Inorganic Biochemistry (https://doi.org/10.1016/j.jinorgbio.2020.111203) co-authored by Zachary Geeraerts, Alisa K. Heskin, Jennifer DuBois, Kenton R. Rodgers, and Gudrun S. Lukat-Rodgers. Zachary Geeraerts had primary responsibility in isolating, preparing and characterizing nitrosyl complexes by vibrational (resonance Raman and infrared) and UV/visible absorbance spectroscopies, and measuring rates for reductive nitrosylation of *Kp*Cld and *Da*Cld ferric nitrosyls. He also had full responsibility in data analysis, interpretation, figure-making, and writing of all sections with guidance from the corresponding authors.

5.2. Introduction

Chlorite dismutases (Clds) are heme *b* containing enzymes that catalyze the unimolecular decomposition of chlorite (ClO_2^-) to chloride (Cl^-) and molecular oxygen (O_2).[1-2] These enzymes belong to the CDE structural superfamily which contain α/β domain proteins that have a strictly conserved histidine residue responsible for coordinating to the heme iron.[3] The Cld protein family consists of two functional Cld clades.[4-5] Both Cld clades contain a conserved distal pocket comprised of four residues: phenylalanine, leucine, threonine, and arginine. Despite having a conserved heme pocket, the two Cld clades differ in their subunit size and quaternary structure. One Cld clade contains pentameric enzymes like the Cld from *Dechloromonas aromatica* (*Da*Cld) which are primarily from perchlorate respiring Proteobacteria.[3] These Clds, found in the periplasmic space, catalyze the detoxification of ClO_2^-, the terminal step in (per)chlorate respiration.[6] The second clade includes dimeric Clds with a truncated *N*-terminus; they are found in non-perchlorate respiring Proteobacteria and Cyanobacteria.[7-8] These Clds are hypothesized to be located within the cytoplasm, due to their lack of a signal peptide for transfer to the periplasmic space, but have no definitive *in vivo* function.[8] It has been proposed that the dimeric Cld from *Klebsiella pneumoniae* (*Kp*Cld) protects against environmental perchlorate and chlorate, whose reduction to ClO_2^- is catalyzed by nitrate reductase.[7]

The resting axial ligation states of five-coordinate high spin (5cHS) and 5cHS/six-coordinate high spin (6cHS) heme in ferric *Da*Cld and *Kp*Cld, respectively, indicate differences in their active sites.[7] The catalytic importance of the conformationally flexible, conserved, and cationic distal arginine is confirmed by substantial loss of ClO_2^- degrading activity upon its mutation to alanine or glutamine.[9-10] In *Da*Cld the arginine is quite effective in confining hypochlorite (ClO^-) within the pocket as it is not detected during catalytic turnover.[7] In contrast,

during the ClO_2^- reaction with *Kp*Cld and the Cld from *Candidatus Nitrospira defluvii* (*Nd*Cld), a pentameric Cld, ClO^- escapes from the heme pocket and is readily detected as HOCl.[7,11]

While bacteria containing dimeric Clds lack any (per)chlorate respiration genes, *K. pneumoniae* specifically has the genes to metabolize nitrogen via both nitrification and denitrification pathways.[12] Common nitrogen metabolites found in both pathways are nitric oxide (NO) and nitrite (NO_2^-). NO is an important signaling molecule in the bacterial processes of biofilm formation, quorum sensing, and symbiosis.[13] Bacteria like *K. pneumoniae* experience high concentrations of NO during the eukaryote response to infection.[14] Bacterial detoxification of high concentrations of NO is achieved by dissimilatory pathways involving reactions catalyzed by various NO and NO_2^- reductases.[15-18]

Many heme proteins are known to interact with NO resulting in a number of reported ligation and oxidations for their respective complexes. For example, NO sensors like mammalian soluble guanyl cyclase (sGC), bacterial nitric oxide sensing (NosP), and heme-nitric oxide / oxygen binding (H-NOX) proteins from *Shewanella oneidensis* form five-coordinate (5c) ferrous NO complexes[19-21] while H-NOX from *Nostoc* sp. and *Thermoanaerobacter tengcongensis* form six-coordinate (6c) ferrous NO adducts with a histidine trans to the NO.[22-23] *Nostoc punctiforme* and *Legionella pneumophila* H-NOX ferrous NO complexes are a temperature-dependent mixture of 5c and 6c species.[24] This temperature dependence on coordination number has also been observed for *Sm*FixL.[25] In contrast, 6c ferric NO adducts are important in the function of nitrophorin (NP) NO donor proteins, cytochrome cd_1 nitrite reductase (NO trans to histidine) and fungal nitric oxide reductase (NO trans to cysteine).[26-28]

The oxidation states of heme nitrosyls are herein distinguished by Enemark-Feltham notation which takes the form of $\{MNO\}^n$ where M is the metal center and n is the sum of *d*-

electrons from the metal and π antibonding electrons from the NO.[29] Ferric heme nitrosyls, $\{FeNO\}^6$ complexes, are generally thermodynamically unstable with respect to reductive nitrosylation, forming ferrous heme nitrosyls, $\{FeNO\}^7$ complexes. The general reaction mechanism involves nucleophilic attack on the nitrosyl nitrogen by a base (commonly hydroxide) followed by the dissociation of nitrous acid leaving behind a reduced pentacoordinate iron center, which is rapidly trapped by any excess NO. The conjugate base of the released HNO_2, NO_2^-, can serve as a nucleophile for subsequent rounds of reductive nitrosylation wherein dinitrogen trioxide (N_2O_3) is released and hydrolyzed to yield two molecules of HNO_2.[30-31] While the $\{FeNO\}^6$ complex of the histidine-ligated heme in NPs are reported to be resistant to reductive nitrosylation[32], the $\{FeNO\}^6$ complexes of many other heme proteins such as myoglobin (Mb), hemoglobin (Hb), and cytochrome *c* undergo reductive nitrosylation.[31] The heme in some of these histidine-ligated proteins undergo *trans* labilization of the proximal iron-histidine bond upon coordination of NO resulting in a five-coordinate $\{FeNO\}^7$ complex. In some proteins like cytochrome *c′* (Cyt *c′*)[33], sGC[19], and H-NOX[20], the final 5c $\{FeNO\}^7$ complex has NO bound on the proximal side of the heme. Although, a definitive physiological role for proximally bound heme nitrosyls remains elusive,[34] it has been suggested that they enable a kinetic trap mechanism that could facilitate release of the rapidly rebinding NO ligand from the heme pocket.[35]

In light of questions about *Kp*Cld function, a role for it in NO storage or transport is investigated by examining whether its heme pocket has characteristics for such activity. This study examines the reactivity of dimeric *Kp*Cld and the pentameric *Da*Cld with NO. Heme pocket variants *Kp*Cld(R128Q) and *Da*Cld(R183Q) are used to address the role of the conserved distal arginine in the formation and reactivities of the various NO complexes. Additionally, the

Cld−NO complexes reveal differences in the *Kp*Cld and *Da*Cld active sites. These differences manifest in various active site ligation and reactivity and are discussed in light of known NO heme protein complexes.

5.3. Materials and Methods

5.3.1. Protein expression and purification.

*Da*Cld and *Da*Cld(R183Q) were expressed and purified as previously described [9,36] with the following modification. A 1:1 stoichiometric equivalence of hemin chloride was added to *Da*Cld after purification by anion exchange chromatography and allowed to incubate for 12 hours at 4 °C in 0.1 M potassium phosphate pH 6.8 buffer. The resulting mixture was purified over a S–200 HR gel filtration column (26 × 750 mm). Protein and hemin quantification were determined by Bradford[37] and hemochromagen[38] assays, respectively, which verified a 1:1 stoichiometric equivalence between bound hemin and protein. Specific activity measurements of *Da*Cld showed a linear increase in O_2 evolution with hemin loaded protein between as isolated and constituted *Da*Cld.

Recombinant *Kp*Cld and *Kp*Cld(R128Q) both with an N-terminal His_6-tag (pET15-b, Merck/Novagen) and a tobacco etch virus (TEV) protease site for His_6-tag removal were expressed in Tuner DE3 *E. coli* cells grown in Terrific Broth supplemented with ampicillin (100 mg/mL). *Kp*Cld was expressed and purified as previously described.[7,39] His_6-tagged TEV(S219V) protease was expressed and isolated according to literature procedures[40] with the following modifications: no glycerol used during chromatographic purification steps and no polyetheleneimine used during lysis. The His_6-tag of *Kp*Cld was removed by incubation with TEV(S219V) at 1 mol TEV per 10 mol Cld in 50 mM sodium phosphate pH 8.0, 2 mM dithiothreitol, and 0.5 mM ethylenediaminetetraacetate overnight at 4 °C. These conditions

resulted in greater than 90% tag-free *Kp*Cld. The proteolysis reaction mixture was passed over a 5 mL Nickel-nitrilotriacetate sepharose column and a linear gradient (20–500 mM imidazole) was used to separate tag-free *Kp*Cld from tagged *Kp*Cld and TEV(S219V) protease. The cleaved *Kp*Cld was passed over a PD–10 desalting column and exchanged into 0.1 M sodium phosphate pH 6.8 buffer to remove imidazole. Purity and cleavage were verified by sodium dodecylsulfate polyacrylamide gel electrophoresis. Purified cleaved *Kp*Cld was then frozen in liquid nitrogen in aliquots and stored at –80 °C. The same procedure was used for the *Kp*Cld(R128Q) variant.

Enzyme activity for all Clds was verified by measuring chlorite-decomposition activity. The luminescence-based NEOFOX® system from Ocean Optics, Inc. was used to measure O_2 evolution during Cld-catalyzed ClO_2^- decomposition under steady state conditions. The probe was calibrated to at least three known $O_2(aq)$ concentrations. Samples were 100 nM in *Kp*Cld, *Kp*Cld(R128Q), *Da*Cld(R183Q) or 10 nM in *Da*Cld, and 2 mM in ClO_2^- in 100 mM phosphate (pH 6.8). The probe was equilibrated in the buffered ClO_2^- solution for 5 minutes prior to initiation of the reaction by introduction of Cld. Kinetic traces were recorded at 0.1 second intervals for 2 minutes.

5.3.2. Preparation of nitrosyl complexes.

The $\{FeNO\}^6$ complexes were generated by equilibrating ferric Cld in $N_2(g)$ for 30–60 minutes prior to the addition of 1 atm NO(g). Natural abundance NO(g) was purified by passage over solid NaOH pellets and through 1 M NaOH(aq). Labeled $^{15}NO(g)$ was obtained directly from a lecture bottle (98%+ purity) without further purification. The $\{FeNO\}^7$ complexes were generated by either reducing $\{FeNO\}^6$ samples directly with sodium dithionite (2–5 mM) or by reducing $N_2(g)$ equilibrated ferric Cld samples followed by exposure to 1 atm NO(g). Stock

sodium dithionite solutions (50 – 100 mM) were generated under N_2(g) in 0.1 M potassium phosphate pH 8 or 0.1 M glycine pH 9.6 buffers.

5.3.3. Vibrational spectroscopy of Cld nitrosyl complexes.

The resonance Raman (rR) spectra of nitrosyl complexes were recorded on a locally built spectrometer. Resonance Raman scattering was excited with either 406.7- or 413.1-nm emission from a Kr^+ laser. The laser beam was focused to a line at the sample using a cylindrical lens. Scattered light was collected in the 135° backscattering geometry using a *f*/1 lens to collect and colimate the lighlt. Rayleigh scattered light was attenuated with a holographic notch filter and the remaining light passed through a polarization scrambler. Collection was *f*-matched to a single *f*/4.7 0.67-m Czerny-Turner spectrograph fitted with a 120×140 mm 1200 groove/mm holographic grating and operated with a 10 μm (0.74 cm^{-1}) slit. The spectrograph was fitted with a LN_2-cooled CCD detector having a 26.8 mm (1340 pixel) × 8.0 mm (400 pixel) image area. The spectrometer was calibrated using known absolute Raman shifts of toluene and dimethylformamide. Unless otherwise noted, all spectra were recorded under ambient conditions from samples contained in 5-mm NMR tubes spinning at ~20 Hz using a locally fabricated spinner. Laser powers ranged from 1 to 2 mW at the sample. All Cld samples for rR spectroscopy ranged from 25–50 μM (heme) in 0.1 M buffer (potassium phosphate and glycine) at indicated pH values. Samples were examined spectrophotometrically before and after laser exposure to monitor sample integrity. For a given set of solution conditions, care was taken to generate natural-abundance and ^{15}N-enriched NO complexes from aliquots of the same Cld solutions in order to match their concentrations. Spectra of pairs of isotopolog samples were recorded with identical acquisition parameters (number of integrations and integration times) and

in temporal proximity to one another on the same day to minimize spectrometer alignment artifacts in the isotope difference spectra.

Raman difference spectra in which either the isotopolog bands of a given mode overlapped, or there were clearly multiple overlapping isotope-sensitive bands were subjected to peak fitting in order to identify FeNO frequencies of the isotopologs. In all cases, the difference spectra were fit with positive bands for spectra of the natural abundance samples and negative bands for the ^{15}NO-enriched samples. Gaussian band shapes were used with the full width at half maximum constrained to the same value (10–25 cm^{-1}) for a given pair of isotopologs. Goodness of fit was based on minimization of χ^2 using a commercial implementation of the Levenberg-Marquardt method.

Fourier-transform infrared absorbance (FTIR) spectra were recorded for both *Kp*Cld and *Da*Cld {FeNO}^{6} complexes in a 30 mm CaF_2 liquid cell. Cld concentrations ranged from 400–1000 μM. A 0.1 M potassium phosphate buffer spectrum recorded under identical sample conditions was used to manually subtract the water background such that the baseline between 1750–2000 cm^{-1} was flat.

5.3.4. Spectrophotometric tracking and kinetic analysis of reductive nitrosylation reactions.

Buffered Cld {FeNO}^{6} solutions were prepared as described in §2.2. Heme concentration was 1.0×10^{-6} M in all reactions. Conversion of {FeNO}^{6} complexes to their {FeNO}^{7} counterparts was monitored by UV-visible absorbance (UV-vis) spectrophotometry at 20.0 °C. Reactions were tracked for 14 to 22 hours. During these reactions there were no effects attributable to O_2 incursion, which would result in the formation of the ferric nitrito complex and the appearance of its ligand to metal charge transfer band at 627 nm.[41] The t_∞ spectrum was recorded after driving the formation of {FeNO}^{7} to completion by adding enough buffered

ascorbate stock solution to make it 2 mM in ascorbate. The kinetic traces of fraction $\{FeNO\}^6$ reduced vs time were modeled by thermodynamically two-term exponential decay function shown in Equation 5.1.

$$\Delta A_t = \Delta A_{\infty 1} \exp(-k_{obs1} t) + \Delta A_{\infty 2} \exp(-k_{obs2} t) \quad \text{(Eq. 5.1)}$$

The apparent rate constant for the [OH^-] dependent pathway, k_{obs1}, is given by Equation 5.2.

$$k_{obs1} = k_{OH^-}[OH^-] + k_{H2O} \quad \text{(Eq. 5.2)}$$

Therefore, the second-order rate constant (k_{OH^-}) was determined from the slope of the plot k_{obs1} vs [OH^-] and the pH insensitive first order rate constant (k_{H2O}) was determined by the y-intercept.

5.3.5. Spectrophotometric tracking of NO-dependent conversion of 6c $\{FeNO\}^7$ to 5c $\{FeNO\}^7$ Cld.

All ferric Cld samples ranged from 5–10 mM and were equilibrated with N_2(g) prior to being reduced with a 5–10 fold excess of sodium dithionite. Aqueous NO solutions were prepared by saturating anaerobic buffer solutions with NO(g) at ambient pressure. Concentrations of stock NO(aq) solutions were determined using the Henry's Law constant K_H = 1.9×10^{-3} $M\cdot atm^{-1}$ at ambient temperature.[42] The resulting NO solution was added in appropriate measure to ferrous Cld samples. UV-vis spectra were recorded as a function of time with a double beam, scanning spectrophotometer for each substoichiometric NO addition to ferrous Cld.

5.3.6. Spectrophotometric determination of pH dependence for 6c ⇌ 5c $\{FeNO\}^7$ Clds.

Multiple anaerobic ferric Cld samples were prepared at the same concentration in the following buffers: potassium phosphate (pH 6.0, 7.0, and 8.0), Tris (pH 8.6), and glycine (pH 9.0, 9.6, and 10). Ferrous Cld samples were prepared with sodium dithionite as described above and then converted to their respective $\{FeNO\}^7$ forms by addition of 1 atm NO(g). UV-vis

spectra of each {FeNO}^{7} sample was recorded with a double beam, scanning spectrophotometer several times to ensure complete complex formation.

5.4. Results

5.4.1. Ferric Clds form {FeNO}^{6} complexes.

Solutions of ferric *Kp*Cld, *Da*Cld, or their distal pocket variants, *Kp*Cld(R128Q) and *Da*Cld(R183Q), equilibrated with NO exhibit UV visible spectra with the Soret band at 416−418 nm and Q bands at 565 (α) and 531 (β) nm (Figure 5.1A). Spin-state marker bands ν_2, ν_3, and ν_{10} in their rR spectra are observed at 1580−1583, 1510, and 1644 cm^{-1} (Figure 5.1B), respectively. These spectral features are consistent with hexacoordinate low-spin (6cLS) {FeNO}^{6} heme complexes.[43-44] Since ν_3 and ν_{10} bands shift to ~1501 and ~1632 cm^{-1}, respectively, upon reduction of the 6cLS {FeNO}^{6} to 6cLS {FeNO}^{7}, they are useful spectral signatures for monitoring for reductive nitrosylation. In fact, the shoulder observed around 1501 cm^{-1} on the ν_3 band for {FeNO}^{6} *Kp*Cld is due to some {FeNO}^{7} which is formed at an accelerated rate upon exposure to laser light (Figures. D1 and D2).

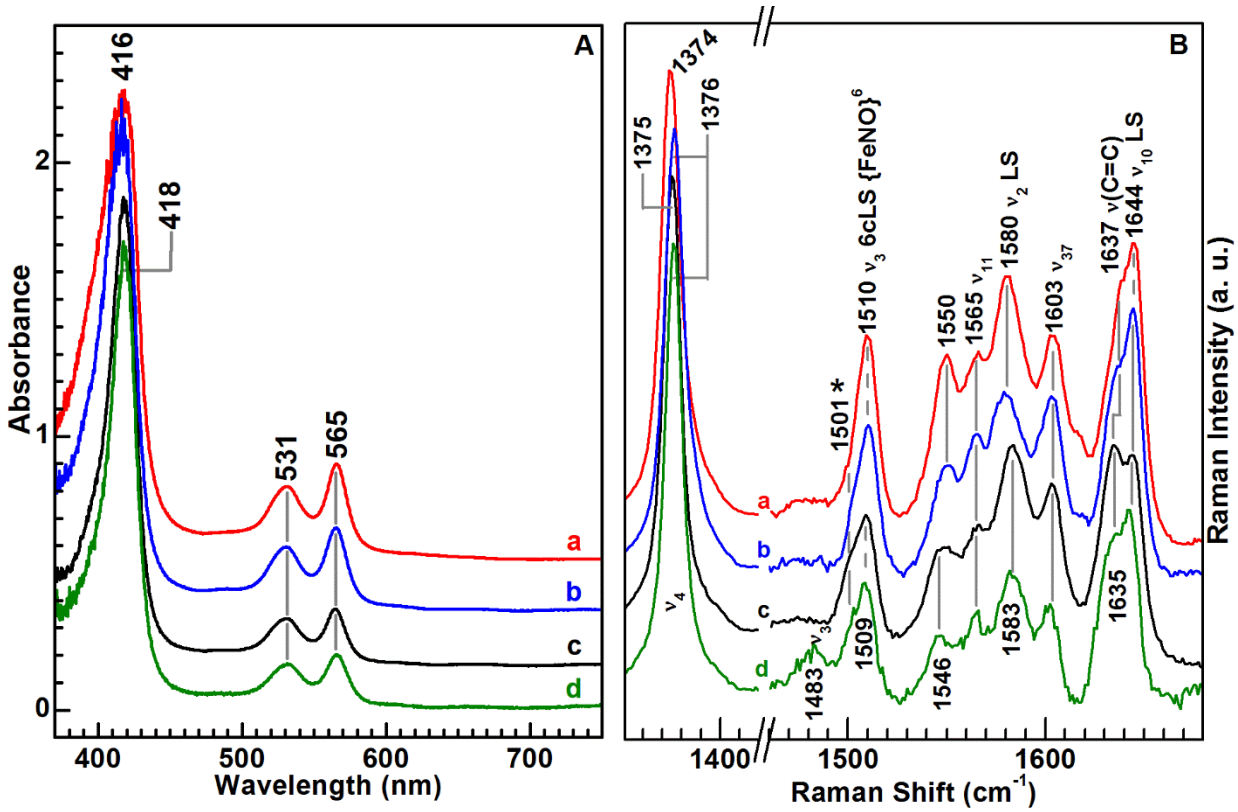

Figure 5.1. {FeNO}^{6} Cld complexes form upon reaction of NO with ferric Clds as illustrated by their UV-visible absorbance spectra (A) and their Soret-excited (413.1 nm) rR spectra (B). Spectra for {FeNO}^{6} Cld complexes in 0.1 M potassium phosphate pH 6.8 under 1 atmosphere NO(g) are shown for a) *Da*Cld (red), b) *Da*Cld(R183Q) (blue), c) *Kp*Cld (black), and d) *Kp*Cld(R128Q) (green). *ν_3 attributed to {FeNO}^{7} formed by photo-induced reduction of {FeNO}^{6}.

*Kp*Cld(R128Q) is the only Cld examined here that exhibits an additional ν_3 band at 1483 cm^{-1} upon exposure to 1 atm NO; such a ν_3 frequency is typically indicative of 6cHS heme. This suggests that a small fraction of the *Kp*Cld(R128Q) has not bound NO. Ferric *Kp*Cld(R128Q) exhibits some characteristics that make it distinct from the wild-type (WT) Clds and the *Da*Cld(R183Q) variant. While the heme resting state is 5cHS in WT *Da*Cld and a mixture of 5cHS and 6cHS in *Da*Cld(R183Q) and WT *Kp*Cld,[7,9,41] ferric *Kp*Cld(R128Q) presents as a mixture of 6cHS and 6cLS with ν_3 band frequencies of 1483 and 1506 cm^{-1}, respectively. This 6cHS/6cLS mixture is not dependent on pH over the range of 7 to 12 (Figure D3A). Similar lack of pH dependence between pH 6.8 and 10 has also been reported for *Da*Cld(R183Q) in both its

spectral characteristics and activity.[9] At pH 5.5 the *Kp*Cld variant is converted completely to a 6cHS species. The UV-vis pH titration reports a pK_a of approximately 6.3 associated with this speciation change (Figure D3B). Mixtures of 6cHS/6cLS heme are observed for the hydroxide complexes of both WT Clds. However, the pK_as for their hydroxide formations are higher (pK_a=8.3±0.1, *Kp*Cld; pK_a=8.7±0.1, *Da*Cld)[7,41] than the one observed here for speciation change of *Kp*Cld(R128Q). To determine if the 6cHS/6cLS *Kp*Cld(R128Q) is due a hydroxide complex in a thermal spin state equilibrium like those known for the WT enzymes, its Soret-excited rR spectra in H_2O, $H_2{}^{18}O$, and ^2H_2O are examined for isotope-sensitive bands indicative of a heme-hydroxide complex (Figure D4). Since no ^2H- or ^{18}O-sensitive bands are observed, even at pH 12, the 6cHS/6cLS species are due to some heme ligand other than hydroxide. The identity of the sixth ligand is currently unknown. In *Kp*Cld(R128Q), the 6cHS/6cLS mixture may be attributable to the glutamine 128 providing either its amide O atom (HS) or N atom (LS) as the iron ligand. Such a 6cLS species due to a distal glutamine binding to the heme *b* of coproheme decarboxylase has been reported.[45] The sixth ligand appears to compete effectively with NO coordination to the ferric iron.

Formation of {FeNO}^{6} Clds are confirmed by identification of three ^{15}NO isotope sensitive bands for each complex using rR and FTIR spectroscopy (Figure 5.2). These bands are assigned to the FeNO bending mode, δ(FeNO), Fe−NO stretch, ν(Fe−NO), and N−O stretch, ν(N−O) of {FeNO}^{6} Clds (Table 5.1) in order of increasing frequency based on nuclear resonance vibrational spectroscopy assignments for nitrosyl complexes of iron porphyrinates[46] and rR assignments for {FeNO}^{6} complexes of Mb[47], NP[48], and FixL from *Sinorhizobiun melilotti* (*Sm*FixL).[49] While both δ(FeNO) and ν(Fe-NO) bands are observed in the rR spectra for all {FeNO}^{6} Clds, they overlap substantially, resulting in $^{14}NO - {}^{15}NO$ difference features whose

maxima and minima do not correspond directly to the mode frequencies. Since the ν(N−O) band was only observed in the rR spectrum of *Da*Cld(R183Q) {FeNO}^{6}, the ν(N−O) frequencies for *Kp*Cld and *Da*Cld complexes were assigned using FTIR spectroscopy. The lack of a ν(N−O) band in the WT Cld rR spectra is due to poor resonance enhancement with 413-nm excitation; enhancement for this mode occurs at 244 nm via resonance with the ligand to metal charge transfer transition.[50] The respective ν(N−O) frequencies observed for *Kp*Cld and *Da*Cld are similar at 1896 and 1898 cm^{-1}. Mutation of the distal arginine to a glutamine in *Da*Cld causes a 15 cm^{-1} increase in the ν(N−O) frequency; FTIR and rR spectra of *Da*Cld(R183Q) {FeNO}^{6} both contain bands at 1911 cm^{-1} (Figures D5 and 5.2).

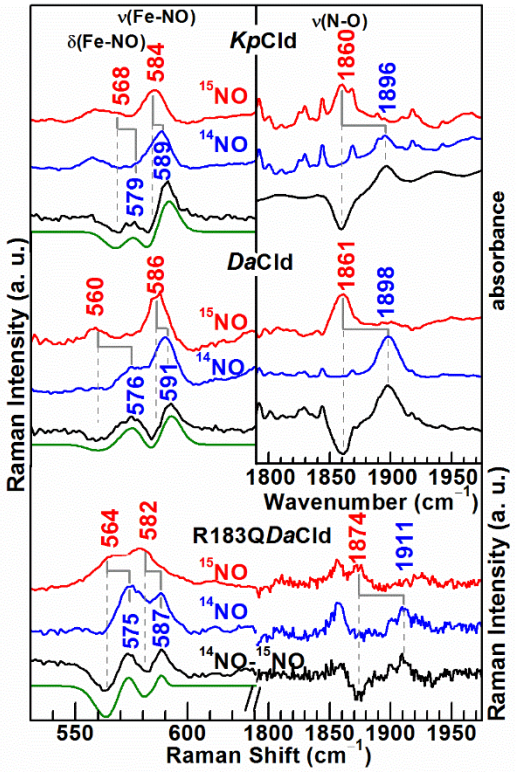

Figure 5.2. Assignment of δ(FeNO), ν(Fe−NO), and ν(N−O) via rR and FTIR indicate generation of {FeNO}^{6} Clds. Soret excited (413.1-nm) resonance Raman spectra of N isotopologs of{FeNO}^{6} Cld complexes in 0.1 M potassium phosphate pH 6.8 under 1 atmosphere NO(*g*). Red, blue, black, and green (smooth) traces: ^{15}NO, ^{14}NO, ^{14}NO − ^{15}NO, and peak fit of ^{14}NO − ^{15}NO, respectively. Inset: High frequency windows for both *Kp*Cld and *Da*Cld are FTIR absorbance spectra. Water vapor rotation-vibration features appear in both *Kp*Cld and *Da*Cld FTIR spectra.

Table 5.1. Vibrational frequencies and absorbance maxima of $\{FeNO\}^n$ Cld complexes

		Raman shift (cm^{-1})				Absorbance maxima (nm)		
Protein	pH	ν_3	δ(Fe−N) (Δ^{15}NO)	ν(Fe−N) (Δ^{15}NO)	ν(N−O) (Δ^{15}NO)	λ_{Soret}	λ_α	λ_β
				6c $\{FeNO\}^6$				
*Kp*Cld	6.8	1510	577 (7)	589 (5)	1896 (36)[a]	418	565	531
*Da*Cld	6.8	1510	575 (16)	591 (5)	1898 (37)[a]	416	565	531
*Da*Cld(R183Q)	6.8	1510	574 (8)	587 (5)	1911 (37)	416	565	531
*Kp*Cld(R128Q)	6.8	1509		589 (6)	n.o.[b]	418	565	531
				5c $\{FeNO\}^7$				
*Kp*Cld	6.8	1506		527 (14)	1680 (34)	401	566	535
*Da*Cld	6.8	1509		525 (9)	1683 (33)	397	566	535
*Da*Cld(R183Q)	6.8	1509		525 (13)	1684 (40)	397	566	535
*Kp*Cld(R128Q)	6.8	1509		525	n.o.[b]	397	566	535
				6c $\{FeNO\}^7$				
*Kp*Cld	9.6	1501		548 (21)	1609 (26)	418	574	542
*Da*Cld	9.6	1502		544 (27)	1599 (19)	415	574	542
*Da*Cld(R183Q)	9.6	1502		539 (27)	1604 (17)	415	574	542

[a] assigned from FTIR spectra; [b] not observed

5.4.2. Reductive nitrosylation of Clds.

All Cld $\{FeNO\}^6$ complexes studied here undergo slow reductive nitrosylation at ambient temperature and pressure to yield $\{FeNO\}^7$. Rates of reductive nitrosylation increase with pH and were tracked spectrophotometrically as a function of time. Due to the exceedingly long time required to affect complete conversion from $\{FeNO\}^6$ to $\{FeNO\}^7$, ascorbate was added after the first kinetic phase to drive the $\{FeNO\}^7$ formation to completion. These effective t_∞ spectra are isosbestic in the Q-band region with all the spectra recorded during the natural time course of the reaction. The spectrum of the ascorbate-treated reaction mixture did not share the isosbestic point in the Soret region of the spectrum due to small ascorbate absorbance in the near-UV. This demonstrates that the $\{FeNO\}^7$ produced during reductive nitrosylation is the same as the product of reduction with ascorbate. Changes in absorbance as a function of time were best

modeled by the two-term exponential function shown in Equation 5.1 (Figure 5.3C). The rate constants obtained from this biphasic behavior are k_{obs1} (faster and pH dependent) and k_{obs2} (slower and pH independent). Amplitudes of the two phases varied, with the slow phase accounting for more than half the total amplitude. This eliminates the possibility of parallel reductive nitrosylation pathways. The kinetic behavior is consistent with the presence of an unreactive form of $\{FeNO\}^6$ that is converted to a reactive form at a rate slower than reductive nitrosylation. This is effectively a slowly established equilibrium followed by a fast product-forming reaction step. Considering that isosbestic behavior is retained throughout the time course (Figures 5.3A and 5.3B), it can be concluded that both pathways yield the same product and that the reactive and unreactive $\{FeNO\}^6$ complexes are spectroscopically indistinguishable. Given that the slow phase was independent of $[OH^-]$, our working hypothesis is that the unreactive form is a kinetic trap and that it reverts only very slowly to the reactive form. *Sm*FixL* exhibits similar behavior.[49]

Previously published studies of $\{FeNO\}^6$ reductive nitrosylation have revealed the rate limiting step of the reaction to be nucleophilic attack of the coordinated N atom of the NO ligand.[31] Reaction mixtures contain three nucleophiles, solvent water, hydroxide and the nitrite produced in the reaction. Thus, the rate law could comprise up to three terms, each showing dependence on one of the nucleophile concentrations. Since the data were well modeled without considering any NO_2^--catalyzed reductive nitrosylation, this nucleophile was not considered in the kinetic analyses reported herein. In order to differentiate the two observed rate constants, reductive nitrosylation of Cld $\{FeNO\}^6$ complexes were monitored at pH 6.8, 8.0, 9.0, and 9.6. These data revealed that k_{obs1} was $[OH^-]$-dependent (Figure 5.3D) and was modeled by Equation 5.2 to obtain values for k_{H2O} and k_{OH-} (Table 5.2). Both k_{H2O} and k_{OH-} values reported here are

several orders of magnitude lower than those reported for HbA, Mb, trHb, but similar to *Sm*FixL*. The pH independent rate constant (k_{obs2}) ranged between 2×10^{-5} and 5×10^{-5} s^{-1} for all three Cld enzymes. At pH 6.8, k_{obs1} and k_{obs2} were kinetically indistinguishable and ΔA vs time was well modeled by a single exponential function for each enzyme. Considering both WT *Da*Cld and *Kp*Cld bind OH^- under alkaline conditions[7,41], we hypothesized that the slow phase could be rate limited by OH^- dissociation. However, the pH independence of the slow phase and the lack of spectral features associated with a Cld−OH^- complex in the $\{FeNO\}^6$ solutions eliminate this mechanistic possibility from further consideration. Moreover, the *Da*Cld(R183Q) variant does not bind OH^-[9] and its reductive nitrosylation is also biphasic. These behaviors are consistent with the hypothesis that Cld $\{FeNO\}^6$ complexes form rapidly upon treatment of ferric Clds with excess NO to yield two spectrally indistinguishable $\{FeNO\}^6$ complexes, one that is reactive towards reductive nitrosylation and one that is not. The nonreactive Cld $\{FeNO\}^6$ converts to the reactive form on the time scale dictated by k_{obs2}.

Table 5.2. Reductive nitrosylation rate constants at 20 °C for select 5c heme proteins with a proximal histidine.

Protein	[NO] (M)	k_{OH^-} ($M^{-1}s^{-1}$)	k_{H2O} (s^{-1})	Distal Residue	Reference
*Da*Cld(R183Q)	1.8×10^{-3}	$6.0\pm0.2\times10^{0}$	$9\pm1\times10^{-6}$	Gln	this work
*Da*Cld	1.8×10^{-3}	$8.4\pm0.2\times10^{0}$	$1.3\pm0.1\times10^{-5}$	Arg	this work
*Kp*Cld	1.8×10^{-3}	$8.8\pm0.3\times10^{0}$	$2.5\pm0.1\times10^{-5}$	Arg	this work
*Sm*FixL*	1.6×10^{-3}	$7\pm1\times10^{0}$	$3\pm2\times10^{-5}$	Arg	[49]
HbA	2.5×10^{-4}	$3.2\pm0.2\times10^{3}$	$1.1\pm0.1\times10^{-3}$	His	[50]
swMb	2.5×10^{-4}	$3.2\pm0.2\times10^{2}$	n.o.[a]	His	[50]
*Gm*LegHb	1.0×10^{-3}	$3.3\pm0.2\times10^{3}$	$3.0\pm0.9\times10^{-4}$	His	[51]
Mt-trHbN	1.9×10^{-3}	$1.7\pm0.2\times10^{2}$	$6.4\pm0.7\times10^{-4}$	Tyr	[52]
Mt-trHbO	1.9×10^{-3}	$2.4\pm0.3\times10^{2}$	$2.9\pm0.3\times10^{-4}$	Tyr	[52]
Cj-trHbP	1.9×10^{-3}	$9\pm1\times10^{2}$	$4.8\pm0.5\times10^{-4}$	Tyr	[52]

[a] not observed.

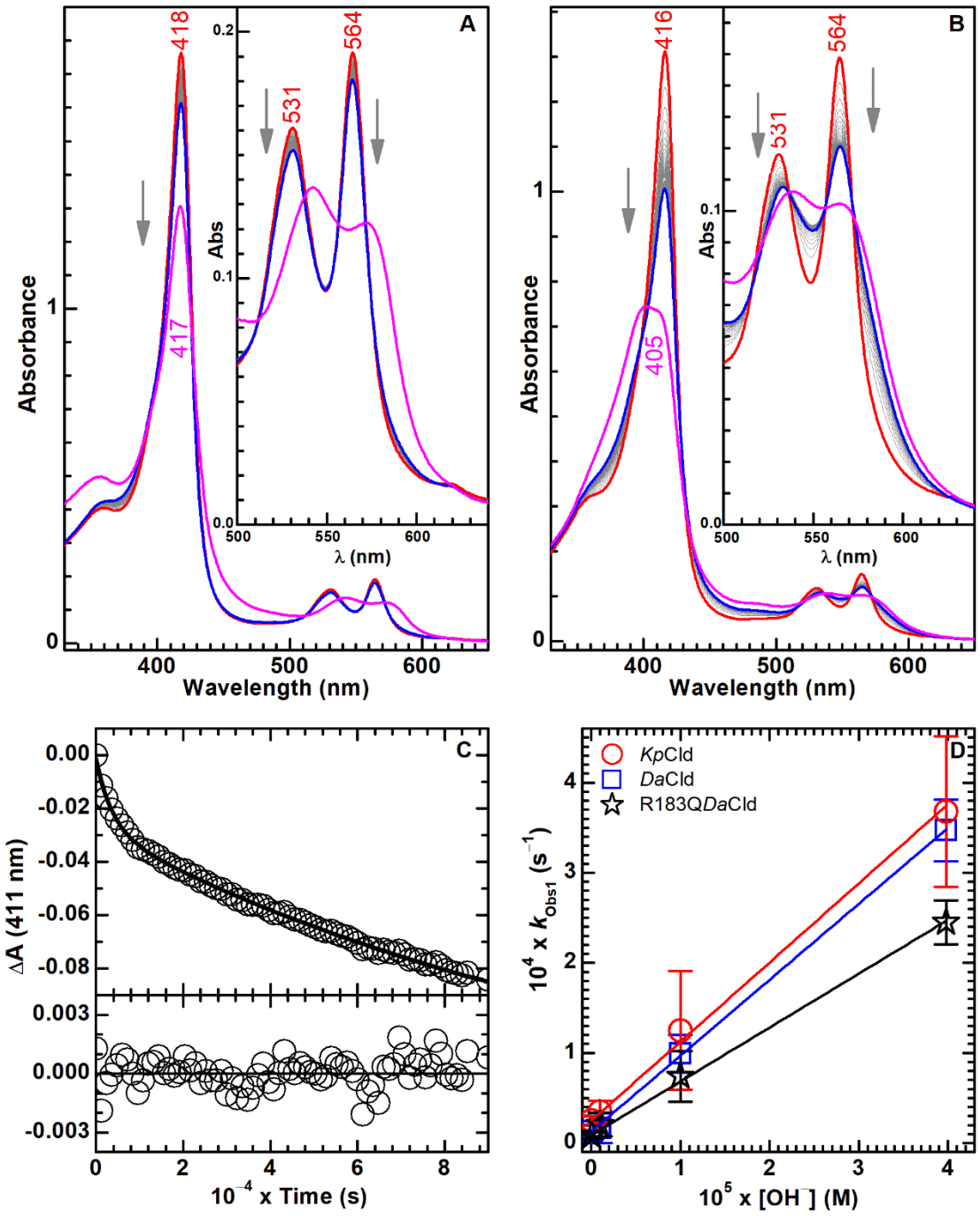

Figure 5.3. {FeNO}^{6} Cld complexes exhibit similar stability with respect to reductive nitrosylation. Time-resolved absorbance spectra of {FeNO}^{6} (red line) converting to {FeNO}^{7} (blue line) over 26 hours and 20 hours for 1.0×10^{-5} M A) *Kp*Cld and B) *Da*Cld at pH 9.0, respectively. Arrows show direction of change with increasing reaction time. Complete reduction to {FeNO}^{7} was achieved upon addition of 2 mM ascorbate (magenta line). C) Representative ΔA vs time trace for *Kp*Cld exhibits biphasic behavior which was fit to a two-term exponential function. D) k_{obs1} vs. [OH^-] for *Kp*Cld, *Da*Cld, and *Da*Cld(R183Q) used to determine values for k_{H2O} and k_{OH-}.

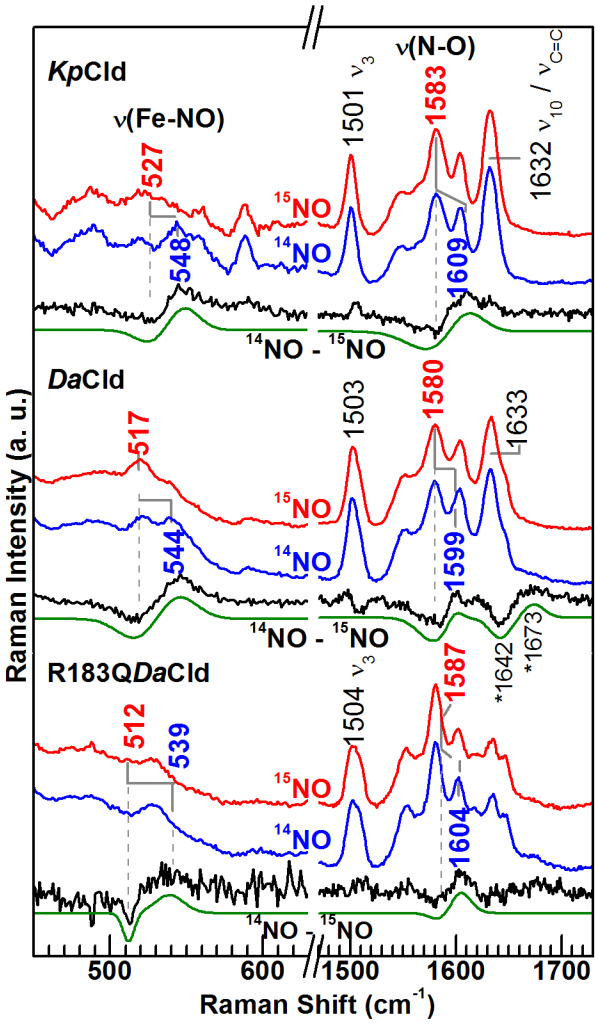

Figure 5.4. Soret-excited rR spectra of {FeNO}^{7} Cld complexes reveal their coordination states under alkaline conditions. Soret excited (413.1-nm) resonance Raman Fe−NO and N−O frequency windows of {FeNO}^{7} Cld complexes in 0.1 M glycine pH 9.6 under 1 atm NO(g). Red spectra = ^{15}NO, blue spectra = ^{14}NO, black spectra = ^{14}NO – ^{15}NO, green (smooth) traces = peak fits to ^{14}NO – ^{15}NO. The ν_3, ν(Fe−NO) and ν(NO) frequencies reveal speciation to be dominated by 6c {FeNO}^{7} *Kp*Cld while the two *Da* enzymes are mixtures of 6c and 5c complexes. *Difference features at 1673 and 1642 cm^{-1} for DaCld may correspond to subtle speciation changes or ν(NO) for 5c {FeNO}^{7}.

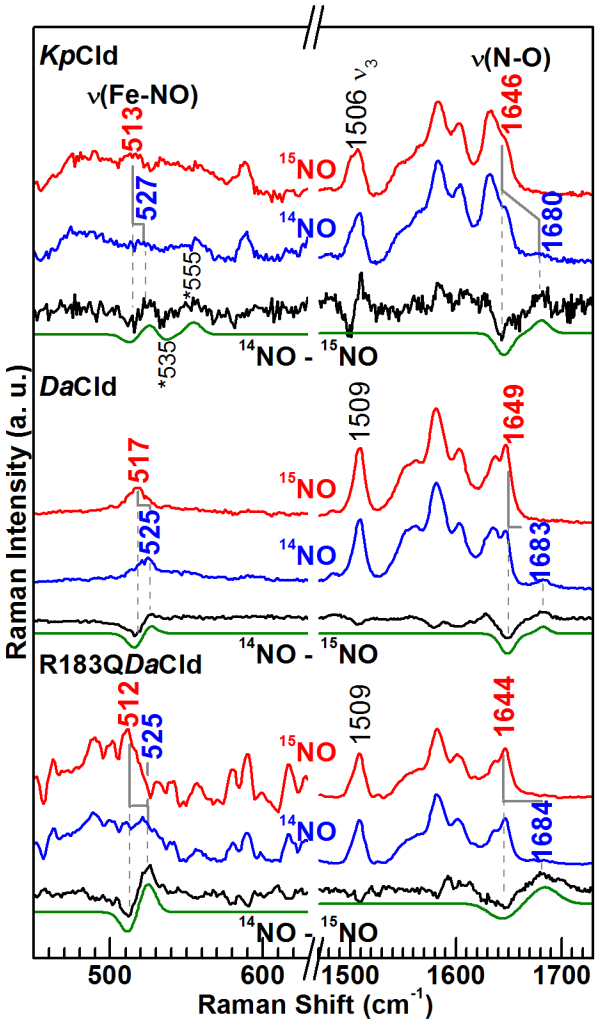

Figure 5.5. Soret-excited rR spectra of N isotopologs of {FeNO}^{7} Clds indicate that they are predominantly 5-coordinate at pH 6.8. Soret excited (406.7-nm) resonance Raman Fe−NO and N−O frequency windows of {FeNO}^{7} Cld complexes in 0.1 M potassium phosphate pH 6.8 under 1 atm NO(g). Red spectra = ^{15}NO, blue spectra = ^{14}NO, black spectra = ^{14}NO – ^{15}NO, green (smooth) traces = peak fits to ^{14}NO – ^{15}NO. The ν_3, ν(Fe−NO) and ν(NO) frequencies indicate that the dominant form is 5cLS. *Difference features at 555 and 534 cm^{-1} for *Kp*Cld may correspond to subtle speciation changes or ν(Fe−NO) for 6c {FeNO}^{7}.

5.4.3. The coordination state of {FeNO}^{7} Cld complexes is pH dependent.

All Cld {FeNO}^{6} complexes form {FeNO}^{7} complexes upon addition of dithionite. Under alkaline conditions (pH 9.6), the spectroscopic signatures of *Kp*Cld {FeNO}^{7} (UV-vis: Soret, 418 nm; α/β bands, 574 nm and 542 nm (Figure D6); rR: ν_3, 1501 cm^{-1} and the sharpness of the ν_{10} and ν(C=C) region (Figure 5.4)) are consistent with formation of a 6cLS complex. The

two isotopically sensitive bands observed for *Kp*Cld {FeNO}^{7} at 1609 and 548 cm^{-1} are assigned as ν(N−O) and ν(Fe−NO), respectively, and are also characteristic of a 6cLS complex.[25,47] At pH 6.0 the *Kp*Cld {FeNO}^{7} UV-vis spectrum has its Soret at 401 nm, a shoulder near 397 nm, α/β bands at 566 nm and 535 nm, and a charge transfer (CT) band at 483 nm (Figure D6). The acidic *Kp*Cld {FeNO}^{7} has a broad, asymmetric n_3 band centered at 1506 cm^{-1}; the width of this band at half height ($\Delta\nu_{½}$ = 16 cm^{-1}) is large compared to its ν_3 band at pH 9.6 ($\Delta\nu_{½}$ = 12 cm^{-1}), suggesting that it comprises multiple unresolved components, consistent with a mixture of species contributing to ν_3 intensity. Three isotope sensitive bands are observed and assigned as follows: 1680 cm^{-1}, 5c ν(N−O); 527 cm^{-1}, 5c ν(Fe−NO); and 555 cm^{-1}, 6c ν(Fe−NO) (Figure 5.5). Observation of two ν(Fe−NO) frequencies is consistent with two species suggested by the broad ν_3 band and lends support to *Kp*Cld being a mixture between 5c and 6c {FeNO}^{7} at acidic pH.

Alkaline *Da*Cld and *Da*Cld(R183Q) {FeNO}^{7} complexes exhibit essentially identical UV-vis spectra (Soret, 415 nm; shoulder, 397 nm; α/β bands, 574 nm and 542 nm; CT band, 483 nm) (Figure D6); their rR spectra exhibit broad ν_3 bands at 1503 cm^{-1} ($\Delta\nu_{½}$ = 16 cm^{-1}) and 1504 cm^{-1} ($\Delta\nu_{½}$ = 17 cm^{-1}), respectively, (Figure 5.4) suggest a mixture of 5cLS and 6cLS heme. In addition, *Da*Cld has two ^{15}NO sensitive bands in the high frequency window, assigned to 6c ν(N−O) (1599 cm^{-1}) and 5c ν(N−O) (1673 cm^{-1}). In the low frequency window, the ^{14}NO – ^{15}NO difference spectra have a single broad difference feature (544/539 cm^{-1}). While the difference features for 6c *Kp*Cld {FeNO}^{7} ν(Fe−NO) fit with bandwidths of 10 cm^{-1}, both *Da* enzymes required 25 cm^{-1} bandwidths to obtain reasonable fits. Given the 5c and 6c ν(N−O) frequencies differ by approximately 19 cm^{-1} (Table 1), the broadness of the *Da*Cld difference feature is consistent with overlap of 5c and 6c ν(Fe−NO) bands such that they are not resolved in

the difference spectra. This, together with the ν(N−O) and ν_3, indicates the WT and R183Q *Da*Cld {FeNO}^{7} complexes are a mixture of 5cLS and 6cLS heme nitrosyls under alkaline conditions.

Under slightly acidic conditions (pH 6.8), speciation of *Da*Cld and *Da*Cld(R183Q) {FeNO}^{7} complexes favors the 5c states based on their UV-vis (λ_{maxB} = 397 nm; λ_{maxQ} = 566, 535 nm; λ_{maxCT} = 483 nm) and rR spectra (ν_3 for 5c {FeNO}^{7}, 1509 cm^{-1}) (Figure 5.5). Two prominent isotope sensitive bands are observed in their rR spectra. They have been assigned as 5c ν(N−O) at 1683/1684 cm^{-1} and to 5c ν(Fe−NO) at 525 cm^{-1} for WT and R183Q *Da*Clds, respectively.

Cld{FeNO}^{7} samples were prepared over a range of pHs for examination by UV-vis spectrophotometry to characterize the pH-dependent transition between the 5c and 6c {FeNO}^{7} complexes of *Da*Cld and *Kp*Cld (Figure 5.6). This transition is reported by the shift in the Soret maximum as a function of pH. Unfortunately, *Da*Cld {FeNO}^{7} could not be completely converted to the 6c form at alkaline pH, and *Kp*Cld did not form a pure 5c {FeNO}^{7} under acidic conditions. Therefore, the pK_a associated with the speciation change could only be estimated; qualitatively the pK_a for the 5c to 6c transition is higher for *Da*Cld than *Kp*Cld. This is consistent with the rR data where at low-pH *Kp*Cld {FeNO}^{7} is a mixture of 5c and 6c species and *Da*Cld {FeNO}^{7} is predominantly 5c while at high-pH the *Kp*Cld complex is 6c and the *Da*Cld is a mixture between 5c and 6c species.

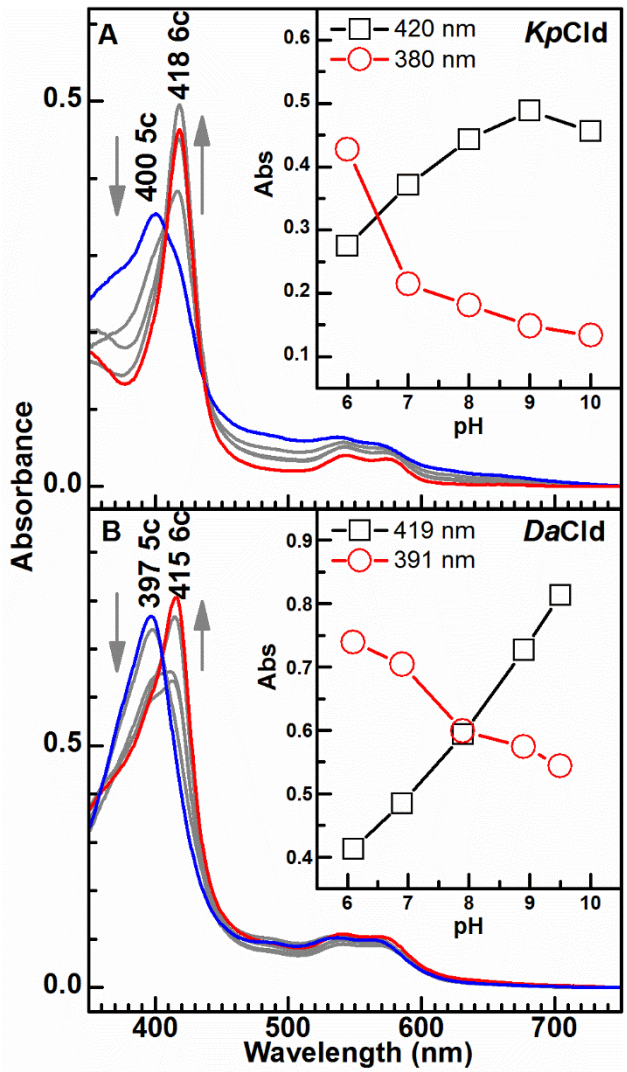

Figure 5.6. Spectrophotometric pH dependence on coordination number for $\{FeNO\}^7$ Cld complexes. pH-dependent UV-vis absorbance spectra of A) *Kp*Cld and B) *Da*Cld $\{FeNO\}^7$. Arrows show the direction of absorbance change with increasing pH. Spectra with bluest and reddest Soret maxima correspond to pH 6 and ~10, respectively. Gray spectra represent pH's between the two extremes. Complete conversion to pure 5c or 6c states was not attained over this pH range. Therefore, a pK_a could not be determined.

5.4.4. Formation of 5c $\{FeNO\}^7$ Clds is [NO] dependent.

Conversion from 6c to 5c $\{FeNO\}^7$ was tracked at pH 6.8 after addition of sub-stoichiometic amounts of aqueous NO to ferrous Clds (Figure 5.7). The spectra do not exhibit clean isosbestic behavior, and spectral features for three heme species are discernable: 5cHS ferrous Cld, 6c $\{FeNO\}^7$, and 5c $\{FeNO\}^7$. As ferrous Cld concentration decreased (evidenced

by decreasing absorbance at 433 nm), spectral features attributable to 6c $\{FeNO\}^7$ appeared (418 nm) and disappeared as those for 5c$\{FeNO\}^7$ grew (400 nm). This slow conversion has also been observed for AXCP under stoichiometric conditions.[53] The interconversion between 6c and 5c $\{FeNO\}^7$ Clds was too fast to be observed in the presence of saturating [NO]. These data support NO-catalyzed conversion of 6c $\{FeNO\}^7$ to 5c $\{FeNO\}^7$ wherein the final product has NO coordinated on the proximal side of the heme, as reported for cyt *c′* [33,53], H-NOX [20,54] and sGC.[19,55]

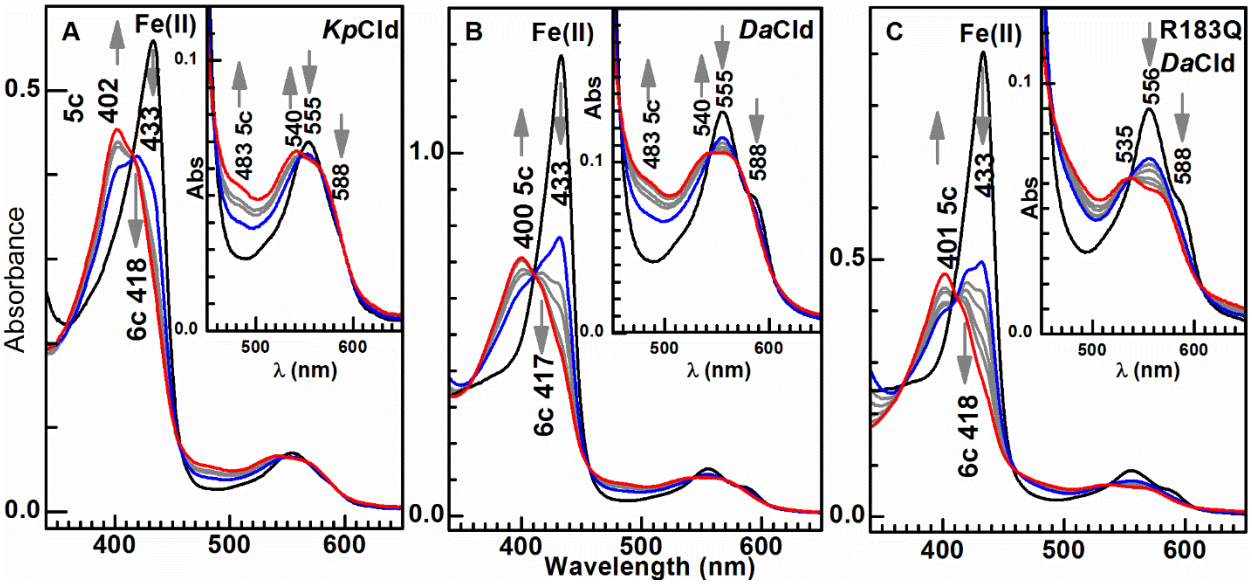

Figure 5.7. Optical absorbance spectra tracking the reaction of ferrous Clds with substoichiometric [NO] yields 6c $\{FeNO\}^7$ and 5c complexes in sequence. A) *Kp*Cld, B) *Da*Cld, and C) *Da*Cld(R183Q) in 0.1 M sodium phosphate buffer at pH 6.8 with 0.5 molar equivalents of NO. Black spectra show starting ferrous Cld while the blue and red spectra indicate initial and final time points after NO addition, respectively. Arrows show directions of absorbance change with increasing reaction time. Total conversion time took 40 minutes for each enzyme to reach their respective end points.

5.5. Discussion

5.5.1. Fe−NO and N−O bonds of {FeNO}^{6} Clds are exceptionally weak under the influence of the distal arginine cation in closed heme pocket conformations.

Figure 5.8 shows the locations of Cld {FeNO}^{6} complexes, along with other proximal histidine-ligated heme proteins, on the ν(Fe−NO) vs ν(N−O) backbonding correlation plot. The two correlation lines with slopes close to −1 are consistent with the positions of {FeNO}^{6} complexes along these lines being modulated by the extent of $Fe^{II}\rightarrow NO^+$ π backbonding.[47] The offsets of the two backbonding correlation lines along the ν(N−O) axis has been explained in terms of Lewis acid-base interactions in the distal pocket of the Mb variants.[47,56] The higher ν(N−O) frequency line is attributed to Lewis acid-base interactions between the NO^+ ligand and either a distal histidine or an exogenous water molecule. The lower ν(N−O) frequency line represents the backbonding correlation in the absence of Lewis donation to the coordinated NO^+ in systems having solvent-inaccessible distal pockets and no endogenous distal bases.[56] One {FeNO}^{6} conformer was observed for each Cld complex reported here. Both open and closed conformers have been observed for the isoelectronic {FeCO}^{6} complexes of *Da*Cld [41] and *Da*Cld(R183Q)[9], and a single open conformer has been reported for that of *Kp*Cld[39]. However, since none of the {FeNO}^{6} Clds reported here fall on the higher ν(N−O) frequency correlation line in Figure 5.8, the heme pockets are concluded to be solvent inaccessible and in their closed conformations.

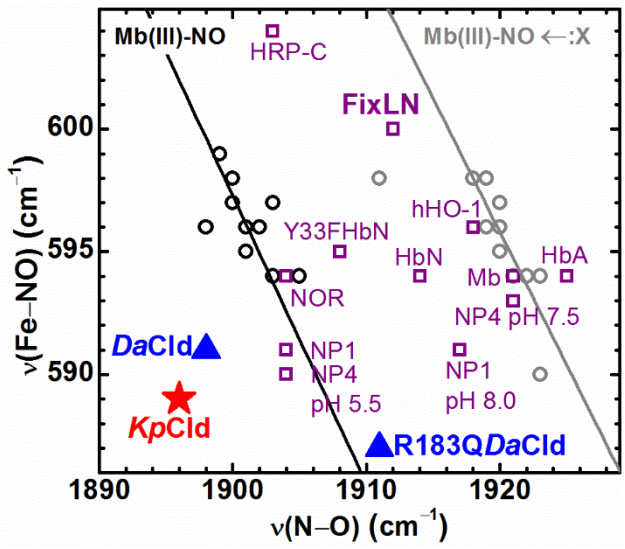

Figure 5.8. Backbonding correlation plot of 6c {FeNO}^{6} complexes reveals closed conformation for {FeNO}^{6} Clds. Both lines were generated from ferric nitrosyl myoglobin mutants[47,56] shown by circles while purple squares correspond to other heme proteins.[25,48,57-63] Proteins falling on the gray line comprise a distal base while those on the black line have none. Blue triangles and red star are *Da*Clds and *Kp*Cld, respectively.

Interestingly, the {FeNO}^{6} complexes of WT *Kp*Cld and *Da*Cld define the low-frequency extreme of ν(N−O), ν(Fe−NO) correlation space for {FeNO}^{6} heme proteins having proximal imidazole ligands reported to date. This suggests that distal {FeNO}^{6} interactions in the Clds exert their influence on FeNO bonding and vibrational dynamics in a way that is distinct from other proteins in Figure 5.8. The very low ν(N−O) / ν(Fe−NO) frequencies for WT *Da*Cld and *Kp*Cld are attributed to the Lewis acidity (or positive charge) of their distal arginine side chains. The nucleophilicity of Lewis bases, such as imidazole and water, favor Fe^{II}–NO^+ character of the {FeNO}^{6} moiety with its formal NO bond order of three, as revealed by their ν(N−O) frequencies ranging from ~25 to 50 cm^{-1} higher than that of free NO (bond order = 2.5, ν(N−O) = 1876 cm^{-1}). Distal Lewis acids, such as the guanidinium side chain of arginine, are expected to destabilize the Fe^{II}–NO^+ form due to repulsive electrostatic interactions with NO^+. In a qualitative sense, the growing electrostatic repulsion between the approaching guanidinium group of a distal arginine and the NO^+ ligand could be mitigated by delocalizing the nitrosonium

charge away from the distal positive charge. Electron transfer from Fe(II) to NO^+ would yield a $Fe^{III}–NO^{\bullet}$ state in which the positive charge has been fully delocalized to the iron center, thereby maximizing the distance between the protein-based positive charge and that localized on the $\{FeNO\}^6$ moiety. Based on DFT computational studies of $\{FeNO\}^6$ porphyrinates, it has been reported that the ground and excited states have $Fe^{II}–NO^+$ and $Fe^{III}–NO^{\bullet}$ character, respectively.[64] The low ν(N−O) and ν(Fe−NO) frequencies of WT $\{FeNO\}^6$ Clds reported here reveal substantially weakened Fe−NO and N−O bonds relative to other $\{FeNO\}^6$ heme proteins. Furthermore, their ν(N−O) frequencies are shifted toward that of free NO relative to other proteins with similar ν(Fe−NO) frequency, consistent with assignment of considerable $Fe^{III}–NO^{\bullet}$ character to the $\{FeNO\}^6$ moiety. Finally, because σ donation from their proximal ligands is not particularly high compared to $\{FeNO\}^6$ HRP with its proximal imidazolate ligand, these weakened FeNO bonds are unlikely to be attributable to proximal effects. Therefore, the results reported here support the conclusion that these WT Clds are the first examples of $\{FeNO\}^6$ heme proteins in which distal factors drive stabilization of the $Fe^{III}–NO^{\bullet}$ excited state. It seems unlikely that the nitrosonium and neutral NO radical states are fully inverted, as the ν(N−O) frequencies remain ~20 cm^{-1} above that of free NO. However, since the frequencies are quite low and only one set of ν(Fe−NO) and ν(N−O) bands is observed, it is most reasonable to suggest that the presence of distal positive charge induces an admixture of the nitrosonium and neutral radical states having an intermediate NO bond order, as illustrated in Scheme 5.1.

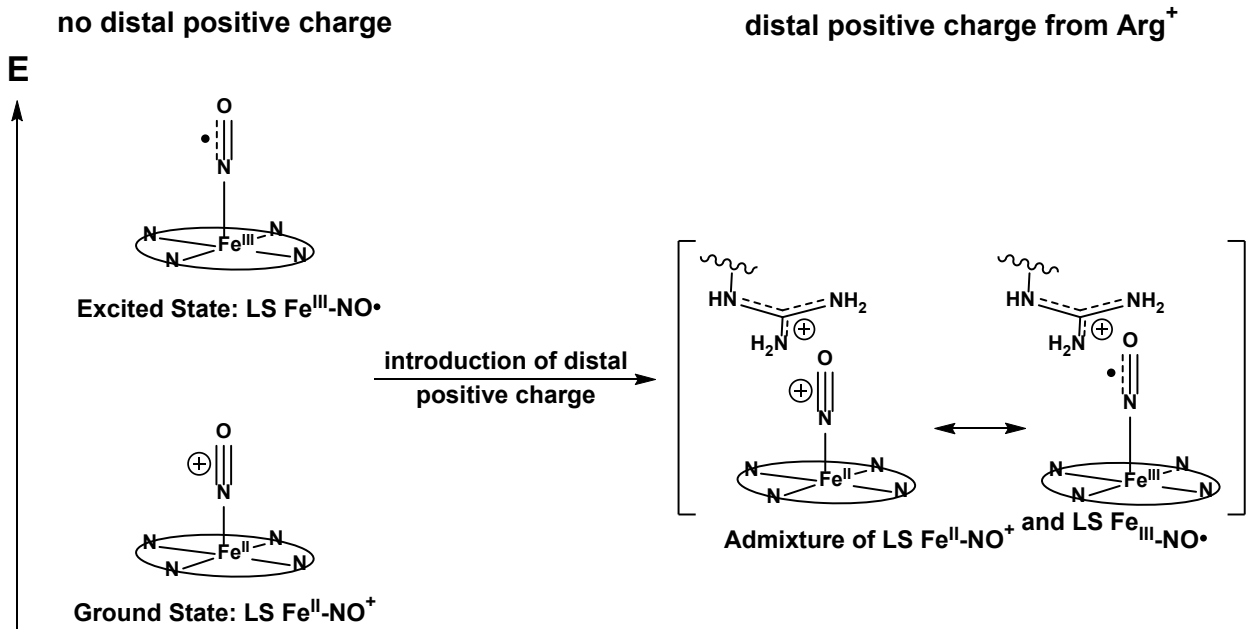

Scheme 5.1. Effect of distal arginine on valence electron distribution in $\{FeNO\}^6$ Clds.

Interestingly, the only other protein in Fig. 8 having a distal arginine residue is the O_2-sensing domain FixLN from *Sinorhizobium meliloti*. The heme environment in FixLN differs from those of the Clds in a couple of ways. First, its Fe^{II}–His bond is relatively weak based on its $\nu(Fe^{II}–His)$ frequency of 212 cm^{-1} [65] and, by virtue of its position on the Lewis donor correlation line in Figure 5.8, likely has an arginine-stabilized water molecule in its distal heme pocket.

Consistent with the cause-and-effect relationship between distal positive charge and very low FeNO frequencies, when the cationic side chain of Arg183 is replaced by the charge-neutral amide of glutamine, its $\{FeNO\}^6$ complex falls at the low-ν(Fe–NO) extreme of the donor-free correlation line. That *Da*Cld(R183Q) $\{FeNO\}^6$ falls on the correlation line is consistent with re-establishment of dominant $Fe^{II}–NO^+$ character in the $\{FeNO\}^6$ moiety and the susceptibility of its backbonding to environmental interactions.

Given the similarity in the distal environments of *Da*Cld and *Kp*Cld, it seems reasonable to consider whether their relative positions in Figure 5.8 are attributable to differential proximal

(*trans*) effects. Their respective ν(Fe^{II}–His) frequencies of 222 cm^{-1} and 229 cm^{-1} reveal more proximal imidazolate character in *Kp*Cld.[7,41] Its correspondingly stronger σ donation is expected to have a greater *trans* effect, resulting in the lower ν(Fe–NO) and ν(N–O) frequencies, which is observed, along with a smaller ∠FeNO in *Kp*Cld than *Da*Cld. An inverse relationship between *trans* donor strength and ∠FeNO was also predicted by previous computational studies[66-67] and recently corroborated experimentally with *trans*-thiolate $\{FeNO\}^6$ compounds.[68] Based on the greater proximal imidazolate character in *Kp*Cld, this relationship would predict it to have the smaller ∠FeNO. However the difference between its ν(Fe–NO) and δ(FeNO) frequencies is smaller than that of *Da*Cld $\{FeNO\}^6$ (Δν = 10 cm^{-1} for *Kp*Cld and 15 cm^{-1} for *Da*Cld), consistent with its ∠FeNO being the larger of the two WT enzymes.[48] Therefore, the relative FeNO frequencies and bond angles cannot be explained in terms of the *trans* effect alone. Earlier computational studies of this *trans* effect, varied *trans* structural and electronic factors independently in order to establish the aforementioned relationship between donor strength and ∠FeNO. Here, there are both distal *and* proximal (i.e. *trans*) forces at play and, as suggested by the apparent inconsistency described above, both influence FeNO bond strengths and angles in combinatorial ways that remain to be clarified.

5.5.2. Structural basis of slow reductive nitrosylation of $\{FeNO\}^6$ Clds

Heme proteins with a proximal histidine and a distal arginine (i.e. Clds and FixL) have k_{H2O} and k_{OH-} of similar magnitudes (Table 5.2). This contrasts with heme proteins having a proximal histidine, and either a distal histidine or tyrosine, whose k_{H2O} and k_{OH-} values are several orders of magnitude larger (i.e. Hb, Mb, trHb, and LegHb).[50-52] While tempting to attribute the sluggish rates of reductive nitrosylation for Clds to the positive charge from their distal arginine, the similarity in k_{H2O} and k_{OH-} values of *Da*Cld(R183Q) to those of the WT Cld enzymes

indicates that this is not the case. A possible explanation is that the WT Clds and the *Da*Cld(R183Q) are characterized by slow conformational dynamics dominated by one or more closed conformers in which access of nucleophiles to the coordinated NO is blocked. In the Cld case either a distal arginine or glutamine can serve this role of slowly and alternately blocking and providing access in the $\{FeNO\}^6$ liganded state. Access of a nucleophile to coordinated NO is likely only possible for the trace fraction of the open conformer present at equilibrium. In this case, pocket access by a reactive nucleophile would be rate limiting for reductive nitrosylation. This would likely be the case, even if there is a water molecule bridging the distal arginine and the reactive N_{NO+} atom, as suggested above for *Sm*FixLN.

Both WT Cld enzymes and *Da*Cld(R183Q) exhibit biphasic reductive nitrosylation similar to *Sm*FixL*.[49] The cause of the slow phase remains elusive. However, based on the kinetic behavior of these systems, it may involve a conformation that is kinetically distinct in its lack of reactivity toward reductive nitrosylation. One possible explanation for the slow phase was incomplete formation of $\{FeNO\}^6$ due to competition from hydroxide coordination. This was ruled out as cause for the slow kinetic phase, as there is no evidence from UV-vis or rR spectroscopy of the ferric heme hydroxides in alkaline $\{FeNO\}^6$ solutions. Thus, it appears that the slow phase is attributable to a kinetically trapped and unreactive fraction of the enzyme that is either intrinsic to the purified enzyme or that forms upon reaction with NO. This trapped state is illustrated in Scheme 5.2. In either case, the UV-vis absorbance spectrum of the $\{FeNO\}^6$ complex is not sensitive to the structural differences that govern their reactivity, suggesting that these differences are structurally remote from the heme.

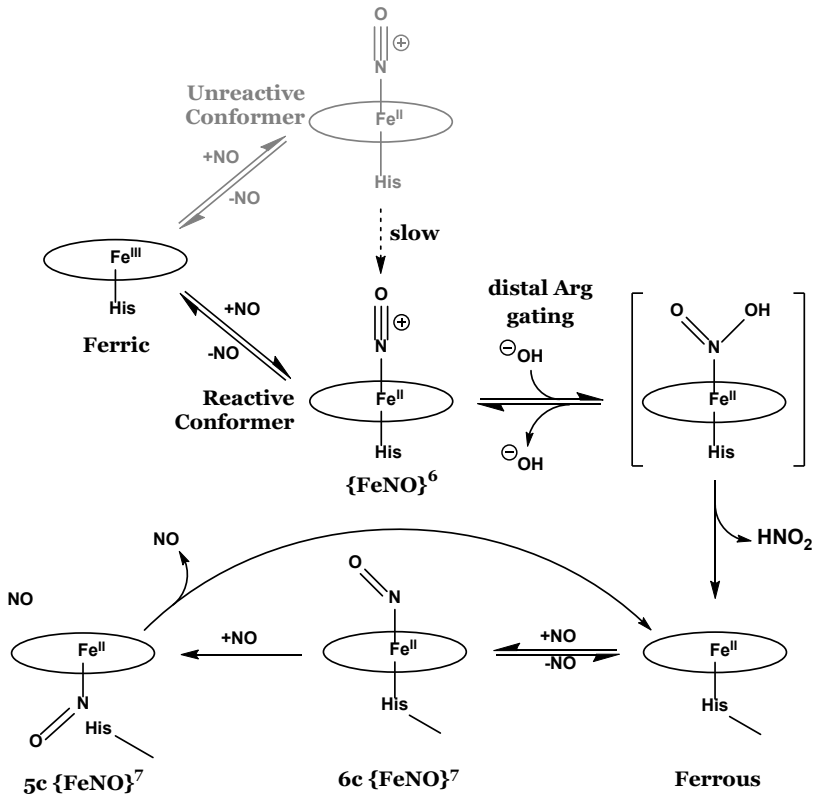

Scheme 5.2. Proposed mechanistic scheme for reductive nitrosylation of Clds.

5.5.3. Hydrogen bonding in the 6c {FeNO}^{7} Clds is directed towards the nitrogen of the NO ligand.

Figure 5.9 shows the ν(Fe−NO) vs ν(N−O) correlation plots for 5c and 6c {FeNO}^{7} complexes of the Clds alongside other histidine-ligated heme proteins. The 6c {FeNO}^{7} complexes fall on two distinct ν(Fe−NO) vs ν(N−O) correlation lines (Figure 5.9A). One reveals a positive correlation between ν(Fe−NO) and ν(N−O) frequencies, for {FeNO}^{7} hemes having hydrogen-bond donation to their N_{NO} atoms. The second shows a negative correlation among complexes having hydrogen-bond donation to the O_{NO} atoms of their NO ligands.[56] Both 6c{FeNO}^{7} WT *Da*Cld and *Kp*Cld complexes fall slightly below the positive correlation line, consistent with hydrogen-bond donation from their distal arginine side chains to N_{NO} in both enzymes. This behavior is in agreement with data on their fluoride and hydroxide complexes, in

which hydrogen bond donation from their distal positively charged arginine residues to the coordinated atom of the ligand is clear from their low ν(Fe−F) and ν(Fe−OH) frequencies, respectively.[69] As hydrogen-bond donation to N_{NO} increases along the positive correlation line, the systematic lowering of their ν(Fe−NO) and ν(N−O) frequencies reveals weakening of both the Fe−NO and N−O bonds. Thus, *Da*Cld, having lower ν(Fe−NO) and ν(N−O) frequencies than *Kp*Cld, exhibits stronger hydrogen-bond donation to N_{NO}. The stronger hydrogen-bonding to the NO ligand in the substrate binding site of *Da*Cld relative to *Kp*Cld is consistent with greater ability of the *Da*Cld distal pocket to polarize the substrate O−Cl bond and lower the kinetic barrier to its heterolytic scission in catalytic ClO_2^- decomposition.

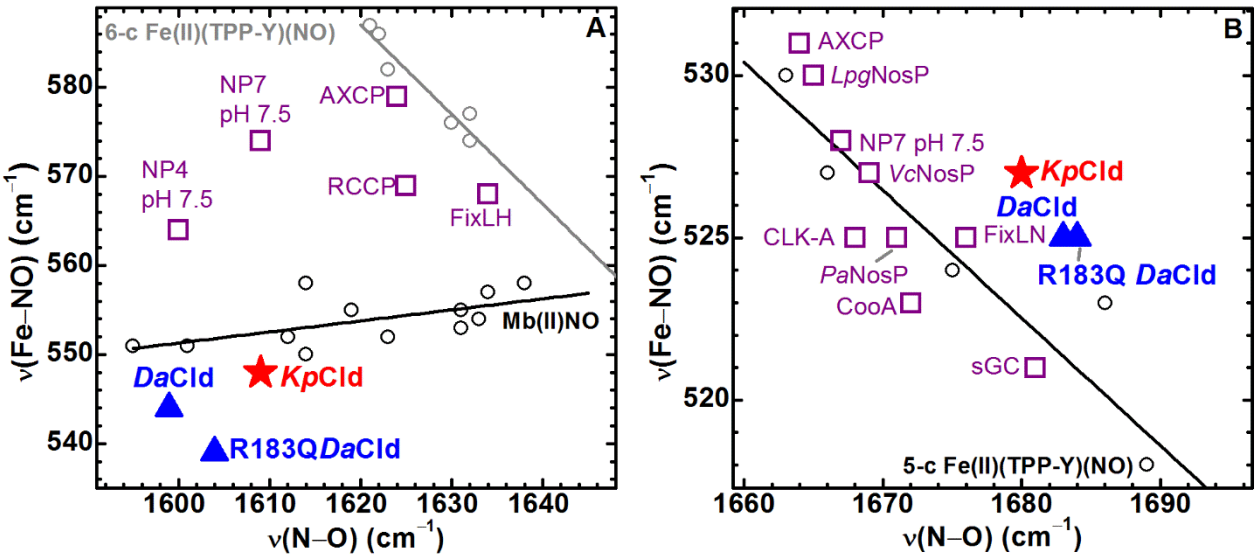

Figure 5.9. Backbonding plots for 6c and 5c $\{FeNO\}^7$. A) Two $\nu(Fe^{II}–NO)/\nu(N–O)$ correlation lines for 6c $\{FeNO\}^7$ complexes represent different hydrogen bond orientations. The negative correlation line was generated from ferrous tetraphenylporphyrin with various ligands (gray) while the positive correlation line was generated from ferrous nitrosyl myoglobin mutants (black).[56] The gray line indicates hydrogen bonding directed toward O_{NO} while the black line indicates hydrogen bonding directed toward N_{NO}. Blue triangles and red star are *Da*Clds and *Kp*Cld, respectively while purple squares correspond to other heme proteins.[53,57,70-73] B) The ν(Fe−NO) vs ν(N−O) backbonding correlation plot of 5c $\{FeNO\}^7$ complexes supports proximal NO binding in Clds. The line was generated from ferrous tetraphenylporphyrin with various ligands (open circles).[56] Blue triangles and red star are *Da*Clds and *Kp*Cld, respectively, while purple squares correspond to other heme proteins.[21,25,41,53,72,74-77]

5.5.4. The pH dependence of 5c:6c {FeNO}^{7} Clds is correlated with acid-base properties of the proximal histidine.

The two 5c {FeNO}^{7} *Da*Cld complexes reported here are co-located on the backbonding correlation plot (Figure 5.9B), consistent with the similarity expected for their NO environments in the proximal *Da*Cld heme pocket. While some effort has been made to distinguish proximal from distal NO binding based on spectroscopic signatures[78-79], position on the backbonding correlation plot alone has yet to provide clear insight into the heme face occupied by NO. Proximal 5c {FeNO}^{7} heme proteins that are known NO sensors (e.g. sGC and H-NOX) respond to changes in [NO] by forming their 5c sensor-on states via two [NO]-dependent steps: NO binding directly to the open distal heme face to yield transient 6c {FeNO}^{7} followed by [NO]-dependent isomerization to give 5c {FeNO}^{7} wherein NO is coordinated to the proximal face.[19,54-55] These two steps support a dampened response to changes in [NO] which might otherwise be physiologically too potent. While a physiological ClO_2^- detoxification function is known for the periplasmic *Da*Cld enzyme it has only been proposed for the cytoplasmic *Kp*Cld.[5] Hence, it is interesting to consider whether the cytoplasmic potential in *K. pneumoniae*, could support formation of the proximal 5c {FeNO}^{7} complex *in vivo*, as that would suggest the possibility of an NO sensing function.

The equilibrium between 6c and 5c {FeNO}^{7} appears to be controlled by the relative proximal Fe−His bond strengths in the Clds. Although the pH dependence alone does not reveal the localization of the controlling acid-base reaction, we note that the enzymes likely have different Fe−His bond strengths, as suggested by their different ν(Fe^{II}–His) frequencies. The extent of the thermodynamic NO *trans* effect on proximal histidine dissociation is expected to correlate inversely with the strength of the Fe−His bond. Thus, greater susceptibility of the

proximal histidine to *trans* labilization by NO is expected for the Cld having the least proximal imidazolate character. Based on ν(Fe^{II}–His) frequencies, that enzyme is *Da*Cld. Consistent with this expectation, the observed susceptibility of the proximal histidine in *Da*Cld to *trans* labilization by NO, as judged by the extent of conversion to 5c $\{FeNO\}^7$ at pH 6, is greater than that for *Kp*Cld. Thus, the pH sensitivity of the 5c:6c population ratio is attributed to the acid-base properties of the distal histidine ligand.

5.5.5. Relevance of these results to catalytic ClO_2^- decomposition.

The behavior of the $\{FeNO\}^6$ Clds is consistent with their established penchant for closed heme pocket conformations in liganded states, which has been suggested to be part of the reason that *Da*Cld has such high catalytic efficiency and specificity. Upon formation of the enzyme substrate complex, the decomposition reaction is sequestered, which prevents escape of reactive chlorine species from the active site[7,36] and diversion of the key intermediates along unproductive or damaging pathways.[80] Especially in the $\{FeNO\}^6$ Clds, the closed solvent-inaccessible and otherwise hydrophobic distal heme pocket supports strong polarization of $Fe–L_{axial}$ moieties by distal positive charge, as revealed by the heretofore unobserved effects of their $Fe^{III}–NO^{\bullet}$ / $Fe^{II}–NO^+$ admixture on the bond strengths and charge distribution in the $\{FeNO\}^6$ moiety. This is consistent with facilitation of polarization-dependent $O–Cl^{III}$ bond scission in the first reaction step of the enzyme-substrate complex (Cld–ClO_2^-). Such polarizing capacity of distal arginine in the heme peroxidases is well established to be crucial in lowering the kinetic barrier to heterolytic cleavage of O–O bond in compound 0 to yield compound I and water.[81] The strong polarizing capacity of the distal arginine revealed here for the Cld $\{FeNO\}^6$ complexes suggests that analogous two-electron coupled heterolytic cleavage of the $O–Cl^{III}$ bond to yield compound I and ClO^- warrants further consideration.

5.6. Conclusions

This study contains the first reported vibrational characterization of both $\{FeNO\}^6$ and $\{FeNO\}^7$ complexes of dimeric and pentameric Clds. Both *Da*Cld (pentameric) and *Kp*Cld (dimeric) form kinetically stable $\{FeNO\}^6$ complexes and have the lowest correlated ν(Fe−NO) / ν(N−O) frequencies on record for heme nitrosyls with proximal histidine ligands. These low frequencies are attributed to Fe^{III}–$NO^{\bullet}$ character of their ground states, in which both NO bond order and π backbonding are both diminished relative to the intrinsic Fe^{II}–NO^{+} ground state. Reductive nitrosylation reactions of the $\{FeNO\}^6$ Clds are slow and biphasic. The closed heme pocket of these ligated states is concluded to be responsible for the slow rates.

Both Clds form mixtures of 6c and proximal 5c $\{FeNO\}^7$ complexes whose equilibrium 5c populations depend on the σ donor strengths of their proximal histidine ligands. The Clds reported here are among the few heme proteins known to form proximal 5c $\{FeNO\}^7$ complexes. Proximal NO coordination in 5c $\{FeNO\}^7$ appears to be intrinsic to the Clds investigated here. Whether this penchant for coordination chemistry heretofore associated with NO sensing speaks to a possible sensor role is an interesting and open question.

5.7. Associated Content

Additional data referred to in the text are in Appendix D: Figures D1 to D7.

5.8. Funding Source

Support from the National Institutes of Health Grants GM114787 (to G. S. L.-R.) and GM090260 (to J. L. D.) is gratefully acknowledged. This work was also supported by a Doctoral Dissertation Fellowship awarded through North Dakota NSF-EPSCoR Grant OIA-1355466 (Z. G.).

5.9. References

1. DuBois, J. L.; Ojha, S., Production of dioxygen in the dark: dismutases of oxyanions. *Met Ions Life Sci* 2015, *15*, 45-87.
2. Schaffner, I.; Hofbauer, S.; Krutzler, M.; Pirker, K. F.; Furtmueller, P. G.; Obinger, C., Mechanism of chlorite degradation to chloride and dioxygen by the enzyme chlorite dismutase. *Arch. Biochem. Biophys.* 2015, *574*, 18-26.
3. Goblirsch, B.; Kurker, R. C.; Streit, B. R.; Wilmot, C. M.; DuBois, J. L., Chlorite dismutases, DyPs, and EfeB: 3 microbial heme enzyme families comprise the CDE structural superfamily. *J. Mol. Biol.* 2011, *408* (3), 379-398.
4. Hofbauer, S.; Schaffner, I.; Furtmueller, P. G.; Obinger, C., Chlorite dismutases - a heme enzyme family for use in bioremediation and generation of molecular oxygen. *Biotechnol. J.* 2014, *9*, 461-473.
5. Celis, A. I.; DuBois, J. L., Substrate, product, and cofactor: The extraordinarily flexible relationship between the CDE superfamily and heme. *Arch. Biochem. Biophys.* 2015, *574*, 3-17.
6. Coates, J. D.; Achenbach, L. A., Microbial perchlorate reduction: rocket-fueled metabolism. *Nat. Rev. Microbiol.* 2004, *2* (7), 569-580.
7. Celis, A. I.; Geeraerts, Z.; Ngmenterebo, D.; Machovina, M. M.; Kurker, R. C.; Rajakumar, K.; Ivancich, A.; Rodgers, K. R.; Lukat-Rodgers, G. S.; DuBois, J. L., A dimeric chlorite dismutase exhibits O2-generating activity and acts as a chlorite antioxidant in Klebsiella pneumoniae MGH 78578. *Biochemistry* 2015, *54* (2), 434-46.
8. Schaffner, I.; Hofbauer, S.; Krutzler, M.; Pirker, K. F.; Bellei, M.; Stadlmayr, G.; Mlynek, G.; Djinovic-Carugo, K.; Battistuzzi, G.; Furtmüller, P. G.; Daims, H.; Obinger, C., Dimeric chlorite dismutase from the nitrogen-fixing cyanobacterium Cyanothece sp. PCC7425. *Mol. Microbiol.* 2015, *96* (5), 1053-1068.
9. Blanc, B.; Mayfield, J. A.; McDonald, C. A.; Lukat-Rodgers, G. S.; Rodgers, K. R.; DuBois, J. L., Understanding how the distal environment directs reactivity in chlorite dismutase: spectroscopy and reactivity of Arg183 mutants. *Biochemistry* 2012, *51* (9), 1895-910.
10. Hofbauer, S.; Gysel, K.; Bellei, M.; Hagmueller, A.; Schaffner, I.; Mlynek, G.; Kostan, J.; Pirker, K. F.; Daims, H.; Furtmueller, P. G.; Battistuzzi, G.; Djinovic-Carugo, K.; Obinger, C., Manipulating conserved heme cavity residues of chlorite dismutase: Effect on structure, redox chemistry, and reactivity. *Biochemistry* 2014, *53*, 77-89.
11. Hofbauer, S.; Gruber, C.; Pirker, K. F.; Suendermann, A.; Schaffner, I.; Jakopitsch, C.; Oostenbrink, C.; Furtmueller, P. G.; Obinger, C., Transiently produced hypochlorite is responsible for the irreversible inhibition of chlorite dismutase. *Biochemistry* 2014, *53*, 3145-3157.
12. Pal, R. R.; Khardenavis, A. A.; Purohit, H. J., Identification and monitoring of nitrification and denitrification genes in Klebsiella pneumoniae EGD-HP19-C for its ability to perform heterotrophic nitrification and aerobic denitrification. *Funct. Integr. Genomics* 2015, *15*, 63-76.
13. Williams, D. E.; Boon, E. M., Towards Understanding the Molecular Basis of Nitric Oxide-Regulated Group Behaviors in Pathogenic Bacteria. *J. Innate Immun.* 2019, *11*, 205-215.

14. Tsai, W. C.; Strieter, R. M.; Zisman, D. A.; Wilkowski, J. M.; Bucknell, K. A.; Chen, G.-H.; Standiford, T. J., Nitric oxide is required for effective innate immunity against Klebsiella pneumoniae. *Infect. Immun.* 1997, *65*, 1870-1875.
15. Poole, R. K.; Hughes, M. N., New functions for the ancient globin family: bacterial responses to nitric oxide and nitrosative stress. *Mol. Microbiol.* 2000, *36*, 775-83.
16. Gardner, A. M.; Helmick, R. A.; Gardner, P. R., Flavorubredoxin, an inducible catalyst for nitric oxide reduction and detoxification in Escherichia coli. *J. Biol. Chem.* 2002, *277*, 8172-8177.
17. Stevanin, T. M.; Moir, J. W. B.; Read, R. C., Nitric oxide detoxification systems enhance survival of Neisseria meningitidis in human macrophages and in nasopharyngeal mucosa. *Infect. Immun.* 2005, *73*, 3322-3329.
18. Mills, P. C.; Rowley, G.; Spiro, S.; Hinton, J. C. D.; Richardson, D. J., A combination of cytochrome c nitrite reductase (NrfA) and flavorubredoxin (NorV) protects Salmonella enterica serovar Typhimurium against killing by NO in anoxic environments. *Microbiology* 2008, *154*, 1218-1228.
19. Martin, E.; Berka, V.; Sharina, I.; Tsai, A.-L., Mechanism of Binding of NO to Soluble Guanylyl Cyclase: Implication for the Second NO Binding to the Heme Proximal Site. *Biochemistry* 2012, *51* (13), 2737-2746.
20. Herzik, M. A., Jr.; Jonnalagadda, R.; Kuriyan, J.; Marletta, M. A., Structural insights into the role of iron-histidine bond cleavage in nitric oxide-induced activation of H-NOX gas sensor proteins. *Proc. Natl. Acad. Sci. U. S. A.* 2014, *111* (40), E4156-64.
21. Bacon, B. A.; Liu, Y.; Kincaid, J. R.; Boon, E. M., Spectral Characterization of a Novel NO Sensing Protein in Bacteria: NosP. *Biochemistry* 2018, *57* (43), 6187-6200.
22. Karow, D. S.; Pan, D.; Tran, R.; Pellicena, P.; Presley, A.; Mathies, R. A.; Marletta, M. A., Spectroscopic Characterization of the Soluble Guanylate Cyclase-like Heme Domains from Vibrio cholerae and Thermoanaerobacter tengcongensis. *Biochemistry* 2004, *43*, 10203-10211.
23. Tsai, A.-L.; Berka, V.; Martin, F.; Ma, X.; van den Akker, F.; Fabian, M.; Olson, J. S., Is Nostoc H-NOX a NO Sensor or Redox Switch? *Biochemistry* 2010, *49*, 6587-6599.
24. Boon, E. M.; Davis, J. H.; Tran, R.; Karow, D. S.; Huang, S. H.; Pan, D.; Miazgowicz, M. M.; Mathies, R. A.; Marletta, M. A., Nitric Oxide Binding to Prokaryotic Homologs of the Soluble Guanylate Cyclase β1 H-NOX Domain. *J. Biol. Chem.* 2006, *281*, 21892-21902.
25. Lukat-Rodgers, G. S.; Rodgers, K. R., Characterization of Ferrous FixL−Nitric Oxide Adducts by Resonance Raman Spectroscopy. *Biochemistry* 1997, *36* (14), 4178-4187.
26. Walker, F. A., Nitric oxide interaction with insect nitrophorins and thoughts on the electron configuration of the {FeNO}6 complex. *J. Inorg. Biochem.* 2005, *99*, 216-236.
27. Wasser, I. M.; de Vries, S.; Moeenne-Loccoz, P.; Schroeder, I.; Karlin, K. D., Nitric Oxide in Biological Denitrification: Fe/Cu Metalloenzyme and Metal Complex NOx Redox Chemistry. *Chem. Rev.* 2002, *102*, 1201-1234.
28. Daiber, A.; Shoun, H.; Ullrich, V., Nitric oxide reductase (P450nor) from Fusarium oxysporum. *J. Inorg. Biochem.* 2005, *99*, 185-193.
29. Enemark, J. H.; Feltham, R. D., Principles of structure, bonding, and reactivity for metal nitrosyl complexes. *Coord. Chem. Rev.* 1974, *13* (4), 339-406.
30. Fernandez, B. O.; Ford, P. C., Nitrite Catalyzes Ferriheme Protein Reductive Nitrosylation. *J. Am. Chem. Soc.* 2003, *125* (35), 10510-10511.

31. Ford, P. C., Reactions of NO and Nitrite with Heme Models and Proteins. *Inorg. Chem.* 2010, *49* (14), 6226-6239.
32. Andersen, J. F.; Ding, X. D.; Balfour, C.; Shokhireva, T. K.; Champagne, D. E.; Walker, F. A.; Montfort, W. R., Kinetics and Equilibria in Ligand Binding by Nitrophorins 1-4: Evidence for Stabilization of a Nitric Oxide-Ferriheme Complex through a Ligand-Induced Conformational Trap. *Biochemistry* 2000, *39* (Copyright (C) 2012 American Chemical Society (ACS). All Rights Reserved.), 10118-10131.
33. Lawson, D. M.; Stevenson, C. E. M.; Andrew, C. R.; Eady, R. R., Unprecedented proximal binding of nitric oxide to heme: implications for guanylate cyclase. *The EMBO Journal* 2000, *19* (21), 5661-5671.
34. Horst, B. G.; Marletta, M. A., Physiological activation and deactivation of soluble guanylate cyclase. *Nitric Oxide* 2018, *77*, 65-74.
35. Andrew, C. R.; Rodgers, K. R.; Eady, R. R., A Novel Kinetic Trap for NO Release from Cytochrome c': A Possible Mechanism for NO Release from Activated Soluble Guanylate Cyclase. *J. Am. Chem. Soc.* 2003, *125* (32), 9548-9549.
36. Streit, B. R.; DuBois, J. L., Chemical and Steady-State Kinetic Analyses of a Heterologously Expressed Heme Dependent Chlorite Dismutase. *Biochemistry* 2008, *47* (19), 5271-5280.
37. Bradford, M. M., A rapid and sensitive method for the quantitation of microgram quantities of protein utilizing the principle of protein-dye binding. *Anal. Biochem.* 1976, *72* (1), 248-254.
38. Berry, E. A.; Trumpower, B. L., Simultaneous determination of hemes a, b, and c from pyridine hemochrome spectra. *Anal. Biochem.* 1987, *161* (1), 1-15.
39. Geeraerts, Z.; Celis, A. I.; Mayfield, J. A.; Lorenz, M.; Rodgers, K. R.; DuBois, J. L.; Lukat-Rodgers, G. S., Distinguishing Active Site Characteristics of Chlorite Dismutases with Their Cyanide Complexes. *Biochemistry* 2018, *57* (9), 1501-1516.
40. Tropea, J. E.; Cherry, S.; Waugh, D. S., Expression and Purification of Soluble His6-Tagged TEV Protease. In *High Throughput Protein Expression and Purification: Methods and Protocols*, Doyle, S. A., Ed. Humana Press: Totowa, NJ, 2009; pp 297-307.
41. Streit, B. R.; Blanc, B.; Lukat-Rodgers, G. S.; Rodgers, K. R.; DuBois, J. L., How active-site protonation state influences the reactivity and ligation of the heme in chlorite dismutase. *J. Am. Chem. Soc.* 2010, *132* (16), 5711-24.
42. Schwartz, S. E.; White, W. H., Solubility equilibria of the nitrogen oxides and oxyacids in dilute aqueous solution. *Adv. Environ. Sci. Eng.* 1981, *4*, 1-45.
43. Li, X. Y.; Czernuszewicz, R. S.; Kincaid, J. R.; Su, Y. O.; Spiro, T. G., Consistent porphyrin force field. 1. Normal-mode analysis for nickel porphine and nickel tetraphenylporphine from resonance Raman and infrared spectra and isotope shifts. *J. Phys. Chem.* 1990, *94* (1), 31-47.
44. Choi, S.; Spiro, T. G.; Langry, K. C.; Smith, K. M.; Budd, D. L.; La Mar, G. N., Structural correlations and vinyl influences in resonance Raman spectra of protoheme complexes and proteins. *J. Am. Chem. Soc.* 1982, *104* (16), 4345-4351.
45. Milazzo, L.; Gabler, T.; Pfanzagl, V.; Michlits, H.; Furtmuller, P. G.; Obinger, C.; Hofbauer, S.; Smulevich, G., The hydrogen bonding network of coproheme in coproheme decarboxylase from Listeria monocytogenes: Effect on structure and catalysis. *J. Inorg. Biochem.* 2019, *195* (Copyright (C) 2019 American Chemical Society (ACS). All Rights Reserved.), 61-70.

46. Li, J.; Peng, Q.; Oliver, A. G.; Alp, E. E.; Hu, M. Y.; Zhao, J.; Sage, J. T.; Scheidt, W. R., Comprehensive Fe-ligand vibration identification in {FeNO}6 hemes. *J. Am. Chem. Soc.* 2014, *136* (52), 18100-10.
47. Soldatova, A. V.; Ibrahim, M.; Olson, J. S.; Czernuszewicz, R. S.; Spiro, T. G., New light on NO bonding in Fe(III) heme proteins from resonance raman spectroscopy and DFT modeling. *J. Am. Chem. Soc.* 2010, *132*, 4614-4625.
48. Maes, E. M.; Walker, F. A.; Montfort, W. R.; Czernuszewicz, R. S., Resonance Raman Spectroscopic Study of Nitrophorin 1, a Nitric Oxide-Binding Heme Protein from Rhodnius prolixus, and Its Nitrosyl and Cyano Adducts. *J. Am. Chem. Soc.* 2001, *123* (47), 11664-11672.
49. Rodgers, R. K.; Lukat-Rodgers, S. G.; Tang, L., Nitrosyl adducts of FixL as probes of heme environment. *J. Biol. Inorg. Chem.* 2000, *5* (5), 642-654.
50. Hoshino, M.; Maeda, M.; Konishi, R.; Seki, H.; Ford, P. C., Studies on the Reaction Mechanism for Reductive Nitrosylation of Ferrihemoproteins in Buffer Solutions. *J. Am. Chem. Soc.* 1996, *118* (24), 5702-5707.
51. Herold, S.; Puppo, A., Kinetics and mechanistic studies of the reactions of metleghemoglobin, ferrylleghemoglobin, and nitrosylleghemoglobin with reactive nitrogen species. *J. Biol. Inorg. Chem.* 2005, *10* (8), 946-57.
52. Ascenzi, P.; di Masi, A.; Tundo, G. R.; Pesce, A.; Visca, P.; Coletta, M., Nitrosylation Mechanisms of Mycobacterium tuberculosis and Campylobacter jejuni Truncated Hemoglobins N, O, and P. *PLOS ONE* 2014, *9* (7), e102811.
53. Andrew, C. R.; George, S. J.; Lawson, D. M.; Eady, R. R., Six- to Five-Coordinate Heme−Nitrosyl Conversion in Cytochrome c‘ and Its Relevance to Guanylate Cyclase. *Biochemistry* 2002, *41* (7), 2353-2360.
54. Wu, G.; Liu, W.; Berka, V.; Tsai, A.-l., The Selectivity of Vibrio cholerae H-NOX for Gaseous Ligands Follows the “Sliding Scale Rule” Hypothesis. Ligand Interactions with both Ferrous and Ferric Vc H-NOX. *Biochemistry* 2013, *52* (52), 9432-9446.
55. Tsai, A.-L.; Berka, V.; Sharina, I.; Martin, E., Dynamic Ligand Exchange in Soluble Guanylyl Cyclase (sGC): IMPLICATIONS FOR sGC REGULATION AND DESENSITIZATION. *J. Biol. Chem.* 2011, *286* (50), 43182-43192.
56. Spiro, T. G.; Soldatova, A. V.; Balakrishnan, G., CO, NO and O2 as vibrational probes of heme protein interactions. *Coord. Chem. Rev.* 2013, *257* (2), 511-527.
57. Benko, B.; Yu, N. T., Resonance Raman studies of nitric oxide binding to ferric and ferrous hemoproteins: detection of Fe(III)--NO stretching, Fe(III)--N--O bending, and Fe(II)--N--O bending vibrations. *Proc. Natl. Acad. Sci. U. S. A.* 1983, *80* (22), 7042-7046.
58. Tomita, T.; Haruta, N.; Aki, M.; Kitagawa, T.; Ikeda-Saito, M., UV Resonance Raman Detection of a Ligand Vibration on Ferric Nitrosyl Heme Proteins. *J. Am. Chem. Soc.* 2001, *123* (11), 2666-2667.
59. Mukai, M.; Ouellet, Y.; Ouellet, H.; Guertin, M.; Yeh, S.-R., NO Binding Induced Conformational Changes in a Truncated Hemoglobin from Mycobacterium tuberculosis. *Biochemistry* 2004, *43* (10), 2764-2770.
60. Ding, X. D.; Weichsel, A.; Andersen, J. F.; Shokhireva, T. K.; Balfour, C.; Pierik, A. J.; Averill, B. A.; Montfort, W. R.; Walker, F. A., Nitric Oxide Binding to the Ferri- and Ferroheme States of Nitrophorin 1, a Reversible NO-Binding Heme Protein from the

Saliva of the Blood-Sucking Insect, Rhodnius prolixus. *J. Am. Chem. Soc.* 1999, *121* (1), 128-138.
61. Zaczek, M. B.; Zareba, A. A.; Czernuszewicz, R. S.; Montfort, W., Structural characterization of *R. prolixus* nitrophorin 4 by UV and visible resonance Raman spectroscopy. *J. of Porphyrins and Phthalocyanines* 2006, *10*, 928-933.
62. Wang, J.; Lu, S.; Moenne-Loccoz, P.; Ortiz, d. M. P. R., Interaction of Nitric Oxide with Human Heme Oxygenase-1. *J. Biol. Chem.* 2003, *278* (Copyright (C) 2013 American Chemical Society (ACS). All Rights Reserved.), 2341-2347.
63. Pinakoulaki, E.; Gemeinhardt, S.; Saraste, M.; Varotsis, C., Nitric-oxide Reductase: Structure and Properties of the Catalytic Site from Resonance Raman Scattering. *J. Biol. Chem.* 2002, *277* (26), 23407-23413.
64. Praneeth, V. K. K.; Paulat, F.; Berto, T. C.; DeBeer George, S.; Nather, C.; Sulok, C. D.; Lehnert, N., Electronic Structure of Six-Coordinate Iron(III)-Porphyrin NO Adducts: The Elusive Iron(III)-NO(radical) State and Its Influence on the Properties of These Complexes. *J. Am. Chem. Soc.* 2008, *130*, 15288-15303.
65. Rodgers, K. R.; Lukat, G. S.; Barron, J. A., Structural Basis for Ligand Discrimination and Response Initiation in the Heme-Based Oxygen Sensor FixL. *Biochemistry* 1996, *35*, 9539-9548.
66. Linder, D. P.; Rodgers, K. R., Fe−N−O Structure and Bonding in Six-Coordinate {FeNO}6 Porphyrinates Containing Imidazole: Implications for Reactivity of Coordinated NO. *Inorg. Chem.* 2005, *44* (5), 1367-1380.
67. Linder, D. P.; Rodgers, K. R., Computational modeling of factors that modulate the unique FeNO bonding in {FeNO}(6) heme-thiolate model complexes. *J. Biol. Inorg. Chem.* 2007, *12* (5), 721-31.
68. Hunt, A. P.; Lehnert, N., The Thiolate Trans Effect in Heme {FeNO}(6) Complexes and Beyond: Insight into the Nature of the Push Effect. *Inorg. Chem.* 2019, *58* (17), 11317-11332.
69. Geeraerts, Z.; Rodgers, K. R.; DuBois, J. L.; Lukat-Rodgers, G. S., Active Sites of O2-Evolving Chlorite Dismutases Probed by Halides and Hydroxides and New Iron–Ligand Vibrational Correlations. *Biochemistry* 2017, *56* (34), 4509-4524.
70. Tsubaki, M.; Yu, N. T., Resonance Raman investigation of nitric oxide bonding in nitrosylhemoglobin A and -myoglobin: detection of bound nitrogen-oxygen stretching and iron-nitric oxide stretching vibrations from the hexacoordinated nitric oxide-heme complex. *Biochemistry* 1982, *21* (6), 1140-1144.
71. Andrew, C. R.; Kemper, L. J.; Busche, T. L.; Tiwari, A. M.; Kecskes, M. C.; Stafford, J. M.; Croft, L. C.; Lu, S.; Moënne-Loccoz, P.; Huston, W.; Moir, J. W. B.; Eady, R. R., Accessibility of the Distal Heme Face, Rather than Fe−His Bond Strength, Determines the Heme-Nitrosyl Coordination Number of Cytochromes c‘: Evidence from Spectroscopic Studies. *Biochemistry* 2005, *44* (24), 8664-8672.
72. He, C.; Neya, S.; Knipp, M., Breaking the proximal Fe(II)-N(His) bond in heme proteins through local structural tension: lessons from the heme b proteins nitrophorin 4, nitrophorin 7, and related site-directed mutant proteins. *Biochemistry* 2011, *50* (Copyright (C) 2012 U.S. National Library of Medicine.), 8559-75.
73. Tomita, T.; Gonzalez, G.; Chang, A. L.; Ikeda-Saito, M.; Gilles-Gonzalez, M. A., A Comparative Resonance Raman Analysis of Heme-Binding PAS Domains: Heme Iron

Coordination Structures of the BjFixL, AxPDEA1, EcDos, and MtDos Proteins. *Biochemistry* 2002, *41* (15), 4819-4826.
74. Deinum, G.; Stone, J. R.; Babcock, G. T.; Marletta, M. A., Binding of nitric oxide and carbon monoxide to soluble guanylate cyclase as observed with Resonance raman spectroscopy. *Biochemistry* 1996, *35*, 1540-7.
75. Tomita, T.; Ogura, T.; Tsuyama, S.; Imai, Y.; Kitagawa, T., Effects of GTP on bound nitric oxide of soluble guanylate cyclase probed by resonance Raman spectroscopy. *Biochemistry* 1997, *36* (Copyright (C) 2013 American Chemical Society (ACS). All Rights Reserved.), 10155-10160.
76. Andrew, C. R.; Green, E. L.; Lawson, D. M.; Eady, R. R., Resonance Raman Studies of Cytochrome c' Support the Binding of NO and CO to Opposite Sides of the Heme: Implications for Ligand Discrimination in Heme-Based Sensors. *Biochemistry* 2001, *40* (13), 4115-4122.
77. Reynolds, M. F.; Parks, R. B.; Burstyn, J. N.; Shelver, D.; Thorsteinsson, M. V.; Kerby, R. L.; Roberts, G. P.; Vogel, K. M.; Spiro, T. G., Electronic Absorption, EPR, and Resonance Raman Spectroscopy of CooA, a CO-Sensing Transcription Activator from R. rubrum, Reveals a Five-Coordinate NO-Heme. *Biochemistry* 2000, *39* (2), 388-396.
78. Kekilli, D.; Petersen, C. A.; Pixton, D. A.; Ghafoor, D. D.; Abdullah, G. H.; Dworkowski, F. S. N.; Wilson, M. T.; Heyes, D. J.; Hardman, S. J. O.; Murphy, L. M.; Strange, R. W.; Scrutton, N. S.; Andrew, C. R.; Hough, M. A., Engineering proximal vs. distal heme-NO coordination via dinitrosyl dynamics: implications for NO sensor design. *Chemical Science* 2017, *8* (3), 1986-1994.
79. Servid, A. E.; McKay, A. L.; Davis, C. A.; Garton, E. M.; Manole, A.; Dobbin, P. S.; Hough, M. A.; Andrew, C. R., Resonance Raman Spectra of Five-Coordinate Heme-Nitrosyl Cytochromes c': Effect of the Proximal Heme-NO Environment. *Biochemistry* 2015, *54* (21), 3320-7.
80. Lee, A. Q.; Streit, B. R.; Zdilla, M. J.; bu-Omar, M. M.; DuBois, J. L., Mechanism of and exquisite selectivity for O-O bond formation by the heme-dependent chlorite dismutase. *Proc. Natl. Acad. Sci. U. S. A.* 2008, *105* (41), 15654-15659.
81. Poulos, T. L., Thirty years of heme peroxidase structural biology. *Arch. Biochem. Biophys.* 2010, *500* (1), 3-12.

6. CHARACTERIZATION OF INTERMEDIATES IN CATALYTIC CHLORITE DECOMPOSITION BY CHLORITE DISMUTASE[5]

6.1. Abstract

The heme-based Cld enzymes catalyze unimolecular decomposition of ClO_2^- to yield Cl^- + O_2 and of BrO_2^- to give Br^- and O_2, albeit with lower catalytic efficiency. Both homopentameric *Da*Cld and homodimeric *Kp*Cld form Cpd II rapidly in pH-dependent reactions with excess $NaClO_2$ or $NaBrO_2$. Reactions with $NaClO_2$ reveal either a protein or $\bullet ClO_2$ radical that coexists with Cpd II, whereas only a protein radical was observed in reactions with $NaBrO_2$. Stopped-flow spectrophotometry of *Da*Cld with $NaBrO_2$ as a function of pH show that Cpd I is the primary accumulating heme intermediate under acidic conditions. Cpd II is the dominant intermediate under alkaline conditions. Reaction mixtures at intermediate pHs were shown by spectral decomposition to comprise Cpd I and Cpd II, wherein protein radical concentration tracked Cpd II formation and loss in specific activity. Therefore, the source of Cpd II is hypothesized to be proton-coupled electron transfer from a heme-pocket amino acid to the oxidized porphyrinate of Cpd I. The favoring of Cpd II + protein radical accumulation in alkaline solution is consistent with the amino acid oxidation being rate limited by transfer of its proton to a deprotonated base, which is most likely a hemin propionate group. Addition of NaClO with Cpd II + protein radical, generated by reaction with peracetic acid, did not yield O_2. Therefore, it is hypothesized that the catalytically active intermediate is Cpd I while Cpd II + protein radical is inactive toward O_2 production. Therefore, these data support a heterolytic O−X bond cleavage pathway for O_2 generation from either the ClO_2^- or the BrO_2^- substrate.

[5] Material in this chapter is currently unpublished and co-authored by Zachary Geeraerts, Olivia Stiller, Gudrun Lukat-Rodgers, and Kenton Rodgers. Zachary Geeraerts had primary responsibility in acquiring, processing, and interpreting all data presented here as original work. He also had full responsibility in figure-making and writing of all sections with guidance from the corresponding authors.

6.2. Introduction

Chlorite dismutase (Cld) is a heme *b* dependent enzyme that catalyzes the rapid and efficient decomposition of chlorite (ClO_2^-) to chloride (Cl^-) and molecular oxygen (O_2). Both clades of functional Clds are found in Gram-negative bacteria. Clade 1 contains Clds mostly found in perchlorate (ClO_4^-) respiring bacteria that undergo (per)chlorate respiration. clade 2 contains Clds found in non-perchlorate respiring bacteria and do not have a known *in vivo* function. The oligomeric state of Clds differs between these two clades where Clade 1 Clds are dominantly pentameric and clade 2 Clds are all dimeric. While both clades catalyze decomposition of ClO_2^-, the Clds found in clade 1 are several orders of magnitude more efficient.

Two mechanistic pathways have been proposed for catalytic ClO_2^- decomposition by Cld. The first involves heterolytic bond cleavage of the O−Cl bond upon formation of the enzyme substrate complex. This pathway leads to formation of a ferryl π cation radical known as Compound I (Cpd I) and a hypochlorite (OCl^-) fragment. This geminate pair then recombines to yield product as illustrated in Scheme 6.1. The second pathway instead undergoes homolytic bond cleavage of the O−Cl bond yielding a one-electron oxidized hemd comprising a ferryl group called Compound II (Cpd II) and a chlorine monoxide ($OCl\cdot$) fragment. Similar to the first pathway, this geminate pair recombines to produce O_2 and Cl^- while regenerating the ferric state of the enzyme.

Previous studies have elucidated potential reactive intermediates with substrate and with surrogate oxidizing agents. Non-native oxidants such as peracetic acid were used to verify the thermodynamic accessibility of Cpd I, in Cld from *Dechloromonas aromatica* (*Da*Cld), a clade 1 enzyme. Cpd II was also observed in reactions with peracetic acid (PAA) through sequential

reduction of Cpd I by either addition of ascorbic acid or by a nearby amino acid, tyrosine or tryptophan.[1] More recently, reactions involving the native substrate and Cld from Cyanothece sp. (CCld), a clade 2 enzyme, have revealed both Cpd I and Cpd II intermediates form. It was concluded that the Cpd II intermediate forms directly through the homolytic bond cleavage pathway and that the heterolytic bond cleavage pathway is not the dominant pathway to O_2 formation.[2]

The pH dependency of catalytic ClO_2^- decomposition remains elusive and cannot be accounted for by the homolytic pathway. The focus of this study is to address the pH dependency of Cld activity by use of both the native substrate, ClO_2^-, and bromite (BrO_2^-), a surrogate substrate that yields O_2. *Da*Cld and the Cld from *Klebsiella pneumoniae* (*Kp*Cld) were used as representatives for their respective clades.

6.3. Experimental Methods

6.3.1. Protein mutagenesis, expression, and purification.

Protein expression, isolation and purification of WT *Da*Cld and *Kp*Cld were carried out as previously described [3-4] The mutant plasmid for *Da*Cld(Y118F) was prepared from the WT *Da*Cld gene in the pET41a expression vector(ref) using a site directed mutagenesis kit and the following primer and its complement: 5'- G CCC TTG AAC TTC ATC AGC AAA G -3'. The mutagenic codon is underlined. Starting with the WT *Kp*Cld gene in a pET15b (Merck/Novagen) expression vector for production of protein with a N-terminal His-tag containing a TEV protease site to facilitate removal of the His-tag post purification,[5] a site directed mutagenesis kit and the primer 5'- C AAT GAA CGC TTC GTG GTG CGC G - 3'and its complement were used to generate the plasmid for *Kp*Cld(Y62F). Mutated plasmids were commercially sequenced to confirm the mutation. These plasmids were transformed into *E. coli* TunerDE3 cells, and the

corresponding proteins were expressed in cultures grown in Terrific Broth supplemented with ampicillin. Soluble mutant proteins were purified as previously described for their WT counterparts.[3-4] Protein purity was verified by sodium dodecyl sulfate polyacrylamide gel electrophoresis (SDS-PAGE). Purified *Da*Cld and its variant were constituted upon incubation with free hemin chloride on ice overnight. Stoichiometric loading was verified by protein and hemin quantification via Bradford and pyridine hemochromogen assays, respectively.[6-7] The His_6-tag on the N-terminus of WT *Kp*Cld and *Kp*Cld(Y62F) was removed from both enzymes with His_6-tagged tobacco etch virus (TEV) variant S219V which was isolated according to literature procedures.[4-5] Cleaved *Kp*Cld was separated from residual tagged *Kp*Cld and TEV(S219V) with a 5-mL Nickel-nitrilotriacetate sepharose column where the components were eluted with a linear gradient (20-500 mM imidazole). Separation, His_6-tag removal, and protein purity were verified by SDS-PAGE.

6.3.2. Activity assay for production of O_2.

A luminescence-based NEOFOX® system from Ocean Optics, Inc. was used to measure O_2 evolution during Cld-catalyzed chlorite or bromite decomposition under steady state conditions. The luminescence of the probe was calibrated to three known $O_2(aq)$ concentrations. O_2 production was measured over a range of pHs in the following buffers: 100 mM phosphate-citrate (pH <6), 100 mM phosphate (pH 6–8), or 100 mM glycine (pH >8). Samples were 10–100 nM Cld and 0.05–2 mM $NaClO_2$ or 5 μM Cld with 0.1–2 mM $NaBrO_2$. The probe was equilibrated in the buffer Cld solutions for 1–2 minutes prior to initiation of the reaction by introduction of oxidant. Kinetic traces were recorded at 0.1 s intervals for 1 – 2 minutes. Constituted WT *Da*Cld and *Kp*Cld specific activity measurements with $NaClO_2$ were consistent with values previously reported.[8-9]

O_2 experiments were performed involving NaClO, NaBrO, and peracetic acid (PAA). NaClO solutions were prepared by serial dilution in H_2O from commercial bleach containing 8.25% NaClO where its concentration was determined by the extinction coefficient (ε_{292} = 350 M^{-1} cm^{-1}).[10] PAA solutions were prepared via serial dilution into H_2O from a 32% (w/w) commercial stock stored at 4 ºC. NaBrO solutions were prepared by serial dilution as described below. Reactions between 5 μM *Da*Cld and 100 μM NaBrO were carried out at pH 5.2, 6.8, and 9.0 at 20 ºC and compared directly with 5 μM *Da*Cld and 100 μM $NaBrO_2$ under the same conditions. The probe was equilibrated in the buffered *Da*Cld solution for 1–2 minutes prior to initiation of the reaction by NaBrO or $NaBrO_2$. Reactions between 80 μM *Da*Cld and 160 μM PAA or NaClO followed by 160 μM NaClO or $NaClO_2$ were carried out at 9.0. The probe was equilibrated in a buffered *Da*Cld solution for 1–2 minutes prior to the addition of PAA or NaClO. After 20–40 seconds elapsed, the second oxidant (NaClO or $NaClO_2$) was added. Kinetic traces were recorded at 0.1 s intervals for 1–2 minutes for all reactions.

6.3.3. Sodium bromite synthesis.

Sodium bromite ($NaBrO_2$) was synthesized by controlled disproportionation of bromine (Br_2) under alkaline conditions based upon published procedures.[11 12]

$$2Br_2(l) + 2Ba(OH)_2(s) \rightarrow Ba(BrO)_2(aq) + BaBr_2(aq) + 2H_2O(l) \quad \text{(Eq. 6.1)}$$

$$2Ba(BrO)_2(aq) \rightarrow Ba(BrO_2)_2(s) + 2BaBr_2(aq) \quad \text{(Eq. 6.2)}$$

The crude extract was reacted with sodium thiosulfate ($Na_2S_2O_3$) which selectively reduced barium hypobromite ($Ba(BrO)_2$) to barium bromide ($BaBr_2$). Excess $BaBr_2$ was removed by addition of silver hydroxide (AgOH). Remaining Ba^{2+} ions were removed by addition of sodium sulfate to precipitate barium sulfate out of solution. Raman spectroscopy was used to verify successful isolation of $NaBrO_2$ as evidenced by its vibrational frequencies (709 cm^{-1}, 680 cm^{-1}

and 324 cm^{-1}).[13] The extinction coefficient for $NaBrO_2$ (ε_{295} = 115 M^{-1} cm^{-1})[11] was used to determine its concentration. A 4.0×10^{-2} M stock $NaBrO_2$ solution in 0.1 M NaOH was stored at –20 ºC.

Sodium hypobromite (NaBrO) was prepared in a similar manner to $NaBrO_2$ but with omission of the reduction of the crude extract from reaction (Equation 6.1) with $Na_2S_2O_3$. The identity and purity of the NaBrO was confirmed by its UV-visible spectrum (λ_{max} = 332 nm)[11] and its vibrational frequency (670 cm^{-1}) [13]. Stock solutions were stored at –20 ºC.

6.3.4. Synthesis of ^{18}O-labelled sodium chlorite.

Isotopically labelled sodium chlorite was synthesized by reduction of ^{18}O-enriched sodium chlorate with hydrogen peroxide in the two steps described in reactions 3 and 4, and based on literature procedures.[14] $NaCl^{18}O_3$ was prepared by oxygen atom exchange (OAE) of sodium chlorate in acidic ^{18}O enriched (97%) water. The OAE reaction was carried out in the presence of 6 M H_2SO_4 and 4 M $NaClO_3$ at 70 ºC.[15] Prior to heating the reaction to accelerate OAE, the acidic chlorate solution was purged with N_2(g) to remove residual ClO_2 formed upon addition of acid to the chlorate solution. After a 1-hour OAE period, the solution was cooled on ice, and 2 M H_2O_2 was added to generate ClO_2 (Equation 6.3). The flask containing the reaction mixture was connected via canula to a flask that contained 4 M NaOH and 2 M H_2O_2. (Equation 6.4). Then the reaction mixture was then warmed to ambient temperature, and the alkaline H_2O_2 solution was cooled in an ice-water bath. A stream of N_2(g) was bubbled through the ClO_2 solution to carry ClO_2(g) to the flask containing the alkaline H_2O_2 solution. The reaction shown in Eq. 4 was allowed to proceed for 2 hours.

$$2NaClO_3(aq) + 2H_2SO_4(aq) + H_2O_2(aq) \rightarrow O_2(g) + ClO_2(g) + 2H_2O(l) + 2NaHSO_4(aq) \quad \text{(Eq. 6.3)}$$

$$2ClO_2(g) + 2NaOH(aq) + H_2O_2(aq) \rightarrow 2NaClO_2(aq) + O_2(g) + 2H_2O(l) \quad \text{(Eq. 6.4)}$$

The resulting ^{18}O-enriched chlorite was crystalized from isopropyl alcohol as the sodium salt, vacuum filtered, air dried, and stored in a desiccator over anhydrous $CaSO_4$. Isotope enrichment of ~70% and chemical purity were determined by Raman spectroscopy. The extinction coefficient for $NaClO_2$ ($\varepsilon_{295} = 155\ M^{-1}\ cm^{-1}$)[16] was used to determine stock solution concentrations.

6.3.5. Coupled time-resolved UV-vis and resonance Raman experiments.

Time-resolved resonance Raman (rR) spectra of the reaction of *Da*Cld and $NaClO_2$ at pH 6.8 and 9.0 and the reaction of *Kp*Cld and $NaClO_2$ at pH 6.0 and 9.0 were obtained at –5 °C. Temperature was controlled with a home-made liquid N_2 boil-off system. Spectra were acquired from 10 – 15 μM (in heme) Cld samples in 5-mm NMR tubes spinning at ~20 Hz using a home-made spinner. UV-visible spectra were monitored during the rR experiment using a diode array spectrometer. The rR spectra were recorded on the locally built, spectrometer previously described in Chapter 5.[4] Resonance Raman scattering was excited with the 413.1-nm emission from a Kr^+ laser. Laser powers ranged from 5 to 10 mW at the sample. The spectrometer was calibrated against the absolute Raman shifts of toluene and dimethylformamide.

6.3.6. Electron paramagnetic resonance experiments.

EPR samples were prepared in 4-mm quartz tubes by rapidly mixing a given Cld with a $NaXO_2$ solution using a T-mixer followed by rapid freezing in an acetone slush bath (−95 °C). Final enzyme concentrations ranged from 25–100 μM. Oxidant concentrations ranged from 25–150 mM $NaClO_2$ and 0.5–2 mM $NaBrO_2$. The 9.3 GHz EPR spectra were recorded at 77 K on a Varian E9 spectrometer equipped with a liquid nitrogen immersion Dewar. The spectra for WT *Da*Cld or *Kp*Cld enzymes reacted with $NaClO_2$ or $NaBrO_2$ at pH 5.2, 6.0, 6.8, and 9.0 were typically recorded using 0.05–0.20 mW microwave power, 2 G modulation amplitude, 100 kHz

modulation frequency. EPR signals were referenced to solid pitch diluted in KCl. Spin quantification was carried out by comparison of the double integral of sample EPR signal over 3200 – 3400 G with the double integral of a 4-amino-2,2,6,6-tetramethylpiperidinyloxy (4-amino TEMPO) standard (98 μM) EPR signal measured under similar conditions.[17] Spectra were simulated with EasySpin software used to determine spectral g-values.[18]

The 413.1 nm-excited resonance Raman spectra of the EPR samples were recorded in the 4 mm quartz tubes while spinning submerged in a liquid nitrogen immersion Dewar at 77 K. The laser power at the samples ranged between 4 – 10 mW. The spectrometer was calibrated against the absolute Raman shifts of liquid toluene.

6.3.7. Stopped-flow spectrophotometry.

Reactions of WT *Da*Cld with $NaBrO_2$ were carried out on a locally modified Applied Photophysics PiStar stopped-flow system at pHs 5.2, 6.0, 6.8, and 9 in a 10 mm pathlength cell at 20 °C. All experiments used 5 μM *Da*Cld (hemin concentration) with concentrations of $NaBrO_2$varying from 5 to 100 μM (after mixing). $NaBrO_2$ solutions were made immediately prior to the stopped-flow experiment from a freshly thawed aliquot of the 4.0×10^{-2} M $NaBrO_2$ stock. Nine measurements were averaged. Reactions between 80 μM *Da*Cld and 80–160 μM PAA (after mixing) were also carried out on the same stopped-flow system at pH 7.1 and 9.0 in a 2 mm pathlength cell at 20 °C. PAA solutions were prepared from a 32% (w/w) PAA stock solution via serial dilution in H_2O within minutes of the experiment. Reactions of WT *Kp*Cld and *Kp*Cld(Y62F) with $NaBrO_2$ and $NaClO_2$ were also carried out on the aforementioned stopped-flow system at 20 °C, pH 5.2 and 6.0. These experiments used 2 μM *Kp*Cld (hemin concentration), 500 μM $NaClO_2$, and 20 μM $NaBrO_2$.

6.4. Results

6.4.1. A low spin reaction intermediate is observed for dimeric and pentameric Clds during chlorite decomposition.

Time-resolved absorbance and Soret-excited rR spectra were collected concurrently from reaction mixtures of *Da*Cld and $NaClO_2$ at −5 ºC. Those spectra are shown in Figure 6.1 and both time courses reveal a LS hemin species at 20 s (first time point) that rapidly decays back to resting enzyme at pH 6.8. The 413.1-nm excited rR spectra (Figure 6.1A) show an upshift in ν_3, a spin state marker band, from 1493 cm^{-1}, a frequency typical of 5cHS hemin to 1510 cm^{-1}, which falls in the frequency range for 6cLS hemin. A frequency upshift of the ν_4 oxidation state marker band, from 1372 cm^{-1} to 1378 cm^{-1} and loss of intensity in the 1523 cm^{-1} ν_{38} marker band, commonly associated with HS hemin, are also observed. Some intensity is lost at 1620 cm^{-1} and gained around 1640 cm^{-1}, these frequencies being associated with HS and LS ν_{10} modes, respectively. Structural changes associated with these changes in vibrational signatures are corroborated by the optical absorbance spectra (Figure 6.1B) where both the Soret and Q bands shift red from their positions in the resting enzyme spectrum. The Soret maximum shifts from ~395 nm to 407 nm while $Q_{0,0}$ shifts from ~540 nm to 551 nm and $Q_{0,1}$ shifts from 510 nm to 522 nm. Additionally, absorbance is lost at the 646 nm CT band. All these spectral signatures are consistent with formation of a LS Fe(IV) species. As the reaction proceeds, the ν_4 frequency shifts back to 1372 cm^{-1} within 5 minutes while the ν_3 band at 1492 cm^{-1}, the ν_{38} band at 1523 cm^{-1}, and intensity at 1620 cm^{-1} are all partially regained. Simultaneously, intensity at 1510 cm^{-1} and intensity gained near 1640 cm^{-1} at short times are lost. These changes reflect the loss of transient LS heme as the HS heme characteristic of the resting enzyme re-emerges. The optical absorbance spectra reflect these changes as well. The Soret maximum shifts from 407 nm to 403

nm within 5 minutes without further change after another 20 minutes. Both $Q_{0,0}$ and $Q_{0,1}$ shift back to ~540 nm and 510 nm, respectively while the CT band at 646 nm gains extinction. These spectral signatures are consistent with a mixture of 5c and 6c HS hemin.

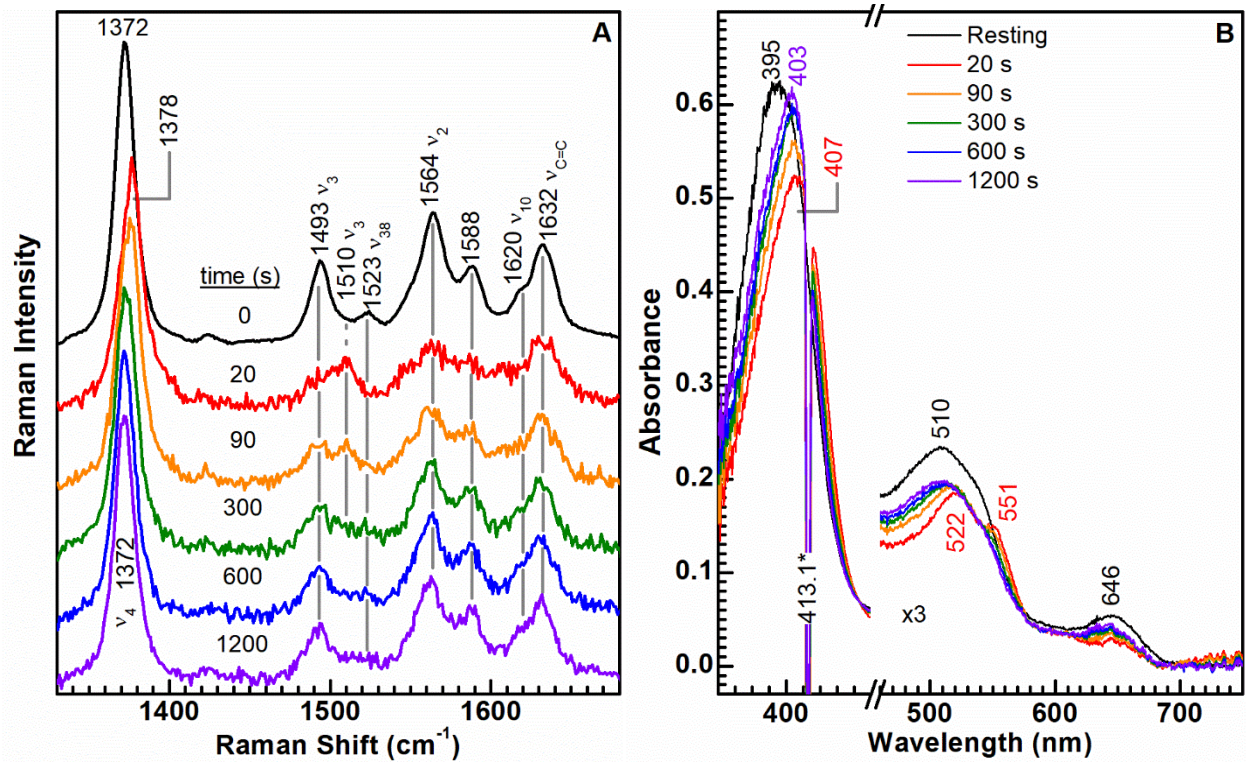

Figure 6.1. Time-resolved reaction between 15 μM *Da*Cld and 50 mM $NaClO_2$ at −5 °C in 0.1 M sodium phosphate pH 6.8 buffer. A) The 413.1-nm excited rR spectra at 6.7 mW power show formation of an intermediate whose spectral signatures are consistent with a high valent iron (ferryl) that decays back to the resting state. B) The optical absorbance spectra collected alongside the rR spectra reveal a change in the absorbance spectrum consistent with a LS hemin that decays gradually back toward the HS resting state.

Data collected at pH 9.0 (Figure 6.2) show similar trends in heme speciation. The resting enzyme spectrum of *Da*Cld at pH 9.0 is dominated by the ferric heme-hydroxide complex (pK_a 8.7) which is in equilibrium between its 6cHS and 6cLS spin states. Some borate from the buffer system may have coordinated as well giving rise to the more intense 6cHS ν_3 band at 1479 cm^{-1} (Figure 6.2A). The first recorded spectrum at pH 9.0 shows diminished ν_3 intensity at 1479 cm^{-1} while the ν_3 band at 1506 cm^{-1} shifts to 1510 cm^{-1} with greater intensity. The ν_4 band also shifts

from 1375 cm^{-1} to 1378 cm^{-1}, all consistent with loss in 6cHS hemin and formation of the 6cLS species observed at pH 6.8. These changes are corroborated by the optical absorbance spectra (Figure 6.2B) wherein Soret extinction is lost at 408 nm and gained at 524 and 552 nm in the Q−band region. The CT band at 606 nm, likely due to coordination of borate, also loses extinction. The loss of this LS species at pH 9.0 is more gradual than at pH 6.8 as it takes nearly 10 minutes for the ν_4 to shift back to 1375 cm^{-1}. The ν_3 envelope regains intensity at 1479 cm^{-1} as the reaction proceeds while losing intensity at 1510 cm^{-1}. This transition back to a ferric spin-crossover resting state is also observed in the absorbance spectrum. These data suggest that, regardless of pH, the enzyme cycles through a common high-valent LS intermediate. Both rR and optical absorbance spectra are similar to that published for *Da*Cld reacted with PAA which forms a Cpd II + amino acid radical species.[1] An isotope labeling experiment was performed at pH 9.0 (Figure E1) using ^{18}O-enriched $NaClO_2$ (>70%) to assign the LS intermediate as either a peroxo or Cpd II, both of which comprise O-coordinated exogenous axial ligands. No isotope-sensitive band was observed in the rR spectrum. This suggests a number of possibilities, including that the oxygen atom for the LS intermediate doesn't originate from $NaClO_2$, the oxygen atom does come from ClO_2^- but readily exchanges with solvent at this pH, or the reactive intermediate does not accumulate to detectable levels during the reaction because subsequent steps promptly consume it. Previous isotope studies revealed that the source of O_2 atoms is from ClO_2^-.[15] Therefore, the likely explanation is due to sub-detectable accumulation of the intermediate.

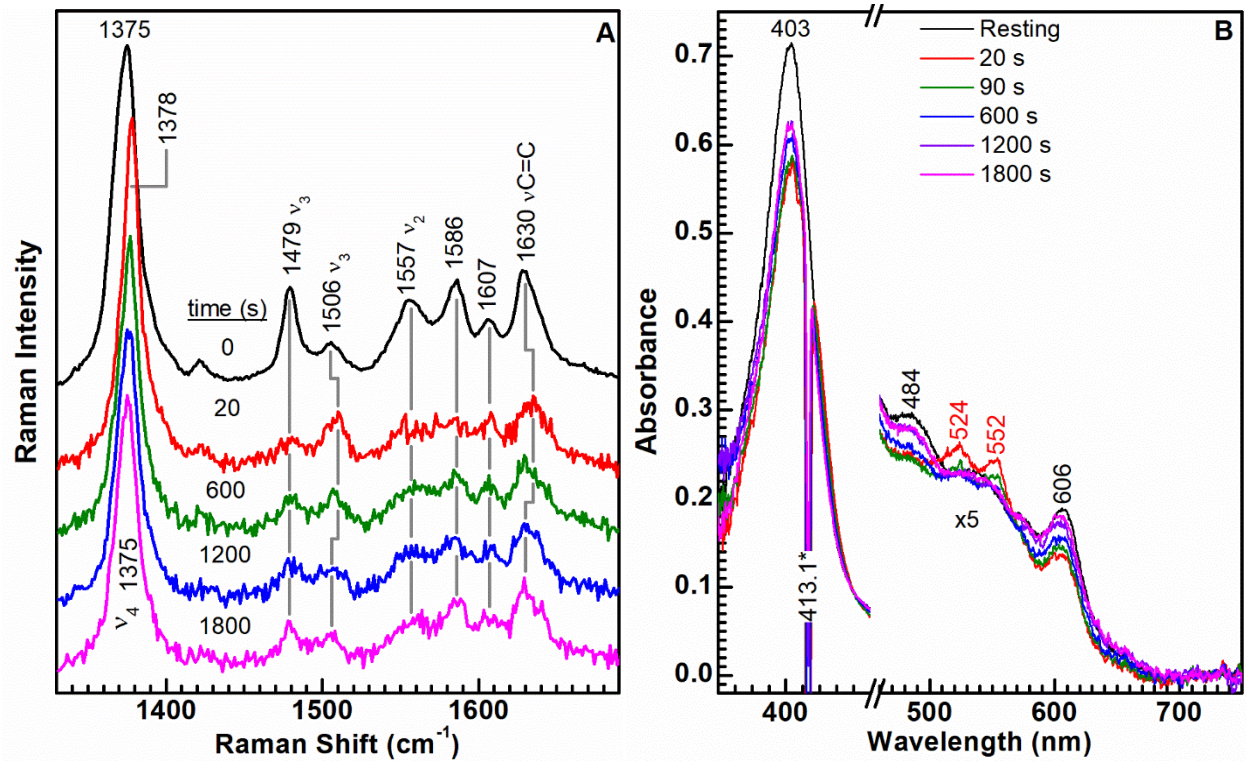

Figure 6.2. Time-resolved reaction between 15 μM *Da*Cld and 36 mM $NaClO_2$ at −5 °C in 0.1 M sodium borate pH 9.0 buffer. A) The 413.1-nm excited rR spectra at 5.3 mW power show formation of an intermediate whose spectral signatures are consistent with a high valent iron (ferryl) that decays slowly back to the starting state. B) The optical absorbance spectra collected alongside the rR spectra reveal a change in the absorbance spectrum consistent with LS hemin that decays gradually back toward the mixed spin system starting state.

A similar trend was observed when tracking the reaction between the homodimeric *Kp*Cld and $NaClO_2$ with rR and absorbance spectroscopy. Figure 6.3 shows a LS intermediate at 20 s that rapidly returns to resting enzyme over the course of five minutes at pH 6.0. The LS intermediate has similar Raman features (Figure 6.3A) as described for *Da*Cld: ν_3 at 1508 cm^{-1}, ν_4 at 1376 cm^{-1}, with an increase in ν_{10} intensity around 1640 cm^{-1}, commonly associated with LS heme. Some HS hemin remains as evidenced by ν_3 intensity at 1484 cm^{-1}, indicative of 6cHS, corresponding to a ferric aqua complex, which is favored at low temperature. As time elapses, the LS signatures lose intensity, ν_3 at 1508 cm^{-1} and ν_4 at 1376 cm^{-1}, while the resting enzyme 6cHS signatures gain intensity, ν_4 at 1371 cm^{-1} and ν_3 at 1484 cm^{-1}. These data are

corroborated by absorbance spectra (Figure 6.3B) recorded during rR spectral acquisition. The UV-visible spectrum of the LS intermediate has a Soret maximum around 413 nm and Q-band maxima at 554 nm and 520 nm. The sharp feature at 413.1 nm is Rayleigh-scattered light from the laser line used to excite rR scattering. The LS intermediate subsequently decays as indicated by absorbance loss at 554 and 520 nm while gaining Q−band absorbance at 505 nm and ligand-to-metal charge transfer (LMCT) absorbance at 640 nm. The Soret maximum also shifts back toward 403 nm from 413 nm, consistent with reformation of HS hemin. Reaction of *Kp*Cld with $NaClO_2$ at pH 9.0 (Figure 6.4) also generates the same LS intermediate and like that which accumulates in the *Da*Cld reaction, it persists longer at pH 9.0 than at pH 6.0. Also, like *Da*Cld, *Kp*Cld coordinates hydroxide with pK_a 8.3[9] Soret excited rR (Figure 6.4A) spectra reveal the spin crossover behavior of the hemin-hydroxide complex in the resting enzyme. The 6cHS and 6cLS ν_3 bands were observed at 1479 cm^{-1} and 1507 cm^{-1}, respectively. Upon reaction with $NaClO_2$, loss of the 6cHS component is evidenced by the absence of Raman intensity at the 1479-cm^{-1} ν_3 and 1564-cm^{-1} ν_2 frequencies commonly associated with HS hemin. Consequently, the LS ν_3 intensity increases and shifts to 1509 cm^{-1} while the LS ν_{10} intensity at 1642 cm^{-1} also increases. Together with the ν_4 increase from 1375 cm^{-1} to 1377 cm^{-1}, these spectral signatures are consistent with the same LS intermediate observed at pH 6.0. These spectral signatures are lost over time and slowly convert back toward the resting enzyme spectrum. Consistent with rR results, the absorbance spectra in Figure 6.4B also exhibit transient features characteristic of the LS intermediate. The Soret band maximum shifts from 407 nm to ~415 nm. The Q−band at ~505 nm, which is associated with the HS hemin, loses absorbance while those associated with the LS hemin shift from 540 and 574 nm to 525 and 556 nm, respectively. The LMCT band at 606 nm also loses all absorbance. This series of absorbance spectra reveal that the enzyme does not fully

return to its HS resting state after reaction with excess ClO_2^-. The optical absorbance spectra for the LS intermediate observed here is similar to that published for ClO_2^- reacted CCld which has been assigned as Cpd II.

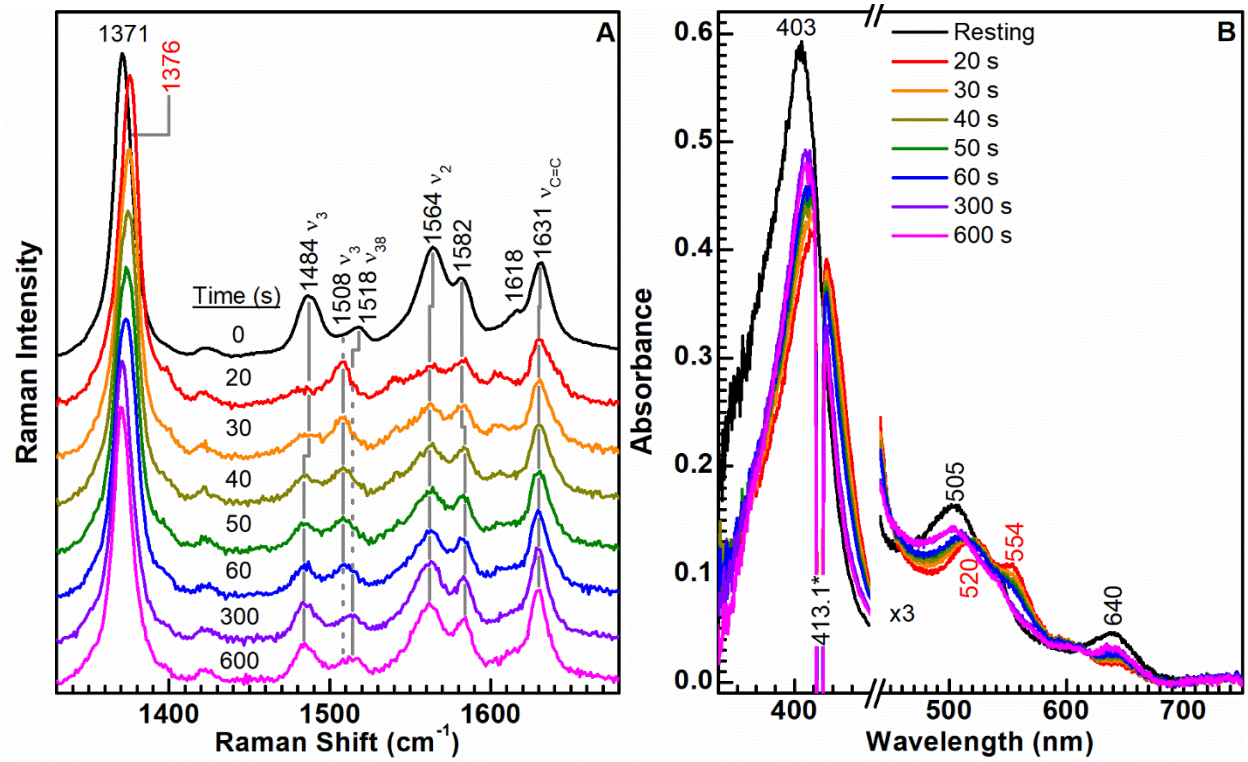

Figure 6.3. Time-resolved reaction between 10 μM *Kp*Cld and 10 mM $NaClO_2$ at −5 °C in 0.1 M sodium phosphate pH 6.0 buffer. A) The 413.1-nm excited rR spectra at 9.6 mW power show formation of an intermediate whose spectral signatures are consistent with a high valent iron (ferryl) that decays rapidly back to the starting state. B) The optical absorbance spectra collected alongside the rR spectra reveal a change in the absorbance spectrum consistent with a LS hemin that decays rapidly back toward the starting HS state. The spike in the spectrum is a 413.1 nm laser line artifact due to simultaneous acquisition of the UV-visible and rR spectra.

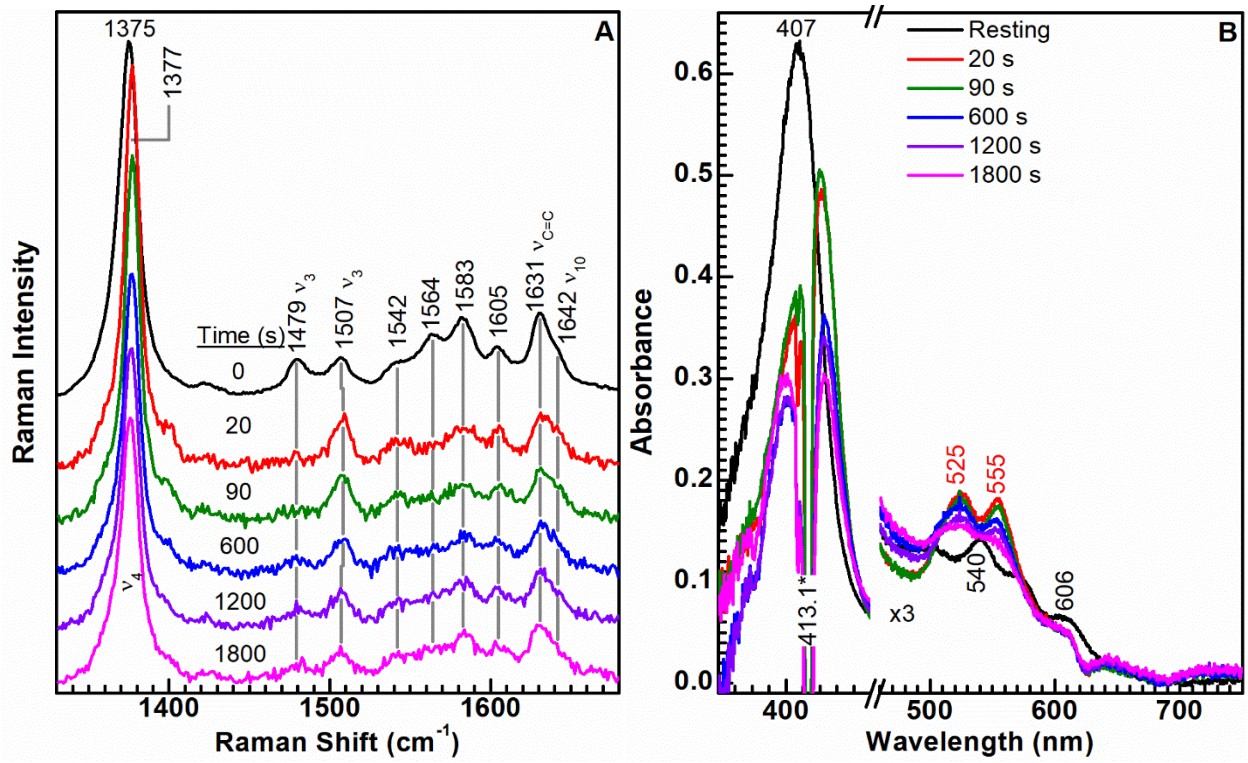

Figure 6.4. Time-resolved reaction between 10 μM *Kp*Cld and 10 mM $NaClO_2$ at −5 °C in 0.1 M sodium borate pH 9.0 buffer. A) The 413.1-nm excited rR spectra at 9.0 mW power show formation of an intermediate whose spectral signatures are consistent with a high valent iron (ferryl) that decays slowly back to the starting state. B) The optical absorbance spectra collected alongside the rR spectra reveal a shift in the absorbance spectrum consistent with a LS hemin that decays gradually back toward the mixed spin state.

6.4.2. Iron-oxygen stretching frequency confirms intermediate is Compound II.

An isotope labeling experiment was performed at pH 9.0 using $NaCl^{18}O_2$ to assign the LS intermediate as either a peroxo (Fe^{III}–O–O) or ferryl (Fe^{IV}=O), both of which comprise O-coordinated exogenous axial ligands. An isotope-sensitive Raman shift was observed for the reaction mixture of *Kp*Cld with $NaCl^{18}O_2$ (Figure E2). The low frequency window (Figure E2A) revealed a difference feature between natural abundance and $NaCl^{18}O_2$. This difference feature was fit to two Gaussian bands with slightly different band widths at 772 cm^{-1} and 749 cm^{-1} for natural abundance and $NaCl^{18}O_2$, respectively. The high-frequency window (Figure E2B) showed the heme speciation between both natural abundance and $NaCl^{18}O_2$ to be identical.

Considering the different peak widths may have been attributable to the overlapping borate buffer bands, the same experiment was carried out in glycine at pH 9 (Figure E3). The same difference feature was observed in the low frequency window with slightly different values from the previous experiment when fit to two Gaussian peaks with identical widths: 775 cm^{-1} for natural abundance $NaClO_2$ and 750 cm^{-1} for $NaCl^{18}O_2$. Again, the high frequency window (Figure E3B) reveals the heme speciation for both reactions are identical. While the frequency value and isotope shift were consistent with the Fe^{IV}=O stretching mode of a ferryl heme,[19] the Fe^{III}–O_2^{2-} stretching mode of a hemin-peroxo complex could not be ruled out.

Therefore, the same reaction was carried out at pH 6 with natural abundance $NaClO_2$ in both natural abundance H_2O and ^{18}O-enriched (85 atom %) H_2O (Figure E4). The low frequency window revealed a subtle difference feature in the same region observed at alkaline pH (Figure E4A). Peak maxima differed slightly when fit to two Gaussian peaks with the same width: 775 cm^{-1} for natural abundance H_2O and 754 cm^{-1} for $H_2{}^{18}O$. The high frequency window (Figure E4B) shows the speciation between the two reactions to be identical and shows that speciation is not purely 6cLS as evidenced by the HS ν_3 at 1482 cm^{-1} owing to the lower amplitudes for the difference feature. These data demonstrate that the intermediate contains a solvent exchangeable oxygen atom which is likely that of a ferryl group. However, this does not preclude the possibility that a ferryl only transiently forms prior to a product-committed intermediate in which the O−O bond has formed, specifically a hemin−peroxyhypochorite complex.

If the ^{18}O-sensitive rR band described above was attributable to a peroxyhypochlorite complex, its analogous Raman shift should occur at lower frequency in a peroxyhypobromite complex due to the reduced mass increase upon replacing Cl with Br. This was addressed by synthesizing $NaBrO_2$ to use as a surrogate substrate. After demonstrating through the O_2

evolution assay that the decomposition of BrO_2^- to Br^- and O_2 (data not shown) is catalyzed by *Kp*Cld at pH 9.0, the reaction with excess $NaBrO_2$ was tracked by rR spectroscopy at −5 ºC (Figure 6.5). The reaction mixture exhibited the same rR features as that with natural abundance $NaClO_2$ (Figure 6.5B). Moreover, the difference feature between the intermediate formed with $NaBrO_2$ and $NaCl^{18}O_2$ was identical to that observed between natural abundance and ^{18}O-enriched $NaClO_2$ (Figure 6.5A). Therefore, it was concluded that the difference in halogen mass does not affect the rR spectrum of the intermediate and that the accumulating LS intermediate is a ferryl heme whose spectral signatures are consistent with Compound II (Cpd II).

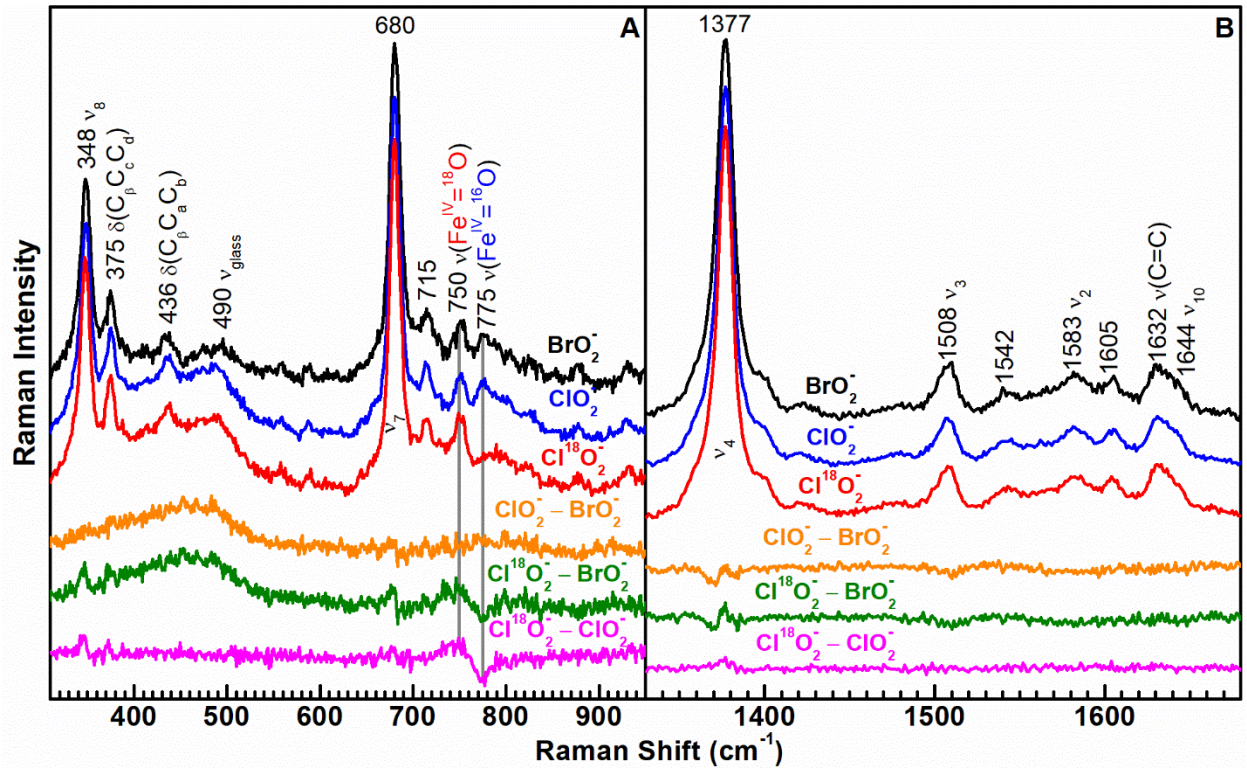

Figure 6.5. Stack plot of 413.1-nm excited rR spectra at 9 mW power one minute after the reaction between 10 μM *Kp*Cld and $NaXO_2$ at −5 °C in 0.1 M sodium borate pH 9.0 buffer. Black spectra correspond to 130 mM $NaBrO_2$ reacted, blue spectra correspond to 10 mM natural abundance $NaClO_2$ reacted, and red spectra correspond to 10 mM $NaCl^{18}O_2$ (77% isotopic enrichment) reacted *Kp*Cld. Orange, green, and magenta difference spectra were generated by one-to-one subtraction as indicated in the figure. A) low frequency window reveals that the ClO_2^- and BrO_2^- reacted *Kp*Cld give rise to the same isotope sensitive difference feature when subtracted from $Cl^{18}O_2^-$ reacted *Kp*Cld. B) high frequency window shows speciation between isotope labeled, natural abundance $NaClO_2$, and $NaBrO_2$ are nearly identical.

6.4.3. pH dependent protein-radical formation is observed for dimeric and pentameric clds during chlorite reaction.

The presence of Cpd II as the prominent intermediate led us to investigate where the corresponding radical resides as Cpd I is known to be readily reduced to Cpd II by tyrosine and tryptophan, both of which occupy the heme pocket. Freeze-quenched samples of *Da*Cld and *Kp*Cld reacted with $NaClO_2$ were first examined by X-band EPR spectroscopy (i.e. before irradiation by violet LASER light to excite rR scattering). Since EPR spectra of stock $NaClO_2$ solutions revealed the presence of some $\bullet ClO_2$ (Figure E5), they were purged with $N_2(g)$ prior to their reaction with Cld. The X-band EPR spectra of reaction mixtures containing *Da*Cld and excess $NaClO_2$ (Figure 6.6A) reveal a radical signature at pH 9.0 that is consistent with $\bullet ClO_2$ (g = 2.023).[20] The radical observed at pH 6.8 is consistent with a protein-based radical (g = 2.0068) previously reported for PAA reacted *Da*Cld[1]; however, may also have $\bullet ClO_2$ superimposed based on intensity at 3279 G arbitrarily increasing the observed g-value and narrowing its width (13 G). Poor S/N did not allow for precise spin quantification of these radicals. Soret-excited rR spectra (Figure 6.6B) showed formation of Cpd II. At pH 9.0 the ν_4 at 1379 cm^{-1}, ν_3 at 1508 cm^{-1}, and ν_{10} around 1640 cm^{-1} are typical of Cpd II. There is also intensity at 1473 cm^{-1} which could be assigned as a 6cHS ν_3 band. However, this frequency is too low to be assigned as a coordinated hydroxide (1479 cm^{-1} HS), borate (1479 cm^{-1} HS), or water (1484 cm^{-1}). Considering the shoulder at 1359 cm^{-1}, typically associated with Fe(II) ν_4, it is likely that some of the ferric hemin underwent photo-induced reduced to 5cHS ferrous heme, for whiche the ν_3 occurs at 1474 cm^{-1}.

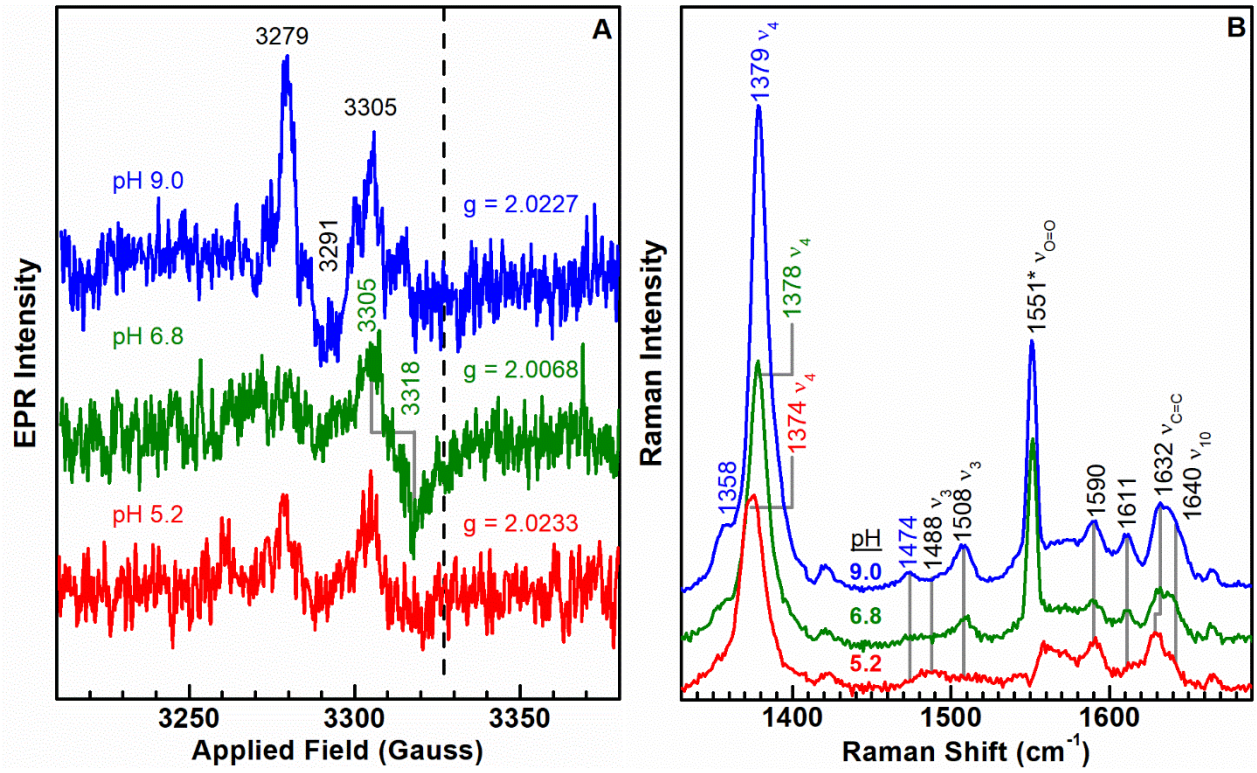

Figure 6.6. Freeze-quenched samples of 30 μM *Da*Cld reacted with 150 mM $NaClO_2$ at pH 5.2, 6.8, and 9.0 where t_{rxn} = 1 second. A) X-band (9.300 GHz) EPR spectra at 77 K using 0.2 mW power reveal radical signatures consistent with chlorine dioxide at pH 5.2 & 9.0 and a protein-based radical at pH 6.8. Dashed line indicates field where an OCl• radical feature would be expected. B) 413.1-nm excited resonance Raman spectra at 77 K using 8.3 mW power shows a greater amount of Cpd II forms with increasing pH. Some evidence for photoinduced reduction to Fe(II) is observed based on the bands at 1359 cm^{-1} and 1473 cm^{-1}. Asterisk denotes dissolved oxygen in the immersion Dewar.

Freeze-quenched samples of *Kp*Cld and $NaClO_2$ were also examined by EPR (Figure 6.7A). These data show spectral signatures characteristic of $•ClO_2$ at pH 9.0 and 6.8 (g_{iso} = 2.0233). An EPR spectrum consistent with a protein-based radical was observed at pH 5.2 (g_{iso} = 2.0056, 19 G width). Similar to *Da*Cld, the Soret-excited rR spectrum of $NaClO_2$ + *Kp*Cld showed evidence of Cpd II at pH 9.0 based on the 1509 cm^{-1} ν_3 (Figure 6.7B). Unlike *Da*Cld, a ν_3 band at the 6cHS frequency of 1484 cm^{-1}, which has been assigned as an aqua complex,[9] dominated throughout the pH range. This partial conversion to Cpd II at t_{rxn} = 1 s may be due to

a lesser excess of $NaClO_2$ than was used for *Da*Cld and, in part, due to the lower reactivity of *Kp*Cld.

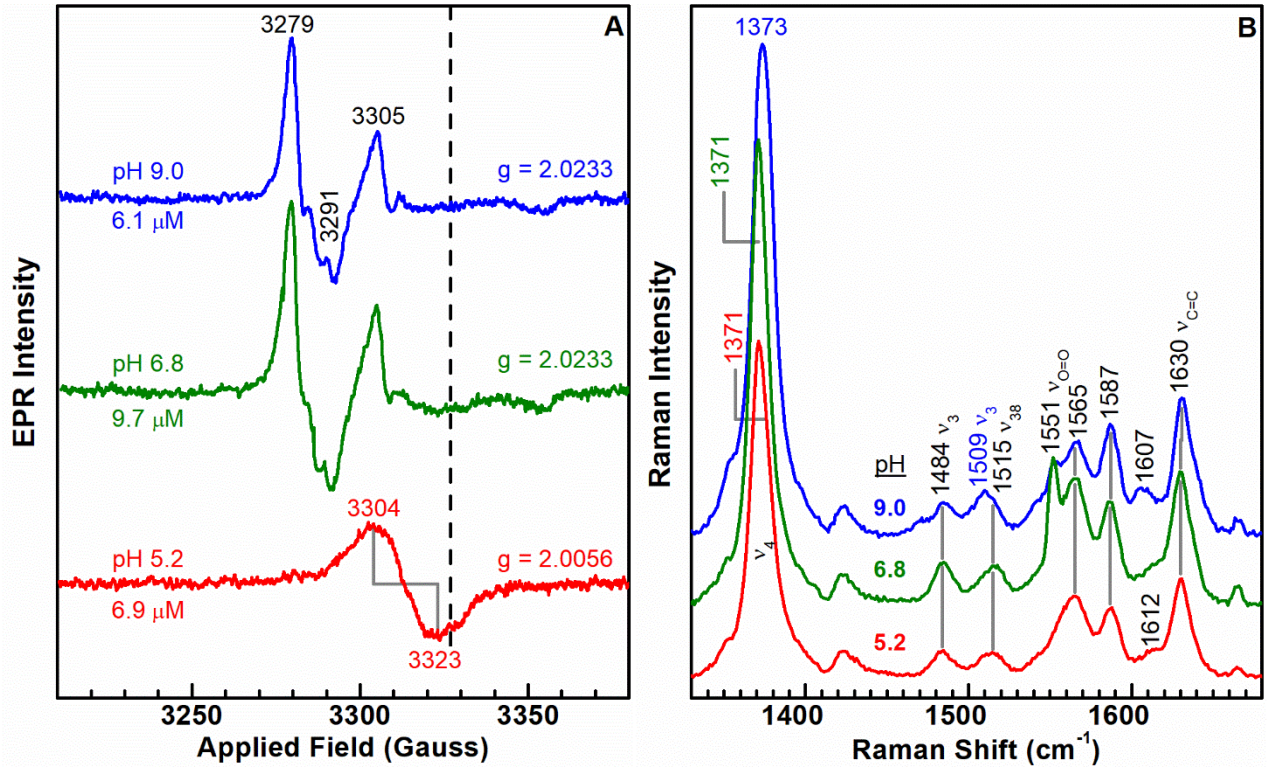

Figure 6.7. Freeze-quenched samples of 30 μM *Kp*Cld reacted with 30 mM $NaClO_2$ at pH 5.2, 6.8, and 9.0 where t_{rxn} = 1 second. A) X-band (9.300 GHz) EPR spectra at 77 K using 0.2 mW power reveal radical signatures consistent with chlorine dioxide at pH 9.0 & 6.8 and a protein-based radical at pH 5.2. Concentrations of the observed radical determined by their respective areas normalized to 4-Amino TEMPO are listed below the corresponding spectra. Dashed line indicates field where an OCl• radical feature would be expected. B) 413.1-nm excited resonance Raman spectra at 77 K using 8.3 mW power shows a greater amount of Cpd II forms with increasing pH. Asterisk denotes dissolved oxygen in the immersion Dewar.

6.4.4. Clds react with bromite to generate O_2.

As indicated earlier $NaBrO_2$ was used as a surrogate substrate for O_2 production in place of $NaClO_2$. Both *Kp*Cld and *Da*Cld react with slight excesses (< 100 mol equivalents) of $NaBrO_2$ to yield stoichiometric amounts of O_2. When catalytic concentrations (1×10^{-8} M) of Cld are reacted with large excesses of $NaBrO_2$ (1×10^{-3} M), no O_2 is detected. This suggests that Cld has a lower turnover number with $NaBrO_2$ than $NaClO_2$ due to rapid enzyme inactivation.

Consequently, O_2 production activity for Cld with $NaBrO_2$ as the substrate is significantly lower than with $NaClO_2$. The Michaelis-Menten equation was used to model initial rate of O_2 production as a function of $NaBrO_2$ concentration for *Da*Cld at pH 5.2 and 20 ºC (Figure 6.8). The resulting fit provided a $k_{cat} = (2.0\pm0.2)\times10^2$ s^{-1} and $K_M = (1.8\pm0.2)\times10^{-3}$ M yielding a k_{cat} / $K_M = (1.2\pm0.2)\times10^5$ M^{-1} s^{-1}. For the *Da*Cld/ $NaClO_2$ reaction at pH 5.2 and 4 ºC k_{cat} = $(2.0\pm0.6)\times10^4$ s^{-1} and $K_M = (6.2\pm0.7)\times10^{-4}$ M yielding a k_{cat} / $K_M = (3.2\pm0.4)\times10^7$ M^{-1} s^{-1}.[8] The k_{cat} for $NaBrO_2$ is three orders of magnitude lower than for $NaClO_2$ while the K_M is one order of magnitude higher. Consequently, the k_{cat} / K_M is two orders of magnitude lower for $NaBrO_2$ than $NaClO_2$. These data demonstrate that *Da*Cld is less efficient and less active toward producing O_2 from $NaBrO_2$. Due to low activities, it was not possible to determine Michaelis-Menten parameters at pH 6.8 and 9.0 (data not shown).

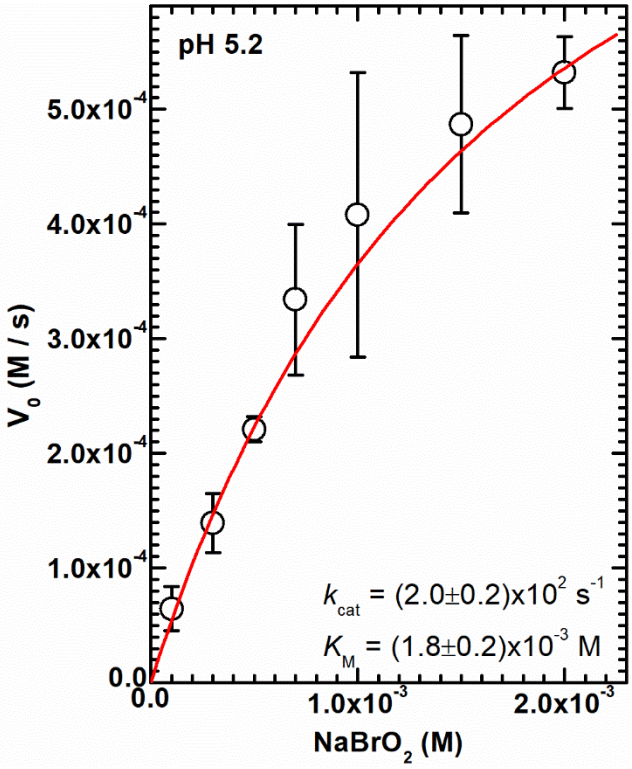

Figure 6.8. Michaelis-Menten curve for 5 µM *Da*Cld + 100–2,000 µM $NaBrO_2$ in 0.1 M sodium citrate pH 5.2 at 20 ºC. Each point represents an average of three or four trials. Error bars correspond to the standard deviation between trials for each point.

Since NaBrO is a common contaminant in $NaBrO_2$ synthesis, a direct comparison between both oxidants was made (Figure E6). No O_2 was detected with NaBrO, but near stoichiometric amounts of O_2 were produced (90±26 μM) when compared with the amount of $NaBrO_2$ added (100 μM). Therefore, all O_2 produced originates from the reaction with $NaBrO_2$ and not any residual NaBrO.

6.4.5. The accumulation of protein-based radical is pH dependent in Cld catalyzed bromite reactions.

To avoid $\bullet ClO_2$ from interfering with interpretation of the EPR spectra at neutral and alkaline pH, reactions were carried out with the surrogate substrate $NaBrO_2$ because during those reactions there were no EPR features attributable to BrO_2. Freeze-quenched reaction mixtures of $NaBrO_2$ and Cld were generated and examined by X-band EPR spectroscopy. The EPR spectra of reaction mixtures with *Da*Cld and $NaBrO_2$ revealed a protein-based radical (g = 2.0044, 19 G width) whose concentration tracked proportionally with increasing pH (Figure 6.9A). The increase in protein-based radical could be tied to an increase in Cpd II. The Soret-excited rR spectra show Cpd II is present at all three pH's suggesting protein radical concentration may not be tied to Cpd II formation. However, it has been documented that Cpd I can be photoreduced to Cpd II with Soret excitation during rR experiments.[21] Therefore, it is possible that the Cpd II observed at the lower pH is due to photoreduction from Cpd I and not due to reduction by a specific amino acid side chain. This explanation is supported by stopped-flow spectrophotometry *vide infra*.

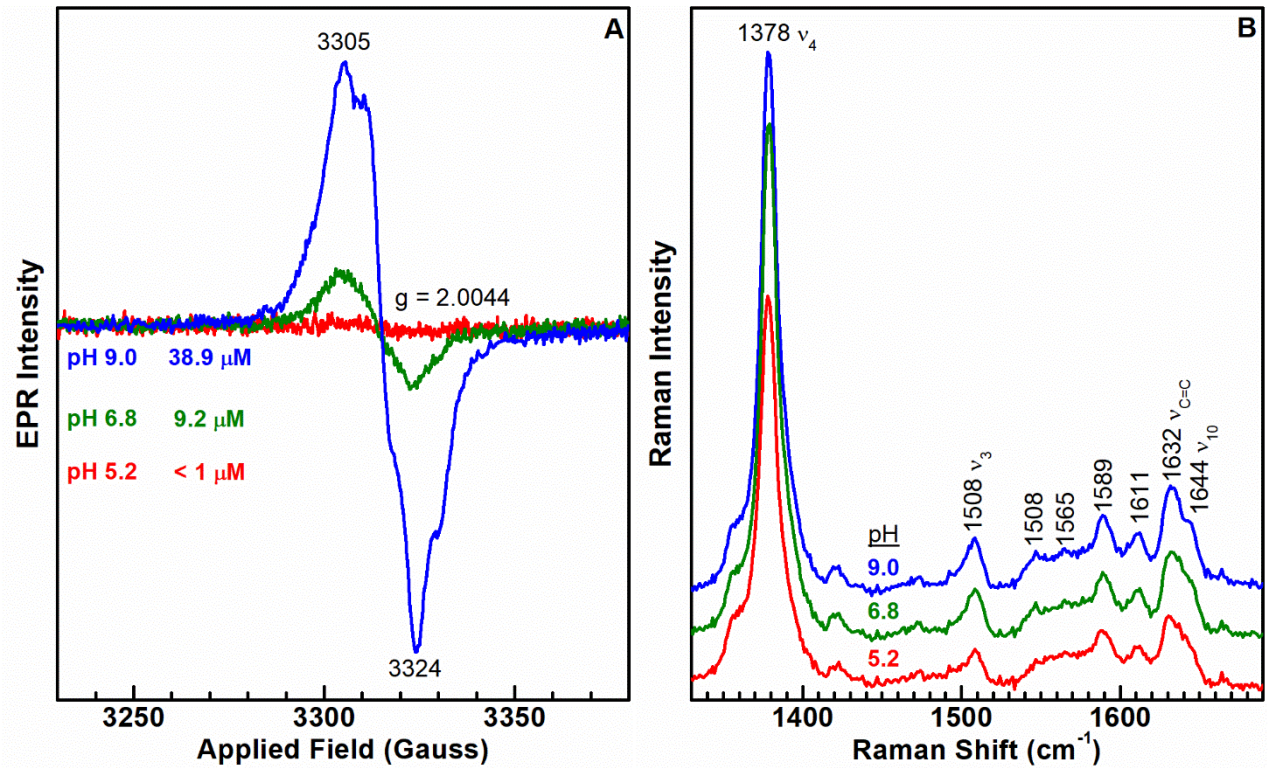

Figure 6.9. Freeze-quenched samples of 100 μM *Da*Cld reacted with 2 mM $NaBrO_2$ at pH 5.2, 6.8, and 9.0 where t_{rxn} = 1 second. A) X-band (9.300 GHz) EPR spectra at 77 K using 0.2 mW power reveal radical signatures consistent with a protein-based radical at pH 6.8 and 9.0 while an absence of radical at pH 5.2. B) 413.1-nm excited resonance Raman spectra at 77 K using 9.8 mW power shows Cpd II across the pH range.

A similar freeze-quenched reaction mixture of $NaBrO_2$ and *Kp*Cld was prepared at pH 9.0 (Figure E7). The EPR spectrum is consistent with a protein-based radical (g_{iso} = 2.0039, 17 G width) whose concentration accounts for 15% of the protein (Figure E7A). The corresponding Soret-excited rR spectrum also reveals a Cpd II spectrum based on the ν_4 at 1377 cm^{-1} and ν_3 at 1508 cm^{-1} along with the presence of HS hemin as evidenced by the broadened ν_3 at ~1480 cm^{-1}. The analogous experiment at pH 6.0 reveals a protein-based radical that accounts for 38% of the protein (Figure 6.11). However, the reaction conditions are not identical; [$NaBrO_2$] was higher at pH 9 and likely damaged the enzyme as evidenced by the poor S/N in the rR spectrum of the same sample (Figure E7B).

6.4.6. Bromite and chlorite substrates yield the same protein-based radical.

Since the EPR spectra of the WT Cld protein-based radicals exhibit very similar features and *g*-values, it was hypothesized that the radical is located on a conserved amino acid. The heme pocket has three tryptophan and two tyrosine side chains within 5 Å of the heme edge that are totally conserved in Clds.[22] However, of those, only one tyrosine and one tryptophan are within hydrogen-bonding distance to the porphyrin, specifically to propionate 6, in both *Da*Cld (Y118 and W155) and *Kp*Cld (Y62 and W97).[9, 23] A previous study investigated the importance of W155 in *Da*Cld and demonstrated it is a structurally critical residue. The W155F mutant destabilized the pentameric oligomeric state, formed a pH insensitive 6cLS complex, and lost all Cld activity.[24] Therefore, neither W155 nor W97 mutations were investigated here. Site-directed mutagenesis was carried out to convert the tyrosine to a phenylalanine in both enzymes. Unfortunately, the *Da*Cld(Y118F) mutant showed severely diminished activity toward $NaClO_2$ and instability in solution (data not shown). This behavior is analogous to that of the tryptophan mutants generated previously. However, the *Kp*Cld(Y62F) mutant retained its $NaClO_2$ decomposition activity with no measurable loss and did not suffer from instability in solution. Therefore, a comparative study was performed between Y62F and wild type *Kp*Cld upon reaction between $NaClO_2$ or $NaBrO_2$. EPR spectra of freeze quenched reaction mixtures comprising $NaClO_2$ and either Y62F or WT *Kp*Cld showed signatures consistent with a protein radical (Figure 6.10A). The peak-to-trough width and *g*-values differ between them: g_{iso} = 2.0032 (14 G) and g_{iso} = 2.0056 (24 G) for Y62F and wild type, respectively. The feature at 3279 G is likely due to some amount of $•ClO_2$ radical superimposed on the protein radical spectrum. Consistent with the small amount of protein radical present (< 1 μM), there are no observable bands in the Soret-excited rR spectra attributable to Cpd II (Figure 6.10B). Similar to previous

$NaClO_2$ reacted *Kp*Cld, the 6cHS aqua complex dominates the rR spectrum based on the ν_3 at 1484 cm^{-1} and ν_{38} at 1515 cm^{-1}.

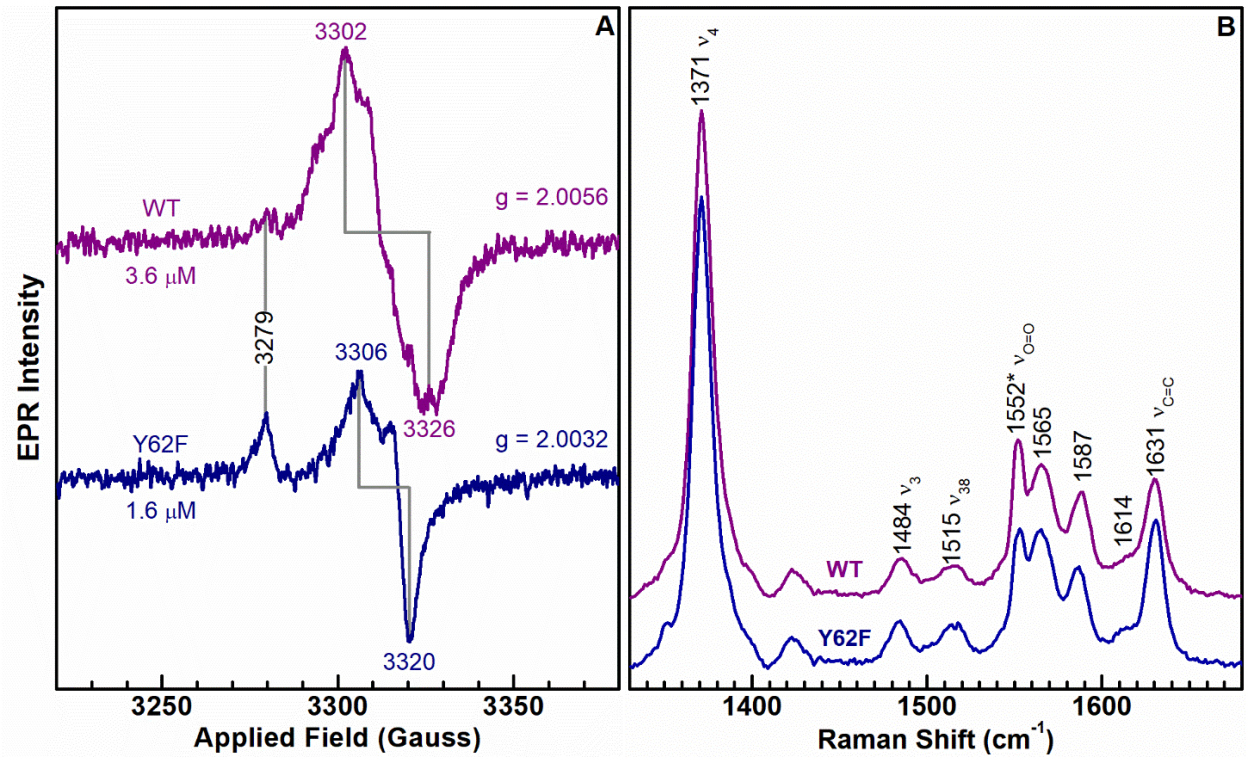

Figure 6.10. Freeze-quenched samples of 25 μM *Kp*Cld (WT in purple and Y62F in blue) reacted with 25 mM $NaClO_2$ at pH 6.0 where t_{rxn} = 1 second. A) X-band (9.300 GHz) EPR spectrum at 77 K using 0.2 mW power reveal radical signatures consistent with a protein-based radical. B) 413.1-nm excited resonance Raman spectra at 77 K using 8.9 mW power shows no evidence of Cpd II. Asterisk denotes dissolved oxygen in the immersion Dewar.

EPR spectra of freeze-quenched reaction mixtures containing $NaBrO_2$ and *Kp*Cld also showed signatures consistent with a protein radical for both the Y62F and wild-type enzymes (Figure 6.11A). No evidence of BrO_2 radical was observed; however, there is intensity at 3284 G in the wild-type spectrum that is not observed in the Y62F spectrum. Consistent with observations for the $NaClO_2$ reaction with *Kp*Cld, the peak-to-trough widths and g_{iso}-values for Y62F (2.0038, 13 G) differ from those of WT *Kp*Cld (2.0050, 21 G) in the $NaBrO_2$ reaction. The radical type may indeed be different between the wild type and Y62F enzymes based on these spectra. However, considering that their *g* values and their respective line widths were the

samefor the $NaClO_2$ and $NaBrO_2$ reaction mixtures suggests that the protein radicals generated are independent of substrate. The concentration of protein radical increased by over a factor of two in the reaction of wild type *Kp*Cld with $NaBrO_2$, but negligibly for *Kp*Cld(Y62F). Consequently, the Soret-excited rR spectra of these samples show some evidence for Cpd II formation based on the ν_3 at 1509 cm^{-1} and ν_{10} at 1644 cm^{-1} (Figure 6.11B). Consistent with only partial conversion to Cpd II, some HS hemin remains as evidenced by the ν_3 intensity at 1484 cm^{-1} and only a a small upshift the ν_4 band to 1373 cm^{-1}.

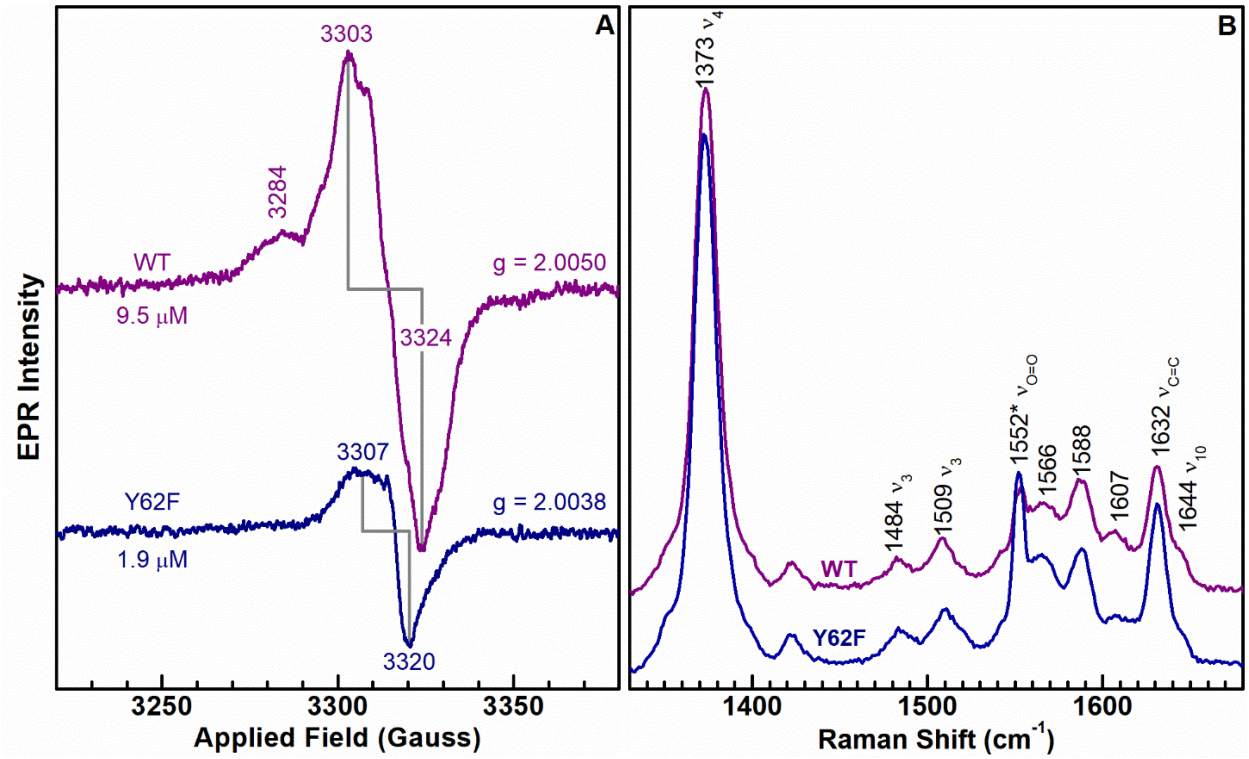

Figure 6.11. Freeze-quenched samples of 25 μM *Kp*Cld (WT in purple and Y62F in blue) reacted with 500 μM $NaBrO_2$ at pH 6.0 where t_{rxn} = 1 second. A) X-band (9.300 GHz) EPR spectrum at 77 K using 0.2 mW power reveal radical signatures consistent with a protein-based radical. B) 413.1-nm excited resonance Raman spectra at 77 K using 8.9 mW power shows some evidence of Cpd II. Asterisk denotes dissolved oxygen in the immersion Dewar.

6.4.7. Accumulation of Compound I is favored at low pH in Cld-catalyzed bromite decomposition.

Stopped-flow spectrophotometry could not be performed for the reaction of *Da*Cld with $NaClO_2$, as the [$NaClO_2$] required for the measurable accumulation of reactive heme intermediates produces enough O_2 to exceed its solubility in H_2O. The resulting bubbles spoil the absorbance measurements to such an extent that the data are not interpretable. Therefore, $NaBrO_2$ was used as a surrogate, O_2-producing substrate. High-valent heme intermediates were observed at lower excesses of $NaBrO_2$, which prevented gas bubbles forming in the optical cell. Side reactions that damage the enzyme are, however, readily observed as will be discussed below. The stopped-flow spectra for the reaction of *Da*Cld with $NaBrO_2$ at pH 5.2 (Figure 6.12A) showed an immediate loss of Soret absorbance with a concomitant absorbance increase to the red of 500 nm. This trend continued for approximately 0.5 s during which the spectra exhibited isosbestic behavior with resting enzyme. The resulting spectrum is consistent with the published Cpd I spectrum, which was generated by reaction of *Da*Cld with PAA at pH 6. The Soret maximum was reported at 397 nm with only ~60% of the resting enzyme extinction at that wavelength.[1] Cpd I then decayed over the course of 10 s to an unknown HS hemin species with a new set of isosbestic points that did not include the resting enzyme spectrum. The resulting spectrum has a Soret maximum at 402 nm and Q-bands at ~544 nm and 510 nm. This HS species decayed slowly with a 10% loss of Soret absorbance over the course of 30 minutes, consistent with slow oxidative degradation of the heme until all the substrate and its partially reduced side products are consumed (Figure 6.12B).

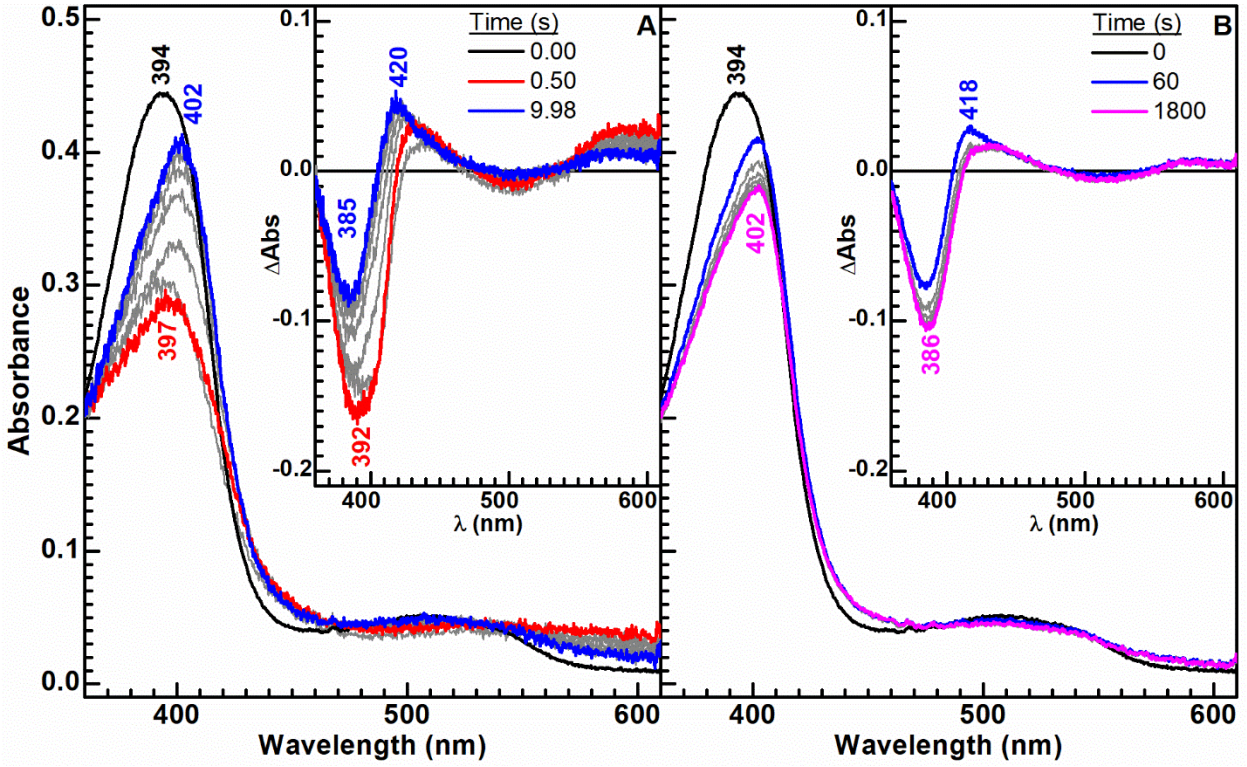

Figure 6.12. Stopped-flow spectra between 5 μM *Da*Cld and 100 μM $NaBrO_2$ in 0.1 M sodium citrate pH 5.2. A) First 10 seconds of the reaction shows brief appearance of Cpd I before it decays to an unknown hemin species. B) The following 30 minutes of the reaction shows a slight decay of the unknown hemin species. Reacted enzyme subtracted by resting enzyme at the corresponding time points. *Fringes are due to emission lines from the Xenon arc lamp.

Stopped-flow spectrophotometry of this reaction at pH 9.0 (Figure 6.13A) revealed markedly different behavior than at pH 5.2. Upon mixing, the Soret maximum shifted from 402 nm to 415 nm along with the emergence of two well-resolved Q-bands at 525 nm and 555 nm within 100 ms and persisted for about a minute. All resting enzyme spectral signatures were lost in this time frame. The resulting spectrum is consistent with the reported Cpd II spectrum upon reaction of *Da*Cld with PAA at pH 8.[1] Cpd II then decayed over the course of ~30 min. to yield a HS hemin species having its Soret maximum at 404 nm with ~40% loss of absorbance relative to the resting enzyme at *t*=0, and unresolved Q-bands (Figure 6.13B). These features are, again, consistent with oxidative heme degradation.

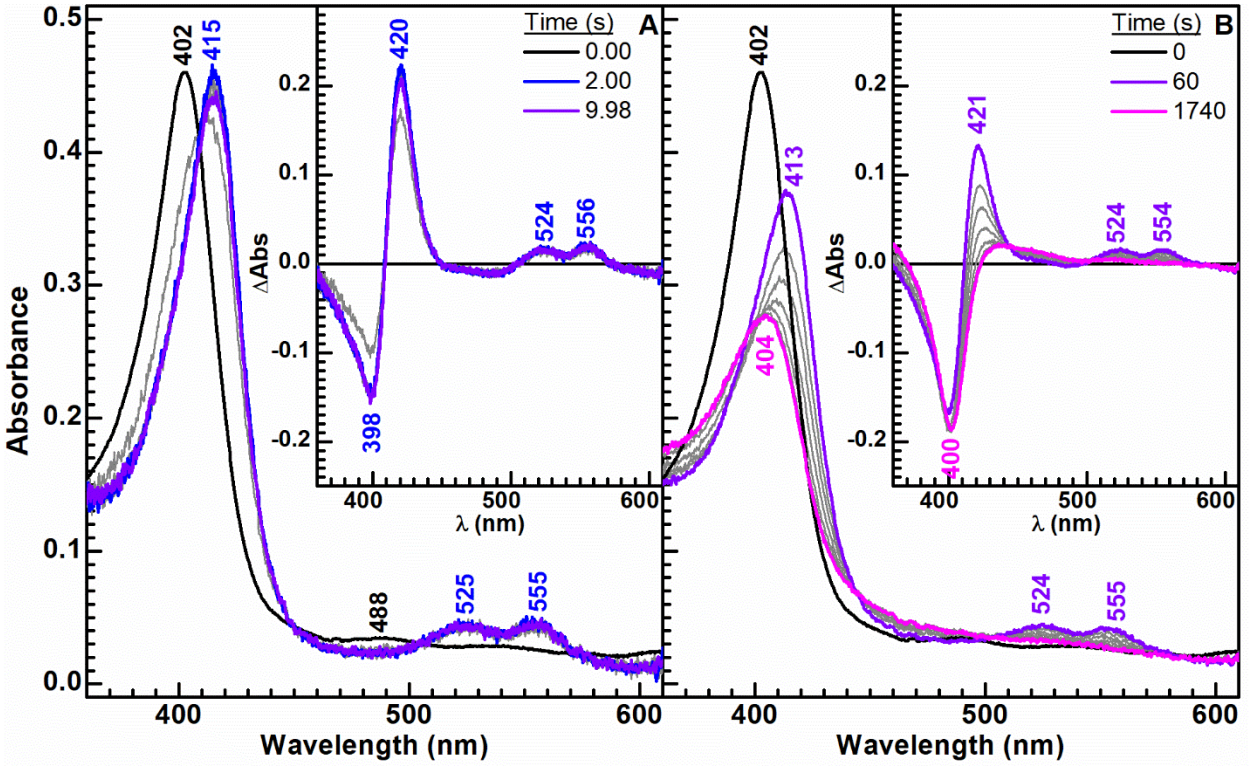

Figure 6.13. Stopped-flow spectra between 5 μM *Da*Cld and 100 μM $NaBrO_2$ in 0.1 M sodium borate pH 9.0. A) First 10 seconds of the reaction shows rapid formation of Cpd II. B) The following 29 minutes of the reaction shows decay of Cpd II to an unknown hemin species. Reacted enzyme subtracted by resting enzyme at the corresponding time points. *Fringes are due to emission lines from the Xenon arc lamp.

At these extremes of pH over which *Da*Cld activity with ClO_2^- varies by two orders of magnitude[8], different heme intermediates were observed on the stopped-flow time scale. Therefore, at intermediate pH's where enzyme activity lies between those at pH 5.2 and 9.0, it was hypothesized that reaction with $NaBrO_2$ would yield a mixture of Cpd I and Cpd II. Hence, the reaction was carried out at pH 6.8 and monitored by stopped-flow spectrophotometry. This reaction yielded a transient spectrum having features resembling Cpd II (Figure E8A). The Soret maximum shifted from 393 nm to 413 nm with the appearance of well- resolved Q-bands at 527 nm and 556 nm within 4 s of mixing. All features associated with the resting enzyme spectrum are lost within this time frame and there were no isosbestic points in the Soret region that contain the resting enzyme spectrum, consistent with more than two species having significant

absorbtivity in this region of the spectrum. The Cpd II-like spectrum decays toward a HS hemin species over the course of 29 minutes, during which the Soret maximum shifts from 410 to 405 nm and loses 10% of its original absorbance. At the same time, Q-band absorbance at 552 nm is lost (Figure E8B). Since the intermediate at this pH did not fully convert to Cpd II nor did its formation share isosbestic behavior with the resting enzyme spectrum, it was concluded that a third and transient heme species was present in the reaction mixture. Given that Cpd I was observed at pH 5.2, it was hypothesized that the second transient heme species was a fraction of the heme was converted to Cpd I. Spectral simulation revealed that the observed transient spectrum is well modelled by a linear combination of Cpd I and Cpd II spectra (Figure 6.14). The Cpd I and Cpd II component spectra used to simulate the transient spectrum were the Cpd I spectrum recorded at pH 5.2 and the Cpd II spectrum recorded at pH 9.0. The spectrum recorded at 20 ms corresponds to 40% Cpd I and 60% Cpd II and the 1 s spectrum reports 35% Cpd I and 65% Cpd II. There are no significant difference features observed between the experimental and simulated spectra. This result suggests the possibility that Cpd I forms first and is converted to Cpd II which, in turn yields a HS hemin species.

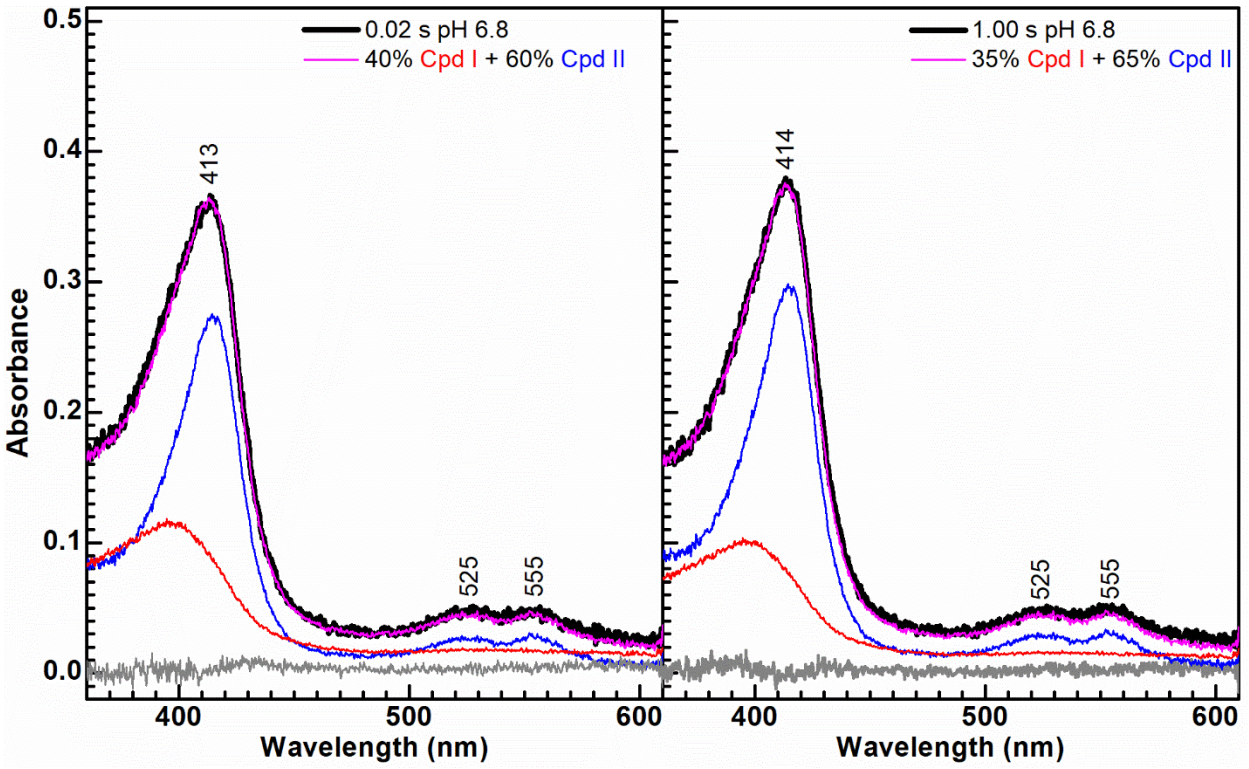

Figure 6.14. Stopped-flow experimental (blue) vs. simulated (red) spectra between 5 μM *Da*Cld and 100 μM $NaBrO_2$ in 0.1 M sodium phosphate pH 6.8. Component spectra used to generate the simulated spectra are shown in gray. The difference spectrum generated by subtracting the simulated spectrum from the experimental spectrum is shown in black. A) The 20 ms experimental spectrum overlaps the simulated sum of 40% Cpd I and 60% Cpd II spectrum. B) The 1 s experimental spectrum overlaps the simulated sum of 35% Cpd I and 65% Cpd II spectrum.

The same experiment carried out at pH 6.0 exhibits a similar trend (Figure 6.15). The Soret band loses 45% of its absorbance and shifts toward 400 nm in the first 20 ms, the Q-bands become unresolved, and absorbance increases to the red of 560 nm. Over the course of the next 2 seconds, the Q-bands partially resolve at 525 nm and 556 nm while the Soret maximum shifts toward 410 nm with a 10% increase in absorbance, then subsequently shifts toward 407 nm and gains ~20% absorbance, while losing absorbance at 556 nm and gaining absorbance around 500 nm in the next 8 seconds (Figure E9A). Over the remaining 20 minutes, absorbance at 525 nm continued to drop while the Soret gradually shifts toward 403 nm with negligible loss in absorbance (Figure E9B). Similar to the pH 6.8 data, no isosbestic point in the Soret region

contained the resting enzyme spectrum during the course of the reaction. This prompted the same spectral analysis that was performed on the spectra recorded at pH 6.8 (Figure 6.15). The simulated spectra reveal that the first spectrum at 20 ms contains 80% Cpd I and 20% Cpd II while the spectrum at 1.0 second contains 70% Cpd I and 30% Cpd II. There are two distinctions in the pH 6.0 data set from the pH 6.8 data set: The baselines do not match between the experimental and simulated spectra at pH 6.0 possibly due to heme bleaching not accounted for in the simulated spectra. Nonetheless, the features and relative absorbances between the simulated and experimental spectra are nigh identical. The trend toward higher accumulation of Cpd I at lower pH parallels the corresponding trend toward higher activity. This correlation supports the hypothesis that Cpd I is the productive intermediate on the O_2 evolving pathway.

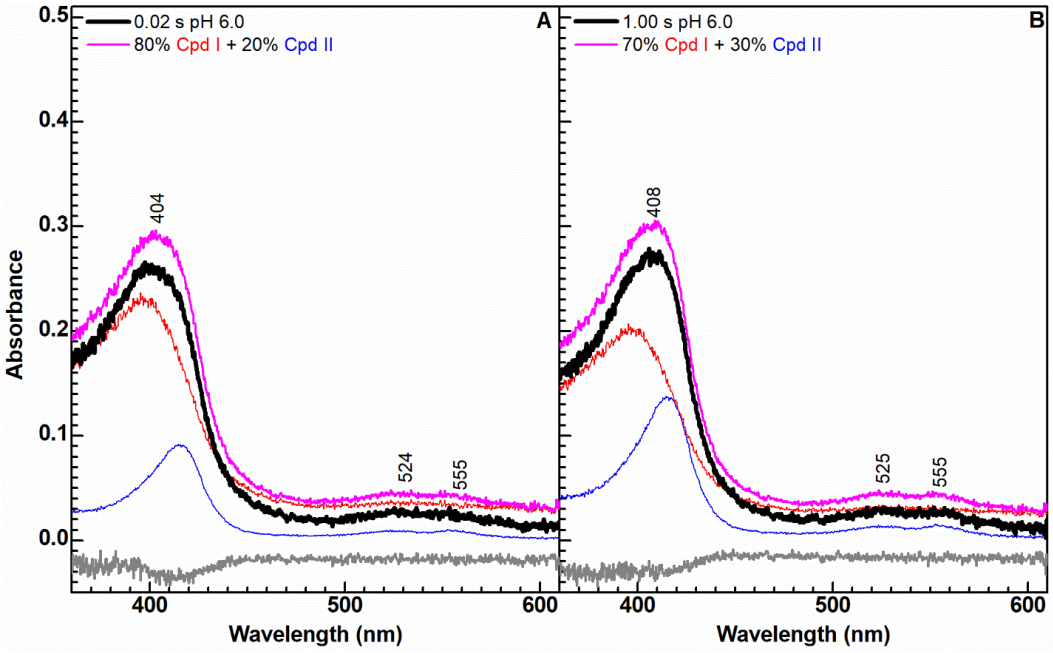

Figure 6.15. Stopped-flow experimental (blue) vs. simulated (red) spectra between 5 μM *Da*Cld and 100 μM $NaBrO_2$ in 0.1 M sodium phosphate pH 6.0. Component spectra used to generate the simulated spectra are shown in gray. The difference spectrum generated by subtracting the simulated spectrum from the experimental spectrum is shown in black. A) The 20 ms experimental spectrum overlaps the simulated sum of 80% Cpd I and 20% Cpd II spectrum. B) The 1 s experimental spectrum overlaps the simulated sum of 70% Cpd I and 30% Cpd II spectrum. Simulated and experimental spectra are slightly off set likely due to differences in baselines.

Stopped-flow spectrophotometry was also used to monitor the reactions of *Kp*Cld with $NaClO_2$ and $NaBrO_2$ at pH 5.2. Early time points for the $NaClO_2$ reaction (Figure E10A) shows a ~20% drop in the Soret extinction and a shift from 403 nm to 406 nm in 100 ms. Over the course of the next 30 seconds, the Soret regains intensity and shifts back toward 403 nm. This contrasts with the $NaBrO_2$ reaction (Figure E10B) where the Soret loses ~40% extinction but does not shift within 0.1 seconds. Over the course of the next 30 seconds, the Soret continues to lose extinction and partially shifts toward 405 nm. The reaction with $NaClO_2$ tracked across long times (Figure E11A) resolved the intermediate species observed at 0.1 seconds in the previous data set: Soret at 406 nm, $Q_{0,0}$ at 556 nm, and $Q_{0,1}$ at 525 nm. These spectral signatures are consistent with a partially formed Cpd II spectrum. Isosbestic behavior is retained as Cpd II decays toward resting enzyme over the course of 20 minutes. The reaction with $NaBrO_2$ (Figure E11B) also resolves an intermediate species not observed in Figure E10B: Soret at 413 nm, $Q_{0,0}$ at 556 nm, and $Q_{0,1}$ at 525 nm. These spectral signatures are also consistent with a more completely formed Cpd II spectrum. However, as the reaction proceeds, a new band at 686 nm gains extinction in 20 seconds and persists for 20 minutes. Unlike $NaClO_2$ the reaction with $NaBrO_2$ does not retain isosbestic behavior with resting enzyme despite the gradual shift of the Soret toward 403 nm from the Cpd II spectrum. The lack of isosbestic behavior may be due to heme degradation during turnover, as suggested the band at 686 nm, which is characteristic of verdoheme.[25] Another possible explanation could involve trace amounts of free-base protoporphyrin IX (H_2PPIX) that is known to contaminate recombinant *Kp*Cld preparations, and is revealed by an absorption band at 621 nm.[26] The decomposition of H_2PPIX is known to yield an extinction increase in the red part of the visible spectrum.[27] However, this process is typically photoinduced and therefore would be expected to show up in both data sets, which it does not.

Thus, it is concluded then that this degradation reaction is $NaBrO_2$ dependent. No spectroscopic evidence for Cpd I is observed in the reactions with either $NaClO_2$ or $NaBrO_2$ at pH 5.2. Thus, either Cpd I does not form or it does not accumulate to a detectable level due to its rapid progression to the O−O bond-forming step of the catalytic reaction, or its reduction to Cpd II by a nearby amino acid. Considering there is evidence for a protein based radical at pH 5.2 in the *Kp*Cld + $NaClO_2$ reaction (*vide supra*) along with O_2 evolution under conditions where there is no protein radical observed for *Da*Cld + $NaClO_2$ or $NaBrO_2$, both of the aforementioned pathways for consumption of a two-electron oxidized heme are likely occurring in parallel. The correlation between lesser of activity of *Kp*Cld and the accumulation of Cpd II + AA• over the entire pH activity profile accounts for the lower ClO_2^- decomposition activity of *Kp*Cld relative to *Da*Cld and is consistent with the earlier stated hypothesis that the Cpd II + AA• state does not yield O_2.

If reduction of Cpd I to Cpd II by an amino acid does indeed compete with recombination of Cpd I with OCl^- to form the O−O bond, then the *Kp*Cld(Y62F) should not form Cpd II assuming Y62 is the sole reducing amino acid. Stopped-flow spectrophotometry was carried out for reactions between *Kp*Cld(Y62F) and excess $NaClO_2$ or $NaBrO_2$ at pH 6.0. This was the lowest pH where the mutant was stable for these experiments. Early time points for the $NaClO_2$ reaction (Figure E12A) show a red shift in the Soret from 403 to 414 nm along with formation of resolved Q−bands at 556 and 525 nm in 100 ms, all consistent with prompt Cpd II formation. Over the course of the next 30 seconds, Cpd II decays back toward resting enzyme. Isosbestic behavior is retained throughout the entire time course. Early time points for the $NaBrO_2$ reaction (Figure E12B) reveal similar trends. The Soret maximum rapidly shifts to 414 nm while Q−bands at 556 and 525 nm resolve within 20 ms, also consistent with a Cpd II spectrum.

However, as the reaction proceeds, the Soret band loses 20% of its extinction from Cpd II and only slightly blue shifts to 413 nm over 30 seconds. Isosbestic behavior is subsequently lost. Tracking the $NaClO_2$ reaction for long times (Figure E13A), showed continuation of the trends seen at short times. The Cpd II spectrum decayed back to resting enzyme within 15 minutes with isosbestic behavior throughout. This contrasts with the long times for the $NaBrO_2$ reaction (Figure E13B). The Cpd II spectrum loses 20% extinction and blue shifts to 406 nm while the Q−bands become unresolved over the course of 15 minutes. Consequently, isosbestic behavior is lost. No spectral features consistent with Cpd I were observed for the *Kp*Cld(Y62F) mutant. Although Cpd II forms more completely with *Kp*Cld(Y62F) than wild type *Kp*Cld, this may be attributable to the differences in pH (6.0 for Y62F compared to 5.2 for WT). Similar to wild type *Kp*Cld, reaction of either $NaClO_2$ or $NaBrO_2$ with *Kp*Cld(Y62F) forms a protein radical at pH 6.0, albeit in lower amounts. Therefore, either Cpd I is rapidly reduced to Cpd II by an amino acid that is exchange coupled with the metal center like the tryptophanyl radical of Compound ES in Cytochrome c peroxidase, which results in a broad EPR signal that can only be observed at low temperatures (i.e. < 4 K)[28-30], Cpd I is reduced rapidly by excess oxidant, or Cpd II forms directly upon one election oxidation of the ferric resting state by either substrate. The latter two possibilities invoke one-election oxidation or reduction of either ClO_2^- or BrO_2^-. Indeed, there is evidence of $\bullet ClO_2$ features superimposed on the EPR spectrum of the *Kp*Cld + ClO_2^- reaction mixture. However, no EPR evidence for •ClO or either oxidized or reduced bromine-centered radicals is seen in these reaction mixtures. Therefore, considering this evidence that a protein radical and Cpd II form, even without the hydrogen-bonded Y62 suggests other amino acids, including the nearby tryptophan, may harbor the hole.

6.4.8. Reaction of Cpd II/AA• with OCl^- does not yield O_2.

The decrease in O_2-evolving activity with increasing pH for both $NaClO_2$ and $NaBrO_2$ raises the question of the reactivity of the Cpd II/AA• state. Specifically, is the two-electron oxidized Cpd II/AA• state incompetent to recombine with OCl^-, leaving less enzyme in the active intermediate state? Or does it do so with less kinetic facility, thereby forming the O–O bond and ultimately O_2 at a slower rate than at lower pH? To address this question, the Cpd II/AA• state was generated by reaction with PAA, as it is known to form rapidly and persist for tens of seconds under alkaline conditions[1] followed by addition of NaOCl. Since this would be a single-turnover experiment, stopped-flow spectrophotometry was performed at high enzyme concentration to determine the time frame of Cpd II formation and its subsequent decay (Figure E14). These data revealed that Cpd II forms in 15 seconds and persists for minutes. Therefore, the single turnover O_2 experiment was performed under similar conditions where NaOCl was added to enough Cpd II to produce a measurable amount of O_2 20 seconds after addition of PAA to *Da*Cld (Figure E15) at pH 9.0. No O_2 was observed. A control was performed with 80 μM $NaClO_2$ (reaction with substrate) and produced near-stoichiometric amounts of O_2. This result strongly supports the conclusion that the Cpd II/AA• does not react with exogenous OCl^- to produce O_2.

To test whether Cpd I + OCl^- produces O_2, that reaction was carried out at pH 7.1 where the HOCl / OCl^- and Cpd I / Cpd II speciation models intersect. These conditions ensured that enough f Cpd I and OCl^- would be present that a rapid reaction would yield a measurable amount of O_2 (Figure E16). The theoretical maximum amount of O_2 produced in this single-turnover experiment would be 20 μM in an 80 μM Cld sample as only 25% of the ferryl species would be Cpd I. Stopped-flow was performed between 80 μM *Da*Cld and 160 μM PAA at pH

7.1 to determine Cpd I / Cpd II formation and decay (Figure E17). The stopped-flow data showed Cpd II within 2.5 s. No detectable O_2 produced in the reaction of 80 μM *Da*Cld with 160 μM PAA followed by 160 μM NaOCl at pH 7.1 (data not shown). Considering that Cpd II dominated the spectrum, it is likely that the rate of Cpd I reduction by an amino acid to Cpd II is out competing the rate of Cpd I formation by PAA. This observation is consistent with that reported at pH 8 for the reaction between PAA and *Da*Cld.[1]

6.5. Discussion

6.5.1. Catalytic $NaXO_2$ decomposition proceeds through heterolytic O−ClO^- bond scission.

Both homolytic and heterolytic O−ClO^- (hereinafter O−Cl) bond cleavage mechanisms have been proposed for catalytic ClO_2^- decomposition by Clds. Several density functional theory (DFT) studies lend support for the homolytic pathway based on the calculation of a higher activation barrier for heterolytic bond cleavage.[31-32] However, it should be noted that only the distal arginine and proximal histidine side chains were included in these calculations. Thus, non-bonding interactions from the heme-pocket were not fully accounted for. Furthermore, peripheral heme substituents were omitted, thereby leaving any inductive or electron withdrawing effects of those substituents on the energy of either bond-scission transition state unaccounted for. Only one study investigated substituent effects on reaction coordinate energies, however, that study focused specifically on water-soluble iron porphyrinates.[33] Thus, the extent to which these interactions impact the the kinetic barriers for O−Cl bond homolysis and heterolysis remains unexplored within the enzyme environment. Therefore, the chemical inaccuracy of the calculations reported to date may undermine the accuracy with which they map the catalyzed reaction coordinate.

The first stopped-flow reaction that yielded observable intermediates with ClO_2^- was reported for CCld, a clade 2 (i.e. dimeric) enzyme.[2] Under acidic conditions, a partially formed Cpd I spectrum was briefly observed at early times (4 ms) based on the prompt loss of Soret extinction and red shift of the LMCT to 650 nm. A more pronounced Cpd II spectrum subsequently emerged before decaying back toward resting enzyme. Under neutral and alkaline conditions, only Cpd II was observed.[2] These observations are consistent with the stopped-flow data reported herein for the dimeric *Kp*Cld wild-type and Y62F at pH 5.2 and 6.0, respectively. Since the earliest time point collected in this study was ~20 ms, the spectral signature for any Cpd I would have already decayed to a substantial extent. Instead, Cpd II was directly observed and remained isosbestic with resting enzyme, suggesting that either Cpd I does not build up to a detectable concentration or, if it does, has reacted within the dead time of the experiment. This contrasts with the stopped-flow data reported herein for *Da*Cld with BrO_2^- at pH 5.2. Cpd I accumulated to concentrations sufficient to be observed directly before reverting back towards resting enzyme as the excess surrogate substrate was consumed. While reactions with BrO_2^- were complicated by catalyst degradation starting at intermediate reaction times, early times showed a clear 1st-order dependence of O_2 production on [BrO_2^-] (Figure 6.8). Therefore, it is well supported that Cpd I is the reactive intermediate that yields O_2 in *Da*Cld catalysis, at least at pH 5.2. However, the fleeting nature of Cpd I clade 2 Clds has caused other investigators to calls into question the mechanistic relevance of Cpd I in O_2 evolution by these enzymes.

Lack of detectable Cpd I concentrations in the CCld reaction with ClO_2 prompted the authors to monitor the CCld reaction with OCl^-, a known two electron oxidant, via stopped-flow spectrophotometry.[2] Cpd I was readily observed at pH 5 and gradually converted to Cpd II over the course of ~7 s. At pH 7 Cpd I was converted to Cpd II within 300 ms. No intermediates were

observed between the reaction of OCl^- and CCld at pH 9. Interestingly, no O_2 evolution was detected polarographically at any pH for the reaction of CCld with excess OCl^-.[2] A similar approach was taken here with *Da*Cld wherein the enzyme was first reacted with stoichiometric PAA and a slight excess of OCl^-. No O_2 was detected at pH 7.1 where the Henderson-Hasselbalch models for the pH dependence of the Cpd I/Cpd II ratio and for HOCl/OCl^- ratio intersect. While these data may appear to support the homolytic bond cleavage pathway, it is highly likely that the rate of Cpd I reduction by an amino acid out competes the diffusion of OCl^- into the heme pocket at pH greater than or approximately equal to pK_a for HOCl. This is supported by the rapid formation of Cpd II for PAA + *Da*Cld at pH 8 (k_{obs} =1.3×10^6 M^{-1} s^{-1}).[1] This represents the very lower limit for the reduction of Cpd I to Cpd II by an amino acid side chain , and may be considerably faster. Additionally, the maximum k_{on} for the binding of CN^-, another anionic diatomic conjugate base of a weak acid ligand, is only ~10^7 $M^{-1}s^{-1}$ for *Da*Cld [34]. This suggests that the rate of Cpd I reduction to Cpd II by an amino acid may well be competitive with the rate at which a diatomic anion can diffuse into the heme pocket. Therefore, it is entirely possible that any fraction of Cpd I formed at higher pH is quickly reduced to Cpd II before OCl^- gets close enough to the ferryl O atom to form the O−O bond. While this explanation works well for the recombination of Cpd I and OCl^-, it does not explain why Cpd I, which persists in acidic solution, does not recombine with HOCl to produce. O_2. This can be inferred from the poor peroxidase activity observed for *Da*Cld. Since there is no catalytic base in the heme pocket, reactions involving H_2O_2 did not yield Cpd I + H_2O, but rather a spectrum corresponding to a LS ferric peroxo complex (either Cpd 0 or Cpd III).[1] Therefore, it is unlikely that the heme pocket facilitates dissociation of the proton in HOCl to form the OCl^- necessary to make the O−O bond, thereby diminishing its reactivity with Cpd I to produce O_2. The reaction

between HOCl and ferric iron itself however is facile. This is likely facilitated by coordination of HOCl to the Lewis acidid Fe(III) center, which acidifies the bound acid, thereby driving its deprotonation at pH<pK_a(HOCl).

Unfortunately, the published study with CCld did not investigate the possibility that a protein-based radical could be detected. The OCl• radical, the expected intermediate of ClO_2^- homolysis, is paramagnetic and has been characterized by X-band EPR in acidic solution (g_{iso} = 1.9972).[20] No EPR signal consistent with OCl• is observed in any reaction between Cld and ClO_2^- at 77 K. However, considering the proximity of a putative OCl• fragment to the heme's *S*=1 Fe(IV) atom, the *S*=½ OCl• fragment could be exchange coupled with the ferryl, thereby broadening the EPR spectrum to such an extent that it would be undetectable at 77 K. This is certainly the case for Cpd I as the porphyrin π cation radical is exchanged coupled with the ferryl and can only be observed as a broadened EPR spectrum at temperatures in the range of 4–10 K.[35] This is also the case for Cpd ES in cytochrome c peroxidase where the *S*=1 Fe(IV) atom and *S*=½ tryptophanyl π cation radical are exchange coupled.[30] All reaction conditions where Cpd II is shown to be the dominant heme species for *Kp*Cld and *Da*Cld reveal either a •ClO_2 radical following reaction with excess ClO_2^-, or a protein-based radical upon reaction with either ClO_2^- or BrO_2^-. Neither •ClO_2 nor the •AA is exchange coupled with the corresponding ferryl. The presence of •ClO_2 can be explained by the one-electron reduction of either Cpd I or Cpd II by excess ClO_2^-. This has been observed directly in Horseradish peroxidase (HRP)[36], human myeloperoxidase (MPO)[37], and bovine lactoperoxidase (LPO)[37]. The Cpd II:AA• state is formed more rapidly in alkaline solution and is not able to recombine with OCl^- to produce O_2 (Figure E15). Therefore, the Cpd I / OCl^- geminate pair is effectively decoupled upon formation of Cpd II:AA•, allowing for diffusion of OCl^- from the heme pocket. This decoupled state appears to

only affect one-electron transfer reactions, such as the oxidation of ClO_2^- to ClO_2. This explanation is consistent with *Kp*Cld producing more $\bullet ClO_2$ than *Da*Cld at each respective pH, as conversion of Cpd I to Cpd II:AA• is more efficient in *Kp*Cld than in *Da*Cld. Additionally, it was previously shown that the OCl^- fragment rapidly leaks out of the heme pocket during turnover in *Kp*Cld[9] and the rate of OCl^- leakage increases with pH in *Nd*Cld.[38] This may contribute to the fraction of Cpd I that is converted to Cpd II:AA•, which may, in turn, add to the $\bullet ClO_2$ yield. Not only does *Kp*Cld produce higher concentrations of $\bullet ClO_2$ with respect to *Da*Cld, it was reacted with less $NaClO_2$ further supporting that decoupling of the O_2 producing state is higher in *Kp*Cld than *Da*Cld.

In contrast to reactions involving ClO_2^-, no bromine-centered radicals were observed for reactions of BrO_2^- with either *Kp*Cld or *Da*Cld. This isn't surprising considering, to the best of the authors knowledge, no EPR spectrum of $\bullet BrO_2$ or •OBr have been reported in aqueous solution at 77 K. Only protein centered radicals were observed. Two amino acids were identified as candidates for housing the observed protein radical in the WT enzymes (Figure 1.3). They are the totally conserved Y62 in *Kp*Cld and Y118 in *Da*Cld, and W97 in *Kp*Cld and W155 in *Da*Cld. These residues are directly hydrogen bonded to propionate 6 (P6). Previous studies have revealed that W155 is important for the structural integrity in *Da*Cld as the corresponding W155F mutation exhibited no ClO_2^- decomposing activity and formed a dimer rather than a pentamer in solution.[24] Similar loss of O_2-evolving activity was observed for *Da*Cld(Y118F), although its oligomeric state was not determined. The effect on ClO_2^- decomposing activity of the analogous mutation in *Kp*Cld(W97F) was not reported.[9] The *Kp*Cld(Y62F) mutant reported here also generated a protein-based radical in the $NaBrO_2$ reaction, albeit at a lower concentration than with WT *Kp*Cld. This is consistent with the protein radical residing on the conserved tyrosine

that is hydrogen bonded to P6 in *Kp*Cld and, by extension, *Da*Cld, as the EPR signatures of the WT enzymes are nearly identical. Consistent with this explanation is the increase in protein radical formation under alkaline conditions.

Two amino acids within the heme pocket are oxidizable by Cpd I: tyrosine and tryptophan (Figure 6.16). Tyrosine is oxidized to tyrosyl radical via proton coupled electron transfer (PCET) reactions that are typically facilitated by a base within H-bonding distance of the phenolic hydrogen.[39] The protonation status of P6 is not known in Clds but has been measured in cytochrome c551 from *Pseudomonas aeruginosa*. Propionate 6 (P6) is solvent exposed and has a pK_a = 3.5 while the buried P7 has a pK_a = 6.0. Mutations removing hydrogen-bond donors to P7 generally increased its measured pK_a.[40] Considering that Y62 and Y118 are both within H-bonding distance of the carboxylate group, it is reasonable to conclude that it can act as a base and facilitate PCET. As the basicity of P6 increases at higher pH, the rate of tyrosyl radical formation would be expected to track the population of deprotonated P6 as pH is increased. The different EPR signal for Y62F may be attributable to protein radical localized on the H-bonded tryptophan, W97. The narrowing of the peak-to-trough width and decrease in the isotropic *g*-value are consistent with a tryptophan-based radical.[41] Unlike tyrosyl radical, tryptophan-based radicals can form via either PCET or a simple electron transfer to yield a cation radical.[41-42] It is unclear which tryptophan radical species is present for Y62F; however, considering the pK_a for tryptophan radical is 4.2, it is likely formed via PCET at pH 6.0. The most compelling evidence resides in the lack of a protein-based radical observed at pH 5.2 for *Da*Cld reacted with $NaBrO_2$. Only Cpd I is observed at this pH and no appreciable amount of Cpd II is detected. Consequently, no protein radical signature was observed at 77 K. These data together lend

support for the intermediate leading to O_2 formation resulting from heterolytic scission of the substrate O−Cl bond.

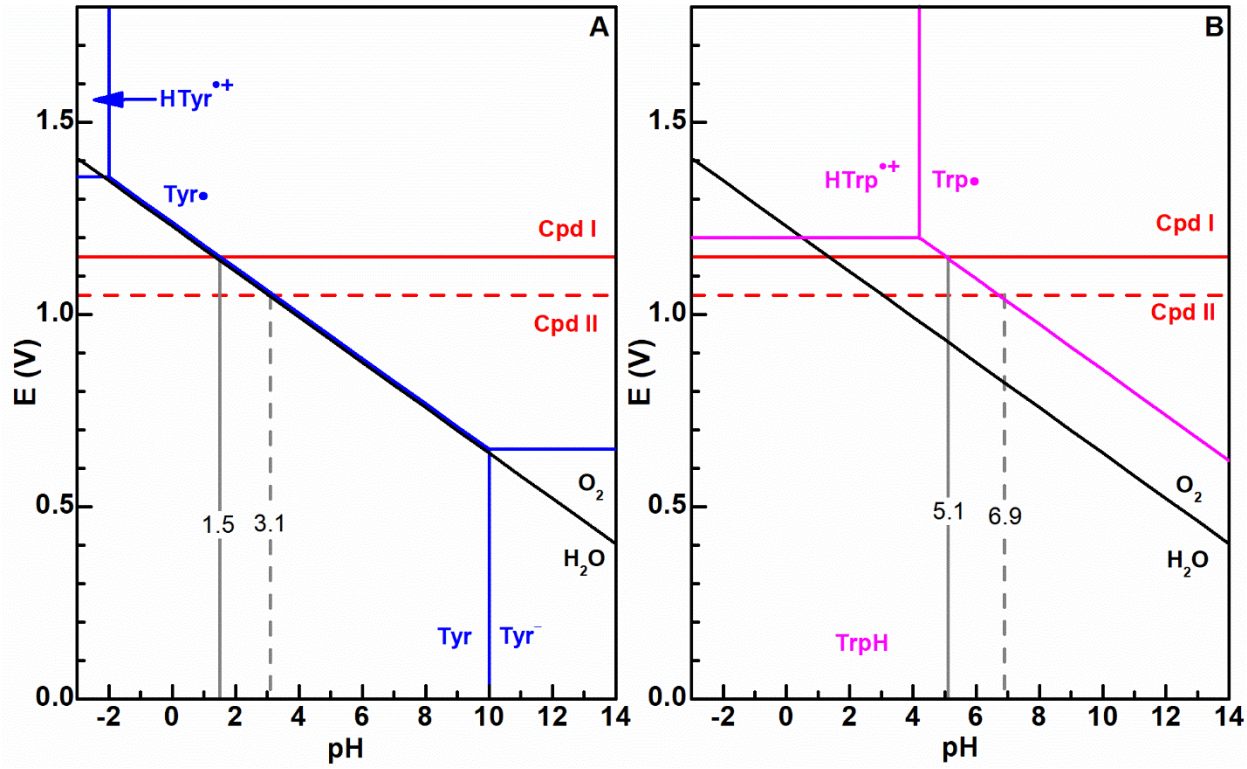

Figure 6.16. Tyrosine and tryptophan amino acids can be oxidized by Cpd I. A) Reduction couples for tyrosine[39] and B) tryptophan[39] species in water. The solid red line indicates the estimated Cpd I | Cpd II reduction potential for *Da*Cld based on the difference in its Fe(III) | Fe(II) potential from HRP.[1] The dashed line is the measured Cpd I | Cpd II reduction potential for HRP. The black line corresponds to the O_2 | H_2O couple. Oxidation of tyrosine without transferring of a proton can only occur below pH -2 while oxidation of a tryptophan can occur at pH 4.2 or lower. Cpd I has the thermodynamic driving force to oxidize tyrosine at pH 1.5 and tryptophan at pH 5.1.

6.5.2. pH dependent catalytic activity tracks the fraction of Fe(IV) present as Cpd I

While the homolytic bond cleavage pathway cannot be definitively ruled out, neither does it explain the pH dependence of O_2 production from catalytic ClO_2^- decomposition by Cld. An initial explanation invoked the possible deprotonation of the distal arginine, an essential residue for efficient catalysis.[8] However, it was later suggested that its pK_a of 13.2 is too high to account for the kinetic pK_a of 6.6. It was subsequently suggested that the ratio of open/closed

conformations was dependent on pH a more reasonable model based on the observation of two distal hydrogen bonding environments reported by the *Da*Cld carbonyl complex.[43] A more recent study confirmed that the distal arginine in CCld remains fully protonated at pH 9.0[2], consistent with its high pK_a for the guanidinium side chain measured reported as 13.8.[44] The carbonyl complex of *Kp*Cld revealed a uniform distal hydrogen-bonding environment consistent with an open conformer.[34] While the distal arginine residue is able to accommodate multiple conformers with a neutral ligand, the inclusion of a charged ligand forces it to adopt a closed conformation.[26, 34] The extent at which the O−Cl bond is polarized by the distal arginine upon binding of ClO_2^- may be attributed, in part, to their differences in activity. However, these hydrogen-bonding effects do not appear to be pH dependent, and therefore can also not be the primary cause for the pH dependency on O_2 production. In light of the data presented in this study, it appears that maximal ClO_2^- decomposing activity occurs when Cpd I is the dominate intermediate while the lowering of activity with increasing pH coincides with more rapid generation of the decoupled Cpd II:AA• state.

This was illustrated in Figure E16 where the fractional amount of Cpd I observed at early times (< 1 second) in *Da*Cld + $NaBrO_2$ stopped-flow reactions tracked pH. The fractional amount of Cpd I vs Cpd II was fit to a Henderson-Hasselbalch model which yielded a pK_a = 6.62±0.03. Interestingly, this value is extremely close to the kinetic pK_a observed for catalytic O_2 production in *Da*Cld (6.6±0.8 for k_{cat} and 6.6±0.4 in k_{cat} / K_M).[8] Considering the proximity between these two values, it is likely that these processes are linked. The recombination of the geminate pair Cpd I:OCl^- is intrinsically 1st-order which is independent of pH. However, the reduction to Cpd II by PCET from an adjacent amino acid radical is proton dependent. Therefore, pH dependent profile on O_2 production is the result of two competing pathways: one

pathway that yields O_2 in a pH independent manner and another pH-dependent pathway that siphons active enzyme into a catalytic dead end from where no O_2 is produced. Generation of the dead-end Cpd II:AA• state is likely linked to the pK_a of P6. This propionate group is shown to be solvent exposed by virtue of a nearby water shown in the x-ray crystal structure of *Da*Cld.[23] Both CCld[2] and *Nw*Cld[45] dimeric enzymes also show several waters that are hydrogen bonded to P6. The acidity of the carboxylic proton is likely modulated by a conserved lysine (K151 in *Da*Cld and K93 in *Kp*Cld) that is directly hydrogen bonded to P6 which will stabilize the carboxylate anion decreasing its pK_a. Therefore, it is reasonable to assign P6 as the proton acceptor in the PCET reaction in which Cpd I is reduced to Cpd II by tyrosine. Coproheme decarboxylase from *Staphylococcus aureus*, previously Cld-like protein, also relies on a deprotonated propionate group to facilitate its oxidative decarboxylation via PCET from the hydrogen bonded catalytic tyrosine.[46] It remains unclear whether the tryptophan based radical requires PCET to form thereby leaving the possibility of a less efficient route to Cpd II:AA• that does not depend on pH.

The ferryl stretching frequency reported herein for *Kp*Cld falls along-side previously reported heme proteins which shows an inverse correlation between their $\nu_{Fe(IV)=O}$ frequencies and $\nu_{Fe(II)-His}$ frequencies (Figure 6.17).[19] This inverse correlation shows the proximal histidine bond strength exerts a trans effect on the distal ferryl bond. The stronger the proximal iron-histidine bond, the weaker the distal ferryl bond. By extension, it would be expected that the $\nu_{Fe(IV)=O}$ frequency for *Da*Cld should be lower as it has a lower $\nu_{Fe(II)-His}$ frequency than *Kp*Cld. The weaker ferryl should be intrinsically more reactive toward geminate pair recombination for production of O_2 by catalytic decomposition of ClO_2^-. However, the rapid formation of the dead-end state in *Kp*Cld may mask this ability. It remains unclear why *Kp*Cld routes to the dead end

Cpd II:AA• state faster than *Da*Cld. This may hint at a possible function that involves PCET in dimeric Clds as ClO_2^- decomposition has not been determined to be their *in vivo* function.

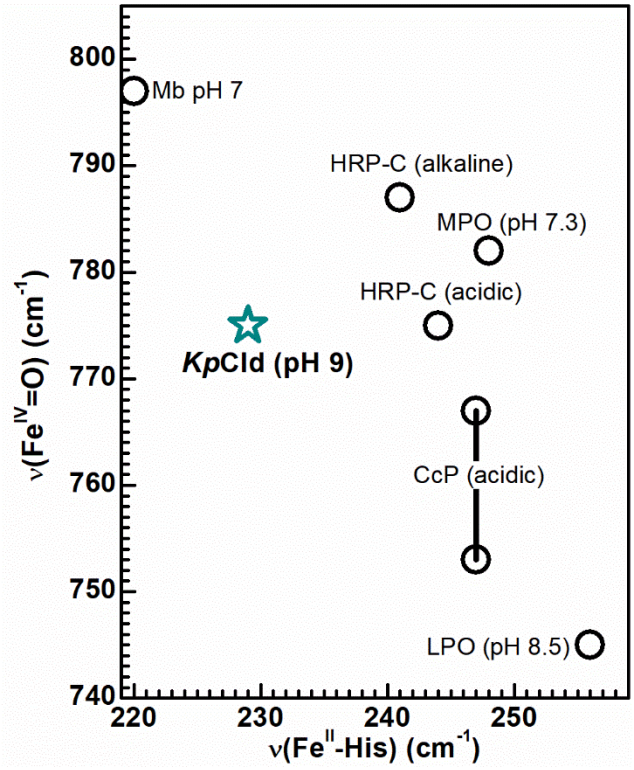

Figure 6.17. Correlation plot between ferryl and ferrous iron-histidine stretching frequencies of select heme proteins.

The proposed mechanistic model for catalytic ClO_2^- decomposition is illustrated in Scheme 6.1. Resting ferric Cld forms the chlorite complex, likely a transition state, through coordination to one of the oxygen atoms. The chlorite complex undergoes heterolytic bond cleavage resulting in Cpd I and an OCl^- geminate pair. Recombination of the geminate pair yields formation of an O−O bond, producing molecular O_2, Cl^-, and regeneration of the ferric resting state in a concerted fashion. However, several side reactions can branch from the Cpd I:OCl^- geminate pair. One pathway involves reduction of Cpd I to Cpd II by a PCET step resulting in an inactivated enzyme toward O_2 production. This inactivated form can also be potentially reached by one electron oxidation of another ClO_2^- molecule. Due to its inability to

recombine with OCl^- to produce O_2, the inactivated form can only return to resting state by subsequent one electron reductions from excess ClO_2^-.

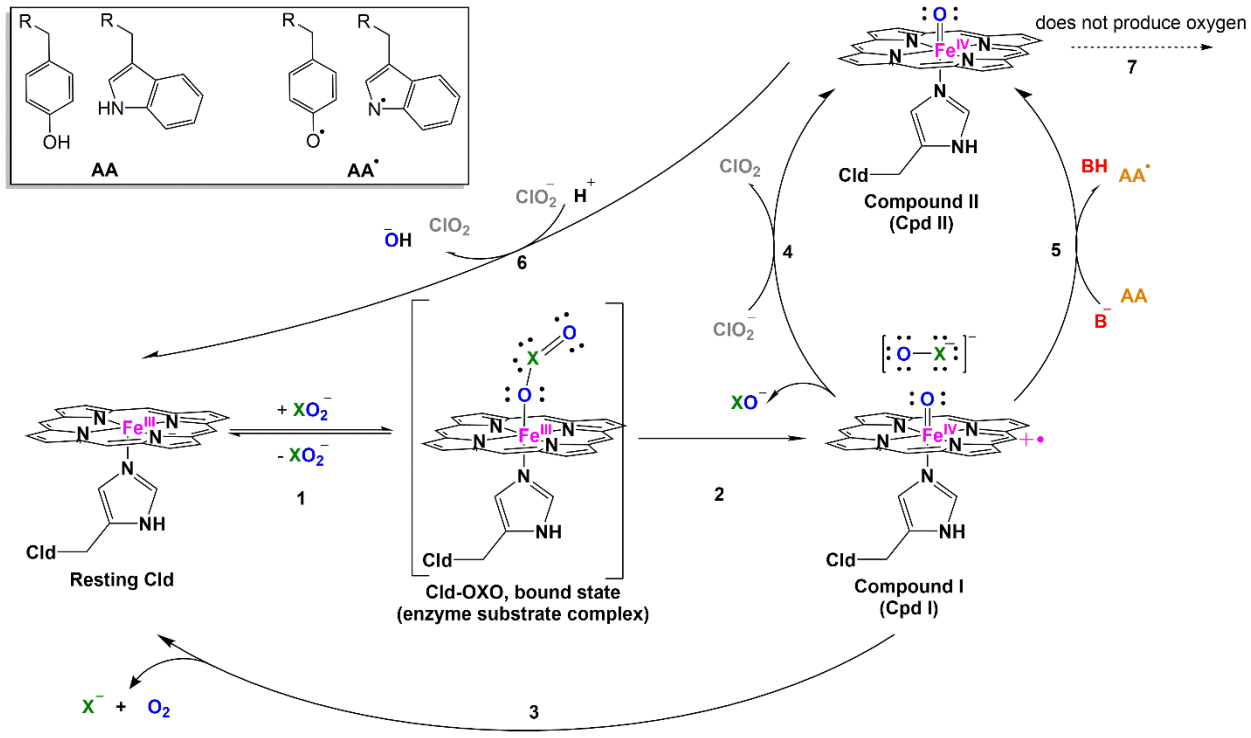

Scheme 6.1. Proposed mechanism for pH dependent catalytic XO_2^- decomposition by Cld. (1) XO_2^- coordinates to the ferric iron center through an oxygen atom. (2) The enzyme substrate complex undergoes heterolytic bond cleavage yielding Cpd I and an OX^- fragment. (3) Cpd I and OX^- fragment recombine to generate oxygen and the corresponding halide in a concerted step. (4) OX^- diffuses out of the pocket before the fragment can recombine. Another molecule of ClO_2^- diffuses into the pocket reducing Cpd I to Cpd II and oxidizing ClO_2^- to ClO_2. (5) Cpd I is reduced to Cpd II by an adjacent amino acid (tyrosine or tryptophan) in a proton coupled electron transfer before the fragment can recombine. (6) Another molecule of ClO_2^- diffuses into the pocket after ClO_2 diffuses out reducing Cpd II to ferric iron. (7) Cpd II persists but does not yield oxygen and undergoes nonspecific redox chemistry poisoning the catalyst.

6.6. Conclusions

Heterolytic bond cleavage models the pH dependent activity profile for catalytic ClO_2^- decomposition by Clds. Cpd I is the O_2-producing intermediate during. Cpd II formation is linked to the oxidization of either tyrosine or tryptophan residues by Cpd I which does not yield O_2. The pK_a for catalytic ClO_2^- decomposition matches the pK_a for the Cpd I : Cpd II population ratio, which is 6.6 for *Da*Cld. This pK_a falls within the known range of pK_a's for heme

propionionic acid groups in other proteins. Therefore, the nearby propionate P6 is assigned as the base that facilitates PCET of the H-bonded aromatic residues. Although the precise structural basis for the intrinsic difference in activity between clade 1 and clade 2 Clds remains elusive, evidence suggests that the rate at which Cpd I oxidizes an adjacent amino acid is faster in the clade 2 *Kp*Cld than in the clade 1 *Da*Cld, thereby effectively reducing the reactive intermediate concentration and therefore the O_2-producing activity.

6.7. Associated Content

Additional data referred to in the text are in Appendix E: Figures E1 to E17.

6.8. Funding Sources

This work was supported by a Doctoral Dissertation Fellowship awarded through North Dakota NSF-EPSCoR Grant OIA-1355466 (Z. G.).

6.9. References

1. Mayfield, J. A.; Blanc, B.; Rodgers, K. R.; Lukat-Rodgers, G. S.; DuBois, J. L., Peroxidase-Type Reactions Suggest a Heterolytic/Nucleophilic O–O Joining Mechanism in the Heme-Dependent Chlorite Dismutase. *Biochemistry* 2013, *52* (40), 6982-6994.
2. Schaffner, I.; Mlynek, G.; Flego, N.; Pühringer, D.; Libiseller-Egger, J.; Coates, L.; Hofbauer, S.; Bellei, M.; Furtmüller, P. G.; Battistuzzi, G.; Smulevich, G.; Djinović-Carugo, K.; Obinger, C., Molecular Mechanism of Enzymatic Chlorite Detoxification: Insights from Structural and Kinetic Studies. *ACS Catalysis* 2017, *7* (11), 7962-7976.
3. Streit, B. R.; DuBois, J. L., Chemical and Steady-State Kinetic Analyses of a Heterologously Expressed Heme Dependent Chlorite Dismutase. *Biochemistry* 2008, *47* (19), 5271-5280.
4. Geeraerts, Z.; Heskin, A. K.; DuBois, J.; Rodgers, K. R.; Lukat-Rodgers, G. S., Structure and reactivity of chlorite dismutase nitrosyls. *Journal of Inorganic Biochemistry* 2020, *211*, 111203.
5. Tropea, J. E.; Cherry, S.; Waugh, D. S., Expression and Purification of Soluble His6-Tagged TEV Protease. In *High Throughput Protein Expression and Purification: Methods and Protocols*, Doyle, S. A., Ed. Humana Press: Totowa, NJ, 2009; pp 297-307.
6. Bradford, M. M., A rapid and sensitive method for the quantitation of microgram quantities of protein utilizing the principle of protein-dye binding. *Analytical Biochemistry* 1976, *72* (1), 248-254.
7. Berry, E. A.; Trumpower, B. L., Simultaneous determination of hemes a, b, and c from pyridine hemochrome spectra. *Analytical Biochemistry* 1987, *161* (1), 1-15.

8. Streit, B. R.; Blanc, B.; Lukat-Rodgers, G. S.; Rodgers, K. R.; DuBois, J. L., How active-site protonation state influences the reactivity and ligation of the heme in chlorite dismutase. *J Am Chem Soc* 2010, *132* (16), 5711-24.
9. Celis, A. I.; Geeraerts, Z.; Ngmenterebo, D.; Machovina, M. M.; Kurker, R. C.; Rajakumar, K.; Ivancich, A.; Rodgers, K. R.; Lukat-Rodgers, G. S.; DuBois, J. L., A dimeric chlorite dismutase exhibits O2-generating activity and acts as a chlorite antioxidant in Klebsiella pneumoniae MGH 78578. *Biochemistry* 2015, *54* (2), 434-46.
10. Morris, J. C., The Acid Ionization Constant of HOCl from 5 to 35°. *The Journal of Physical Chemistry* 1966, *70* (12), 3798-3805.
11. Wang, L.; Nicoson, J. S.; Huff Hartz, K. E.; Francisco, J. S.; Margerum, D. W., Bromite Ion Catalysis of the Disproportionation of Chlorine Dioxide with Nucleophile Assistance of Electron-Transfer Reactions between ClO2 and BrO2 in Basic Solution. *Inorganic Chemistry* 2002, *41* (1), 108-113.
12. Noszticzius, Z.; Noszticzius, E.; Schelly, Z. A., Use of ion-selective electrodes for monitoring oscillating reactions. 2. Potential response of bromide- iodide-selective electrodes in slow corrosive processes. Disproportionation of bromous and iodous acids. A Lotka-Volterra model for the halate driven oscillators. *The Journal of Physical Chemistry* 1983, *87* (3), 510-524.
13. Evans, J. C.; Lo, G. Y. S., Vibrational spectra of BrO-, BrO2-, Br3-, and Br5. *Inorganic Chemistry* 1967, *6* (8), 1483-1486.
14. Qian, Y.; Chen, Y.; Jiang, Y.; Zhang, L., A clean production process of sodium chlorite from sodium chlorate. *Journal of Cleaner Production* 2007, *15* (10), 920-926.
15. Lee, A. Q.; Streit, B. R.; Zdilla, M. J.; Abu-Omar, M. M.; DuBois, J. L., Mechanism of and exquisite selectivity for O–O bond formation by the heme-dependent chlorite dismutase. *Proceedings of the National Academy of Sciences* 2008, *105* (41), 15654.
16. Philippi, M.; dos Santos, H. S.; Martins, A. O.; Azevedo, C. M. N.; Pires, M., Alternative spectrophotometric method for standardization of chlorite aqueous solutions. *Analytica Chimica Acta* 2007, *585* (2), 361-365.
17. Dave Barr, S. S. E., and Gareth R. Eaton, Workshop on Quantitative EPR. *31st Annual International EPR Symposium*, 120.
18. Stoll, S.; Schweiger, A., EasySpin, a comprehensive software package for spectral simulation and analysis in EPR. *Journal of Magnetic Resonance* 2006, *178* (1), 42-55.
19. Oertling, W. A.; Kean, R. T.; Wever, R.; Babcock, G. T., Factors affecting the iron-oxygen vibrations of ferrous oxy and ferryl oxo heme proteins and model compounds. *Inorganic Chemistry* 1990, *29* (14), 2633-2645.
20. Atkins, P. W.; Brivati, J. A.; Keen, N.; Symons, M. C. R.; Trevalion, P. A., 935. Oxides and oxy-ions of the non-metals. Part III. Oxy-radicals of chlorine. *Journal of the Chemical Society (Resumed)* 1962, (0), 4785-4793.
21. Van Wart, H. E.; Zimmer, J., Resonance Raman studies of the photoreduction of horseradish peroxidase compounds I and II. *Journal of the American Chemical Society* 1985, *107* (11), 3379-3381.
22. Zámocký, M.; Hofbauer, S.; Schaffner, I.; Gasselhuber, B.; Nicolussi, A.; Soudi, M.; Pirker, K. F.; Furtmüller, P. G.; Obinger, C., Independent evolution of four heme peroxidase superfamilies. (1096-0384 (Electronic)).

23. Goblirsch, B. R.; Streit, B. R.; DuBois, J. L.; Wilmot, C. M., Structural features promoting dioxygen production by Dechloromonas aromatica chlorite dismutase. *JBIC Journal of Biological Inorganic Chemistry* 2010, *15* (6), 879-888.
24. Blanc, B.; Rodgers, K. R.; Lukat-Rodgers, G. S.; DuBois, J. L., Understanding the roles of strictly conserved tryptophan residues in O2 producing chlorite dismutases. *Dalton Transactions* 2013, *42* (9), 3156-3169.
25. Matsui, T.; Nakajima A Fau - Fujii, H.; Fujii H Fau - Matera, K. M.; Matera Km Fau - Migita, C. T.; Migita Ct Fau - Yoshida, T.; Yoshida T Fau - Ikeda-Saito, M.; Ikeda-Saito, M., O(2)- and H(2)O(2)-dependent verdoheme degradation by heme oxygenase: reaction mechanisms and potential physiological roles of the dual pathway degradation. (0021-9258 (Print)).
26. Geeraerts, Z.; Rodgers, K. R.; DuBois, J. L.; Lukat-Rodgers, G. S., Active Sites of O2-Evolving Chlorite Dismutases Probed by Halides and Hydroxides and New Iron–Ligand Vibrational Correlations. *Biochemistry* 2017, *56* (34), 4509-4524.
27. Ericson, M. B.; Grapengiesser S Fau - Gudmundson, F.; Gudmundson F Fau - Wennberg, A. M.; Wennberg Am Fau - Larkö, O.; Larkö O Fau - Moan, J.; Moan J Fau - Rosén, A.; Rosén, A., A spectroscopic study of the photobleaching of protoporphyrin IX in solution. (0268-8921 (Print)).
28. Sivaraja, M.; Goodin, D. B.; Smith, M.; Hoffman, B. M., Identification by ENDOR of Trp191 as the free-radical site in cytochrome c peroxidase compound ES. *Science* 1989, *245* (4919), 738.
29. Houseman, A. L. P.; Doan, P. E.; Goodwin, D. B.; Hoffman, B. M., Comprehensive explanation of the anomalous EPR spectra of wild-type and mutant cytochrome c peroxidase compound ES. *Biochemistry* 1993, *32* (16), 4430-4443.
30. Huyett, J. E.; Doan, P. E.; Gurbiel, R.; Houseman, A. L. P.; Sivaraja, M.; Goodin, D. B.; Hoffman, B. M., Compound ES of Cytochrome c Peroxidase Contains a Trp .pi.-Cation Radical: Characterization by Continuous Wave and Pulsed Q-Band External Nuclear Double Resonance Spectroscopy. *Journal of the American Chemical Society* 1995, *117* (35), 9033-9041.
31. Sun, S.; Li Zs Fau - Chen, S.-L.; Chen, S. L., A dominant homolytic O-Cl bond cleavage with low-spin triplet-state Fe(IV)=O formed is revealed in the mechanism of heme-dependent chlorite dismutase. (1477-9234 (Electronic)).
32. Su, J.-X.; Chen, S.-L., Significant electron transfer in heme catalysis: The case of chlorite dismutase. *Journal of Catalysis* 2017, *348*, 40-46.
33. Keith, J. M.; Abu-Omar, M. M.; Hall, M. B., Computational Investigation of the Concerted Dismutation of Chlorite Ion by Water-Soluble Iron Porphyrins. *Inorganic Chemistry* 2011, *50* (17), 7928-7930.
34. Geeraerts, Z.; Celis, A. I.; Mayfield, J. A.; Lorenz, M.; Rodgers, K. R.; DuBois, J. L.; Lukat-Rodgers, G. S., Distinguishing Active Site Characteristics of Chlorite Dismutases with Their Cyanide Complexes. *Biochemistry* 2018, *57* (9), 1501-1516.
35. Bracci, M.; Van Doorslaer, S.; García-Rubio, I., EPR of Compound I: An Illustrated Revision of the Theoretical Model. *Applied Magnetic Resonance* 2020, *51* (11), 1559-1589.
36. Jakopitsch, C.; Spalteholz, H.; Furtmüller, P. G.; Arnhold, J.; Obinger, C., Mechanism of reaction of horseradish peroxidase with chlorite and chlorine dioxide. *Journal of Inorganic Biochemistry* 2008, *102* (2), 293-302.

37. Jakopitsch, C.; Pirker, K. F.; Flemmig, J.; Hofbauer, S.; Schlorke, D.; Furtmüller, P. G.; Arnhold, J.; Obinger, C., Mechanism of reaction of chlorite with mammalian heme peroxidases. *Journal of Inorganic Biochemistry* 2014, *135*, 10-19.
38. Hofbauer, S.; Gruber, C.; Pirker, K. F.; Sündermann, A.; Schaffner, I.; Jakopitsch, C.; Oostenbrink, C.; Furtmüller, P. G.; Obinger, C., Transiently Produced Hypochlorite Is Responsible for the Irreversible Inhibition of Chlorite Dismutase. *Biochemistry* 2014, *53* (19), 3145-3157.
39. Mahmoudi, L.; Kissner, R.; Nauser, T.; Koppenol, W. H., Electrode Potentials of l-Tryptophan, l-Tyrosine, 3-Nitro-l-tyrosine, 2,3-Difluoro-l-tyrosine, and 2,3,5-Trifluoro-l-tyrosine. *Biochemistry* 2016, *55* (20), 2849-2856.
40. Mikami, S.-i.; Tai, H.; Yamamoto, Y., Effect of the Redox-Dependent Ionization State of the Heme Propionic Acid Side Chain on the Entropic Contribution to the Redox Potential of Pseudomonas aeruginosa Cytochrome c551. *Biochemistry* 2009, *48* (33), 8062-8069.
41. Davis, I.; Koto, T.; Terrell, J. R.; Kozhanov, A.; Krzystek, J.; Liu, A., High-Frequency/High-Field Electron Paramagnetic Resonance and Theoretical Studies of Tryptophan-Based Radicals. *The Journal of Physical Chemistry A* 2018, *122* (12), 3170-3176.
42. Un, S., The g-values and hyperfine coupling of amino acid radicals in proteins: comparison of experimental measurements with ab initio calculations. *Magnetic Resonance in Chemistry* 2005, *43* (S1), S229-S236.
43. Blanc, B.; Mayfield, J. A.; McDonald, C. A.; Lukat-Rodgers, G. S.; Rodgers, K. R.; DuBois, J. L., Understanding how the distal environment directs reactivity in chlorite dismutase: spectroscopy and reactivity of Arg183 mutants. *Biochemistry* 2012, *51* (9), 1895-910.
44. Fitch, C. A.; Platzer, G.; Okon, M.; Garcia-Moreno, B. E.; McIntosh, L. P., Arginine: Its pKa value revisited. *Protein Sci* 2015, *24* (5), 752-761.
45. Mlynek, G.; Sjöblom, B.; Kostan, J.; Füreder, S.; Maixner, F.; Gysel, K.; Furtmüller, P. G.; Obinger, C.; Wagner, M.; Daims, H.; Djinović-Carugo, K., Unexpected Diversity of Chlorite Dismutases: a Catalytically Efficient Dimeric Enzyme from <span class="named-content genus-species" id="named-content-1">Nitrobacter winogradskyi</span&gt. *Journal of Bacteriology* 2011, *193* (10), 2408.
46. Streit, B. R.; Celis, A. I.; Moraski, G. C.; Shisler, K. A.; Shepard, E. M.; Rodgers, K. R.; Lukat-Rodgers, G. S.; DuBois, J. L., Decarboxylation involving a ferryl, propionate, and a tyrosyl group in a radical relay yields heme b. *Journal of Biological Chemistry* 2018, *293* (11), 3989-3999.

APPENDIX A

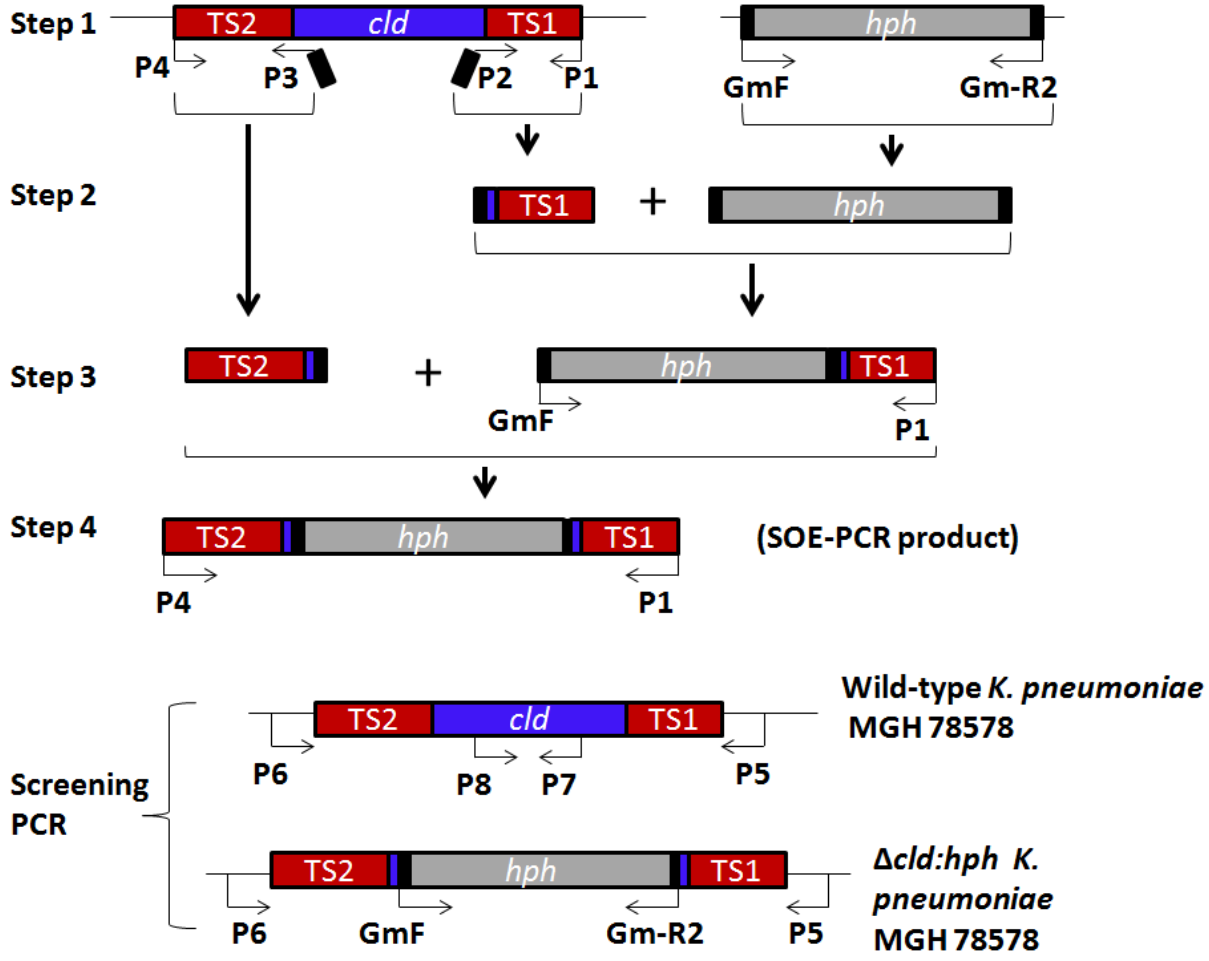

Figure A1. Schematic outlining the SOE-PCR and PCR validation strategy used to generate the Δ*cld* strain. See text for further details.

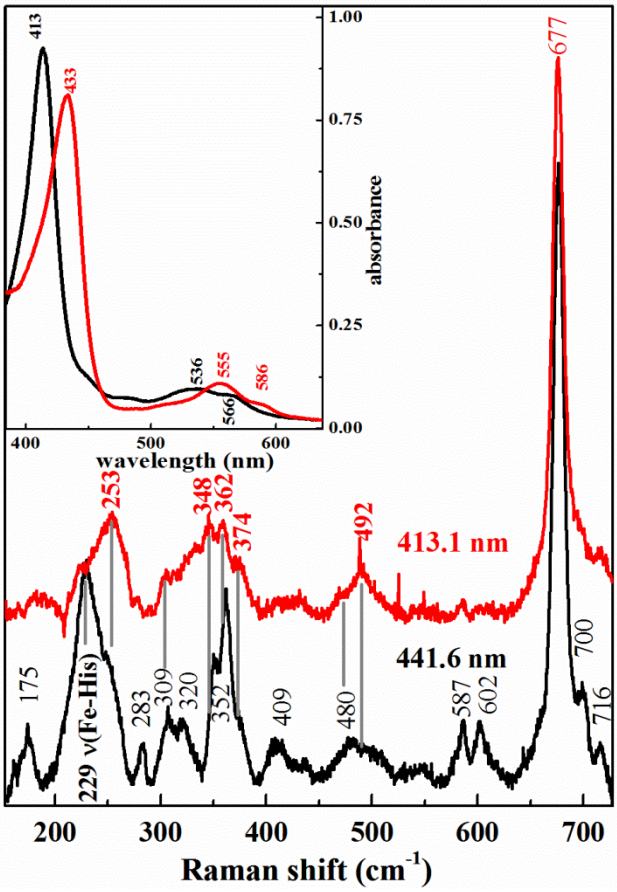

Figure A2. The iron histidine stretch of ferrous *Kp*Cld is resonance enhanced with 441.6 nm excitation. Comparison of rR spectra of ferrous *Kp*Cld pH 7.0 with 413.1 (red) and 441.6 nm (black) excitation. Inset: UV-visible spectra of ferric (black) and ferrous (red) KpCld pH 7.0 in 100 mM potassium phosphate buffer.

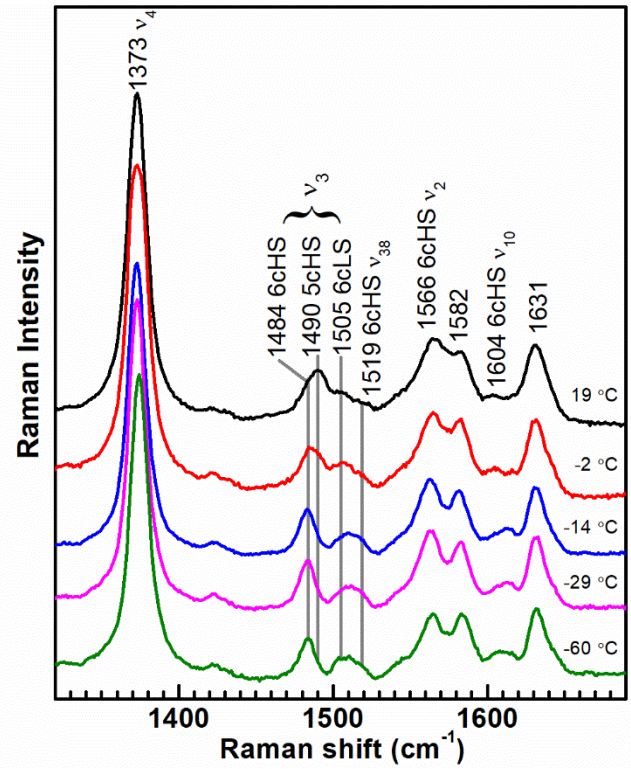

Figure A3. Temperature dependence of the rR spectrum of ferric *Kp*Cld pH 6.0 indicates exothermic binding of water to the heme. The high frequency rR spectra of ferric *Kp*Cld in 100 mM potassium phosphate pH 6.0 at the indicated temperatures were acquired with 413.1 nm excitation and 4 mW power at the sample. Temperature was controlled with a liquid N_2 boil off system. As the temperature is decreased, the broad ν_3 envelop encompassing contributions from 5cHS and 6cHS heme species sharpens to a symmetrical band consistent with a 6cHS aqua *Kp*Cld complex. As the 6cHS grows in, as judged by sharpening to the ν_3 band, ν_{38} associated with this 6cHS complex also becomes prominent and overlaps with the ν_3 that suggests a small amount of 6cLS species at room temperature. Band assignments were made by analogy to metMb.

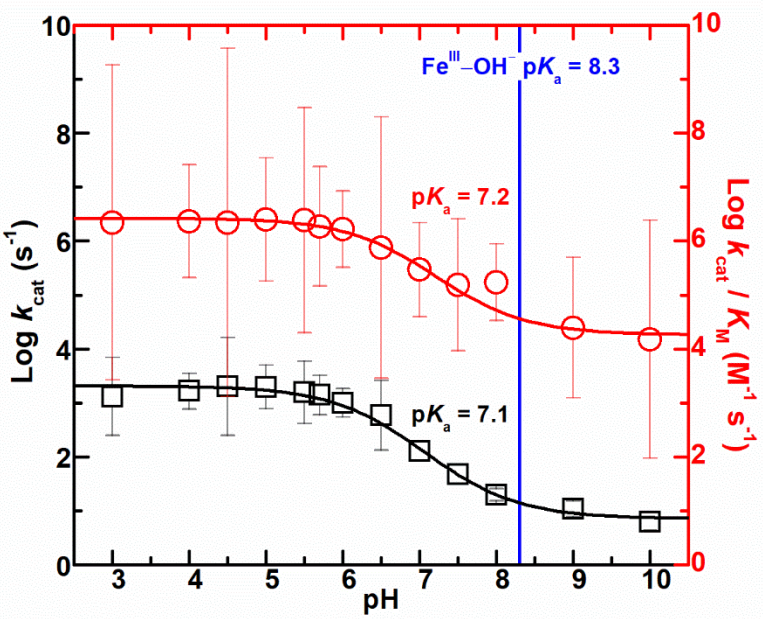

Figure A4. Plots of the log(k_{cat}) (black squares) and the log(k_{cat}/K_M) (red circles) for the chlorite decomposition reaction as a function of pH. Initial rates of chlorite-decomposing activity in the steady state were measured with a luminescence-based probe used to measure O_2 evolution by *Kp*Cld. Samples were 12 nM WT *Kp*Cld and 0.05 – 2 mM chlorite in the following buffer solutions: 50 mM phosphate-citrate (pH < 6), 100 mM phosphate (pH 6 – 8), or glycine (pH >8). Plots of log(k_{cat}) and the log(k_{cat}/K_M) both show a single clear turning point corresponding to a pK_a of 7.0. This enzyme-localized (as opposed to heme-localized) deprotonation event decreases the enyzme activity and efficiency. The optimum activity is observed near pH 5.0 where k_{cat} and k_{cat}/K_M have values of $(1.9\pm0.2)\times10^3$ s^{-1} and $(2.5\pm0.4)\times10^6$ $M^{-1}s^{-1}$, respectively. Above the enzyme-localized pK_a (~7), k_{cat} and k_{cat}/K_M drop to $(1.1\pm1.6)\times10^1$ s^{-1} and $(2.4\pm0.7)\times10^4$ $M^{-1}s^{-1}$ (pH 9.0), respectively.

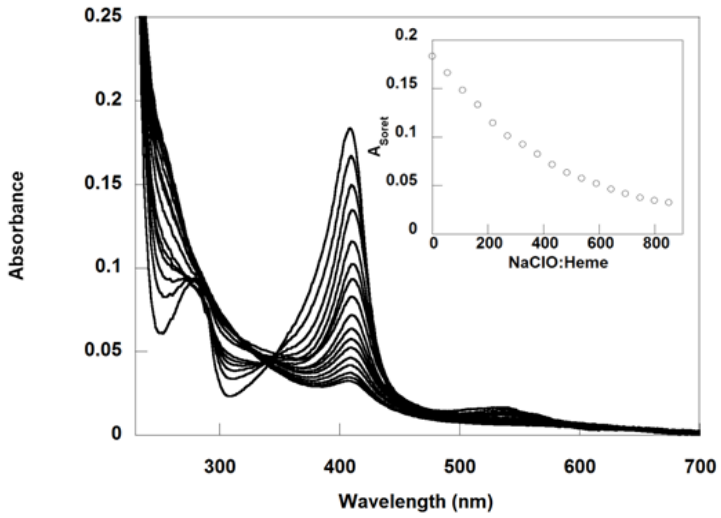

Figure A5. Titration of *Kp*Cld heme spectrum with NaClO. 50µL of 7.3 µM heme-bound *Kp*Cld was added to 950µL citrate-phosphate buffer (50 mM, pH 6.0, room temperature) in a UV/vis cuvette. A defined concentration of sodium hypochlorite was added and the solution was rapidly mixed. (Shown here is 0.90 mM an amount sufficient to nearly eliminate the heme Soret band. Several concentrations of NaClO were examined.) Spectra were scanned every 6s until the Soret band no longer changed. The inset shows the final Soret band absorbance plotted versus increasing [NaClO], generated from a series of experiments like the representative one shown here. The curve reaches an asymptote near 800 equivalents of NaClO per heme.

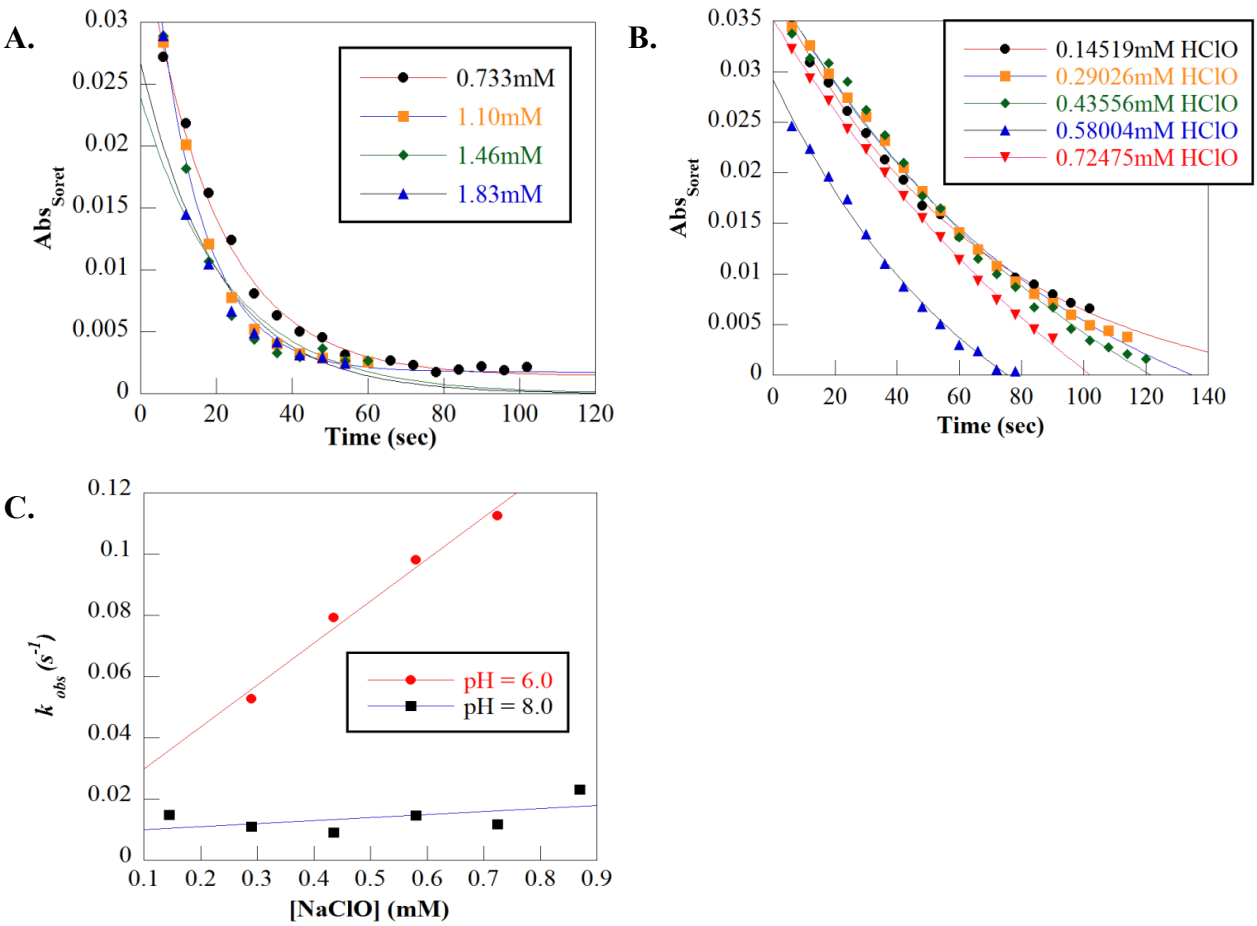

Figure A6. 50µL of 7.3 µM heme-bound *Kp*Cld was added to 950 µL 50 mM citrate-phosphate buffer, pH 6.0 or 8.0, in a UV/vis cuvette at room temperature. NaClO was added to final concentrations ranging from 0.15mM – 0.9mM. Immediately following each NaClO addition, the solution was mixed rapidly by pipetting up and the reaction monitored over time in scanning mode (250–700 nm) with scans every 6s. The reaction was monitored to completion, until the Soret band was eliminated and/or changes in the spectra ceased. First order rate constants (k_{obs}) were fit to the resulting single exponential curves A) and B), pH 6 and 8 respectively, describing the change in the Soret band absorbance versus time. The values of k_{obs} were plotted versus [NaClO] to generate a second-order rate constant from the slope of the line C).

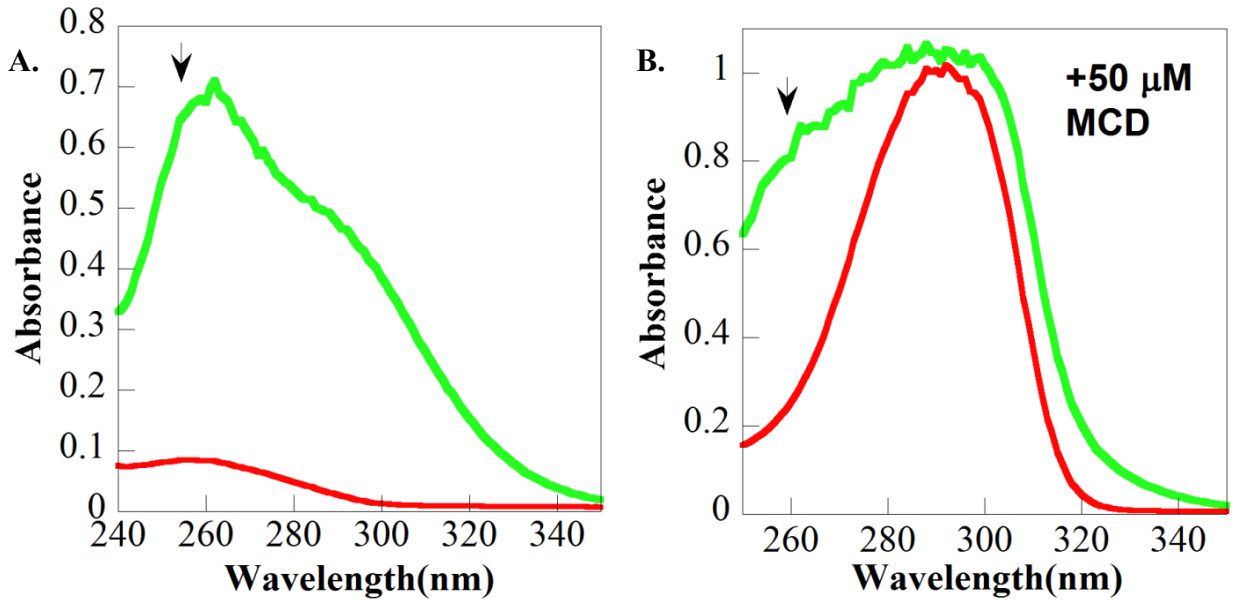

Figure A7. Trappable HOCl is not formed in appreciable quantities during the *Da*Cld reaction. The reaction between *Da*Cld and chlorite was monitored under conditions similar to those shown in the text in Figure 5A–C. Only the initial spectra (t_0, green) and final spectra (t_{30min}, red) are shown. A) 5mM ClO_2^- was added to 0.1µM of *Da*Cld in 50 mM potassium phosphate buffer, pH 7.4. 88% of the initially present ClO_2^- was degraded, according to iodometric titration of the end products. B) The reaction was run under the same condtions but in the presence of 50 mM MCD ($\lambda max \sim 290$ nm). While most of the chlorite ($\lambda max \sim 260$ nm) is eliminated under these conditions, little MCD is converted to its chlorinated product DCD, which has no absorbance at this wavelength.

Table A1. Bacterial strains and plasmids used in this study.

Strain/ plasmid	Genotype/Features	Reference /Sources
Strain		
Klebsiella pneumoniae MGH 78578	Wild-type *K. pneumoniae* strain	ATCC
KR3478	*K. pneumoniae* MGH 78578 carrying pKOBEGApra	This study
KR3444	Δ*cld K. pneumoniae* MGH 78578 (Colony A)	This study
KR3523	Δ*cld K. pneumoniae* MGH 78578 (Colony B)	This study
Plasmid		
pKOBEGApra	Arabinose-inducible lambda Red expression plasmid; apramycin resistance	1
pJTAG-hyg	FRT-*hph*-FRT, hygromycin resistance cassette	2

1. Chaveroche MK, Ghigo JM, d'Enfert C. 2000. A rapid method for efficient gene replacement in the filamentous fungus Aspergillus nidulans. Nucleic Acids Res 28: E97.
2. Zhang Y, Jiang X, Wang Y, Li G, Tian Y, Liu H, Ai F, Ma Y, Wang B, Ruan F, Rajakumar K. 2014. Contribution of β-Lactamases and porin proteins OmpK35 and OmpK36 to carbapenem resistance in clinical isolates of KPC-2-producing *Klebsiella pneumoniae.* Antimicrob Agents Chemother 58:1214–1217.

Table A2. Oligonucleotide primers used in this study.

Primer number	Primer Name	Use/ target	Sequence (5'→3')[a]
-	GmF	FRT-*hph*-FRT	CGAATTAGCTTCAAAAGCGCTCTGA
-	GmR	FRT-*hph*-FRT	CGAATTGGGGATCTTGAAGTTCCT
-	EBGNHe-5	*gam, bet, exo*	CCCGCTAGCGAAAAGATGTTTCGTGAAGC
-	EBGh3-3	*gam, bet, exo*	GGGAAGCTTATTATCGTGAGGATGCGTCA
P1	cld-TS1-R	TS1	CCGTTATGTCATGCCTACCC
P2	cld-TS1-Fp/GmF	TS1	TCAGAGCGCTTTTGAAGCTAATTCGATTCATCAGT TTCCTCTCAG
P3	cld-TS2-Rp/GmR	TS2	AGGAACTTCAAGATCCCCAATTCGTAGTATCAGG TTTAACTGCG
P4	cld-TS2-F	TS2	CAACAACTGGGTGGAAAACC
P5	cld-upstr-TS1-Rp	Screening	CAATTGGAACGGGGGCTTTG
P6	cld-downstr-TS2-Fp	Screening	GAACCTTCCTGGGTGACTGG
P7	cld-internal-F	*cld*	AAGTCGAAGGGTTCGCTCTC
P8	cld-internal-R	*cld*	TCGCGGGATAACGAGTAACG

[a] Underlined nucleotides corresponding to primers P2 and P3 are complementary to matching sequences of primers GmF and GmR, respectively.

APPENDIX B

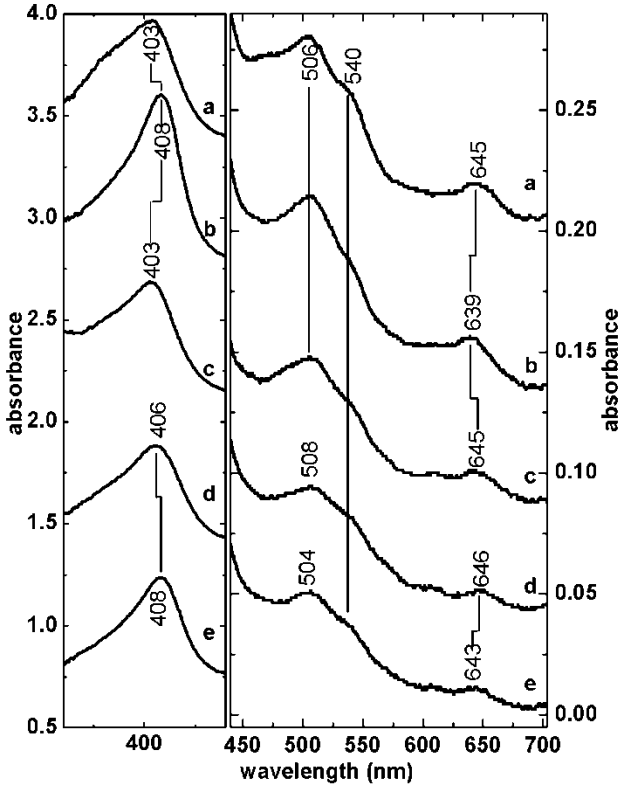

Figure B1. Chloride ion binding to *Kp*Cld is responsible for the changes in the CT and Soret bands. Effect of 100 mM chloride ion and 100 mM sulfate ion on ferric KpCld is examined by UV-visible spectroscopy. Spectra are shifted along the ordinate axis for illustration of the subtle changes in the presence of Cl^-. Cld under the following conditions: a) 100 mM sodium phosphate buffer pH 5.7, b) 100 mM NaCl, 100 mM sodium phosphate buffer pH 5.7 (identical spectrum is obtained in 100 mM KCl, 100 mM potassium phosphate buffer pH 5.7.), c) 100 mM sodium sulfate, 100 mM sodium phosphate buffer pH 5.7, d) 100 mM sodium phosphate pH 7.5, and e) 100 mM NaCl, 100 mM sodium phosphate buffer pH 7.5. The effect of chloride ion is observed at both pH 5.7 and 7.5.

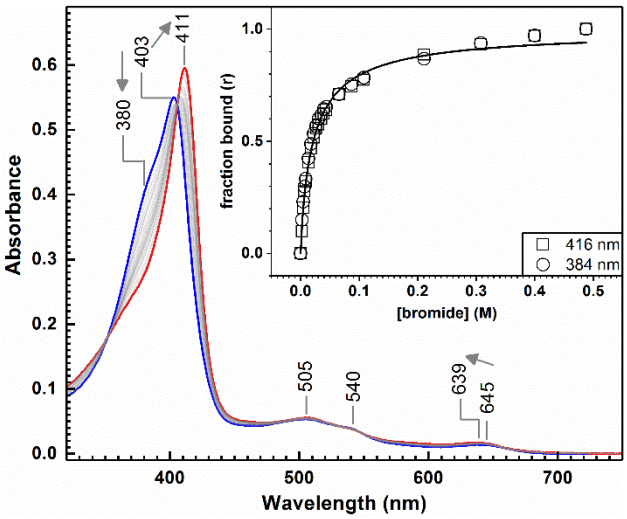

Figure B2. Spectrophotometric titration of *Kp*Cld with bromide. The spectrophotometric titration of *Kp*Cld in 100 mM sodium phosphate pH 6 is shown with the initial spectrum (0 mM Br^-) in blue and the final spectrum (488 mM Br^-) in red. Spectra corresponding to intermediate concentrations of bromide are grey. Aliquots of a stock bromide solution prepared in the same buffer were added to the enzyme to increase the bromide ion concentration in 0.002 – 0.100 M steps. Equilibrium was reached prior to each sequential addition. Arrows indicate the direction of change in the spectra as the bromide concentration increases. Inset: The fraction of *Kp*Cld with bromide bound ($r = (A_{Br} - A_{initial})/(A_{final} - A_{initial})$) calculated using the absorbance data at 416 and 384 nm, the wavelengths of greatest change in the titration, are plotted as a function of bromide concentration. The line shows the fit obtained using a single binding isotherm model (eqn 1) where the $K_D = (2.0 \pm 0.4) \times 10^{-2}$ M.

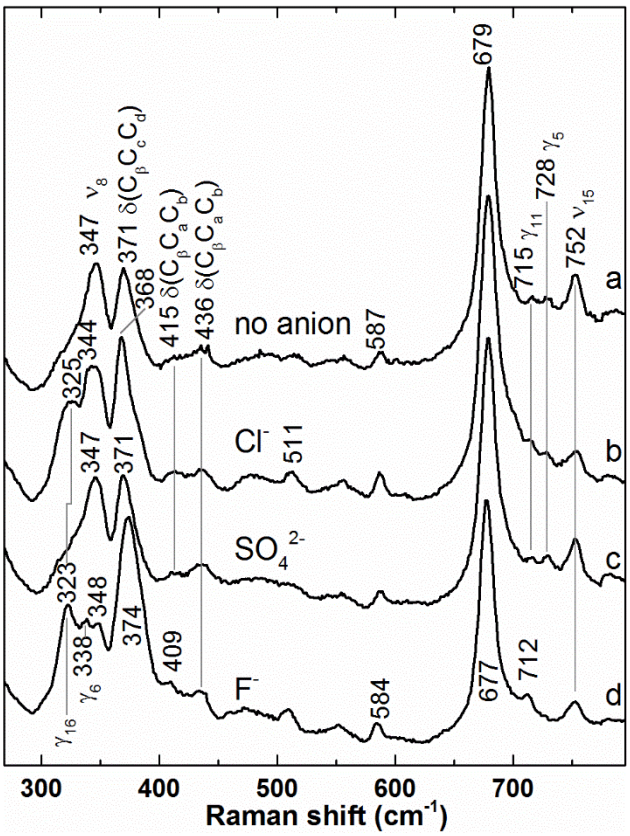

Figure B3. Differences are observed in low frequency rR spectra upon 6cHS heme formation in *Kp*Cld. All samples were in 100 mM sodium phosphate pH 5.7 with the following anions added: a) no anion, b) 100 mM sodium chloride, c) 100 mM sodium sulfate, and d) 500 mM sodium fluoride. Spectra a-c were obtained with 413.1 nm excitation and 3 mW at the sample; d was obtained with 406.7 nm excitation and 5 mW at the sample.

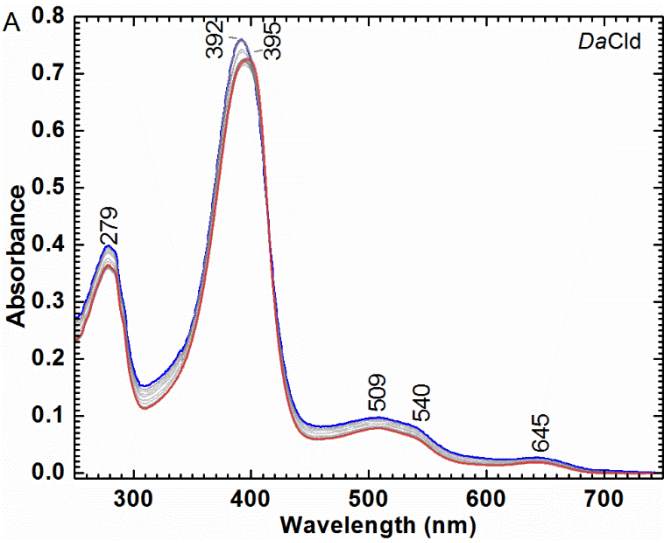

Figure B4. Spectrophotometric titration of *Da*Cld with chloride. 7.6 µM *Da*Cld in 100 mM sodium phosphate buffer pH 6.0 was titrated with Cl^- by increasing [Cl^-] in 20 mM increments from 0 to 400 mM: 0 mM Cl^-, blue; 20 mM Cl^- increments, grey; and 400 mM Cl^-, red.

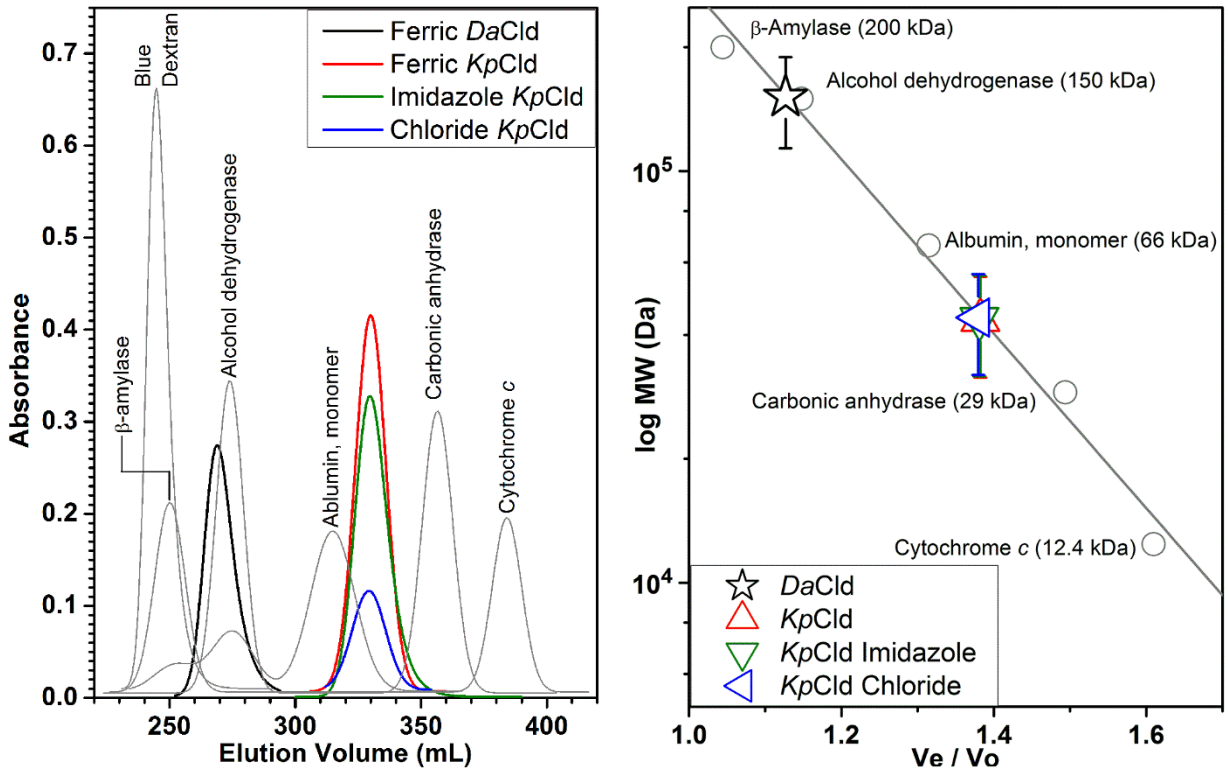

Figure B5. Size exclusion chromatography was used to demonstrate that *Kp*Cld is dimeric in the presence and absence of chloride ion. A) Absorbance maxima as a function of elution volumes are plotted and fit to either a Gaussian or exponentially modified Gaussian function in order to determine peak centers for each marker/Cld. Void volume (V_o) was determined by blue dextran while elution volumes (V_e) as a function of molecular weight were determined by five calibration proteins: β-amylase, alcohol dehydrogenase, carbonic anhydrase, albumin, and cytochrome *c* (gray peaks). Ferric *Da*Cld (black peak) has an elution volume at 269 mL while ferric *Kp*Cld (red peak) has an elution volume at 330 mL indicating *Kp*Cld has a smaller hydrodynamic radius and by extension a lower order oligomeric state. *Kp*Cld elution volume is not affected by coordination or spin state when in the presence of either 10 mM imidazole (green peak) or 200 mM sodium chloride (blue peak). B) Calibration curve displaying log molecular weight in daltons (Da) as a function of V_e/V_o ratio. Markers used to generate the calibration curve are shown as open circles (gray). Ferric *Da*Cld (open black star) has a molecular weight of $(1.5\pm0.4)\times10^5$ Da which is consistent with the reported crystallized pentamer. Ferric *Kp*Cld (open red triangle), *Kp*Cld in 10 mM imidazole (open green triangle), and *Kp*Cld in 200 mM sodium chloride (open blue triangle) has a molecular weight of $(4\pm1)\times10^4$ Da, consistent with its oligomeric state in solution being dimeric regardless of coordination or spin state. Reported uncertainties are propagated from the standard error generated by the calibration curve fit.

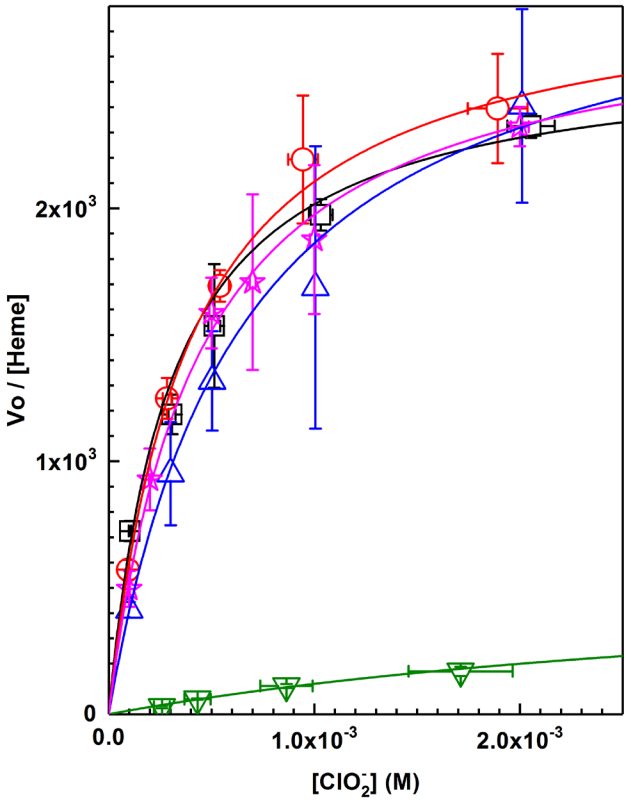

Figure B6. The effect of chloride, fluoride, perchlorate, and cyanide ions on the Michaelis-Menten plot of *Kp*Cld in 0.1 M sodium phosphate pH 6 at 25 °C: no ligand (black squares), 200 mM NaCl (red circles) 50 mM NaF (blue triangles) 100 mM $NaClO_4$, (magenta stars), 50μM KCN (green inverted triangles). Vertical error bars are the standard deviation between at least three trials. Horizontal error bars correspond to the uncertainty in concentration propagated from the extinction coefficient used to determine them.

Table B1. *Kp*Cld Michaelis-Menten fit parameters for the effects of various anions on the chlorite decomposition reaction. Reactions were carried out at 25 °C in 0.1 M sodium phosphate pH 6.

Ligand (M)	k_{cat} (s^{-1})	K_M (M)	k_{cat} / K_M ($M^{-1}s^{-1}$)
None	$(2.6\pm0.1)\times10^{3}$	$(3.0\pm0.4)\times10^{-4}$	$(9\pm1)\times10^{6}$
F^- (5.0×10^{-2})	$(3.1\pm0.1)\times10^{3}$	$(6.5\pm0.4)\times10^{-4}$	$(4.7\pm0.4)\times10^{6}$
Cl^- (2.0×10^{-1})	$(2.91\pm0.07)\times10^{3}$	$(3.8\pm0.2)\times10^{-4}$	$(7.6\pm0.4)\times10^{6}$
ClO_4^- (1.0×10^{-1})	$(2.83\pm0.06)\times10^{3}$	$(4.3\pm0.3)\times10^{-4}$	$(6.6\pm0.5)\times10^{6}$
CN^- (5.0×10^{-5})	$(6\pm3)\times10^{2}$	$(4\pm3)\times10^{-3}$	$(2\pm1)\times10^{5}$

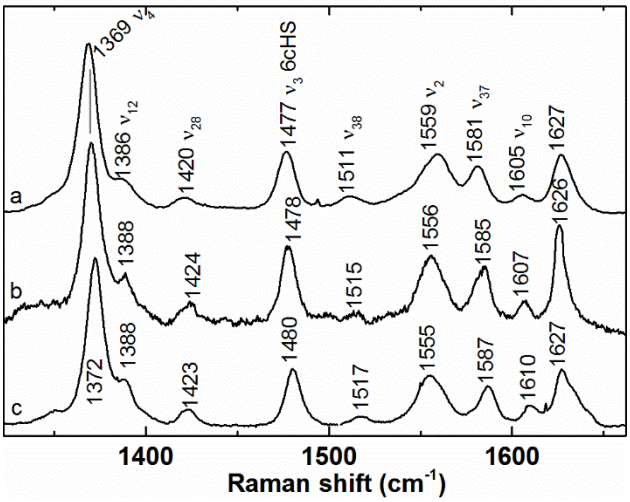

Figure B7. Heme site in ferric fluoride complexes of Clds as detected in the high frequency window of their Soret-excited rR spectra. a) *Kp*Cld−F pH 5.8, b) *Da*Cld(W227F)−F pH 6.8, and c) *Da*Cld−F pH 5.8. Spectra were obtained with 406.7-nm excitation; 12 mW at the sample. Samples were in 100 mM sodium phosphate buffer at the indicated pHs with 500 mM NaF.

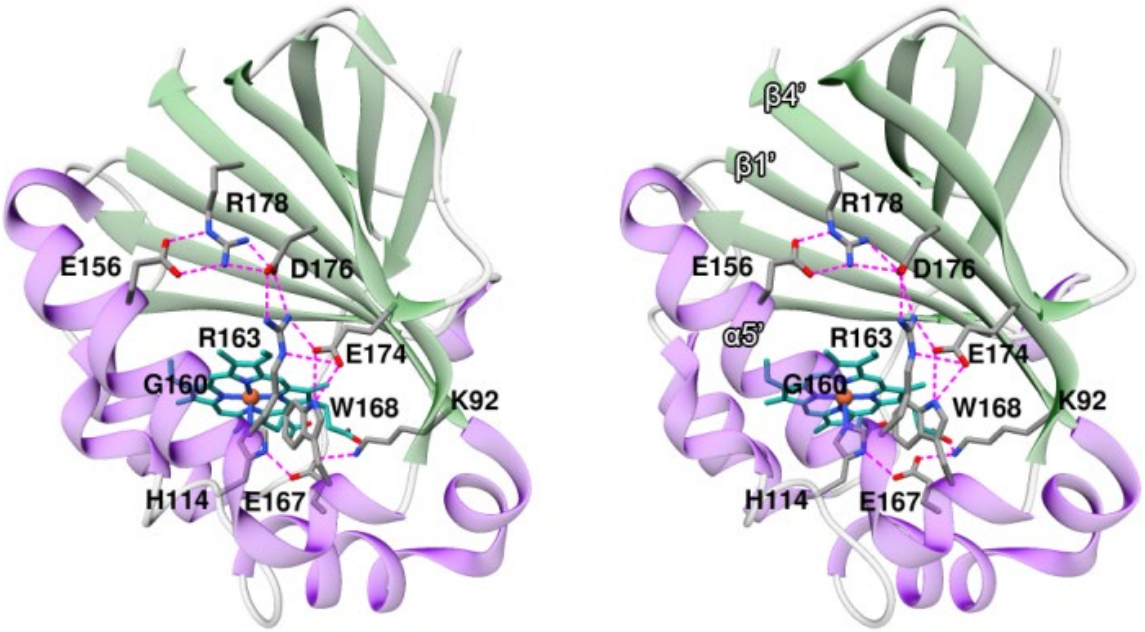

Figure B8. Cross-eyed stereo view of the crystal structure of *Nw*Cld (3QPI)[1] depicting residues with nonbonding interactions (2.7 – 3.6 Å) between α5' and β4' as indicated by dashed magenta lines. These residues are hydrophilic suggesting their interactions are primarily ionic in nature.

B.1. Correlations observed between ν(Fe^{III}–F) or ν(Fe^{III}–OH) and ν(Fe^{II}–His) for Clds and other heme proteins

Table B2. ν(Fe^{III}–F), ν(Fe^{III}–OH) and ν(Fe^{II}–His) frequencies for heme proteins with proximal His ligands and various distal H-bond donors. Equilibrium bond lengths, $r_{Fe\text{-}X}$, were calculated from stretching frequencies using Badger's rule.

Protein	ν(Fe^{III}–F) (cm^{-1})[a]	$r_{Fe\text{-}F}$ (Å)	LS ν(Fe^{III}–OH) (cm^{-1})	LS $r_{Fe\text{-}OH}$ (Å)	HS ν(Fe^{III}–OH) (cm^{-1})	HS $r_{Fe\text{-}OH}$ (Å)	ν(Fe^{II}–His) (cm^{-1})	ref
Arg in distal pocket								
*Kp*Cld	385	2.65	509	2.44	444	2.57	229	This work, [2]
*Da*Cld pH 8.0	390	2.63	514	2.43	440	2.58	224	This work, [3]
*Da*Cld pH 5.8	391	2.63					222	This work, [3]
*Da*Cld(W227F)	393	2.63	526	2.41			220	This work, [4]
*Sm*FixLN			539	2.39	479	2.49	212	[5]
*Cd*HmuT(Y235A)	393	2.63	521	2.42	433	2.59	221	[6]
HRP-C (H42L)			493	2.47			238	[7]
His in distal pocket								
hhMb pH 7.0	460	2.47	550	2.37	491	2.47	220	[8, 9]
swMb pH 7.0	462	2.47			490	2.47	220	[9, 10]
swMb pH 7.0[b]	461	2.47					220	[10-12]
hhMb pH 5.2	411	2.58					220	[9, 10]
swMb pH 5.4[b]	399	2.61					220	[10-12]
swMb pH 5.2	410	2.58					220	[9, 10]
Hb pH 7.0	468	2.45	553	2.36	492	2.47	215	[8, 13]
Hb pH 4.9	407	2.59					215	[11, 13]
Hb α subunit[b]	466	2.46					219	[14, 15]
Hb β subunit[b]	471	2.45					223	[14, 15]
*Pa*PhuS			546	2.37			222	[16]
DHP	462	2.47			491	2.47	233	[17, 18]
His & Arg in distal pocket								
HRP-C (alkaline)			503	2.45			241	[8, 19, 20]
HRP-C (acidic)	385	2.65					244	[9, 19, 21]
HRP-A1			516	2.42			244	[20]

[a]Excitation into CT2 of fluoride complex unless otherwise indicated. [b]Excitation into CT1 of fluoride complex.

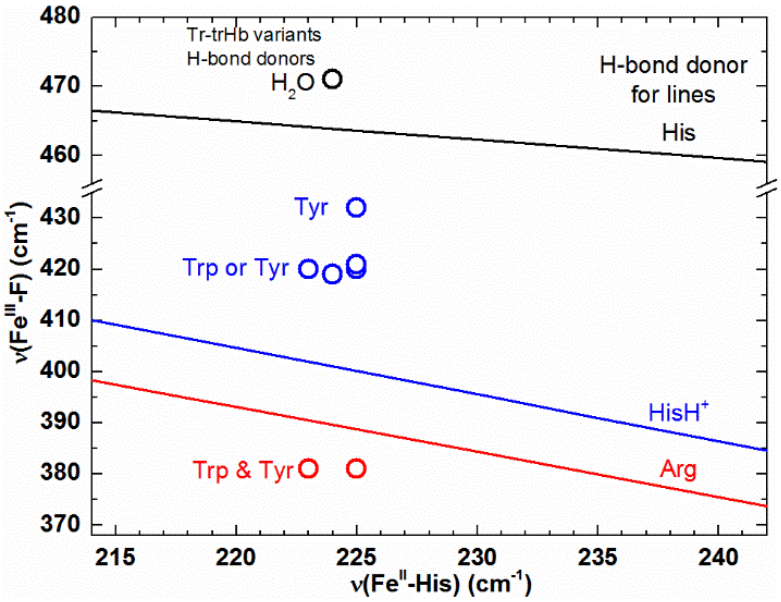

Figure B9. Vertical position of the ν(Fe^{III}–F)/ν(Fe^{II}–His) correlation lines is indicative of the number of H-bonds are donated from the distal pocket. The solid lines are the correlation lines presented in the manuscript that correspond to the following number of H-bonds donated from distal amino acid residues: two H-bonds (Arg as donor), red line; one H-bond ($HisH^+$ as donor), blue line; weak amino acid donor or water, black line. A series of *Tr*-trHb WT and variant fluoride complexes have been reported to show a direct correlation between CT1 energy and ν(Fe-F) frequency; placement of these variant-fluoride complexes on the CT1/ ν(Fe–F) correlation line has been explained by increases in H-bond donors. Since the ν(Fe^{II}–His) frequency ranges from 223-225 cm^{-1} for these *Tr*-trHb proteins,[22] they can be used to test the suggestion that vertical placement on the ν(Fe^{III}–F)/ν(Fe^{II}–His) plot is indicative of the number of distal H-bonds from amino acids. *Tr*-trHb proteins are shown on the ν(Fe^{III}–F)/ν(Fe^{II}–His) plot as follows: *Tr*-trHb complexes with 2 distal H-bond donors (Trp and Tyr) are WT and ASV and YB10F variants, red circle; complexes with single distal H-bond donor are variants WG8F, YCD1F, YCD1F/WG8F, YB10F/YCD1F and a second conformer observed for WT, ASV, and YB10F, blue circles; and water as the sole H-bond donor occurs in the triple mutant YB10F/YCD1F/WG8F, black circle. Data points were compiled from references [22-24].

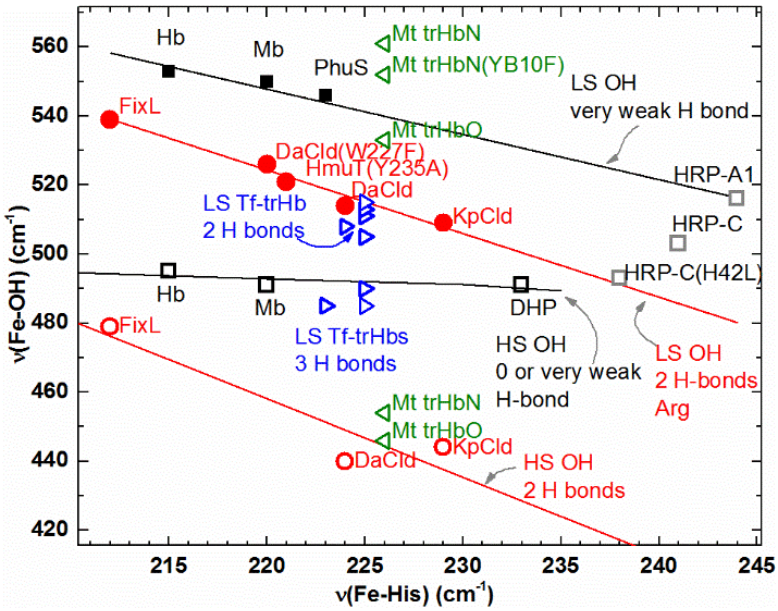

Figure B10. Vertical position of the ν(Fe^{III}–OH)/ν(Fe^{II}–His) correlation lines is indicative of the number of H-bonds are donated from the distal pocket. Data for trHbs has been added to the correlation plot from Figure 7B. The truncated Hbs (trHbs) have distal pockets with different H-bond donors than those discussed in the manuscript: *Mt* trHbN (green triangles), B10 Tyr and E11 Gln;[25] *Mt* trHbO (green triangles), CD1 Tyr and G8 Trp;[25] *Tf* trHb (blue triangles), CD1 Tyr, G8 Trp and water.[9, 22, 23] Points for WT and ASV *Tf* trHb correspond to hydroxide complexes with 3 H-bonds due to CD1 Tyr, G8 Trp and water. A series of *Tf* trHb mutants with two H-bonds to the bound hydroxide fall on the correlation line defined by Clds with 2 H-bonds supplied by Arg.[26] This suggests that the H-bond donating strength felt by the hydroxide is comparable between the 2 H-bonds from Arg and the case where one is from a Tyr and 1 is from Trp. The blue star is a *Tf* trHb mutant (YCD1F/WG8F) that MD simulation suggests has a single H-bond from water to hydroxide;[26] its position on the correlation plot suggests that it probably has two H-bonds, possibly one from water and one from B10 Tyr that normally indirectly (by H-bonding to a water which donates a H-bond to coordinated OH^-) stabilizes OH^- binding. The LS OH^- complexes of trHbN and trHbO are close to the LS OH^- correlation line that indicates little or no H-bond donation to the coordinated OH^- while their HS OH^- complexes fall on or close to the correlation line defined by 2 H-bonds. For trHbN those would be supplied by B10 Tyr and E11 Gln; in trHbO CD1 Tyr and G8 Trp residues are the likely H-bond donors. The ν(Fe^{II}–His) frequencies were compiled from following references: *Tf* trHb,[22, 26] *Mt* trHbN and *Mt* trHbO[25]

B.2. References

1. Mlynek, G., Sjoeblom, B., Kostan, J., Fuereder, S., Maixner, F., Gysel, K., Furtmueller, P. G., Obinger, C., Wagner, M., Daims, H., and Djinovic-Carugo, K. (2011) Unexpected diversity of chlorite dismutases: a catalytically efficient dimeric enzyme from *Nitrobacter winogradskyi*, *J. Bact. 193*, 2408-2417.
2. Celis, A. I., Geeraerts, Z., Ngmenterebo, D., Machovina, M. M., Kurker, R. C., Rajakumar, K., Ivancich, A., Rodgers, K. R., Lukat-Rodgers, G. S., and DuBois, J. L.

(2015) A Dimeric Chlorite Dismutase Exhibits O2-Generating Activity and Acts as a Chlorite Antioxidant in *Klebsiella pneumoniae* MGH 78578, *Biochemistry 54*, 434-446.
3. Streit, B. R., Blanc, B., Lukat-Rodgers, G. S., Rodgers, K. R., and DuBois, J. L. (2010) How Active-Site Protonation State Influences the Reactivity and Ligation of the Heme in Chlorite Dismutase, *J. Am. Chem. Soc. 132*, 5711-5724.
4. Blanc, B., Rodgers, K. R., Lukat-Rodgers, G. S., and DuBois, J. L. (2013) Understanding the roles of strictly conserved tryptophan residues in O2 producing chlorite dismutases, *Dalton Trans. 42*, 3156-3169.
5. Lukat-Rodgers, G. S., and Rodgers, K. R. (1998) Spin-state equilibria and axial ligand bonding in FixL hydroxide: a resonance Raman study, *J. Biol. Inorg. Chem. 3*, 274-281.
6. Draganova, E. B., Akbas, N., Adrian, S. A., Lukat-Rodgers, G. S., Collins, D. P., Dawson, J. H., Allen, C. E., Schmitt, M. P., Rodgers, K. R., and Dixon, D. W. (2015) Heme Binding by Corynebacterium diphtheriae HmuT: Function and Heme Environment, *Biochemistry 54*, 6598-6609.
7. Howes, B. D., Rodriguez-Lopez, J. N., Smith, A. T., and Smulevich, G. (1997) Mutation of Distal Residues of Horseradish Peroxidase: Influence on Substrate Binding and Cavity Properties, *Biochemistry 36*, 1532-1543.
8. Feis, A., Marzocchi, M. P., Paoli, M., and Smulevich, G. (1994) Spin State and Axial Ligand Bonding in the Hydroxide Complexes of Metmyoglobin, Methemoglobin, and Horseradish Peroxidase at Room and Low Temperatures, *Biochemistry 33*, 4577-4583.
9. Droghetti, E., Nicoletti, F. P., Bonamore, A., Sciamanna, N., Boffi, A., Feis, A., and Smulevich, G. (2011) The optical spectra of fluoride complexes can effectively probe H-bonding interactions in the distal cavity of heme proteins, *J. Inorg. Biochem. 105*, 1338-1343.
10. Kitagawa, T., Nagai, K., and Tsubaki, M. (1979) Assignment of the iron-nitrogen (His F8) stretching band in the resonance Raman spectra of deoxymyoglobin, *FEBS Letters 104*, 376-378.
11. Asher, S. A., Adams, M. L., and Schuster, T. M. (1981) Resonance Raman and absorption spectroscopic detection of distal histidine-fluoride interactions in human methemoglobin fluoride and sperm whale metmyoglobin fluoride: measurements of distal histidine ionization constants, *Biochemistry 20*, 3339-3346.
12. Asher, S. A., and Schuster, T. M. (1979) Resonance Raman examination of axial ligand bonding and spin-state equilibriums in metmyoglobin hydroxide and other heme derivatives, *Biochemistry 18*, 5377-5387.
13. Jeyarajah, S., and Kincaid, J. R. (1990) Resonance Raman studies of hemoglobins reconstituted with mesoheme. Unperturbed iron-histidine stretching frequencies in a functionally altered hemoglobin, *Biochemistry 29*, 5087-5094.
14. Asher, S. A., and Schuster, T. M. (1981) Differences in iron-fluoride bonding between the isolated subunits of human methemoglobin fluoride and sperm whale metmyoglobin fluoride as measured by resonance Raman spectroscopy, *Biochemistry 20*, 1866-1873.
15. Podstawka, E., Mak, P. J., Kincaid, J. R., and Proniewicz, L. M. (2006) Low frequency resonance Raman spectra of isolated α and β subunits of hemoglobin and their deuterated analogues, *Biopolymers 83*, 455-466.
16. Lansky, I. B., Lukat-Rodgers, G. S., Block, D., Rodgers, K. R., Ratliff, M., and Wilks, A. (2006) The Cytoplasmic Heme-binding Protein (PhuS) from the Heme Uptake System of

Pseudomonas aeruginosa Is an Intracellular Heme-trafficking Protein to the δ-Regioselective Heme Oxygenase, *J. Biol. Chem. 281*, 13652-13662.
17. Belyea, J., Belyea, C. M., Lappi, S., and Franzen, S. (2006) Resonance Raman Study of Ferric Heme Adducts of Dehaloperoxidase from Amphitrite ornata, *Biochemistry 45*, 14275-14284.
18. Franzen, S., Roach, M. P., Chen, Y.-P., Dyer, R. B., Woodruff, W. H., and Dawson, J. H. (1998) The Unusual Reactivities of *Amphitrite ornata* Dehaloperoxidase and *Notomatus lobatus* Chloroperoxidase Do Not Arise from a Histidine Imidazolate Proximal Heme Iron Ligand, *J. Am. Chem. Soc. 120*, 4658-4661.
19. Teraoka, J., and Kitagawa, T. (1981) Structural implication of the heme-linked ionization of horseradish peroxidase probed by the iron-histidine stretching Raman line, *J. Biol. Chem. 256*, 3969-3977.
20. Sitter, A. J., Shifflett, J. R., and Terner, J. (1988) Resonance Raman spectroscopic evidence for heme iron-hydroxide ligation in peroxidase alkaline forms, *J Biol Chem 263*, 13032-13038.
21. Smulevich, G., Feis, A., Focardi, C., Tams, J., and Welinder, K. G. (1994) Resonance Raman Study of the Active Site of Coprinus cinereus Peroxidase, *Biochemistry 33*, 15425-15432.
22. Droghetti, E., Nicoletti, F. P., Bonamore, A., Boechi, L., Arroyo, M. P., Estrin, D. A., Boffi, A., Smulevich, G., and Feis, A. (2010) Heme pocket structural properties of a bacterial truncated hemoglobin from Thermobifida fusca, *Biochemistry 49*, 10394-10402.
23. Nicoletti, F. P., Droghetti, E., Boechi, L., Bonamore, A., Sciamanna, N., Estrin, D. A., Feis, A., Boffi, A., and Smulevich, G. (2011) Fluoride as a Probe for H-Bonding Interactions in the Active Site of Heme Proteins: The Case of Thermobifida fusca Hemoglobin, *J. Am. Chem. Soc. 133*, 20970-20980.
24. Nicoletti, F. P., Droghetti, E., Howes, B. D., Bustamante, J. P., Bonamore, A., Sciamanna, N., Estrin, D. A., Feis, A., Boffi, A., and Smulevich, G. (2013) H-bonding networks of the distal residues and water molecules in the active site of Thermobifida fusca hemoglobin, *Biochim. Biophys. Acta, Proteins Proteomics 1834*, 1901-1909.
25. Egawa, T., and Yeh, S.-R. (2005) Structural and functional properties of hemoglobins from unicellular organisms as revealed by resonance Raman spectroscopy, *J. Inorg. Biochem. 99*, 72-96.
26. Nicoletti, F. P., Bustamante, J. P., Droghetti, E., Howes, B. D., Fittipaldi, M., Bonamore, A., Baiocco, P., Feis, A., Boffi, A., Estrin, D. A., and Smulevich, G. (2014) Interplay of the H-Bond Donor-Acceptor Role of the Distal Residues in Hydroxyl Ligand Stabilization of Thermobifida fusca Truncated Hemoglobin, *Biochemistry 53*, 8021-8030.

APPENDIX C

Table C1. Michaelis-Menten fit parameters for *Kp* and *Da*Cld chlorite decomposition reaction. Reactions were carried out in 0.1 M sodium phosphate buffer, pH 6.0 at 25 °C.

enzyme	k_{cat} (s^{-1})	K_M (M)	k_{cat} / K_M ($M^{-1}s^{-1}$)
*Kp*Cld	$(2.6\pm0.1)\times10^{3}$	$(3.0\pm0.4)\times10^{-4}$	$(9\pm1)\times10^{6}$
*Kp*Cld−CN^{-}	$(6\pm3)\times10^{2}$	$(4\pm3)\times10^{-3}$	$(2\pm1)\times10^{5}$
*Da*Cld	$(2.3\pm0.4)\times10^{4}$	$(5\pm2)\times10^{-4}$	$(4\pm1)\times10^{7}$

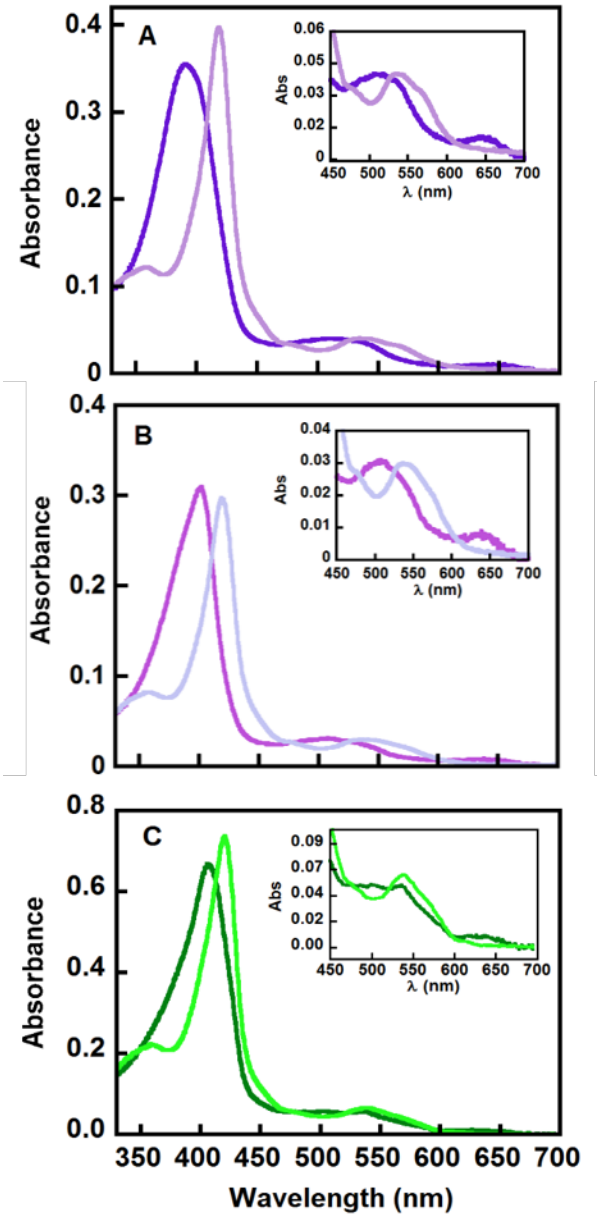

Figure C1. Cyanoferric Clds optical absorbance spectrum is characteristically different than their respective resting spectrum. UV/Visible spectra of A) WT *Da*Cld, B) its R183Q mutant, and C) *Kp*Cld, along with their cyano complexes measured at pH 7.0. In each case, the spectrum for the cyano-complex is blue shifted relative to the unligated complex and is plotted in a lighter color. *Da*Cld and its mutant were diluted to 3 μM in 0.2 M citrate-phosphate buffer and spectra measured before/after addition of 0.1 and 1 mM KCN, respectively. 2.5 μM *Kp*Cld was mixed with 20 μM KCN and spectra were recorded. The insets show the visible bands in each case on an amplified scale.

C.1. UV/Visible (UV/vis) properties of Clds and their complexes with cyanide.

The UV/vis spectra for WT *Da*Cld and its cyanide complex are shown in Figure C1A. At pH 7.0, the ligand-free enzyme has a Soret band at 393 nm, a broad visible band (β/α) centered near 510 nm, and a charge-transfer (CT) band at 644 nm (0.2 M citrate-phosphate, 25 °C). These features have been previously ascribed to the enzyme's five-coordinate high-spin (5cHS) heme. An alkaline form of the enzyme with a distinct UV/vis spectrum (not shown) predominates at higher pH (pK_a = 8.7). It has Soret and visible bands at 410, 574, and 539 nm, respectively, which are typical of a 6 coordinate low spin (6cLS) histidine- and hydroxide-bound ferric heme. The cyano complex of *Da*Cld has a red-shifted Soret band centered at 418 nm with a shoulder at 360 nm. A prominent visible band appears at 540 nm with a shoulder at 565 nm. These features, which do not change with pH, are consistent with a 6cLS cyano complex. The *Da*Cld(R183Q) variant resembles WT *Da*Cld but with a slightly red- shifted Soret band at 402 nm, β/α bands at 509 and 530 nm (shoulder), and a CT band at 635 nm (Figure C1B). Its cyano complex has UV/vis spectral features that are similarly pH-independent and nearly identical to those for the WT.

The UV/Vis spectra of *Kp*Cld and its cyano complex are shown in Figure C1C. Consistent with previous reports, the free enzyme has a Soret peak at 405 nm, β/α bands at 505 (540 nm shoulder), and a CT band at 645 nm (0.2 M citrate phosphate, pH 7.0, 25 °C). The red-shifted Soret has previously been ascribed to a more water-accessible active site with mixed 5c/6c HS coordination due to water ligation evident from the resonance Raman (rR) spectra. *Kp*Cld like *Da*Cld has a hydroxide-ligated 6cLS alkaline form (pK_a = 8.3), with a Soret absorbance at 413 nm and visible bands at 540, 572, and 603 (shoulder) nm (not shown). The

pH-independent spectrum for the cyano complex is very similar to that for *Da*Cld, with a red shifted the Soret band (419 nm) and visible bands at 538 and 565 nm.

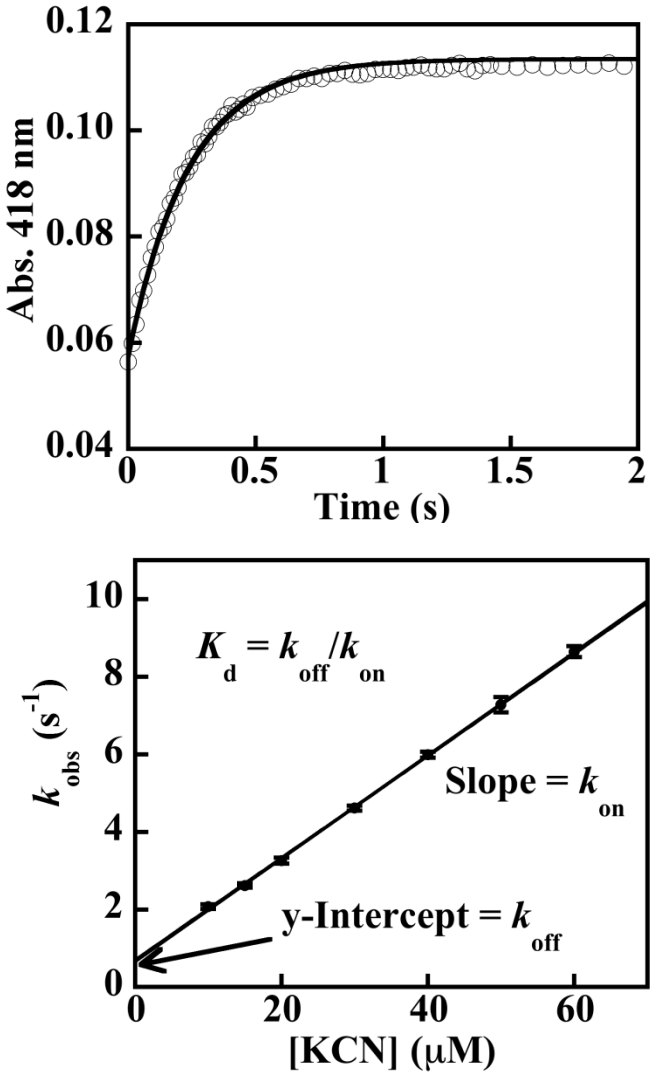

Figure C2. Representative data illustrating the formation of a ferric heme-cyano complexes of WT *Da*Cld over time. (Top) A representative trace showing the change in absorbance at 418 nm upon binding of cyanide by *Da*Cld WT in 0.2 M citrate-phosphate buffer, pH 5.5, 20 °C. Enzyme (1 μM) was mixed with 100 μM KCN. The open circles show the measured absorbance values which are fit to a single-exponential curve, equation 2 in the text. (Bottom) Representative linear fit of k_{obs} versus [KCN]. Values of k_{obs} measured from traces like those shown (Top) are plotted as a function of KCN. Data here from values collected with 1 μM *Da*Cld WT in 0.2 M citrate-phosphate buffer, pH 5.5, 20 °C mixed with KCN (10 - 60 μM). Each point represents an average of no less than 5 measurements and the error is reported as the standard deviation of those values. Data are fit to a linear expression, as described in equation 3 in the text, where the slope of each line gives k_{on} ($M^{-1}s^{-1}$) and y-intercept gives k_{off} (s^{-1}).

Table C2. Kinetic and equilibrium constants for WT *Da*Cld, *Da*Cld(R183Q), and *Kp*Cld reaction with cyanide as a function of pH at 20 °C.

	k_{on} ($\times 10^{-4}$) ($M^{-1}s^{-1}$)			k_{off} (s^{-1})			K_D (μM)		
pH	WT *Da*Cld	*Da*Cld (R183Q)	WT *Kp*Cld	WT *Da*Cld	*Da*Cld (R183Q)	WT *Kp*Cld[a]	WT *Da*Cld[b]	*Da*Cld (R183Q)[b]	WT *Kp*Cld[c]
8.5	1300 (40)	5.7 (0.6)	960 (80)	42 (7)	0.2 (0.2)	0.1 (0.1)	3.3 (0.5)	3 (4)	0.01 (0.01)
8.0	830 (400)	2.2 (0.3)	600 (10)	26 (12)	0.36 (0.2)	0.04 (0.02)	3 (2)	16 (8)	0.0060 (0.003)
7.5	390 (20)	0.8 (0.1)	330 (6)	2.9 (0.8)	0.2 (0.1)		0.7 (0.2)	28 (12)	
7.0	130 (20)	0.3 (0.1)	120 (1)	0.8 (0.6)	0.17 (0.02)	0.006 (0.003)	0.6 (0.4)	60 (6)	0.0050 (0.003)
6.5	44 (1)	0.07 (0.01)	47 (2)	0.8 (0.1)	0.75 (0.08)		1.9 (0.2)	1000 (100)	
6.0	13 (1)	0.02 (0.01)	20 (1)	0.7 (0.1)	0.34 (0.06)	0.016 (0.001)	5.2 (0.4)	1400 (300)	0.079 (0.005)
5.5	3.9 (0.1)	0.005 (0.002)	12 (1)	0.70 (0.02)	1.1 (0.1)		19 (1)	20000 (2000)	
5.0	1.0 (0.2)	0.002 (0.001)	2.9 (0.1)	0.9 (0.2)	0.23 (0.08)	0.011 (0.003)	84 (20)	12000 (5000)	0.39 (0.01)
4.5			1.1 (0.4)						
4.0			0.70 (0.05)						

[a]*Kp*Cld values for k_{off} were calculated from k_{on} and spectrophotometrically determined K_D. In plots of k_{obs} versus [KCN], k_{off} extrapolated to zero within experimental error (negative values near the origin). In each case, k_{off} is on the order of 10% or less of the corresponding value for k_{on}. We interpret these results as indicative of a small k_{off} across the pH range.
[b]K_D calculated from.k_{on} and k_{off}.
[c]K_D determined spectrophotometrically.
[d]Same value was determined with a spectrophotometric titration (See Figure 4.3).

Table C3. Comparison of resonance Raman isotope-sensitive frequencies (cm^{-1}) for cyanoferric Cld complexes as obtained by curve fitting analysis.

	$^{12}C^{14}N^-$	$^{13}C^{14}N^-$	$^{12}C^{15}N^-$	$^{13}C^{15}N^-$	$\Delta(^{12}C^{14}N-^{13}C^{15}N)$	Γ (cm^{-1})
*Da*Cld pH 5.8	441.4	438.5	438.4	435.7	5.7	12.4
	396.2	391.7	395.9	389.3	6.9	16
	309.2	307.4	307.7	308.0	1.2	14
*Da*Cld pH 8.8	440.5	438.0	437.5	434.0	6.5	12.4
	398.0	391.4	397.0	395.0	3	16
	309.3	308.3	309.1	308.2	1.1	16
*Da*Cld(R183Q) pH 5.8	441.2	439.3	438.8	435.7	5.5	17
	403.0	398.5	401.0	397.8	5.2	16
	375.0	373.7	374.8	373.9	1.1	12
	361.1	359.1	360.9	360.2	0.9	14
	304.9	303.9	304.1	302.5	2.4	13
*Kp*Cld pH 5.8	438.5	437.0	436.9	435.6	2.9	12
	371.5	371.1	371.5	370.7	0.8	10
	355.7	354.9	355.8	354.7	1.0	14
	306.0	304.0	306.0	303.0	3.0	18
*Kp*Cld pH 8.0	440.2	437.8	438.4	437.1	3.1	10
	373.2	373.0	373.4	372.8	0.4	8.5
	358.5	357.7	358.6	357.6	0.9	13

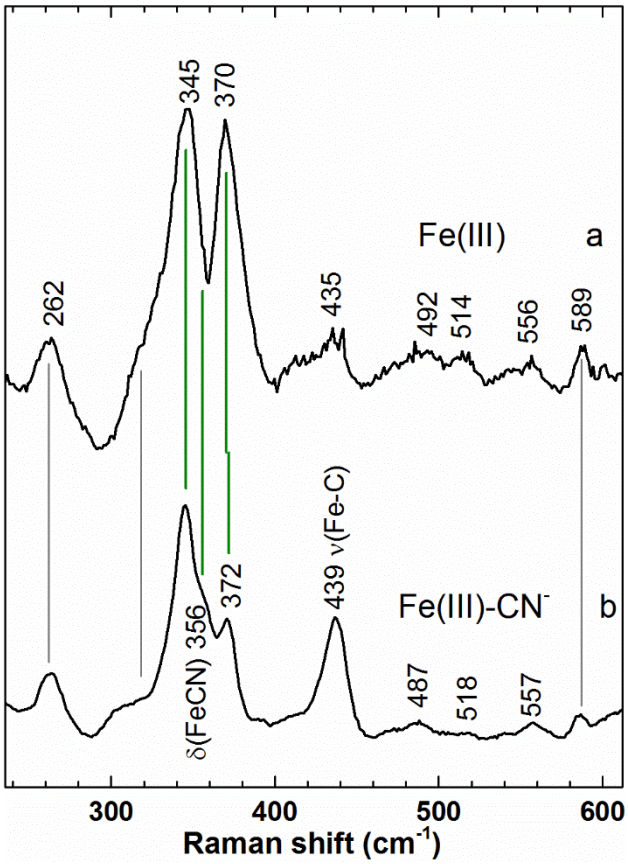

Figure C3. Comparison of low frequency rR spectra of ferric *Kp*Cld and *Kp*Cld−CN^-. Samples were in 100 mM sodium phosphate pH 5.8 with a) no anion and b) 25 mM sodium cyanide. Spectra were obtained with 413.1 nm excitation and a) 3 mW at the sample and b) 12 mW at the sample.

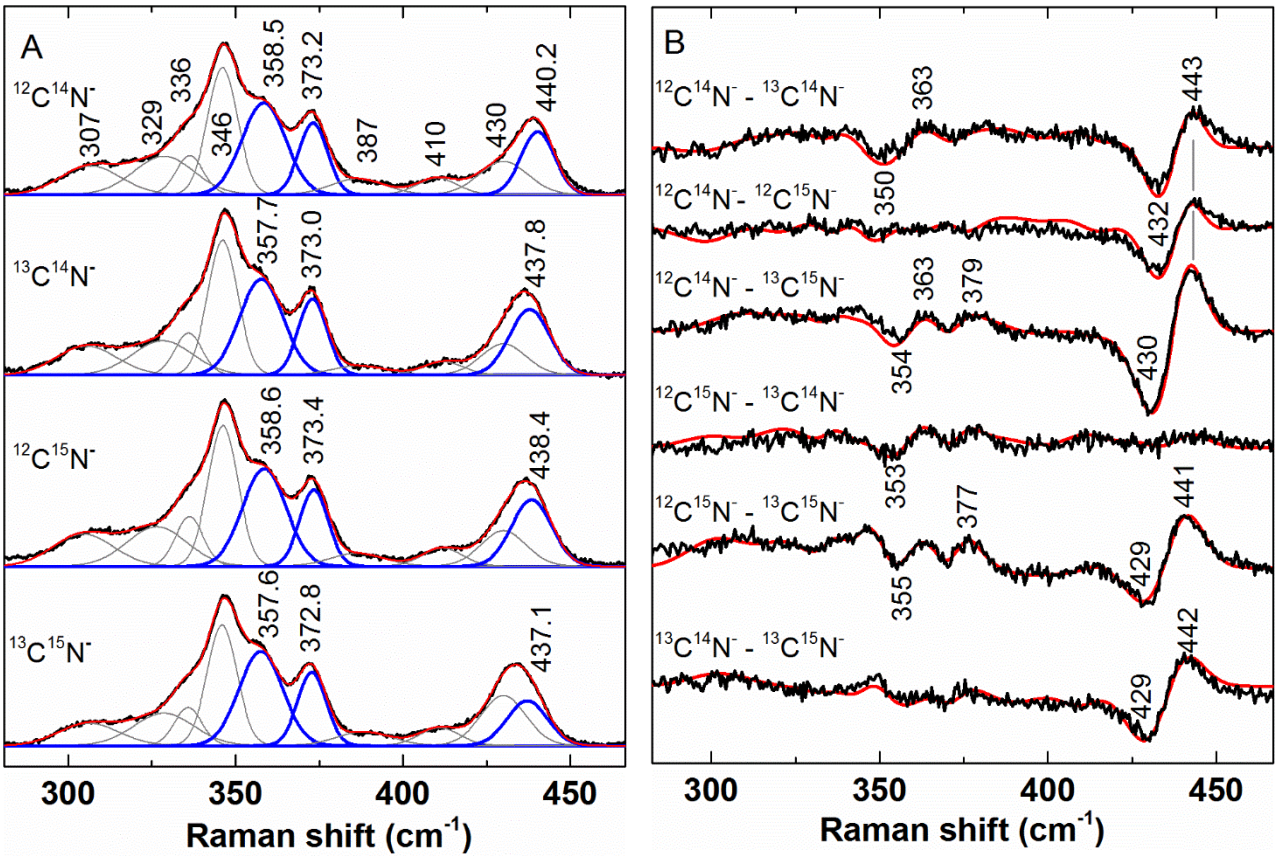

Figure C4. Fits of cyanoferric *Kp*Cld isotopologs at high pH. A) Low-frequency resonance Raman spectra of isotopically labeled cyanoferric *Kp*Cld pH 8.0. The cyanoferric *Kp*Cld complexes were 20 µM *Kp*Cld and 25 mM cyanide in 100 mM Tris/sulfate buffer. The excitation frequency was 413.1 nm; laser power at the sample was 12 mW. Spectra were acquired at 20 °C. Original spectral data are shown in black, bands used to fit the spectra are grey and blue; the calculated spectra are shown in red. Bands in blue are responsible for the difference features shown in B. B) Cyanide isotope difference spectra generated by digital subtraction of the spectra shown in A. Difference spectra generated from subtraction of spectral data are shown in black; the fit difference spectra are shown in red. Fits for the difference spectra were obtained by generating fits for the experimental spectra and then subtracting those fits.

A band at 440.2 cm^{-1} in the rR spectrum of *Kp*Cld-CN$^-$ exhibits a zigzag isotope shift pattern as the cyanide mass is changed in the following order: $^{12}C^{14}N^-$, $^{13}C^{14}N^-$, $^{12}C^{15}N^-$, $^{13}C^{15}N^-$. Its observed isotope shift between $^{12}C^{14}N^-$ and $^{13}C^{15}N^-$ complexes is 3.1 cm^{-1}. Despite the zigzag isotope shift pattern, this band has considerable contribution from an ν(FeCN) mode based on the [$^{12}C^{14}N^-$ – $^{12}C^{15}N^-$] and [$^{13}C^{14}N^-$ – $^{13}C^{15}N^-$] difference spectra (see Chapter 4 text).

Small isotopic shifts are attributed to coupling interactions between Fe−C−N fragment and heme vibrational modes.

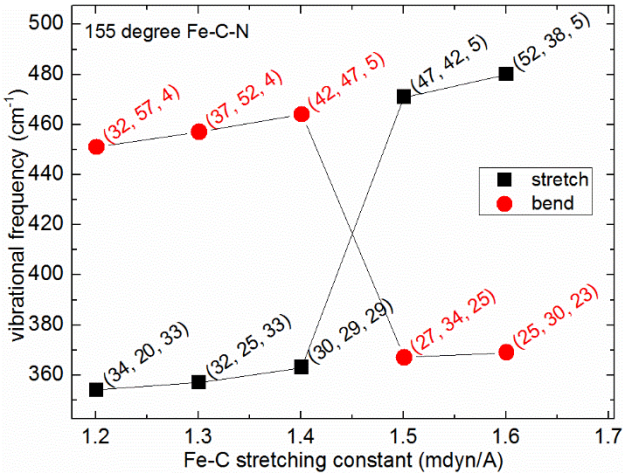

Figure C5. Effect of increasing the Fe-C stretching force constant at a FeCN bond angle of 155º on the potential energy distribution (PED) and frequency of the primarily stretching (ν) and primarily bending (δ) normal modes. PED containing the stretching and bending internal coordinate contributions are shown in parenthesis: (%ν(FeC), %δ(FeCN), %ν(HisFe)).[1]

C.2. Relative contributions of the FeCN and FeHis stretches are deterministic for the frequency ordering of the "stretch" and "bend" assignments.

The most deterministic contribution to the frequencies of these two modes is their Fe−His stretching character. The contribution of Fe−Im stretching to the higher frequency mode is 4 to 5% while the PED of the lower frequency mode ranges from 23 to 33% Fe−His stretch. As f_{Fe-C} increases from 1.2 to 1.4 mdyn/Å, the contribution of Fe−C stretch to the low-frequency mode tracks the decreasing contribution of Fe−His stretch to the PED while the smaller FeCN bending contribution rises to meet them both at 1.4 mdyn/Å. Over this f_{Fe-C} range, the low frequency mode is assigned as a Fe–C stretch. Over the same f_{Fe-C} range, the high-frequency mode is slightly dominated by FeCN bending and it is referred to as the bending mode. Further increase in f_{Fe-C} causes the stretching contribution to the low-frequency mode to fall below that of the bend. Thus, for $f_{Fe-C} \geq 1.5$, the bending contribution to the low-frequency mode is greater than

that of the stretch. In this situation, it is labelled a bending mode. The high-frequency mode is slightly dominated by Fe−CN stretching when $f_{Fe\text{-}C}$ is ≥1.5. Consequently, it is labelled as the Fe−C stretching mode.

Table C4. Comparison of observed stretching and bending frequencies and isotope shifts for Fe−C−N unit in *Kp*Cld−CN^- and NP1−CN^-.

complex	Observed mode (cm^{-1}) (Δ $^{13}C^{14}N$, $^{12}C^{15}N$, $^{13}C^{15}N$)	Potential energy distribution (%)[a]	Ref.
*Kp*Cld pH 5.8	438.5 (1.3, 1.6, 3.1)	ν(FeCN) + δ(FeCN) + ν(FeIm)	This work
	355.7 (0.3, 0.1, 1.1)	δ(FeCN) + δ(ImFeC) + ν(FeIm)	
*Kp*Cld pH 8.0	440.2 (2.4, 1.8, 3.1)	ν(FeCN) + δ(FeCN) + ν(FeIm)	This work
	358.5 (0.8, 0.1, 0.9)	δ(FeCN) + δ(ImFeC) + ν(FeIm)	
	∠(Fe−C−N) =155.0		
NP1 pH 7.0 Bent	442.8 (2.4, 1.8, 3.2)	ν(FeCN) + δ(FeCN) + ν(FeIm) (75) (19) (11)	[2]
	356.6 (1.0, 0.0, 1.2)	δ(FeCN) + δ(ImFeC) + ν(FeIm) (46) (16) (11)	
	∠(Fe−C−N) =172.9		
NP1 pH 7.0 "nearly linear"	454.4 (1.4, 1.8, 3.0)	ν(FeCN) + ν(FeIm) (84) (14)	[2]
	396.8 (4.8, 0.0, 5.2)	δ(FeCN) + δ(ImFeC) (75) (16)	

[a]Calculated potential energy distribution (%) with respect to force constants for the natural abundance molecule.

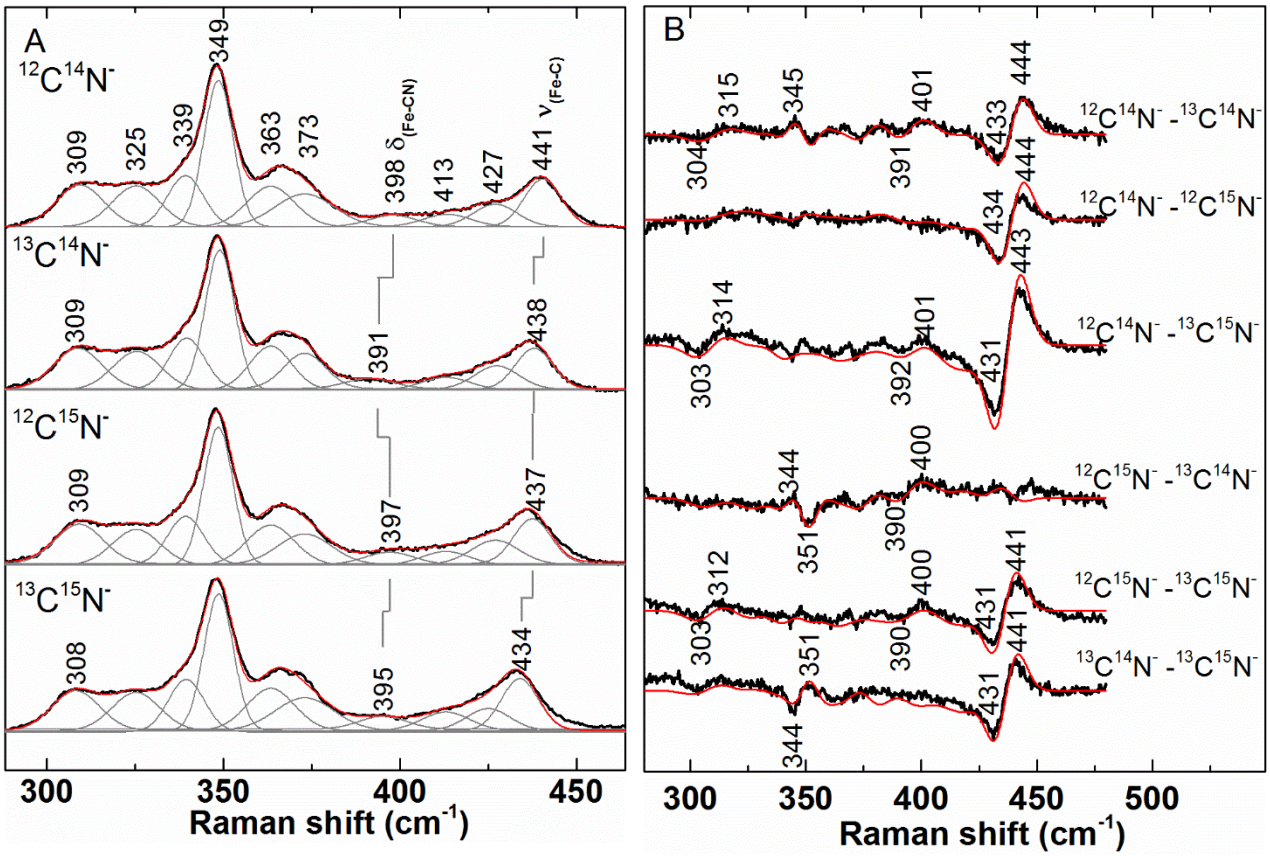

Figure C6. Fits of the cyanoferric *Da*Cld isotopologs at high pH. A) Low-frequency resonance Raman spectra (240-470 cm^{-1}) of isotopically labeled cyanoferric *Da*Cld pH 8.8. The cyanoferric *Da*Cld complexes were 25 μM *Da*Cld and 25 mM cyanide in 100 mM Tris/sulfate buffer. The excitation frequency was 413.1 nm; laser power at the sample was 12 mW. Spectra were acquired at 20 °C. Original spectral data are shown in black, bands used to fit the spectra are grey and the calculated spectra are shown in red. B) Cyanoferric *Da*Cld isotope difference spectra generated by digital subtraction of the spectra shown in A. Difference spectra generated from subtraction of spectral data are shown in black; the fit difference spectra are shown in red. Fits for the difference spectra were obtained by generating fits for the experimental spectra and then subtracting those fits.

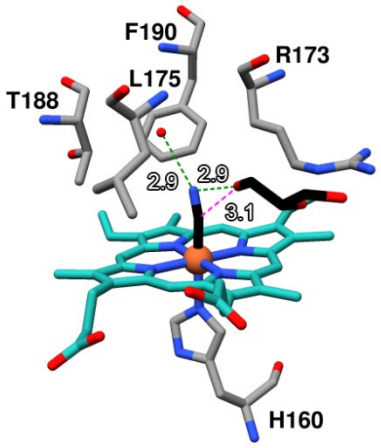

Figure C7. Structure of the heme pocket of *Nd*Cld−CN^- (pdb: 3NN2)[3]. Heme carbons are cyan, protein carbons are gray, and the ligand carbon is black. The Fe-C-N angle is this monomer is 158.6°. The Fe-C-N angle ranges from 140.9 to 177.0° within the pentamer. Presumed H-bonds to the first coordinated atom are shown as magenta dashed lines with the distances indicated in angstroms. A water and glycerol molecule are crystalized within the heme pocket located 2.878 Å and 2.862 Å away from the nitrogen of the cyanide as indicated by grey dashed lines.

C.3. References

1. Lopez-Garriga, J. J., Oertling, W. A., Kean, R. T., Hoogland, H., Wever, R., and Babcock, G. T. (1990) Metal-ligand vibrations of cyanoferric myeloperoxidase and cyanoferric horseradish peroxidase: evidence for a constrained heme pocket in myeloperoxidase, *Biochemistry 29*, 9387-9395.
2. Maes, E. M., Walker, F. A., Montfort, W. R., and Czernuszewicz, R. S. (2001) Resonance Raman Spectroscopic Study of Nitrophorin 1, a Nitric Oxide-Binding Heme Protein from Rhodnius prolixus, and Its Nitrosyl and Cyano Adducts, *J. Am. Chem. Soc. 123*, 11664-11672.
3. Kostan, J., Sjoeblom, B., Maixner, F., Mlynek, G., Furtmueller, P. G., Obinger, C., Wagner, M., Daims, H., and Djinovic-Carugo, K. (2010) Structural and functional characterisation of the chlorite dismutase from the nitrite-oxidizing bacterium "Candidatus Nitrospira defluvii": Identification of a catalytically important amino acid residue, *J.Struct.Biol. 172*, 331-342.

APPENDIX D

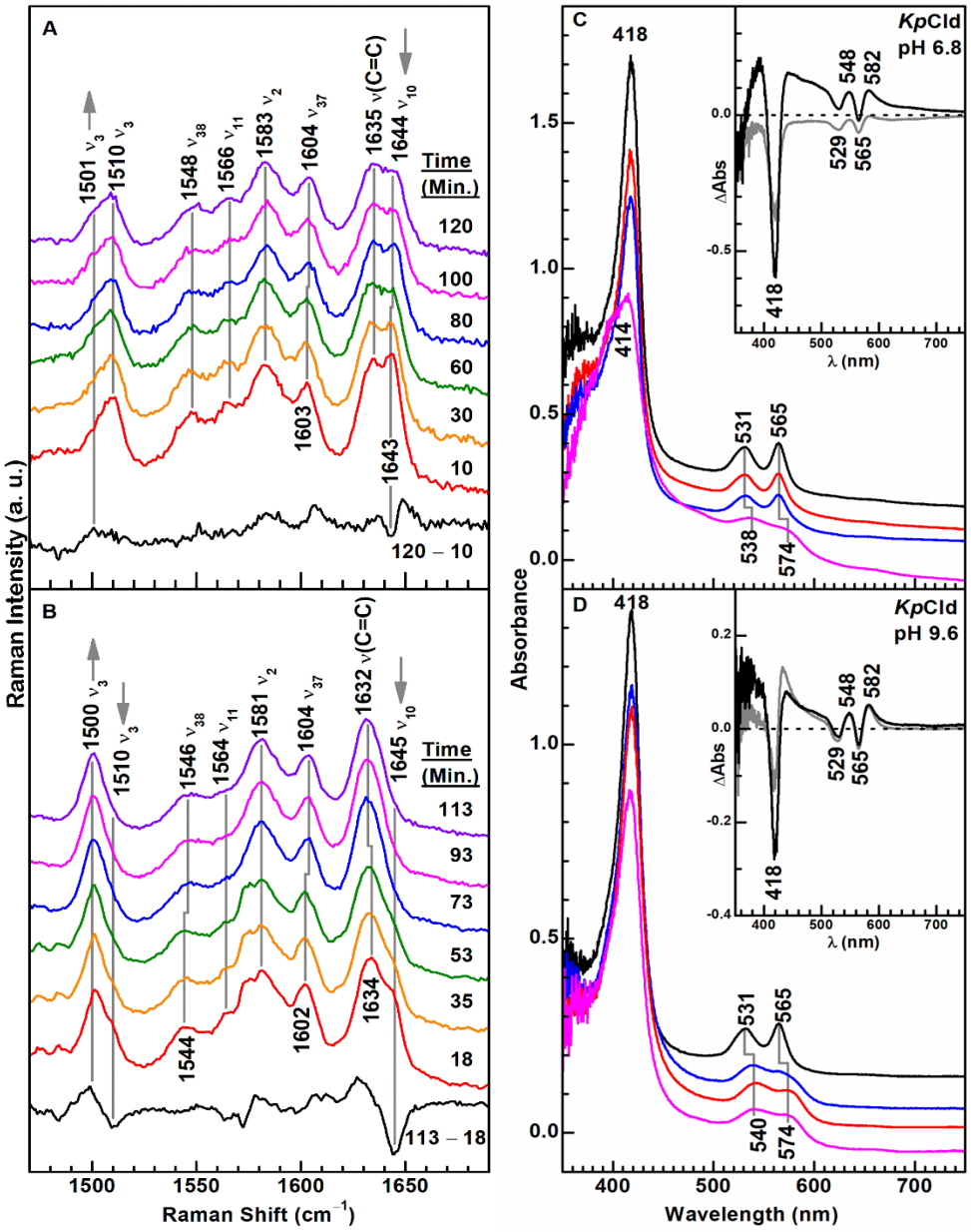

Figure D1. Photoinduced reduction of *Kp*Cld {FeNO}^{6} is observed upon exposure to 413.1 nm LASER light. Time-resolved Soret excited rR of *Kp*Cld {FeNO}^{6} in A) 0.1 M potassium phosphate pH 6.8 (1.5 mW power) and B) 0.1 M glycine pH 9.6 (3.7 mW power). Listed times indicate the total duration of LASER exposure for the sample. Time-resolved optical absorbance spectra of *Kp*Cld {FeNO}^{6} rR sample in C) 0.1 M potassium phosphate pH 6.8 and D) 0.1 M glycine pH 9.6. Black, red, and blue spectra indicate no LASER exposure, 1 hour LASER exposure, and 2 hours LASER exposure, respectively. Magenta spectra were recorded after reduction with dithionite. *Insets:* gray ΔA spectra; spectrum recorded after 2 hours of exposure to LASER light minus the spectrum recorded before LASER exposure; black ΔA spectra; reduced by dithionite minus no LASER exposure.

When *Kp*Cld {FeNO}^{6} was exposed to 413.1-nm LASER light, its rR spectra collected as a function of the time show a loss of band intensity at 1510 and 1644 cm^{-1} with an increase in intensity at 1501 and 1635 cm^{-1} at pH 6.8. These spectral changes occur faster at pH 9.6 such that ν_{10} at 1645 cm^{-1} and ν_3 at 1510 cm^{-1} lose all intensity suggesting a more complete conversion to {FeNO}^{7} species in the same time frame. UV-Vis spectra recorded before and after rR are consistent with a change in speciation based on the broadening of the Q-bands and drop in intensity of the Soret band. This is in contrast to the very slow reductive nitrosylation of *Kp*Cld in the absence of LASER light (Figure 5.3).

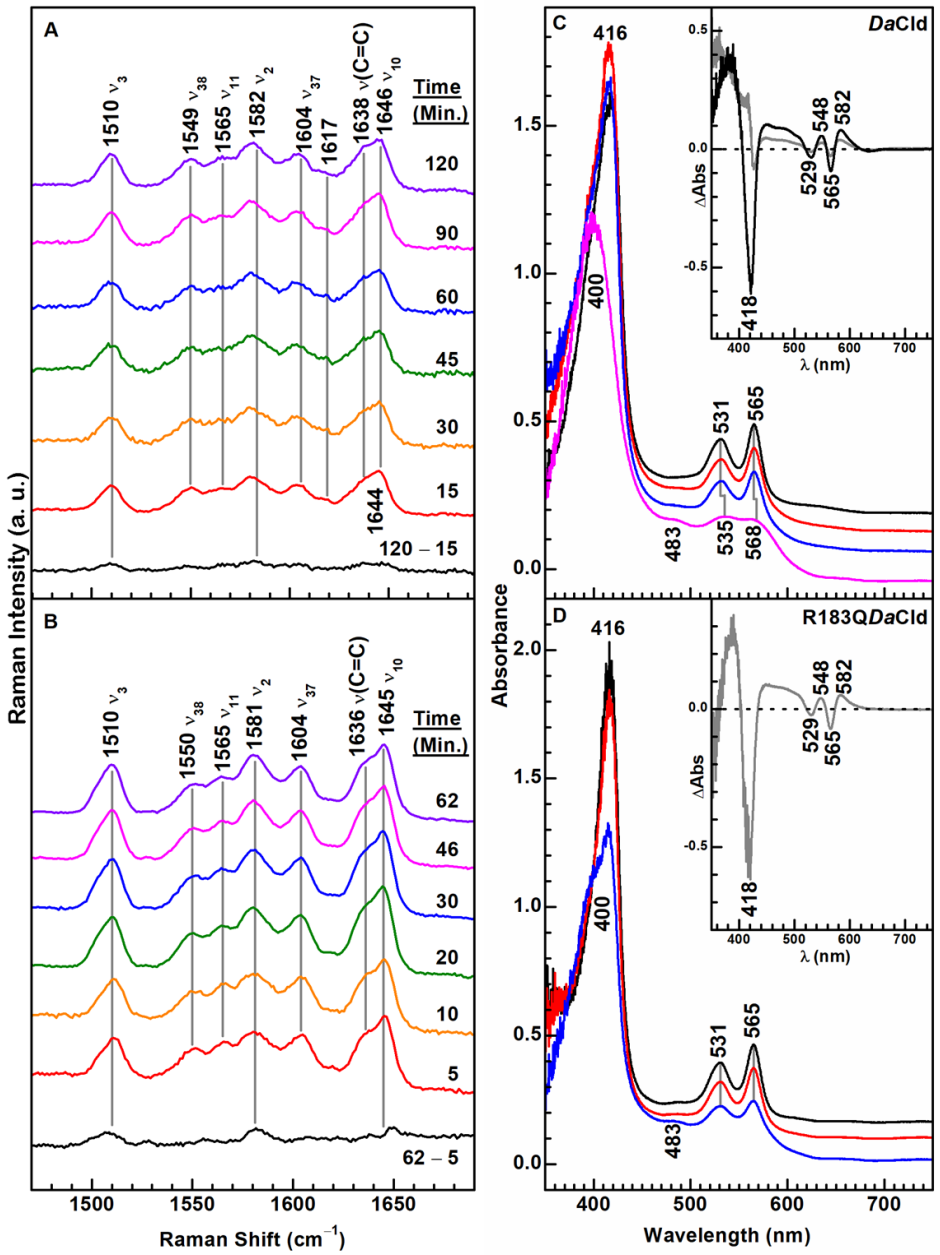

Figure D2. The $\{FeNO\}^6$ complexes of the *Da*Cld enzymes do not exhibit obvious rR spectral features corresponding to photoinduced reduction at pH 6.8. Time-resolved Soret (413.1-nm) excited rR of A) *Da*Cld (1.5 mW power) and B) *Da*Cld(R183Q) (6.6 mW power)$\{FeNO\}^6$ in 0.1 M potassium phosphate pH 6.8. Listed times indicate the total duration of LASER exposure for the sample. Time-resolved optical absorbance spectra of C) *Da*Cld and D) *Da*Cld(R183Q) $\{FeNO\}^6$ in 0.1 M potassium phosphate pH 6.8. Black, red, and blue spectra indicate no LASER exposure, 1 hour laser exposure, and 2 hours laser exposure, respectively, for *Da*Cld and no LASER exposure, 30 minutes, and 60 minutes, respectively, for *Da*Cld(R183Q). Magenta spectra, when shown, are post reduction with dithionite. Insets*:* gray ΔA spectra; spectrum recorded after 2 hours of exposure to LASER light minus the spectrum recorded before LASER exposure; black ΔA spectrum; reduced by dithionite minus no LASER exposure.

Resonance Raman spectra collected as a function of the time that *Da*Cld or R183Q variant $\{FeNO\}^6$ complexes were exposed to 413.1-nm LASER light at pH 6.8 do not reveal spectral changes consistent with photoinduced reduction (Figure D2). These spectral changes are expected to be less pronounced than those associated with the photoinduced reduction of *Kp*Cld $\{FeNO\}^6$ because 6cLS $\{FeNO\}^6$ and 5cLS $\{FeNO\}^7$ have similar core-size marker frequencies (Figures 5.4 & 5.5). The most prominent change is a ~2 cm^{-1} shift in the ν_{10} from 1644 cm^{-1} to 1646 cm^{-1} for *Da*Cld while *Da*Cld(R183Q) shows no measurable change. Nonetheless, the UV-Vis spectra recorded before and after rR clearly show spectral changes consistent with formation of 5cLS $\{FeNO\}^7$ as evidenced by broadening and blue shifting of the Soret band along with broadening of the Q-bands (Figure D2). An additional absorbance band at ~480 nm also appears with formation of 5cLS $\{FeNO\}^7$.

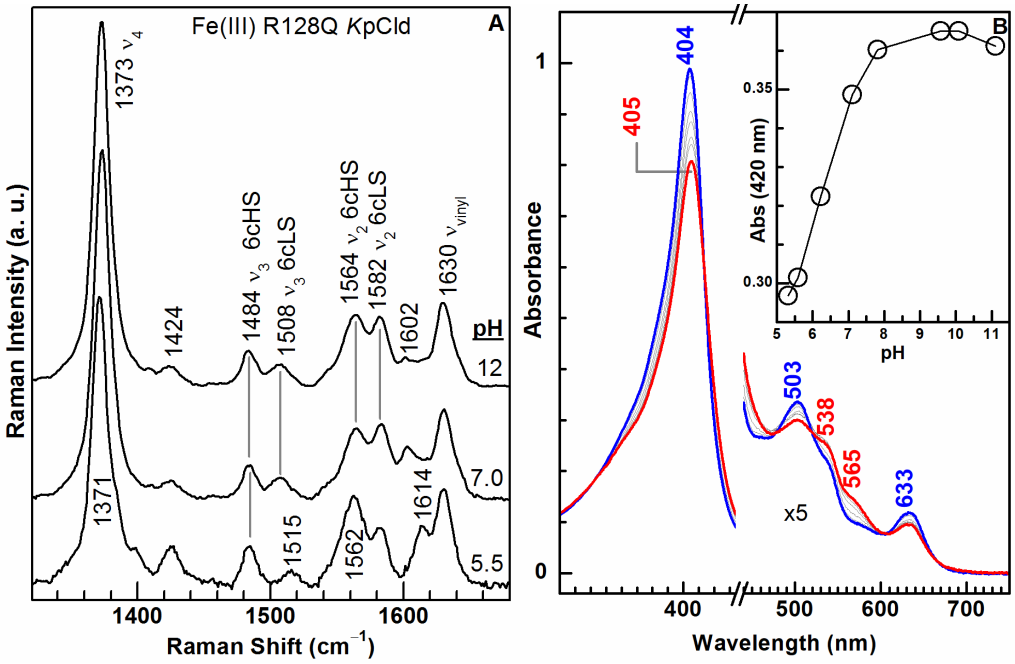

Figure D3. The pH titration of ferric *Kp*Cld(R128Q) indicates a speciation change at low pH. A) Spectra were recorded with 413.1-nm excitation of *Kp*Cld(R128Q) in 0.1 M potassium phosphate pH 5.5, 7.8 and 12. B) UV/vis pH titration for *Kp*Cld(R128Q). The blue spectrum is at pH 5.3 and the red one is at pH 11.1 with the gray spectra corresponding to the intermediate pHs shown in the inset. Inset: Absorbance at 420 nm as a function of pH. The pK_a is estimated at 6.3 based on these spectra. This is consistent with changes in the rR spectra between pH 5.5 and 7.0.

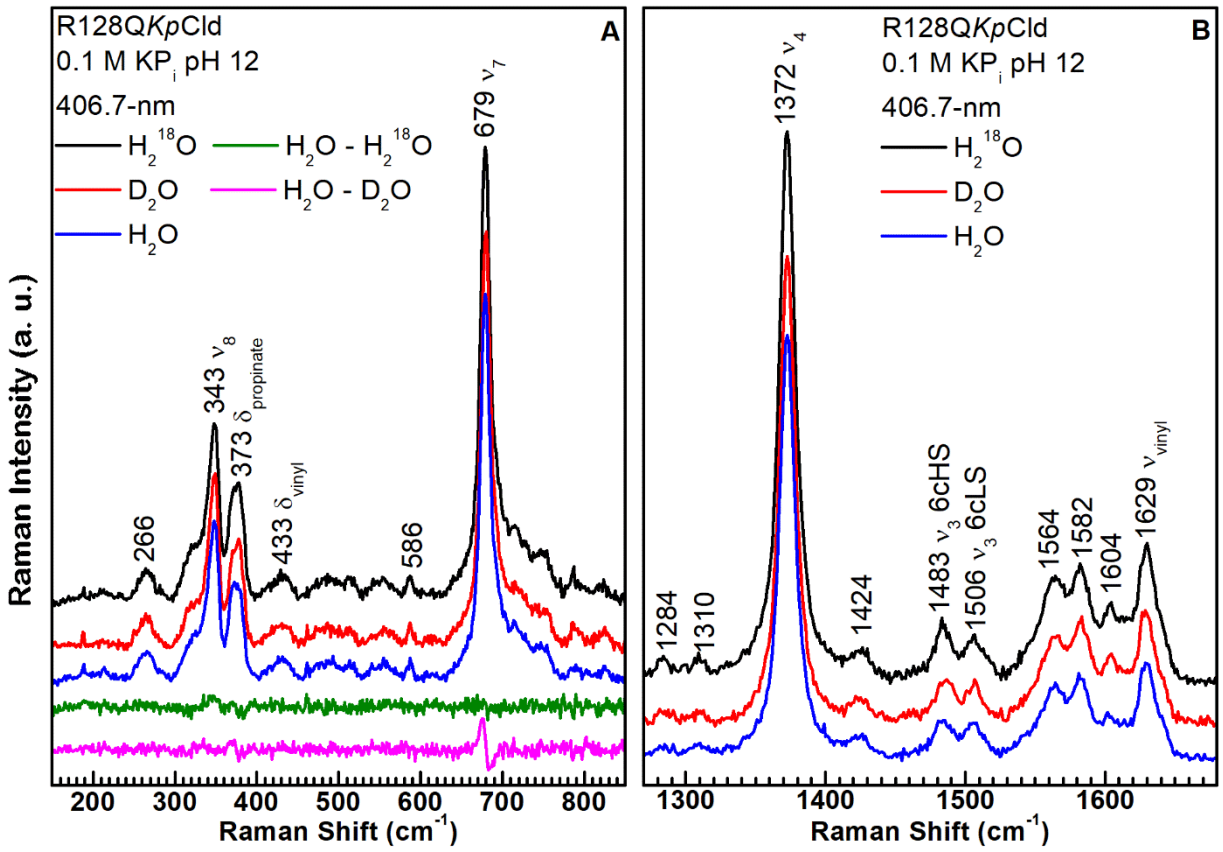

Figure D4. *Kp*Cld(R128Q) does not form a hydroxide complex as revealed by the absence of isotopically-sensitive bands in the Soret-excited rR spectra. A) Low frequency window of 406.7 nm excited rR spectra of *Kp*Cld(R128Q) at pH 12 prepared in H_2O (black), ^2H_2O (red), and $H_2{}^{18}O$ (Blue) and the difference spectra generated by subtraction of the following spectra [H_2O − $H_2{}^{18}O$] (green) and [H_2O − ^2H_2O] (magneta) are shown. B) High frequency window of rR spectra that correspond to *Kp*Cld(R128Q) at pH 12 prepared in H_2O (black), ^2H_2O (red), and $H_2{}^{18}O$ (Blue). Samples in ^2H_2O and $H_2{}^{18}O$ were prepared by dilution of a concentrated stock protein solution into 100 mM potassium phosphate pH 12 buffer prepared in D_2O (99.9% D) or $H_2{}^{18}O$ (96% ^{18}O). Final enrichments were 80%.

Heme-hydroxide complexes can be identified and characterized by their low-frequency rR signatures. If the Fe−OH moiety is present, the mode(s) having significant Fe−OH stretching character are definitively identified by their ^{18}O and ^2H isotope shifts observed for samples prepared in $H_2{}^{18}O$ and ^2H_2O, respectively. For *Kp*Cld the ν_{Fe-OH} modes identified by isotopic substitution are observed at 509 and 442 cm^{-1} and assigned to the Fe−OH stretching modes for

the LS and HS heme hydroxides, respectively.[1] These isotopically-sensitive bands are not observed for alkaline *Kp*Cld(R128Q).

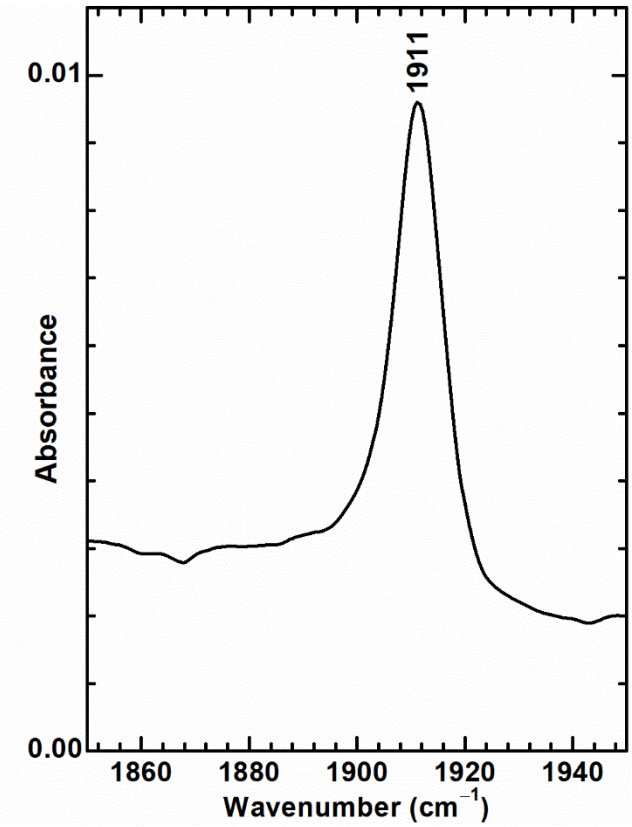

Figure D5. The FTIR spectrum of *Da*Cld(R183Q) {FeNO}^{6}. This ν(N–O) frequency is the same as that assigned in the rR spectrum of *Da*Cld(R183Q) {FeNO}^{6}.

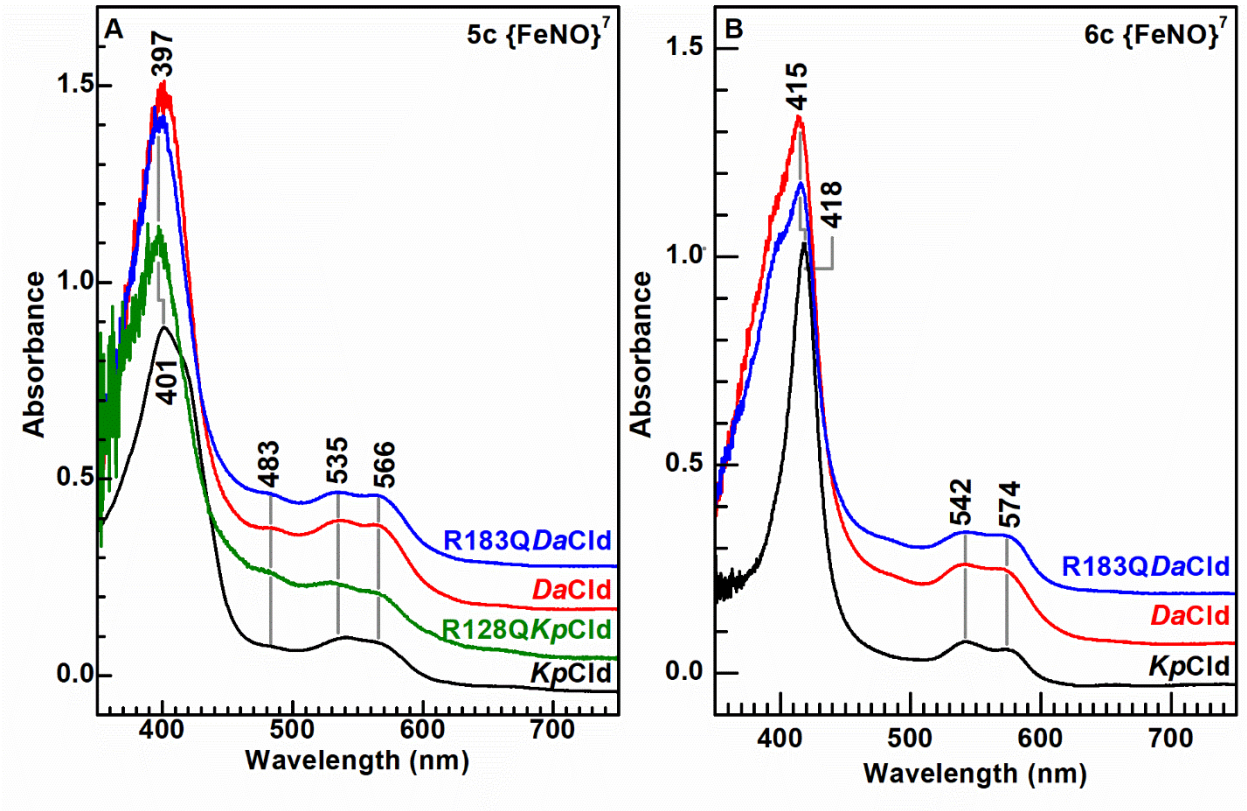

Figure D6. Cld $\{FeNO\}^7$ complexes generated by addition of NO to ferrous Clds are sensitive to pH as judged by their UV visible spectra. A) Optical absorbance spectra of Cld $\{FeNO\}^7$ complexes in 0.1 M phosphate pH 6 under 1 atmosphere NO (g). B) Optical absorbance spectra of Cld $\{FeNO\}^7$ complexes in 0.1 M glycine pH 9.6 under 1 atmosphere NO (g). *Kp*Cld (black),*Kp*Cld(R128Q) (green), *Da*Cld (red), and *Da*Cld(R183Q) (blue).

D.1. References

1. Celis, A. I.; Geeraerts, Z.; Ngmenterebo, D.; Machovina, M. M.; Kurker, R. C.; Rajakumar, K.; Ivancich, A.; Rodgers, K. R.; Lukat-Rodgers, G. S.; DuBois, J. L. Biochemistry 54 (2015) 434-446.

APPENDIX E

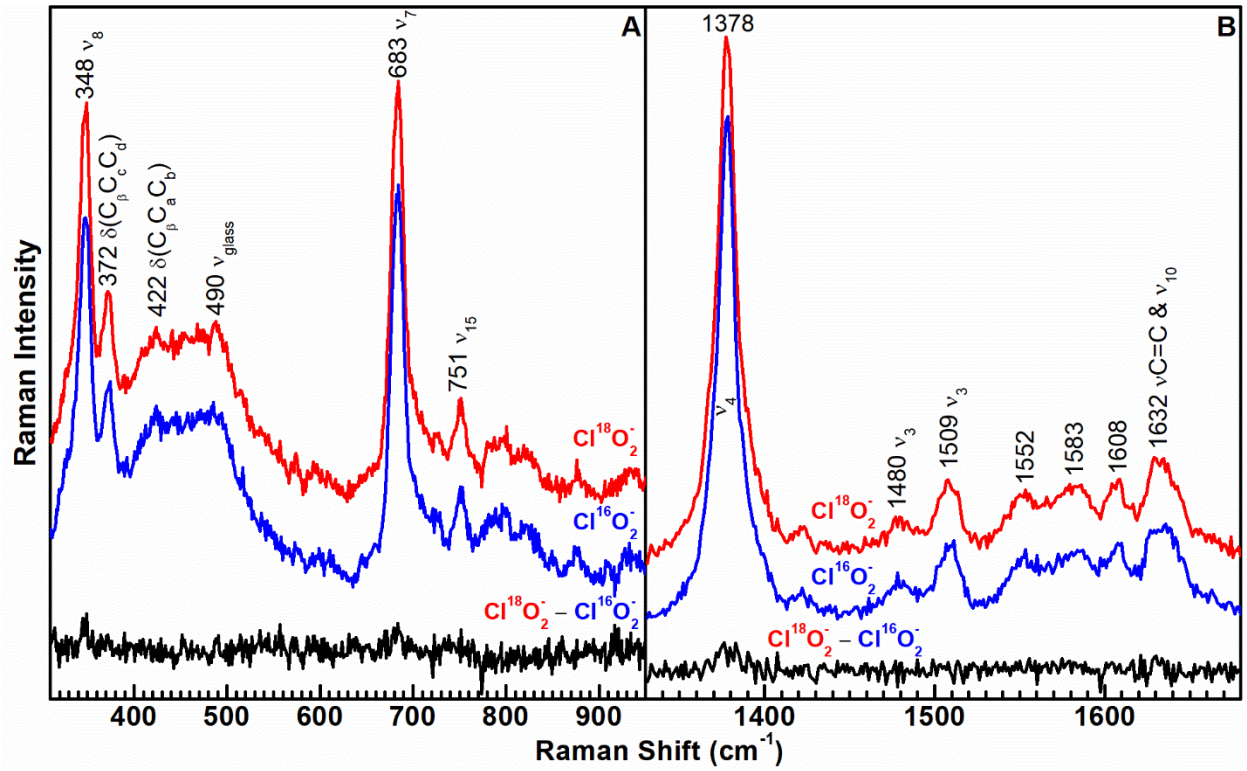

Figure E1. Time-resolved 413.1-nm excited rR spectra at 7.6 mW power of the reaction between 15 μM *Da*Cld and 50 mM $NaClO_2$ (natural abundance and ^{18}O enriched) at −5 °C in 0.1 M sodium borate pH 9.0 buffer. Red spectra correspond to $NaCl^{18}O_2$ reacted with *Da*Cld, blue spectra indicate natural abundance $NaClO_2$, and black spectra were generated by subtracting $NaCl^{18}O_2$ reacted *Da*Cld by natural abundance $NaClO_2$ reacted *Da*Cld. A) low frequency window reveals no isotope difference feature. B) high frequency window shows speciation between isotope labeled and natural abundance $NaClO_2$ are identical.

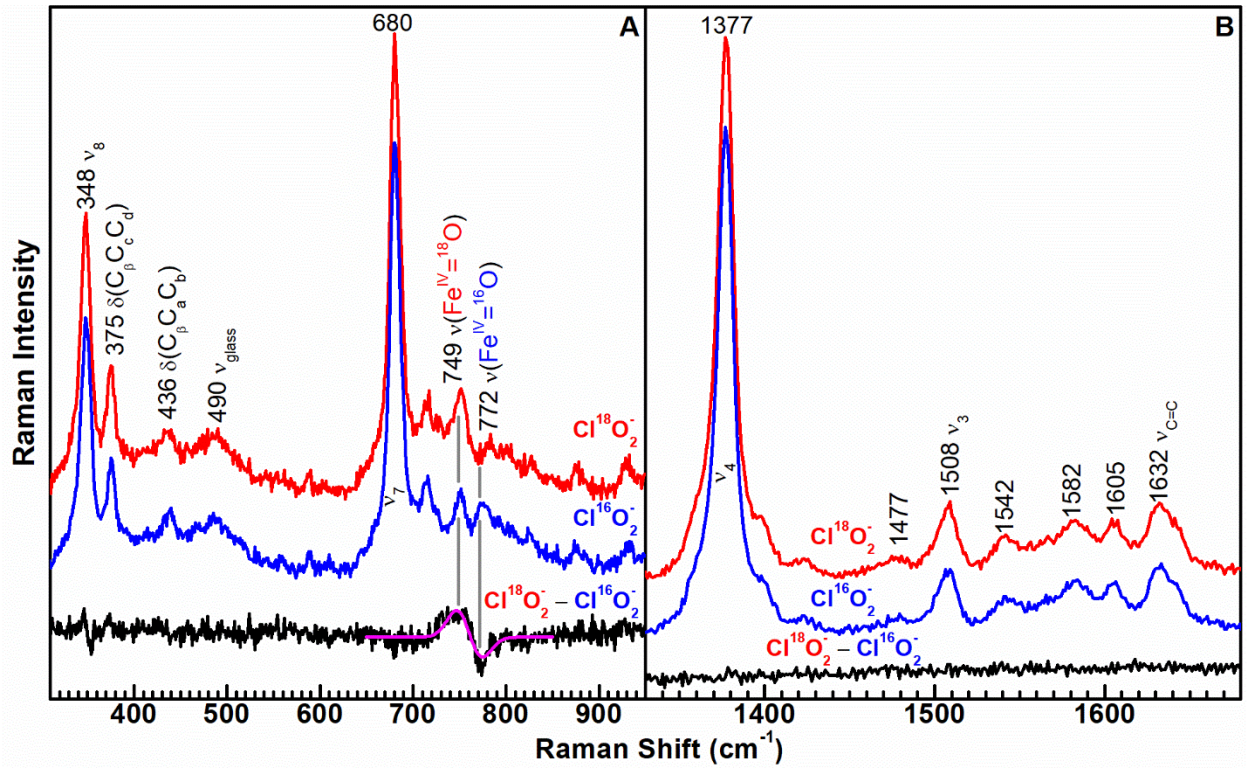

Figure E2. Time-resolved 413.1-nm excited rR spectra at 9.0 mW power of the reaction between 10 µM *Kp*Cld and 10 mM $NaClO_2$ (natural abundance and ^{18}O enriched) at −5 °C in 0.1 M sodium borate pH 9.0 buffer. Red spectra correspond to $NaCl^{18}O_2$ reacted with *Kp*Cld, blue spectra indicate natural abundance $NaClO_2$, and black spectra were generated by subtracting $NaCl^{18}O_2$ reacted *Kp*Cld by natural abundance $NaClO_2$ reacted *Kp*Cld. A) low frequency window reveals one isotope difference feature. The magenta line is the cumulative fit of the observed difference feature. B) high frequency window shows speciation between isotope labeled and natural abundance $NaClO_2$ are identical.

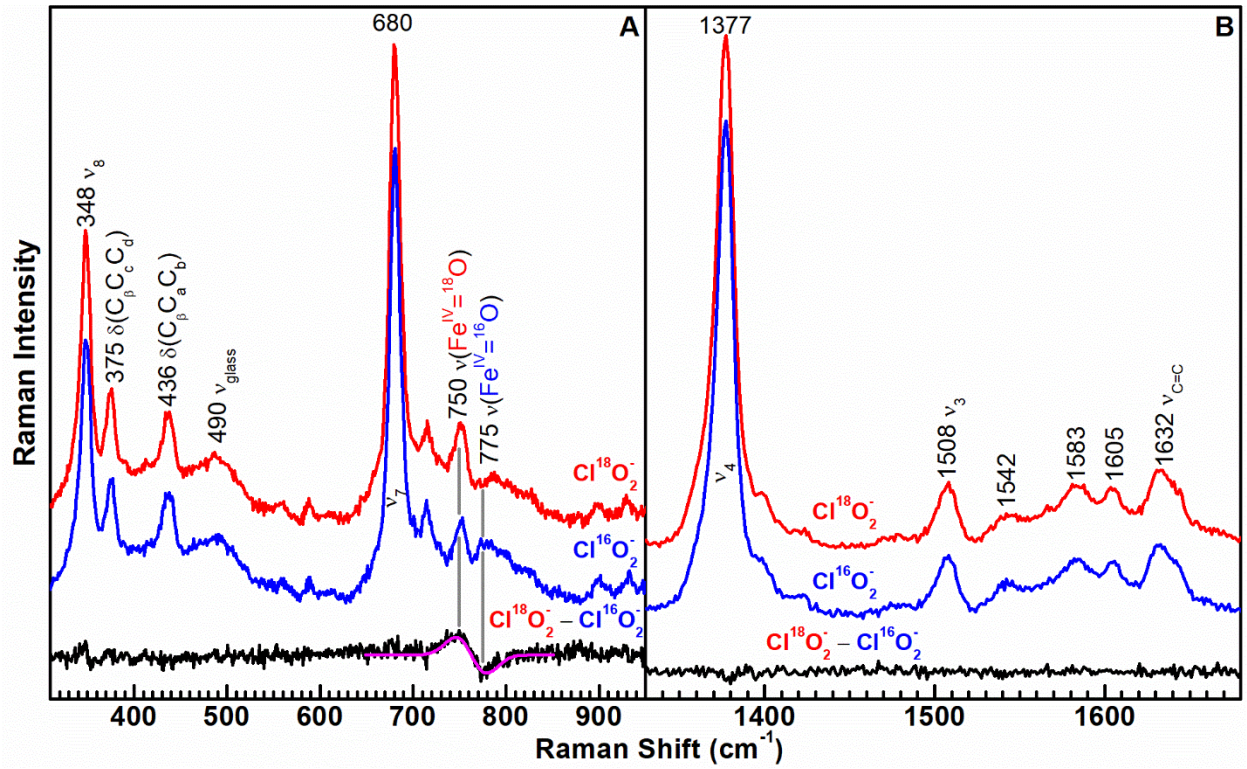

Figure E3. Time-resolved 413.1-nm excited rR spectra at 9.0 mW power of the reaction between 10 μM *Kp*Cld and 10 mM $NaClO_2$ (natural abundance and ^{18}O enriched) at −5 °C in 0.1 M glycine pH 9.0 buffer. Red spectra correspond to $NaCl^{18}O_2$ reacted with *Kp*Cld, blue spectra indicate natural abundance $NaClO_2$, and black spectra were generated by subtracting $NaCl^{18}O_2$ reacted *Kp*Cld by natural abundance $NaClO_2$ reacted *Kp*Cld. A) low frequency window reveals one isotope difference feature. The magenta line is the cumulative fit of the observed difference feature. B) high frequency window shows speciation between isotope labeled and natural abundance $NaClO_2$ are identical.

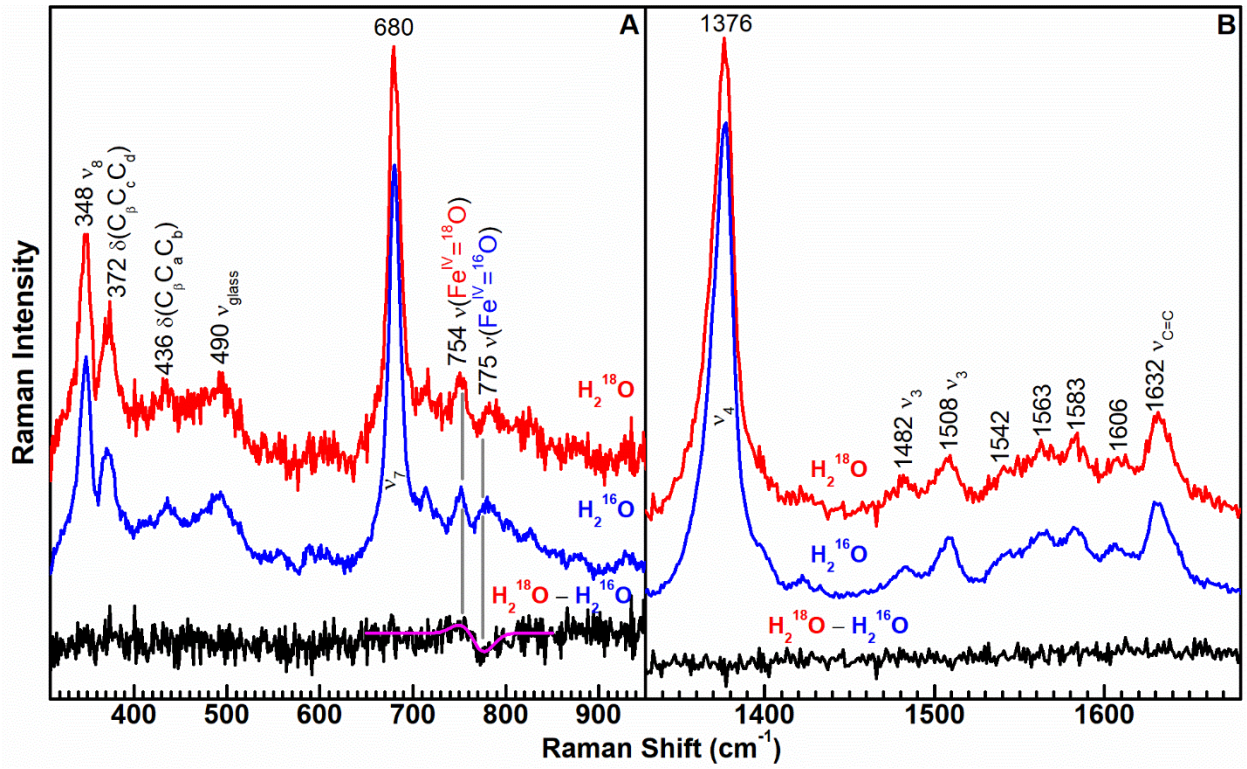

Figure E4. Time-resolved 413.1-nm excited rR spectra at 9.4 mW of the reaction between 10 μM *Kp*Cld and 10 mM $NaClO_2$ at −5 °C in 0.05 M sodium phosphate pH 6.0 buffer with natural abundance and ^{18}O enriched H_2O. Red spectra correspond to $NaClO_2$ reacted with *Kp*Cld in $H_2{}^{18}O$ (85% isotope enrichment), blue spectra indicate $NaClO_2$ reacted *Kp*Cld in natural abundance H_2O, and black spectra were generated by subtracting $H_2{}^{18}O$ from natural abundance H_2O. The magenta line is the cumulative fit of the observed difference feature. A) low frequency window reveals one isotope difference feature. B) high frequency window shows speciation between isotope labeled and natural abundance $NaClO_2$ are identical.

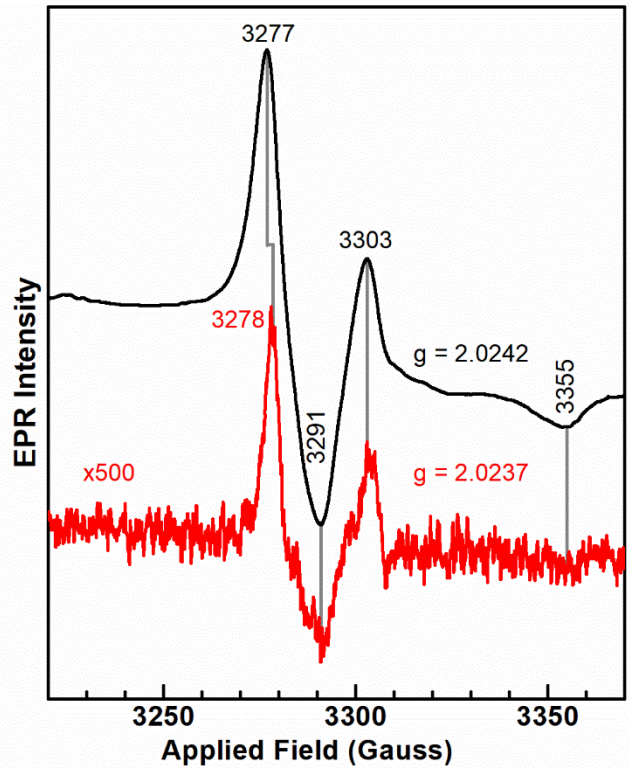

Figure E5. X-band EPR spectra at 0.2 mW power of 280 mM $NaClO_2$ stock at 77 K in dilute HCl (black) and H_2O (red). EPR features are consistent with ClO_2(*aq*) Concentrations are estimated to be 94 mM and 70 µM, respectively.

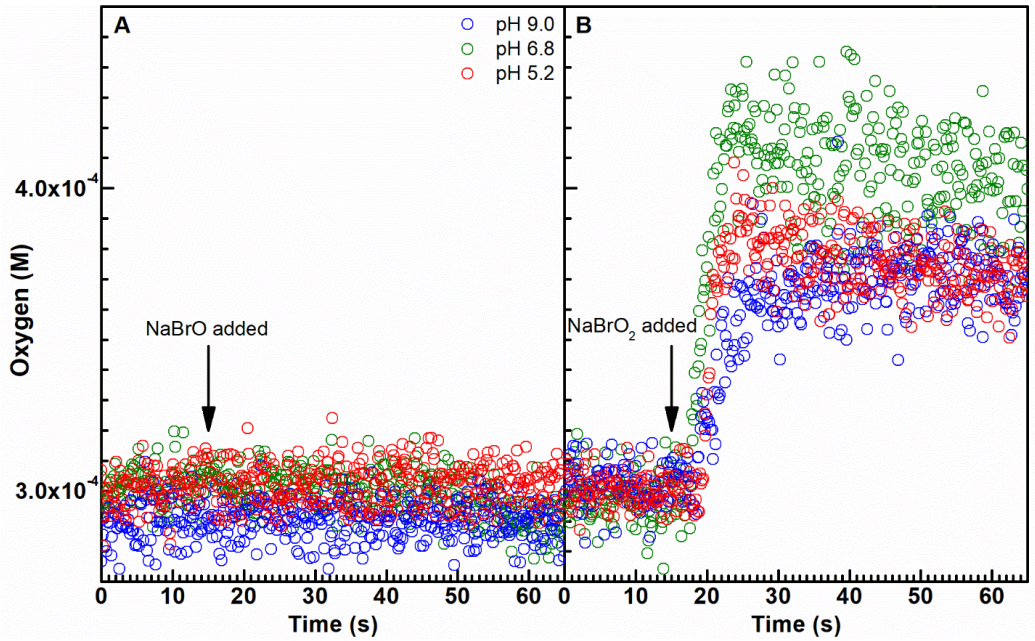

Figure E6. Cld catalytically decomposes BrO_2^- to O_2. Assay of 5 µM *Da*Cld with 100 µM NaBrO A) or 100 mM $NaBrO_2$ B) at pH 5.2 (red), 6.8 (green), and 9.0 (blue). All reactions were initiated with oxidant after ~15 seconds elapsed. No scans were averaged per point.

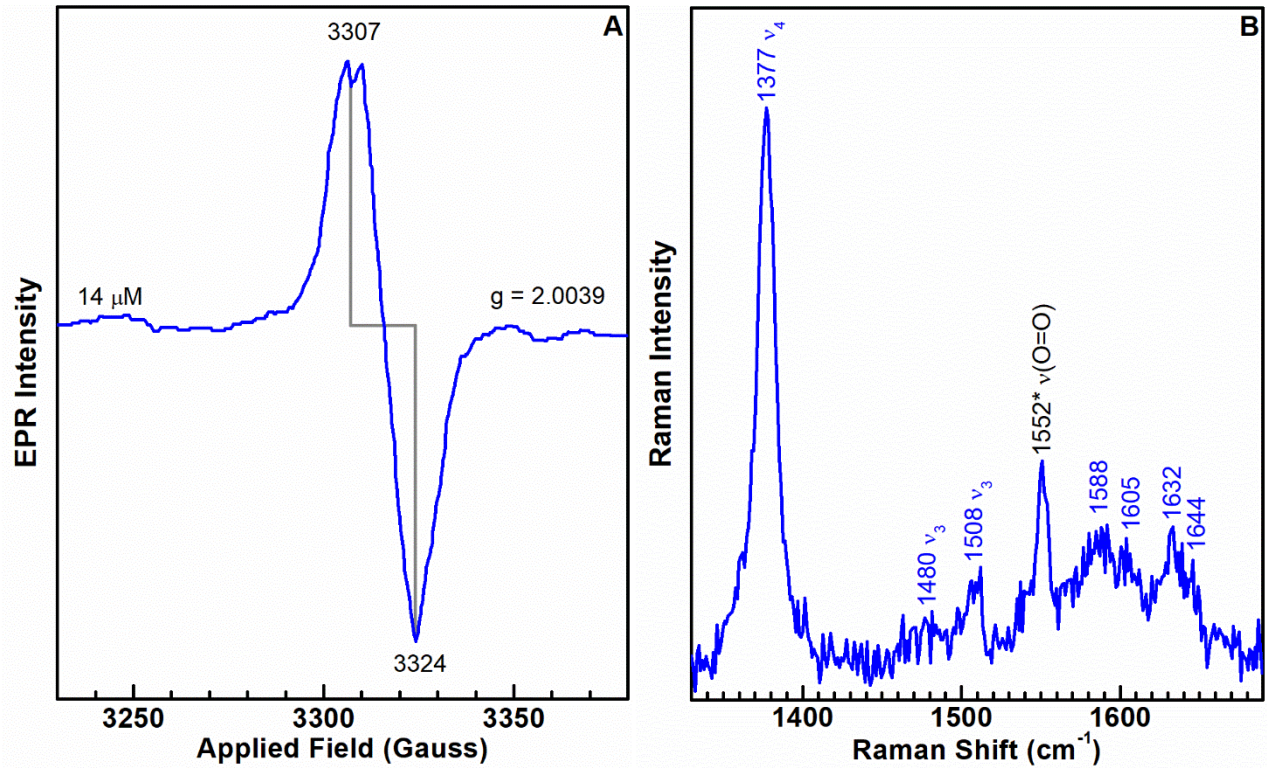

Figure E7. Freeze-quenched samples of 94 μM *Kp*Cld reacted with 1 mM $NaBrO_2$ at pH 9.0 where t_{rxn} = 1 second. A) X-band (9.300 GHz) EPR spectrum at 77 K using 0.05 mW power reveal radical signatures consistent with a protein-based radical. B) 413.1-nm excited resonance Raman spectra at 77 K using 4.4 mW power shows Cpd II. Asterisk denotes dissolved oxygen in the immersion Dewar.

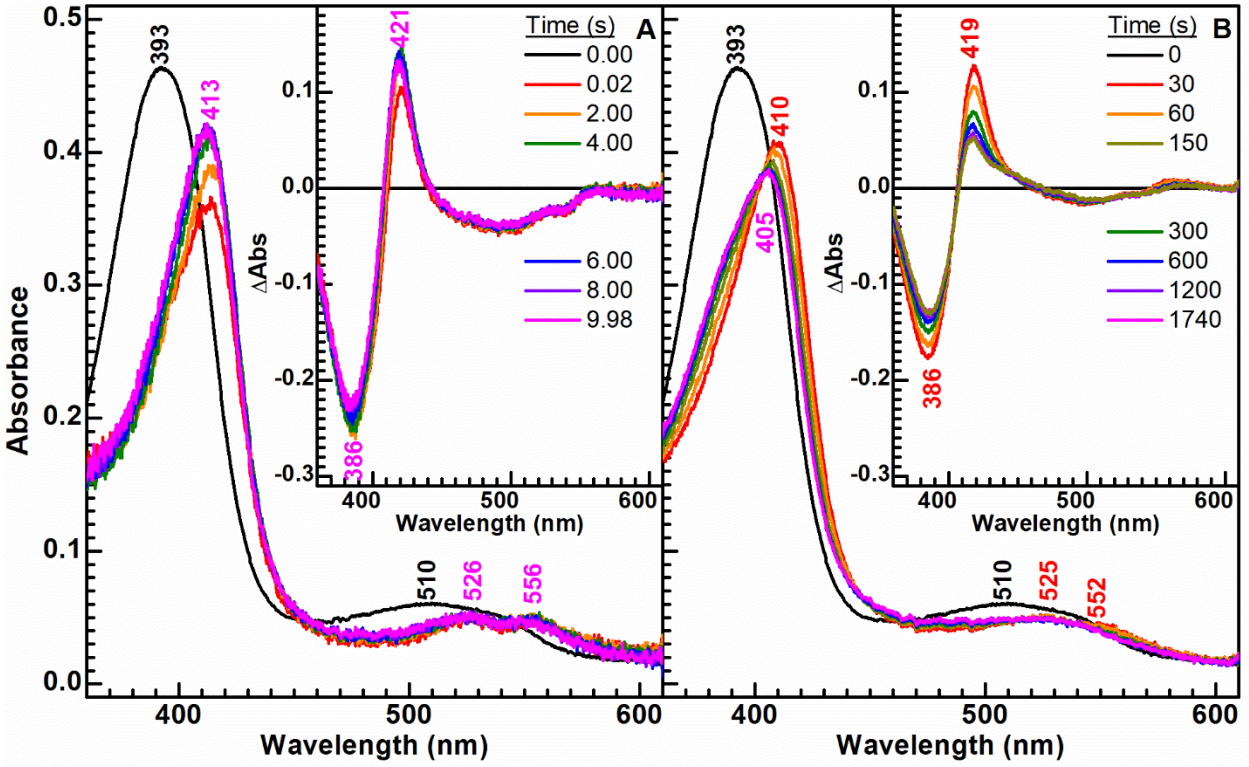

Figure E8. Stopped-flow spectra between 5 µM *Da*Cld and 100 µM $NaBrO_2$ in 0.1 M sodium phosphate pH 6.8. A) First 10 seconds of the reaction shows rapid formation of Cpd II. B) The following 29 minutes of the reaction shows decay of Cpd II to an unknown hemin species. Inset: Reacted enzyme subtracted by resting enzyme at the corresponding time points. *Fringes are due to emission lines from the Xenon arc lamp.

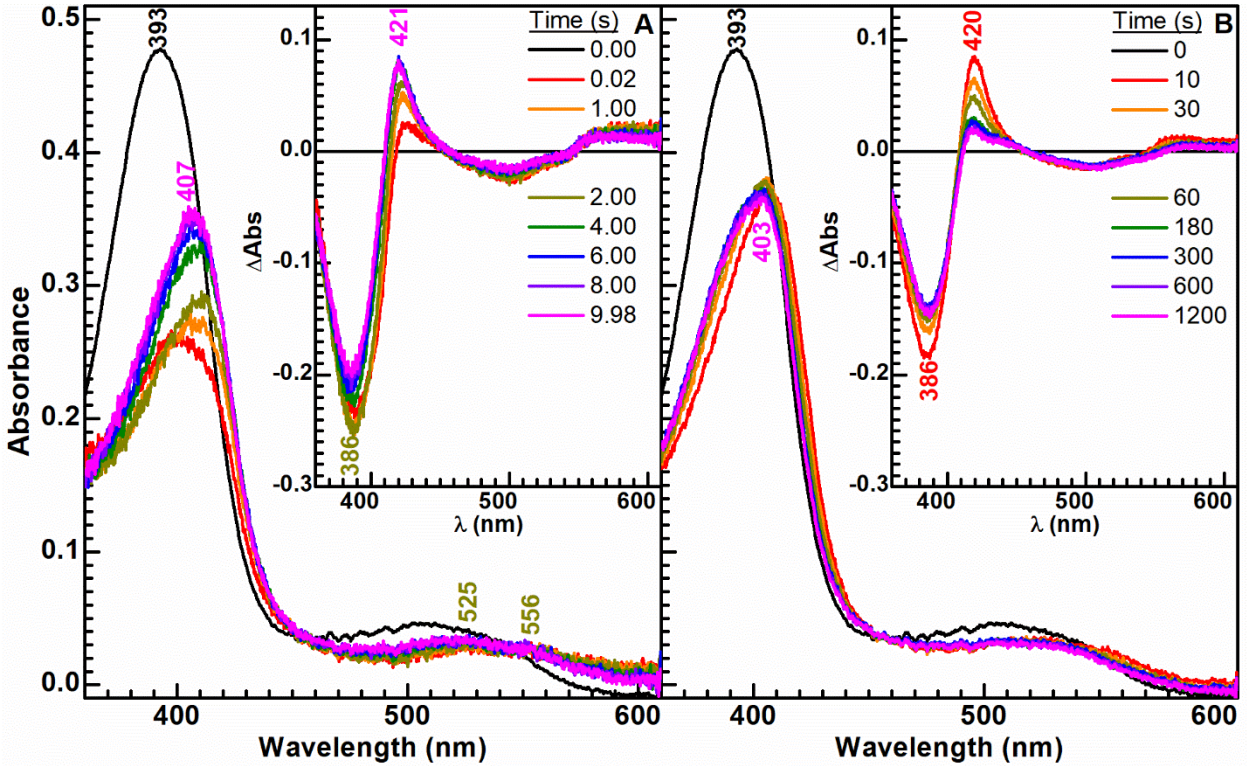

Figure E9. Stopped-flow spectra between 5 μM *Da*Cld and 100 μM $NaBrO_2$ in 0.1 M sodium phosphate pH 6.0. A) First 10 seconds of the reaction shows partial formation of Cpd I and Cpd II prior to rapidly decaying to an unknown hemin species. B) The following 20 minutes of the reaction shows complete loss of Cpd II to the unknown hemin species. Inset: Reacted enzyme subtracted by resting enzyme at the corresponding time points. *Fringes are due to emission lines from the Xenon arc lamp.

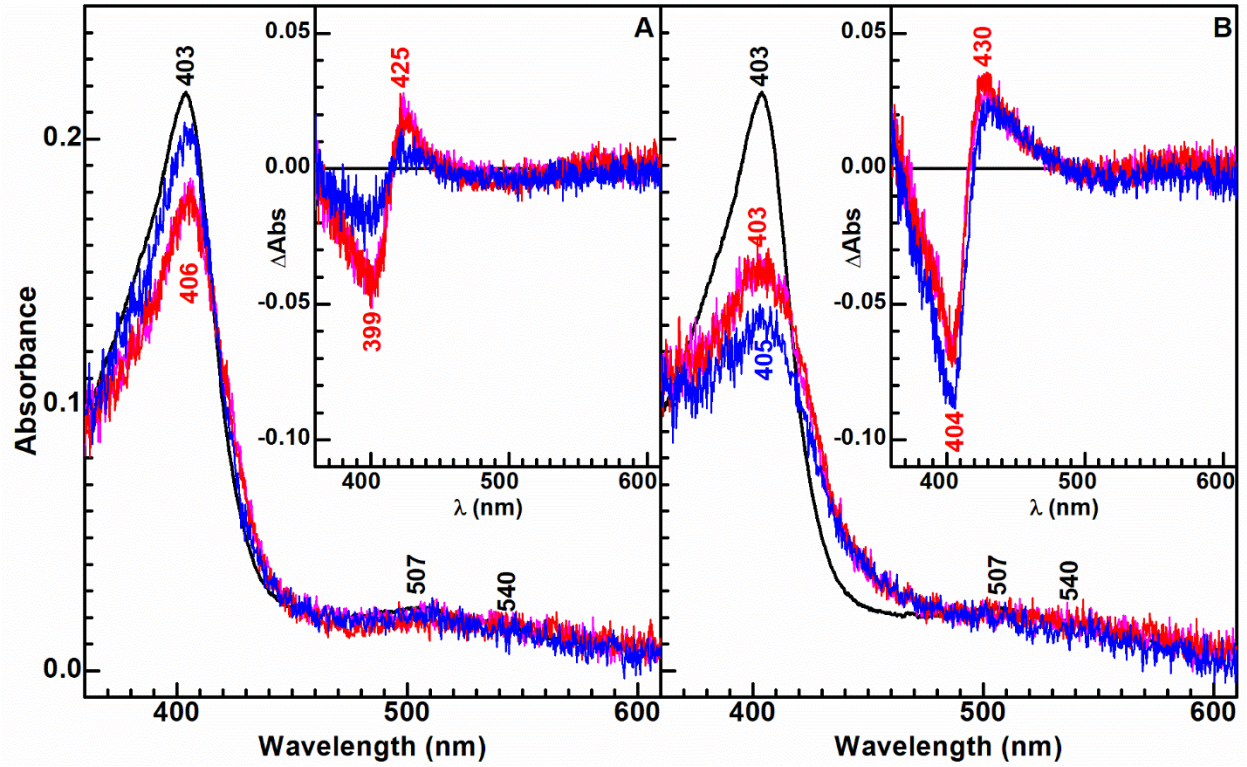

Figure E10. Stopped-flow spectra of 2 μM *Kp*Cld reacted with A) 500 μM $NaClO_2$ and B) 20 μM $NaBrO_2$ in 0.1 M sodium phosphate pH 5.2 at 20 °C at short times. Resting enzyme spectrum is shown in black, t = 0.02 s shown in magenta, t = 0.1 s shown in red, and t = 30 s shown in blue for both data sets. Inset: Reacted enzyme subtracted by resting enzyme at the aforementioned time points.

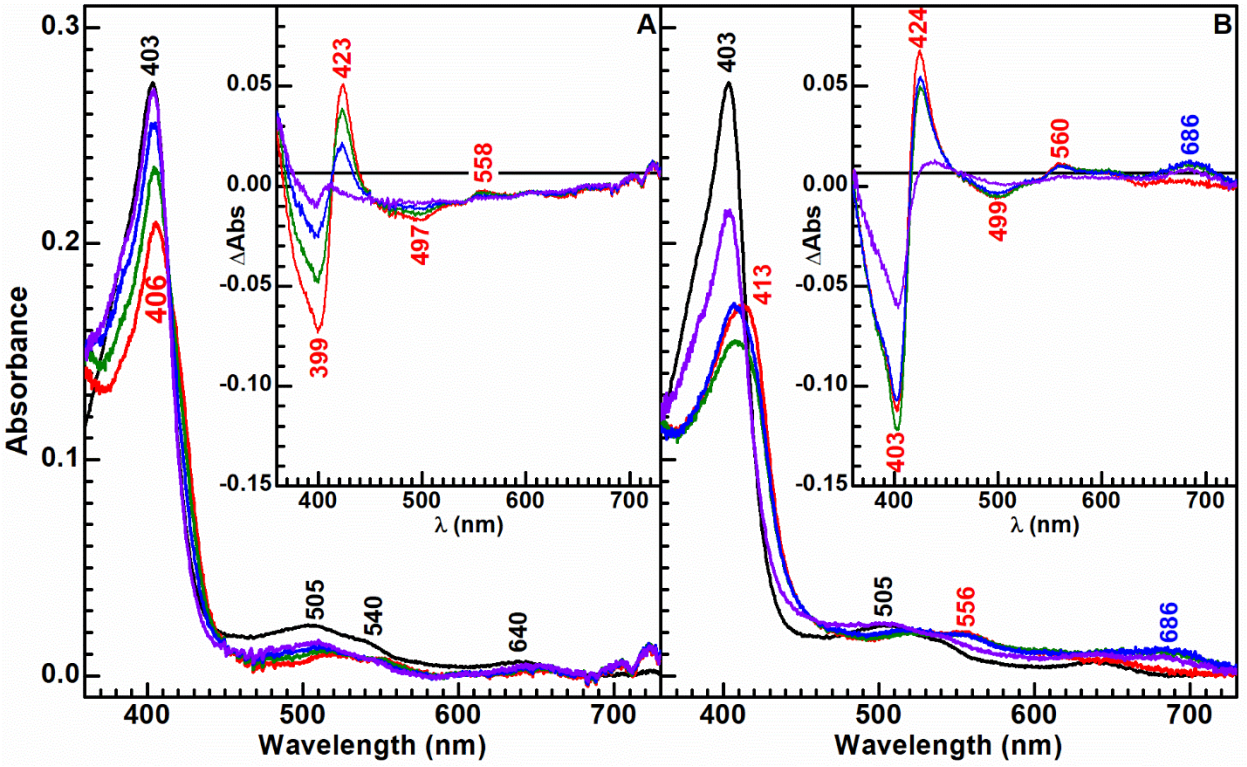

Figure E11. Stopped-flow spectra of 2 μM *Kp*Cld reacted with A) 500 μM $NaClO_2$ and B) 20 μM $NaBrO_2$ in 0.1 M sodium phosphate pH 5.2 at 20 °C at long times. Resting enzyme spectrum is shown in black, t = 0.2 s in red, t = 5 s in green, t = 20 s in blue, and t = 1200 s in violet for both data sets. Inset: Reacted enzyme subtracted by resting enzyme at the aforementioned time points. *Fringes between are due to emission lines from the Xenon arc lamp.

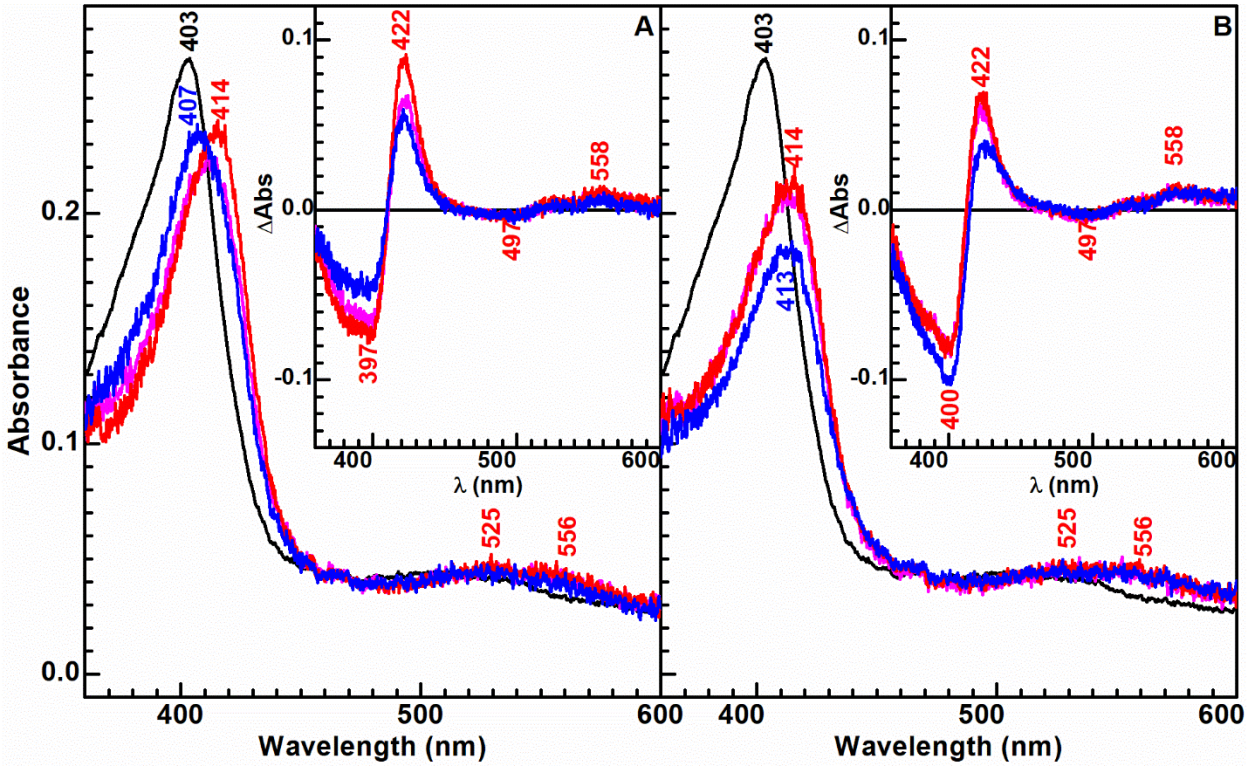

Figure E12. Stopped-flow spectra of 2 μM *Kp*Cld(Y62F) reacted with A) 500 μM $NaClO_2$ and B) 20 μM $NaBrO_2$ in 0.1 M sodium phosphate pH 6.0 at 20 °C at short times. Resting enzyme spectrum is shown in black, t = 0.02 s in magenta, t = 0.1 s in red, and t = 30 s in blue for both data sets. Inset: Reacted enzyme subtracted by resting enzyme at the aforementioned time points.

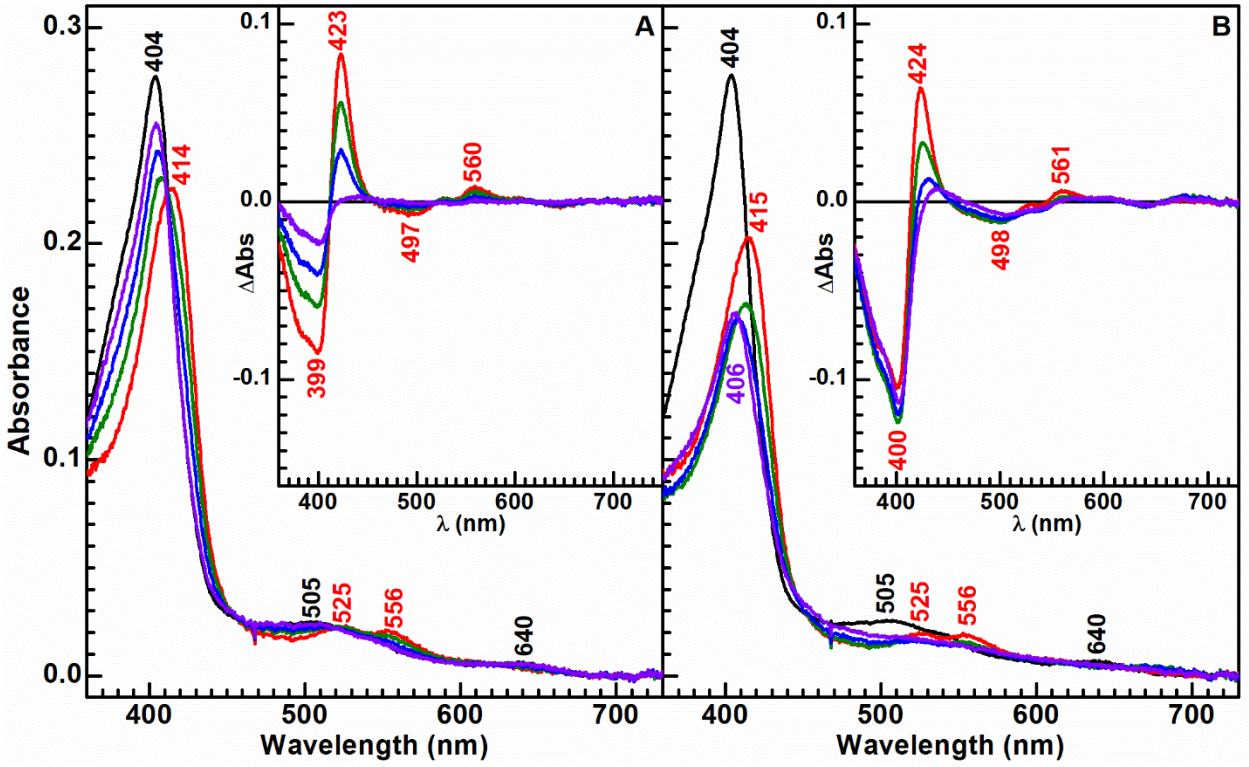

Figure E13. Stopped-flow spectra of 2 μM *Kp*Cld(Y62F) reacted with A) 500 μM $NaClO_2$ and B) 20 μM $NaBrO_2$ in 0.1 M sodium phosphate pH 6.0 at 20 °C at long times. Resting enzyme spectrum is shown in black, t = 1 s in red, t = 30 s in green, t = 150 s in blue, and t = 900 s in violet for both data sets. Inset: Reacted enzyme subtracted by resting enzyme at the aforementioned time points.

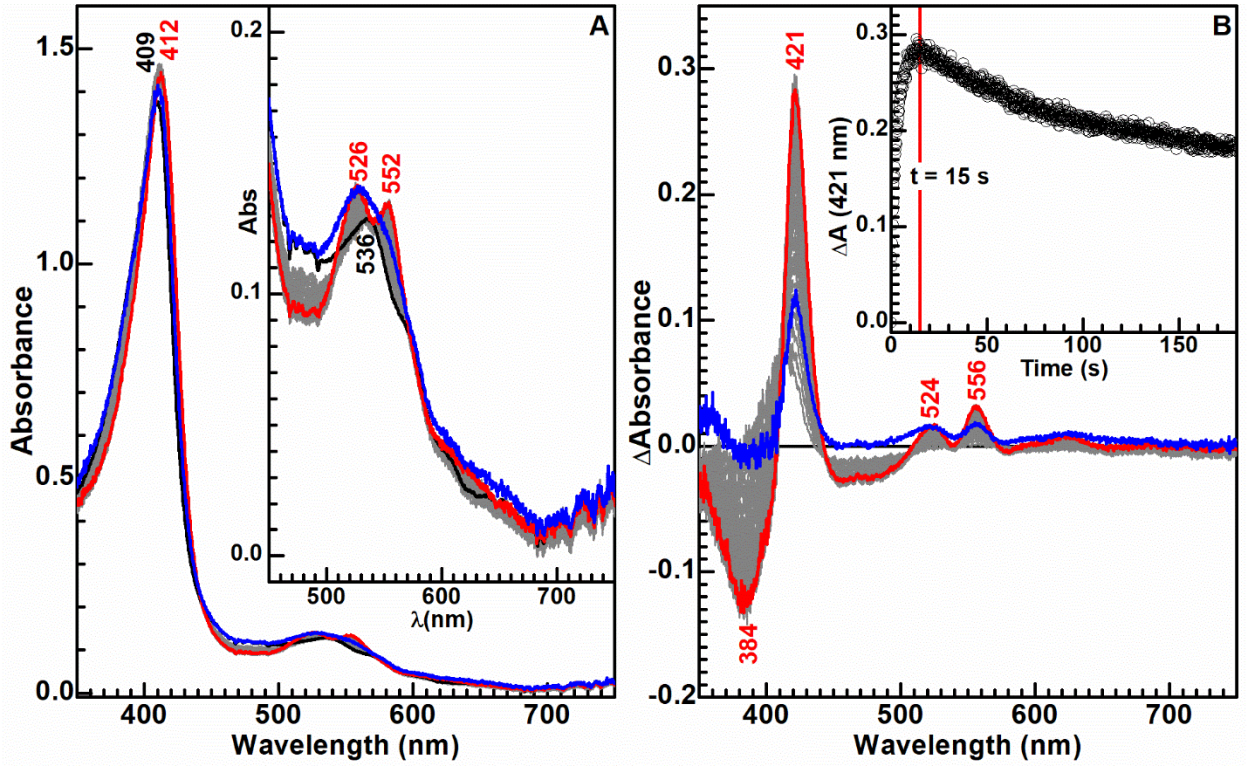

Figure E14. Reaction of 80 μM *Da*Cld and 80 μM PAA in 0.1 M glycine pH 9.0 yields Cpd II. A) Stopped-flow absorbance spectra shows resting enzyme (black) convert over to Cpd II (red) in 15 seconds while gradually decaying back to resting enzyme over the course of 10 minutes (blue).Remaining spectra (gray) correspond to time points every 0.2 seconds for the first 15 seconds. Inset: Q-band region of the time-resolved absorbance spectra. B) Time-resolved difference spectra of reacted enzyme subtracted by resting enzyme Time zero (black) reveals difference features up to 15 seconds (red) which gradually fade over the remaining time course (blue). Remaining spectra (gray) correspond to time points every 0.2 seconds for the first 15 seconds. Inset: Q-band region of the time-resolved absorbance spectra. *Fringes are due to emission lines from the Xenon arc lamp.

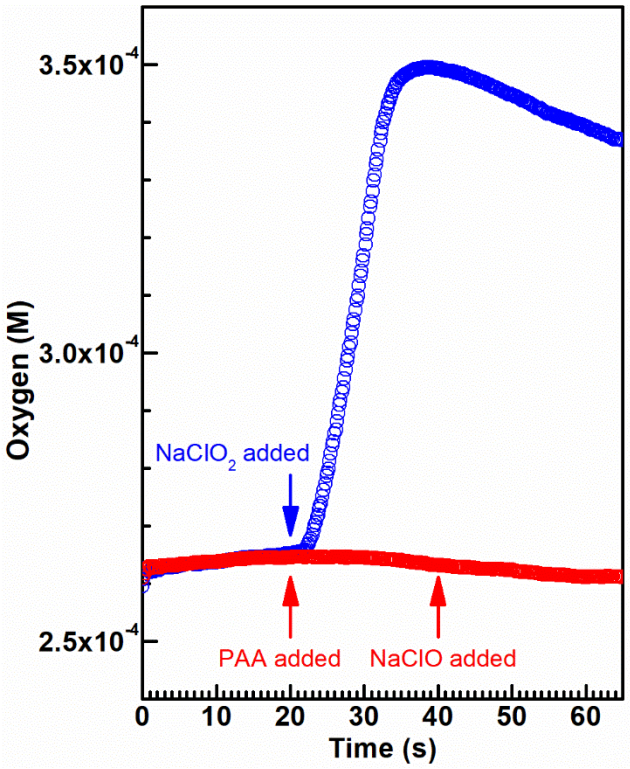

Figure E15. O_2 assay of 80 μM *Da*Cld with 80 μM $NaClO_2$ (blue) and 80 μM PAA + 80 μM NaClO (red) in 0.1 M glycine pH 9.0 at 20 C. The first oxidant was added after 20 seconds elapsed for both reactions while the second oxidant was added after 40 seconds elapsed. 100 scans were averaged per point.

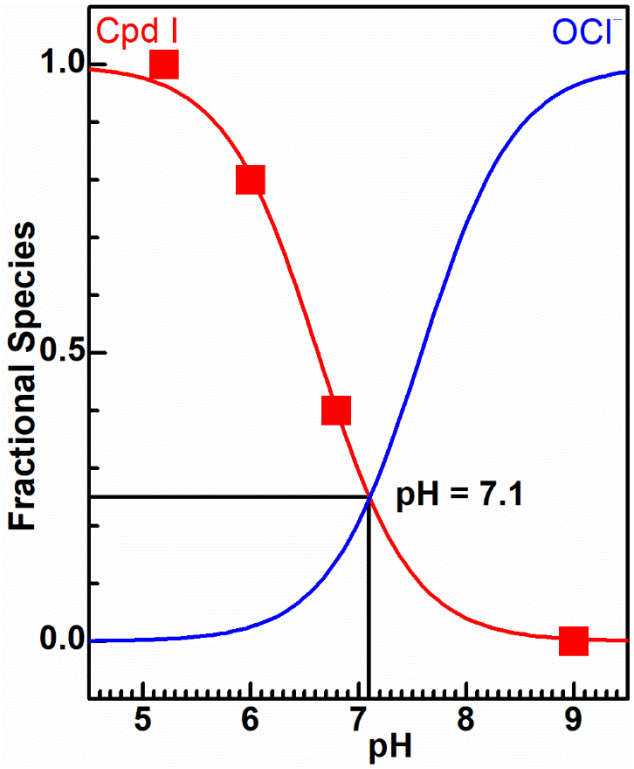

Figure E16. Fractional speciation diagram of Cpd I (red) and OCl^- (blue) as a function of pH. The fractional speciation of Cpd I was calculated based on the stopped-flow data of *Da*Cld reacted with $NaBrO_2$ and fit to a Henderson-Hasselbalch model. The respective models for Cpd I and OCl^- speciation intersect at pH 7.1 and coexist with a fractional speciation of 0.25 each.

s

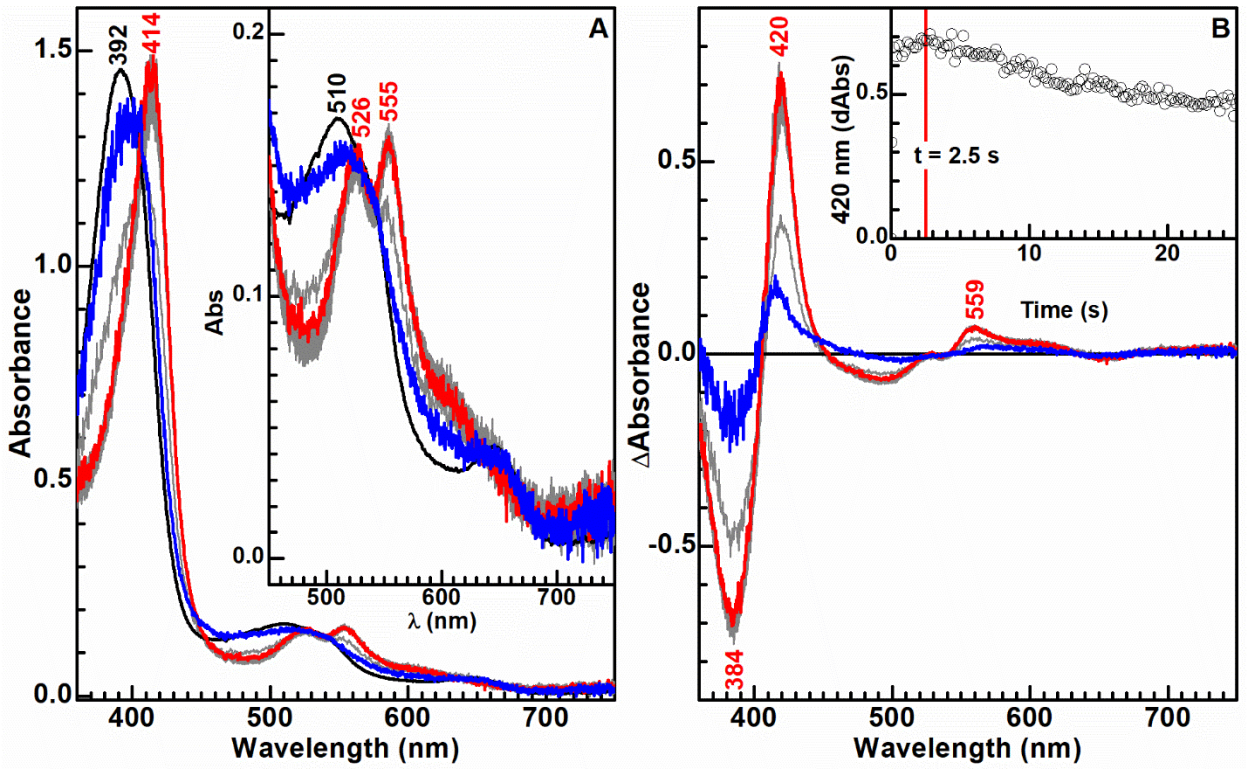

Figure E17. Stopped-flow spectra between 80 μM *Da*Cld and 160 μM PAA in 0.1 M sodium phosphate pH 7.1. A) Time-resolved absorbance spectra shows resting enzyme (black) convert over to Cpd II (red) in 2.5 seconds while gradually decaying back to resting enzyme over the course of 10 minutes (blue).Remaining spectra (gray) correspond to time points every 0.2 seconds for the first 2.5 seconds. Inset: Q-band region of the time-resolved absorbance spectra. B) Time-resolved difference spectra of reacted enzyme subtracted by resting enzyme. Time zero (black) reveals difference features up to 2.5 seconds (red) which gradually fade over the remaining time course (blue). Remaining spectra (gray) correspond to time points every 0.2 seconds for the first 2.5 seconds. Inset: Q-band region of the time-resolved absorbance spectra. *Fringes are due to emission lines from the Xenon arc lamp.